TRANSACTIONS
OF THE ASME
Series D

Journal of BASIC ENGINEERING

June 1959

Divisions: LUBRICATION • HYDRAULIC • INSTRUMENTS AND REGULATORS
METALS ENGINEERING • Research Committees: AUTOMATIC REGULATION THEORY
EFFECT OF TEMPERATURE ON THE PROPERTIES OF METALS • FLUID METERS
PREVENTION OF FRACTURE IN METALS • MECHANICAL PRESSURE ELEMENTS
LUBRICATION • PLASTIC FLOW OF METALS

Published Quarterly by
THE AMERICAN SOCIETY OF MECHANICAL ENGINEERS

TRANSACTIONS OF THE ASME
Series D

Journal of
BASIC ENGINEERING
VOLUME 81 • SERIES D • NUMBER 2
June 1959

CONTENTS

101 **Elastic and Damping Properties of Cylindrical Journal Bearings**
B. Sternlicht

109 **Axial, Relative Motion of a Circular Step Bearing**
L. Licht

118 **Friction and Wear of Metals to 1000 C**
E. P. Kingsbury and E. Rabinowicz

123 **Friction Factors for Turbulent Flow in Curved Pipes**
H. Ito

135 **Characteristics of a Self-Lubricated Stepped Thrust Pad of Infinite Width With Compressible Lubricant**
K. C. Kochi

147 **Direct Measurement of Net Positive Suction Head**
R. B. Jacobs, K. B. Martin, and R. J. Hardy

153 **Transitional Phenomena in Ultrasonic Shock Waves Emitted by Cavitation on Hydrofoils**
F. Numachi

167 **Cavitation and NPSH Requirements of Various Liquids**
Victor Salemann

181 **The Unsteady Wake Interaction in Turbomachinery and Its Effect on Cavitation**
Hsuan Yeh and J. J. Eisenhuth

190 **Thermal-Stress Ratchet Mechanism in Pressure Vessels**
D. R. Miller

197 **Refractory Metal Facings for Protection of Metal Surfaces Subjected to Repeated High-Temperature Pulses**
Aaron Cohen and Edward Homer

203 **The Failure of Structural Metals Subjected to Strain-Cycling Conditions**
R. W. Swindeman and D. A. Douglas

213 **Evaluation of Material Wear and Self-Welding in Sodium-Cooled Reactor Systems**
R. B. Jerman, R. C. Williams, and D. O. Leeser

226 **Irradiation of Haynes-25 and Inconel-X Compression Springs in High-Temperature High-Pressure Water**
R. L. Mehan

233 **Energy Losses of Balls Rolling on Plates**
R. C. Drutowski

239 **On the Effect of Lubricant Inertia in the Theory of Hydrodynamic Lubrication**
A. A. Milne

EDITORIAL DEPARTMENT

Editor, J. J. JAKLITSCH, JR.
Editor Emeritus, GEORGE A. STETSON
Consulting Editor, LEO BLODGETT
Production, JEAN NORTH
Art Editor, HENRY BALFOUR

OFFICERS OF THE ASME

President, G. B. WARREN
Secretary, O. B. SCHIER, II
Treasurer, E. J. KATES
Assistant Treasurer, H. J. BAUER

PUBLICATIONS COMMITTEE

Chairman, JOHN de S. COUTINHO
B. G. A. SKROTZKI
HENDLEY N. BLACKMON
R. D. MINDLIN
MARTIN GOLAND

Junior Representatives
A. T. WUSKA
A. S. GOLDSTEIN

REGIONAL ADVISORY BOARD

Region I, ROY L. PARSELL
Region II, GLENN R. FRYLING
Region III, F. J. HEINZE
Region IV, FRANCIS C. SMITH
Region V, H. M. CATHER
Region VI, C. R. EARLE
Region VII, M. POPOVICH
Region VIII, LINN HELANDER

Published quarterly by The American Society of Mechanical Engineers. Publication office at 20th and Northampton Streets, Easton, Pa. The editorial department is located at the headquarters of the Society, 29 West Thirty-Ninth Street, New York 18, N.Y. Cable address, "Mechaneer," New York. Price $3.00 a copy, $10.00 annually; to members, $1.50 a copy, $5.00 annually. Add 50 cents for postage to all countries outside the United States, Canada, and Pan American Union. Changes of address must be received at Society headquarters seven weeks before they are to be effective on the mailing list. Please send old as well as new address. . . . By-Law: The Society shall not be responsible for statements or opinions advanced in papers or . . . printed in its publications (B13, Par. 4). . . . Application to mail at second-class postage rates is pending at the Post Office at Easton, Pa. . . . © Copyrighted, 1959, by The American Society of Mechanical Engineers. Reprints from this publication may be made on condition that full credit be given the Transactions of the ASME, Series D — Journal of Basic Engineering, and the author, and that date of publication be stated.

TRANSACTIONS OF THE ASME
is indexed by the Engineering Index, Inc.

245 **Surface Finish and Clearance Effects on Journal-Bearing Load Capacity and Friction**
F. W. Ocvirk and G. B. DuBois

254 **Statistical Optimization of Regulators Employing a Binary Error Criterion**
J. H. Milsum

263 **An Introduction to the Time-Modulated Acceleration Switching Electrohydraulic Servomechanism**
S. A. Murtaugh, Jr.

272 **Discussion on previously published paper**
B. Sternlicht and R. C. Elwell

TRANSACTIONS OF THE ASME Series E

Journal of
APPLIED MECHANICS
Vol. 81 • Series E • No. 2

CONTENTS FOR JUNE, 1959

TECHNICAL PAPERS

161 Effect of a Nonisothermal Free Stream on Boundary-Layer Heat Transfer, E. M. Sparrow and J. L. Gregg. (58—A-42)

166 Visual Studies of the Wall Layers in the Turbulent Boundary Layer, S. J. Kline and P. W. Runstadler. (58—A-64)

171 Unsteady Laminar Boundary Layers Over an Arbitrary Cylinder, Kwang-Tzu Yang. (58—A-49)

179 On Journal Bearings of Finite Length With Variable Viscosity, L. N. Tao. (58—A-75)

184 Analysis of Complex Kinematic Chains With Influence Coefficients, J. Modrey. (58—A-74)

189 A Theory of Oil Whip, Yukio Hori. (59—APM-2)

199 On Critical Speeds of a Shaft Supported by a Ball Bearing, Toshio Yamamoto. (59—APM-12)

205 Root-Locus Analysis of Structural Coupling in Control Systems, R. H. Cannon, Jr. (58—A-65)

210 Normal Vibrations of Uniform Plate Carrying Any Number of Finite Masses, W. F. Stokey and C. F. Zorowski. (58—A-28)

217 Transients in Simple Undamped Oscillators Under Inertial Disturbances, Antongiulio Dornig. (58—A-58)

224 On Laterally Loaded Semicircular Plate With Clamped Edges, W. H. Jurney. (59—APM-3)

227 Direct Determination of Stresses in Plane Elasticity Problems, P. S. Theocaris. (58—A-43)

235 Stresses in a Stretched Slab Having a Spherical Cavity, Chih-Bing Ling. (58—A-45)

241 Influence Coefficients for Edge-Loaded Short, Thin, Conical Frustums, J. H. Baltrukonis

246 Upper and Lower Bounds for Special Eigenvalues, F. C. Appl and C. F. Zorowski. (59—APM-18)

251 Analysis of a Compression Test of a Model of a Granular Medium, C. W. Thurston and H. Deresiewicz. (58—A-48)

259 A Reassessment of Deformation Theories of Plasticity, Bernard Budiansky. (58—A-54)

265 Collapse Loads of Rings and Flanges Under Uniform Twisting Moment, Burton Paul. (58—A-55)

271 Creep of Thick-Walled Tubes Under Internal Pressure, F. P. J. Rimrott. (59—APM-6)

276 Strain-Hardening Solutions to Plate Problems, Nicholas Perrone and P. G. Hodge, Jr.

285 Determination of Creep Deflection of a Rivet in Double Shear, Joseph Marin. (58—A-47)

DESIGN DATA AND METHODS

290 The Frequency of Vibration of Rectangular Isotropic Plates, H. J. Fletcher

BRIEF NOTES

291 Large Deflections of a Clamped Elliptical Plate, W. A. Nash and I. D. Cooley. **293** Thermal Stress at Spherical Cavities, A. L. Florence and J. N. Goodier. **294** Deflection of a Thick Ring in Diametral Compression, Alexander Blake. **296** The Biot-Willis Coefficients for a Sandstone, I. Fatt. **297** Circular Plates on Elastic Foundation, G. D. Galletly. **298** Frequencies of Vibration of Stiffened Plates, R. L. Thorkildsen and W. H. Hoppmann, II. **300** Design of a π Network for Heat-Flow Analog, D. G. Stephenson and G. O. Starke. **301** Stress Distribution in a Square Tube, M. A. Sadowsky and E. E. Zwicky, Jr.

DISCUSSION

303 Discussion of previously published papers by R. H. Cannon, Jr.; C. G. Van Niekerk; M. Hetényi and P. H. McDonald, Jr.; K. A. Foss; N. J. Huffington, Jr., and W. H. Hoppmann, II; T. J. Harvey; H. Tramposch and G. Gerard; C. E. Crede; C. J. Ancker, Jr., and J. N. Goodier; H. Poritsky and F. A. Fend; K. L. Johnson; J. H. Haywood and L. B. Wilson.

317 **BOOK REVIEWS**

TRANSACTIONS OF THE ASME
Series A

Journal of
ENGINEERING FOR POWER
Volume 81 • Series A • Number 2

CONTENTS FOR APRIL, 1959

111 The Control System of a 225,000-Kw Double-Automatic Extraction Steam Turbine and Related Reducing Stations, by M. A. Eggenberger and P. G. Ipsen. (58—SA-36)
123 Design of 321-Mw Cross-Compound Steam Turbine—River Rouge Unit No. 3, by C. D. Wilson. (58—SA-22)
133 Five Years' Experience on the Consolidated Edison System With Protection of Turbine Generators and Boilers by Automatic Tripping, by W. C. Beattie, H. A. Bauman, J. M. Driscoll, P. T. Onderdonk, and R. L. Webb. (58—Pwr-8)
142 A Simplified Regenerator Theory, by W. F. Schalkwijk. (58—A-135)
151 Development of a Smooth Running, Double-Spool, Gas-Turbine Rotor System, by J. R. Schnittger. (58—A-197)
161 M-252 Alloy for Heavy-Duty Gas-Turbine Buckets, by G. R. Fusner and D. L. Newhouse. (58—A-191)
177 The Calibration of Thermocouples by Freezing-Point Baths and Empirical Equations, by R. P. Benedict. (58—A-175)
189 Theoretical Stresses Near a Circular Opening in a Flat Plate, Reinforced With a Cylindrical Outlet, by E. O. Waters. (58—A-171)
201 Effect of Steam-Turbine Reheat on Speed-Governor Performance, by Charles Concordia. (58—A-36)
208 Load Capacity Tests on Tapered-Land and Pivoted-Shoe Thrust Bearings for Large Steam-Turbine Application, by R. E. Brandon and H. C. Bahr. (58—A-172)

TRANSACTIONS OF THE ASME
Series B

Journal of
ENGINEERING FOR INDUSTRY
Volume 81 • Series B • Number 2

CONTENTS FOR MAY, 1959

95 The Strength of Thick-Walled Cylinders, by B. Crossland, S. M. Jorgensen, and J. A. Bones. (58—Pet-20)
115 Steady-State Creep Analysis of the Weight Loadings of Furnace Tubes on Multiple Supports, by J. L. Jacobowitz and C. K. Mader. (58—Pet-14)
126 How to Replace Gears by Mechanisms (Linkages), by Kurt Hain and Gerhard Marx. (58—SA-33)
131 The Effect of a Lead Additive on the Machinability of Alloy Steels, by Norman Zlatin and J. V. Gould. (58—SA-53)
139 Controlled Contact Cutting Tools, by B. T. Chao and K. J. Trigger. (58—SA-42)
152 A Study of the Effects of Tool Flank Wear on Tool Chip Interface Temperature, by D. R. Olberts. (58—SA-41)
159 Synthesis of Path-Generating Mechanisms by Means of a Programmed Digital Computer, by Ferdinand Freudenstein and G. N. Sandor. (58—A-85)
169 Synthesis of the Four-Bar Linkage to Match Prescribed Velocity Ratios, by Philip Barkan and E. J. Tuohy. (58—A-115)
178 High-Range Plasticity of Metals Beyond Normal Work-Hardening, by E. V. Crane and W. S. Wagner. (58—A-132)
183 Self-Excited Vibrations in Metal Cutting, by N. H. Cook. (58—A-189)

TRANSACTIONS OF THE ASME
Series C

Journal of
HEAT TRANSFER
Vol. 81 • Series C • No. 2

CONTENTS FOR MAY, 1959

95 Heat and Mass Transfer From a Rotating Disk, by F. Kreith, J. H. Taylor, and J. P. Chong.
106 Numerical and Machine Solutions of Transient Heat-Conduction Problems Involving Melting or Freezing, Part I, by W. D. Murray and Fred Landis. (58—HT-16)
113 A Theory of Rotating Condensation by E. M. Sparrow and J. L. Gregg. (58—A-70)
121 Laminar Heat Transfer in Rectangular Channels, by L. S. Han. (58—A-124)
129 Heat Transfer to Water in Thin Rectangular Channels, by S. Levy, R. A. Fuller, and R. O. Niemi. (58—A-127)
144 Combined Geometric and Network Analog Computer for Transient Heat Flow, by Victor Paschkis. (58—A-69)
151 Heat Transfer From an Annular Fin of Constant Thickness, by H. H. Keller and E. V. Somers. (58—A-116)
157 A Variational Method for Fully Developed Laminar Heat Transfer in Ducts, by E. M. Sparrow and R. Siegel. (58—A-92)
168 The Effect of Surface Roughness on the Convection Heat-Transfer Coefficient for Fully Developed Turbulent Flow in Ducts With Uniform Heat Flux, by R. T. Lancet. (58—A-122)

B. STERNLICHT

General Engineering Laboratory,
General Electric Company,
Schenectady, N. Y.
Assoc. Mem. ASME

Elastic and Damping Properties of Cylindrical Journal Bearings

Introduction

The knowledge of hydrodynamic damping and elastic properties of journal bearings is desirable for the accurate determination of the critical speed of a shaft and for the anticipation of its behavior in the neighborhood of such speeds. It is also required for judging the stability of the rotating shaft against self-excited vibrations [1, 2, 3].[1]

The equations that describe the motion of the journal center may be given by the differential equation

$$\left.\begin{aligned} M\ddot{x} + B_{xx}\dot{x} + B_{xy}\dot{y} + K_{xx}x + K_{xy}y &= G\cos(\omega t + \phi) \\ M\ddot{y} + B_{yx}\dot{x} + B_{yy}\dot{y} + K_{yx}x + K_{yy}y &= G\sin(\omega t + \phi) \end{aligned}\right\} \quad (1)$$

The stiffness and dissipation functions in this equation are dependent on Sommerfeld numbers and therefore, in turn, on the eccentricity ratio. This paper gives values for these parameters as functions of eccentricity ratio. These parameters are determined from the solution of Reynolds two-dimensional equation with squeeze-film considerations included.

The paper is divided into four parts: (1) Derivation of the equations; (2) consideration of special cases; (3) solution with arbitrary direction for the squeeze-film velocity; (4) conclusions and recommendations.

Derivation of Equations

Reynolds equation for two-dimensional flow with squeeze-film effect is the starting point for the analysis of the journal bearing. It is written in the following form for the configuration in Fig. 1:

$$\frac{\partial}{\partial x'}\left(\frac{h'^3}{\mu'}\right)\frac{\partial P'}{\partial x'} + \frac{\partial}{\partial z'}\left(\frac{h'^3}{\mu'}\frac{\partial P'}{\partial z'}\right) = 6U'\frac{\partial h'}{\partial x'} - 12\,V' \quad (2)$$

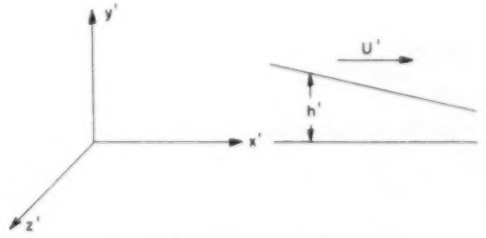

Fig. 1 Co-ordinate axes of bearing

[1] Numbers in brackets designate References at end of paper.

Contributed by the Lubrication Division of THE AMERICAN SOCIETY OF MECHANICAL ENGINEERS and presented at the ASLE-ASME Lubrication Conference, Los Angeles, Calif., October 13-15, 1958.

NOTE: Statements and opinions advanced in papers are to be understood as individual expressions of their authors and not those of the Society. Manuscript received at ASME Headquarters, July 11, 1958. Paper No. 58—Lub-3.

Nomenclature

a = coefficients
B = dissipation function, lb sec/in.
C = diametral clearance, in.
C_V = specific heat at constant volume, in²/sec² deg F
D = diameter of bearing, in.
e = eccentricity, in.
F = dimensionless force
G = rotating force
h = film thickness, in.
K = stiffness function, lb/in.
L = axial length of bearing, in.
M = mass of rotor apportioned to the bearing, lb sec²/in.
n = eccentricity ratio
N = rps
P = pressure, psi
t = time, sec
T = temperature, deg F
U = relative velocity between journal and bearing, in/sec
V = "squeeze-film" velocity, in/sec
x, y, z = rectangular co-ordinates of a point
α = attitude angle, deg
β = angle between journal locus and the line of center, deg
Δ = increment
θ = angle, deg
ϕ = angle between the rotating force and line of center, deg
μ = viscosity, lb sec/in.²
ω = angular velocity, radians/sec

Subscripts

i = index defining the value z in the journal bearing mesh running from 1 to n
j = index defining the value x or θ in the journal bearing mesh running from 1 to m
av = average
H = horizontal
R = radial
T = tangential
V = vertical

Superscripts

$'$ = dimensional
k = iteration number
$\cdot$ = first derivative
$y'y'$ = axis along the displacement
$x'x'$ = axis perpendicular to the displacement
$\cdot\cdot$ = second derivative

Conversions

$$F = \frac{F'}{L'D'\mu_{av}'N'\left(\frac{D'}{C'}\right)^2}$$

$$K = \frac{F'}{2e'L'\mu_{av}'N'\left(\frac{D'}{C'}\right)^2}$$

$$K' = \frac{F'}{e'} = 2KL'\mu_{av}'N'\left(\frac{D'}{C'}\right)^2, \text{ lb/in.}$$

$$B = \frac{F'}{V'L'\mu_{av}'\left(\frac{D'}{C'}\right)^2}$$

$$B' = \frac{F'}{V'} = BL'\mu_{av}'\left(\frac{D'}{C'}\right)^2, \text{ lb sec/in.}$$

Neglecting the effect of curvature, it is possible to analyze a cylindrical bearing using the configuration of Fig. 1. The circumferential co-ordinate is x' and the width co-ordinate is z' for a journal bearing. The film thickness in the bearing with a certain eccentricity e can be calculated approximately from the following equation (see Fig. 2):

$$h' = \frac{C'}{2} + e' \cos(\theta - \alpha) \tag{3}$$

In order to write Reynolds' equation in dimensionless form, the following dimensionless quantities are defined:

$$\left.\begin{aligned}
x &= \frac{1}{2}\theta = \frac{x'}{D'} \\
z &= \frac{z'}{L'} \\
h &= \frac{h'}{C'} \\
\mu &= \frac{\mu'}{\mu_{av}'} \\
P &= \frac{P'}{\mu_{av}' N'} \left(\frac{C'}{D'}\right)^2 \\
n &= \frac{2e'}{C'} \\
U' &= \pi D' N' \\
V' &= -V_R' \cos(\theta - \alpha) + V_T' \cos(\theta - \alpha - 90°) \\
-\frac{12V'}{C'N'} &= \frac{12V_R'}{C'N'} \cos(\theta - \alpha) - \frac{12V_T'}{C'N'} \cos(\theta - \alpha - 90°)
\end{aligned}\right\} \tag{4}$$

Substituting (4) into Equation (2) the following dimensionless form is obtained for Reynolds' equation:

$$\frac{\partial}{\partial x}\left(\frac{h^3}{\mu}\frac{\partial P}{\partial x}\right) + \left(\frac{D'}{L'}\right)^2 \frac{\partial}{\partial z}\left(\frac{h^3}{\mu}\frac{\partial P}{\partial z}\right) = 6\pi \frac{\partial h}{\partial x} - \frac{12}{C'N'} V' \tag{5}$$

Substituting Equation (4) in Equation (3) we obtain

$$h = \frac{1}{2} + \frac{1}{2} n \cos(\theta - \alpha) \tag{6}$$

In order to solve this expression, the method of finite differences will be used. Thus any pressure $P_{i,j}$ in the field may be represented by Equation (7).

$$P_{i,j} = \frac{18.84\left(\frac{h_{i,j-1/2} - h_{i,j+1/2}}{\Delta x}\right) + \frac{12V'}{C'N'_{i,j}} + \left(\frac{D'}{L'}\right)^2 \left[\frac{h^3}{\mu}\Big|_{i+1/2,j} \frac{P_{i+1,j}}{\Delta z^2} + \frac{h^3}{\mu}\Big|_{i-1/2,j} \frac{P_{i-1,j}}{\Delta z^2}\right] + \frac{h^3}{\mu}\Big|_{i,j+1/2} \frac{P_{i,j+1}}{\Delta x^2} + \frac{h^3}{\mu}\Big|_{i,j-1/2} \frac{P_{i,j-1}}{\Delta x^2}}{\left(\frac{D'}{L'}\right)^2 \left[\frac{h^3}{\mu}\Big|_{i+1/2,j} \frac{1}{\Delta z^2} + \frac{h^3}{\mu}\Big|_{i-1/2,j} \frac{1}{\Delta z^2}\right] + \frac{h^3}{\mu}\Big|_{i,j+1/2} \frac{1}{\Delta x^2} + \frac{h^3}{\mu}\Big|_{i,j-1/2} \frac{1}{\Delta x^2}} \tag{7}$$

Equation (7) is of the form:

$$P_{i,j} = a_0 + a_1 P_{i+1,j} + a_2 P_{i-1,j} + a_3 P_{i,j+1} + a_4 P_{i,j-1} \tag{8}$$

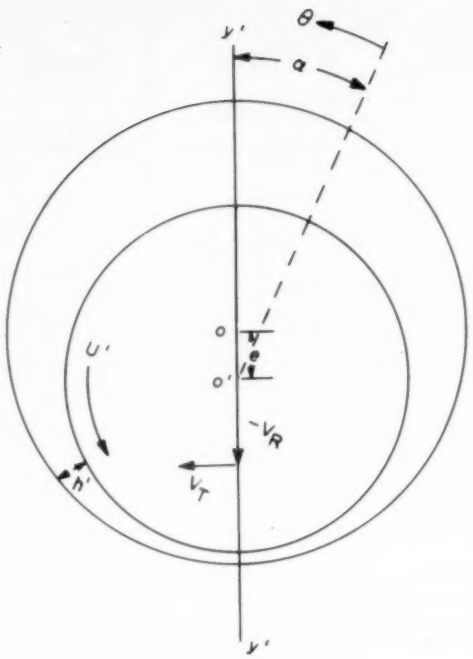

Fig. 2 Bearing nomenclature

Once the size of the field has been selected, it is but a matter of solving Equation (8) for each point in the field; this is done by an iterative process. In this analysis the field size was chosen to be 18×18. Note that in Equation (7) both the film thickness and fluid viscosity must be known at intermediate points. The film thickness at every point can be solved from Equation (6). In order to calculate the viscosity, the energy equation must be solved for temperature at every point from which the viscosity at every point can be computed [4]. In this analysis isothermal conditions are assumed; thus average viscosity is considered throughout the fluid film. It is further assumed that no negative pressures can exist at any point in the film. Therefore any pressures below zero are assigned a value of zero.

With the dimensionless pressure computed throughout the fluid, it is next possible to calculate the dimensionless components of force in both vertical and horizontal direction for the specific value of L'/D', α, n, and $\frac{12V'}{C'N'}$. This is done using the following two equations:

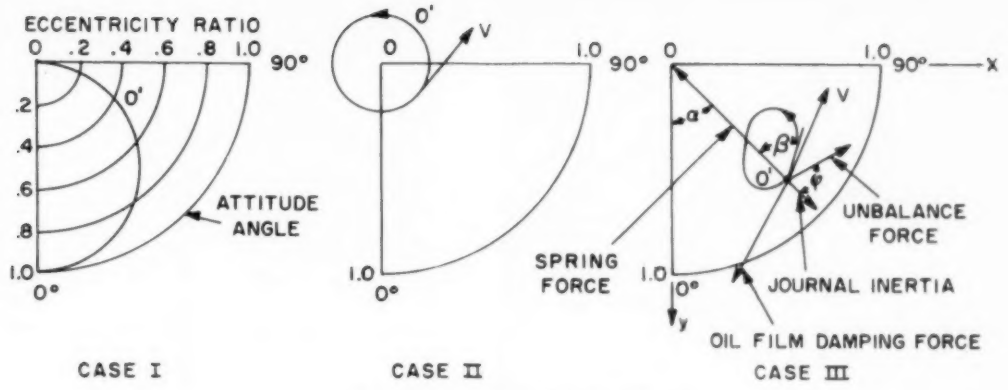

Fig. 3 Three cases representing journal locus

$$F_V = -\sum_{j=1}^{m}\sum_{i=1}^{n} P_{i,j}{}^{k} \cos\theta_{i,j}\,\Delta x\,\Delta z \tag{9}$$

$$F_H = \sum_{j=1}^{m}\sum_{i=1}^{n} P_{i,j}{}^{k} \sin\theta_{i,j}\,\Delta x\,\Delta z \tag{10}$$

The total force is equal to the sum of the horizontal and vertical component.

$$F = \sqrt{F_V{}^2 + F_H{}^2}, \qquad \alpha = \tan^{-1}\frac{F_H}{F_V} \tag{11}$$

Considerations of Special Cases

For a system without a driving force such as unbalance, the right-hand sides of Equations (1) are equal to zero and the squeeze film velocity $\left(\frac{12V'}{C'N'}\right)$ in the Reynolds equation is equal to zero. Under this condition the journal will follow a steady-state locus as represented by case I of Fig. 3.

For vertical shaft machines with plain cylindrical journal bearings the same reactive hydrodynamic force acts in all directions; thus the stiffness in all directions is equal. In the absence of unbalance force the shaft center will coincide with the bearing center. With unbalance force present, the journal center will follow a circular path as illustrated by case II of Fig. 3.

Case III in Fig. 3 represents a locus of journal center in which the stiffness and dissipation along the x and y-axis are not equal. This is present in journal bearings which have no symmetry in the quadrants described by two mutually perpendicular axes (e.g., elliptical bearings, three lobe bearing, etc.) or for a journal bearing which, in the presence of gravity load and driving force, operates with a locus which is not symmetrical about the bearing center.

Equation (1) is general and applies to all the cases described. If we consider this equation as applied to bearings then we see that all the constants can be determined purely from hydrodynamic considerations. Consider a small angular displacement of the journal $d\alpha$ from some position of equilibrium e and α. From the geometry of the fluid film, it is assumed that the resultant film force acting on the journal will not change appreciably in magnitude, but will change its direction by the angle of the displacement. Therefore the hydrodynamic forces F_x and F_y on the journal for small displacement (x, y) are [5]

$$\left.\begin{aligned} F_x = \frac{F'O}{e} &= F[x(\sin\alpha\tan\beta + \cos\alpha) \\ &\quad - y(\sin\alpha - \cos\alpha\tan\beta)] \end{aligned}\right\} \tag{12}$$

$$\left.\begin{aligned} F_y = \frac{\partial F}{\partial e}\Delta e = \frac{\partial F}{\partial e}(x\sin\alpha + y\cos\alpha) \end{aligned}\right\} \begin{matrix}(12)\\(cont.)\end{matrix}$$

Knowing these forces, the displacement and the velocity, the stiffness and dissipation can be computed:

$$\left.\begin{aligned} K_{xx} &= \frac{F}{e}(\sin\alpha\tan\beta + \cos\alpha) \\ K_{xy} &= -\frac{F}{e}(\sin\alpha - \cos\alpha\tan\beta) \qquad \text{(cross coupling term)} \\ K_{yx} &= \frac{\partial F}{\partial e}\sin\alpha = \frac{\partial F_T}{\partial e} \qquad \text{(cross coupling term)} \\ K_{yy} &= \frac{\partial F}{\partial e}\cos\alpha = \frac{\partial F_R}{\partial e} \\ B_{xx} &= B_{y'y'}\sin^2\alpha + F_{x'x'}\cos^2\alpha \\ B_{yy} &= B_{y'y'}\cos^2\alpha + B_{x'x'}\sin^2\alpha \\ B_{xy} &\text{ and } B_{yx} \text{ are small in comparison to } B_{xx} \text{ and } B_{yy} \\ &\text{and therefore may be neglected.} \end{aligned}\right\} \tag{13}$$

One of the dynamic operations investigated, and which is discussed in this paper, produced a purely radial journal displacement. For this case the squeeze film velocity acts along a radial line and its magnitude is varying. The analysis indicates that with a purely radial velocity a maximum damping force results. A further discussion of this point will follow.

Using the nomenclature represented in Fig. 4, results of vertical and horizontal components of force as functions of eccentricity ratio and radial velocity are given in Table 1 for three L'/D' ratios. These results were obtained from solution of Equation (5). Fig. 5 shows results for $L'/D' = 1$.

The values along the ordinate for zero radial velocity are the general steady-state solutions to Reynolds' equation without squeeze-film velocity (case I, Fig. 3.) Note that with a radial velocity present and acting in the direction which tends to decrease the minimum film thickness, the vertical and horizontal components of force increase. This increase in force is proportional to velocity and it acts in a direction tending to damp out the oscillations; it is the damping force. Fig. 6 shows the loci of the force vector as a function of eccentricity ratio and of different radial velocities under counterclockwise journal rotation. We note that as the radial velocity increases in the negative sense the angle α between the hydrodynamic force and the displacement tends to decrease. The reverse is true for increasing positive values of the radial velocity.

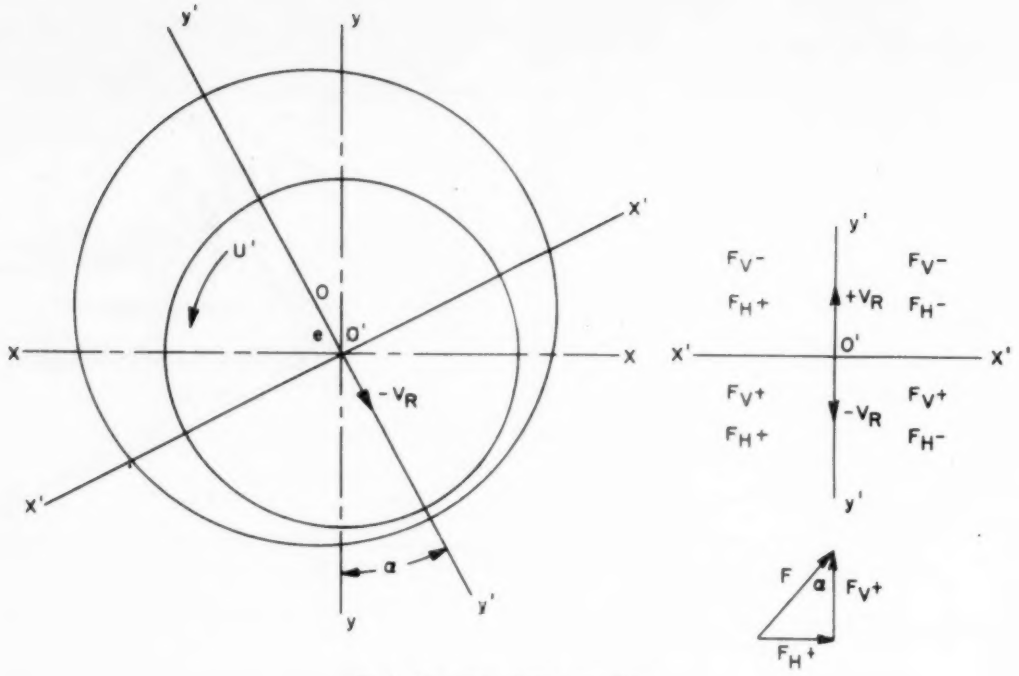

Fig. 4 Force and velocity nomenclature

Table 1

		$L'/D' = 0.5$				$L'/D' = 1.0$				$L'/D' = 1.5$			
n	V_R/CN	F_V	F_H	F	α	F_V	F_H	F	α	F_V	F_H	F	α
0.1	−6.0	11.2	9.2	14.5	140.4	33.2	31.5	45.9	136.8	64.9	56.5	86.0	138.9
	−4.0	7.4	6.4	9.8	139.1	23.9	21.4	32.1	138.2	43.0	38.0	57.4	138.5
	−2.0	3.6	3.4	4.9	137.0	11.7	10.9	16.0	137.0	20.0	20.5	28.6	134.3
	−1.0	1.4	1.6	2.2	130.3	4.5	4.9	6.7	132.6	8.4	10.8	13.7	127.9
	0	0	0.2	0.2	98.3	0.1	0.7	0.7	100.1	0.3	1.3	1.3	102.4
0.3	−6.0	20.3	13.0	24.1	147.4	62.0	40.0	73.8	147.2	104.0	72.0	126.5	145.3
	−4.0	13.5	9.0	16.2	146.3	41.2	27.5	49.5	146.3	68.5	48.5	83.9	144.7
	−2.0	7.2	5.0	8.8	145.4	19.5	15.0	24.6	142.4	34.0	26.0	42.8	142.6
	−1.0	3.6	2.8	4.6	142.0	7.8	7.8	11.0	135.2	17.5	15.3	23.2	138.8
	0	0.3	0.8	0.8	111.8	1.0	2.4	2.54	111.9	1.6	4.0	4.3	112.1
	0.6	−0.3	−0.1	0.3	342.3	−0.6	−0.4	0.8	330.5	−1.0	−0.5	1.1	331.5
	2.0	−1.0	−1.7	2.0	300.8	−2.0	−4.3	4.8	295.5	−3.2	−8.5	9.1	290.6
	4.0	−2.0	−4.2	4.6	295.5	−4.4	−12.8	13.5	288.8	−6.0	−21.0	21.8	286.0
	18.0	−8.7	−20.5	22.3	293.0	−19.6	−65.0	67.9	286.8	−26.0	−105.0	108.2	283.9
0.5	−6.0	45.0	19.6	49.1	156.5	123.0	56.0	135.3	155.5	182.0	91.5	203.7	153.3
	−4.0	30.0	13.8	33.0	155.3	80.0	39.5	89.2	153.7	122.0	63.5	137.5	152.5
	−2.0	15.6	7.8	17.4	153.6	39.0	21.8	44.7	150.8	62.5	35.0	71.6	150.7
	−1.0	8.1	4.7	9.4	149.9	17.3	11.9	21.0	145.5	31.8	22.0	38.7	145.3
	0	1.1	1.6	1.9	125.6	3.2	4.7	5.7	123.8	4.8	7.4	8.8	122.8
	0.6	−0.2	0.2	0.3	35.6	−0.6	0.6	0.8	47.5	−0.7	0.8	48.3	48.0
	2.0	−0.8	−1.2	1.4	303.2	−1.5	−2.3	2.7	303.0	−2.2	−6.0	6.4	289.7
	4.0	−1.4	−2.2	2.6	301.2	−2.8	−10.6	11.0	284.8	−3.6	−17.0	17.4	282.0
	18.0	−4.8	−19.2	19.8	284.0	−10.3	−58.5	59.4	280.0	−13.7	−95.0	96.0	278.2
0.7	−6.0	136.0	36.5	140.7	165.0	290.0	87.0	302.8	163.3	420.0	125.0	438.2	163.4
	−4.0	92.5	26.0	96.1	164.3	205.0	62.5	214.2	163.0	278.0	90.0	292.2	162.1
	−2.0	45.0	15.0	47.4	161.6	98.0	36.5	104.4	159.6	139.0	53.5	149.0	159.0
	−1.0	19.5	9.6	21.7	153.8	42.5	21.0	47.4	153.7	67.5	32.0	74.7	154.6
	0	4.1	3.5	5.4	139.7	9.6	8.8	13.0	137.5	13.1	13.0	18.5	135.5
0.8	−6.0	332.0	58.0	337.6	170.1	650.0	124.0	661.8	169.2	780.0	165.0	797.5	168.0
	−4.0	220.0	42.0	224.0	169.2	425.0	88.0	433.6	168.3	520.0	118.0	532.9	167.2
	−2.0	113.0	25.0	115.8	167.5	215.0	52.5	221.4	166.3	265.0	71.0	274.4	165.0
	−1.0	56.5	16.0	58.7	163.5	112.0	34.3	116.6	163.0	133.0	46.5	140.7	160.8
	0	8.8	5.8	10.5	146.5	18.3	13.1	22.5	144.4	23.6	18.0	29.7	142.7
	0.6	0.1	0.9	0.9	96.3	0.2	2.4	2.4	93.0	0.3	3.5	3.5	94.2
	2.0	−0.5	−0.6	0.7	309.2	−1.1	−1.3	1.7	309.6	−1.5	−2.5	2.9	301.0
	4.0	−0.8	−2.4	2.6	288.7	−2.0	−7.2	7.5	285.4	−2.5	−11.2	11.5	282.5
	18.0	−0.6	−18.6	18.6	271.8	−0.4	−54.5	54.5	270.5	−0.1	−84.0	84.0	270.0

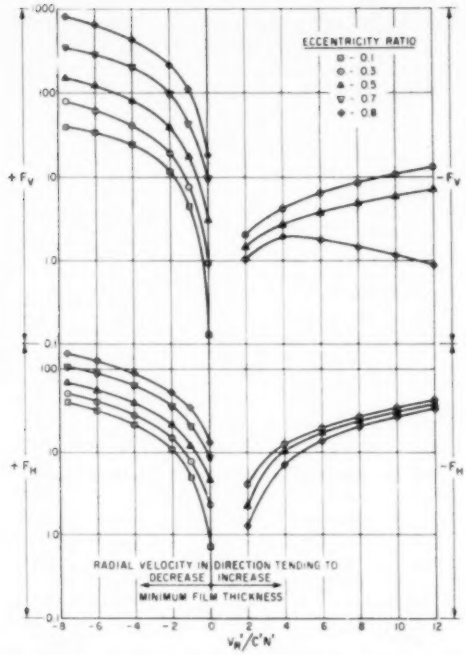

Fig. 5 Dimensionless component of force as a function of dimensionless radial velocity

The values of stiffness and dissipation functions are obtained next. It becomes convenient to evaluate these parameters along the $x'x'$ and $y'y'$-axes.

Thus:

$$\left.\begin{aligned} K_{y'y'} &= \frac{\partial F}{\partial e}\cos\alpha + \frac{F}{e}\sin\alpha\tan\beta \\ K_{y'x'} &= \frac{F}{e}\sin\alpha \\ K_{x'x'} &= \frac{F}{e}\cos\alpha \\ K_{x'y'} &= \frac{F}{e}\cos\alpha\tan\beta - \frac{\partial F}{\partial e}\sin\alpha \end{aligned}\right\} \quad (14)$$

For the dynamic case under consideration $\beta = 0$ and the displacement is only along the $y'y'$-axis. Therefore the only stiffnesses of interest are:

$$\left.\begin{aligned} K_{y'y'} &= \frac{\partial F}{\partial e}\cos\alpha = \frac{\partial F_R}{\partial e} \\ K_{x'y'} &= -\frac{\partial F}{\partial e}\sin\alpha = -\frac{\partial F_T}{\partial e} \end{aligned}\right\} \quad (15)$$

These parameters are plotted versus eccentricity ratio in Figs. 7 and 8.

Since the velocity is along the $y'y'$-axis and since $B_{x'y'}$ is small in comparison to $B_{y'y'}$ only one dissipation function is of interest and it is the $B_{y'y'}$ which is represented by Fig. 9.

The upper branch of the curve is radial velocity in the direction tending to decrease the minimum film thickness. The lower branch is for the reverse condition.

Three types of problems can be analyzed using Equation (1), the type of problem is defined hereafter. In the first type the journal displacement velocity, acceleration, and mass are known. Thus from Figs. 7 through 9 it is possible to calculate the stiffness and dissipation functions and from Equation (1) calculate the driving force. In the second type of problem, the driving force and mass are known. By making few simplifying assumptions about the squeeze-film velocity and acceleration it is possible to calculate the displacement or amplitude of vibration. In the third type of problem it is possible to calculate the critical speed of the system in which the fluid film stiffness is included. This information is very important in predicting both stability and dynamic behavior of rotating equipment supported on elastic fluid film.

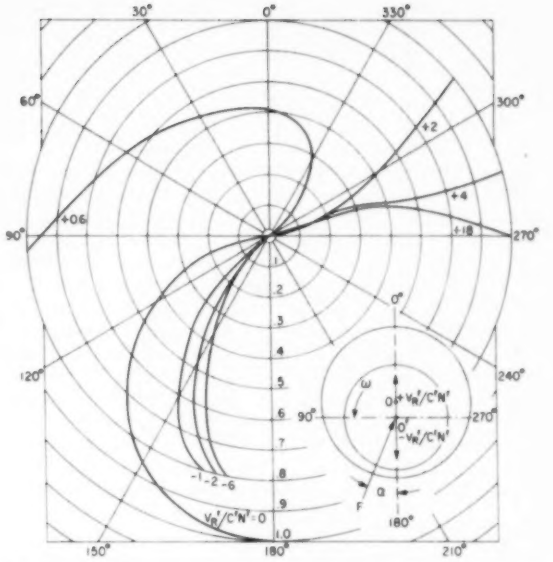

Fig. 6 Loci of force vector as a function of eccentricity ratio and radial velocity

Solution With Arbitrary Direction for the Squeeze-Film Velocity

Under dynamic operating conditions the journal center moves along some locus. The amount of energy absorbed by the fluid system per cycle is the integral of the damping force times the squeeze-film velocity. The damping force depends on eccentricity ratio and direction of the squeeze-film velocity. It was hypothesized that maximum damping occurs when the squeeze-film velocity acts along the line of centers in the direction tending to reduce the minimum film thickness. To verify this point an analysis was made for cylindrical journal bearing with $L'/D' = 1$. Solutions were obtained for squeeze-film velocity acting at several arbitrary angles to the line of centers. Fig. 10 shows the magnitude and direction of the force vector which is computed from Equation (5) for the respective directions of squeeze film velocity. The squeeze-film velocity $V'/C'N'$ in all cases was equal to 1.2 and it was acting at eccentricity ratio of 0.5. Note that the maximum force was calculated when the velocity acted along the line of centers in direction tending to reduce minimum film thickness. Table 2 shows the effect of eccentricity ratio, squeeze-film velocity, and direction on the hydrodynamic force. We note from these results that dissipation $B_{y'y'}$ for run 5-6 is 2.13 larger than for run 2-3. The values of dissipation versus eccentricity ratio presented in Fig. 9, which were calculated for purely radial velocity, yield the maximum values of damping for

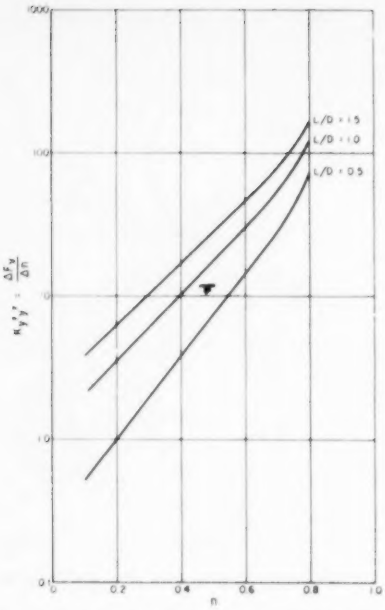

Fig. 7 Stiffness as a function of eccentricity ratio

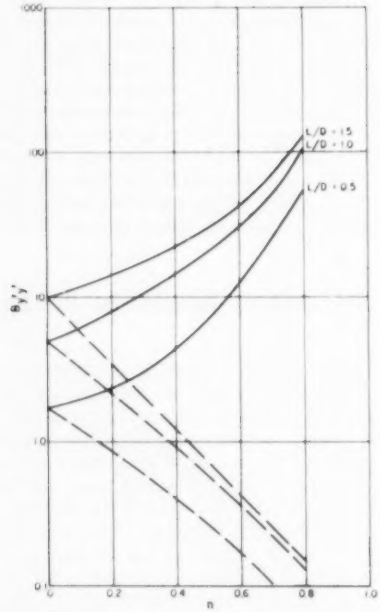

Fig. 9 Dissipation as a function of eccentricity ratio

Table 2

Run	n	V/CN	F_V	F_H	F	$B_{y'y'}$
1	0.3	0.95|120°	5.9	7.6	9.6|127.8°	
2	0.5	0.95|120°	12.6	11.6	17.1|137.4°	9.2
3	0.5	1.20|120°	14.9	12.9	19.7|139.2°	
4	0.3	0.95|180°	7.5	7.4	10.5|135.4°	
5	0.5	0.95|180°	16.1	11.2	19.6|145.2°	19.6
6	0.5	1.20|180°	21.0	13.5	25.0|147.3°	

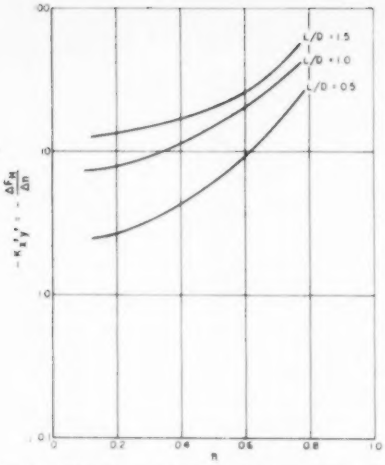

Fig. 8 Stiffness as a function of eccentricity ratio

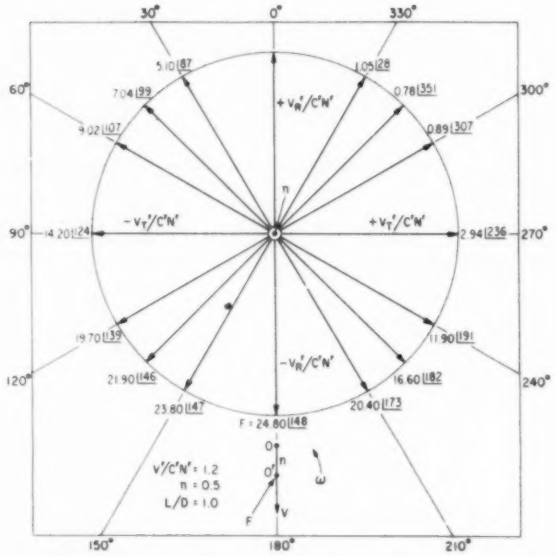

Fig. 10 Magnitude and direction of hydrodynamic force as a function of the direction of squeeze-film velocity

a plain cylindrical journal bearing. This information is very useful to the design engineer in checking whether he can tolerate the maximum amplitude of vibration. In the event that this amplitude is too large, he then has to reduce the driving force by better balancing his rotor.

Conclusions

1 The paper presents techniques for calculation of fluid stiffness and dissipation functions for journal bearings. The knowledge of these parameters is very important in predicting critical speed and amplitude of vibration.

2 Bearing geometry plays a very important role on stiffness and dissipation functions. Figs. 7 through 9 show the effect of L'/D' ratio and eccentricity ratio on these parameters.

3 The damping energy depends on both the shape of the locus and the squeeze-film velocity.

4 The cross terms of dissipation Equation (1) are small and may be neglected in dynamic analysis.

5 If the driving force and mass are known and a simplifying assumption is made about the squeeze-film velocity and acceleration it is possible to estimate the journal displacement.

6 Squeeze-film velocity acting along the line of centers and in the direction tending to reduce minimum film thickness yields maximum dissipation.

7 The analysis presented here is applicable to any bearing geometry. Film shapes other than that given in Equation (3) may be used when the bearing is other than cylindrical.

Recommendations

1 Energy considerations and pressure effect on viscosity should be considered in rigorous analysis. This is presently being programmed for the IBM-704 computer and will be presented at a later date.

2 Inertia effects and cavitation in dynamically loaded bearings deserve additional study. Experiments should be undertaken to establish the boundary conditions in cavitation. Under dynamic loads babbitt fatigue often occurs at the bonding surface if the bonding is poor. In practice there are several examples of plucking of babbitt material from the surface. This has occurred in the absence of "shaft currents" and may be explained by the presence of cavitation. This observation should be studied further.

3 Careful experiments should be conducted on dynamically loaded bearings in which journal misalignment should be kept to an absolute minimum. Measurements of vertical and horizontal displacement of the journal center with respect to time and load should be taken. From these data it is possible to calculate the stiffness and dissipation and the driving force along any two mutually perpendicular axes. The experimental results can then be compared to theoretical results. This can be done for any bearing geometry. (It may be worth mentioning that such experiments have been conducted for several bearing configurations in the presence of unbalancing rotating load and the results compare very well.)

4 In dynamically loaded bearings the hydrodynamic pressures may be extremely high and the effect of pressure on viscosity may play an important role on load carrying capacity [6]. It is recommended that this point be considered in further analysis.

Acknowledgment

The author greatly appreciates the help of Mr. Charles Bedford and Mr. J. Lund of the Medium Steam Turbine, Generator and Gear Department who are presently programming this analysis with energy considerations on the IBM-704 digital computer. He would like also to thank Mrs. P. Mall and Miss M. E. Haas of the Bearing and Lubricant center who have aided in the programming of the analysis on the IBM 650 computer.

References

1 G. F. Boeker and B. Sternlicht, "Investigation of Translatory Fluid Whirl in Vertical Machines," TRANS. ASME, vol. 78, 1956, pp. 13–19.

2 H. Poritsky, "Contribution to the Theory of Oil Whip," TRANS. ASME, vol. 75, 1953, pp. 1153–1161.

3 A. C. Hagg and P. C. Warner, "Oil Whip of Flexible Rotors," TRANS. ASME, vol. 75, 1953, pp. 1339–1344.

4 B. Sternlicht, "Energy and Reynolds Considerations in Thrust Bearing Analysis," IME Conference on Lubrication and Wear, October, 1957, Paper 21.

5 A. C. Hagg, "The Influence of Oil-Film Journal Bearings on the Stability of Rotating Machines," *Journal of Applied Mechanics*, vol. 13, TRANS. ASME, vol. 68, 1946, pp. A-211–220.

6 B. Sternlicht, "Influence of Pressure and Temperature on Oil Viscosity in Thrust Bearings," TRANS. ASME, vol. 80, 1958, pp. 1108–1112.

DISCUSSION

Burt L. Newkirk[2]

The application of digital computers to bearing analysis is an important step in progress, and the material presented in this paper is of great interest. One remarkable point is that the forces due to squeeze film velocity have such large components normal to the direction of motion.

It would be very helpful if tests could be made to determine, for a few simple cases, how closely calculated results represent the behavior of rotors running on journal bearings. This is not to question the analysis, but to give an indication of the adequacy of the basic assumptions [Equation (1)] to express the physical conditions.

An independent and different experimental study of the properties of fluid films in journal bearings is desirable also. This would be an exploratory program set up to study the behavior of a shaft running on a fluid film in a journal bearing, but with no primary object of testing indications of analysis.

It is recognized that the quasielasticity and damping of the fluid films affect appreciably the numerical values of the critical speeds and the fluid film whirls, especially for rotors having "calculated" critical speeds above 5000 rpm. However, important details of the resulting behavior of the rotors might be determined experimentally, and this should be a parallel approach. For example, a rotor having a calculated critical speed of about 10,000 rpm might be supported on very rigid standards, with a ball bearing at one end and a journal bearing at the other end. Bearing clearance, L/D ratio, oil viscosity, and unbalance might be varied, and the paths and frequencies of the journal motions studied.

A parallel study of this sort would probably help the interpretation of calculated results and suggest further applications of digital computers to bearing analysis.

Author's Closure

The author wishes to thank Dr. Newkirk for his valuable com-

[2] Consultant, Schenectady, N. Y. Fellow ASME.

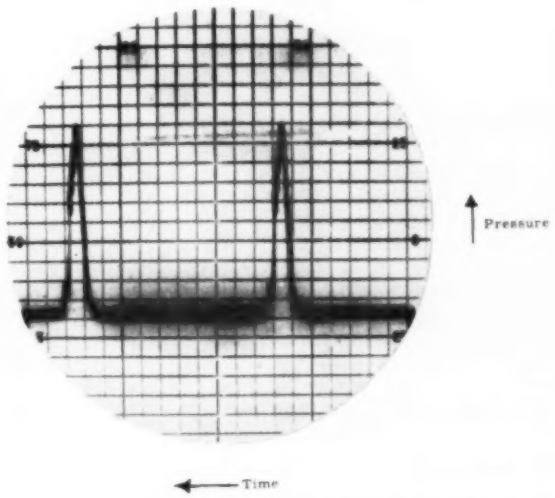

Fig. 11 Typical dynamic load pressure on piston
(Peak pressure: 600 psig; base pressure: 0 psig; period: 0.0335 sec)

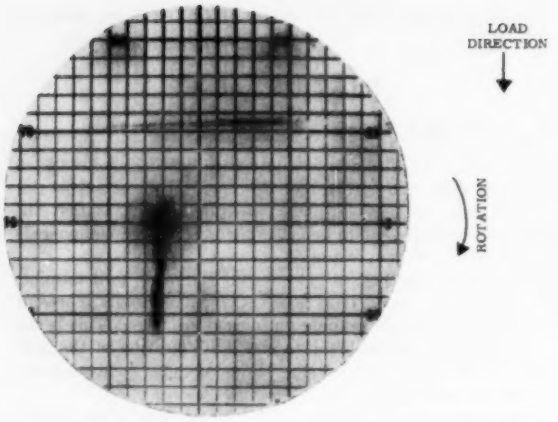

Fig. 12 Typical dynamic load shaft locus in front gage plane, plain bearing
(Oil hole inlet at top of picture; load: 837-psi peak on bearing; length of locus: 0.00088 in.)

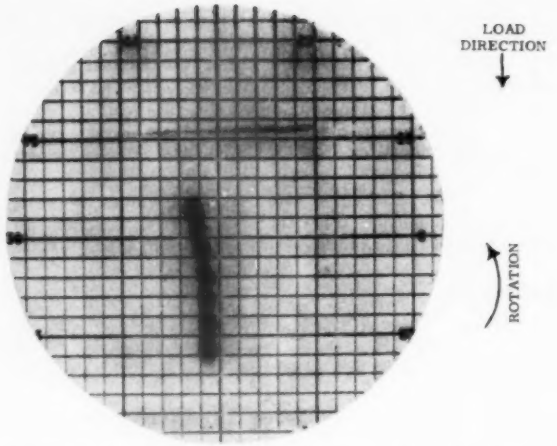

Fig. 13 Steady load shaft locus in front gage plane, plain bearing
(Oil hole inlet at top of picture; loads: 0, 49, 97, 146, 195, 243, 292 lb on piston; displacement between 0 and 292 lb; points: 0.00107 in.; 292 lb = 450 psi)

ments. It is quite true that experimental analyses of the properties of fluid films in journal bearings are very few and this procedure should be extended so as to gain a better understanding of the phenomenon. Through these experiments we may obtain a better physical picture of fluid film behavior.

I might add at this point that the analysis presented in this paper was actually undertaken to verify some experimental work that we were conducting at the time. Test equipment was constructed to duplicate loading in one of our apparatus. The type of loading that was applied is shown in Fig. 11. The magnitude of this load could be varied. Fig. 12 shows an oscilloscope picture of the shaft locus for a dynamic load and Fig. 13 shows shaft locus under static load. Note in comparing Figs. 12 and 13 that the eccentricity for the dynamic load was lower than that for the static load even though the dynamic load was of higher magnitude. This difference is attributed to "squeeze-film" velocity as predicted by theory. In general, our theoretical results correlated well with experimental results. One of the problems encountered in the experimental procedure was that it was extremely difficult to eliminate misalignment. The bearing and shaft axes must be aligned if theory is to be compared to the experiment. Small misalignments will considerably reduce the squeeze film force.

It is essential to include the fluid film stiffness in rigorous analysis of critical speeds. We are able to correlate closely the theoretically calculated critical speeds with those obtained on test if we include fluid and pedestal stiffness in analysis. The fluid damping characteristics and magnitude of unbalance must be known in predicting rotor vibrational amplitudes. Stiffness and damping are also essential in predicting fluid film whirls.

The experiment proposed by Dr. Newkirk would be most valuable in that it will be a controlled experiment in which one variable will be varied at a time. I would like to encourage other investigators to pursue this very important dynamic problem. The results will be most rewarding for they will have multiplicity of applications. Misalignment must be avoided in experiment if theory is to be compared to practice.

Axial, Relative Motion of a Circular Step Bearing

L. LICHT

Research Engineer, The Franklin Institute Laboratories, Philadelphia, Pa.

Equations relating the flow of the lubricant and the axial motion of an externally pressurized thrust bearing are developed. The bearing is shown to be stable when the fluid is incompressible.

Expressions for local stiffness and damping coefficients, useful in the evaluation of the dynamic response of the bearing, are given.

An analog computer solution of the equation of motion is compared with the results of the corresponding, small displacement equation.

Introduction

THE analysis is made for a unidirectional thrust plate, having a central recess as shown diagrammatically in Fig. 1. It can be extended to thrust bearings capable of supporting loads in both directions and having different pocket arrangements.

It is assumed that the bearing is restrained to permit only axial, relative motion and that a truly incompressible fluid of constant viscosity is supplied from a constant pressure reservoir. External drag effects are not considered in the equation of motion.[1]

A simplified version of the Navier-Stokes equation (as applicable to laminar, viscous flow) in conjunction with the continuity equation, describes the flow in the annular and recess regions. After pressure terms are eliminated, a nonlinear differential equation in terms of displacement and its time derivatives results. This, in turn, is linearized, giving a second-order differential equation in terms of perturbation displacements.

[1] The inclusion of a velocity-proportional term would describe the external damping effect adequately without introducing additional difficulties into the analysis.

Contributed by the Lubrication Division of THE AMERICAN SOCIETY OF MECHANICAL ENGINEERS and presented at the ASLE-ASME Lubrication Conference, Los Angeles, Calif., October 13–15, 1958.

NOTE: Statements and opinions advanced in papers are to be understood as individual expressions of their authors and not those of the Society. Manuscript received at ASME Headquarters, May 26, 1958. Paper No. 58—Lub-1.

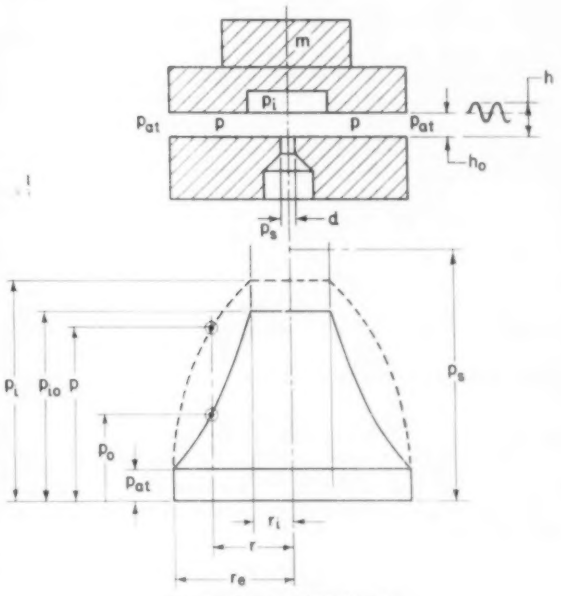

Fig. 1 Diagram of the bearing

Nomenclature

Linear Dimensions

r_s = radius of recess, in.
$r = r_s R$ = radial distance from bearing center, in.
$r_e = r_s R_e$ = outer radius of bearing, in.
$d = 2r_s D$ = supply nozzle diameter, in.
h_0 = width of annulus, equilibrium, in.
$h = h_0 H$ = width of annulus, in.
$\hat{\delta} = h_0(1 - H) = h_0\Delta$ = deviation in annular width from the equilibrium value h_0, in. ($\delta \ll h_0$)

Pressures

p_{s0} = pressure in the recess, equilibrium, psia
$p_s = p_{s0}P_s$ = pressure in the recess, psia
$p_0 = p_{s0}P_0$ = pressure in the annulus, equilibrium, psia
$p = p_{s0}P$ = pressure in the annulus, psia
$p_s = p_{s0}P_s$ = supply pressure, psia
$p_{at} = p_{s0}P_{at}$ = atmospheric (ambient) pressure, psia

Other Quantities

L = load on bearing, lb
m = mass, lb-sec²/in.
q_0 = volume rate of flow, equilibrium, in.³/sec
$q_1 = q_0 Q_1$ = volume rate of flow into recess, in.³/sec
$q_2 = q_0 Q_2$ = volume rate of flow from recess, in.³/sec
ρ = fluid mass density, lb-sec²/in.⁴
μ = fluid viscosity, lb-sec/in.²
g = acceleration of gravity, in./sec²
f = local, natural frequency, 1/sec (see Appendix 2)
k_s = local, static stiffness, lb/in. (see Appendix 2)
k_d = dynamic stiffness, lb/in.
b = damping coefficient, lb-sec/in.
$t = \tau/f$ = time, sec
$n = mg/L$ = (weight of mass/load on bearing) ratio
$\frac{d}{d\tau} = (\cdot)$ = denotes differentiation with respect to the dimensionless time variable

Analysis

By combining the reduced Navier-Stokes equation with the continuity equation, we obtain an equation that applies to the annular region:

$$\frac{1}{r}\frac{\partial}{\partial r}\left(r\frac{\partial p}{\partial r}\right) = \frac{12\mu}{h^3}\frac{dh}{dt} \tag{1}$$

The continuity equation for the cylindrical volume above the recess area is represented by:

$$\pi r_i^2\frac{dh}{dt} = q_1 - q_2 = \frac{\pi d^2}{4}\left[\frac{2}{\rho}(p_s - p_i)\right]^{1/2} + \frac{\pi r_i}{6\mu}\left[\frac{\partial p}{\partial r}\right]_{r=r_i} \tag{2}$$

The equation of motion of the thrust plate and the attached mass is:

$$m\frac{d^2h}{dt^2} = \pi r_i^2(p_i - p_{s0}) + \int_{r_i}^{r_e} 2\pi(p - p_0)r\,dr \tag{3}$$

The dimensionless equivalents of equations (1), (2), and (3) are:

$$\frac{1}{R}\frac{\partial}{\partial R}\left(R\frac{\partial P}{\partial R}\right) = \frac{12\mu f r_i^2}{p_{s0}h_0^2}\frac{\dot{H}}{H^3} \tag{4}$$

$$\dot{H} = \frac{D^2\left(\frac{2p_{s0}}{\rho}\right)^{1/2}}{fh_0}(P_s - P_i)^{1/2} + \frac{p_{s0}h_0^2}{6fr_i^2}H^3\left[\frac{\partial P}{\partial R}\right]_{R=1} \tag{5}$$

$$\ddot{H} = \frac{\pi r_i^2 p_{s0}}{mf^2h_0}(P_i - 1) + \frac{2\pi r_i^2 p_{s0}}{mf^2h_0}\int_1^{R_e}(P - P_0)R\,dR \tag{6}$$

where, in equation (6), P_0 is given by:

$$P_0 - P_{at} = -\frac{6\mu D^2 r_i^2\left(\frac{2p_{s0}}{\rho}\right)^{1/2}(P_s - 1)^{1/2}}{p_{s0}h_0^3}\log\frac{R}{R_e} \tag{7}$$

The next step is the integration of equation (4), subject to the following boundary conditions:

$$\left.\begin{aligned} P(1,\tau) &= P_i(\tau) \\ \text{and} \\ P(R_e,\tau) &= P_{at} \end{aligned}\right\} \tag{8}$$

This results in the following expression for the dimensionless pressure in the annulus:

$$P(R,\tau) = P_i(\tau)\left[1 - \frac{\log R}{\log R_e}\right] + P_{at}\frac{\log R}{\log R_e} + \frac{3\mu f r_i^2}{p_{s0}h_0^2}\left[(R^2 - 1) - \frac{R_e^2 - 1}{\log R_e}\log R\right]\frac{\dot{H}}{H^3} \tag{9}$$

Substituting equations (9) and (7) into the integral in equation (6) gives, upon integration:

$$\left.\begin{aligned} &\frac{2\pi r_i^2 p_{s0}}{mf^2h_0}\int_1^{R_e}(P - P_0)R\,dR \\ &\quad = \frac{\pi r_i^2 p_{s0}}{2mf^2h_0}\left(\frac{R_e^2 - 1}{\log R_e} - 2\right)(P_i - P_{at}) \\ &\quad + \frac{3\pi\mu r_i^4}{2mfh_0^3}\left[\frac{(R_e^2 - 1)^2}{\log R_e} - (R_e^4 - 1)\right]\frac{\dot{H}}{H^3} \\ &\quad + \frac{3\mu\pi r_i^4 D^2\left(\frac{2p_{s0}}{\rho}\right)^{1/2}(P_s - 1)^{1/2}}{mf^2h_0^4}\left[2\log R_e - (R_e^2 - 1)\right] \end{aligned}\right\} \tag{10}$$

(cont.)

so that equation (6) can now be written as:

$$\left.\begin{aligned} \ddot{H} = \frac{\pi r_i^2 p_{s0}}{mf^2h_0}&\left[(P_i - 1) + \left(\frac{R_e^2 - 1}{2\log R_e} - 1\right)(P_i - P_{at})\right] \\ &+ \frac{3\pi\mu r_i^4}{2mfh_0^3}\left[\frac{(R_e^2 - 1)^2}{\log R_e} - (R_e^4 - 1)\right]\frac{\dot{H}}{H^3} \\ &+ \frac{3\pi\mu r_i^4 D^2\left(\frac{2p_{s0}}{\rho}\right)^{1/2}(P_s - 1)^{1/2}}{mf^2h_0^4}\left[2\log R_e - (R_e^2 - 1)\right] \end{aligned}\right\} \tag{11}$$

From equation (9) one obtains, by differentiation:

$$\left[\frac{\partial P}{\partial R}\right]_{R=1} = -\frac{P_i - P_{at}}{\log R_e} + \frac{3\mu f r_i^2}{p_{s0}h_0^2}\left[2 - \frac{R_e^2 - 1}{\log R_e}\right]\frac{\dot{H}}{H^3} \tag{12}$$

and the substitution of equation (12) in (5) gives:

$$\dot{H} + \left(\frac{p_{s0}h_0^2}{3\mu f r_i^2}\right)\left(\frac{P_i - P_{at}}{R_e^2 - 1}\right)H^3 = \frac{2\log R_e D^2\left(\frac{2p_{s0}}{\rho}\right)^{1/2}}{(R_e^2 - 1)fh_0}(P_s - P_i)^{1/2} \tag{13}$$

The elimination of P_i between equations (11) and (13) results in the following equations in terms of H and its derivatives:

$$H^3\left(C_1\ddot{H} + C_2\frac{\dot{H}}{H^3} + C_3\right) = \left(C_4 + C_5\frac{\dot{H}}{H^3} + C_6\ddot{H}\right)^{1/3} \tag{14}$$

Here, the C's represent constants which include the bearing and fluid parameters. Their explicit expressions are listed in Appendix 3.

Squaring equation (14), introducing the perturbation displacement and its derivatives,

$$\left.\begin{aligned} h &= h_0 + \delta \quad (\delta \ll h_0) \\ H &= 1 + \Delta \quad (\Delta \ll 1) \\ \dot{H} &= \dot{\Delta} \\ \ddot{H} &= \ddot{\Delta} \end{aligned}\right\} \tag{15}$$

and neglecting their squares and cross-products as quantities of higher order, equation (14) reduces to:

$$\ddot{\Delta} + \left(\frac{2C_2C_3 - C_5}{2C_1C_3 - C_6}\right)\dot{\Delta} + \left(\frac{9C_3^2 - 3C_4}{2C_1C_3 - C_6}\right)\Delta = \frac{C_4 - C_3^2}{2C_1C_3 - C_6} \tag{16}$$

and, since $C_4 = C_3^2$, we have:

$$\ddot{\Delta} + \beta\dot{\Delta} + \theta\Delta = 0 \tag{17}$$

where

$$\beta = \frac{2C_2C_3 - C_5}{2C_1C_3 - C_6}$$

$$= \frac{\pi\left[\frac{h_0 g}{6n(2P_s - P_{at} - 1)}\right]^{1/2}}{D^2\left(\frac{2p_{s0}}{\rho}\right)^{1/4}(P_s - 1)}\left\{(R_e^2 + 1)(2P_s - P_{at} - 1) - (R_e^2 - 1)\frac{1 - P_{at}}{\log R_e}\right\} \tag{18}$$

$$\theta = \frac{6C_3^2}{2C_1C_3 - C_2} = 4\pi^2 \tag{19}$$

and the dimensional equivalent of (17):

$$m\frac{d^2\delta}{dt^2} + b\frac{d\delta}{dt} + k_d\delta = 0 \tag{20}$$

where

$$\left.\begin{aligned} b &= mf\beta \\ k_d &= mf^2\theta \end{aligned}\right\} \tag{21}$$

Discussion of Results

The conditions of stability are that the coefficients of equation (17) be positive: e.g., $\beta > 0$; $\theta > 0$. Since $\theta = 4\pi^2$ is always positive, one needs only to examine the quantity which appears within the brackets of the expression for the dimensionless coefficient β in (18).

For $\beta > 0$

$$\left.\begin{aligned} &(R_e^2 + 1)(2P_s - P_{at} - 1) > \frac{R_e^2 - 1}{\log R_e}(1 - P_{at}) \\ &\text{or} \\ &\frac{R_e^2 + 1}{R_e^2 - 1}\log R_e > \frac{1 - P_{at}}{2P_s - P_{at} - 1} \end{aligned}\right\} \tag{22}$$

It can easily be seen that unity is the smallest and the largest value which the left side and right side of the inequality (22) can respectively assume. Consequently the bearing is stable for all ratios of radii and pressures.

At this point we also note that the local, static, and dynamic stiffness coefficients are equal, viz.:

$$k_d = mf^2\theta = \frac{m}{(2\pi)^2}\frac{k_s}{m}\theta = k_s \tag{23}$$

The local stiffness and damping coefficients are useful in evaluating the response of the bearing for small deviations from any equilibrium value.

Equation (17) predicts stability in the sense that small oscillations do not grow with time. The region of resonance is also indicated for small periodic disturbances whose frequency is equal to the "natural, local frequency" of the bearing.

The analog computer solutions of equation (14) and the corresponding perturbation displacement equation (17) are presented graphically in Figs. 2, 3, and 4. In each figure, $n = \frac{1}{4}$, 1, 4 refers to the ratio mg/L. Dimensionless displacements $H = h/h_0$ and $\Delta = \delta/H_0$ are plotted against dimensionless time $\tau = ft$ where f is the local, natural frequency, and are shown one above the other. The upper graph represents the solution of equation (14) and the lower that of equation (17).

Although equation (17) is valid only for small displacements, the same initial deflections of $\Delta(0) = -1/4, -1/2, -3/4$ are applied as in the nonlinear case of equation (14), where the corresponding values are $H(0) = 3/4, 1/2, 1/4$.

The similarity between the graphs which represent the two solutions is rather remarkable, particularly in view of the much greater complexity of equation (14) and the magnitude of the initial deflections applied in the case of equation (17).

From the solution of the nonlinear equation it appears that the bearing is stable regardless of the magnitude of the initial displacement. This confirms the predictions made on the basis of the linearized equation.

In addition, the linearized equation appears to represent the motion of the bearing quite well even beyond the region of small displacements.

It is noted that the bearing is overdamped for small values of mg/L and values of the pressure ratio p_{i0}/p_s tending toward unity, whereas a noticeable overshoot occurs when the opposite is the case.

Acknowledgments

This paper is based on the work performed under contract administered by the Office of Naval Research and supported jointly by the Department of Defense, Atomic Energy Commission, and the Maritime Administration.

The author wishes to express his gratitude to Prof. H. Elrod of the Mechanical Engineering Department, Columbia University, for his expert advice and constructive criticism, and to Prof. Dudley D. Fuller, also of the Columbia faculty, for his constant encouragement and guidance.

Bibliography

1 A. Stodola, "Kritische Wellenstörung infolge der Nachgiebigkeit des Oelpolsters im Lager," *Schweizerische Bauzeitung*, vol. 85, 21, May, 1925.

2 F. R. Archibald, "Load Capacity and Time Relations for Squeeze Films," TRANS. ASME, vol. 78, 1956, p. 29.

3 D. D. Fuller, "Hydrostatic Lubrication," *Machine Design*, vol. 19, August, 1947, pp. 115–120.

APPENDIX 1

The rate of flow at equilibrium is given by:

$$q_0 = \frac{\pi d^2}{4}\left[\frac{2}{\rho}(p_s - p_{i0})\right]^{1/2} \tag{24}$$

as well as by [3][2]

$$q_0 = \frac{\pi h_0^3}{6\mu \log \frac{r_e}{r_i}}(p_{i0} - p_{at}) \tag{25}$$

so that

$$h_0 = \left[\frac{6\mu \log \frac{r_e}{r_i} D^2 r_i^2 \left(\frac{2p_{i0}}{\rho}\right)^{1/2}(P_s - 1)^{1/2}}{p_{i0} - p_{at}}\right]^{1/3} \tag{26}$$

APPENDIX 2

Local Static Stiffness and Natural Frequency

Defining the local, static stiffness as:

$$k_s = -\frac{dL}{dh_0} \tag{27}$$

and the local, natural frequency as:

$$f = \frac{1}{2\pi}\left(\frac{k_s}{m}\right)^{1/2} = \frac{1}{2\pi}\left(\frac{k_s g}{nL}\right)^{1/2} \tag{28}$$

where

$$n = \frac{\text{Weight of mass}}{\text{Load on bearing}} = \frac{mg}{L} \tag{29}$$

and with the load $\sim$ pressure $\sim$ flow relations given by [3]

[2] Numbers in brackets refer to Bibliography at end of paper.

$$L = \frac{\pi}{2}(p_{s0} - p_{at})\frac{r_e^2 - r_i^2}{\log \frac{r_e}{r_i}} \tag{30}$$

$$p_{s0} - p_{at} = \frac{6\mu q_0}{\pi h_0^3}\log\frac{r_e}{r_i} \tag{31}$$

$$q_0 = \frac{\pi d^2}{4}\left[\frac{2}{\rho}(p_s - p_{s0})\right]^{1/2} \tag{32}$$

we have

$$k_s = -\frac{dL}{dh_0} = -\frac{dL}{dp_{s0}}\frac{dp_{s0}}{dh_0} = -\frac{\pi}{2}\frac{r_e^2 - r_i^2}{\log\frac{r_e}{r_i}}\frac{dp_{s0}}{dh_0} \tag{33}$$

From (31) and (32) we obtain:

$$p_{s0} - p_{at} = \frac{6\mu}{\pi h_0^3}\frac{\pi d^2}{4}\left[\frac{2}{\rho}(p_s - p_{s0})\right]^{1/2}\log\frac{r_e}{r_i} \tag{34}$$

Squaring (34) and rearranging terms we have:

$$h_0^6 = \frac{9}{2}\frac{\mu^2 d^4}{\rho}\left(\log\frac{r_e}{r_i}\right)^2\frac{p_s - p_{s0}}{(p_{s0} - p_{at})^2} \tag{35}$$

Differentiation of (35) results in:

$$-\frac{dp_{s0}}{dh_0} = \frac{4\rho h_0^5}{3\mu^2 d^4\left(\log\frac{r_e}{r_i}\right)^2}\cdot\frac{(p_{s0} - p_{at})^2}{(2p_s - p_{s0} - p_{at})} \tag{36}$$

Substitution of (36) in (33) gives:

$$k_s = \frac{\pi}{24}\frac{\rho p_{s0}^2(1 - P_{at})^2(R_e^2 - 1)h_0^5}{\mu^2 r_i^2 D^2(\log R_e)^2(2P_s - P_{at} - 1)} \tag{37}$$

and substituting (37) in (28) we obtain:

$$f = \frac{1 - P_{at}}{4\pi\mu D^2 r_i^2\log R_e}\left[\frac{g\rho p_{s0}h_0^5}{3n(2P_s - P_{at} - 1)}\right]^{1/2} \tag{38}$$

APPENDIX 3

The constants of equation (14) are as follows:

$$C_1 = \frac{mf^2\left(\frac{h_0}{r_i}\right)^4}{3\mu\pi D^2\left(\frac{2p_{s0}}{\rho}\right)^{1/2}(R_e^2 - 1)} = \frac{3(P_s - 1)^{3/2}}{2\pi^2(2P_s - P_{at} - 1)}$$

$$C_2 = \frac{fh_0(R_e^2 + 1)}{2D^2\left(\frac{2p_{s0}}{\rho}\right)^{1/2}} = \frac{3}{2}\frac{(R_e^2 + 1)(P_s - 1)^{1/2}}{\pi D^2\left(\frac{2p_{s0}}{\rho}\right)^{1/2}}\left[\frac{gh_0}{6n(2P_s - P_{at} - 1)}\right]^{1/2}$$

$$C_3 = \left\{(P_s - 1)^{1/2}\left(1 - \frac{2\log R_e}{R_e^2 - 1}\right) + \frac{p_{s0}(1 - P_{at})h_0^3}{3\mu r_i^2 D^2\left(\frac{2p_{s0}}{\rho}\right)^{1/2}(R_e^2 - 1)}\right\} = (P_s - 1)^{1/2}$$

$$C_4 = C_3^2 = \left\{(P_s - P_{at}) - (1 - P_{at})\frac{2\log R_e}{R_e^2 - 1} + \frac{6\mu D^2 r_i^2\left(\frac{2p_{s0}}{\rho}\right)^{1/2}(P_s - 1)^{1/2}\log R_e[2\log R_e - (R_e^2 - 1)]}{p_{s0}h_0^3(R_e^2 - 1)}\right\} = P_s - 1$$

$$C_5 = \frac{3\mu f r_i^2}{p_{s0}h_0^2}[(R_e^2 - 1) - (R_e^2 + 1)\log R_e] = \frac{3}{2}\frac{1 - P_{at}}{\pi D^2\left(\frac{2p_{s0}}{\rho}\right)^{1/2}}\left[\frac{R_e^2 - 1}{\log R_e} - (R_e^2 + 1)\right]\left[\frac{gh_0}{6n(2P_s - P_{at} - 1)}\right]^{1/2}$$

$$C_6 = -\frac{2mf^2h_0\log R_e}{\pi r_i^2 p_{s0}(R_e^2 - 1)} = -\frac{3}{2}\frac{(1 - P_{at})(P_s - 1)}{\pi^2(2P_s - P_{at} - 1)}$$

In replacing m, f, and h_0 in these expressions, use was made of the equations and the results of Appendix 1, and Appendix 2, namely:

$$h_0 = \left\{\frac{6\mu D^2 r_i^2\left(\frac{2p_{s0}}{\rho}\right)^{1/2}(P_s - 1)^{1/2}\log R_e}{p_{s0}(1 - P_{at})}\right\}^{1/3}$$

$$m = \frac{nL}{g} = \frac{n}{g}\frac{\pi r_i^2 p_{s0}}{2}(1 - P_{at})\frac{R_e^2 - 1}{\log R_e}$$

$$= \frac{1 - P_{at}}{4\pi\mu D^2 r_i^2\log R_e}\left[\frac{g\rho p_{s0}h_0^5}{3n(2P_s - P_{at} - 1)}\right]^{1/2}$$

$P_s = 20$ atm.

$\mu = 1.67 \times 10^{-5} \ \frac{\text{lb-sec}}{\text{in.}^2}$ $\qquad \frac{r_e}{r_i} = 3$

$\rho = 7.93 \times 10^{-5} \ \frac{\text{lb-sec}^2}{\text{in.}^4}$ $\qquad \frac{p_{io}}{p_s} = .9$

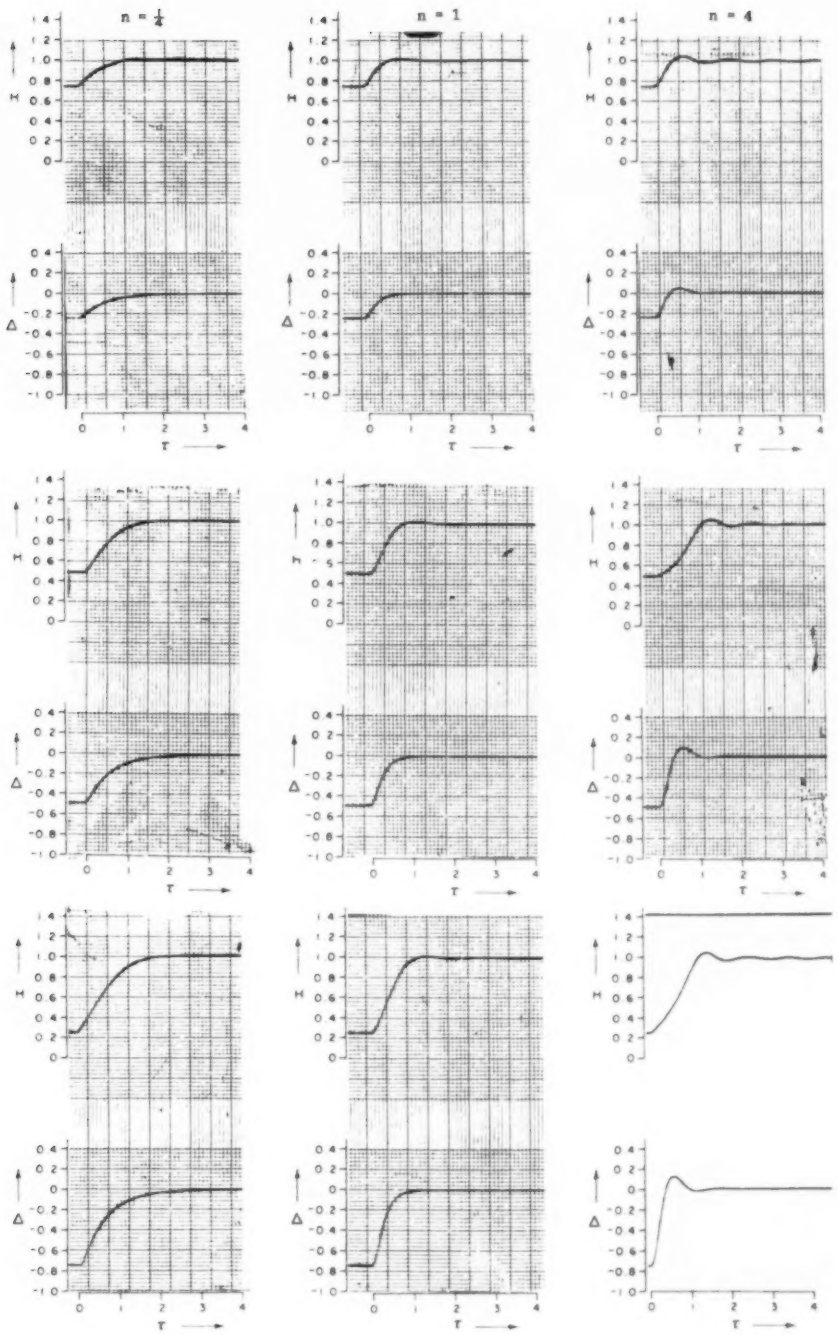

Fig. 2 Computer solution of equations (14) and (17) when $p_{io}/p_s = 0.9$

P_s = 20 atm.

$\mu = 1.67 \times 10^{-5} \frac{\text{lb-sec}}{\text{in.}^2}$ $\qquad \frac{r_e}{r_i} = 3$

$\rho = 7.93 \times 10^{-5} \frac{\text{lb-sec}^2}{\text{in.}^4}$ $\qquad \frac{P_{io}}{P_s} = .7$

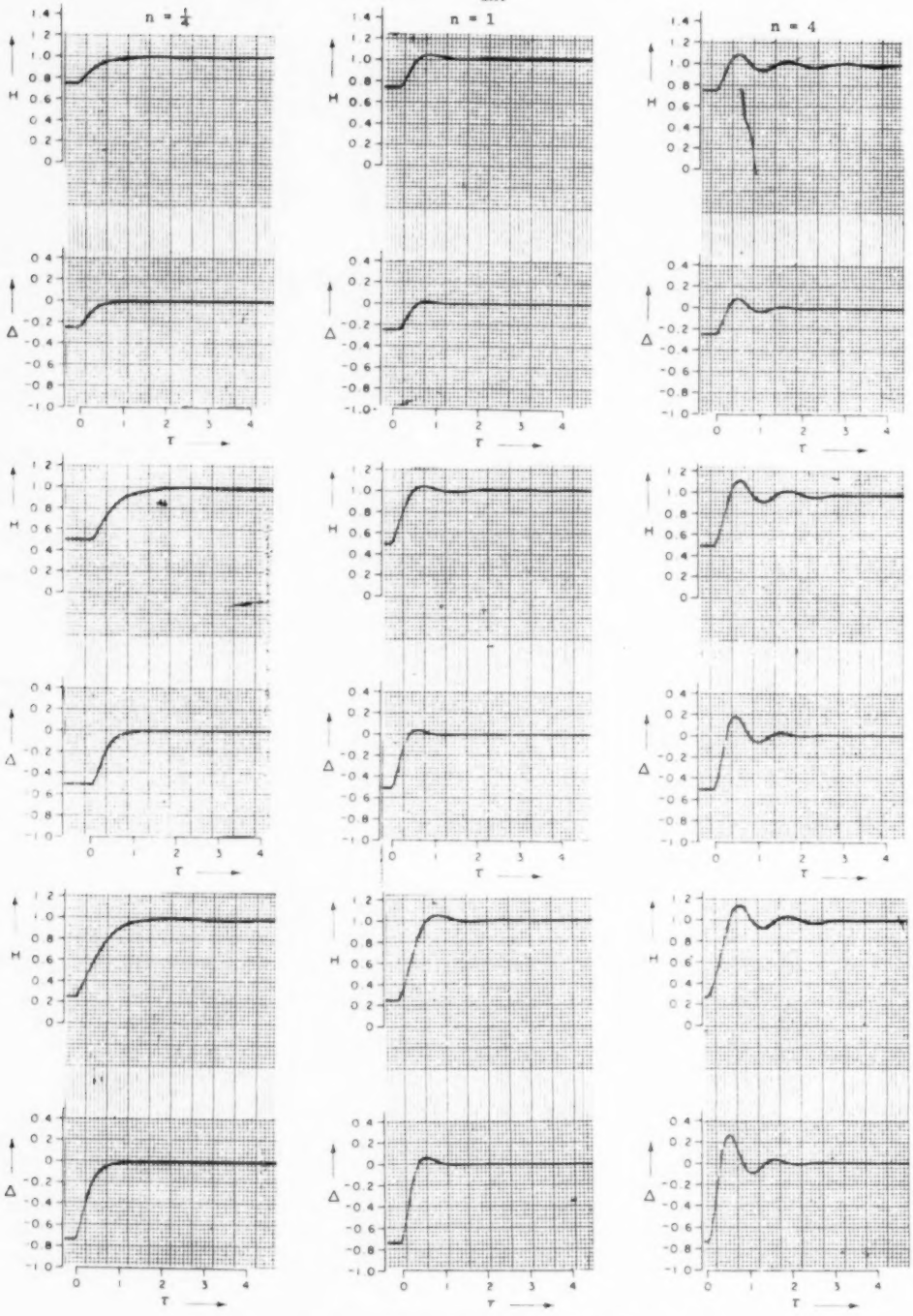

Fig. 3 Computer solution of equations (14) and (17) when $p_{io}/p_s = 0.7$

P_s = 20 atm.

$\mu = 1.67 \times 10^{-5}$ $\frac{\text{lb-sec}}{\text{in.}^2}$ $\qquad \frac{r_e}{r_i} = 3$

$\rho = 7.93 \times 10^{-5}$ $\frac{\text{lb-sec}^2}{\text{in.}^4}$ $\qquad \frac{P_{io}}{P_s} = .5$

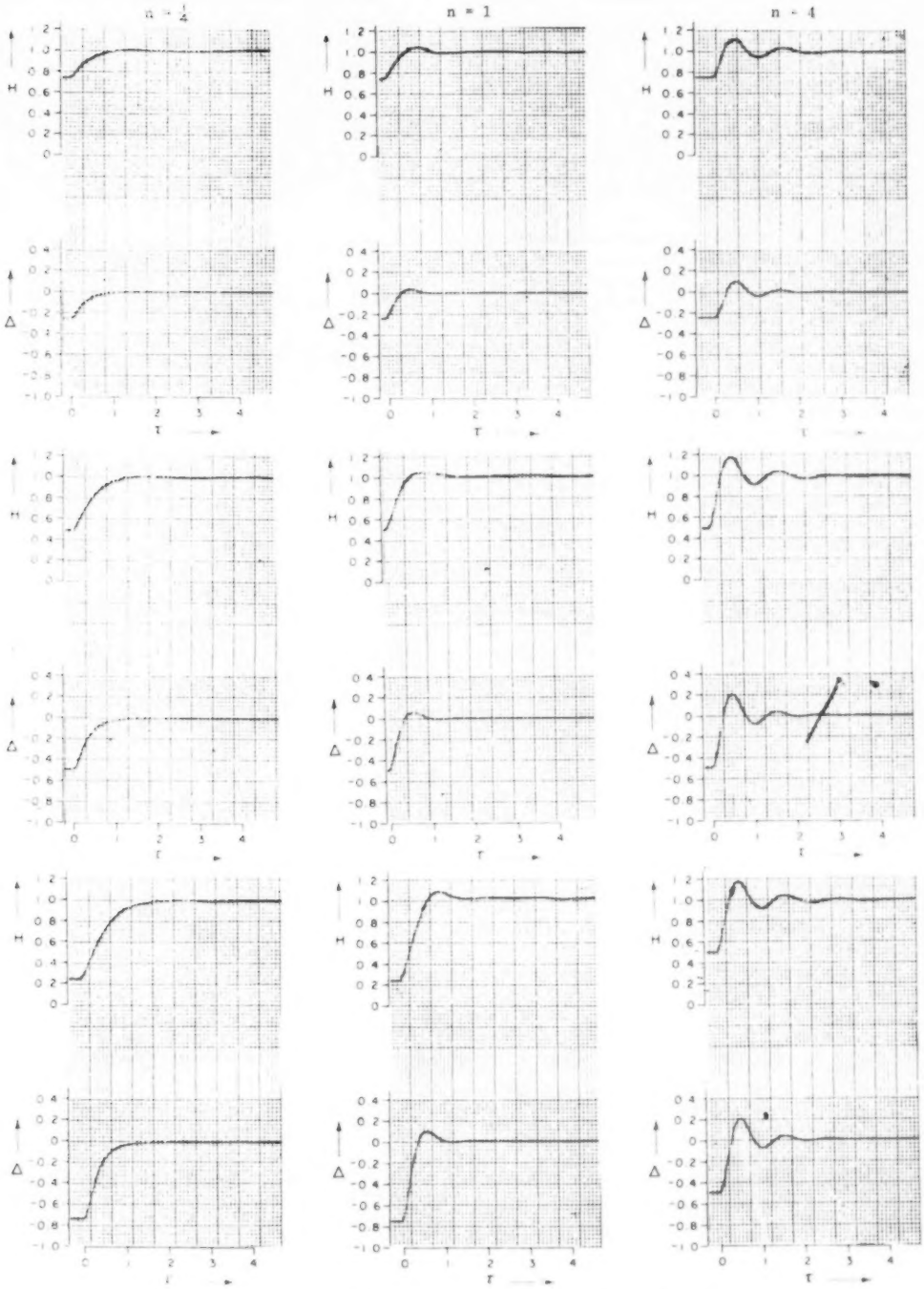

Fig. 4 Computer solution of equations (14) and (17) when $p_{io}/p_s = 0.5$

DISCUSSION

Herbert Richardson[3]

The author's very careful and thorough analysis is a valuable contribution to the literature on pressurized-fluid bearings. He has shown that for most practical purposes the fluid film characteristics of this type of bearing can be approximated by a linear differential equation consisting of a displacement term plus a velocity term. That is, the bearing film is characterized by an equivalent spring stiffness and an equivalent viscous damping. Although the author has studied the case where the fluid film is loaded only by a mass and an external force, knowledge of the film characteristics will permit analysis of more complex systems which incorporate this type of pressurized bearing.

The author is particularly to be commended for his use of an analog computer to show the range of applicability of the perturbation analysis. His observation that the linearized equation describes the bearing behavior well for relatively large perturbations is in accordance with this writer's experience with a variety of dynamic systems. Generally, the perturbation method yields excellent results in systems that have "well-behaved" or slowly varying nonlinearities but breaks down when "hard" or discontinuous nonlinearities (e.g., coulomb friction, hysteresis, and dead zone) are encountered.

In developing his analysis, the author has employed the classical assumptions of lubrication theory. Although the convective acceleration terms in the momentum equation probably are negligible over a wide range of parameters, there will be a range of frequencies f above which the local accelerations (partial derivative of velocity with respect to time) will become significant. This effect would probably introduce an acceleration-dependent term into the equation for fluid-film force. A determination of the frequency range within which this effect is negligible would be a valuable addition to the paper.

In conclusion, the writer would like to suggest that the author extend his analysis to include and evaluate the effects of liquid compressibility. Luming,[4] in an experimental and analytical study of the dynamics of pocket-type pressurized journal bearings, found that compressibility of the liquid in the pockets could not be neglected in a bearing that has small clearance, large stiffness, and is subject to light loads, even though the pocket volume appears geometrically small.

H. J. Sneck[5]

The question of whether it is permissible to use steady-state flow equation (1) to describe a nonsteady flow phenomena would seem to require some investigation. A modification of the continuity equation (2) of the paper is discussed here and a possible criterion for the upper limit of the permissible vibrational frequency is also suggested.

Equation (1) is obtained by the reduction and combination of the following equations for incompressible flow:

$$\frac{\partial V_r}{\partial r} + \frac{V_r}{r} + \frac{\partial V_z}{\partial z} = 0 \tag{39}$$

$$\rho\left(\frac{\partial V_r}{\partial t} + V_r\frac{\partial V_r}{\partial r} + V_z\frac{\partial V_r}{\partial z}\right) = -\frac{\partial P}{\partial r} + \mu\left(\frac{\partial V_r^2}{\partial z^2} + \frac{1}{r}\frac{\partial V_r}{\partial r} - \frac{V_r}{r^2} + \frac{\partial^2 V}{\partial r^2}\right) \tag{40}$$

where

V_r = radial velocity component
V_z = axial velocity component
ρ = mass density
P = pressure

Introducing the nondimensional characteristic quantities

$$\left.\begin{aligned} r &= Rr' & t &= \frac{h}{\frac{dh}{dt}}t' \\ z &= hz' & & \\ V_z &= \frac{dh}{dt}V_z' & & \\ V_r &= \frac{R}{h}\frac{dh}{dt}V_r' & P &= \rho V_r^2 P' \end{aligned}\right\} \tag{41}$$

in a manner similar to that employed by Brand[6] gives

$$\left.\begin{aligned} &\frac{\partial V_r'}{\partial r'} + \frac{V_r'}{r'} + \frac{\partial V_z'}{\partial z'} = 0 \\ &\frac{\partial V_r'}{\partial t'} + V_r'\frac{\partial V_r'}{\partial r'} + V_z'\frac{\partial V_r'}{\partial z'} \\ &\qquad = -\frac{\partial P'}{\partial r'} + \left(\frac{\mu}{\rho R\frac{dh}{dt}}\right)\frac{R}{h}\frac{\partial V_r'^2}{\partial z'^2} \end{aligned}\right\} \tag{42}$$

where all the primed terms are of the order of magnitude one, and terms of higher order have been dropped. From this, it is possible to conclude that the inertia terms omitted from equation (1) must be included when

$$\frac{\mu}{\rho h\frac{dh}{dt}} \sim 1.0 \tag{43}$$

In order to estimate the magnitude of the maximum allowable velocity dh/dt, take as an example

$$\rho = 2.0 \text{ slugs/ft}^3$$

$$\mu = (10^{-5})\frac{\text{lb sec}}{\text{ft}^2}$$

$$h_0 = 0.010 \text{ in.}$$

$$\delta = 0.001 \text{ in.}$$

$$\frac{dh}{dt} = \frac{\mu}{\rho h} = \frac{(10^{-5})}{2.0\,\frac{(0.010)}{12}} = 0.6 \text{ ft/sec}$$

but

[3] Assistant Professor of Mechanical Engineering, Massachusetts Institute of Technology, Cambridge, Mass.

[4] M. Luming, "Dynamic Analysis of Externally Pressurized Bearings" S.M. thesis, Dept. of Mechanical Engineering, Massachusetts Institute of Technology, Cambridge, Mass., February, 1954.

[5] General Engineering Laboratory, General Electric Company, Schenectady, N. Y.

[6] R. S. Brand, "Inertia Forces in Lubricating Films," *Journal of Applied Mechanics*, vol. 22, TRANS. ASME, vol. 77, 1955, p. 363.

$$\left(\frac{dh}{dt}\right)_{\max} \approx 2\pi f\delta$$

$$f = \frac{12(0.6)}{2\pi(0.001)} \simeq 10^3 \text{ cps}$$

From this it would appear that the omission of the inertia terms might not impose a serious restriction on the validity of the results.

It would be interesting to see if the predictions of the paper and the criterion mentioned here are verified by experimental evidence.

Since the phenomena studied in the paper is essentially one of unsteady motion, it is natural to expect that the equations of motion will contain terms to account for the fluid inertial forces involved. When they do not appear, as is the case in equations (1) and (2), there is a tendency to question the validity of the results.

Equation (2) contains the term

$$\frac{\pi d^2}{4}\left[\frac{2}{\rho}(P_s - P_i)\right]^{1/2}$$

which describes the flow of the fluid through an orifice. Usual practice requires the modification of this equation by a multiplying coefficient to account for flow losses and the contraction of the jet in steady flow. This coefficient has been omitted here, but could easily be included. Just how this coefficient should be altered in the case of unsteady flow through an orifice and if its inclusion has any major influence on the result would be of interest.

Author's Closure

The author wishes to thank Professor Richardson for his encouraging comment and to express his appreciation of Mr. Sneck's contribution to the discussion.

He is aware, of course, of the limitations which the neglect of the acceleration and compressibility terms in the basic equations imposes upon the range of validity of this approach. Mr. Sneck's reference to the Brand paper and the numerical example represent, therefore, a desirable supplement to this paper.

No account was taken of entrance effects at the sharp edge of the recess and, perhaps not inconsistently, the nozzle flow equation was given in its idealized form. The question as to how valid the inclusion of a steady-flow discharge coefficient is in the case of unsteady flow through a nozzle would seem to depend on the ratio of the local and convective accelerations. The criterion is the magnitude of the so-called Strouhal number,[7] the requirement for the applicability of quasi-steady flow theory being that:

$$N_s \equiv \frac{df}{\bar{U}} \ll 1$$

in which

N_s = Strouhal number
d = nozzle (orifice) diameter
f = frequency of oscillation
$\bar{U}$ = average flow velocity

Using the values given in Mr. Sneck's numerical example and pressure ratios $p_s : p_{t0} : p_{at} = 20:16:1$, we have approximately:

$\bar{U} \approx 1.10 \times 10^3$ in/sec
$d \approx 0.132$ in.
$f = 1000$ cps

so that

$$N_s \approx \frac{0.132 \times 10^3}{1.10 \times 10^3} = 0.120$$

It would appear therefore that the use of a steady-flow discharge coefficient involves no serious error.

In this paper, the emphasis was put on the distributed parameter treatment of the problem and the definite similarities existing between the solutions of the nonlinear and linearized equations. The work was a precursor of an investigation into the unstable behavior of externally pressurized gas bearings. The analytical phase of this investigation is now concluded and it is hoped that the experimental part will be completed before the end of this year.

[7] A. K. Oppenheim and E. G. Chilton, "Pulsating-Flow Measurement—A Literature Survey," TRANS. ASME, vol. 77, 1955, pp. 231–248.

Friction and Wear of Metals to 1000 C

E. P. KINGSBURY
E. RABINOWICZ

Department of Mechanical Engineering, Massachusetts Institute of Technology, Cambridge, Mass.

Sliding experiments using mainly the metals zinc, copper, titanium, and 1020 steel were carried out on a pin-on-disk friction apparatus incorporated in a metallurgical furnace. At room temperatures the results with steel, but not with the other metals, depended markedly on the atmospheric moisture content. As temperatures were raised to 400 C the friction and wear rate of the steel reached a maximum at 100 C and then diminished, while with the other metals the friction remained constant and the wear rate increased. These and other results are discussed in terms of the W/p ratio for the metals, W being the surface energy and p the hardness. It is postulated that materials with low W/p ratios should have favorable friction properties at high temperatures.

Introduction

THE evaluation of the frictional properties of materials at elevated temperatures, once a field of study of only mild academic interest, has recently become a subject of technological importance. High performance machinery like gas turbines contains bearings sliding at high environmental temperatures, and a severe design limitation is imposed by the need to keep the temperature of these bearings below the maximum effective temperature of available lubricants. In other applications high temperatures are produced by high sliding speeds, and again there are difficulties in providing suitable sliding conditions. Futhermore, it appears that each system yet evaluated is a special case so that it is difficult to find an over-all inclusive picture.

Hence in order to investigate frictional phenomena at elevated temperatures, an apparatus was constructed to measure friction and wear at temperatures to 1000 C.

The Friction Apparatus

Equipment previously described in the literature generally achieved elevated temperatures at the sliding interface by applying heat to one of the contacting specimens, thus heating the other by conduction across the interface [1].[1] Large thermal gradients and accompanying temperature uncertainties are consequently present while, owing to the large heat losses, maximum temperatures have been limited to 300 C. An alternative design permitted only limited loads and movements [2]. A more promising approach seemed to be to build a friction apparatus of a type frequently used for room temperature studies, but to enclose it in a metallurgical furnace to obtain good temperature control.

The friction part of the apparatus is quite similar to a design previously described [3], the latter in turn based upon a machine used by Bisson and co-workers [4]. The sliding geometry is the same as in the Bowden-Leben apparatus [1] and consists of a vertical rod, the "rider," axially loaded and sliding on a horizontal plate, the "flat." These sliding members may be of any material or combination of materials provided they are moderately rigid

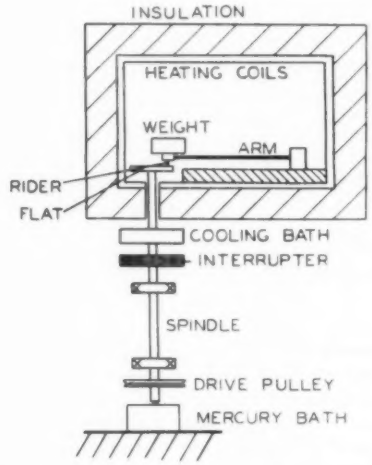

Fig. 1 Schematic drawing of the friction apparatus

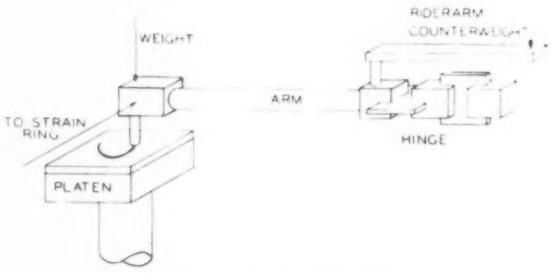

Fig. 2 Illustration of the sliding geometry

The normal force is provided by a dead weight supported on the rider, and the frictional force is measured as that lateral force which is required to keep the rider stationary when the flat is slid past it. Figs. 1 and 2 show the arrangement adopted. The flat is rotated on the end of a hollow spindle which extends downward through the bottom of the furnace to a variable speed drive. The rider is held vertical by a rider arm. The necessary movements of this arm, first a small vertical rotation to provide the normal load, and second a small horizontal rotation for friction force measurements, are allowed by two leaf springs mounted in the horizontal and vertical planes, or by equivalent

[1] Numbers in brackets designate References at end of paper.

Contributed by the Lubrication Division of THE AMERICAN SOCIETY OF MECHANICAL ENGINEERS and presented at the ASLE-ASME Lubrication Conference, Los Angeles, Calif., October 13–15, 1958.

NOTE: Statements and opinions advanced in papers are to be understood as individual expressions of their authors and not those of the Society. Manuscript received at ASME Headquarters, July 15, 1958. Paper No. 58—Lub-6.

mechanisms. The friction force is transmitted by a light rod fastened to the rider arm, passing through the furnace door to an aluminum strain ring, and measured with SR-4 gages. The output of this strain ring is connected to a recording potentiometer.

Temperatures inside the furnace are measured with two thermocouples. One is mounted inside the hollow spindle directly under the flat. Its signal is transmitted through a mercury bath slip ring to a potentiometer. The second couple is mounted through the furnace door in such a manner that when the door is closed the junction is suspended just above the flat. Various heating coils inside the furnace are independently supplied by variable transformers and adjusted so that the two thermocouples read the same temperature. Under these conditions the temperature uncertainties near the sliding interface are very small.

In operation the equipment has proved very flexible. It has been possible to hold the temperature at 68 C, just under the melting temperature of Wood's metal, yet other friction determinations have been made at temperatures up to 1000 C. The normal load is variable between 100 and 3000 g and the sliding velocity between 0.001 and 100 cm/sec.

Two quantities were measured in the tests, f the coefficient of friction and V_s the "specific wear." The latter is defined as the total volume of material lost from a specimen during a run of a given length under a given load, divided by that length and load. The units of V_s used here are $cm^3/cm\ kg$.

In some experiments it became evident that the absolute humidity of the test atmosphere played an important role in determining friction and wear. In order to study this effect more closely the apparatus was modified so that prehumidified air (at room temperature) could be continuously admitted to the region around the rubbing interface. The air was prepared by passing it through saturated solutions of various inorganic chemicals in water. Except for this, no effort to provide a controlled atmosphere was made in any of the tests.

Owing to the construction of the machine, two types of increasing temperature tests could be made. In the first, the rate of temperature increase was small compared to the rotation speed of the flat so that a point on the wear track passed many times under the rider. In the second, the rate of temperature increase was great compared to the rotation speed of the flat so that the thermal expansion of the rider support could be used as a radial feed. Thus a spiral wear track was generated, each point on the track passing only once under the rider.

It was decided to concentrate attention mainly on four metals: Copper, a low carbon steel (1020), zinc, and titanium. The steel and titanium were chosen because of their present and potential applicability at elevated temperatures, copper and zinc because of their use in previous friction studies. Surfaces were prepared by abrasion with suitable emery paper and then jarred to remove any loose abrasive particles.

Experimental Results

Initial experiments using steel specimens showed very irregular friction and wear results. It was found that changes in partial pressure of water vapor due to changes in the weather were affecting the tests. Hence a study of the effect of water vapor content of the atmosphere at room temperature was undertaken for three of the test metals. Results are shown in Figs. 3 and 4, which plot, respectively, friction coefficient and specific wear as a function of water partial pressure. It is seen that the only effect is on steel and that for this metal increased water content causes both the friction and wear to decrease, the latter by a factor of about seven from the driest obtainable conditions. Our results for the friction of steel and copper agree quite well

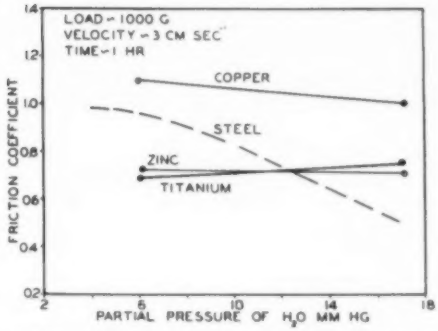

Fig. 3 Friction coefficients at room temperature as a function of atmospheric moisture

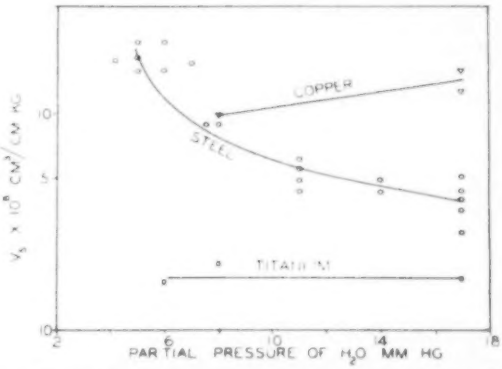

Fig. 4 Wear rates at room temperature as a function of atmospheric moisture

with those of Daniels and West [5] who investigated the effect of moisture on this property for these metals.

As the temperature was raised above 100 C, the effect of changes in moisture content seemed to become negligibly small. In Figs. 5 and 6 are plotted friction and specific wear for the test metals in the temperature range from 25 to 400 C. With the exception of steel, the friction remained nearly constant, but the wear increased. The steel showed irregular friction traces and decreasing wear at the higher temperatures.

Titanium with surfaces prepared at room temperatures is known to have very poor frictional properties, but experiments on titanium prepared by surface grinding suggested that a layer with better frictional properties might be formed at high temperatures [8]. To investigate this possibility, friction tests were run to 1000 C, making use of the single or multiple pass technique just described. Fig. 7 shows the results obtained. Up to about 700 C, the friction values are nearly the same; above that temperature, there is a marked difference, the multiple pass values being far lower.

Fig. 8 shows the friction as a function of temperature for copper sliding on aluminum. These metals form a eutectic at 548 C and the drop in friction at about this temperature is spectacular and in good agreement with the work of Umeda and Nakano [10] who investigated other eutectic-forming combinations. Eutectic-forming materials, however, cannot be used in their present form as high-temperature bearing combinations, because large scale melting occurs.

Discussion

Some interest attaches to the question of whether the increase

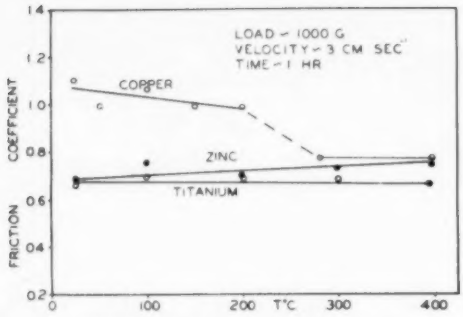

Fig. 5 Friction coefficients as a function of temperature. The values for steel were so erratic that they have been omitted.

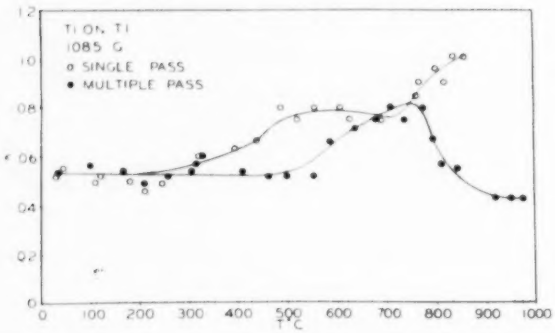

Fig. 7 Friction of titanium as a function of temperature. Note the difference at high temperatures between single-pass and multiple-pass conditions.

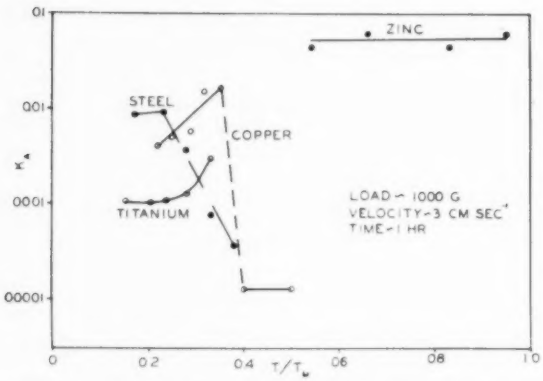

Fig. 9 Wear constant K plotted as a function of the ratio of the sliding temperature to the melting temperature

in wear rate shown in Fig. 6 results merely from thermal softening of the metals or from other causes. Fig. 9 plots the Archard [6] wear constant K (defined as

$$K = 3PV/Wl = 3PV,$$

where P is the hardness of the metal and V the volume removed under a normal load W and path length l) against T/T_m where T_m is the melting temperature of the metal. It will be seen that with the exception of steel above 100 C, the influence of temperature on the wear coefficient now becomes much smaller especially

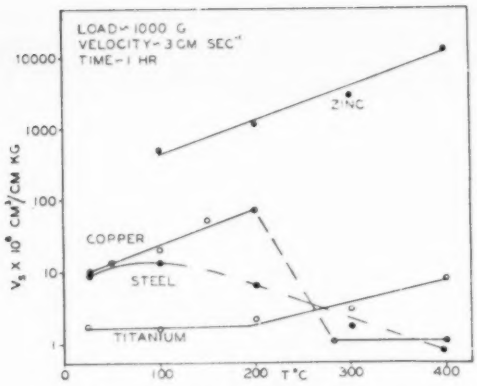

Fig. 6 Wear rates as a function of temperature

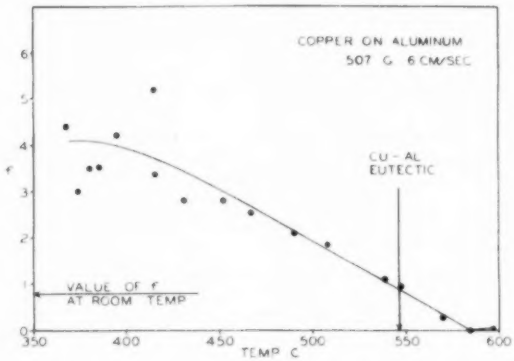

Fig. 8 Friction as a function of temperature for copper on aluminum. Note the sharp drop in friction near the eutectic temperature.

for zinc, for which tests were taken to within 20 C of its melting point. A similar conclusion has been reached by Lancaster [7] working with brass on tool steel.

The anomalous behavior of steel is perhaps due to the formation of a protective film derived from atmospheric water vapor as indicated in Figs. 3 and 4. This same type of behavior is seen also in Fig. 7 which contrasts the single-pass and multiple-pass tests for titanium. It would appear that the oxide layer formed on titanium at 700 C has favorable frictional properties, but that it is brittle if allowed to get too thick (c.f., Hanzel [9]). The layer is kept thin and effective when running over the same surface repeatedly, but becomes thick and brittle under single-pass conditions. Work on other materials (to be published) suggests that similar changes in sliding conditions due to changes in oxide composition, structure, and conformability are very commonly observed in sliding systems at elevated temperatures.

The independence of friction coefficient on temperature may be explained on the basis of the current theory of friction which states that the friction coefficient for two surfaces in sliding contact is s/p where s is the shear strength of the interface or of the weaker of the two materials and p is the flow pressure of the weaker material. Since f is the ratio of two similar material properties, the effect of temperature is canceled out.

This theory also suggests that friction coefficients should range from 0.5 for unlubricated surfaces to much lower values for surfaces lubricated by a low shear strength material.

However, much higher friction values, in the range 5 to 0.5, are readily observed for sliding metals, and associated with them

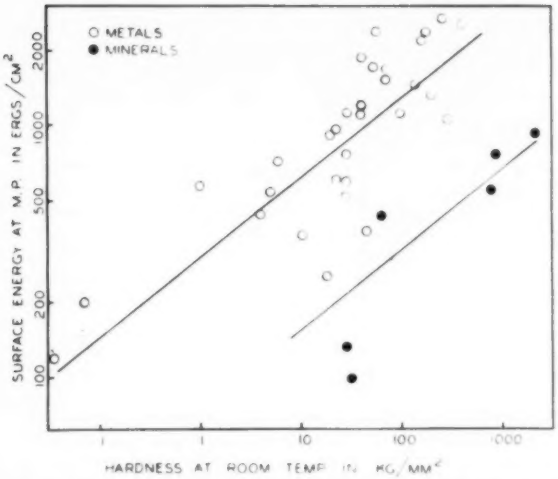

Fig. 10 Plot of surface tension as a function of hardness for the metals tabulated by Bondi [12] and Taylor [13], also a few nonmetals. The surface tensions increase as a low power (between 1/3 and 1/4) of the hardness.

are violent fluctuations of the instantaneous values of the friction force and greatly increased surface damage, metal transfer, and wear. This behavior, called "galling," results from the coagulation of individual metal junctions (diameter 10^{-3} cm) into superjunctions of diameter 10^{-2} to 10^{-1} cm or more, accompanied by a marked increase in the real area of contact.

In a recent paper [15] one of us has postulated that this coagulation occurs in systems with high values of W_{ab} cot θ/p, where W_{ab} is the adhesional energy and θ the average angle of roughness of the surfaces. From a published table of surface tensions of metals [12, 13] we may deduce that W for various metals varies as some low power of p, say $p^{1/4}$ (Fig. 10), so that we expect that softer metals gall more readily than harder ones. Of the four metals used in our tests, three, namely, zinc, copper, and titanium, appear to be well within the galling range when unlubricated. Only the steel, the hardest, is close to the limit. In dry atmosphere it galls, but the presence of moisture lowers the surface energy sufficiently (either by adsorption or through the formation of oxides) to bring the steel below the galling limit. Similar results were obtained by Daniels and West [5] who observed high friction not greatly reducible by moisture with the soft metals tin, aluminum, copper, and silver, but friction reducible by a factor of 2 in the presence of moisture with the harder iron, steel, nickel, and chromium.

When the temperature is raised the W/p ratio is increased, since W is nearly independent of temperature but p falls markedly, reaching 0 at the metal's melting point. Hence the tendency to galling becomes greater. This effect is resisted, however, by the greater oxidation-rate of metals at higher temperatures, which may lead to the formation of a low-surface energy oxide thus reducing W and preventing galling. In our experiments, this appears to have happened with the titanium above 700 C and the steel above 100 C. Sata [11] has made similar observations on steel.

This discussion suggests that good resistance to galling and hence favorable friction properties at high temperatures might be found among hard nonmetals, since these tend to have very low W/p ratios. We have been testing a few of these materials and they appear to have some merit and deserve further investigation.

Nonmetals, as is well known, have not been much used in moderate temperature sliding applications. The reason seems to be that, when a lubricant is present, it is helpful to use a material with high surface energy so that the energy of adhesion of the lubricant is high [14]. Only at high temperatures, when use of a lubricant becomes impossible, does this consideration lose its importance, and then the hard nonmetal seems to be the preferable material.

Acknowledgments

We should like to thank Prof. Brandon G. Rightmire for helpful discussions, and the office of Ordance Research for sponsorship of this work under Contract No. DA-19-020-ORD-3471.

References

1 F. P. Bowden and D. Tabor, "The Friction and Lubrication of Solids," Clarendon Press, Oxford, England, 1950, chapter 4.
2 F. P. Bowden and J. E. Young, "Friction of Diamond, Graphite, and Carbon, and the Influence of Surface Films," *Proceedings, Royal Society*, series A, vol. 208, 1951, pp. 444–455.
3 E. Rabinowicz, "The Boundary Friction of Very Well Lubricated Surfaces," *Lubrication Engineering*, vol. 10, 1954, pp. 205–208.
4 R. L. Johnson, M. A. Swikert, and E. E. Bisson, "Friction at High Sliding Velocities," NACA TN 1442, 1947.
5 R. O. Daniels and A. C. West, "The Influence of Moisture on the Friction and Surface Damage of Clean Metals," *Lubrication Engineering*, vol. 11, 1955, p. 261.
6 J. F. Archard, "Contact and Rubbing of Flat Surfaces," *Journal of Applied Physics*, vol. 24, 1953, pp. 981–988.
7 J. K. Lancaster, "The Influence of Temperature on Metallic Wear," *Proceedings, Physical Society*, section B, vol. 70, 1957, pp. 112–118.
8 E. Rabinowicz, "The Frictional Properties of Titanium," Annual Progress Report to Bureau of Aeronautics, U. S. Navy, Project NO as 51-1185, 1952.
9 R. W. Hansel, "Surface Hardening Processes for Titanium and Its Alloys," *Metal Progress*, vol. 65, no. 3, 1954, pp. 89–96.
10 K. Umeda and Y. Nakano, "Solid-Solubility Effect of Metallic Surface Friction," *Physical Review*, vol. 75, 1949, p. 1621.
11 T. Sata, "Thermal Effects on Metal Wear," Proceedings, Third Japan Congress of Applied Mechanics, pp. 153–156.
12 A. Bondi, "The Spreading of Liquid Metals on Solid Surfaces," *Chemical Review*, vol. 52, 1953, pp. 417–485.
13 J. W. Taylor, "Estimation of Some Unknown Surface Tensions for Metals," *Metallurgia*, vol. 50, 1954, pp. 161–165.
14 E. P. Kingsbury, "Some Aspects of the Thermal Desorption of a Boundary Lubricant," *Journal of Applied Physics*, vol. 29, 1958, pp. 888–891.
15 E. Rabinowicz, "Theoretical Criteria for the Effectiveness of a Lubricant Film," *Trans. ASLE*, vol. 1, 1958, pp. 96–100.

DISCUSSION

M. Godet[2]

The importance and timeliness of the study undertaken by the authors is such that it is useless to elaborate on that point. The need for information in this field exists and it is indeed gratifying to see that the problem is being investigated by men who have already contributed enormously in closely related fields.

Needless to say, industry is keenly interested in high-temperature lubrication and has already under development lubricants which will operate up to 400 C (i.e., polyphenyl ethers). The dry friction data obtained at even higher temperatures presented in this paper provide useful information for further lubrication developments.

The friction apparatus just described is certainly simple and versatile, and should be able to lend itself to the study of very many parameters, the most important of which have been investigated in this paper. However, in fully evaluating the data presented here it is regrettable that, in their efforts to present a concise paper incorporating a thorough discussion, the authors could only lightly touch upon the description of the apparatus and hardly elaborate on the experimental techniques followed.

[2] Shell Development Company, Emeryville, Calif.

Necessarily any measurement of wear is arbitrary and correlation between different studies can be attempted only if the experiments are explained in the greatest detail. The relative effect of different kinds of wear, such as wear by abrasion, scoring, or chemical action is also of interest to the reader, and any attempt to define and evaluate them would be very helpful.

Some information about the surfaces before and after the experiment would be valuable in attempting to assess the importance of surface finish on wear.

Changes in atmospheric conditions have a marked effect on the coefficient of friction and wear. In noting this phenomenon, the authors substantiate results obtained by others (Cocks, ASLE, vol. 1, no. 1) who showed in a setup which is similar to the one used here that the introduction of an inert gas in the experimental chamber leads to very large and highly erratic values for the forces required to overcome friction. This suggests that the oxide coating which is allowed to build up in the presence of oxygen is material in preventing the stick-slip action often encountered between two metal surfaces rubbing against one another.

This simple observation in itself leads to a very wide investigation program in which various metals with differing surface activities could be studied for friction and wear. Consequently, it would be interesting to investigate at elevated temperatures the difference between the behavior of ironlike metals which can undergo a volume-type corrosion with aluminum-type metals which only undergo surface corrosion. The authors have insisted on the importance of the oxide film on frictional effects and information about the thickness, the rate of build-up of these oxide layers would be of help to assess the mechanism under study. Proceeding along these lines, the authors have in the ingenious single-pass and multipass device showed that a new surface at high temperature gives a higher coefficient of friction than a surface which has already been traveled and "run in," due, according to them, to the presence in the single-pass case of a brittle thick layer as opposed to the presence in the multipass case of a thin and effective coating. This leads us to believe that there is an optimum oxide-film thickness under a given set of conditions which would give a minimum coefficient of friction and minimum wear. It would, of course, be of great value to find out whether, as in the case of E.P. lubricants, the oxide films are constantly reformed and attrited or whether the same oxide film is kept pliable by repeated passage of the rider on the flat. Possibly the use of radioactive tracing techniques could be of help here. Should the surfaces be renewed and destroyed, information about the build-up rate of the oxide could be obtained by varying the speed of rotation of the flat.

The discussion of the rate of build-up of oxides on metal surfaces leads one to the study of the surface energy of various metals, a field in which the authors have contributed immensely. As certainly the ability of a metal particle to change its shape is proportional to its surface energy W and inversely proportional to its flow (or deformation) pressure p, it would be desirable to obtain metals with low values of W/p resisting in the manner any tendency the metal particles might have to gather and cause galling, which is responsible for dramatic increases in wear.

Here the use of nonmetals with low W/p values announced by the authors appears very promising and it is hoped that further information on the subject will be available very soon.

Carl Goodzeit[3]

This discussion will be limited to one particular area of this paper, one that is important from a practical standpoint—seizure or galling between sliding surfaces.

Whether at high or low temperature, the principles underlying the mechanism of galling are the same. That is, galling occurs when the junction formed at the real area of contact between sliding surfaces becomes stronger than the base materials. The strength of such junctions depends principally on the area of the junction and, equally as important, on the adhesive strength of the material in contact at the junctions. We have concluded from theory as well as from many tests with different combinations of metals that dissimilar materials tend to resist galling while similar materials promote this. Thus we have generally concluded that the first thing to do in a seizure situation is not to use similar materials.

We have found that weak intermetallic junctions are associated with metal pairs that do not alloy by virtue of their dissimilarity in atomic size, crystal structure, and bond type. On this basis, we can also conclude that galling at high temperature can be avoided through the use of dissimilar metals with sufficient strength and corrosion resistance at operating temperature.

Thus the writer would like to ask the authors if they would care to comment on how the dissimilarity of a pair of sliding materials would effect galling according to the criterion for the coagulation of metal junctions presented in this paper.

[3] Senior Research Engineer, Research Laboratories, General Motors Corporation, Detroit, Mich. Assoc. Mem. ASME.

Authors' Closure

The discussions of Dr. Godet and Dr. Goodzeit are much appreciated. In answer to Dr. Godet, we wish to state that the reason for not elaborating the condition of the surfaces before the tests is our feeling that the initial conditions, whatever they might be, would not persist under repeated traverses of the surfaces. Eventually an equilibrium surface configuration is arrived at, determined by the sliding conditions themselves but not by the initial surface conditions. By making each test of sufficient length (about 1 hr), we ensure that most of the running time is spent under the equilibrium conditions. The difficulties with steel, which are several times referred to in the paper, arise precisely from this point, that, in the middle of a test (say, about 20 min of running time), the sliding conditions would change from high friction, high wear to low friction, low wear. This behavior was only encountered with the steel; with the other metals, equilibrium conditions were reached after about 1 min. No really satisfactory explanation for this difference in behavior occurs to us.

In answer to Dr. Goodzeit, we agree entirely that metal pairs which do not alloy are much less likely to seize than are metal pairs which do alloy. Indeed, the experimental work of Dr. Goodzeit and his colleagues is conclusive proof of this fact. When considering metals of similar hardness, this alloying criterion is a very valuable one. It is our feeling that the reason the criterion "works" is the fact that metal pairs which do alloy are likely to have larger energies of adhesion than metal pairs which do not. Thus the influence on our W factor is direct.

However, the alloying criterion is not entirely satisfactory in that it omits the important factor of hardness. Thus indium, the softest metal stable in air, galls readily when slid against other clean metals, whether or not they are similar in atomic size, crystal structure, or bond type. This cannot be readily explained using the alloying criterion but, using the W/p criterion, we would argue that it was because the surface tension of indium is relatively high (and hence the energy of adhesion of indium against other metals is also relatively high), but p for indium is very low, so that when indium is slid against other metals galling takes place because of the high W/p ratio.

Friction Factors for Turbulent Flow in Curved Pipes

H. ITŌ

Assistant Professor of the Institute of High Speed Mechanics, Tohoku University, Sendai, Japan

The object of this paper is to furnish the engineer with reliable data on the friction factors to be used in computing the pressure losses for turbulent flow in smooth curved pipes. The empirical formulas proposed, backed by theoretical considerations, appear to define the influence of curvature upon the law of resistance with satisfactory accuracy.

Introduction

THE PROBLEM of the determination of the law of resistance for turbulent flow through straight pipes has been the subject of many exhaustive investigations. Comparatively few records are available, however, with regard to the influence of curvature, especially for turbulent flow.

Such curved pipes are largely used in heating and refrigeration in order to transfer heat from one fluid to another, and the clarification of the law of resistance offers an important indication in deciding the pressure required to obtain the necessary circulation and the rate of heat transfer for a given circulation.

In curved pipes there exists a secondary flow by the action of a centrifugal force, and it has attracted the attention of many investigators. Unfortunately, these researches [1–13][1] are confined mainly to the case of laminar flow. For the case of turbulent flow, the chief interest of the hydraulic engineer, no theoretical investigations have been published about the law of resistance, and comparatively few experimental records [6, 7, 9, and 10] are available, so far as the author is aware.

Recently, Hawthorne [14] and Detra [15] analyzed the secondary flow in curved pipes. However, since both of them are grounded on the inviscid-fluid theory, they have nothing to contribute to the clarification of the law of resistance which is the main subject of the present investigation.

It is the purpose of this paper to present results of measurements on the frictional resistance for turbulent flow through curved pipes, and further to furnish empirical formulas which express the friction factors for turbulent flow through curved pipes with satisfactory accuracy.

[1] Numbers in brackets designate References at end of paper.

Contributed by the Fluid Mechanics Subcommittee of the Hydraulics Division and presented at the Semi-Annual Meeting, Detroit, Mich., June 15–19, 1958, of THE AMERICAN SOCIETY OF MECHANICAL ENGINEERS.

NOTE: Statements and opinions advanced in papers are to be understood as individual expressions of their authors and not those of the Society. Manuscript received at ASME Headquarters, February 21, 1958. Paper No. 58—SA-14.

Table 1 Dimensions of curved pipes which were tested

Curved pipe no.	ID, $2r_0$, cm	Radius of curvature, R, cm	Radius ratio, R/r_0
1	1.604	520.0	648
2	1.604	200.0	250
3	1.596	80.37	100
4	3.491	69.72	40.0
5	1.577	12.90	16.4

Experimental Apparatus

All the experimental pipes used to measure the friction factors were of smooth, drawn-copper tubing, specially selected for straightness and uniformity of their bores. The dimensions of curved pipes tested are found in Table 1. The arrangement of experimental apparatus is illustrated in Fig. 1. The water, led

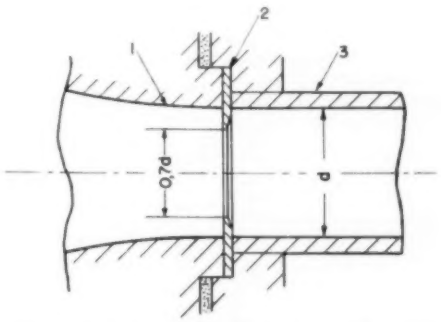

Fig. 2 Thin-plate orifice used to impose disturbed conditions at entry and its arrangements: 1 Bell-mouth entrance, 2 thin-plate orifice, 3 upstream tangent (drawn-copper tubing)

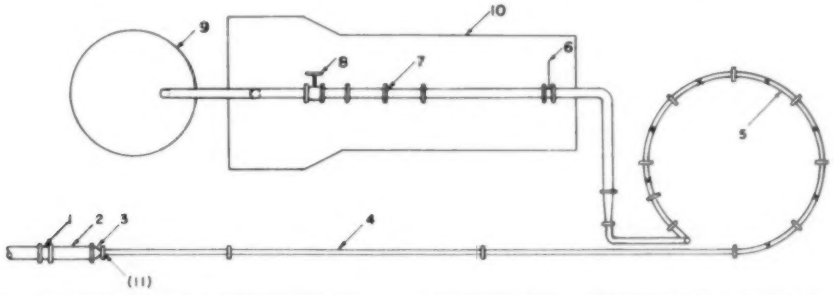

Fig. 1 Arrangement of experimental apparatus: 1 Honeycomb flow straightener, 2 3-in. pipe, 3 bell-mouth entrance, 4 upstream tangent (drawn-copper tubing same as 5), 5 curved pipe (drawn-copper tubing), 6 thermometer, 7 orifice meter, 8 valve, 9 weighing tank, 10 triangular weir with a vertex angle 90 deg, 11 thin-plate orifice to impose disturbed conditions, X piezometers

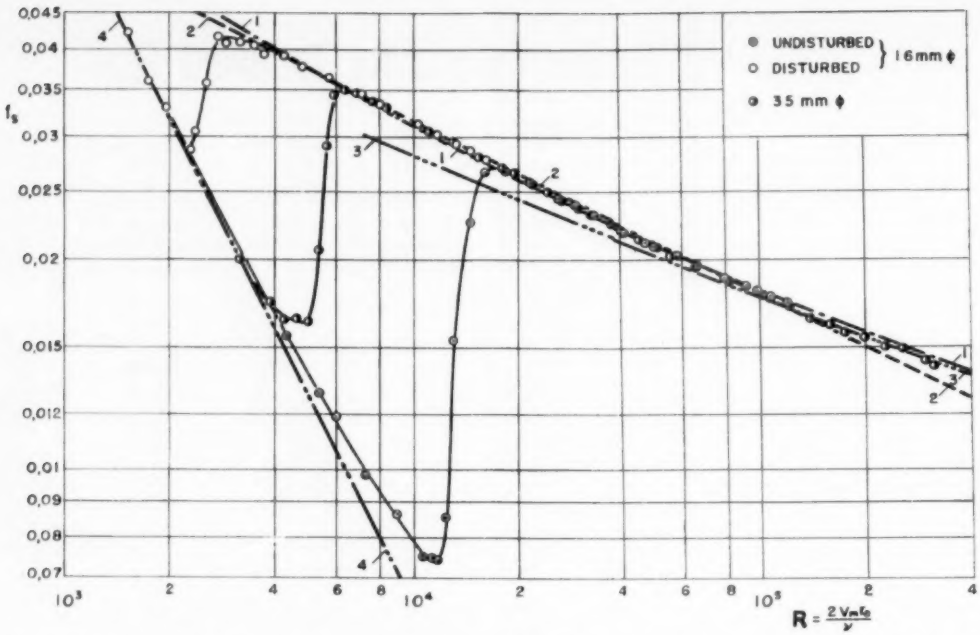

Fig. 3 Friction factors for the straight, drawn-copper pipes used in the tests: 1 Logarithmic resistance formula, 2 Blasius' resistance formula, 3 Nikuradse's resistance formula, 4 Hagen-Poiseuille law

from a surge tank or from a constant-level tank, after passing through the "honeycomb" flow straightener and the bell-mouth entrance, enters the experimental pipe. The axial length of the curved pipe was determined to be sufficiently long so that together with the long upstream tangent the entrance effects might be completely eliminated within the testing length of the pipe. In cases where pipes of 16-mm ID were used, the measured critical Reynolds number was unusually high. In such cases experiments were also conducted for the disturbed conditions at entry to the straight pipe. The plate used to introduce disturbances has a form similar to that of a thin-plate orifice. Its dimensions and arrangements are seen in Fig. 2.

The friction factors f_s for the straight, drawn-copper pipes used in the tests are shown plotted against the Reynolds number in Fig. 3. The measured results are in close agreement with the resistance formulas [16–18] for smooth straight pipes.

Friction Factors for Fully Developed Flow in Curved Pipes

The friction factor of a curved pipe, denoted by f_c, is defined by the equation

$$h = f_c \frac{l_c}{d} \frac{v_m^2}{2g} \tag{1}$$

in which h is the loss of head in friction, l_c and d the axial length and internal diameter of the curved pipe, v_m the mean velocity of flow, and g the acceleration of gravity.

The measured friction factors of the fully developed flow in curved pipes are shown in Fig. 4. With regard to the friction factors of turbulent flow, the measured results for pipe No. 1, which has the largest radius of curvature in our experimental pipes, practically coincide with the Blasius formula for the lower Reynolds numbers. While for pipe No. 5, where the radius of curvature is the smallest, a considerable increase in resistance is observed.

The ratio of the friction factor of a curved pipe to that of a straight pipe in the case of laminar flow is expressed in Fig. 5 in ordinary manner [6 and 9] as a function of the Dean number $\mathbf{R}(r_0/R)^{1/2}$ where r_0 is the radius of the cross section, R the radius of curvature of pipe axis, and $\mathbf{R}$ the Reynolds number $2v_m r_0/\nu$ (ν being the kinematic viscosity of the fluid). In Fig. 5 the results of the previous experimenters [6, 9, 10] are included together with the empirical formulas [6, 9, and 19] for laminar flow. These results may be expressed in a somewhat different form: In Fig. 6, $f_c(R/r_0)^{1/2}$ is expressed as a function of the Dean number $\mathbf{R}(r_0/R)^{1/2}$, which, being referred to Figs. 7 and 8, seems to be the more comprehensible presentation than in the former case.

Resistance Formulas for Fully Developed Turbulent Flow in Smooth Curved Pipes

Resistance Formula for Turbulent Flow Deduced From the $^1/_7$th-Power Velocity Distribution Law. The experimental results of the author are plotted in Fig. 7, together with those of the previous investigators [6, 9, 10, 20, and 21], as a function of the nondimensional number $\mathbf{R}(r_0/R)^2$. Although the radius ratios of the curved pipes in these experiments differ widely, all the experimental results conform satisfactorily to a single curve for fully developed turbulent flow. The following empirical formula was deduced from the experimental results

$$f_c\left(\frac{R}{r_0}\right)^{1/2} = 0.029 + 0.304[\mathbf{R}(r_0/R)^2]^{-0.25} \tag{2}$$

This equation gives good agreement with experimental results in the range

$$300 > \mathbf{R}(r_0/R)^2 > 0.034$$

Below $\mathbf{R}(r_0/R)^2 = 0.034$, the friction factor of a curved pipe practically coincides with that of a straight pipe.

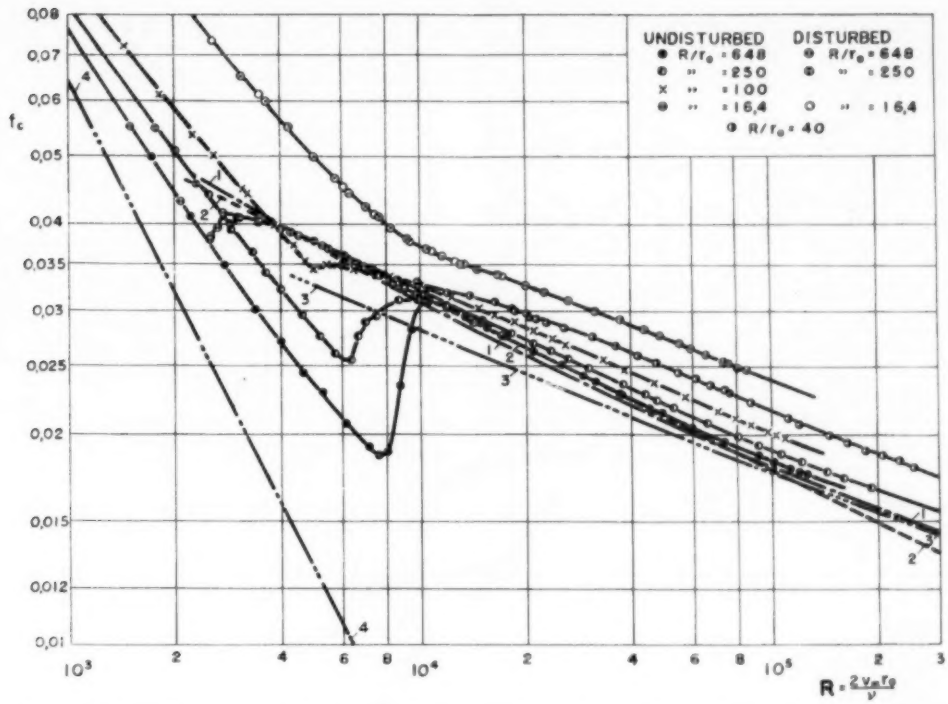

Fig. 4 Friction factors for curved pipes: 1 Logarithmic resistance formula, 2 Blasius' resistance formula, 3 Nikuradse's resistance formula, 4 Hagen-Poiseuille law

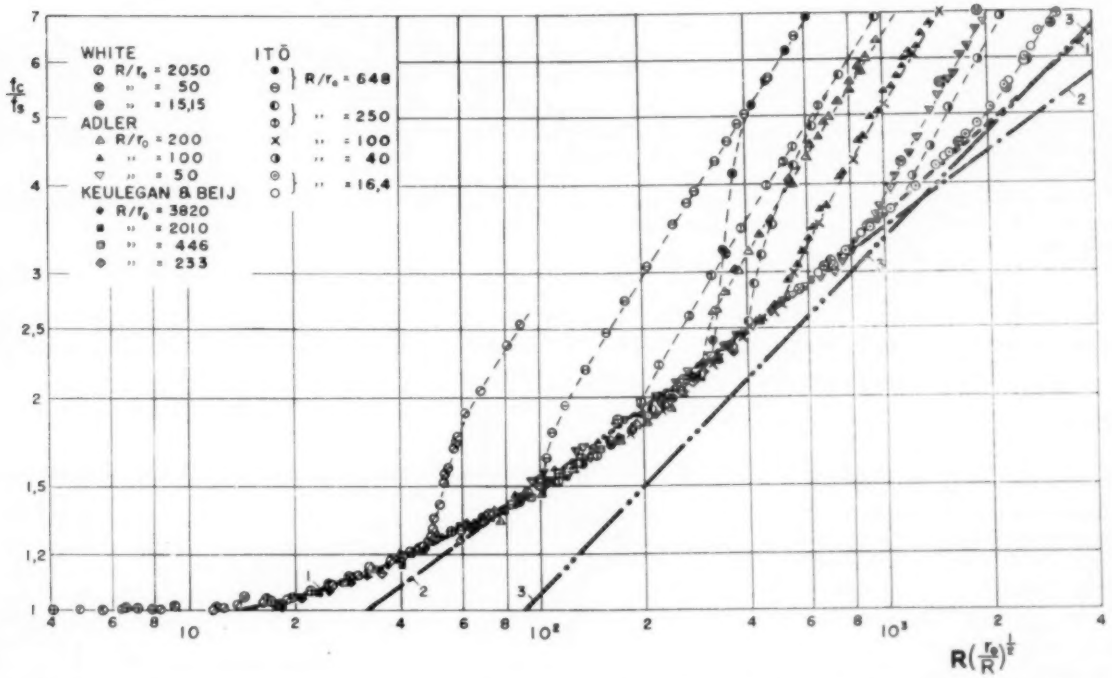

Fig. 5 Friction factor for laminar flow in curved pipes as a function of the Dean number, $R(r_0/R)^{1/2}$: 1 White's empirical formula, 2 Prandtl's empirical formula, 3 Adler's theoretical formula

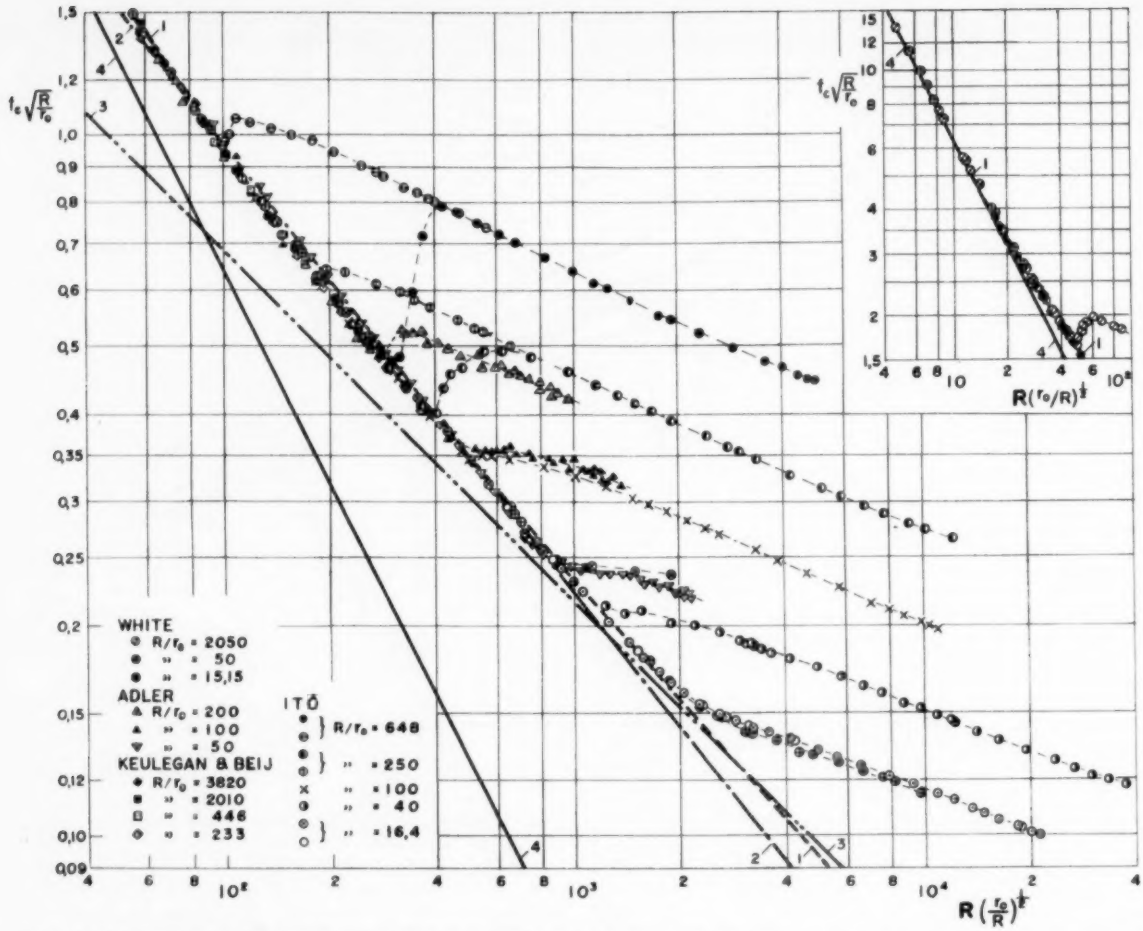

Fig. 6 Friction factor for laminar flow in curved pipes as a function of the Dean number, $R(r_0/R)^{1/2}$: 1 White's empirical formula, 2 Prandtl's empirical formula, 3 Adler's theoretical formula, 4 Hagen-Poiseuille law

For large values of $R(r_0/R)^2$ the following empirical formula was deduced, and it may be used for values of the parameter $R(r_0/R)^2$ exceeding 6.

$$f_c\left(\frac{R}{r_0}\right)^{1/2} = \frac{0.316}{[R(r_0/R)^2]^{1/4}} \tag{3}$$

By making use of the Blasius formula

$$f_s = 0.316R^{-1/4} \tag{4}$$

the equation (3) may be expressed in an alternative form

$$\frac{f_c}{f_s} = 1.00\left[R\left(\frac{r_0}{R}\right)^2\right]^{1/20} \tag{5}$$

Resistance Formula for Turbulent Flow Deduced From the Logarithmic Velocity-Distribution Law. The experimental results were plotted in Fig. 8 as a function of the nondimensional number $Y^2(r_0/R)^{1/2}$ where Y is defined by the equation

$$Y^2e^Y = R(R/r_0)^{1/2} \tag{6}$$

In Fig. 8 the experimental results of the previous investigators were included for comparison. In this case, too, all the experimental results conform satisfactorily to a single curve for fully developed turbulent flow. The following empirical formula was deduced from the experimental results and it may be used for values of the parameter $Y^2(r_0/R)^{1/2}$ less than 12

$$f_c\left(\frac{R}{r_0}\right)^{1/2} = 0.0323 + 1.6[Y^2(r_0/R)^{1/2}]^{-1.27} \tag{7}$$

For large values of $Y^2(r_0/R)^{1/2}$ the following empirical formula was deduced from the experiments and holds with sufficient accuracy for values of $Y^2(r_0/R)^{1/2}$ greater than 5.3

$$f_c = \frac{1.186}{Y^2} \tag{8}$$

Eliminating Y from (6) and (8), the equation (8) may be expressed in an alternative form

$$\frac{1}{f_c^{1/2}} = 2.11\log_{10}\left[R\left(\frac{R}{r_0}\right)^{1/2} f_c^{1/2}\right] - 0.23 \tag{9}$$

The empirical formula (9) is also found as follows: According to equation (9) the law of friction of a curved pipe should give a straight line if $1/(f_c)^{1/2}$ is plotted against $\log_{10}\left[R\left(\frac{R}{r_0}\right)^{1/2} f_c^{1/2}\right]$. This was done and, as seen from Fig. 9, where the results of measurements were plotted, this feature agrees extremely well with

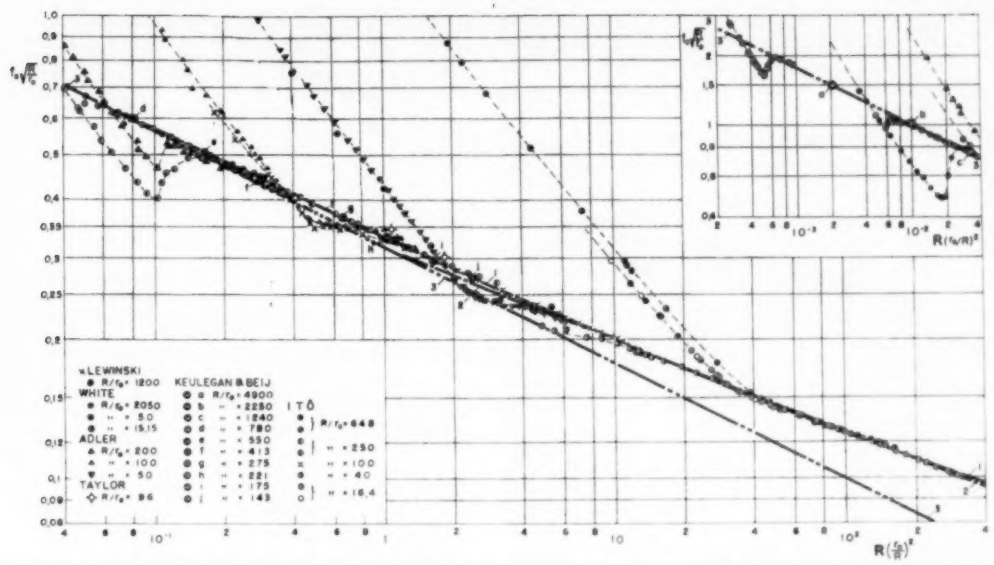

Fig. 7 Friction factor for turbulent flow in curved pipes as a function of the nondimensional number, $R(r_0/R)^2$: 1 Equation (2), 2 equation (3) or (5), 3 Blasius' resistance formula

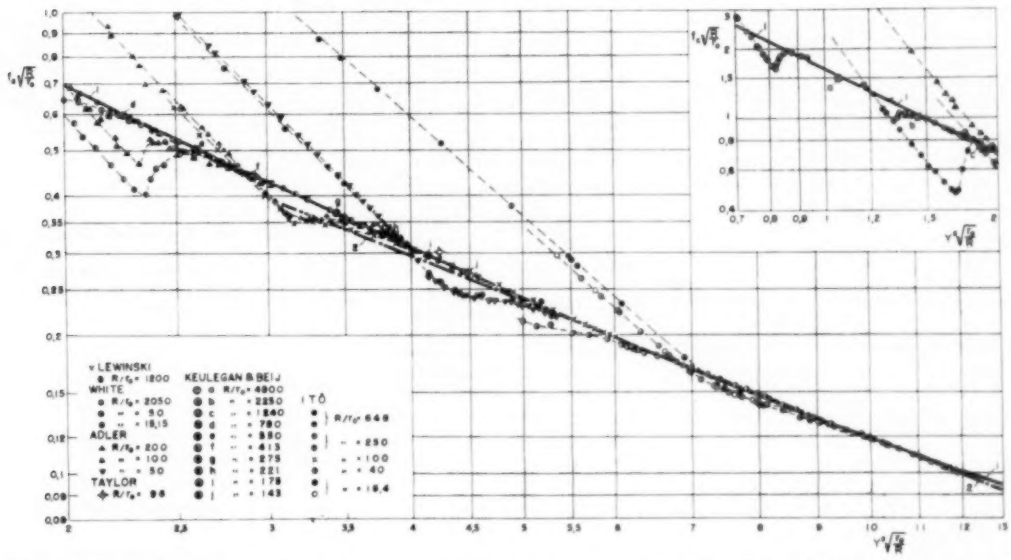

Fig. 8 Friction factor for turbulent flow in curved pipes as a function of the nondimensional number, $Y^2(r_0/R)^{1/2}$: 1 Equation (7), 2 equation (8) or (9)

experiments on curved pipes whose radius ratio is less than 50.

The Transition From Laminar to Turbulent Flow

The critical Reynolds numbers obtained in the present investigation are shown in Fig. 10 together with those obtained by previous investigators [6, 9, 10, and 22], as a function of the Dean number at transition point. There seems to be a lower critical Reynolds number for a curved pipe, which starts at about 2.3×10^2 for zero Dean number (straight pipe) and increases as the critical Dean number increases. The measured results are approximated by the following empirical equation

$$\mathbf{R}_{crit} = 420[\mathbf{R}(r_0/R)^{1/2}]^{0.33} \tag{10}$$

This equation is rewritten in a more convenient form

$$\mathbf{R}_{crit} = 2\left(\frac{r_0}{R}\right)^{0.33} \times 10^4 \tag{11}$$

This equation gives good agreement with experimental results in the range

$$15 < R/r_0 < 8.6 \times 10^2$$

For $R/r_0 > 8.6 \times 10^2$, the critical Reynolds number for a curved

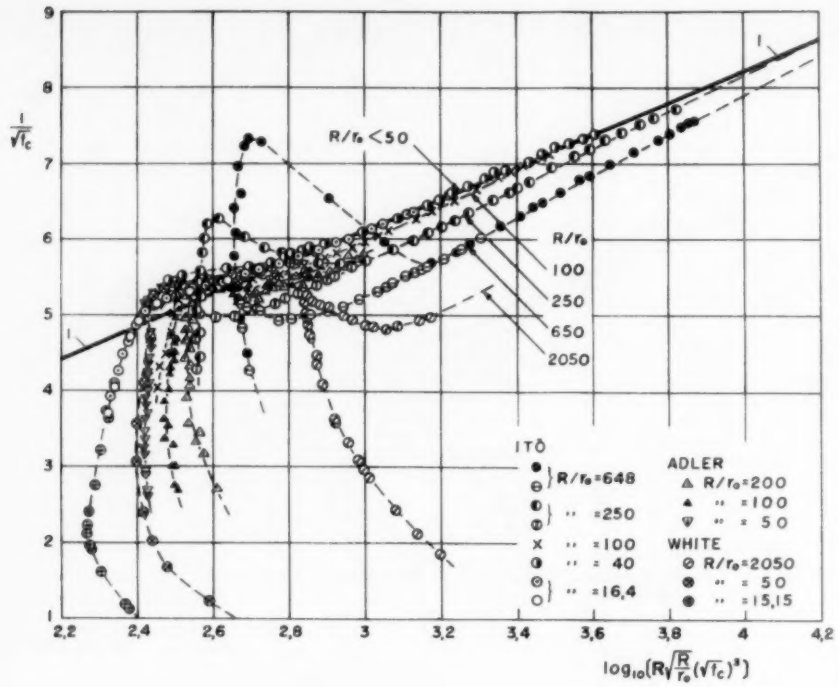

Fig. 9 Logarithmic representation of the friction factor for curved pipes. The straight line, 1, represents equation (9), while steep experimental curves represent laminar flow region.

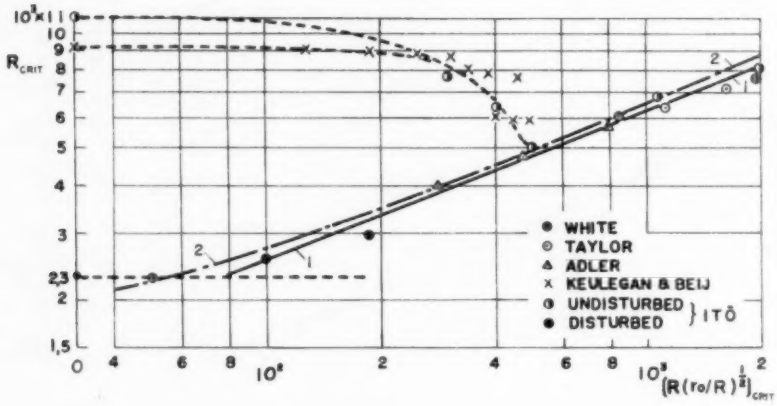

Fig. 10 Critical Reynolds number for curved pipes as a function of the critical Dean number: 1 Equation (11), 2 White's empirical equation ($f_c = 0.036$)

pipe practically coincides with that for a straight pipe. Equation (11) may be used to estimate a lower critical Reynolds number for a curved pipe.

Acknowledgments

In concluding this paper, the author wishes to express his thanks to Prof. F. Numachi, Director of the Institute, for his kind advice in the course of this work. The author also wishes to acknowledge his indebtness to Mr. K. Imai, Assistant, who aided him in the experimental work.

References

1 J. H. Grindley and A. H. Gibson, "On the Frictional Resistance to the Flow of Air Through a Pipe," *Proceedings of the Royal Society (London)*, ser. A, vol. 80, 1908, pp. 114–139.

2 J. Eustice, "Flow of Water in Curved Pipes," *Proceedings of the Royal Society (London)*, ser. A, vol. 84, 1910, pp. 107–118.

3 J. Eustice, "Experiments on Stream-Line Motion in Curved Pipes," *Proceedings of the Royal Society (London)*, ser. A, vol. 85, 1911, pp. 119–131.

4 W. R. Dean, "Note on the Motion of Fluid in a Curved Pipe," *The London, Edinburgh & Dublin Philosophical Magazine and Journal of Science*, vol. 4, 1927, pp. 208–223.

5 W. R. Dean, "The Stream-Line Motion of Fluid in a Curved Pipe," *The London, Edinburgh & Dublin Philosophical Magazine and Journal of Science*, vol. 5, 1928, pp. 673–695.

6 C. M. White, "Streamline Flow Through Curved Pipes," *Proceedings of the Royal Society (London)*, ser. A, vol. 123, 1929, pp. 645–663.

7 K. Tomita, "On the Flow of Water in Coiled Pipes," *Journal of the Japan Society of Mechanical Engineers*, vol. 35, 1932, pp. 293–304.

8 O. Miyagi, "Flow in a Curved Pipe and Its Stability," *Journal of the Japan Society of Mechanical Engineers*, vol. 35, 1932, pp. 1121–1124.

9 M. Adler, "Strömung in gekrümmten Rohren," *Zeitschrift für angewandte Mathematik und Mechanik*, vol. 14, 1934, pp. 257–275.

10 G. H. Keulegan and K. H. Beij, "Pressure Losses for Fluid Flow in Curved Pipes," *Journal of Research, National Bureau of Standards*, vol. 18, 1937, pp. 89–114.

11 F. Kitō, "On Secondary Vortex Generated in a Bent-Pipe of Elliptical Cross Section," *Journal of the Japan Society of Applied Mechanics*, vol. 3, 1950, pp. 73–75.
12 H. Itō, "Theory on Laminar Flows Through Curved Pipes of Elliptic and Rectangular Cross Sections," *Reports of the Institute of High Speed Mechanics, Tōhoku University*, vol. 1, 1951, pp. 1–16.
13 H. G. Cuming, "The Secondary Flow in Curved Pipes," Aeronautical Research Council, Reports and Memoranda, No. 2880, 1955.
14 W. R. Hawthorne, "Secondary Circulation in Fluid Flow," *Proceedings of the Royal Society (London)*, ser. A, vol. 206, 1951, pp. 374–387.
15 R. W. Detra, "The Secondary Flow in Curved Pipes," *Mitteilungen aus dem Institut für Aerodynamik, E.T.H. Zürich*, Nr. 20, 1953.
16 H. Blasius, "Das Ähnlichkeitsgesetz bei Riebungsvorgängen in Flüssigkeiten," Forschungsheft 131, 1913.
17 L. Prandtl, "Neuere Ergebnisse der Turbulenzforschung," *Zeitschrift des Vereines Deutscher Ingenieure*, vol. 77, 1933, pp. 105–114.
18 J. Nikuradse, "Gesetzmässigkeiten der turbulenten Strömung in glatten Rohren," Forschungsheft 356, 1932.
19 H. Schlichting, "Boundary Layer Theory," Translated by J. Kestin, Pergamon Press, London, England, 1955, p. 427.
20 D. Thoma, "Der hydraulische Verlust in Form-Stücken," The Transactions of the Tokyo Sectional Meeting, World Power Conference, Tokyo, Japan, 1929, vol. 2, p. 461.
21 Sir Geoffrey Taylor, "The Dispersion of Matter in Turbulent Flow Through a Pipe," *Proceedings of the Royal Society (London)*, ser. A, vol. 223, 1954, pp. 446–468.
22 G. I. Taylor, "The Criterion for Turbulence in Curved Pipes," *Proceedings of the Royal Society (London)*, ser. A, vol. 124, 1929, pp. 243–249.
23 G. S. Williams, C. W. Hubbell, and G. H. Fenkell, "Experiments at Detroit, Mich., on the Effect of Curvature Upon the Flow of Water in Pipes," *Trans. ASCE*, vol. 47, 1902, pp. 1–369.
24 J. R. Weske, "Investigations of the Flow in Curved Ducts at Large Reynolds Numbers," *Journal of Applied Mechanics*, vol. 15, TRANS. ASME, vol. 70, 1948, pp. 344–348.
25 H. Itō, "On the Pressure Losses for Turbulent Flow in Smooth Pipe Bends," *Reports of the Institute of High Speed Mechanics, Tōhoku University*, vol. 6, 1956, pp. 55–102.
26 H. Itō, "On the Pressure Loss of Turbulent Flow Through Curved Pipes," *The Memoirs of the Institute of High Speed Mechanics, Tōhoku University*, vol. 7, 1952, pp. 63–76.

APPENDIX

An approximate analysis based on the concept of a shedding layer will be presented. The results, although of asymptotic character for large values of variables, will serve in some respects for the interpretation of the tests.

Nomenclature

The following nomenclature is used in the appendix:

p = static pressure
r = radial distance from the center of circular cross section of the pipe
r_0 = radius of circular cross section of pipe
R = radius of curvature of pipe axis
$\mathbf{R}$ = $2v_m r_0/\nu$, Reynolds number
v_m = mean axial velocity
v_ψ, v_φ = velocity components in the shedding layer
v_* = $(\tau_w/\rho)^{1/2}$, friction velocity formed with the wall shearing stress τ_w
δ = thickness of shedding layer
f_c = friction factor for a curved pipe
ν = kinematic viscosity of the fluid
ξ = $r_0 - r$, distance normal to wall
ρ = mass density of the fluid
τ_w = shearing stress at pipe wall
τ_ψ, τ_φ = components of the wall shearing stress τ_w
φ = angle measured in the plane of the curved-pipe axis
ψ = angle in transverse plane with respect to outward direction of symmetry line

Subscripts

1 = values at the edge of the shedding layer
ψ = values in ψ-direction
φ = values in φ-direction

Asymptotic Expression for Friction Factors Deduced From the 1/7th-Power Velocity Distribution Law

Experimental measurements[2] show that, if the curvature is marked, the distribution of velocity in a pipe is entirely altered by the secondary flow, the greatest axial velocity being near the outside wall; the secondary flow takes place chiefly in a sort of boundary layer in the regions near the walls. This layer is called shedding layer.[3] The thickness of the shedding layer is defined to be equal to the distance from the wall to the point where the peripheral velocity component changes its sense, hence[4]

$$v_{\varphi 1} = 0, \quad v_\varphi > 0 \quad \text{for} \quad \xi < \delta, \quad v_\varphi < 0 \quad \text{for} \quad \xi > \delta \tag{12}$$

The thickness of the shedding layer is assumed to be smal compared with the radius of the pipe. Variations of the static pressure within the layer normal to the wall are neglected. It is assumed that the fluid is incompressible and that the curvature of the pipe is small, that is, r_0/R is small. The momentum integral equations for the shedding layer[5] are, since $v_{\varphi 1} = 0$,

$$\rho \frac{\partial}{\partial \psi} \int_0^\delta v_\psi^2 d\xi = -\tau_\psi r_0 + \rho \frac{\delta r_0}{R} v_{\varphi 1}^2 \sin \psi - \rho \frac{r_0}{R} \sin \psi \int_0^\delta v_\varphi^2 d\xi \tag{13}$$

$$\rho \left[\frac{\partial}{\partial \psi} \int_0^\delta v_\varphi r_\varphi d\xi - v_{\varphi 1} \frac{\partial}{\partial \psi} \int_0^\delta v_\psi d\xi \right] = -\tau_\varphi r_0 - \frac{\delta r_0}{R} \frac{\partial p}{\partial \varphi} \tag{14}$$

where

$$\frac{\partial p}{\partial \varphi} = -\frac{2R}{\pi r_0} \int_0^\pi \tau_\varphi R d\psi \tag{15}$$

changes of the pattern of flow along the axis of the pipe being disregarded.

To make use of equations (13) and (14), velocity distributions are assumed for v_φ and v_ψ normal to the wall. On the assumption that it is sufficiently accurate to take the velocity component v_φ to be proportional to $\xi^{1/7}$ throughout the shedding layer, we assume that

$$v_\varphi = v_{\varphi 1} \left(\frac{\xi}{\delta} \right)^{1/7} \tag{16}$$

On the other hand, v_ψ rises from zero at the wall to a positive value, and falls again to zero at the edge of the shedding layer. If, near the wall, it is rising to the value $Kv_{\varphi 1}$, where K is to be determined later, then near the wall we should put $v_\psi = Kv_{\varphi 1}(\xi/\delta)^{1/7}$; in order to leave this form near the wall and to make v_ψ vanish at $\xi = \delta$, we write

$$v_\psi = Kv_{\varphi 1} \left(\frac{\xi}{\delta} \right)^{1/7} \left(1 - \frac{\xi}{\delta} \right) \tag{17}$$

Thus, near the wall, the velocity of the fluid is

[2] Reference [9], p. 274, or reference [23], p. 300.
[3] Reference [24], p. 345.
[4] Outside the shedding layer, v_ψ is of order δ/r_0, compared with the peripheral velocity in the shedding layer.
[5] Reference [9], p. 262, or reference [25], p. 59.

$$v = v_1 \left(\frac{\xi}{\delta}\right)^{1/7} \tag{18}$$

where

$$v_1 = v_{\varphi 1}(1 + K^2)^{1/2} \tag{19}$$

The shear stress at the wall can be expressed in terms of the velocity and distance from the wall as[6]

$$\tau_w = 0.0225\rho v^{7/4}(\nu/\xi)^{1/4} \tag{20}$$

Then with the velocity profile given in (18) and (19) we obtain

$$\tau_w = 0.0225\rho v_1^{7/4}(\nu/\delta)^{1/4} \tag{21}$$

and

$$\tau_\varphi = \frac{1}{(1 + K^2)^{1/2}}\tau_w, \quad \tau_\psi = \frac{K}{(1 + K^2)^{1/2}}\tau_w \tag{22}$$

These wall shear stresses and the assumed velocity profiles are now substituted into the equations (13) and (14). However, the asymptotic expression of the type (3) may be readily obtained from an order-of-magnitude consideration without entering into the detailed numerical calculation as follows:

Since K is small compared with unity, we have

$$v_\varphi \sim v_m, \quad v_\psi \sim Kv_m \tag{23}$$

and

$$\tau_\varphi \sim \tau_w, \quad \tau_\psi \sim K\tau_w \tag{24}$$

where

$$\tau_w \sim \rho v_m^2 \mathbf{R}^{-1/4}\left(\frac{\delta}{r_0}\right)^{-1/4} \tag{25}$$

in virtue of (21). Then the order of magnitude of each term in the equation (13), after division by $\rho v_m^2 r_0$, is

$$\underbrace{\rho \frac{\partial}{\partial \psi}\int_0^\delta v_\varphi^2 d\xi}_{K^2 \cdot \frac{\delta}{r_0}} = \underbrace{-\tau_\psi r_0}_{K\mathbf{R}^{-1/4}\left(\frac{\delta}{r_0}\right)^{-1/4}} + \underbrace{\rho \frac{\delta r_0}{R} v_{\varphi 1}^2 \sin\psi}_{\frac{\delta}{r_0}\cdot\frac{r_0}{R}} - \underbrace{\rho \frac{r_0}{R} \sin\psi \int_0^\delta v_\varphi^2 d\xi}_{\frac{\delta}{r_0}\cdot\frac{r_0}{R}} \tag{26}$$

Each term in the equation must be the same order of magnitude. Hence we shall have

$$K \sim (r_0/R)^{1/2} \tag{27}$$

and

$$\frac{\delta}{r_0} \sim \left[\mathbf{R}\left(\frac{r_0}{R}\right)^2\right]^{-1/5} \tag{28}$$

From (24) and (25) it follows that

$$\tau_\varphi \sim \rho v_m^2 \mathbf{R}^{-1/4}\left(\frac{r_0}{R}\right)^{1/10} \tag{29}$$

and hence from (15)

$$-\frac{\partial p}{\partial \varphi} \sim \rho v_m^2 \mathbf{R}^{-1/4}\left(\frac{r_0}{R}\right)^{-9/10} \tag{30}$$

The friction factor of a curved pipe is defined by the equation

$$f_c = -\left(\frac{\partial p}{R\partial\varphi}\right)\frac{4r_0}{\rho v_m^2} \tag{31}$$

From (30) it follows that

$$f_c\left(\frac{R}{r_0}\right)^{1/2} \sim \left[\mathbf{R}\left(\frac{r_0}{R}\right)^2\right]^{-1/5} \tag{32}$$

[6] Reference [19], p. 405.

Hence for large values for $\mathbf{R}(r_0/R)^2$ we have the asymptotic expression of the type

$$f_c\left(\frac{R}{r_0}\right)^{1/2} = \frac{\text{const.}}{[\mathbf{R}(r_0/R)^2]^{1/5}} \tag{33}$$

The momentum integral equations (13) and (14) were solved numerically for K and δ prior to the experiments with the assumed velocity profiles (16) and (17) and with the wall shear stresses (21) and (22). The axial-velocity components V_φ in the central core of the fluid were assumed to be

$$V_\varphi = A + Br\cos\psi \tag{34}$$

where A and B are constants, the ratio B/A being determined by the condition of continuity of the secondary flow. Omitting the details of the calculations, which are available in reference [26], we have the main results as follows:

(a) The friction factor is given by

$$f_c\left(\frac{R}{r_0}\right)^{1/2} = \frac{0.29}{[\mathbf{R}(r_0/R)^2]^{1/5}} \tag{35}$$

The numerical coefficient is slightly different from that in (3) and the difference may be attributed to somewhat rough and semi-empirical nature of the calculation.

(b) The theoretical thickness of the shedding layer is compared in Figs. 12 and 13 with measured velocity profiles.[7] The results seem to justify the concept of shedding layer for large values of $\mathbf{R}(r_0/R)^2$.

Asymptotic Expression for Friction Factors Deduced From the Logarithmic Velocity Distribution Law

In this case we assume that, close to the wall

$$v_\varphi = \frac{1}{(1 + K^2)^{1/2}}v, \quad v_\psi = \frac{K}{(1 + K^2)^{1/4}}v \tag{36}$$

[7] Reference [9], p. 274, and reference [23], p. 301.

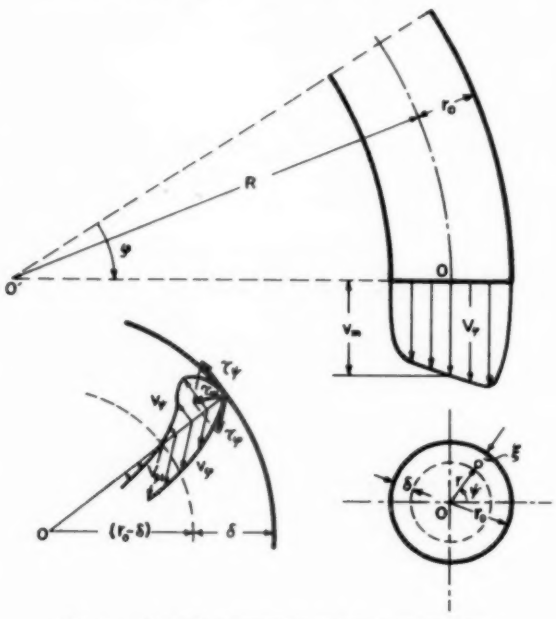

Fig. 11 Schematic presentation of flow in curved pipes

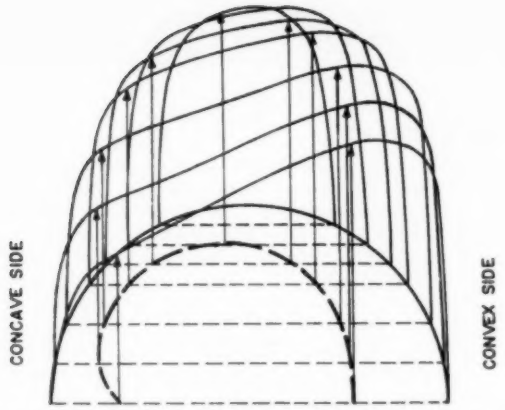

Fig. 12(a) Axial-velocity profile in a curved pipe (Adler [9]), and the theoretical thickness of shedding layer, where $R/r_0 = 50$, $R = 8.54 \times 10^3$, and $R(r_0/R)^2 = 3.42$

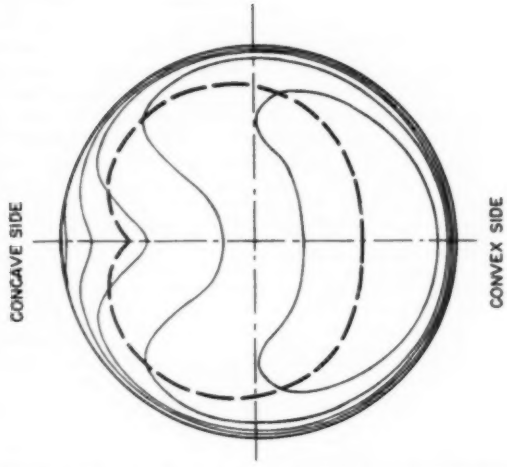

Fig. 12(b) Diagram showing lines of constant axial velocity (Adler [9]), and the theoretical thickness of shedding layer [same as Fig. 12(a)]

where

$$v_1 - v = -Av_* \log_e \left(\frac{\xi}{\delta}\right) \tag{37}$$

$$v_1 = v_{\varphi 1}(1 + K^2)^{1/2} \tag{38}$$

and A is given as about 2.5. Hence

$$\tau_\varphi = \frac{1}{(1 + K^2)^{1/2}}\tau_w, \qquad \tau_\psi = \frac{K}{(1 + K^2)^{1/2}}\tau_w \tag{39}$$

and $\tau_w (= \rho v_*^2)$ is given by

$$\frac{v_{\varphi 1}(1 + K^2)^{1/2}}{v_*} = A \log_e \frac{v_*\delta}{\nu} + B \tag{40}$$

where A has the same value as before, and B is about 5.5.

The component v_ψ must vanish at $\xi = \delta$. However, without further assumption for v_ψ, the asymptotic expression of the type (9) is obtainable directly from the afore-mentioned conditions.

For brevity we write

$$Y \sim v_m/v_* \tag{41}$$

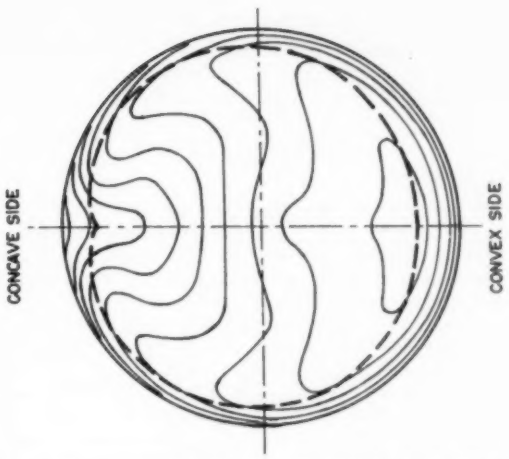

Fig. 13 Diagram showing lines of constant axial velocity (Saph and Schoder [23]) and the theoretical thickness of shedding layer, where $R/r_0 = 19.2$, $R = 6.52 \times 10^4$, and $R(r_0/R)^2 = 178$

Since K is small compared with unity, we have, from (36), (39), and (40)

$$v_\varphi \sim v_m, \quad v_\psi \sim Kv_m \tag{42}$$

$$\tau_\varphi \sim \rho v_m^2/Y^2, \quad \tau_\psi \sim K\rho v_m^2/Y^2 \tag{43}$$

and

$$\frac{\delta}{r_0} \sim \frac{Y}{\mathsf{R}}\, e^Y \tag{44}$$

Then the order of magnitude of each term in the equation (13), after division by $\rho v_m^2 r_0$, is

$$\underbrace{\rho \frac{\partial}{\partial \psi}\int_0^\delta v_\psi^2 d\xi}_{K^2 \cdot \frac{Y}{\mathsf{R}} \cdot e^Y} = \underbrace{-\tau_\psi r_0}_{\frac{K}{Y^2}} + \underbrace{\rho \frac{\delta r_0}{R} v_{\varphi 1}^2 \sin\psi}_{\frac{r_0}{R} \cdot \frac{Y}{\mathsf{R}} \cdot e^Y} - \underbrace{\rho \frac{r_0}{R} \sin\psi \int_0^\delta v_\varphi^2 d\xi}_{\frac{r_0}{R} \cdot \frac{Y}{\mathsf{R}} \cdot e^Y} \tag{45}$$

Each term must be the same order of magnitude. Hence we have

$$K \sim (r_0/R)^{1/2} \tag{46}$$

$$Y^2 e^Y \sim \mathsf{R}(R/r_0)^{1/2} \tag{47}$$

Now the pressure gradient in the φ-direction is given, from (15) and (43), by

$$-\frac{\partial p}{\partial \varphi} \sim \frac{R}{r_0}\frac{\rho v_m^2}{Y^2} \tag{48}$$

Hence from (31) it follows that

$$f_c \sim Y^{-2} \tag{49}$$

Eliminating Y from (47) and (49) we have the asymptotic expression of the type

$$\frac{1}{f_c^{1/2}} = k_1 \log\left[\mathsf{R}\left(\frac{R}{r_0}\right)^{1/2} f_c^{1/2}\right] + k_2 \tag{50}$$

where k_1 and k_2 are constants.

An approximate unpublished calculation similar to that given in the case of the 1/7th-power velocity distribution, leads to the conclusion that

$$k_1 = 2.0, \quad k_2 = -0.33 \tag{51}$$

The numerical coefficients are slightly different from that in (9), and the difference may again be attributed to somewhat rough and semiempirical nature of the calculations.

DISCUSSION

J. D. Hamilton[8]

One aspect of this interesting paper deals with the friction factor for straight pipes. This subject has been investigated recently at the writer's laboratory in connection with some tests on pressure loss of valves and fittings used in oil hydraulics. It was required to check the friction factor of the steel pipe used in the tests. The test fluids were mineral oils of 37.5 and 160 centistokes viscosity at 22 deg C and the flow range gave Reynolds numbers from 100 to 20,000.

The test arrangement was similar to the author's setup for his straight length of pipe. A bell-mouth entry connected a 4-in-diam supply pipe to the test pipe which had a bore of 0.830 in., Fig. 14.

First tests repeatedly revealed an apparent continuance of laminar flow to a Reynolds number of 9000 with a transition region of 9000 to 13,000.

It was suspected that boundary pressures were being measured at P_1 and P_2 rather than the mean pressure, possibly caused by an unusual velocity profile in the pipe. To check this, a 100-diameters length pipe was fitted upstream of the 100-diameters test length (instead of the previous pipe which had been only 20 diameters long) to allow a normal velocity profile to be established. The result of this was to give an apparent transition region of 3500 to 5000 Reynolds number.

A disturbance, in this case a needle valve, was inserted just after the bell mouth and the resultant friction factors showed a transition range of 2000 to 3000 Reynolds number.

Does the author consider that similar conditions may have existed in his test rig and that the high critical Reynolds numbers shown in Fig. 3 of the paper reflect true flow conditions in the pipe? Will he state the lengths of the straight pipes used in his tests and describe the method of obtaining the pressure at the piezometer stations?

[8] Department of Scientific and Industrial Research, Fluid Mechanics Division Mechanical Engineering Research Laboratory, Glasgow, Scotland.

L. MacG. Trefethen[9]

The author has presented very useful experimental results, and a turbulent-flow analysis the importance of which he understates in his presentation. Now that this information is available, it is possible to compare it with data obtained from the analogous case of flow in rotating radial tubes, and thus to demonstrate that the secondary-flow effects are, to a close approximation, independent of the nature of the transverse body force, in turbulent as well as in laminar flow.

The writer has suggested[10] that this type of secondary flow and such of its effects as increased friction factors are determined by the magnitude of the total transverse body force (and also, of course, by the tube diameter and the properties of the fluid). This transverse body force can be approximated easily if the assumption is made that all the fluid moves at mean velocity, V, an assumption which is not quite correct but which leads to the simple conclusion that, if (f_c/f_s) for laminar flow in a bent tube is a function of $N_{Re}(r_0/R)^{1/2}$, then (f/f_s) for laminar flow in a rotating tube will be the same function of $N_{Re}(\omega 2r_0/V)^{1/2}$, where ω is the angular speed of rotation of the tube about an axis perpendicular to the tube, and f and f_s are the rotating and stationary friction factors, respectively. Crude experiments[10] with rotating tubes demonstrated that this function is approximately the same for laminar flow. More recent and more accurate experiments[11] show this clearly. As plotted in Fig. 15, laminar-flow

[9] Professor of Mechanical Engineering, Tufts University, Medford, Mass.

[10] L. Trefethen, "Fluid Flow in Radial Rotating Tubes," *Actes, IX^e Congrès International de Méchanique Appliquée*, vol. 2, Université de Bruxelles, 1957, pp. 341–350.

[11] L. Trefethen, "Flow in Rotating Radial Ducts: Report R55GL 350 on Laminar Flow in Rotating, Heated Horizontal, and Bent Tubes, Extended Into Transition and Turbulent Regions," General Electric Company, Report No. 55GL350-A, August, 1957.

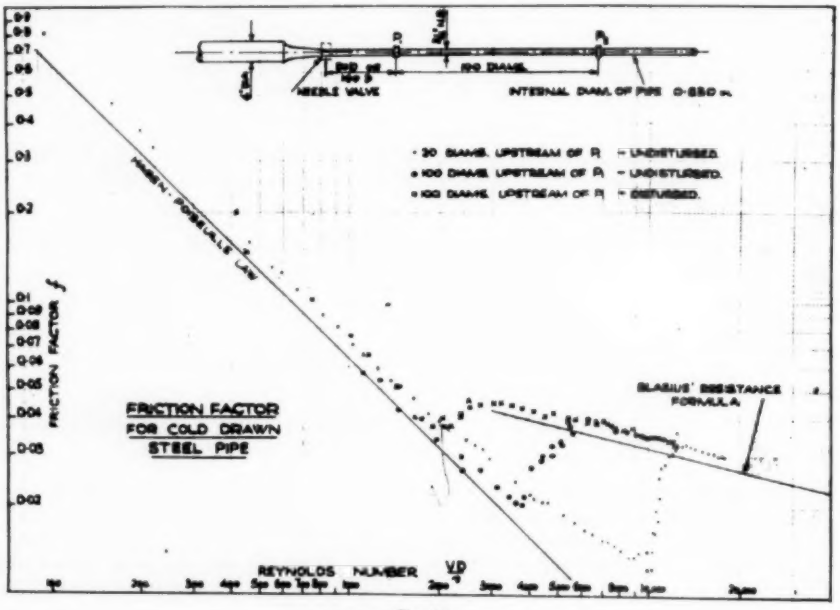
NEEDLE VALVE
INTERNAL DIAM. OF PIPE 0.830 in.
FRICTION FACTOR FOR COLD DRAWN STEEL PIPE
FRICTION FACTOR f
REYNOLDS NUMBER VD/ν
BLASIUS' RESISTANCE FORMULA

Fig. 14

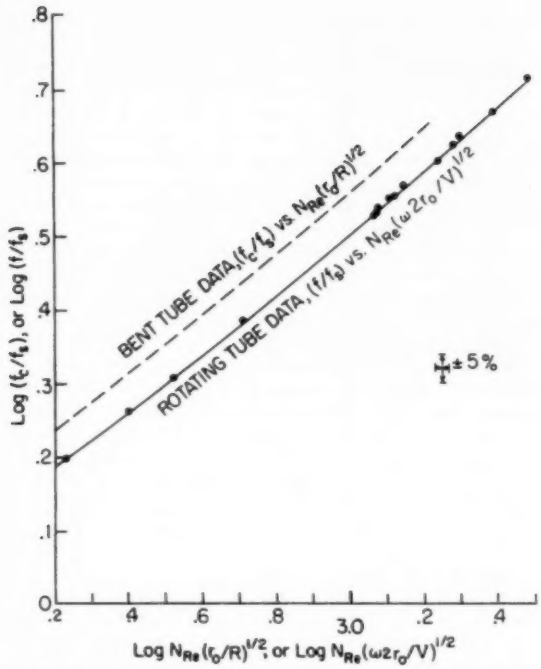
BENT TUBE DATA, (f_c/f_s) vs $N_{Re}(r_0/R)^{1/2}$
ROTATING TUBE DATA, (f/f_s) vs. $N_{Re}(\omega 2r_0/V)^{1/2}$
±5%
Log (f_c/f_s), or Log (f/f_s)
Log $N_{Re}(r_0/R)^{1/2}$, or Log $N_{Re}(\omega 2r_0/V)^{1/2}$

Fig. 15 Comparison of laminar-flow data for bent tubes [6] with data for radial rotating tubes[11]

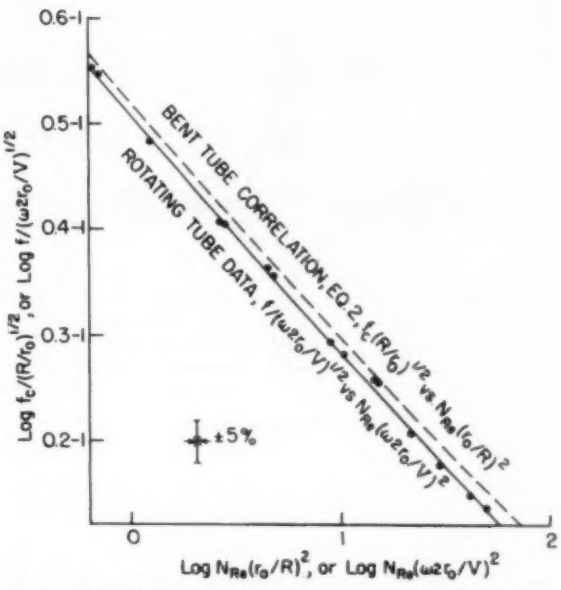
BENT TUBE CORRELATION, EQ. 2, $f_c(R/r_0)^{1/2}$ vs $N_{Re}(r_0/R)^2$
ROTATING TUBE DATA, $f/(\omega 2r_0/V)^{1/2}$ vs $N_{Re}(\omega 2r_0/V)^2$
±5%
Log $f_c/(R/r_0)^{1/2}$, or Log $f/(\omega 2r_0/V)^{1/2}$
Log $N_{Re}(r_0/R)^2$, or Log $N_{Re}(\omega 2r_0/V)^2$

Fig. 16 Comparison of author's turbulent-flow correlation for bent tubes with data for radial rotating tubes[11]

data for rotating tubes are about 13 per cent below the laminar-flow data for bent tubes, within a secondary flow effect on friction factors ranging up to 500 per cent.

This 13 per cent discrepancy between laminar-flow data is largely due to the foregoing assumption that all fluid moves at mean velocity, not to inapplicability of the concept that the total transverse body force determines the secondary flow. The Coriolis force on a particle is proportional to its velocity, whereas centrifugal force is proportional to its velocity squared. Since velocity profiles are not flat, the similarity method just outlined ascribes equal total transverse body forces to cases where, in fact, the bent-tube force would be greater. The writer has integrated one known velocity profile, in order to estimate the discrepancy to be expected when both bent and rotating-tube data are plotted as in Fig. 15, and obtained the unfortunate prediction of 13 per cent. (The data are not that accurate.) Therefore the conclusion is suggested that friction factors in the two cases are alike to within about 2 per cent on the basis of equality of total transverse body forces. If body forces are represented by the mean velocities, and integration of the profile thus avoided, the simple method of plotting used in Fig. 15 results, and the rotating-tube friction-factor ratios lie about 13 per cent below the bent-tube values. (A similar relationship apparently holds for heat-transfer coefficients in heated horizontal tubes.[10,11])

Similar conclusions now appear to hold for turbulent flow. The writer obtained turbulent-flow data for rotating tubes,[11] but the increase over nonrotating turbulent-flow friction factors is so insensitive to Reynolds number that the turbulent range covered did not allow for empirical determination of that dependence. The author's analysis in his Appendix suggests such a dependence for bent tubes, and his bent-tube data conform closely to his analytical prediction. With the same similarity assumptions made as the foregoing in the laminar-flow case, it can be shown that if, in turbulent flow in bent tubes, $f_c(R/r_0)^{1/2}$ is a function of $N_{Re}(r_0/R)^2$, then, for turbulent flow in rotating tubes, $f/(\omega 2r_0/V)^{1/2}$ should be the same function of $N_{Re}(\omega 2r_0/V)^2$. The rotating-tube data are compared, on this basis, with the author's proposed bent-tube correlation, Equation (2), in Fig. 16 of this discussion, and again the rotating-tube data are lower, this time by about 2 to 5 per cent. The same effect of velocity profiles which applied to the laminar-flow comparison would apply here, but, since the profiles are flatter in turbulent flow, the discrepancy might be expected to be less. The writer has not integrated a turbulent-flow profile to estimate what this discrepancy might be.

The writer would suggest that much of the author's paper can be applied to rotating tubes as well as to bent tubes, and appreciates the opportunity his turbulent flow data and analysis have provided to demonstrate the close similarity which exists between turbulent-flow effects in bent and rotating tubes. This analogy is useful, since it permits one to model experiments between systems, to use data from one system in another, and to tie together in one's thinking several varieties of what are essentially the same phenomena. By this time it is probably not surprising to note that the critical Reynolds-number increase also appears to be the same for the two systems.

The rotating-tube experiments and conclusions[11] will be published shortly.

Author's Closure

The author wishes to express his sincere thanks to Mr. Hamilton and to Professor Trefethen for their interest and discussion, and for their presentation of valuable experimental information.

Mr. Hamilton has asked the details of the author's test arrangement for the straight-pipe experiments. In this case, a straight pipe of about 250 diameters long (later used as an upstream tangent) was connected at the exit of the bell mouth directly, and the pressure drops were measured between the two piezometer stations distant 125 and 225 diameters, respectively, from the exit of the bell mouth. The details of the piezometer station are shown in Fig. 17. In each station there were four piezometer openings, 0.5 mm in diam, drilled at 90-deg intervals in the circumference. Sufficient care was taken to scrape off the burrs

Fig. 17 Piezometer station

so that the inside edge of each hole may be flush with the surface. These holes were connected, respectively, to a multitube manometer by rubber tubings.

Mr. Hamilton has asked whether similar conditions as his tests may have existed in the author's test rig. This is difficult to answer readily since in the author's experiments, although the insertion of the thin-plate orifice lowered the critical Reynolds number from 1.1×10^4 to 2.3×10^3 as shown in Fig. 3, the experiments with a different location of the upstream piezometer station were not carried out. However, with a smooth entry, the high critical Reynolds numbers shown in Fig. 3 or 14 are not surprising in view of many experimental informations now available.[12] The author should like to mention that in such cases laminar flow is inherently unstable, and the least disturbance appears to transform laminar flow into turbulent flow. In some of the author's earlier experiments, the transition was observed to take place at a Reynolds number of about 8×10^3 more or less, instead of 1.1×10^4. In this case, a vibration (although hardly perceived) of the 3-in. supply pipe, which was caused by the vibration of a $2^1/_2$-in. vertical pipe used as a bypass from the constant-level tank, was observed. This fact was soon found, and the vertical bypass pipe was fixed to the ground so as to eliminate the vibration of the supply pipe. Then tests were repeated, and the results shown in Fig. 3 were obtained. Therefore, in the author's tests, the elimination of the vibration of the 3-in. supply pipe was essential to maintain laminar flow up to values of the Reynolds number exceeding 10^4.

Professor Trefethen has suggested that much of the author's paper can be applied to rotating tubes, and has shown a close similarity which exists between turbulent-flow effects in bent and rotating tubes. The author is happy to learn such application of the bent-tube experiments which he had not noticed before this.

With the trend toward high-speed high-mass-flow fluid machinery, the secondary flow effects now become increasingly significant in many problems in hydraulic engineering. Professor Trefethen's findings will be a useful addition to the literature on secondary flows in rotating systems.

In conclusion, the author takes this occasion to express his sincere thanks to Professor R. E. Kronauer, Harvard University, for his able presentation of the paper at the Detroit meeting on behalf of the author.

[12] S. Goldstein, "Modern Developments in Fluid Dynamics," Clarendon Press, Oxford, England, 1938, vol. 1, p. 319; Reference [10], p. 109.

Characteristics of a Self-Lubricated Stepped Thrust Pad of Infinite Width With Compressible Lubricant

KIKUO C. KOCHI

Senior Research Engineer, Preliminary Guidance Anaylsis, Autonetics, North American Aviation, Inc., Downey, Calif.

Harrison's equation for the pressure in a gas-lubricated bearing of infinite width is solved for a thrust pad with stepped configuration. Analytic expressions for the pressure and load are developed. Numerical results are presented graphically. The analytic expressions together with the numerical data permit most of those characteristics of the stepped pad of practical interest to be completely determinable. Determination of optimum design parameters is given by a pair of graphs.

AN EXPLICIT pressure solution is exceedingly difficult to obtain from Harrison's pressure equation for gas-lubricated bearings, even for bearings of simple geometry, because the differential equation is nonlinear. Exact integrals do exist to Harrison's equation[1] but the pressure is found to be contained implicitly in difficult transcendental equations. To the author's knowledge, there is no known exact explicit pressure solution to Harrison's equation for any bearing geometry, where the lubricant film is assumed to be compressible.

Usually either a linearizing perturbation or an exact numerical method is employed to obtain pressure-distribution curves and bearing-load-carrying capacity from Harrison's equation. If perturbation techniques are used, the analytic results obtained, while giving a fairly accurate qualitative structure of the solution, will have design applicability restricted by the approximating assumptions. This is found to be true[2] in the case of J. S. Ausman's perturbation solution for the cylindrical journal bearing of infinite width where the accuracy of his solution is confined to lightly loaded journal bearings; i.e., it gives accurate solutions for journal eccentricities less than one half. On the other hand, exact numerical methods, while giving accurate solutions for any given set of bearing-parameter values, are restricted to that particular set of values, and involved numerical work is necessary to extract additional information. Moreover, the qualitative characteristics of the bearing as, for example, optimum design configuration, would be exceedingly difficult to ascertain. An example of this instance is Harrison's solution for a bearing with double-ramp configuration.

In this paper Harrison's equation is solved for a stepped thrust pad. It is found that, for this particular configuration, the usual difficulties of the pressure solution outlined in the foregoing are largely overcome; that is, the over-all qualitative structure of the pressure and load, optimum bearing parameters, asymptotic solutions, exact numerical solutions, and design curves can be determined with relative ease. A method is presented whereby additional numerical results can be obtained with minimum effort. The pressure solution is found to be contained in a set of transcendental equations. However, they are such that relatively simple graphical methods can be developed to obtain numerical results. The load expression is developed from the pressure solution employing a simple transformation.

The design problem for a stepped thrust pad is reduced to a pair of graphs. One graph gives the maximum load-carrying capacity in terms of the nondimensional parameters β and s. The

[1] W. J. Harrison, "The Hydrodynamical Theory of Lubrication With Special Reference to Air as a Lubricant," *Trans. Cambridge Philosophical Society*, vol. 22, 1913, p. 16.

[2] J. S. Ausman, "The Fluid Dynamic Theory of Gas-Lubricated Bearings," TRANS. ASME, vol. 79, 1957, p. 1218.

Contributed by the Aviation Committee of the Instruments and Regulators Division and presented at a joint session of the Aviation and Instruments and Regulators Divisions at the Annual Meeting, New York, N. Y., November 30–December 5, 1958, of THE AMERICAN SOCIETY OF MECHANICAL ENGINEERS.

NOTE: Statements and opinions advanced in papers are to be understood as individual expressions of their authors and not those of the Society. Manuscript received at ASME Headquarters, September 15, 1958. Paper No. 58—A-194.

Nomenclature

c_1 = length between pad step and trailing edge of bearing
c_2 = length between pad step and leading edge of bearing
h = bearing clearance height
h_1 = clearance in Region I
h_2 = clearance in Region II
l = total length of bearing
L = load per unit width
P = pressure in bearing
P_0 = ambient pressure
P_1 = pressure in Region I
P_2 = pressure in Region II
P_s = maximum pressure or pressure occurring at step
Q = mass flow rate of lubricant
$s = h_1/\Delta$ = ratio of minimum clearance height to difference in clearances
U = relative speed of upper member of pad to lower member
x = linear measure along bearing length
$\beta = (3\mu Ul)/(P_0\Delta^2)$ = nondimensional parameter
γ' = constant of integration proportional to mass flow rate of lubricant
γ_1 = arbitrary constant
γ_2 = arbitrary constant
$\Delta = h_2 - h_1$ = difference in clearance heights
$\eta = c_1/l$ = ratio of length between step and trailing edge to total bearing length
ξ_1 = arbitrary constant
ξ_2 = arbitrary constant
μ = viscosity of lubricant (assumed constant)
$\psi_1 = P_1/P_0$ = ratio of pressure in Region I to ambient
$\psi_2 = P_2/P_0$ = ratio of pressure in Region II to ambient

parameter β depends directly upon viscosity, speed, bearing length, and inversely upon ambient pressure, and the square of the step height. Parameter s is the ratio of the minimum clearance height to the step height and is essentially a measure of the stiffness of the bearing. Maximum load is defined as the load which is obtained for an optimum value of η, the ratio of the length of the step from the trailing edge of the bearing to the total bearing length, and for an optimum value of β, keeping s fixed. In design considerations then, the parameters optimum β, s, and optimum η will yield the optimum bearing configuration maximizing the load. The second graph permits the determination of optimum η for fixed values of β and s. Aside from the one serious restriction due to the infinite width assumption, these curves with the additional curves included in this paper, permit most of the practical characteristics of the bearing to be determined completely.

A constructional feature of the stepped bearing, which may prove to be a real advantage, is that the stepped configuration is sufficiently simple to machine to the close tolerance required for hydrodynamic bearings. It is much easier to shape a step into a flat surface than to shape it into any other profile.

One other advantage which is only conjectured here is that the stepped pad of optimum parameters may yield the maximum load-carrying capacity over all other configurations. One is led to this, rather heuristically, by Lord Rayleigh's variational proof[3] of this fact for incompressible lubricants.

Pressure-Differential Equation

Harrison[1] has shown that for gas-lubricated bearings of infinite width with isothermal pressure-density relationship, the pressure-differential equation is given by

$$\frac{dP}{dx} = -\frac{6\mu U}{h^2} + \frac{\gamma'}{Ph^3} \tag{1}$$

where μ is the dynamic viscosity of the lubricant (assumed constant), U is the relative speed of the upper and lower members of the bearing, h the clearance height, P the pressure, x the linear measure along the bearing length, and γ' a constant of integration. It can be shown that γ' is proportional to μQ where Q is the mass flow rate of the lubricant per unit width.

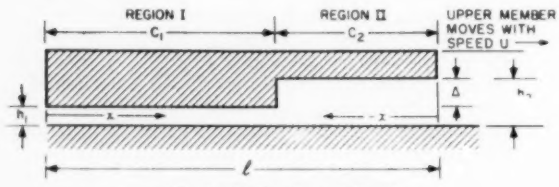

Fig. 1 Profile of stepped pad

Fig. 1 shows a cross section of a stepped thrust pad. The nomenclature employed for the dimensions of the pad correspond to those indicated in this figure. Region I defines the section of the pad where the clearance height is smaller (h_1), and Region II the section where it is larger (h_2). For convenience in obtaining the pressure solution for each region, the origin of the co-ordinate system for Region I is assumed to be located at the trailing edge of the bearing and for Region II at the leading edge. It will be assumed hereafter that parameters with subscripts 1 and 2 will be associated with Regions I and II, respectively.

The pressure solution must satisfy the following boundary conditions:

$$P_1(x = 0) = P_0 = P_2(x = 0) \tag{2}$$

$$P_1(x = c_1) = P_s = P_2(x = -c_2) \tag{3}$$

where P_0 is the ambient pressure and P_s the pressure at the bearing step.

It was indicated previously that the constant γ' is proportional to the mass flow rate of the lubricant at any point in the bearing. The volume flow is then proportional to γ'/P. Continuity of the volume flow at the step of the bearing together with the condition for pressure continuity, Equation (3), requires that γ' be the same constant for Regions I and II. This gives rise to the following equations:

$$\frac{dP_1}{dx} = \frac{-6\mu U}{h_1^2} + \frac{\gamma_1}{P_1}, \qquad 0 \le x \le c_1 \tag{4}$$

$$\frac{dP_2}{dx} = \frac{-6\mu U}{h_2^2} + \frac{\gamma_2}{P_2}, \qquad -c_2 \le x \le 0 \tag{5}$$

where

$$\gamma_1 = \frac{\gamma'}{h_1^3}, \qquad \gamma_2 = \frac{\gamma'}{h_2^3}$$

From the foregoing relationships for γ_1 and γ_2, it follows that

$$\gamma_1 = \frac{h_2^3}{h_1^3}\gamma_2 \tag{6}$$

This equation essentially summarizes the condition for volume flow-rate continuity at the step of the bearing.

Pressure Integral

Equation (1) is readily integrable since the clearance h is a constant for each region. Let

$$\alpha = \frac{6\mu U}{h^2}, \qquad \gamma = \frac{\gamma'}{h^3} \tag{7}$$

then Equation (1) can be put into the form

$$\int_{P_0}^{P} \frac{P\,dP}{-\alpha P + \gamma} = \int_0^x dx \tag{8}$$

where boundary condition (2) is imposed for the lower limit of integration. Integration with respect to Equations (4) and (5) yields the following transcendental equations for the pressure in Regions I and II, respectively:

$$\frac{P_1}{P_0} - 1 + \frac{\gamma_1}{\alpha_1 P_0}\ln\left(\frac{\dfrac{-P_1}{P_0} + \dfrac{\gamma_1}{\alpha_1 P_0}}{-1 + \dfrac{\gamma_1}{\alpha_1 P_0}}\right) = -\frac{\alpha_1 x}{P_0}, \quad 0 \le x \le c_1 \tag{9}$$

$$\frac{P_2}{P_0} - 1 + \frac{\gamma_2}{\alpha_2 P_0}\ln\left(\frac{\dfrac{-P_2}{P_0} + \dfrac{\gamma_2}{\alpha_2 P_0}}{-1 + \dfrac{\gamma_2}{\alpha_2 P_0}}\right) = -\frac{\alpha_2 x}{P_0}, \quad -c_2 \le x \le 0 \tag{10}$$

where

$$\alpha_1 = \frac{6\mu U}{h_1^2}, \qquad \alpha_2 = \frac{6\mu U}{h_2^2} \tag{11}$$

Boundary condition (3) implies the following:

$$\frac{P_s}{P_0} - 1 + \frac{\gamma_1}{\alpha_1 P_0}\ln\left(\frac{\dfrac{-P_s}{P_0} + \dfrac{\gamma_1}{\alpha_1 P_0}}{-1 + \dfrac{\gamma_1}{\alpha_1 P_0}}\right) = -\frac{\alpha_1 c_1}{P_0} \tag{12}$$

[3] Lord Rayleigh, "Notes on the Theory of Lubrication," *Philosophical Magazine*, vol. 35, 1918, pp. 1–12.

$$\frac{P_s}{P_0} - 1 + \frac{\gamma_2}{\alpha_2 P_0} \ln \left(\frac{\dfrac{-P_s}{P_0} + \dfrac{\gamma_2}{\alpha_2 P_0}}{-1 + \dfrac{\gamma_2}{\alpha_2 P_0}} \right) = \frac{\alpha_2 c_2}{P_0} \tag{13}$$

The complete pressure solution is given by the set of five equations: Equations (6), (9), (10), (12), and (13). Equations (6), (12), and (13) will determine the constants of integration P_s, γ_1, and γ_2, in terms of the given physical parameters of the bearing. Substitution of these determined values into Equations (9) and (10) will yield the pressure distribution. It is needless to say that while the foregoing procedure to obtain the pressure solution appears simple in principle, it nevertheless involves a certain amount of preliminary tedious numerical work.

In order to handle the foregoing pressure solution more conveniently define the nondimensional parameters

$$\left.\begin{aligned} \psi_1 &= P_1/P_s \\ \psi_2 &= P_2/P_0 \\ \eta &= e_1/l \\ s &= h_1/\Delta \\ \xi_1 &= \gamma_1/(\alpha_1 P_0) \\ \xi_2 &= \gamma_2/(\alpha_2 P_0) \\ \beta &= (3\mu U l)/(P_0 \Delta^2) \end{aligned}\right\} \tag{14}$$

Substitution of these parameters into Equations (6), (9)–(13) and rearranging terms will yield the following nondimensionalized equations:

$$\xi_1 \ln \left(\frac{\xi_1 - \psi_1}{\xi_1 - 1} \right) = -2\beta \frac{\eta}{s^2} \frac{x}{c_1} - (\psi_1 - 1), \; 0 \le x \le c_1 \tag{15}$$

$$\xi_2 \ln \left(\frac{\xi_2 - \psi_2}{\xi_2 - 1} \right) = -2\beta \frac{(1-\eta)}{(1+s)^2} \frac{x}{c_2} - (\psi_2 - 1), \; -c_2 \le x \le 0 \tag{16}$$

$$\xi_1 \ln \left(\frac{\xi_1 - \psi_s}{\xi_1 - 1} \right) = -2\beta \frac{\eta}{s^2} - (\psi_s - 1) \tag{17}$$

$$\xi_2 \ln \left(\frac{\xi_2 - \psi_s}{\xi_2 - 1} \right) = 2\beta \frac{(1-\eta)}{(1+s)^2} - (\psi_s - 1) \tag{18}$$

$$\xi_1 = (1 + 1/s)\, \xi_2 \tag{19}$$

Independent parameters in these equations which completely specify the pressure distribution are s, β, η, x/c_1, and x/c_2. The unknown dependent variables to be solved for in the foregoing equations are ψ_s, ξ_1, ξ_2, ψ_1, and ψ_2. Hereafter the word pressure will refer to the nondimensionalized pressure ψ.

Numerical Methods for Pressure Solution

Because of their transcendental nature it is necessary to employ graphical techniques to the solution of Equations (15)–(19). It is noted incidentally that these equations would be difficult to program for computing machines. In Figs. 2 and 3 the left sides of Equations (15), (17), and (16), (18) are, respectively, plotted for

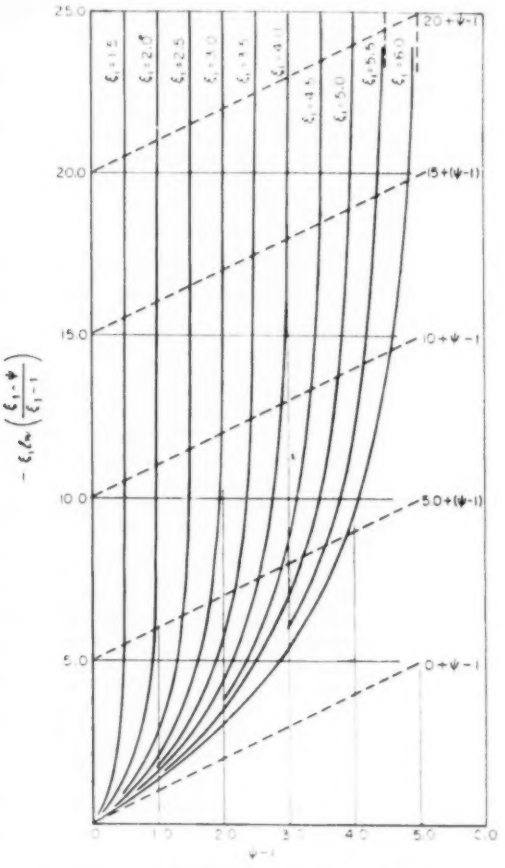

Fig. 2 Plot of function $\xi_1 \ln (-\psi + \xi_1)/(-1 + \xi_1)$

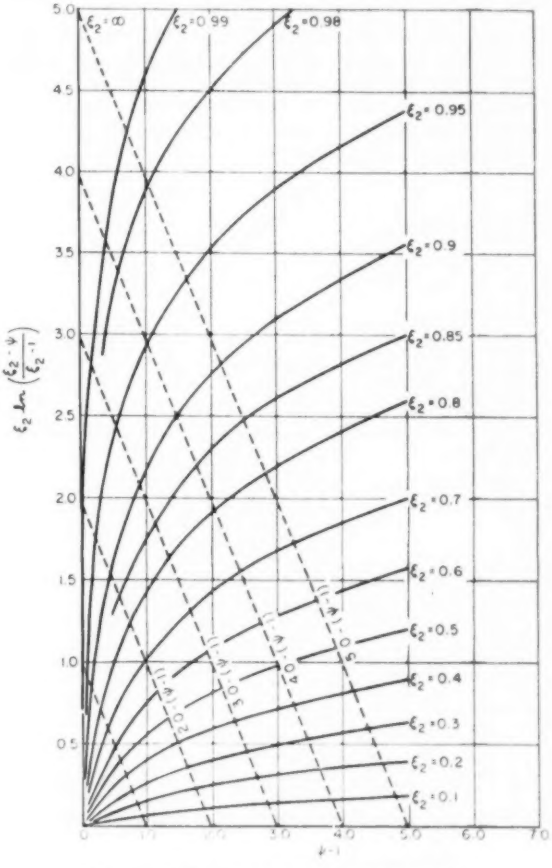

Fig. 3 Plot of function $\xi_2 \ln (-\psi + \xi_2)/(-1 + \xi_2)$

various values of ξ_1 and ξ_2 and with $\psi - 1$ as the abscissa. The right sides of these equations which are straight lines are plotted in as dotted lines. These curves are used to facilitate the numerical work involved in determining the pressure distribution.

To determine the pressure distribution in the bearing for a particular set of the independent parameters, the procedure outlined in the following is used:

First, the set of Equations (17), (18), and (19) is solved simultaneously for ψ_s the pressure at the step of the bearing, and ξ_1, ξ_2 which are arbitrary constants. This solution is accomplished by obtaining from Fig 2 a plot of ψ_s against ξ_1 and from Fig 3 a plot of ψ_s against ξ_2; eliminating either ξ_1 or ξ_2 using Equation (19); plotting the resulting two curves of ψ_s against either ξ_1 or ξ_2; and from this obtaining the solution which is given by the intersection of these two curves.

Next, having determined ξ_1 and ξ_2, the respective values are substituted into Equations (15) and (16). For each value of x/c_1 and x/c_2, which defines the position in the bearing at which the pressure is being determined, there is a unique pressure solution ψ_1 and ψ_2 given by these equations. Referring again to Figs. 2 and 3, the right and left sides of Equations (15) and (16) are interpolated into the series of curves shown in the respective figures and each of the values ψ_1 and ψ_2 is obtained directly by the intersections of the right and left sides of these equations. This is repeated for a sufficient number of points x/c_1 and x/c_2 until a complete pressure profile is obtained.

Load

A simple transformation can be used to give the load in terms of ψ_s, ξ_1, and ξ_2, which values were determined from Equations (17), (18), and (19). The load is given by the integral of the pressure above ambient over the bearing area. For infinite-width bearings, the load given as load per unit width is expressed by the following integral for Region I:

$$\frac{L_1}{lP_0} = \int_0^{c_1} \frac{c_1}{l}\left(\frac{P_1}{P_0} - 1\right)\frac{dx}{c_1} = \int_0^{c_1} \eta(\psi_1 - 1)\frac{dx}{c_1} \tag{20}$$

$$= \frac{\eta}{c_1}\int_1^{\psi_s} (\psi_1 - 1)\frac{dx}{d\psi_1}\,d\psi_1 \tag{21}$$

The pressure ψ_1 is a continuous function with bearing length in Region I. The integral (21) exists if $d\psi_1/dx \neq 0$. It can be shown that $d\psi_1/dx$ approaches zero asymptotically for large values of β; however, it never assumes the value zero for any particular value of β. Thus integral (21) exists and will yield the load capacity.

From Equation (4) it follows that

$$\frac{d\psi_1}{dx} = -\frac{2\beta}{s^2}\frac{1}{l}\left(\frac{\psi_1 - \xi_1}{\psi_1}\right) \tag{22}$$

Substituting (22) into (21) and integrating the result yields the following expression for the load in Region I:

$$\frac{L_1}{lP_0} = \frac{s^2}{2\beta}\left[(\xi_1 - 1)\frac{2\beta\eta}{s^2} - \frac{(\psi_s^2 - 1)}{2}\right] \tag{23}$$

By an identical argument the load in Region II is given as

$$\frac{L_2}{lP_0} = \frac{(1+s)^2}{2\beta}\left[(\xi_2 - 1)\frac{2\beta(1-\eta)}{(1+s)^2} + \frac{\psi_s^2 - 1}{2}\right] \tag{24}$$

Total load L is given by the sum of Equations (23) and (24)

$$\frac{L}{P_0 l} = \frac{\psi_s^2 - 1}{2}\left(\frac{1+2s}{2\beta}\right) + (\xi_2 - 1) + (\xi_1 - \xi_2)\eta \tag{25}$$

Qualitative Structure of Pressure Distribution and Load

Before entering into a detailed discussion of the numerical results, it would be instructive to describe, qualitatively, the characteristics of Equations (15)–(19) and (25).

For small values of β the pressure and the load reduce to the case of incompressible flow. The pressure and load expressions for this case have been developed by Archibald.[4] In terms of the notations used here these expressions assume the following form:

$$\psi_s - 1 = \frac{P_s - P_0}{P_0} = \frac{2\beta}{\dfrac{s^3}{\eta} + \dfrac{(1+s)^2}{1-\eta}} \tag{26}$$

$$\psi_1 - 1 = \frac{P_1 - P_0}{P_0} = (\psi_s - 1)\frac{x}{c_1}, \quad 0 \leq x \leq c_1 \tag{27}$$

$$\psi_2 - 1 = \frac{P_2 - P_0}{P_0} = (\psi_s - 1)\frac{x}{c_2}, \quad 0 \leq x \leq c_2 \tag{28}$$

$$\frac{L}{lP_0} = \frac{1}{2}(\psi_s - 1) \tag{29}$$

Space does not permit a proof of this statement; however, the reader may readily verify that Equations (15)–(19) and (25) reduce to (26)–(29) by taking a first-order perturbation of the parameter β about zero with respect to the former set of equations.

As β approaches infinity the compressibility effect of the gas predominates. In Equations (17) and (18) it is seen that as $\beta \to \infty$, $\xi_1 \to \psi_s$, and $\xi_2 \to 1$. Using Equations (15), (16), (19), and (25) it follows that

$$\psi_s = \frac{h_2}{h_1} = \left(1 + \frac{1}{s}\right) \tag{30}$$

$$\psi_1 = \psi_s \tag{31}$$

$$\psi_2 = 1 \tag{32}$$

$$\frac{L}{lP_0} = (\psi_s - 1)\eta = \frac{\eta}{s} \tag{33}$$

Thus the pressure and load characteristics are determined only by the dimensions of the bearing. The foregoing equation for the pressure can be written as

$$P_1 h_1 = P_2 h_2 \tag{34}$$

which is essentially the isothermal compressibility equation of an ideal gas. It is also seen from these equations that the maximum pressure ψ_s can never exceed the ratio of the larger clearance to the smaller. Hence the upper limit to the pressure attainable in the bearing is limited by this ratio.

Parameters ξ_1 and ξ_2 are positive. This is immediately noted when it is recognized that they are directly associated with the lubricant volume flow which must be positive to obtain load-carrying capacity.

Nondimensionalized pressures ψ_1, ψ_2, ψ_s are greater than unity; that is, the pressure in the bearing is above ambient at every point in the bearing. Physical arguments indicate that the convergence which is effected by the step can give rise to only a positive pressure build-up. Mathematically it is seen from Equations (15)–(19) that values less than unity are untenable. Moreover, these equations show that ψ and ψ_2 both increase monotonically toward ψ_s, the pressure at the step. For this reason, ψ_s is also the maximum pressure in the bearing.

The following inequalities are valid: $\xi_1 \geq \psi_s$ and $\xi_2 \leq 1$. These conditions are absolutely necessary if Equations (17) and (18) are

[4] F. R. Archibald, "A Simple Hydrodynamic Thrust Bearing," TRANS. ASME, vol. 72, 1950, pp. 393–400.

to yield valid results; otherwise it is seen that mathematical inconsistencies arise in these equations. The foregoing inequalities are important in that they aid in narrowing the range of values which must be considered in the numerical solution of the transcendental pressure equations, Equations (15)–(19).

The proof for these inequalities rests upon the fact that the right side of Equations (17) and (18) are, respectively, negative and positive for all physically reasonable parameter values. It is easy to see that the right side of (17) is always negative since all the parameters are positive and $\psi_s \geq 1$. From this fact it can easily be shown that $\xi_1 \geq \psi_s$ must hold. For the second inequality it is necessary to show that the right side of (18) is positive. It is sufficient to show that the following inequality is always valid:

$$2\beta \frac{(1-\eta)}{(1+s)^2} > (\psi_s - 1) \text{ compressible}$$

The maximum pressure for incompressible lubricant is always greater than for the compressible lubricants. Therefore it follows from Equation (26) that

$$\frac{2\beta}{\frac{s^3}{\eta} + \frac{(1+s)^3}{1-\eta}} > (\psi_s - 1) \text{ compressible}$$

But it is also true that

$$\frac{2\beta(1-\eta)}{(1+s)^2} > \frac{2\beta}{\frac{s^3}{\eta} + \frac{(1+s)^3}{1-\eta}}$$

Hence the right side of Equation (18) is always positive. The inequality $\xi_2 \leq 1$ can now be established without difficulty.

Two singularities for the cases $\eta = c_1/l = 0$ and $\eta = 1$ appear in the pressure solution, Equations (15)–(19). These are not serious but require an explanation. If $\eta = 0$ is substituted into Equations (17) and (18) it is seen that the only tenable solution for (17) is that $\psi_s = 1$, while (18) will be inconsistent for this value. However, boundary conditions and continuity of the pressure which are primary requisites for a valid solution imply that the pressure at the step ψ_s must be equal to the ambient pressure when $\eta = 0$. Hence $\psi_s = 1$ is the correct solution and, because the pressure in the bearing must be greater than or equal to ambient, the pressure distribution also must be ambient, and the resulting load-carrying capacity is zero. Fig. 2 partially bears out this argument. It is seen that the dotted straight line corresponding to $\eta = 0$ of the right side of Equation (17) passes through the origin so that $\psi_s = 1$. A similar argument can be used to show that the identical results given in the foregoing is obtained for the case $\eta = 1$ using Fig. 3.

As the independent parameter $s \to \infty$ the pressure solution will approach the solution for incompressible lubricant; that is, this solution will be given by the case where $\beta \to 0$ which has been discussed in the foregoing.

For $s \to 0$ the pressure solution shows that $\psi_s \to \xi_1$ and $\psi_1 \to \psi_s$ except where $x/c_1 = 0$. Thus the pressure in Region I approaches the maximum pressure. No inference for the asymptotic solution can be drawn for the pressure ψ_2 in Region II.

Numerical Results and Discussion

1 Maximum Pressure. Figs. 4–6 show the variation of the maximum pressure above ambient, i.e., the pressure occurring at the step, with the parameter β as the abscissa and for several typical values of the parameter s keeping η fixed. Representative values selected for η in these three graphs are $\eta = 1/4$, $1/2$, and $3/4$, that is, the step is located one quarter, one half, and three quarters of the total bearing length from the trailing edge of the bearing. These curves clearly show how the maximum pressure is influenced by the compressible nature of the lubricating film.

For comparative purposes and to emphasize the differences between compressible and incompressible lubricants, the asymptotic maximum pressures for the cases $\beta \to 0$ and $\beta \to \infty$ are shown as dotted lines in these figures. These are plots of Equations (26) and (30), respectively.

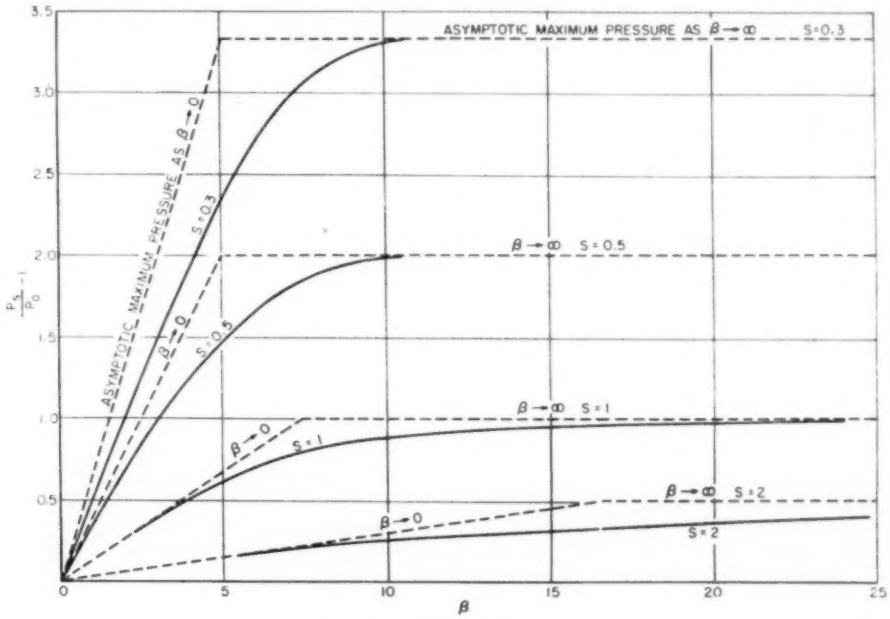

Fig. 4 Maximum pressure for $\eta = 1/4$

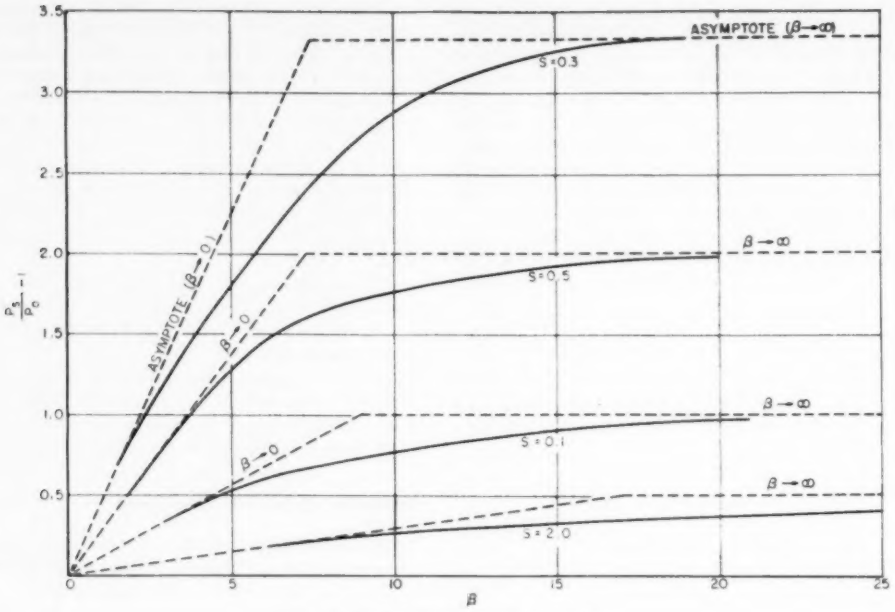

Fig. 5 Maximum pressure for $\eta = 1/2$

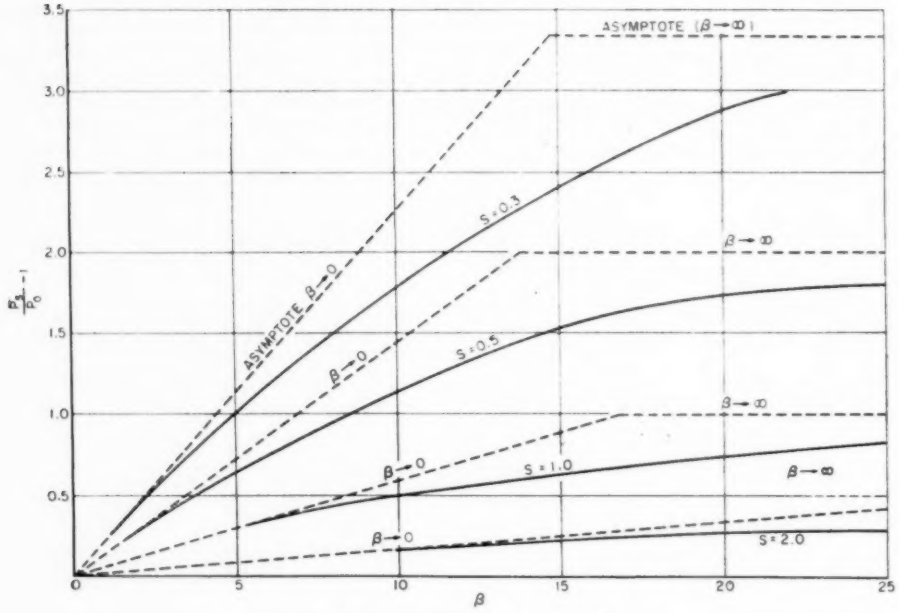

Fig. 6 Maximum pressure for $\eta = 3/4$

The afore-mentioned figures together with the asymptotic solutions permit the characteristics of the maximum pressure in the bearing to be known completely. For any fixed value of β the maximum pressure increases with decrease in the parameter s. For any β the maximum pressure above ambient does not exceed $1/s$. In the regions of small β the maximum pressure is asymptotic to the incompressible solution, always remaining less than this solution and approaching it as $\beta \to 0$.

In the case of the incompressible solution, Equation (26), it can be shown that an optimum η exists which optimizes the maximum pressure. On determining the maximum of Equation (26) with respect to the parameter η the following relationship will be obtained for the optimum η:

$$\frac{1 - \eta_{opt}}{\eta_{opt}} = \left(\frac{1+s}{s}\right)^{1/s} \tag{35}$$

Typically for $s = 0.3$ the optimum η is equal to 0.1 and the optimum maximum pressure above ambient is $(\psi_s - 1)_{opt} = 0.74\beta$. Thus the maximum slope of the incompressible solution will be 0.74. For all other values of η then, the slope decreases approaching zero as $\eta \to 0$ or $\eta \to 1$.

Pressure Distribution. In Figs. 7–9, pressure-distribution curves are typically shown for $\beta = 5$ with s as the parameter and for several values of η. The numerical examples given for s and η correspond to those chosen in Figs. 4–6 for the maximum-pressure curves. Again it is emphasized that, while some of these figures appear to show the pressure slope at the step in Region I to be zero, actually there is a finite slope which is different from zero.

It is interesting to note here that if the incompressible solution, Equations (27) and (28), which is given by straight lines is plotted on these graphs using equivalent parameter values, the load which is the integral of these curves, in some cases, can be greater for the compressible case than the incompressible. Hence compressible lubricant can yield higher load-carrying capacity than the incompressible. Actually this conclusion is not realistic inasmuch as the viscosity and therefore β is significantly different in magnitude for the two cases.

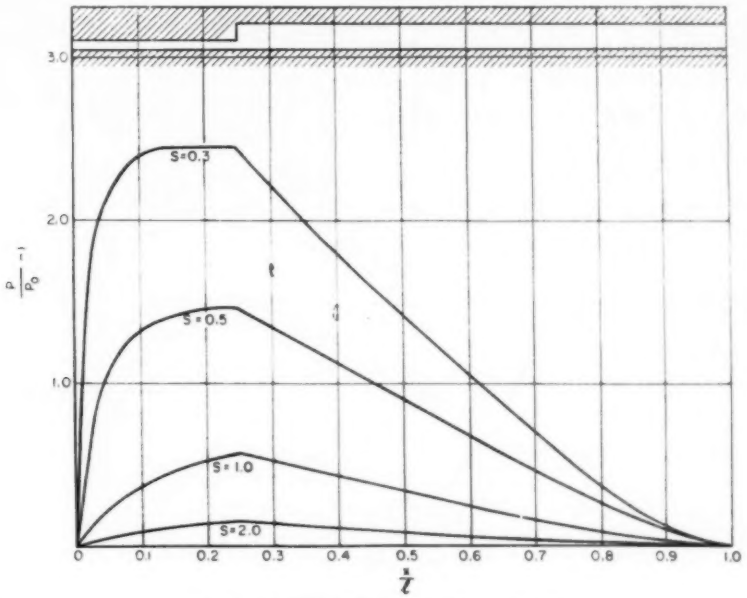

Fig. 7 Pressure profile for $\eta = 1/4$ and $\beta = 5$

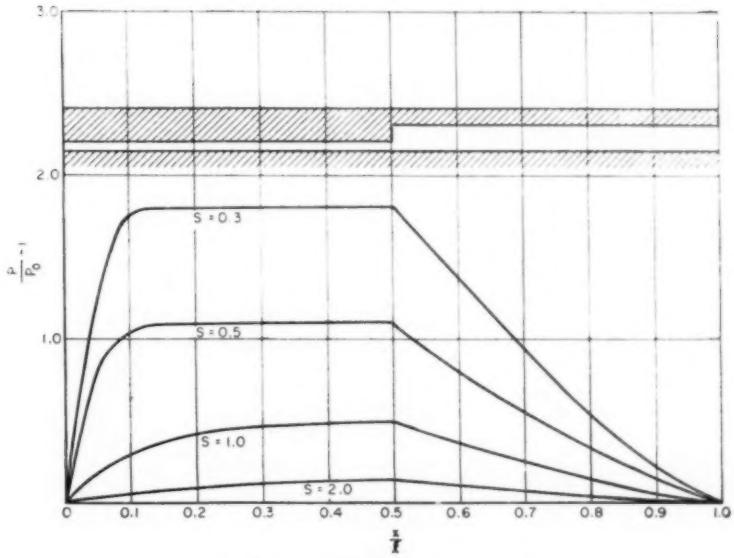

Fig. 8 Pressure profile for $\eta = 1/2$ and $\beta = 5$

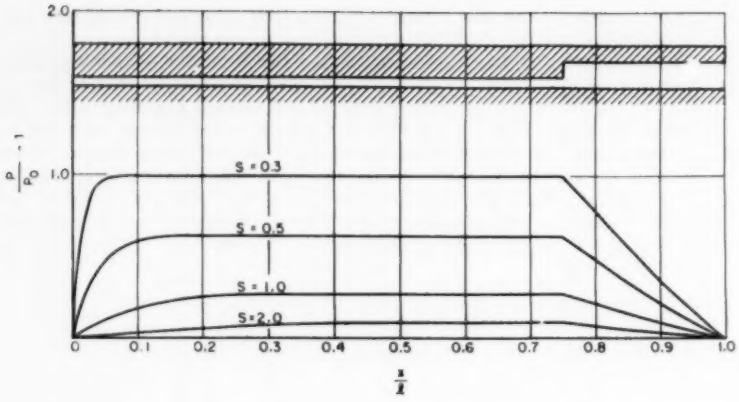

Fig. 9 Pressure profile for $\eta = 3/4$ and $\beta = 5$

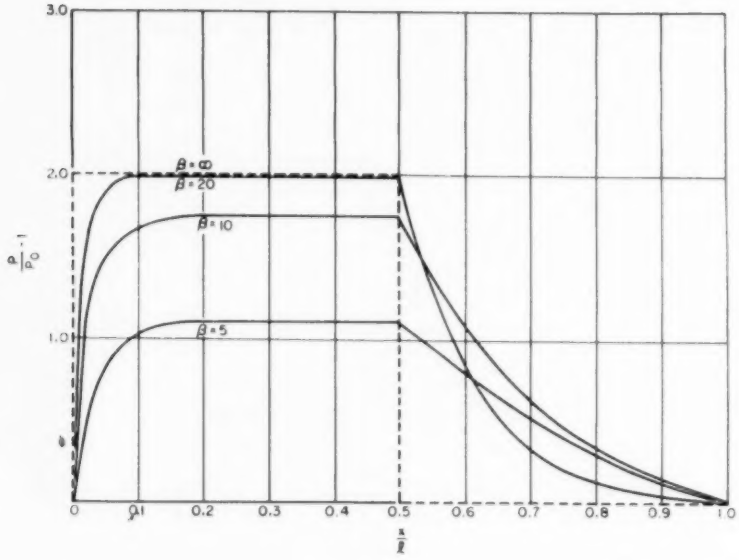

Fig. 10 Pressure distribution for various values of β at $s = 0.5$

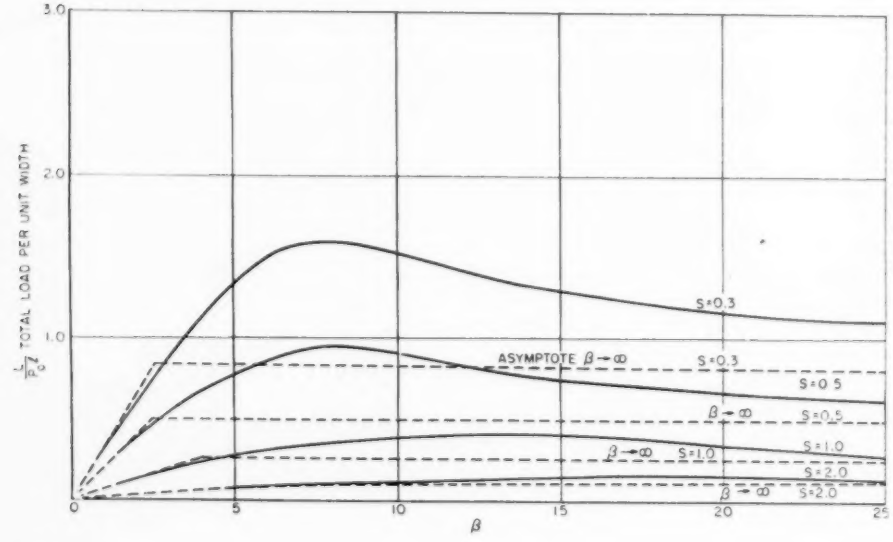

Fig. 11 Load per unit width for $\eta = 1/4$

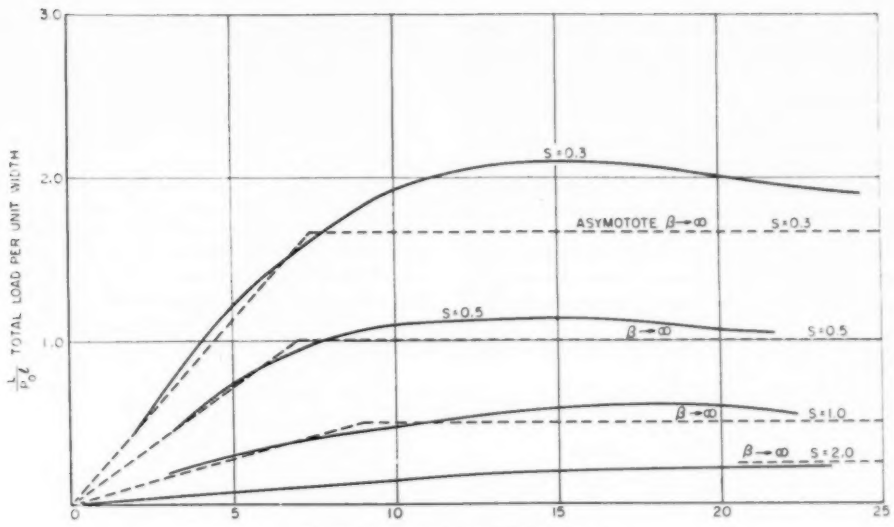

Fig. 12 Load per unit width for $\eta = 1/2$

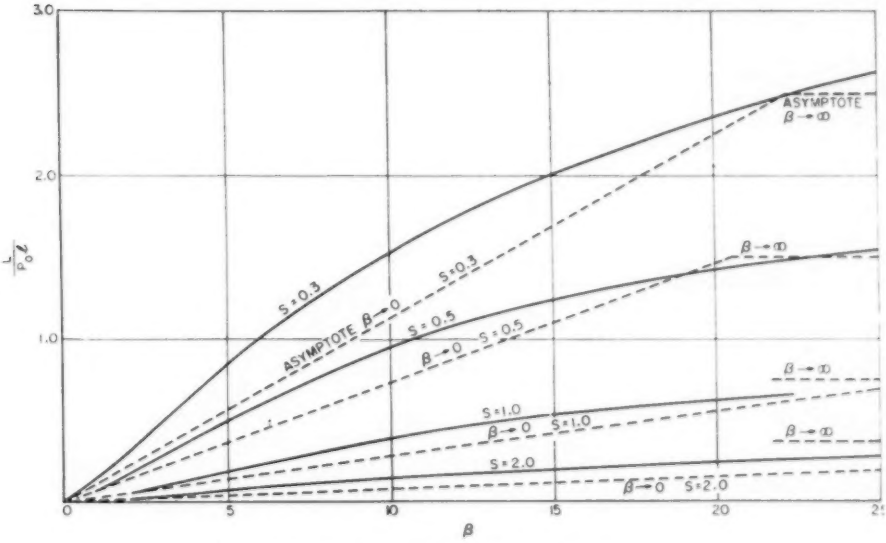

Fig. 13 Load per unit width for $\eta = 3/4$

Fig. 10 shows the pressure-distribution curves for various values of β with $s = 0.5$ and $\eta = 0.5$. The dotted line shown is the asymptotic pressure distribution as $\beta \to \infty$.

The characteristics of the pressure distribution can be described as follows: For small β or large s the pressure distribution is given by the case $\beta \to 0$ which gives a triangular-shaped distribution with the apex at the step and the two vertexes at the ends of the bearing, Equations (27) and (28). As β increases the pressure above ambient at the step increases, Figs. 4–6, toward the ratio $1/s$, and the pressure distribution in Region I approaches the constant value $1/s$ while in Region II it decreases to ambient. This increase of the pressure in Region I and the corresponding decrease in Region II as $\beta \to \infty$ gives rise to an optimum β which maximizes the integral of the pressure curves (load). This will be discussed more in detail.

Load. Total load capacity of the stepped thrust pad is typically described by the series of curves shown in Figs. 11–13. The asymptotic cases $\beta \to 0$ and $\beta \to \infty$, Equations (29) and (33), are also shown in these figures.

It is particularly noted that the maximum load occurs at a value of β which is not necessarily infinite. This is tantamount to obtaining maximum load at comparatively low operating speeds. It is an effect not present with incompressible lubricants, and not heretofore noticed in connection with gas bearings.

The reason for the presence of this phenomenon in the gas-lubricated stepped pad is that the nonlinear pressure distribution in Region I closely approaches the constant maximum pressure $\psi_a - 1$ at comparatively low values of β (optimum β), while in Region II the pressure distribution is considerably higher than ambient. As a result, the load which is the area of the pressure curves is larger at these values of β than for β equal to infinity. Typically in Fig. 10 it is noted that at $s = 0.5$ the pressure dis-

tribution in Region I is close to its maximum distribution when $\beta > 10$ while in Region II the pressure distribution is considerably greater than ambient. As β increases, the pressure distribution in Region I remains relatively unchanged while in Region II the distribution drops asymptotically toward ambient, approaching in the limit the dotted line shown in this figure. Thus the area of the pressure curve is greater than what it would be at $\beta \to \infty$.

Figs. 14 and 15 typically show cross plots of the total load at $s = 0.3$ and $s = 0.5$ with η as the abscissa and for several values of β. In these figures are also shown the locus of maximum load from which a plot of optimum η versus β can be obtained. These figures show that as $\beta \to \infty$ the optimum η tends toward unity. It can be established that this is a general characteristic for all values of s.

Design Curves. Since β and η are the two optimizing parameters which will maximize the load, it would be useful to characterize this fact by a set of curves.

Fig. 16 shows a series of curves which give the maximum load in terms of s and optimum β. Each of these curves is essentially the envelope of the set of load curves given in Figs. 11–13 for a fixed value of s. (They were obtained graphically from these figures.)

In Fig. 17 is shown a series of curves which give the variation of optimum η with optimum β for several values of s. These curves as previously explained are obtained by cross-plotting the load curves, Figs. 11–13 against η for several values of β keeping s fixed. These curves show that if optimum β is chosen very large then optimum η should be close to unity.

The two graphs, Figs. 16 and 17, are sufficient to permit the determination of optimum parameters for the stepped pad.

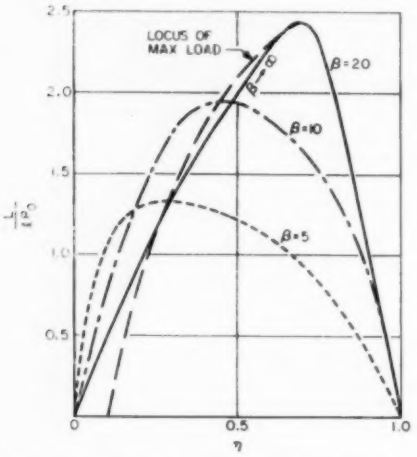

Fig. 14 Load per unit width versus η for various β and $s = 0.3$

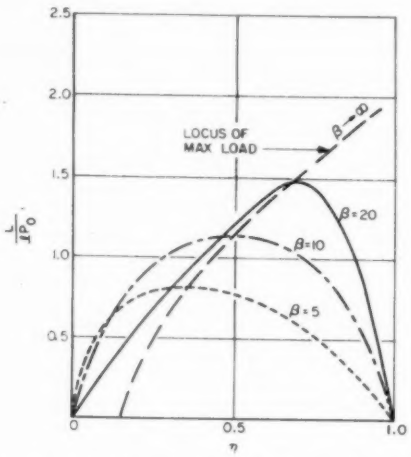

Fig. 15 Load per unit width versus η for various β and $s = 0.5$

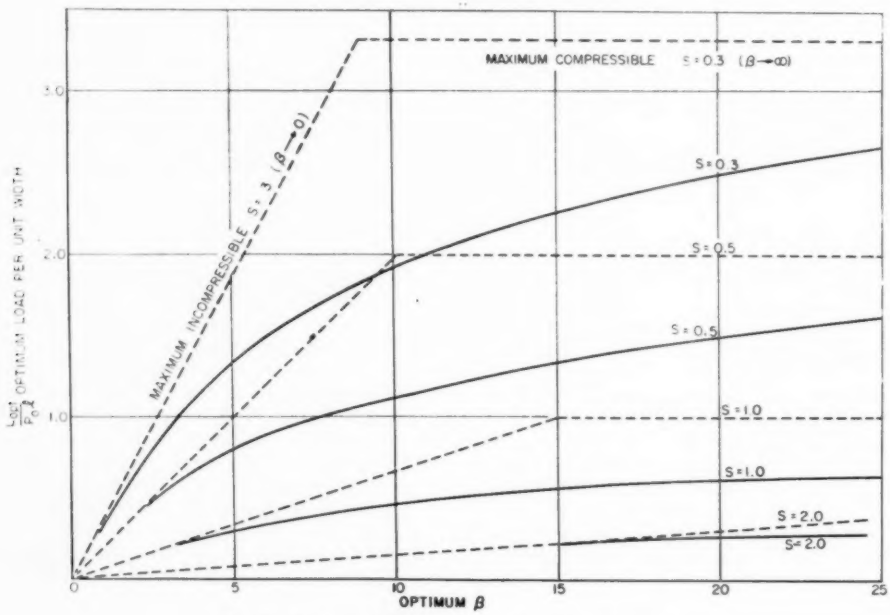

Fig. 16 Maximum load per unit width versus optimum β

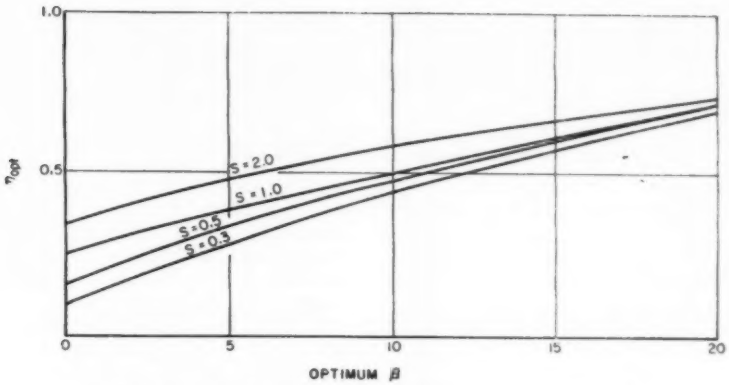

Fig. 17 Variation of optimum η with optimum β for various values of s

Typically, optimum β and s will be selected on the basis of the desired load from Fig. 16 and the corresponding optimum η can be determined from Fig. 17. In Fig. 16 there will be a set of values of β_{opt}, s, and η_{opt} which gives the required load; the particular choice for these parameters can be based upon other optimizing considerations which do not depend upon the foregoing discussion. For example, there may be an upper limit to the operating speed, in which case a smaller speed may be selected at a different value of s, and optimum η which still yields the same load.

In Fig. 16 are also shown the asymptotic maximum load curves for $\beta \to 0$ and $\beta \to \infty$. The expression for the asymptotic maximum load for $\beta \to 0$ is

$$\frac{L_{max}}{P_0 l} = \frac{\beta \eta_{opt}^2}{s^3} \tag{36}$$

where η_{opt} is determined in terms of s from Equation (35). This is the equation which is plotted in Fig. 16.

The asymptotic maximum load for $\beta \to \infty$ plotted in Fig. 16 is

$$\frac{L_{max}}{P_0 l} = \frac{1}{s} \tag{37}$$

This equation requires some justification. It is obtained in the following way: For large β the maximum pressure is $1/s$ and the pressure in Region I becomes asymptotically equal to this value. Thus total load is proportional to η/s and this is maximum as $\eta \to 1$. It is of course remembered that for $\eta = 1$ the load is zero. However, Fig. 17 bears out that, as $\beta \to \infty$, optimum $\eta \to 1$.

Analytic Expression for Maximum Load. Because of the importance of the curves shown in Fig. 16 and also because they are somewhat tedious to obtain for other values of s, a simple approximate formula is developed which will characterize these curves with a reasonable accuracy. It is noted that the reciprocal of the maximum load is very closely given by the sum of the reciprocals of the asymptotic maximum loads, $\beta \to 0$ and $\beta \to \infty$; That is

$$\frac{P_0 l}{L_{max}} = \frac{P_0 l}{L_{max}(\beta \to 0)} + \frac{P_0 l}{L_{max}(\beta \to \infty)} \tag{38}$$

$$= \frac{s^3}{\beta \eta_{opt}^2} + s \tag{39}$$

where η_{opt} is given by Equation (35), and the two terms on the right side of (39) are obtained from Equations (36) and (37).

Conclusions

The analysis and the graphs presented herein permit most of the characteristics of a stepped thrust pad of infinite width to be determined with a minimum amount of effort.

Acknowledgment

This study was supported under Air Force Contract [AF 33(616)—2137]. The author is indebted to Dr. J. S. Ausman and Mr. W. Wildman for their many helpful suggestions given during the course of this research.

DISCUSSION

W. A. Gross[5]

The author has presented a valuable paper which compares well with the high standard previously established by the gas-bearing work of his associates. The curves presented will be of great value to the designer. Previously published works on the gas-lubricated infinitely long step bearing[6,7] have not made such a complete presentation of the results.

It would be well to emphasize the restrictions relating to finite bearing length. Since significant losses in load capacity result as the length-to-breadth ratio decreases, the writer would like to have this effect discussed with respect to Figs. 14 and 15.

It is claimed that, for small values of the bearing number β, the pressure and load reduce to the values predicted in incompressible flow theory. Although these conditions are approached, it is possible to obtain a more precise bounding condition for $\beta \to 0$. The Reynolds' equation for the infinitely long isothermal gas film is,

$$\frac{d}{dx}\left[h^3 p \frac{dp}{dx}\right] = -6\mu U \frac{d}{dx}(ph) \tag{40}$$

[5] Member of Laboratory Staff Applied Mechanics, IBM Research Laboratory, San Jose, Calif. Mem. ASME.

[6] V. N. Constantinescu, "Consideratii Asupra Calculului Lagarelor de Alungire Infinita Lubrificate cu Gaze, Compuse din Suprafete Plane"(Methods for Calculating Characteristics of Infinitely Long Slider Bearings Consisting of Plane Surfaces and Lubricated by Gas), *Studii Si Cercetari de Mecanica Aplicata*, vol. 7, 1956, pp. 741–771.

[7] W. A. Gross, "Film Lubrication IV: Compressible Lubrication of Infinitely Long Slider and Journal Bearings," IBM Research Paper, RJ-RR-117, June 25, 1958.

Apply this now to Region I of Fig. 1, letting the normalized distance be $X = x/l$, and using the normalizations (14),

$$\frac{d}{dX}\left[\psi_1 \frac{d\psi_1}{dX}\right] = -\left(\frac{2\beta}{s^2}\right)\frac{d\psi_1}{dX} \tag{41}$$

Thus,

$$\frac{d^2(\psi_1)^2}{dX^2} = 0, \tag{42}$$

and

$$\psi_1 = [1 + (\psi_s^2 - 1)X]^{1/2} \tag{43}$$

When pressure profiles for small bearing numbers are plotted, it is apparent that the limit is (43) rather than

$$\psi_1 = 1 + (\psi_s - 1)X \tag{44}$$

as predicted by the theory for an incompressible film.

The pressure at the step is established by the bearing load rather than the requirement that flow be continuous across the step. For Region I, the unit bearing load is,

$$\left(\frac{L_1}{P_0 c_1}\right)_{\beta \to 0} = \frac{2\psi_s^2 - \psi_s - 1}{3(\psi_s + 1)}. \tag{45}$$

The center of pressure for Region I is given by

$$\left(\frac{\bar{x}}{c_1}\right)_{\beta \to 0} = \frac{4[3(\psi_s^5 - 1) - 5(\psi_s^3 - 1)] - 15(\psi_s^2 - 1)^2}{10(\psi_s^2 - 1)[2(\psi_s^3 - 1) - 3(\psi_s^2 - 1)]} \tag{46}$$

Similar results may be obtained for Region II.

Author's Closure

The author wishes to thank Dr. Gross for his comments and interest in the problem. He quite agrees that the solution for infinite width bearings leaves much to be desired when applied to finite width bearings.

For the stepped bearings an approximate finite width solution has been obtained from the Reynolds equation by perturbation methods, and this solution has been programmed on an IBM 701. However, this approximate solution, although reasonably good for qualitative purposes, is not always accurate in the quantitative prediction of the bearing characteristics. The study on the infinite width bearing was primarily motivated to sharpen the finite width solution. It is intended to submit in a subsequent paper the results of the study on the characteristics of the finite bearing.

In connection with the foregoing the load curves in Figs. 14 and 15 will be altered as the length-to-width ratio is varied. However the numerical results with the approximate finite width solution indicate that optimum η is relatively unaffected by variations in the length-to-width ratio. The curves given in Fig. 17 therefore appear to be valid for predicting optimum η for the finite width bearing.

With regard to the simplified solution for small values of β, Equation (42), one fails to see why Equation (43) can be a better approximation than Equation (44). The solution Equation (43) is based upon the premise that $\beta = 0$. The solution Equation (44) is the asymptotic solution of Equations (15) through (19) as β approaches zero. Hence it appears that Equation (44) is necessarily a better approximation than Equation (43) for small values of β.

This contention can be shown rigorously: Suppose Equation (43) is a better approximation. From Equation (42) the pressure distribution in region 2 can then be written as

$$\psi_2 = \left(1 + (\psi_s^2 - 1)\frac{x}{C_2}\right)^{1/2}, \quad -C_2 \leq x \leq 0 \tag{47}$$

Equations (43) and (47) must satisfy the continuity equation

$$\left\{\frac{6MUh_1}{po} + h_1^3 \frac{d\psi_1}{dx}\right\}_{x=c_1} = \left\{\frac{6MUh_2}{po} + h_2^3 \frac{d\psi_2}{dx}\right\}_{x=-c_2} \tag{48}$$

which implies that

$$\frac{1}{2}\frac{\psi_s^2 - 1}{\psi_s} = \frac{2\beta}{\frac{s^3}{\eta} + \frac{(1+s)^3}{(1-\eta)}} \tag{49}$$

or equivalently

$$\psi_s - 1 = \frac{2\psi_s}{\psi_s + 1}\,\frac{2\beta}{\frac{s^3}{\eta}\,\frac{(1+s)^3}{(1-\eta)}} = \left\{\frac{2\psi_s}{\psi_s + 1}\right\}(\psi_s - 1)_{\text{incompressible}} \tag{50}$$

Since $\psi_s > 1$ the conclusion is that

$$\psi_s - 1 > (\psi_s - 1)_{\text{incompressible}} \tag{51}$$

implying that Equation (42) will lead one to overestimate the pressure for even small values of β. From the maximum pressure curves (Figs. 4 through 6) it is seen that for all values of β the maximum pressure is always less than in the incompressible case represented by the straight dotted lines. The conclusion is that Equation (42) cannot be a valid approximation for small values of β.

Direct Measurement of Net Positive Suction Head[1]

ROBERT B. JACOBS[2]
KENNETH B. MARTIN[2]
RICHARD J. HARDY[3]

A simple, reliable, and accurate method for measuring net positive suction head is described, difficulties which may be encountered in its application are discussed, and test information indicating its reliability and accuracy is presented. The device which embodies the method consists of a vapor-pressure bulb that measures the vapor pressure of the liquid, a pressure tap that measures stagnation pressure, and a pressure gage to indicate (and record, if desired) the difference between the two pressures.

Introduction

The net positive suction head (NPSH) is the difference between the actual stagnation pressure and the vapor pressure of the liquid at the suction of a pump. It is one of the more important quantities which must be determined during the evaluation of pump characteristics, especially with regard to cavitation. The purpose of this paper is to describe a simple, reliable, and accurate method for measuring NPSH.

The usual methods for determining NPSH vary in details because of differences in pumps and test equipment, but they require the measurement of both pressure and temperature. If the stagnation pressure (total head) cannot be measured directly, separate determinations of the static and dynamic pressures are made, the latter requiring flow measurements. From the temperature measurements and vapor pressure data, the vapor pressure is obtained. A subtraction then gives the NPSH.

The usual methods, however, are not satisfactory for some fluids. For example, the determination of NPSH with liquid hydrogen to an accuracy of one inch requires a temperature measurement accurate to about 0.0005 K. The only simple, inexpensive device that will give this accuracy is the vapor pressure thermometer. Although it is not used as a thermometer, this device is the basis of the method for measuring NPSH that is described here. The scale of the indicator can be calibrated to read NPSH directly; no computations are necessary.

Description of Method

Fig. 1 is a schematic of the simplest type of installation, the pump being submerged in a sump. This configuration is used by the authors when determining NPSH with liquid hydrogen and liquid nitrogen. The system consists of three elements: 1, A stagnation pressure tube; 2, a vapor-pressure bulb and tube; and 3, a differential pressure measuring device. The stagnation pressure tube transmits the stagnation pressure to one side of the differential pressure device while the vapor-pressure tube transmits the vapor pressure to the other. If the scale of the differential pressure device is calibrated in height of liquid the NPSH will be directly indicated. (It should be noted that, in this sump configuration, there is an insignificant decrease in NPSH between the location of the instrumentation and the entrance to the first stage impeller; this is a friction effect.)

The Stagnation Pressure Tube. The stagnation pressure tube (see Fig. 1) is merely a tube with its lower end open to the liquid at the pump suction. If the liquid is prevented from rising in the tube, the pressure communicated to the differential pressure device is that existing in the liquid at the open end of the tube. (If desired, a correction for the hydrostatic head of gas in the tube can be made.) The authors have used two methods to prevent liquid from rising in the tube: 1, The tube is insulated with a vacuum jacket. The heat conducted down the tube evaporates any liquid which may rise in the tube. An electric heater is installed at the lower end of the tube to supplement the heat conduction; it has not had to be used. 2, A very small flow of helium gas is forced down the tube, thus keeping out all liquid. The flow must be small so that only a negligible pressure difference down the tube is created. (The helium should be prevented from entering the pump.) In installations where the pressure in a suction pipe must be measured, the stagnation pressure tube must be a total head device and should have a minimum effect on the fluid flow. It should be noted that, except for friction effects in the

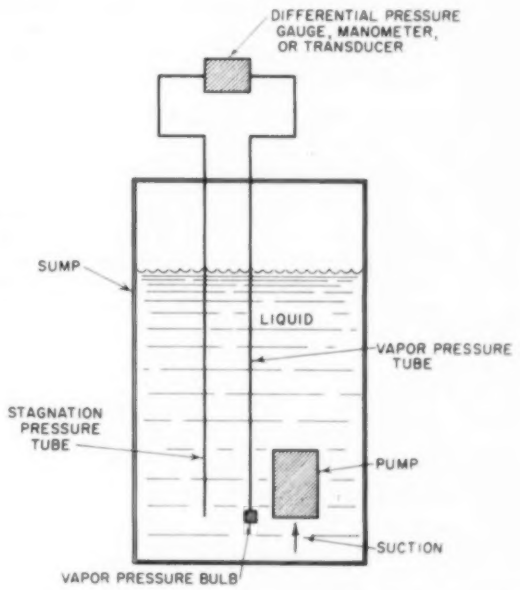

Fig. 1 Schematic of vapor-pressure device for measuring NPSH

---

[1] This work was supported by the U. S. Atomic Energy Commission.
[2] National Bureau of Standards, Boulder, Colo.
[3] U. S. Naval Ordnance Laboratory, Corona, Calif.
Contributed by the Pumping Machinery Subcommittee of the Hydraulic Division and presented at the Annual Meeting, New York, N. Y., November 30–December 5, 1958, of The American Society of Mechanical Engineers.

Note: Statements and opinions advanced in papers are to be understood as individual expressions of their authors and not those of the Society. Manuscript received at ASME Headquarters, April 25, 1958. Paper No. 58—A-38.

suction pipe, the NPSH measured in a sump should not differ from that measured in a suction pipe.

The Vapor Pressure Bulb and Tube. As this part of the system is merely a vapor-pressure thermometer, it should fulfill the design requirements for such a device. It is filled with material which is, as nearly as possible, identical to the fluid being pumped. The amount of material introduced into this part of the system is readily determined from the internal volume of the bulb, tubing, and differential pressure device; when the bulb is at its operating temperature, the liquid-vapor interface must be in the bulb.

The importance of the identity of the composition of the fluid in the vapor-pressure bulb and that of the fluid being pumped must be stressed. If the fluids differ appreciably, they must be analyzed and corrective computations be made. For example, if nitrogen being pumped has a 2 per cent oxygen impurity while that in the vapor-pressure bulb has none, an error of over 10 inches in the NPSH will result; more than this amount of oxygen can condense from the atmosphere into liquid nitrogen as a result of poor handling technique. As another example, consider the effect of ortho-para composition in liquid hydrogen: If the ortho-para composition in the vapor-pressure bulb differs from that entering the pump by 5 per cent, the NPSH will be in error by about 12 in. Difficulties from this source can be overcome by placing catalyst in the vapor-pressure bulb and in the pump sump to insure that equilibrium hydrogen exists in both places.

Because petroleum fuels are mixtures of many fractions and their compositions vary widely, it is probable that great care will have to be exercised when using this NPSH device with them. The vapor-pressure bulb may therefore have to be refilled each time a new batch of fuel is used. The method of filling the bulb must be such that the liquid does not fractionate during filling. With water, as with all liquids, the air must be thoroughly removed from the vapor-pressure system (e.g., by evacuation) before the working liquid is introduced.

Liquids with low boiling points can produce very high pressures in the vapor-pressure system when allowed to warm to room temperature; provision must therefore be made to protect the system and differential pressure device. (With hydrogen, the pressure can rise to over 20,000 psia.) These high pressures can be avoided by allowing the gas to expand into an auxiliary volume when the system warms, or by permitting the gas to escape from the vapor bulb, replenishing it each time the system is cooled. In the latter case it is important that the escape passage have a capacity sufficient to handle the vapor which can forth exceedingly rapidly.

The volume of the bulb must be large enough so that the liquid-vapor interface always remains in the bulb. As condensation should take place only in the bulb it must be the coldest part of the system; if there is liquid in the vapor-pressure tube an error will be introduced. For liquefied gases, the authors have enclosed the vapor-pressure tube, which is made of stainless steel, in a vacuum-insulated jacket from its room temperature end down to the bulb. The heat conduction down the tube is sufficient to prevent the undesired condensation; if this were not the case, an electric heater could be installed in the jacket. The use of such a heater would be necessary in cases where the temperature of the pumped liquid is near or above ambient temperature. Obviously, the vapor bulb should be designed and placed so that it has a minimum effect on the pump characteristics.

It is apparent that the pressure within the vapor-pressure bulb is the vapor pressure of the surrounding liquid, and if the bulb is in the pump suction, it is the vapor pressure needed to compute the NPSH.

The Differential Pressure Device. The differential pressure device measures the difference between the pressure in the stagnation pressure tube and that in the vapor-pressure bulb, and thus (if the scale is calibrated in height of liquid) the NPSH. Depending upon the liquid and the accuracy required, it can be a gage, manometer, transducer, etc.

Discussion and Test Results

The device just described embodies a very simple and straightforward method for determining NPSH. It is the only one, known to the authors, which will yield sufficient accuracy with liquid hydrogen. [All of the pumps which the authors have tested with liquid hydrogen (from 1725 rpm to over 12,000 rpm) have required NPSH's of less than 6 in. to prevent symptoms of cavitation.] If the NPSH is to be known to within one inch (of liquid hydrogen) the ordinary methods would require a temperature measurement accurate to about 0.0005 K; this vapor-pressure method, however, only requires a pressure measurement accurate to 1.75 mm H_2O.

Fig. 2 shows the actual appearance of the vapor-pressure device used by the authors during their liquid hydrogen and liquid nitrogen pumping tests. The vapor pressure bulb is a half torus with an internal volume of about 8 cu in., containing about one cubic inch of catalyst. Not shown in the figure are: 1, The external valving required to protect the differential pressure device; 2, the differential pressure device which, for hydrogen, is a transducer with a range of ± 0.1 psid; and 3, the auxiliary volume which limits the pressure in the warm system (with hydrogen) to about 400 psia.

Fig. 3 gives the results of a test conducted to determine the reliability of the vapor-pressure device by comparing the NPSH indicated by it with that indicated by a conventional setup. Liquid nitrogen was the working substance. The NPSH was varied over the period shown by changing the stagnation pressure and the liquid temperature, and the indication of each NPSH measuring device was recorded. (Fig. 3 will be discussed later.)

The vapor-pressure device used a 0 to 100 in. of H_2O differential pressure gage for differential pressure measurement; this reading was accurate to better than one inch of liquid nitrogen.

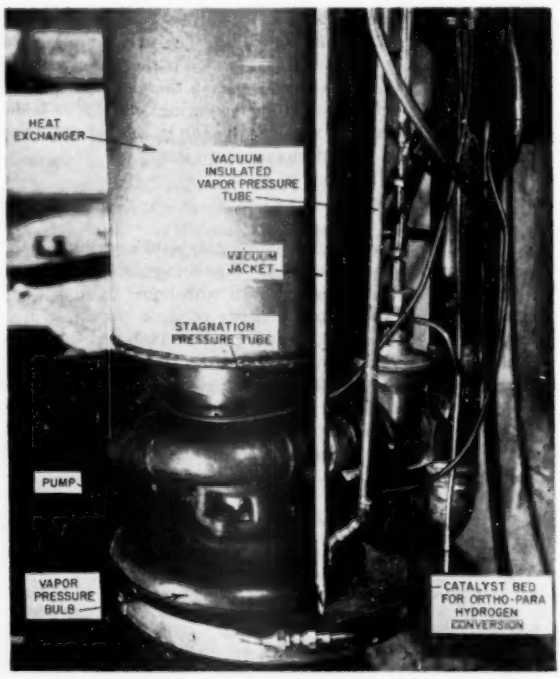

Fig. 2 Test setup with sump removed

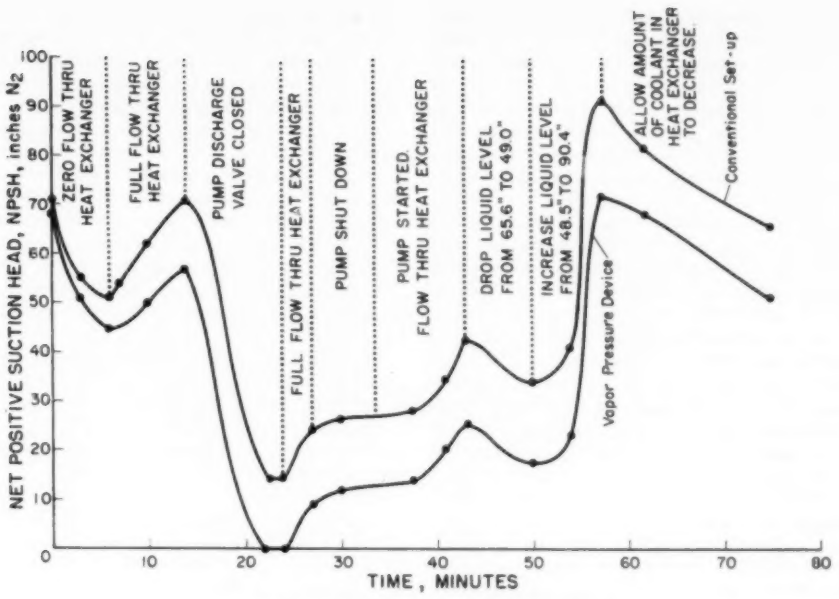
NET POSITIVE SUCTION HEAD, NPSH, inches N_2
TIME, MINUTES
ZERO FLOW THRU HEAT EXCHANGER
FULL FLOW THRU HEAT EXCHANGER
PUMP DISCHARGE VALVE CLOSED
FULL FLOW THRU HEAT EXCHANGER
PUMP SHUT DOWN
PUMP STARTED FLOW THRU HEAT EXCHANGER
DROP LIQUID LEVEL FROM 65.6" TO 49.0"
INCREASE LIQUID LEVEL FROM 48.5" TO 90.4"
ALLOW AMOUNT OF COOLANT IN HEAT EXCHANGER TO DECREASE
Conventional Set-up
Vapor Pressure Device

Fig. 3 NPSH measurements with liquid nitrogen

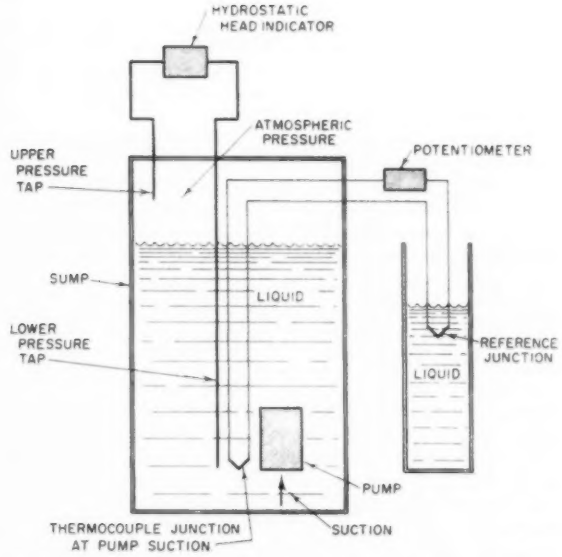

Fig. 4 Conventional setup for measuring NPSH with a liquid at or near its boiling point

The conventional setup is shown in Fig. 4. The surfaces of the liquid in both the sump and the reference junction container were at atmospheric pressure. The reference junction was well tempered and was located near the surface of the liquid which was boiling violently. Thus if both bodies of liquid have the same composition, the thermocouple setup measures the difference between the temperature of the liquid at the pump suction and the boiling point corresponding to the pressure on the surface of the liquid in the sump. The hydrostatic head indicator measures the difference in pressure between the surface of the liquid and the pump suction. Thus if the difference in vapor pressure, corresponding to the measured temperature difference, is subtracted from the hydrostatic head, the NPSH is obtained.

The hydrostatic head indicator (in Fig. 4) was a 0 to 100 in. of H_2O differential pressure gage (of the same type that was used on the vapor-pressure system) with an accuracy of better than one inch of liquid nitrogen. The thermocouples were gold with a 2.1 atomic per cent impurity of cobalt versus copper; their sensitivity at liquid nitrogen temperature is approximately 35 microvolts per degree Kelvin. The potentiometer had a least reading of 1/2 microvolt and reproduced readings to 2 microvolts. The temperature measurements were thus accurate to about 0.059 K. This corresponds to a vapor pressure measurement that is accurate to 2.34 in. of liquid nitrogen.

Therefore in Fig. 3, the vapor-pressure-device curve is reliable to about one inch of liquid nitrogen, while the conventional-setup curve is reliable to about 2.3 in. of liquid nitrogen.

The NPSH was varied during the test by changing both the pressure and the temperature at the pump suction. The pressure was altered by changing the liquid level (hydrostatic head). The temperature was altered in the following manner: After being discharged from the pump, the liquid passed through a heat exchanger (see Fig. 2) where it was cooled by liquid nitrogen boiling at atmospheric pressure. The degree of cooling was varied by changing the amount of coolant in the heat exchanger and by changing the proportion of the pump discharge that flowed through the heat exchanger. The temperature of the liquid at the pump suction could thus be varied from the normal boiling point to the saturation temperature corresponding to the suction pressure; the NPSH could be varied from zero to the maximum liquid level attainable in the apparatus. (The maximum can be increased by pressurizing the sump. However, the 22-ft liquid level attainable in the authors' apparatus was sufficient for the tests which have been performed.) In the test shown in Fig. 3, the NPSH range is seen to be from 0 to 6 ft. The pump used in this test was an aircraft fuel booster pump that effectively handles liquid-gas mixtures. It is known that the pump was cavitating at the lower values of NPSH; however, this situation has no bearing on the present discussion. The notations on Fig. 3 indicate the methods used to vary the NPSH.

Fig. 3 shows that the values of NPSH indicated by the two methods differed by about 15 in., the conventional setup consistently yielding higher results than the vapor-pressure apparatus. The purpose of the test was not to prove the superiority of one method relative to the other, but merely to indicate the reliability and accuracy of the vapor-pressure device. It is therefore necessary that differences in the results obtained by the two methods be explained, and to indicate, if possible, which curve is more likely to be correct.

The authors have two reasons for believing that the curve obtained from vapor-pressure device is the more accurate and therefore that the device is reliable: 1, The vapor-pressure-device curve indicates the behavior expected during the test; 2, an explanation of why the conventional-setup curve can be erroneous has been found, but no potential source of inaccuracy has been found in the vapor-pressure device.

The explanation of the first reason is that at time equal to 14½ min (see Fig. 3), the pump discharge valve was closed; thus all of the energy which entered the sump through the pump shaft should increase the liquid temperature and rapidly reduce the NPSH to zero. (Because of the extremely effective insulation of the sump and the location of the sensing elements, it is not possible for the NPSH to tend to a steady-state value greater than zero. On the other hand, as the turbulence in the sump was very great, it is improbable that the liquid would become sufficiently superheated to cause the NPSH to tend toward a negative steady-state value.) The figure shows that the vapor-pressure device indicated the expected behavior, i. e., the NPSH did go to zero.

In the second place, the NPSH indicated by the conventional setup could be erroneous because the composition of the liquid at the reference junction could be different from that of the liquid in the sump. As mentioned previously, unless care is taken, appreciable amounts of oxygen will condense from the atmosphere into liquid nitrogen that is being poured into, or is standing in, an open container. If this occurred with the nitrogen at the reference junction (and this is very possible) its temperature would be too high; this would make the temperature at the pump suction appear too low, and thus indicate an NPSH that is too high. An oxygen impurity of only 3 per cent would cause the discrepancy between the curves in Fig. 3. On the other hand, because the nitrogen in both the vapor bulb and the sump was obtained from the same container and was not exposed to the atmosphere, the required identity of composition was achieved with the vapor-pressure device.

DISCUSSION

S. Prelowski[4] and G. H. Caine[4]

This method of measuring NPSH directly was suggested to Pesco by the authors for our use in a pump-development program for liquid para hydrogen which we conducted at NBS with NBS technical advice and assistance in 1957 and 1958.

The method, because of its directness and the theoretical simplicity of its idea, is of much interest for measuring quite small values of NPSH, or measuring it with theoretically possible accuracy in a liquid such as hydrogen which (*a*) has a rapidly changing vapor pressure with temperature, and (*b*) has a low, extremely difficult to measure absolute temperature, as the authors have noted.

For this reason it is hoped that some of the practical limitations and precautions in its use can be resolved. Some of these are as follows:

1 The same tube which is used to measure vapor pressure from the vapor bulb to an outside measuring device is also a conducting path for heat to or from the vapor bulb. So also is the vacuum jacketing tube around it (which the authors used and which we also employed). While thin-wall 300 series stainless tube was used for both, and this has poor heat conductivity, heat conduction to the bulb cannnot be completely eliminated. Consider that 1 deg C change in liquid-hydrogen temperature causes a change in vapor pressure equivalent roughly to 125 ft head of liquid, at the particular conditions of test. Then an increase of only $^1/_{1000}$ C in bulb temperature would cause a corresponding 1-in. increase of vapor pressure, and the same decrease in NPSH. One inch of NPSH is also most appreciable compared with a typical 3 to 6-in. static inlet head before cavitation effects become appreciable on our various pumps.

It is seen that even a very small amount of heat conduction down the tubes could cause appreciable error in NPSH measurements.

With any finite conductivity down the tubes, some definite, if small, thermal gradient must exist between the bulb and the liquid inside it and outside it. Inside the bulb, at the place where the tubes are attached, it can be expected that the fluid will be boiling more intensely, and the recondensing of the vapor will take place in parts of the bulb more distant from the place of attachment.

Consequently, the vapor pressure measured will be some kind of a mean value of these two extremes in the bulb, and slightly higher than the vapor pressure outside the bulb.

We believe that this as well as other possible errors which the authors have mentioned may have caused at least a part of the difference between their curves in Fig. 3.

For our use of this method, we had reached a zero NPSH reading by it with about 12 to 15 in. of liquid hydrogen above the pump inlet. At liquid levels below this we had NPSH readings before the pump inlet which were at times several inches negative. It is difficult to find this acceptable in view of the agitated condition of fluid in the dewar.

We wonder whether there was any negative indication between about 22 and 24 min in Fig. 3.

A partial remedy of tube conduction might be elimination of the outer jacketing tube, and a helix made of the pressure tube to give less axial heat leak, with a nonmetallic insulator as a bulb mechanical support.

2 Another possible difficulty is that there is a difference of state between liquid inside the bulb and the liquid outside the bulb, because the liquid inside the bulb is quiet, whereas liquid outside the bulb is agitated.

3 A third need for precaution (and a possible source of difficulty) is in getting proper representative samples of liquid in the bulb. This is a problem where we do not deal with a pure substance, but rather a multicomponent liquid. Even with relatively pure liquids we are usually dealing with dissolved gases in the liquid which change the vapor nucleation, vapor pressure, and temperature of the liquid, and these also change during the course of a test. This necessitates frequent sampling of the bulb and test tank contents. Some attention to better and more convenient methods of sampling is in order. It would be most useful.

4 A necessary precaution is location of the bulb in such a place where no significant pressure and temperature gradients exist because of velocity or vorticity of fluids in the inlets.

5 Other limitations to either the conventional temperature system, or the bulb method described is that we have found net *negative* suction heads at times, where the level of boiling hydrogen was indicated as actually below the level of the impeller inlet. Also, consistently on all pumps tried on liquid hydrogen, we have found a velocity head in the inlet greatly exceeding either the static head of boiling liquid or the lesser NPSH possible, on minimum inlet levels before cavitation surges appeared. These effects we believe are due to liquid evaporation (change of *PVT*

[4] Pesco Products Division, Borg Warner Corporation, Bedford, Ohio.

relations in the inlet) with vapor formation in the inlet which the bulb cannot measure.

The bulb method of the authors is not only direct, but also has proved extremely sensitive as was required for our tests. For these reasons we hope that the practical difficulties and limitations in its use can be resolved. We would certainly welcome suggestions on these for our applications.

Victor Salemann[5]

The writer has had experience using a method similar to the one described in this paper, but adapted to liquids hotter than the surroundings. Rather than fight condensation in the tubing, the system was inverted such that all tubing was filled with liquid, Fig. 5.

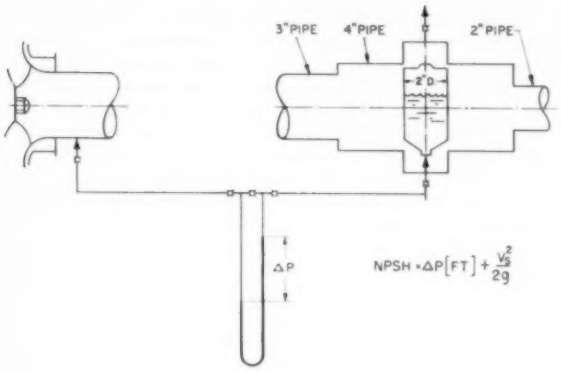

Fig. 5

There are several points on the requirements for a vapor-pressure thermometer that were not mentioned or stressed enough in the paper.

1 There must be no heat transfer between the bulb and the outside: This would create a temperature difference between bulb and pumped fluid, introducing an error. For instance, in the authors' example, a 1-in. error will be produced in the NPSH measurement using liquid hydrogen if there is a difference of only 0.0005 deg K between bulb and pumped liquid. In the authors' setup, a heater was installed on the vapor-pressure tube and some heat transfer was allowed down the tube. The writer does not suggest that this caused a measurable error, but it may have.

2 When mixtures are used in the bulb the vapor pressure in the bulb would depend on the vapor and liquid volumes and would vary if the volumes vary, as they would if a manometer is used as a differential pressure-measuring device. Even if the volumes do not vary, there is the question of what volume ratio should be used. If cavitation inception is to be found, the volume of vapor should be very small compared to the volume of the liquid. This may be difficult to achieve and be sure that there always is a small volume of vapor.

3 Coming back to the heat-transfer problem, care must be taken that the pumped liquid does not cavitate on the surface of the vapor bulb, as this would cause a drop in surface temperature introducing an error. This difficulty is easily encountered in suction pipe installations. Also, there should be no heat transfer to and from the pumped liquid between the bulb and the impeller.

[5] Research and Development Section, Worthington Corporation, Harrison, N. J. Assoc. Mem. ASME.

4 The writer's only questions pertain to the reliability of both methods. The authors mention that there was considerable turbulence in the sump during the operation of the pump at shutoff. Was this turbulence created by other means than the pump itself? If so, and if the liquid was also agitated during the shutdown period, the NPSH should approach the value of the liquid level, as it does at zero time on the curve. In the conventiona setup, the accuracy of the hydrostatic pressure-measuring device can always be checked by the elevation of the liquid above the pump. Did these values correspond? Finally, it seems that the reference junction should be placed at the liquid surface in the sump, rather than in a separate container, to reduce the uncertainty of the composition of the liquids. Is there any practical reason against it?

Authors' Closure

We wish to thank Messrs. Prelowski, Caine, and Salemann for presenting their experience with the NPSH vapor-pressure device, especially the difficulties encountered, and for posing some pertinent questions. Recording their difficulties here materially increases the value of this paper.

The question concerning thermal equilibrium between the vapor bulb and the surrounding fluid, which is the first item in both discussions, can be resolved by considering the vapor pressure tube and bulb as a compound fin and solving the steady-state, one-dimensional heat-transfer problem. The calculation indicates that heat transfer to (or from) the bulb via the supporting tubing can, in fact, introduce appreciable error. As this error is an inverse exponential function of the length of the conducting path, the "partial remedy" which Messrs. Prelowski and Caine suggest is quite satisfactory. Consider, for example, a vapor bulb supported by a length of $^1/_8$-in. OD $\times$ 0.010-in. wall stainless-steel tube immersed in liquid hydrogen flowing with a Reynolds number of 2000 (used to calculate the heat-transfer coefficient). Assume that the temperature of the warmer end of the tube differs from that of the hydrogen by 1 deg K. Then if the support tube is 3 in. long, the temperature of the bulb will differ from that of the hydrogen by about 0.0008 deg K. If, however, the tube is 10 in. long the error will be less than 10^{-10} deg K. The results of these computations and the construction of our vapor pressure system indicate that heat conduction could have introduced a measurable error in our hydrogen experiments. In the liquid nitrogen test shown in Fig. 3, the effective temperature of the vapor bulb would have had to have been 0.22 deg K higher than that of liquid to account for the difference between the curves. It is unlikely this temperature difference could exist in the nitrogen test. Furthermore, the facts that the NPSH went to zero at 22 minutes, as expected, and that our measurements were good to 1 in. of liquid nitrogen (corresponding to 0.027 deg K) lead us to believe that no measurable error was introduced into the nitrogen test (in Fig. 3) by heat conduction. We did not notice any negative NPSH indications in our tests, but this source of error could certainly have contributed to the negative NPSH's which Mr. Caine measured. In any event this problem should be borne in mind by anyone designing this type of instrumentation.

The same basic question is raised by item 2 in both discussions: How does one define the vapor pressure which is significant in pump cavitation criteria. Obviously, the answer is not readily obtained. The difficulty is not caused by the use of any particular method of NPSH measurement, but rather by the question of whether the proper vapor pressure is a function of temperature only. An additional problem caused by the highly agitated fluid outside the bulb is that of obtaining an accurate value for the stagnation pressure.

Answering Mr. Salemann's specific questions: The turbulence in the sump during shutoff was induced by the pump. The ac-

curacy of the hydrostatic pressure measuring device in the conventional setup was checked as suggested and was found to be very good. There was a practical reason for not floating the reference junction in the sump; as the liquid level varied over 20 ft during some of the tests, it was anticipated that the leads would become fouled when the level was below its maximum.

It should be emphasized that the vapor-pressure device should not be used indiscriminately; there are situations for which a crude mercury-in-glass thermometer would be more desirable. The criterion is whether or not the accuracy, simplicity, and cost of a vapor-pressure thermometer makes its use more desirable than another type of thermometer.

Table 1 was compiled to illustrate this point: The pertinent information for water at various temperatures, octane, butane, oxygen, nitrogen, and hydrogen is tabulated. The specific gravity is included so that the reader can determine the relative accuracy of the pressure measurements required to obtain a given accuracy of the NPSH. The fourth column is the slope of the vapor-pressure curve, expressed as the temperature change which is equivalent to a pressure change that corresponds to a head change of one inch; it therefore gives the necessary accuracy of a temperature measurement if the NPSH determination is to have an accuracy of one inch. It is immediately apparent that, for a NPSH accuracy of 1 in. with water at 70 deg F or with octane at 90 deg F, an ordinary mercury thermometer is adequate.

However, for hot water, butane, and the three liquefied gases, rather precise temperature measurements are required and use of the vapor-bulb device is desirable. In the fifth column of Table 1 is tabulated the thermocouple potentials (in microvolts) which correspond to the temperature differences given in column four; for most of the examples, the potentiometric system would have to be able to detect a fraction of a microvolt.

The sixth and seventh columns in Table 1 are included to indicate whether or not an NPSH measurement accurate to one inch is, in fact, accurate enough. Column six lists the NPSH requirements which have been measured for pumps with the indicated liquids, while column seven gives the per-cent error (based upon these requirements) represented by an NPSH accuracy of one inch. Whether or not these errors are acceptable depends upon the particular investigation. Of course, pressure instrumentation with accuracies of much better than one inch of head are available; however, with hydrogen an error of less than 0.2 in. is not attainable with presently available commercial equipment.

It is desirable to add a comment which is relevant to the material in the last paragraph in the section on "Discussion and Test Results." It was stated that a temperature at the reference junction, in Fig. 4, which was too high could account for the difference in the curves in Fig. 3. It was also stated that the liquid surrounding the reference junction was boiling violently. It is therefore possible that the liquid around the reference junction was superheated; a superheat of only 0.22 deg K would cause the difference in Fig. 3. It is therefore possible that both superheating and oxygen impurity at the reference junction caused the difference between the curves in Fig. 3.

Table 1

Liquid	Temperature (°F)	Specific Gravity	$(dT/dp)_{v.p.}$ (°F/inch)	$(dT/dp)_{v.p.}$ (μv/inch)	Example of Required NPSH (ft)	Error due to NPSH accuracy of 1 inch (%)
WATER	70	0.998	2.96	68 [1]	6.5 (1600) [3]	1.3
"	212	0.958	0.121	3.14 [1]		
"	300	0.918	0.033	0.915 [1]	4 (1600) [3]	2.1
"	400	0.858	0.0111	0.334 [1]		
OCTANE	90	0.7	2.023	46.5 [1]		
BUTANE	94	0.6	0.028	0.635 [1]	1.5 (1600) [3]	5.5
OXYGEN	−298	1.149	0.041	0.824 [2]		
NITROGEN	−321	0.807	0.027	0.510 [2]	7 (1350) [3]	1.2
HYDROGEN	−424	0.0709	0.001	0.009 [2]	0.17 (1350) [3]	50

ACCURACY OF TEMPERATURE AND PRESSURE MEASUREMENTS REQUIRED FOR NPSH DETERMINATIONS

NOTES

(1) Copper − Constantan thermocouple

(2) Gold (2.1 atomic % Cobalt) − Copper thermocouple

(3) These numbers are specific speed

Transitional Phenomena in Ultrasonic Shock Waves Emitted by Cavitation on Hydrofoils

F. NUMACHI

Professor, Tohoku University (Faculty of Engineering); Director, Institute of High Speed Mechanics, Sendai, Japan. Mem. ASME.

In some cases during the experiments described in past reports [1, 2][1] which dealt with cavitation-induced ultrasonic shock waves, extremely anomalous values were obtained in the imparted pressure of the shock waves. The paper deals with an investigation into the nature of these shock-wave anomalies, and it is demonstrated that these anomalies can be caused not only in closed-circuit cavitation tunnels but can be produced in any flow subjected to preliminary cavitation at a point upstream of the point of principal cavitation. The nature of the anomalies occurring in the shock-wave spectrum was studied, and its relation to cavitation-bubble size was made clear.

THERE are three well-known kinds of trouble due to cavitation that arise in hydraulic machinery: (*a*) Drop in the hydraulic efficiency of the machine; (*b*) damage to the machine from erosion, leading to shorter life; (*c*) vibrations evoked by cavitation. Studies from the point of view of hydrodynamics and of materials have been undertaken in the past to counter these troubles, but the author considers that new approaches can be suggested for the studies on materials through basic research work aimed at clarifying the different aspects of cavitation occurrence. It is to be proved by future workers whether investigations on ultrasonic shock waves emitted in conjunction with cavitation would contribute to the same end.

According to present knowledge, erosion by cavitation is attributed mainly to the shock pressure developed when the cavitation bubbles extinguish themselves. It is therefore thought that a study of the nature of the shock waves emitted by cavitation should bring significant results in solving the problem of erosion fatigue. Furthermore, such a study could contribute also in establishing a method of detecting cavitation occurrence by "listening" for the ultrasonic waves that accompany cavitation. The study could provide an indication of the most suitable frequency to which to tune the detector for the purpose.

Some published papers report on shock waves caused by the extinction of a single bubble [3], shock waves accompanying nozzle cavitation [4], and similar waves emitted by cavitation on a revolving thin rod [5], but these reports do not give the relations connecting the shock waves to the hydromechanical data, particularly cavitation coefficient.

The author has already described in past reports [1, 2] the nature of the ultrasonic shock waves emitted by hydrofoils under cavitation. On some occasions during these experiments, marked anomalies were observed in the spectrum of these shock waves. In all these experiments the shock-wave spectra were measured after obtaining the desired cavitation coefficient[2] k_d by regulating the flow velocity and maintaining it during the measurements. The anomalies were observed in the cases (*b*) and (*c*) below:

(*a*) The flow velocity is gradually increased and then regulated until a predetermined ultimate value of cavitation coefficient k_d is obtained, where it is maintained for some minutes. We might call this "stabilized cavitation."

(*b*) The flow is first accelerated to a point where cavitation is overdeveloped (for instance, until it reaches the tail of the specimen), and flow thus subjected to preliminary cavitation is then slowed down to the velocity corresponding to the predetermined ultimate value of cavitation coefficient k_d. In this case an anomalously high but decreasing shock-wave pressure is recorded during about 3 minutes following the attainment of k_d. This phenomenon might be named "reducing transition cavitation."

(*c*) After first raising the velocity to the predetermined value of k_d, the pump motor is shut off (the flow coming to a stop in about 50 sec); within several minutes the pump is restarted and the flow velocity made to regain the value of k_d (the time from restarting to regaining the velocity is about 30 sec). In this case several minutes are required for the shock-wave pressure to build up again to the ultimate stable value. This phenomenon might be called "regenerating transition cavitation."

The following points concerning these transitional phenomena are successively examined in the paper:

1 The conditions under which the phenomena of the cases (*b*) and (*c*) occur, and the evolution in time of the mean shock-wave pressure.[3]

---

[1] Numbers in brackets indicate References at end of paper.

Contributed by the Cavitation Committee of the Hydraulics Division and presented at the Annual Meeting, November 30–December 5, 1958, New York, N. Y., of THE AMERICAN SOCIETY OF MECHANICAL ENGINEERS.

NOTE: Statements advanced in papers are to be understood as individual expressions of their authors and not those of the Society. Manuscript received at ASME Headquarters, August 7, 1958. Paper No. 58—A-117.

[2] The cavitation coefficient k_d is the value represented by

$$k_d = (p_\infty - p_d) \Big/ \frac{1}{2}\rho v_\infty^2$$

where

p_∞, v_∞ = static pressure and velocity upstream of profile
p_d = vapor pressure at water temperature t_w
ρ = density of water

[3] The mean shock-wave pressure p_m and the individual impulse pressure p_i are defined as follows [1]:

From the output oscillogram of the chosen reception frequency the input voltage U is obtained, based on which the total shock-wave pressure acting on the detector element

$$K_s = \frac{\epsilon UF}{4\pi s d_{31}} \qquad (1)$$

2 The effect on these phenomena of differences in the period during which the preliminary cavitation is maintained (case *b*) or during which the flow is interrupted (case *c*).

3 The spectrum of the shock waves during transition.

4 The effect of differences in water temperature on the transitional shock-wave spectrum.

5 Frequency distribution of the impulse pressures[3] of individual shock waves during transitional and stabilized cavitation.

6 The possibility of analogous transitional phenomena occurring in hydraulic machinery.

7 Relation between shock-wave pressure and bubble size.

Experimental Apparatus and Method

The profile form utilized for the present series of experiments was the Clark Y of 11.7 per cent thickness ratio, the same as in the two previous reports already mentioned; the cavitation tunnel used was the one utilized in the experiments of Report 1 [1, 6]. An open-end cavitation tunnel [2] was used for experiments aimed at determining whether the transitional phenomena also could be produced where the flow did not follow a closed circuit.

The device for measuring the sound waves, the method of computing the shock-wave pressures, that of selecting the location of the measuring points, of calculating the impulse pressures imparted by individual shock waves, and so on, have already been fully discussed [1, 2] and will therefore not be repeated here. It may be noted that during these experiments, the static pressure H_s prevailing immediately upstream of the specimen was 3.3 m aq, and before starting each experiment the water temperature was left free to accord with the prevailing surrounding atmosphere. The degree of air content of the water a/a_s (where a is quantity of dissolved air, a_s is quantity of dissolved air in saturated water at the same temperature) was measured before and after experiments, and was found to be stable at a value of 1.07. The value of a/a_s also was measured before and after the experiments involving the transitional phenomena, and it was found to be unaffected. The method of determining the quantity of dissolved air has been reported already [7].

Experimental Results

Nature of Transitional Phenomena. Figs. 1 and 2 depict the evolution in time of the transition shock-wave pressure as it tends toward the stabilized state. In these figures the mean shock-wave pressure p_{sm} is plotted on the ordinate against the lapse of time z on the abscissa, the origin of which is placed at the instant where the flow, after being subjected to preliminary cavitation, regains the velocity corresponding to the ultimate cavitation coefficient k_d. It will be seen from these figures that the aspect of the transitional phenomena differs according to the period z_0 during which the flow is subjected to preliminary cavitation. λ, used as parameter in the figures, and given as a measure of the size of the cavitation, represents the distance of the tail end of the cavitation measured from the leading edge of the profile, in percentage of the chord length l. To explain an example, the curve joining the observed points marked by small circles (o) in Fig. 1 represents the evolution of the mean shock-wave pressure p_{sm} during a period of 3 min after attainment of the ultimate cavitation coefficient[3] ($k_d = 1.55$, $\lambda/l = 38$ per cent), following a 30-sec z_0 period of overdeveloped preliminary cavitation [$k_{d0} = 1.36$, $(\lambda/l)_0 = 75$ per cent]. The time required to reduce the flow velocity from $k_{d0} = 1.36$ or $= 1.23$ down to $k_d = 1.55$ is 10 ~ 20 sec. The value of 1.55 was adopted for k_d because this is the velocity at which the highest mean shock-wave pressures are produced by waves around 250 or 350 kilocycles (kc) (which frequencies are, in turn, those at which the most intense waves are produced with an incident angle of 5 deg and with water temperature at 7 C). Therefore it must be noted that the mean pressures recorded with overdeveloped cavitation ($k_{d0} = 1.36$ or 1.23) are lower than at $k_d = 1.55$ [1].

Similarly, in Fig. 2, the curves joining the two kinds of crossmarks represent experiments made with $z_0 = 0$ (preliminary cavitation not maintained for any period, the flow velocity being reduced immediately upon attainment of the predetermined k_{d0} [$(\lambda/l)_0 = 100$ per cent, $k_{d0} = 1.23$ or $(\lambda/l)_0 = 75$ per cent, $k_{d0} = 1.36$]). In these cases it takes about 30 sec for the shock wave to build up to its maximum transitional value. We calculated the time required for a cavitation bubble to complete the circuit of the tunnel to be as given in Table 1.

Table 1 Calculated times required for circuit of cavitation tunnel

No.	$(\lambda/l)_0$ or λ/l, per cent	k_{d0} or k_d	Flow velocity, (m per sec)	Calculated circuit time
1	100	1.23	10.75	1′37″
2	75	1.36	10.44	1′40″
3			10.38	1′41″
4			10.24	1′42″
5	38	1.55	10.05	1′44″

The actual velocity will be continually diminishing during the reducing transition from the preliminary (k_{d0}) to the ultimate state (k_d) of cavitation, and the foregoing table gives the circuit times for circulation velocities corresponding to k_{d0}, and to k_d, as well as intermediate values between the two, obtained by computing the mean values between them. No account has been taken of the volume occupied by the dead water in the tunnel, and the actual circuit times must thus be smaller than these calculated values.

Fig. 3 represents the case of regenerating cavitation, in which the flow is first subjected to preliminary cavitation at k_d, the pump motor then shut off (the motor coming to stop in 30 sec, and the water circulation 20 sec thereafter), the pump restarted after the lapse of a predetermined period of stoppage z_0 (2 min and so on, in the case of Fig. 3) and the flow made to regain the velocity corresponding to $k_d = 1.55$ (attained in about 1 min). The origin of the abscissa z is placed at the instant where the flow, after being subjected to the stoppage of lapse z_0, regains the velocity corresponding to the ultimate value of cavitation coefficient k_d.

Incidentally, the water was sampled 2 min and 15 min after the circulation stopped, during the interruption of the flow, but no appreciable difference between the two cases could be detected concerning air content, though the precise state of dissociation in the dissolved air could not be determined.

---

where

K_s = total pressure force of shock wave (in g)
ϵ = dielectric constant of the detector crystal = 4.5
U = induced voltage (in $cm^{1/2} g^{1/2} s^{-1}$ esu) on the crystal detector
F, s = surface area (cm^2) and thickness (cm) of the detector
d_{11} = piezoelectric modulus in the X-direction of the detector = 6.5×10^{-8} ($cm^{1/2} g^{-1/2} s$)

The individual impulse pressures

$$p_i = K_s/F = \frac{\epsilon U}{4\pi s d_{11}} \tag{2}$$

which are represented by the heights of the individual lines appearing on the oscillogram.

The mean shock-wave pressure p_{sm} (kg/cm^2) is the total pressure recorded for a given frequency on the oscillogram divided by F, the surface area of the detector, and by τ, the exposure time of the oscillogram; thus

$$p_{sm} = \frac{\Sigma K_s}{F\tau} = \frac{\epsilon 10^{-3}}{4\pi s d_{11}\tau} \Sigma U \tag{3}$$

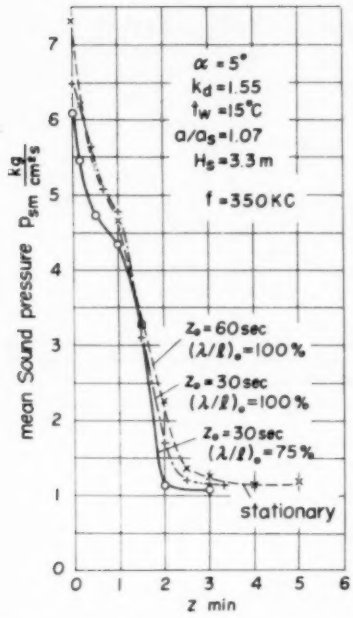

Fig. 1 Evolution in time of transient mean shock-wave pressure p_{sm}, from anomalous to stabilized state—reducing cavitation

z_0: Period of time during which preliminary cavitation was maintained, sec
$(\lambda/l)_0$: Size of preliminary cavitation (represented in percentage of profile chord l)
α = 5 deg, k_d = 1.55, t_w = 15 C
Static pressure H_s = 3.3 m aq, f = 350 kc

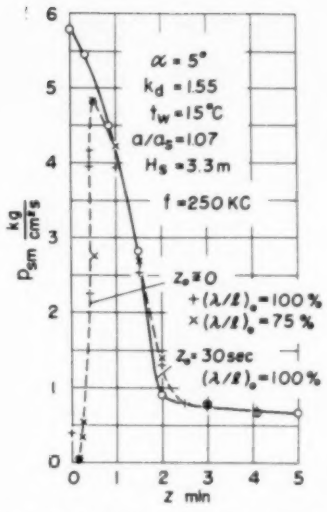

Fig. 2 Evolution in time of transient mean shock-wave pressure p_{sm}, from anomalous to stabilized state—reducing cavitation

z_0: Period of time during which preliminary cavitation was maintained, sec
$(\lambda/l)_0$: Size of preliminary cavitation (represented in percentage of profile chord l)
α = 5 deg, k_d = 1.55, t_w = 15 C,
H_s = 3.3 m, f = 250 kc

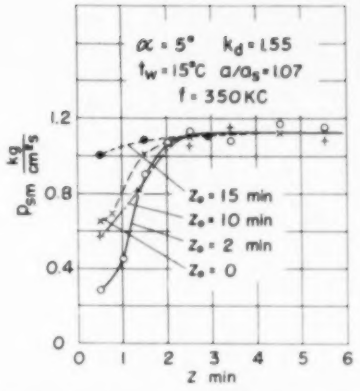

Fig. 3 Evolution in time of transient mean shock-wave pressure p_{sm}, from anomalous to stabilized state—regenerating cavitation

z_0: Period of time during which flow was stopped, sec
α = 5 deg, k_d = 1.55, t_w = 15 C,
H_s = 3.3 m, f = 350 kc

It was ascertained that these transitional phenomena occurred only with the use of the closed-circuit cavitation tunnel, and could not be observed with an open end tunnel [2], and further, that there was good agreement between the values of p_{sm} at the stabilized cavitation obtained with the two kinds of tunnel.

We can draw the following conclusions from the Figs. 1 to 3:

1 The wave pressures recorded during reducing cavitation are several times greater than those observed with stabilized flow, not to speak of comparison with overdeveloped cavitation.

2 Wave pressures of regenerating cavitation can be as low as a small fraction of that of stabilized cavitation.

3 The time required for the transition of the wave pressure from anomalous to stabilized states is about 3 min for both reducing and regenerating cavitation.

4 The mean shock-wave pressure p_{sm} during reducing cavitation does not vary appreciably according to the nature of the preliminary cavitation, but tends to be higher with a higher degree of overdevelopment [greater $(\lambda/l)_0$] and with a longer z_0.

5 With regenerating cavitation p_{sm} appears to be the more attenuated the shorter the period z_0 of flow interruption, except for case of $z_0 = 0$.

6 The transitional phenomena do not occur under ordinary conditions in open-end tunnel experiments.

7 No difference between the results on closed circuit and open-end tunnels can be detected in respect of the values of p_{sm} recorded after attainment of k_d.

The Spectrum of Transitional Cavitation Shock Waves. The spectra of the shock waves produced at a given moment z during the transitional stage are shown in Figs. 4 to 11, where the mean wave pressure p_{sm} is plotted against wave frequency. Figs. 4 and 5 represent the spectra at the instant z = 30 sec after initiation of reducing cavitation (curves b) in comparison with those under stabilized cavitation (curves a), for two cases k_d = 1.55 and 1.45, respectively. In Figs. 6 and 7, cases of regenerating cavitation (curves c) are similarly compared with stabilized states (curves a). In each case the incident angle was 5 deg. For incident angles of 0 and 7 deg, the curves a, b, and c are grouped together in the Figs. 8 to 11. Figs. 8 and 9 represent two cases where p_{sm} is high (α = 0 deg, k_d = 0.9 and 0.7, respectively, t_w being 7 C), while Figs. 10 to 11 illustrate examples of low p_{sm} (α = 7 deg). In Fig. 12 the mean wave pressure p_{sm} for 250 kc at a given instant z = 30 sec during transitional cavitation is shown, together with that of stabilized cavitation, as a function of cavitation coefficient. The size of the cavitation is also indicated by the positions of the head (λ_0) and tail (λ) of the cavitation.

The following points emerge from these figures:

1 Value p_{sm} during transition departs from the values under stabilized state with varying degree according to the wave frequency, Figs. 4 to 11.

2 However, with a given k_{d0} the spectra of the shock waves for the three cases corresponding to a, b, and c follow the same common pattern, and have their peaks and troughs approximately at the same points of frequency on the spectrum, Figs. 4 to 11.

3 The velocity (cavitation coefficient) at which the maximum wave pressure is produced at a given frequency (250 kc) differs slightly between cases of transitional and stabilized cavitation, Fig. 12.

Conditions Under Which Transitional Phenomena Occur, and Accompanying Changes in Lift and Drag. It has been ascertained that the transitional shock waves occur only when the preliminary cavitation to which the flow is subjected, represented by $(\lambda/l)_0$ and k_{d0}, and that to which the flow is ultimately subjected, λ/l and k_d, both fulfill certain conditions. The preliminary and ultimate cavitation must fall within the limits indicated in Table 2.

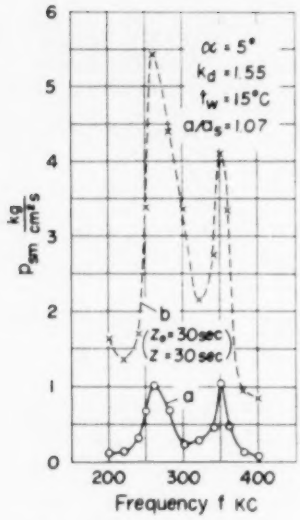

Fig. 4 Comparison between reducing (curve *b*) and stabilized (curve *a*) states of shock-wave spectra

α = 5 deg, k_d = 1.55, t_w = 15 C, H_s = 3.3 m
For curve *b*: z_0 = 30 sec, $(\lambda/l)_0$ = 100 per cent, k_{d0} = 1.23
Spectrum of transient shock waves as of the instant z = 30 sec after flow velocity diminished to k_d = 1.55 (λ/l = 38 per cent)

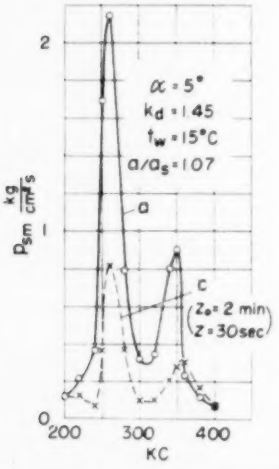

Fig. 7 Comparison between regenerating (curve *c*) and stabilized (curve *a*) states of shock-wave spectra

α = 5 deg, k_d = 1.45, t_w = 15 C, H_s = 3.3 m
For curve *c*: z_0 = 2 min
z = 30 sec, λ/l = 42 per cent, k_d = 1.45

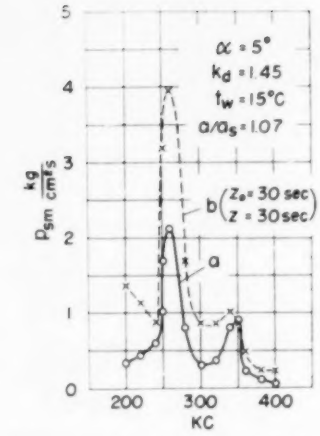

Fig. 5 Comparison between reducing (curve *b*) and stabilized (curve *a*) states of shock-wave spectra

α = 5 deg, k_d = 1.45, t_w = 15 C, H_s = 3.3 m
For curve *b*: z_0 = 0 sec, $(\lambda/l)_0$ = 100 per cent, k_{d0} = 1.23
z = 30 sec, λ/l = 42 per cent, k_d = 1.45

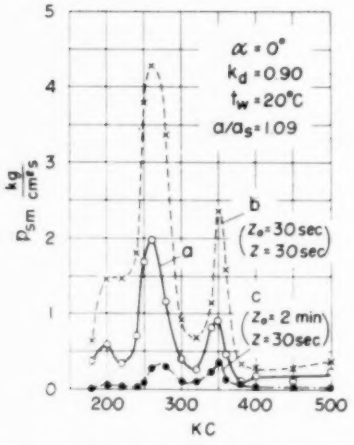

Fig. 8 Comparison of shock-wave spectra of stabilized (*a*), reducing (*b*), and regenerating (*c*) states

α = 0 deg, k_d = 0.90, t_w = 20 C, H_s = 3.3 m
For curve *b*: z_0 = 30 sec, $(\lambda/l)_0$ = 110 per cent, k_{d0} = 0.65
z = 30 sec, λ/l = 43 per cent, k_d = 0.90
For curve *c*: z_0 = 2 min
z = 30 sec, λ/l = 43 per cent, k_d = 0.90

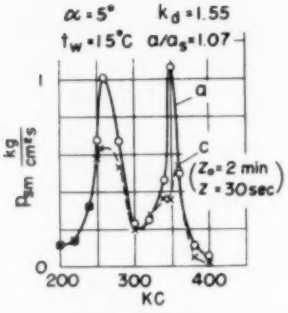

Fig. 6 Comparison between regenerating (curve *c*) and stabilized (curve *a*) states of shock-wave spectra

α = 5 deg, k_d = 1.55, t_w = 15 C, H_s = 3.3 m
For curve *c*: z_0 = 2 min
z = 30 sec, λ/l = 38 per cent, k_d = 1.55

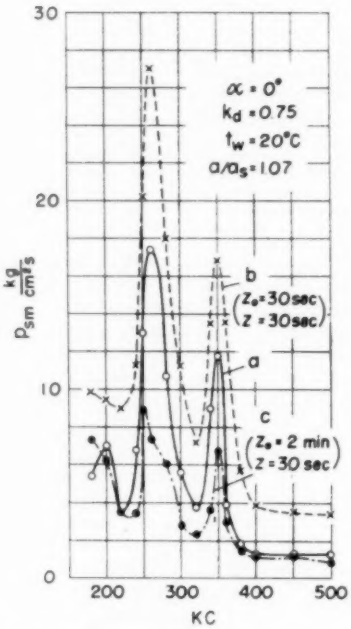

Fig. 9 Comparison of shock-wave spectra of stabilized (*a*), reducing (*b*), and regenerating (*c*) states

α = 0 deg, k_d = 0.75, t_w = 20 C, H_s = 3.3 m
For curve *b*: z_0 = 30 sec, $(\lambda/l)_0$ = 110 per cent, k_{d0} = 0.65
z = 30 sec, λ/l = 90 per cent, k_d = 0.75
For curve *c*: z_0 = 2 min
z = 30 sec, λ/l = 90 per cent, k_d = 0.75

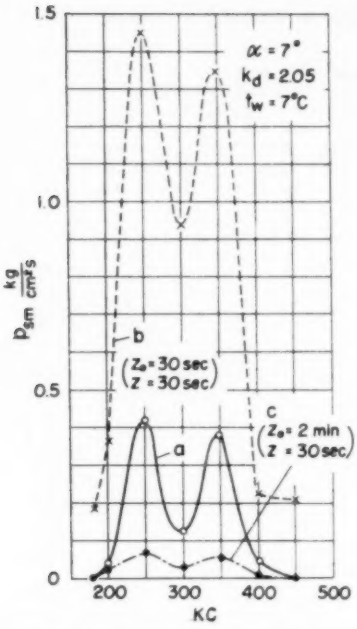

Fig. 10 Comparison of shock-wave spectra of stabilized (a), reducing (b), and regenerating (c) states

α = 7 deg, k_d = 2.05, t_w = 7 C, H_s = 3.3 m
For curve b: z_0 = 30 sec, $(\lambda/l)_0$ = 110 per cent, k_{d0} = 1.40
z = 30 sec, λ/l = 22 per cent, k_d = 2.05
For curve c: z_0 = 2 min
z = 30 sec, λ/l = 22 per cent, k_d = 2.05

The limits in Table 2 for k_d are indicated in Fig. 13 by the range marked b (for reducing cavitation) and c (for regenerating cavitation). It will be seen that the upper limit of the range c coincides with cavitation incipience for all angles of incidence. It must further be noted that the period of subjection to preliminary cavitation z_0 has no effect on this range, in either reducing or regenerating cavitation.

The effect of the transitional phenomena on the lift and drag[4] was next examined for different values of k_d, the measurements being made by a method already reported [6]. The degree of development of the preliminary cavitation during these tests was within the range of k_{d0} given in Table 2, and z_0 was 30 sec for reducing cavitation and z_0 = 2 min for regenerating cavitation. As a result it was found that:

1 No difference in the values of lift coefficient could be detected during reducing and regenerating cavitation as compared to the ultimate stabilized state.

2 The same could be said of the drag coefficient with regenerating cavitation, but with reducing cavitation a discrepancy of up to 6.5 per cent (with α = 7 deg and k_d = 0.7) was recorded in the drag coefficient in comparison with the stabilized state.

3 The transitional shock wave occurs only when the ultimate cavitation falls within the limit, represented by k_d and λ/l, Table 2.

4 The anomalous shock wave of the reducing cavitation occurs only when the preliminary cavitation to which the flow is sub-

[4] The lift and drag coefficients C_a and C_w are computed according to the following formula:

$$C_a = A \Big/ \frac{1}{2}\rho v_\infty^2 F, \qquad C_w = W \Big/ \frac{1}{2}\rho v_\infty^2 F$$

where

A, W = measured lift and drag
v_∞ = mean flow velocity upstream of profile
F = profile area = chord × breadth

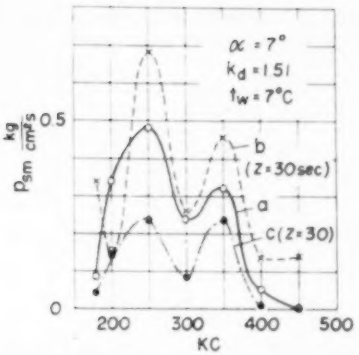

Fig. 11 Comparison of shock-wave spectra of stabilized (a), reducing (b), and regenerating (c) states

α = 7 deg, k_d = 1.51, t_w = 7 C, H_s = 3.3 m
For curve b: z_0 = 30 sec, $(\lambda/l)_0$ = 110 per cent, k_{d0} = 1.40
z = 30 sec, λ/l = 92 per cent, k_d = 1.51
For curve c: z_0 = 2 min
z = 30 sec, λ/l = 92 per cent, k_d = 1.51

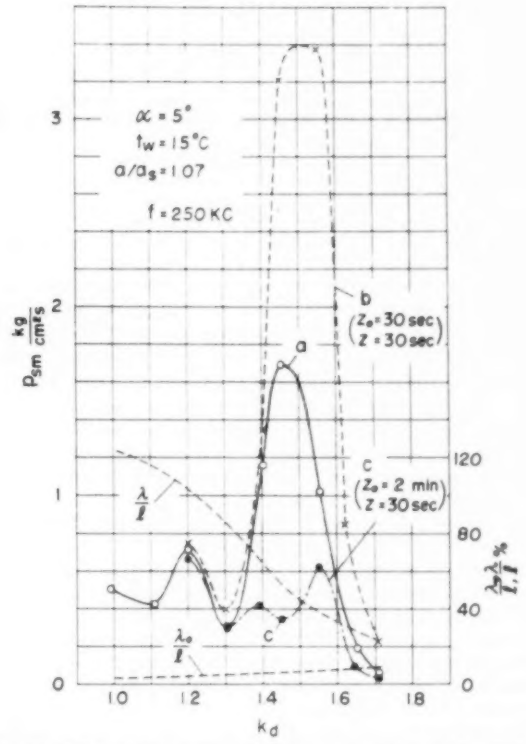

Fig. 12 Relation between mean shock-wave pressure p_{sm} and cavitation coefficient k_d.

α = 5 deg, t_w = 15 C, H_s = 3.3 m, f = 250 kc
a: Stabilized cavitation
b: Reducing cavitation (z_0 = 30 sec, $(\lambda/l)_0$ = 110 per cent, k_{d0} = 1.15, z = 30 sec)
c: Regenerating cavitation (z_0 = 2 min, z = 30 sec)

Table 2 Limiting ranges for preliminary and ultimate cavitation for production of transient anomalous shock waves

Incident angle, deg α	Preliminary cavitation $(\lambda/l)_0$, per cent	Preliminary cavitation k_{d0}	Ultimate cavitation: Reducing cavitation λ/l, per cent	Ultimate cavitation: Reducing cavitation k_d	Ultimate cavitation: Regenerating cavitation λ/l, per cent	Ultimate cavitation: Regenerating cavitation k_d
0	70 ~ 130	0.82 ~ 0.5	40 ~ 118	0.92 ~ 0.6	40 ~ 118	0.92 ~ 0.6
3	75 ~ 130	1.12 ~ 0.7	40 ~ 100	1.25 ~ 1.0	40 ~ 100	1.25 ~ 1.0
5	75 ~ 130	1.36 ~ 0.9	36 ~ 90	1.60 ~ 1.3	32 ~ 90	1.72 ~ 1.3

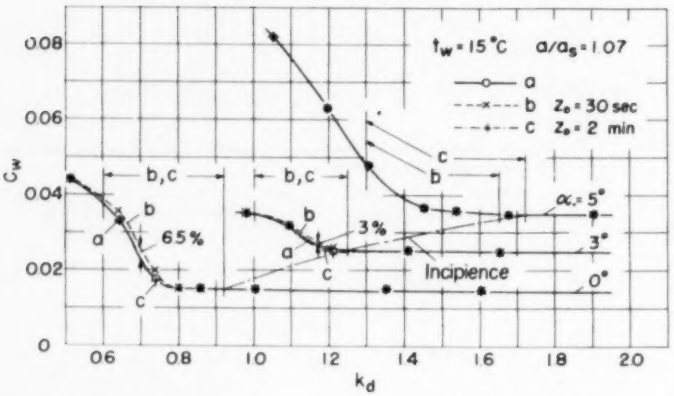

Fig. 13 Comparison of drag coefficients for stabilized (a), reducing (b), and regenerating (c) cavitation

t_w = 15 C, a/a_s = 1.07, H_s = 3.3 m
For curve b: z_0 = 30 sec For curve c: z_0 = 2 min

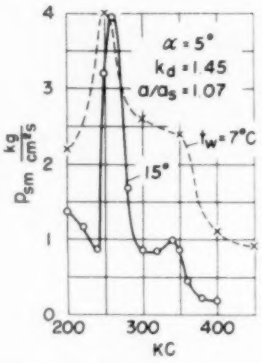

Fig. 14 Influence of differences in water temperature on the wave spectrum in reducing cavitation

α = 5 deg, k_d = 1.45, H_s = 3.3 m
z_0 = 30 sec, $(\lambda/l)_0$ = 100 per cent, k_{d0} = 1.23
z = 30 sec, λ/l = 42 per cent, k_d = 1.45

jected, represented by k_{d0} and $(\lambda/l)_0$, fulfill the limited condition, Table 2.

Influence of Temperature on Transitional Shock-Wave Spectrum. The spectra of transitional shock-wave pressures are shown for different water temperatures in Figs. 14 (reducing cavitation) and 15 (regenerating cavitation). The following points emerge from these curves:

1 The maximum values of mean shock-wave pressure p_{sm} do not vary appreciably with temperature in reducing cavitation, but change considerably in the case of regenerating cavitation.

2 The frequencies that give maximum p_{sm} do not vary much with temperature.

3 The influence of temperature on p_{sm} varies according to the frequency.

Frequency of Occurrence of Individual Shock-Wave Impulses of Different Intensities. The imparted pressures p_i of the individual shock waves appearing on a 250-kc oscillogram were measured [2], and the number of recorded impulses in each category of imparted pressure intensity was plotted as a histogram against the frequency of occurrence during a period of 1 sec (Fig. 16, corresponding to the experiments represented in Figs. 5 and 7; Fig. 17, corresponding to Figs. 14 and 15). The following points emerge from these figures:

1 The number of impulses imparted during reducing cavitation is markedly superior in all categories of p_i, as compared to that of the stabilized state.

2 In the case of regenerating cavitation this number is markedly inferior.

3 In comparison with the cases of reducing and stabilized cavitation, a relatively large number of extremely faint impulses occurs in regenerating cavitation.

About 4150 oscillograms were taken in the foregoing experiments.

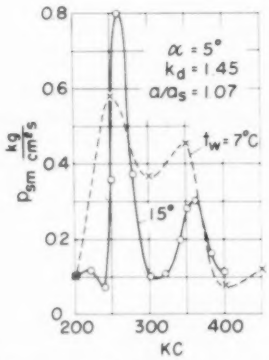

Fig. 15 Influence of differences in water temperature on the wave spectrum of regenerating cavitation

α = 5 deg, k_d = 1.45, H_s = 3.3 m
z_0 = 2 min
z = 30 sec, λ/l = 42 per cent, k_d = 1.45

Shock-Wave-Pressure Anomalies Caused by Independent Preliminary Cavitation Occurring Upstream of the Principal Cavitation

Considerations Concerning the Anomalous Phenomena. The nature of the anomalous phenomena discussed in the foregoing suggests the involvement, at least in part, of bubble nuclei, necessary for cavitation incipience, as one of the causing factors. In reducing cavitation, the innumerable bubble nuclei formed by the extinction of the bubbles caused by the overdeveloped preliminary cavitation circulate back to the test stretch of the tunnel, thus bringing about the anomalous phenomenon.

The limiting ranges of $(\lambda/l)_0$ mentioned in the section Condi-

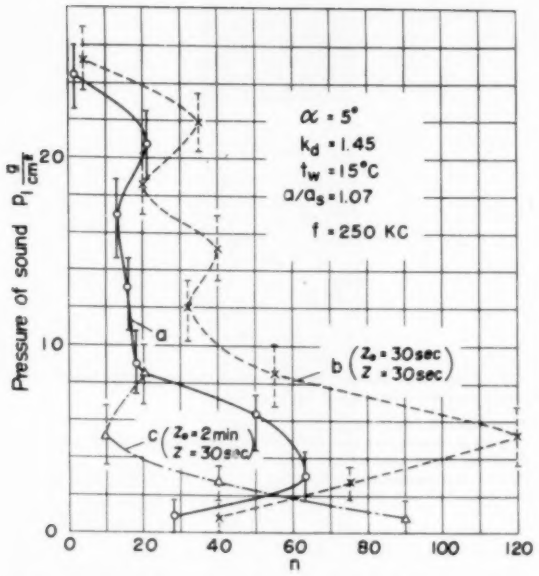

Fig. 16 Frequency (n per sec) distribution of individual shock-wave impulses according to their intensity p_i

$\alpha = 5$ deg, $k_d = 1.45$, $t_w = 15$ C, $H_s = 3.3$ m, $f = 250$ kc
a: Stabilized cavitation, *b*: Reducing cavitation,
c: Regenerating cavitation
For curve *b*: $z_0 = 30$ sec, $(\lambda/l)_0 = 100$ per cent, $k_{d0} = 1.23$
$z = 30$ sec, $\lambda/l = 42$ per cent, $k_d = 1.45$
For curve *c*: $z_0 = 2$ min
$z = 30$ sec, $\lambda/l = 42$ per cent, $k_d = 1.45$

tions Under Which Transitional Phenomena Occur, may be explained as follows: An excessive velocity during the preliminary cavitation, e.g., $(\lambda/l)_0 > 130$ per cent at $\alpha = 5$ deg, causes a veritable cavity around the specimen profile, which disfavors the formation of minute bubbles which would later transform into bubble nuclei. To the contrary, the faint preliminary cavitation, e.g., $(\lambda/l)_0 < 75$ per cent at $\alpha = 5$ deg, yields only insufficient formation of minute bubbles which would transform into bubble nuclei.

Regenerating cavitation might be explained as a phenomenon in which the stoppage of the flow after subjection to the preliminary cavitation causes the disappearance of a large part of the bubble nuclei. Though no satisfactory explanation can be given of the fact that p_{sm} is less attenuated with $z_0 = 0$ than with $z_0 = 2$ min, Fig. 3, nevertheless it may be stated that regenerating cavitation presupposes the existence of some form of preliminary cavitation to which the flow is previously subjected.

Those considerations led us to realize the possibility of producing the anomalous phenomenon with an open-end tunnel, by subjecting the flow to independent preliminary cavitation upstream of the test stretch, to compare the results with those obtained with a closed-circuit tunnel.

Device for Producing Independent Cavitation Upstream of Test Stretch. A cavitation-producing propeller K, Fig. 18,[5] was inserted in the circuit of the cavitation tunnel [2, 6] at a point upstream of the test stretch. This cavitation tunnel can be operated both as closed-circuit [6] and open-end [2] systems.

[5] A propeller designed to produce profuse cavitation; 250 mm diam, 1450 rpm, powered by a 2-hp motor.

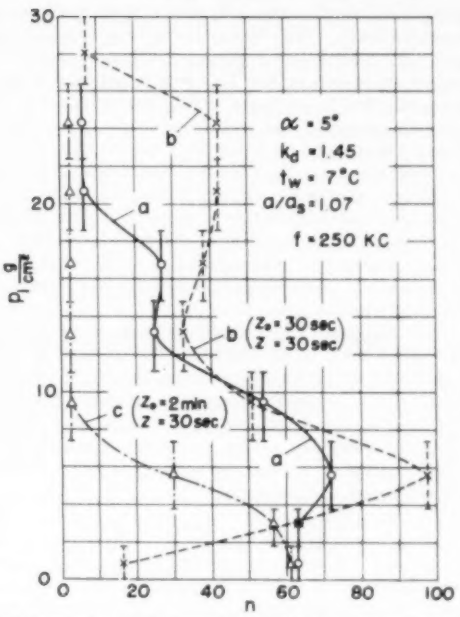

Fig. 17 Frequency distribution of individual shock-wave impulses according to their intensity p_i

$\alpha = 5$ deg, $k_d = 1.45$, $t_w = 7$ C, $H_s = 3.3$ m, $f = 250$ kc
a: Stabilized cavitation, *b*: Reducing cavitation,
c: Regenerating cavitation
For curve *b*: $z_0 = 30$ sec, $(\lambda/l)_0 = 100$ per cent, $k_{d0} = 1.23$
$z = 30$ sec, $\lambda/l = 42$ per cent, $k_d = 1.45$
For curve *c*: $z_0 = 2$ min
$z = 30$ sec, $\lambda/l = 42$ per cent $k_d = 1.45$

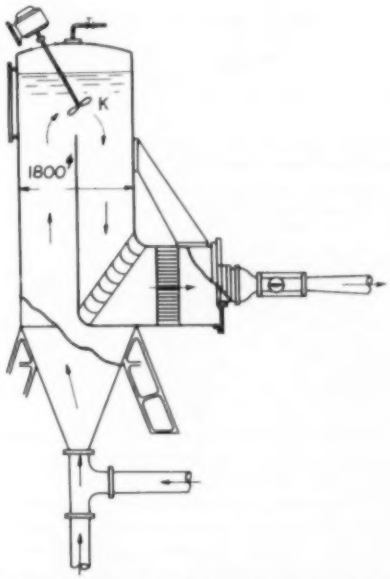

Fig. 18 Device for producing independent upstream cavitation
K: Cavitation-producing propeller: 250 mm diam, powered by a 2-hp motor at 1450 rpm

Experiments With the Closed-Circuit System on the Effects of Independent Preliminary Cavitation. The effect of the increase in bubble nuclei formed by the independent preliminary cavitation was studied. The results are shown in Fig. 19, curve *b*, obtained under the conditions inscribed in the figure. Stabilized cavitation was produced on the specimen; the cavitation-producing propeller was then brought into action for 40 sec and stopped. This instant of stoppage was taken as origin for the co-ordinate of the curve, which clearly illustrates how the mean shock-wave pressure p_{sm}, initially anomalously high, settles down in the course of about 2 min, to the stable ultimate value. Thus an anomalous phenomenon, analogous to that of reducing cavitation, was obtained without recourse to overdeveloped preliminary cavitation, simply by the superposition of an auxiliary point of cavitation upstream of the principal point. The anomalously high, transient, shock-wave pressures may be attributed to the increase in bubble nuclei caused by the cavitation-producing propeller. The size of cavitation on the test profile during the transitional period diminished from $\lambda_0/l = 7$ per cent, $\lambda/l = 46$ per cent at $z = 0$ down to the stabilized $\lambda_0/l = 7$ per cent, $\lambda/l = 44$ per cent at $z = 2$ min, λ_0 being the distance of the head of cavitation measured from the leading edge of the profile.

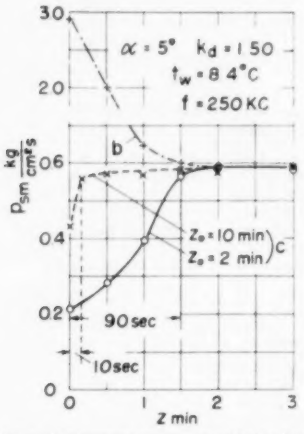

Fig. 19 Anomalous shock-wave pressures obtained with independent upstream cavitation—closed-circuit system

(*b*): $z = 0$ at instant at which propeller motor was shut off
(*c*): $z = 0$ at 30 sec after restarting propeller K
$\alpha = 5$ deg, $k_d = 1.50$, $t_w = 8.4$ C, $f = 250$ kc

Curves *c* in the same figure give the results of experiments in producing effects analogous to regenerating cavitation with the upstream cavitation. Similarly to the previous experiment, stabilized cavitation was first produced on the specimen profile, and the propeller K then started, operated for 40 sec, and stopped. At the same instant the main pump motor was shut off (the motor coming to a stop in about 30 sec, and the flow itself 20 sec later). After a predetermined period z_0 measured from the instant when the motor was shut off ($z_0 = 2$ min in the present case) the pump was restarted. The curve (*c*) depicts the evolution of p_{sm} as it gradually builds up to the stable value. The origins of the curves (*c*) are placed at 30 sec after the instant when the pump motor is switched on again. The curves follow a pattern quite similar to that of regenerating cavitation, shown in Fig. 3, curve (*c*). The size of cavitation during this transitional stage changed from $\lambda_0/l = 7$ per cent, $\lambda/l = 42 \sim 43$ per cent at $z = 0$ to $\lambda_0/l = 7$ per cent, $\lambda/l = 44$ per cent at $z = 2$ min.

Experiments With an Open-End System. Effects analogous to regenerating cavitation cannot be produced with this system.

Fig. 20 depicts the evolution of p_{sm} measured during an experiment simulating reducing cavitation. After obtaining a stabilized cavitation ($\alpha = 5$ deg, $k_d = 1.50$) on the specimen profile, the cavitation propeller K was started (point z_a in Fig. 20); the anomalously high p_{sm} was observed to reach its full strength in about 20 sec (point z_b); the propeller motor was shut off at point z_c, but the anomalous pressure was observed to persist for about 95 sec (period $z_d - z_a$). The size of cavitation was observed by eye to diminish from $\lambda_0/l = 7$ per cent, $\lambda/l = 46$ per cent at z_c to $\lambda_0/l = 7$ per cent, $\lambda/l = 44$ per cent (stabilized) at z_d. Thus it was definitely proved that anomalously high shock-wave pressures could occur without overdeveloped cavitation being produced at any point, when the flow was subjected to independent preliminary cavitation at a point upstream of the principal cavitation point.

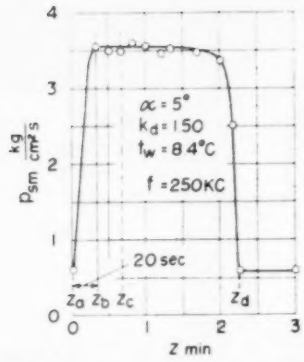

Fig. 20 Anomalous shock-wave pressures obtained with independent upstream cavitation—open-end system

z_a: Propeller K brought into action
z_b: Transient anomalous pressure reaches full development
z_c: Propeller motor shut off ($z_c - z_a = 40$ sec)
z_d: Transient phenomenon terminates ($z_d - z_c = 95$ sec)
$\alpha = 5$ deg, $k_d = 1.50$, $t_w = 8.4$ C, $f = 250$ kc

It may be imagined that conditions similar to this experiment, which might be called "superposed cavitation," may occur in ordinary hydraulic machinery. Thus it must be thought that abnormally high shock-wave pressures can be produced in hydraulic machinery when the flow is subjected to superposed cavitation.

No satisfactory explanation can be given to the fact that with the closed-circuit system the p_{sm} begins to decline immediately upon stoppage of the propeller K, curve (*b*), Fig. 19, while with the open-end system the anomalous pressure is maintained for some moments, Fig. 20, though it must of course have some relation with the difference between the two systems.

The effect of the superposed cavitation on the lift and drag was next examined. As a result it was found that no difference in the values of lift coefficient could be detected as compared to the ordinary simple cavitation.

In the drag coefficient the discrepancy of the same degree with the reducing cavitation, Fig. 13, was recorded in comparison with the ordinary simple cavitation.

Summary of Results on Experiments With Independent Preliminary Cavitation. (*a*) The attenuating effect of regenerating cavitation can be produced even when the flow is subjected to superposed preliminary cavitation, though this should produce a large amount of bubble nuclei.

(*b*) The size of cavitation during this attenuated transient phenomenon is observed by eye to appear about 2 per cent smaller than after stabilization.

(*c*) Under normal conditions of cavitation on the profile, the superposition of an auxiliary point of cavitation further upstream

causes the mean shock-wave pressure to rise to a level several times higher than normal, in a manner analogous to the case of reducing cavitation.

(*d*) With superposed cavitation, the shock-wave pressures are anomalously high both with open-end and closed-circuit systems.

(*e*) The size of cavitation during the transient period was observed to appear about 2 per cent greater than after stabilization.

(*f*) The anomalously high pressures accompanying superposed cavitation diminish promptly upon removal of the auxiliary cavitation in the case of a closed system, but persist for some moments with an open-end system.

(*g*) With superposed cavitation, no difference in the value of lift coefficient and a slight change in the value of drag coefficient could be detected as compared to the ordinary simple cavitation.

Considerations Concerning Cavitation Bubbles

Observation of the Bubbles. The relation of the mean shock-wave pressure p_{sm} and the individual impulse pressure p_i to the status of the bubbles was examined with the use of high-speed photography (6300 frames per sec, see Fig. 21, Photos 1–3). Individual bubbles were photographed at successive stages of development and decline, and the evolution in their size examined.

The top pictures of Photos 1–3 were taken with extended exposes of $(2 \sim 2.25) \times 10^{-4}$ sec in order to show the form of the bubbles more clearly. The photographs were taken during experiments with $\alpha = 5$ deg and $k_d = 1.45$. A total of 12,630 frames of photo 1 and 4210 frames each of photos 2 and 3 were used for the data of Figs. 22 and 23.

The bubbles appearing in all the pictures taken were measured and the evolution of their sizes noted. The bubbles do not present accurate spheres but are shaped like ellipsoids of rotation. Since the photographs do not permit the determination of the bubble dimension in the direction perpendicular to the profile surface, the bubble size is represented simply by its axial length (d_b on the top picture of Photo 3).

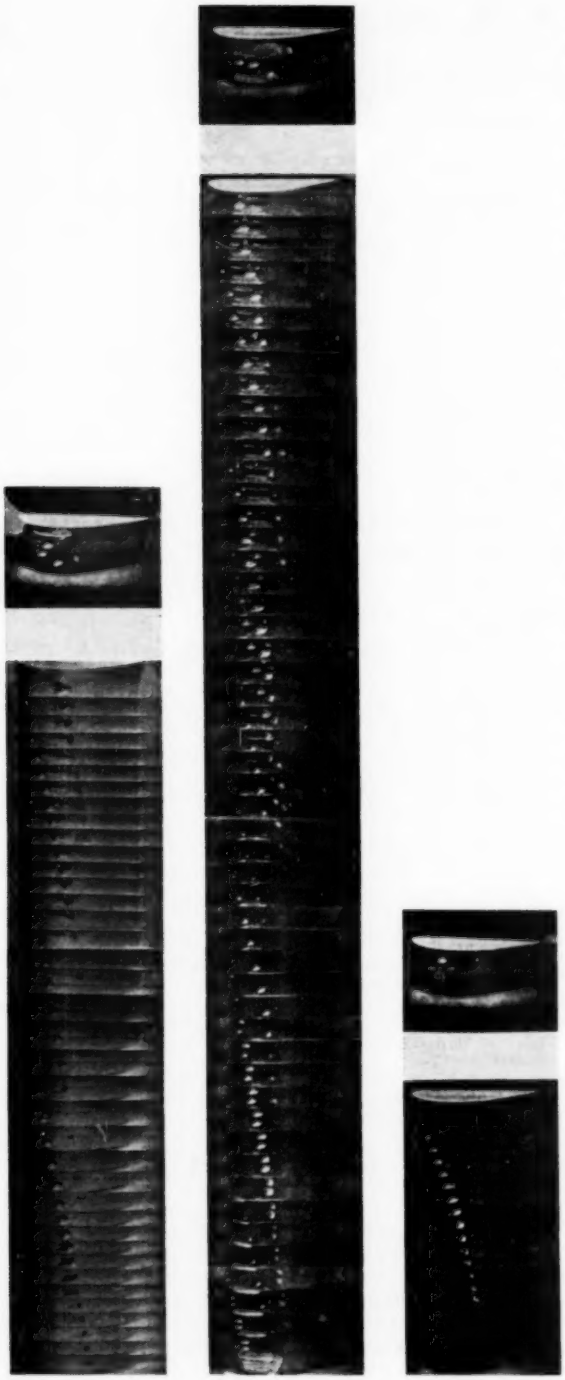

Photo 1: Stabilized cavitation

Photo 2: Reducing cavitation

Photo 3: Regenerating cavitation

Fig. 21 (Photos 1–3) Bubbles taken with extended exposures (top) and those with high-speed photography (below)

$\alpha = 5$ deg, $k_d = 1.45$, $t_w = 7$ C

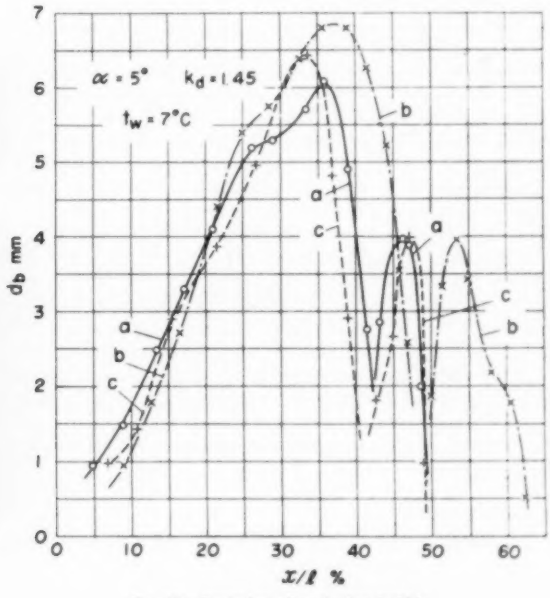

Fig. 22 Evolution of cavitation bubble

a: Stabilized cavitation, b: Reducing cavitation, c: Regenerating cavitation

$\alpha = 5$ deg, $k_d = 1.45$, $t_w = 7$ C

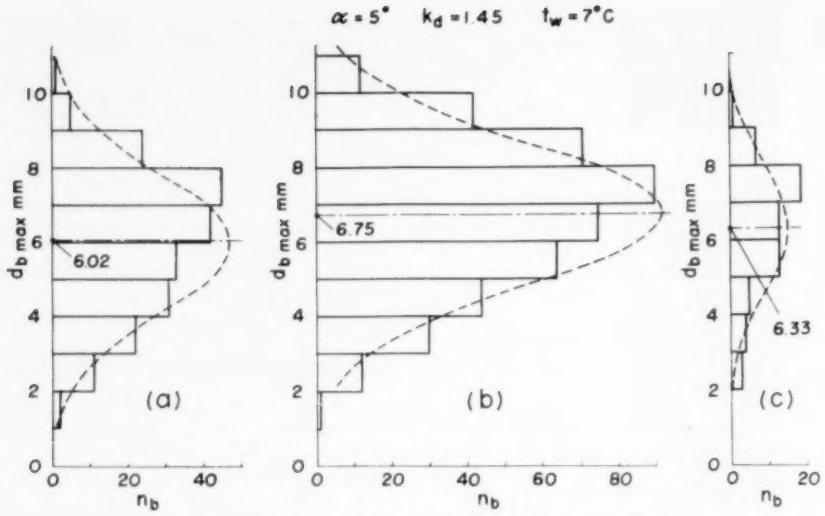

Fig. 23 Frequency (n_b per sec) distribution of bubble sizes d_{bmax}, mm
a: Stabilized cavitation, b: Reducing cavitation, c: Regenerating cavitation
α = 5 deg, k_d = 1.45, t_w = 7 C

Evolution of the Size of Cavitation Bubbles. A study of the photographs indicated that there were three kinds of bubbles [8]: Traveling cavitation, rebounded traveling cavitation, and fixed cavitation. It has already been reported [9] that the phenomenon which contributes most to the production of the shock waves is that of the traveling cavitation extinguishing itself. Fig. 22 depicts the evolution of the sizes of three random examples of traveling bubbles, during stabilized (curve *a*), reducing (curve *b*), and regenerating (curve *c*) cavitation. The bubble size, d_b, is plotted against the positions held by the bubble during its passage towards the profile tail (the positions being represented in percentage of the chord, measured from the leading edge of the profile). It is seen that the bubble of reducing cavitation (curve *b*) develops to a greater size as compared to the other cases. In this example the curve (*c*) representing a case of regenerating cavitation rises above the curve (*a*), of a stabilized cavitation bubble, since the curves are random examples and not statistical results.

Bubble Sizes and Their Frequency Distribution. All the cavitation bubbles (excepting fixed cavitation) appearing on the profile surface were classified according to their category of size d_{bmax} at the greatest development, and their frequency n_b (per sec) plotted in a histogram of 1-mm intervals between size categories, Fig. 23. It will be seen that, as compared to stabilized cavitation (curve *a*), the number of bubbles produced is markedly higher with reducing cavitation (curve *b*), and markedly lower with regenerating cavitation (curve *c*), though the median sizes do not appear to differ significantly. This explains qualitatively the p_i-n relation given in Fig. 17; namely, the relation between the intensity p_i of shock-wave impulse and the frequency of occurrence n.

Acknowledgment

In conclusion, the author wishes to acknowledge the valuable assistance provided by Assistants Messrs. I. Chida and H. Takeuchi, and also the help by Messrs. M. Hongo, M. Ansai, and R. Satō. The apparatus for high-speed photography was purchased with a grant-in-aid from the Ministry of Education. The pump utilized for the open-end tunnel experiments was donated by the Tōhoku Electric Power Company.

References

1 F. Numachi, "Ultraschallwelle am Tragflügelprofil bei Hohlsog/Teil I," *Forschung auf dem Gebiete des Ingenieurwesens*, vol. 22, 1956, pp. 77–84.

2 F. Numachi, "Ultraschallwelle am Tragflügelprofil bei Hohlsog/Teil II," *Forschung auf dem Gebiete des Ingenieurwesens*, vol. 24, 1958, pp. 73–78.

3 M. F. M. Osborne, "The Shock Produced by a Collapsing Cavity in Water," TRANS. ASME, vol. 69, 1947, pp. 253–266.

4 M. Harrison, "An Experimental Study of Single Bubble Cavitation Noise," *Journal of Acoustical Society of America*, vol. 24, 1952, pp. 776–782.

5 R. H. Mellen, "Ultrasonic Spectrum of Cavitation Noise in Water," *Journal of Acoustical Society of America*, vol. 26, 1954, pp. 356–360.

6 F. Numachi, "Kraftmessungen an vier Flügelprofilen bei Hohlsog," *Forschung auf dem Gebiete des Ingenieurwesens*, vol. 11, 1940, pp. 303–308.

7 F. Numachi, "Über die Kavitationsentstehung mit besonderem Bezug auf den Luftgehalt des Wassers," *Ingenieur-Archiv*, vol. 7, 1936, pp. 396–409.

8 R. T. Knapp, "Cavitation Mechanics and Its Relation to the Design of Hydraulic Equipment," *Engineering*, vol. 173, 1952, pp. 566–569.

9 F. Numachi, "Kavitationsblasen und Ultraschallwelle am Tragflügelprofil," *Forschung auf dem Gebiete des Ingenieurwesens*, vol. 24, 1958, pp. 125–132.

DISCUSSION

J. W. Daily[6]

The author's interesting experiments have disclosed the significant phenomenon of cavitation activity being increased as the result of upstream cavitation. Among its chief consequences is the likelihood that cavitation erosion is accelerated by this effect. Should this prove true, the importance as regards hydraulic machinery cannot be overestimated.

The explanation relating increased cavitation activity to an increase in the bubble-nuclei population by the upstream cavitation agrees qualitatively with the present understanding of the role of gas nuclei in the cavitation process, and the writer finds this general explanation most plausible. As regards the detailed

[6] Professor of Hydraulics, Hydrodynamics Laboratory, Massachusetts Institute of Technology, Cambridge, Mass.

interpretation of the author's test results, however, the writer has some questions as follows:

Considering the author's experiments and his interpretation of them the following factors seem to be involved:

A Factors that apparently produce extra nuclei in the water approaching the test hydrofoil:

(1) Recirculation of nuclei generated by cavitation of the test hydrofoil itself.

(2) Artificial generation of nuclei by separate upstream cavitation.

B Factors that reduce the nuclei population in the approaching flow:

(1) Elimination of recirculation.

(2) Elimination of upstream cavitation.

(3) Allowing re-solution of bubble nuclei (by flow stoppage) before the nuclei reach the test hydrofoil.

While the author's findings from his tests of reducing cavitation in the closed circuit and simulated reducing cavitation with both the closed and open circuits are consistent with the foregoing items, some of the other results suggest some inconsistencies. (*a*) The author's Figs. 3 and 19 show that for regenerating cavitation and simulated regenerating cavitation in the closed circuit the anomalous effects are *reduced* as the stoppage period z_0 *increases*. This seems to suggest more nuclei after a long z_0 than for short period, rather than a greater deficiency as would be expected. Certainly, with an increased deficiency of nuclei, an increasingly anomalous behavior should be expected rather than vice versa. The finding suggests the influence of some unknown additional factor in this experiment. (*b*) The author states that the stabilized value of p_{sm} for a particular k_d was the same for open and closed-circuit tests of the hydrofoil alone. This suggests no effect of recirculation of nuclei generated by cavitation on the test hydrofoil which is inconsistent with items A(1) and B(1) and consequently with the findings from both the decreasing and regenerating cavitation. The author's comments on these points would be appreciated.

In the case of reducing cavitation, the excess cavitation was obtained by increasing the velocity. It is assumed that similar effects (though perhaps smaller in magnitude) would be obtained were the cavitation coefficient adjusted by varying the absolute pressure instead. Perhaps the author has information regarding this method of operation.

With regard to the experimental method of measuring the cavitation shock-wave pressures, it would be helpful if the author could provide the details of the pickup design and its accuracy and directional discrimination, as well as an explanation of the method of evaluating the instantaneous pressure pulses.

Author's Closure

The author wishes to express his appreciation of the understanding discussion given by Professor Daily and wants to answer him.

As to the first question, that is, inconsistency between the orders of z_0 and attenuation of p_{sm} in Figs. 3 and 19, the author stated in the text of his paper that he could not explain it. It means he affirms that there could be influence of some unknown additional factor. The following are to be considered as questions outside of the amount of nuclei. That is, some conditions seem to be necessary to materialize themselves for cavitation nuclei to grow to cavitation bubbles. For instance, it is considered that, in case of regenerating process where flow velocity increases from zero to the velocity of ultimate cavitation, the generation of boundary layer or a certain form of velocity distribution therein is necessary. That means it is possible to assume that relations between these factors, those in B(3)N, stated hereafter, and z_0 are not too simple.

As to the second question, the author would like to answer as follows:

Professor Daily quoted items A(1) to A(2) and B(1) to B(3) as representing author's experiment and his interpretation. The author, however, wants to revise A(1), B(1), and B(3) as follows:

A(1)N Recirculation of nuclei generated by "reducing cavitation" of the test hydrofoil in a "transitional period" almost

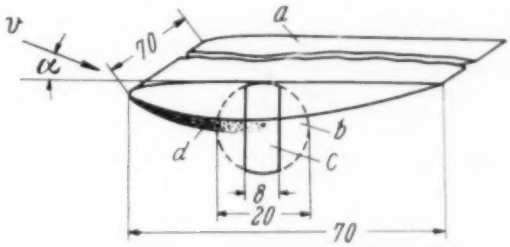

Fig. 24 Specimen hydrofoil profile and crystal pickup
- a Profile: Clark Y
- b Outline of ordinary crystal cross section
- c Cross section of crystal actually used
- d Visible cavitation
- v Velocity of flow
- α Incidence angle

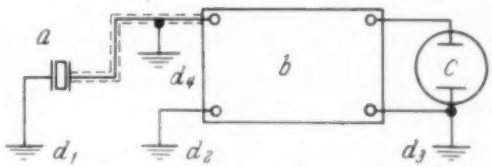

Fig. 25 Arrangement of receiving device
- a Crystal pickup
- b Amplifier—detector
- c Cathode ray oscilloscope
- d_1–d_4 Earth

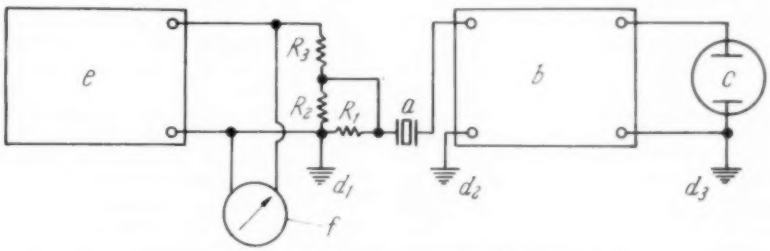

Fig. 26 Calibrating arrangement for the receiver
- a Crystal pickup
- b Amplifier—detector
- c Cathode ray oscilloscope
- d_1–d_4 Earth
- e High frequency wave generator
- f Bult voltmeter

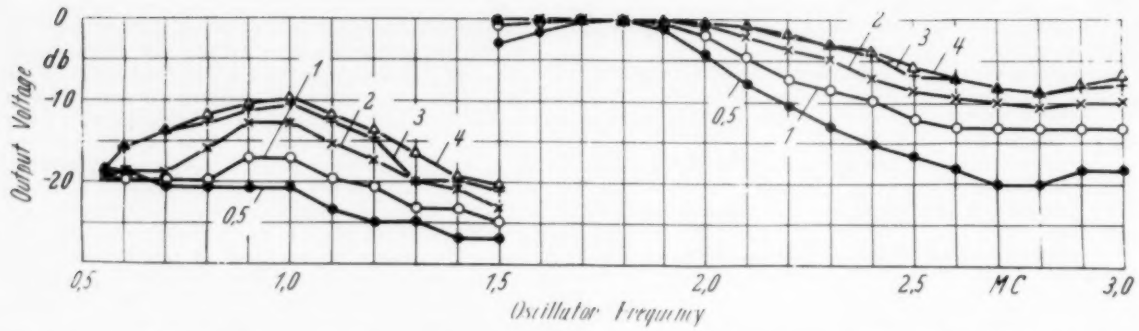

Fig. 27 Change in gain with frequency for different pickups—range 0.5 ~ 3.0 MC, pickups with resonance at 0.5, 1.0, 2.0, 3.0, and 4.0 MC

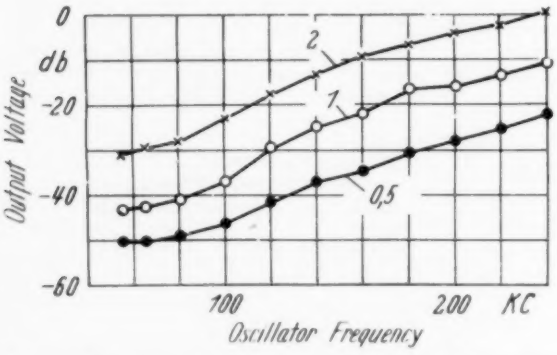

Fig. 28 Change in gain with frequency for different pickups—range 200 ~ 600 KC, pickups with resonance at 0.5, 1.0, 2.0, and 3.0 MC

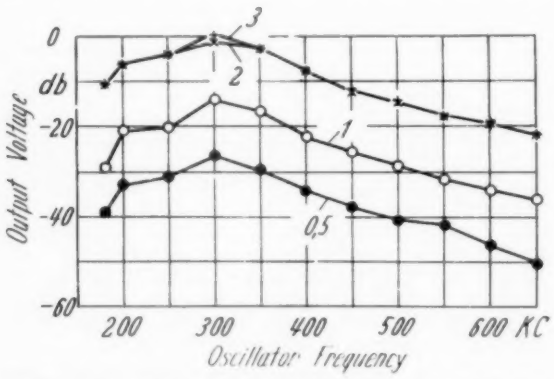

Fig. 29 Change in gain with frequency for different pickups—range 40 ~ 240 KC, pickups with resonance at 0.5, 1.0, and 2.0 MC

equal to a short time required by only one circulation of flow in the tunnel (cf. Figs. 2 and 19).

B(1)N "Regeneration process," consisting chiefly of the elimination of flow circulation and raising velocity, to make the transitional attenuation of a short time almost equal to the time required of by only one circulation of flow in the tunnel.

B(3)N Ditto with Professor Daily's. Further, the author wants to add that some part of cavitation bubbles may not reduce themselves back to nuclei but expel themselves from water where velocity is small, for instance, in the upper part of the tank in Fig. 18.

The author believes that there is no inconsistency through this correction, but he will add some more by way of explanation.

It should be interpreted that in the closed-circuit tests, the increase or decrease of nuclei shown by transitional anomalies recovers their normal quantity. And the following will prove the statement. That is, there is no evidence in the closed-circuit tests that indicates shock pressure p_{sm} of ultrasonic wave emitted by the stabilized cavitation under a constant value of k_d rising with the lapse of time. That is again to be interpreted that no accumulation of nuclei takes place in the tunnel. Then, in case the water used in the open-circuit tests is used in the closed-circuit tests, the stabilized value of p_{sm} ought to be the same in both cases.

On Professor Daily's question of adjusting the cavitation coefficient by varying the absolute pressure to obtain reduced cavitation, the author conducted qualitative test and found the possibility of the said method, though he did not make comparison of the values of p_{sm} in pressure method and velocity method. When k_d-value of ultimate cavitation is taken as 1.55 and the value of excess cavitation 1.36, the statical head is required to be dropped by 1 m aq to obtain the excess cavitation and the time needed for it is 45 ~ 50 sec instead of 2 ~ 3 sec. And the time required to reduce the flow from $k_d = 1.36$ down to $k_d = 1.55$ is about 60 sec instead of 20 sec.

In conclusion, the experimental method of measuring shock-wave pressure is as follows:

(*1*) *Hydrofoil Setting.* The specimen hydrofoil measures 70 mm both in chord and width (Fig. 24); one end is fixed to the wall (of bronze) of the cavitation tunnel; a plexiglas window forms the opposite wall at this point. A free space 0.05 mm wide was left between the specimen and the window for experiments in lift and drag determination, but in the present case, the specimen was made to press directly on the window to provide for the transmission of ultrasonic waves to the hydrophone.

(*2*) *Ultrasonic Wave Receiving Device.* The hydrophone, an X-cut crystal, is held against the plexiglas window: The impulses induced by the ultrasonic waves and transmitted through the window are amplified and measured by a cathode ray oscilloscope. The layout is outlined schematically in Fig. 25. The apparatus is designed to possess a sufficient degree of frequency selectivity to meet the present requirements. The quartz pickup, originally a cylinder 20 mm in diameter, was cut on two sides leaving a width of 8 mm (cross section indicated by a continuous line in Fig. 24), with the view to limiting as far as possible the collecting area and thus focusing the measuring point.

(*3*) *Calibrating the Receiver Gain.* The over-all gain characteristics of the receiver were calibrated by the device shown in Fig. 26: A modulated wave of constant power from a high frequency wave generator (e) was applied after appropriate attenuation (by R_2 and R_3), to the two ends of a low resistance leak (R_1) inserted between the pickup (a) and earth. The pickup output was amplified and detected (by b), and measured by oscilloscope (c). The results of calibration are shown in Figs. 27 to 29, for three fre-

quency bands between 0.5 and 3 MC. Different receiver sets with characteristics suited to each band were used, which accounts for the different levels of gain recorded in the diagrams in Figs. 27 to 29.

The ultrasonic waves are attenuated by about 12 per cent through reflection during their passage through the plexiglas window, and this has been taken account of in the calculations. Further, though sound waves would be generated all along width of the specimen, it can be assumed that only those emanating from the vicinity of the window reach and penetrate it to enter the pickup, considering that the rest of the waves have to pass through a thick layer of cavitation bubbles, known to have a high shielding effect on supersonic waves.[7]

The same consideration precludes the possibility of waves reflected from the opposite and surrounding walls having any appreciable effect.

(4) *Calculation of Shock Pressure.* One of the oscillograms taken is shown in Fig. 30. The method of calculating out the shock pressure p_i and p_{sm} is stated in footnote 7 of the text.

Preliminary Experiments.

(1) *Selecting the Quartz Pickup.* The supersonic waves produced by cavitation can be expected to have a very wide frequency range, depending also on the incident angle and cavitation coefficient. In order to select a pickup suitable for receiving such a range of frequencies, 5 different models (with resonance occurring, respectively, at 0.5, 1.0, 2.0, 3.0, and 4.0 MC) were tested on a given cavitation phenomenon (Clark Y 11.7 per cent, incidence angle $\alpha = 0$ deg, cavitation coefficient $k_d = 0.8$). The result, given in Fig. 31, shows that in this case no waves above 2.5 MC were involved. The same figure also shows how pickups with resonance below 2.5 MC distort the spectrum by exaggerated amplification of waves around the resonance frequencies. A pickup with resonance at 3 MC was chosen for detecting waves in the range 0.5 ~ 2.5 MC. Similar tests were made for selecting pickups to be used with amplifiers for detecting waves in the range 150 ~ 650 KC (Fig. 32) and 55 ~ 250 KC (Fig. 33). The tests

[7] J. Saneyoshi, "Theoretical Studies on Absorption and Reflection of Ultrasonic Waves in Water Containing Bubbles," *Bulletin, Tōkyō Institute of Technology*, series B, no. 1, 1953, pp. 1-30.

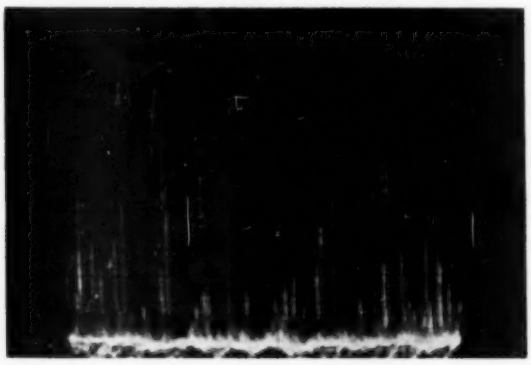

Fig. 30 An example of oscillograms

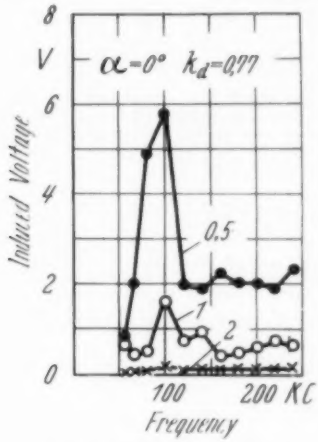

Fig. 32 Spectrum of cavitation waves obtained with pickups possessing different resonance frequencies—frequency band 150 ~ 650 KC, k_d = 0.77, pickup resonance frequencies 0.5, 1.0, 2.0, and 3.0 MC, profile Clark Y, α = 0 deg

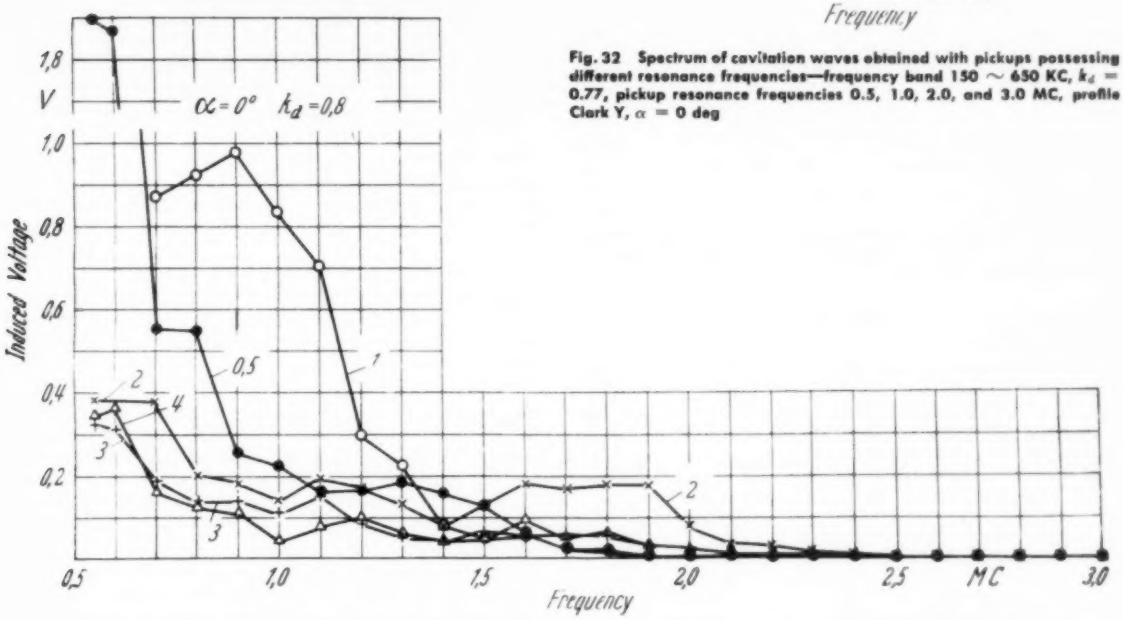

Fig. 31 Spectrum of cavitation waves obtained with pickups possessing different resonance frequencies—frequency band 0.5 ~ 3.0 MC, k_d = 0.8, pickup resonance frequencies 0.5, 1.0, 2.0, 3.0, and 4.0 MC, profile Clark Y, α = 0 deg

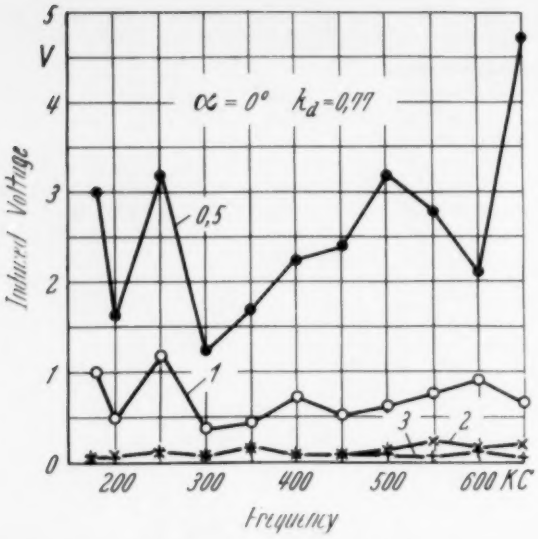

Fig. 33 Spectrum of cavitation waves obtained with pickups possessing different resonance frequencies—frequency band 55 ~ 250 KC, k_d = 0.77, pickup resonance frequencies 0.5, 1.0, and 2.0 MC, profile Clark Y, α = 0 deg

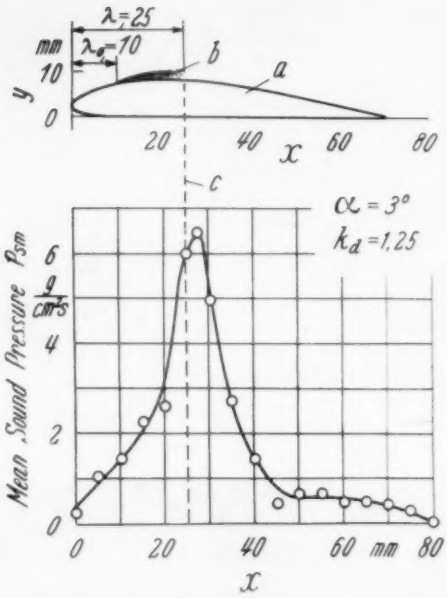

Fig. 34 Variation of wave intensity along chord—α = 3 deg, k_d = 1.25 frequency of shock wave = 1.7 MC. (a) Profile, (b) visible incipient, cavitation, (c) line indicating position of visible cavitation tail, head λ_0 = 10 mm, tail λ = 25 mm.

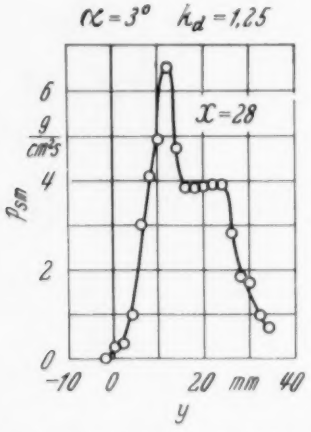

Fig. 35 Variation of wave intensity along the thickness (y-direction) of profile (along the straight line perpendicular to the chord at the point of maximum intensity along chord)

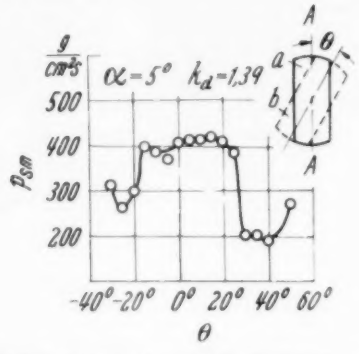

Fig. 36 Variation of measured wave intensity according to angle θ of pickup crystal. Incident angle α = 5 deg, k_d = 1.39, frequency f = 300 KC.

were further repeated with different values of incident angle and cavitation coefficient.

(2) *Determination of Measuring Point.* Cavitation waves are believed to be generated by the shock of extinguishing cavitation bubbles. The point of maximum wave intensity can therefore be expected to be in the vicinity of the tail of visibility cavitation (dotted line c in Fig. 34).

By moving the pickup along the chord of the profile the actual point of maximum intensity was found to be slightly displaced downstream from the tail of visible cavitation. The pickup was further displaced perpendicularly to the chord (along the y-axis in Fig. 34) to determine the point of highest intensity on the whole cross section (Fig. 35).

As concerns the angular position of the pickup the results of tests, shown in Fig. 36, indicate that within a range of ±20 deg the angle θ given to the pickup does not significantly affect the measured values. A guide was fixed to the cylindrical metal mounting of the pickup to keep its angle within these limits.

Cavitation and NPSH Requirements of Various Liquids

VICTOR SALEMANN

Group Supervisor,
Research and Development Section,
Worthington Corporation,
Harrison, N. J.
Assoc. Mem. ASME

Test results on the net positive suction head, NPSH, requirements for centrifugal pumps handling water up to 420 F, some hydrocarbons, and Freon-11 are presented. Satisfactory pump performance was observed with net positive suction heads less than those required by the pump on cold water. A direct measurement of NPSH was attempted and is reported. The cavitation process is discussed and a correlation and method of prediction for all liquids is proposed.

NET POSITIVE SUCTION HEAD is defined as the difference between the absolute suction head and vapor pressure at suction temperature. The minimum required NPSH is usually found by test, in which total head and efficiency are measured as a function of a cavitation coefficient. When converted to or tested at constant speed, a deviation from the initially constant value results when cavitation begins. Noise and vibration usually accompany cavitation and are also used as a means of detection. Generally, a small percentage drop in head is used to define the minimum required NPSH.

It has been known for some time that pumps operating on hydrocarbons can perform satisfactorily when supplied with less NPSH than the minimum required for cold water. Head, capacity, and efficiency experience little change and apparently no cavitation erosion takes place.

The need for better experimental measurements for hydrocarbon NPSH resulted in a series of tests in which the NPSH requirements at several temperatures for water, benzene, butane, butane-propane mixtures, gasoline, kerosene, and Freon-11 were determined and a general correlation attempted.

Previous Work

Stahl and Stepanoff [1][1] presented experimental results on a pump handling water up to 300 F and demonstrated that less NPSH was required at the higher temperatures. They also proposed that thermodynamic effects limit the flashing of water into steam caused by a given pressure drop below the initial vapor pressure which they called "dynamic depression" and that the volume of the vapor thus formed decreases as the temperature increases. They also compared the vapor volume created by "depressing" butane at room temperature a given amount with that of water at 300 F and concluded that since these volumes were in the same order of magnitude the two fluids should exhibit similar reduced NPSH requirements. They finally proposed to use a parameter, B, defined as the vapor-to-liquid-volume ratio created by flashing due to a small pressure drop below initial saturation pressure. This parameter is calculated and compared for two liquids or for the same liquid at two temperatures but using the same "depression." From the comparison some conclusion can be drawn as to the relative cavitating characteristics of the two liquids. Furthermore, from the order of magnitude of the parameter it is possible to conclude whether such a pressure drop in the pump is possible and, therefore, whether a corresponding NPSH reduction can be expected.

Jacobs, et al. [2], present data on pumping liquefied gases and a theoretical derivation of thermodynamic and viscous friction effects. They first expressed the volume ratio of vapor to vapor-liquid mixture generated by a given drop of pressure below initial saturation pressure as a function of fluid properties. Assuming that this volume ratio, which they called V, is a constant for a

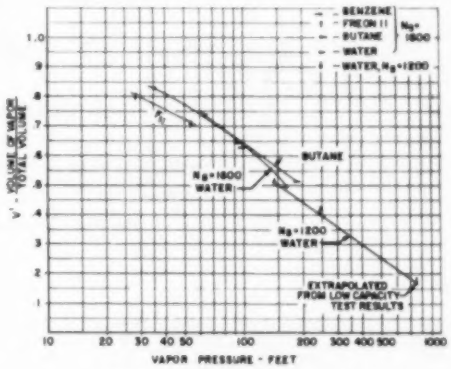

Fig. 1 V' versus vapor pressure

[1] Numbers in brackets designate References at end of paper.

Contributed by the Hydraulic Division and presented at the Annual Meeting, New York, N. Y., November 30–December 5, 1958, of THE AMERICAN SOCIETY OF MECHANICAL ENGINEERS.

NOTE: Statements and opinions advanced in papers are to be understood as individual expressions of their authors and not those of the Society. Manuscript received at ASME Headquarters, August 4, 1958. Paper No. 58—A-82.

Nomenclature

B = vapor volume / liquid volume
h_f = enthalpy of liquid
h_{fg} = enthalpy of evaporation
v_g = specific volume of vapor
v_f = specific volume of liquid
V' = vapor volume / total volume
V = total volume
P = pressure
Δp_{vv} = pressure difference across suction vane
N_s = specific speed
N = rotational speed

Subscripts

A denotes fluid and temperature
B denotes fluid and temperature
c = cavitating
L = liquid
m = minimum noncavitating
v = vapor

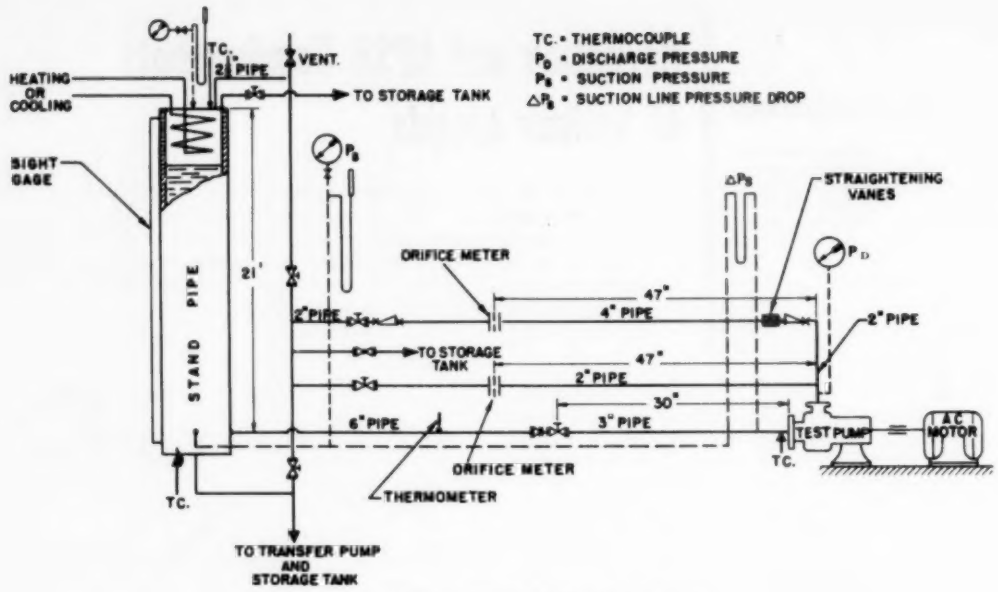

Fig. 2(a) Schematic view of test stand, $N_s = 1600$

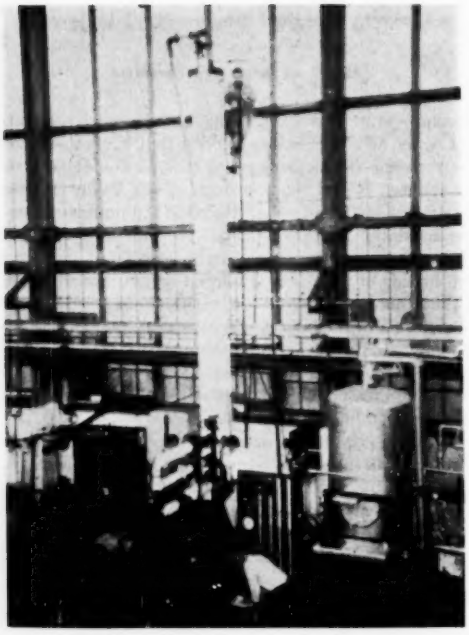

Fig. 2(b) Photograph of test stand, $N_s = 1600$

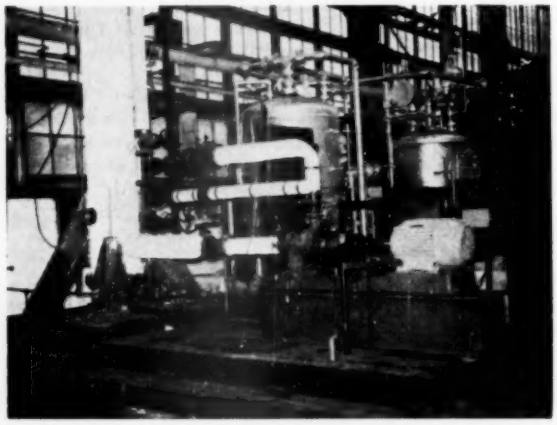

Fig. 2(c) Photograph of test stand, $N_s = 1600$

pump the ratio of V's for a pump operating on two fluids should equal unity. They then substitute the expression for V' in terms of fluid properties and dynamic depression, and solve for the ratio of dynamic depressions. As a result they developed a "Cavitation Tendency Quotient" which for constant capacity may be expressed as

$$\frac{T_A}{T_B} = \frac{[\mathrm{NPSH}_m - \mathrm{NPSH}_e]_A}{[\mathrm{NPSH}_m - \mathrm{NPSH}_e]_B} = \frac{f\left(\frac{v_g}{v_f}, h_{fg}, \frac{\partial h_f}{\partial p}\right)_A}{f\left(\frac{v_g}{v_f}, h_{fg}, \frac{\partial h_f}{\partial p}\right)_B}$$

This parameter should be useful to extrapolate results to other temperatures and liquids, if the physical properties are known.

The Appendix contains illustrations and sample computations of parameters B and V' for the convenience of readers not acquainted with the material in References [1] and [2].

Test Apparatus and Procedure

Two test stands and two pumps were used in the investigation. Most of the testing was done on a single-stage refinery-type pump of $N_s = 1600$ and 280-gpm design capacity. This pump was operated in the system shown in Figs. 2(*a*, *b*, and *c*). This sys-

tem permitted testing by suction-line throttling, by varying the pressure above the liquid level, and by varying the level itself. For most liquids, vapor pressure was maintained above the liquid level. The NPSH could therefore be computed from pressure and temperature measurements at the suction flange and also by subtracting the suction-pipe losses from the level in the standpipe.

Vapor pressure was measured in the case of mixtures and compared with values calculated from Raoult's and Dalton's laws in the case of known butane-propane mixtures. For tests on gasoline and kerosene, the vapor pressure was measured by the Reid and the "bubble-point" method. The latter is preferable for liquids containing gases and unknown mixtures where the vapor pressure depends on the evaporated quantity.

Test results on commercial gasoline indicated that the Reid method of vapor-pressure determination may be sufficiently accurate for liquid mixtures of closely similar properties. NPSH equal to that for cold water was observed for gasoline at room temperature using vapor pressure obtained by the Reid method but at pumping temperature. Tests on kerosene, however, resulted in NPSH requirements above those for water when Reid vapor pressure was used. Repeated tests resulted in progressively lower values. The apparent discrepancy was due to the fact that vapor pressure above the liquid was obtained by an ejector, which evidently "distilled" some of the volatile components during each test. After a number of hours, most volatile components were drawn off and the NPSH requirements of the remaining liquid approached those of cold water.

A vapor-pressure determination by the Reid and bubble-point method was made on a fresh batch of kerosene. Results are plotted on Fig. 4 and indicate the presence of a small quantity of highly volatile constituents or dissolved gas.

An attempt was made to measure the difference between vapor pressure and static pressure directly on water above 300 F. This was necessary as pressures and temperatures could not be measured with enough precision to calculate NPSH with sufficient accuracy. The apparatus used is shown schematically in Fig. 5. A similar apparatus was used by R. B. Jacobs, et al. [3], in their work on cryogenic liquids, and for similar reasons. In spite of precautions against heat transfer to the outside, Fig. 7, and for better heat transfer between bulb and fluid, Fig. 6, the

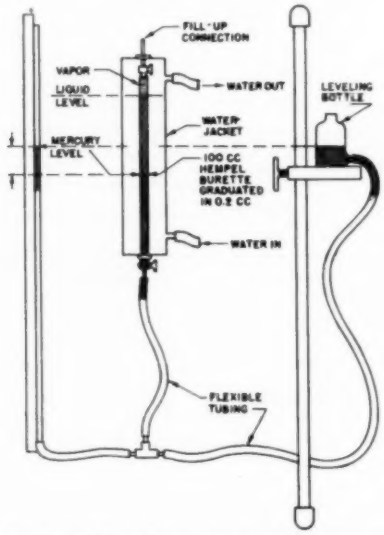

Fig. 3 Bubble-point-pressure measuring apparatus

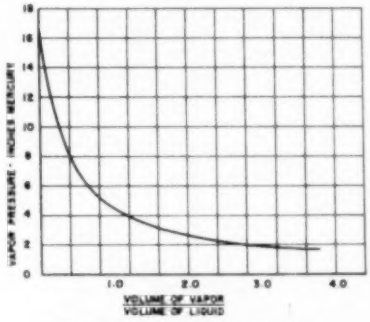

Fig. 4 Vapor pressure of kerosene

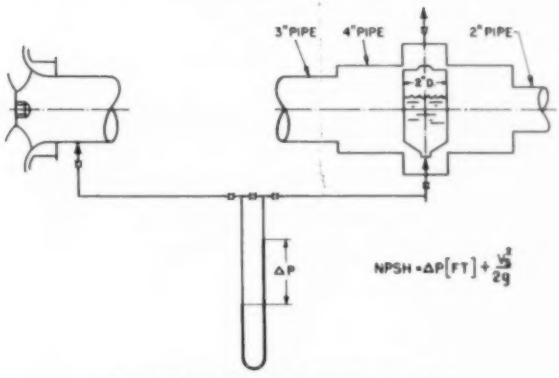

Fig. 5 Schematic view of vapor-pressure bulb

(a)

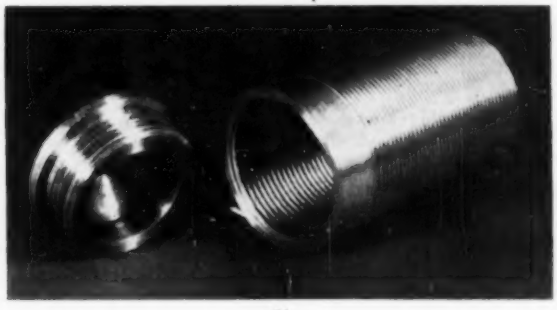

(b)

Fig. 6 Photograph of vapor-pressure bulb

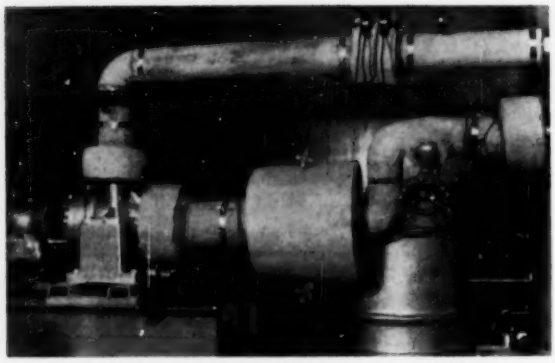

Fig. 7(a) Photograph of test stand, $N_s = 1200$

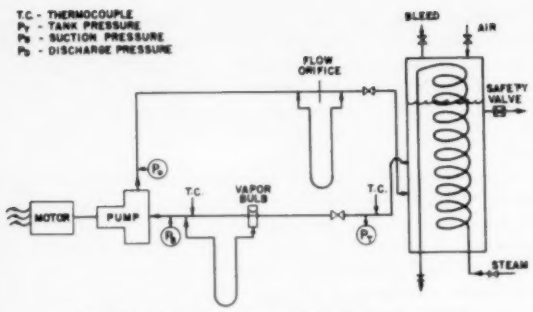

Fig. 7(b) Schematic view of test stand, $N_s = 1200$

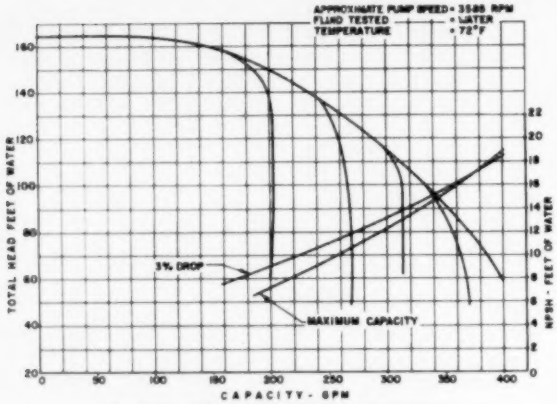

Fig. 8(a) Cold-water cavitating performance

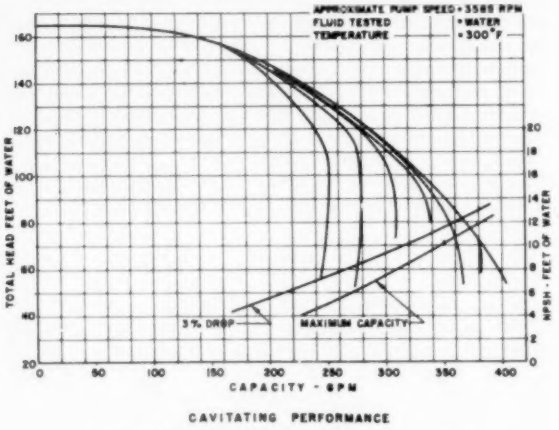

Fig. 8(b) 300-F water cavitating performance

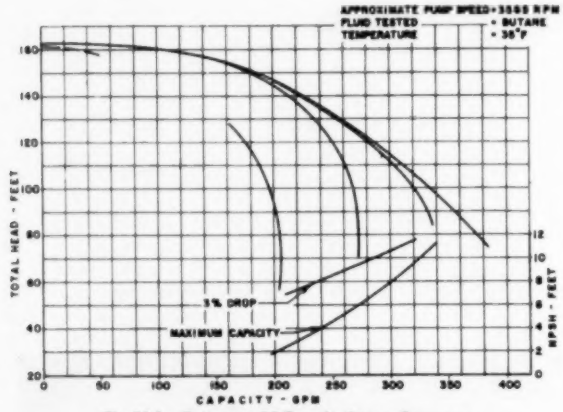

Fig 9(a) Butane at 35 F cavitating performance

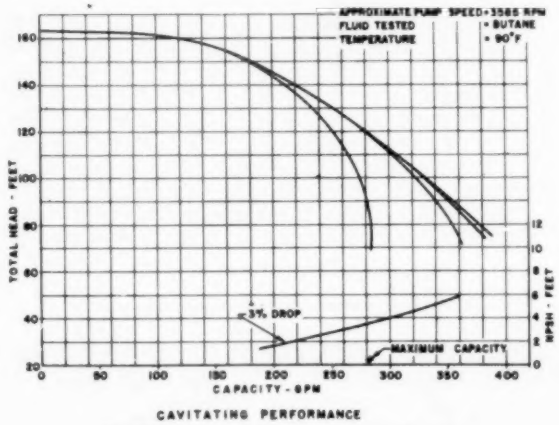

Fig. 9(b) Butane at 90 F cavitating performance

apparatus could not be made to indicate zero when the water in the suction pipe was flashing due to a throttled suction valve. The manometer on Fig. 5, under steady conditions, would not indicate less than about 1-in-Hg positive difference between suction and vapor pressure. The design of the chamber containing the bulb was suspected of causing flashing at the bulb and recondensation after, thus producing a slightly cooler fluid around the bulb. A temperature difference of only 0.13 F would account for this pressure difference.

Since NPSH at 400 F was expected to be approaching zero, and the apparatus could not be made to read zero, it was decided to run tests by setting a capacity and measuring the head while the temperature was allowed to drop. Vapor pressure was previously obtained above the liquid level and NPSH could then be calculated from suction losses and the level. As seen on Fig. 7, the entire suction line was insulated and no temperature difference could be detected from one end of the line to the other. Thermocouples wired with opposing emf were used in conjunction with a light-beam potentiometer. The data thus obtained were used to extrapolate to design capacity to obtain NPSH requirements at

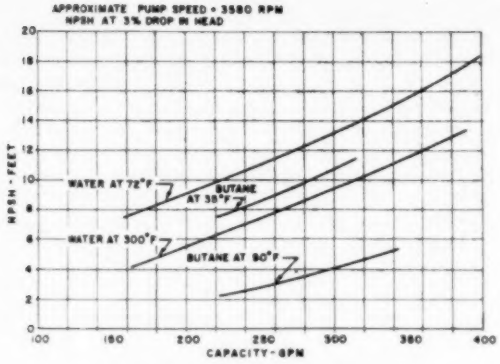

Fig. 10 NPSH versus capacity comparison

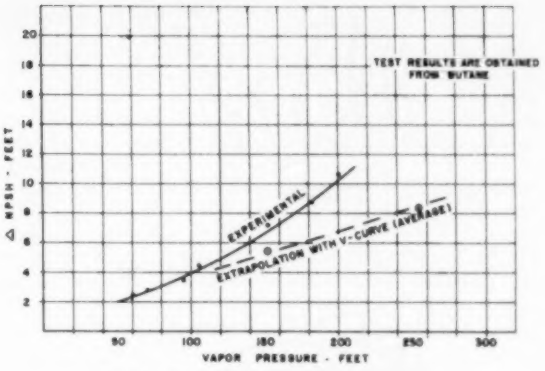

Fig. 11 Correction for paraffin hydrocarbons

Table 1 Test results, NPSH requirements at design flow and 3 per cent drop in head

Fluid	Temperature, F	NPSH, ft, min. accuracy ±0.5 ft	ΔNPSH
	Pump N_s = 1600, N = 3585 rpm		
Water	70	12.3	0.0
	250	11.0	1.3
	300	8.6	3.7
Butane	35	9.8	2.5
	55	8.8	3.5
	90	3.5	8.8
Butane + 3 per cent propane by weight	35	9.5	2.8
	55	7.8	4.5
	90	1.6	10.7
Benzene	180	12.4	(−0.1)
	230	9.7	2.6
Kerosene degasified	70	12.4	(−0.1)
Gasoline (Reid)	70	13.3	(−1.0)
Freon-11	85	10.2	2.1
	120	8.4	3.9
	Pump N_s = 1200, N = 3585 rpm		
Water	70	12.0	0
	290	9.5	2.5
	325	6.0	6.0
	410[a]	2.0	10.0

[a] Extrapolated from lower capacity. NPSH accuracy for this point is estimated at 2 ft.

these elevated temperatures. At higher capacities, suction-pipe losses exceeded the available NPSH such that flashing is assumed to have begun in the piping prior to the impeller.

Test Results

Typical performance curves at nearly constant NPSH are shown in Figs. 8 and 9. NPSH curves for the corresponding temperatures are shown in Fig. 10. The reduction in required NPSH as compared to cold water, at design point, is given in Table 1. Fig. 1 shows V' calculated for an NPSH corresponding to the maximum capacity, plotted against vapor pressure in feet. This curve is then used to obtain NPSH values for any other liquid if its properties are known. Fig. 11 as an NPSH correction chart for paraffin hydrocarbons. This generalization was possible by using equations for properties of hydrocarbons as published

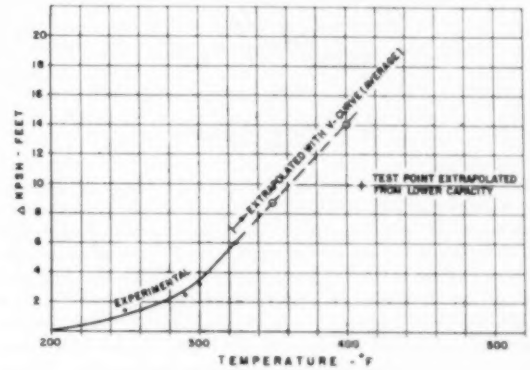

Fig. 12 Correction for hot water

by the Bureau of Standards [4]. Finally, Fig. 12 is a correction chart for hot water. Both charts are for the pump tested.

Discussion

The difference between cold water NPSH and NPSH for other temperatures and fluids was used as dynamic depression to calculate V' or percentage vapor by volume generated by the cavitation process. It had been assumed here that a pump should handle the same volume percentage of vapor irrespective of temperature. It was with surprise that the author discovered that this was not the case. The percentage of vapor (parameter V') was calculated assuming:

1 Constant temperature across a channel.

2 "Homogeneous" type of vapor formation or identical local vapor formation for all fluids and temperatures.

3 The difference between limiting cold water NPSH and limiting NPSH at other conditions was set equal to the "dynamic depression" of the fluid below vapor pressure corresponding to suction temperature.

To justify these assumptions, a model of the cavitating flow must be established. Stable cavities in the low-pressure regions rotating with the vanes or cavities nucleating at one point, growing until the flow sweeps them away and then collapsing, may be assumed. Both these processes have been shown directly or are confirmed by localized cavitation damage. But both these processes exist only at relatively low pressures. A fluid at high pressure and temperature should tend to "cavitate" more uniformly resulting in a more homogeneous mixture. This is true because

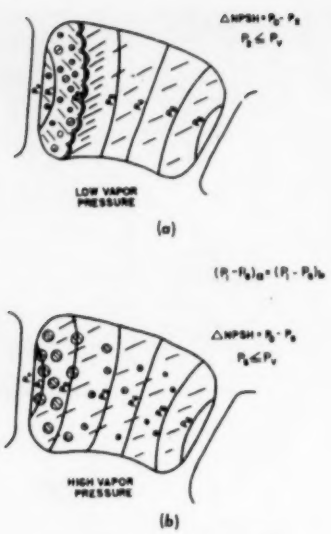

Fig. 13 Modes of cavitation

the pressure differences across a flow path depend on the velocity distribution and are unaffected by the ambient pressure. At high pressures, however, a much larger "depression" is necessary to produce an appreciable volume of vapor. Thus although the flashing is more intense in the low-pressure zones, the fluid will flash across the whole channel (compare Figs. 13 *a* and *b*).

The modes of cavitation may be identified according to the region in which the controlling parameters fall when plotted on Fig. 14. The value of B for a depression of 1 ft, called $B(1)$ is plotted against $\frac{1}{\Delta p_{sv}}$, which denotes the pressure difference across a suction vane (which should be equal to the difference across the channel), expressed in feet. Regions of local and uniform cavitation and a qualitative line, to be found by test, dividing the regions of light and severe reduction of pump performance are indicated.

It is now evident that the first two assumptions are not justified at all conditions. In a relatively cold liquid that flashes locally, temperature differences must exist between the liquid in high-pressure zones and the liquid-vapor mixture in the low-pressure zone. The second assumption may be justified only at relatively high pressures, while the alternative assumption is not justified at all. The third assumption is justified if the flow conditions are the same. If "limiting" is taken to mean the minimum NPSH required to suppress cavitation entirely, this would be true as the velocity and pressure distribution would not have been disturbed by cavitation. However, the same NPSH is required for all fluids if cavitation is to be suppressed entirely. The new concept in cavitation as first brought out by Stahl and Stepanoff is limited or "harmless" cavitation, and not lack of cavitation in liquids other than cold water. Cold-water NPSH at cavitation inception is a good approximation for limiting or minimum noncavitating NPSH. Since cavitation progresses very quickly in cold water, as evidenced by the steep breakoff curve on Fig. 8(*a*) the difference between minimum noncavitating NPSH and NPSH at the first measurable sign of cavitation is small, and assumption (3) is justified. With relatively hot liquids, which are assumed to cavitate homogeneously, the assumption is also reasonably justified, because a small percentage of uniformly distributed vapor would not disturb the flow conditions.

It is now possible to discuss the plot of V' against vapor pressure in feet, Fig. 1. Since the same pump was used for most of the testing and a pump with similar suction geometry employed for the tests on water above 300 F, the velocity and pressure distribution at the design flow are assumed identical for all fluids. The vapor pressure, when expressed in feet, is in the proper units to be used as a parameter in conjunction with the pressure distribution, if various density liquids are to be compared. Pressure differences across the channel and the B or V' parameter of the liquid for a given depression control the mode in which vapor is generated, in concentrated "cavities" or more evenly distributed. The parameter V' is a measure of the amount of vapor developed with an experimentally determined depression, set equal to ΔNPSH. This value of V' is the percentage of vapor in the cavitating region that will result in a measurable drop in performance. It should be correlated with the mode of cavitation resulting from pump and fluid characteristics. As a first approximation, vapor pressure is used to identify the mode. Thus, if V' is plotted against vapor pressure a family of curves for various suction geometries and possibly some fluid properties should result.

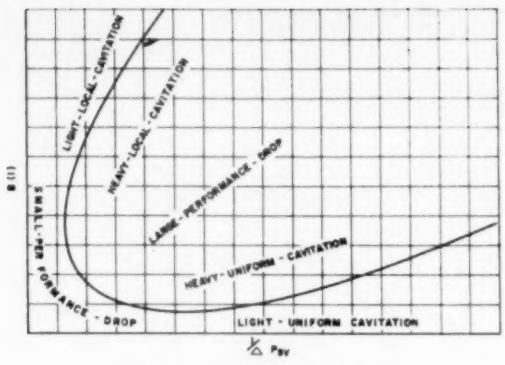
LIGHT - LOCAL - CAVITATION
HEAVY - LOCAL - CAVITATION
LARGE - PERFORMANCE - DROP
HEAVY - UNIFORM - CAVITATION
SMALL - PERFORMANCE - DROP
LIGHT - UNIFORM CAVITATION
B (1)
$\frac{1}{\Delta P_{sv}}$

Fig. 14 Regions of cavitation modes

A fairly smooth curve is obtained when V', as based on test results for all fluids, is plotted against vapor pressure. A wide scatter of points resulted when NPSH values based on a 3-per-cent-drop in head were used. This was due to experimental errors in head measurement. Scatter of points based on NPSH at maximum capacity is much smaller. The magnitude of V', see Fig. 1, is in both cases surprisingly high at low vapor pressures, and it is difficult to believe that the pump would produce 97 per cent of noncavitating head with 70 per cent vapor by volume in the suction. However, as pointed out previously, cavitation occurs at low vapor pressures only locally and 70-per-cent-vapor content pertains only to the lowest pressure region that does experience cavitation. In view of dissimilar modes of cavitation and therefore flow conditions, the assumption made by Stahl and Stepanoff, that "the same value of $\frac{V_v}{V_L}(B)$ would mean the same extent of cavitation and the same damage to performance" is questioned since, although the $\frac{V_v}{V_L}$ may be the same in the lowest pressure region, cavitation may be localized in one case or engulf the entire channel in another.

A similar assumption was made by Jacobs, et al., in their theoretical derivation of the Cavitation Tendency Quotient. They assumed that, for all liquids, a pump will handle the same percentage vapor under cavitating conditions and set it equal to V', which is calculated as a result of the dynamic depression. However, V' is the percentage vapor in the lowest pressure region, the over-all percentage across a channel is smaller and

will vary from liquid to liquid and from temperature to temperature if V' is kept constant. Furthermore, if different modes of cavitation exist, the same over-all percentage will not result in similar performance.

It is recognized that vapor pressure alone is not sufficient to describe the mode of cavitation. Since test results for one particular pump, run at one speed and capacity, were to be correlated, only the influence of the fluid properties on the mode need be considered. This is best described by the parameter B, calculated for a given depression. A depression of 1 ft was chosen, and V' based on experimental NPSH results was plotted against $B(1)$. Fig. 15 shows that the butane curve moves away from water and

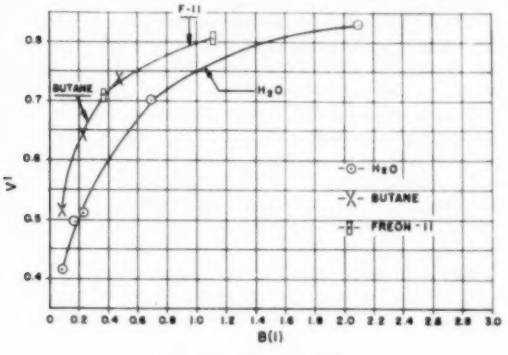

Fig. 15 V' versus $B(1)$

toward Freon-11, and that there is a distinct difference between water and the other two fluids. The reason for the failure of this representation is not known.

It should be stressed that Reid vapor pressure may be quite inadequate for calculating NPSH, as this vapor pressure is measured at a vapor-to-liquid-volume ratio of 4:1. Since the experimental values of V' denote the per cent vapor in the lowest pressure region, the vapor pressure to be used is that corresponding to V' if limited cavitation is tolerable. If cavitation is to be suppressed entirely, the initial bubble-point pressure, at negligible vapor volume, should be used (vapor pressure at B and $V' = 0$ on Fig. 4). According to present test data, vapor percentages of 30 to 70 per cent are common for limited cavitation. Vapor pressures should thus be measured under conditions where the vapor-volume percentage is the same, between 30 and 70 per cent, which corresponds to a vapor-to-liquid volume ratio of 0.4 to 2.3.

Surface-tension effects, neglected here, should be stronger at low temperature and reduce the vapor percentage somewhat. Except for very small bubbles, they are small compared to thermodynamic effects. Thermodynamic equilibrium is also assumed in the calculation of V', with all sensible heat liberated by the pressure drop being transferred into latent heat of the vapor. Actually, some energy will go into accelerating the fluid, and superheated water may exist for a small portion of the time of travel through the low-pressure region. Consequently, not all the sensible heat is liberated.

Conclusions

Test results confirmed previous work in this field; demonstrating that a pump will perform satisfactorily under cavitating conditions with less NPSH than required for cold water. The more favorable performance during cavitation, as well as reduced noise and vibration, suggest that a different mode of cavitation exists at high pressures.

Practical difficulties in obtaining accurate measurements for NPSH calculations at high pressures and temperatures make direct measurement desirable.

Tests on liquid mixtures and liquids containing gas in solution must be conducted in a manner approximating application conditions, losses of light fractions prevented, and a bubble method used in obtaining vapor pressure.

Future Investigations

Certainly more experimental work is necessary to corroborate this correlation. NPSH measurements on ordinary pumps are quite difficult at high vapor pressures. It may be wise, when experimental work in this line is contemplated, to test a pump that requires NPSH in the order of 100 ft rather than 10 ft.

Other suction geometries should be tested and families of V' curves obtained. In the analysis, metastable superheated state of the liquid should be considered, that is, the possibility of the liquid existing as such at pressures below its vapor pressure, resulting from lack of time for nucleation, or creation of vapor bubbles, and slow heat transfer. Initial liquid conditions affecting the nucleation and growth of bubbles such as solid particles or gas bubbles should be investigated. The very low V' values at high temperatures for water obtained by the author may be a result of sufficient nuclei in the liquid, as flashing was expected already in the suction pipe during the test runs. Throttling the suction line may produce similar effects, as air or vapor generated at the valve may not be quite reabsorbed before entering the impeller.

This investigation did not concern itself with cavitation damage under these conditions. Although the test pump was operated for hours under cavitating conditions, no damage was found. This, however, is insufficient evidence, and the cavitation-erosion question under these conditions must still be answered.

Acknowledgments

The author expresses his gratitude to the members of the Research Section for their co-operation in the test work and data processing, and especially to Mr. A. Agostinelli for his advice on correlation and presentation of results.

References

1 H. A. Stahl and A. J. Stepanoff, "Thermodynamic Aspects of Cavitation in Centrifugal Pumps," TRANS. ASME, vol. 78, 1956, p. 1691.

2 R. B. Jacobs, K. B. Martin, G. J. Van Wylen, and B. W. Birmingham, unpublished report, National Bureau of Standards.

3 R. B. Jacobs, K. B. Martin, and R. T. Hardy, "Direct Measurement of Net Positive Suction Head," published in this issue, pp. 147–152.

4 NBS Miscellaneous Publication No. 97, "Thermal Properties of Petroleum Products."

APPENDIX

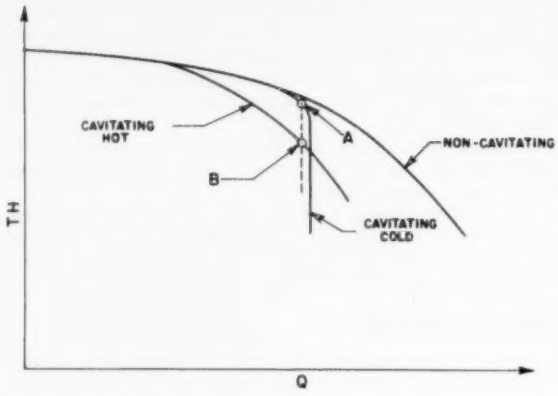

Sample Calculations

$$\Delta\text{NPSH} = \text{NPSH at } A - \text{NPSH at } B$$

$$V' = \frac{\text{volume of vapor}}{\text{volume of mixture}} \text{ (per lb of fluid)}$$

$$B = \frac{\text{volume of vapor}}{\text{volume of liquid}} \text{ (per lb of fluid)}$$

for a given ΔNPSH

$$V' = \frac{Xv_g}{v_f + Xv_g} \qquad X = \frac{\Delta\text{NPSH} \times \Delta h_f/\Delta p}{h_{fg}}$$

$$B = X\frac{v_g}{v_f}$$

Example

Reference fluid (A), cold water
Test fluid (B), water at 300 F
NPSH at (A) = 12.3 ft
NPSH at (B) = 8.6 ft
ΔNPSH = 3.7 ft
h_{fg} (at 300 F) = 910.1 Btu/lb
v_f (at 300 F) = 0.01745 ft³/lb
v_g (at 300 F) = 6.466 ft³/lb
Vapor pressure (at 300 F) = 67.013 psia

$$\frac{\Delta h_f}{\Delta p} = \frac{h_f(302\text{ F}) - h_f(298\text{ F})}{p_{sat}(302\text{ F}) - p_{sat}(298\text{ F})} = \frac{271.66 - 267.53}{69.046 - 65.028} = 1.03\ \frac{\text{Btu/lb}}{\text{psi}}$$

(p_{sat} = saturation pressure)

$$\text{NPSH (in psi)} = \frac{3.7}{0.01745 \times 144} = 1.47 \text{ psi}$$

$$X = \frac{1.47\ 1.03}{910.1} = 0.001665$$

$$V' = \frac{0.001665 \cdot 6.466}{0.01745 + 0.00165 \times 6.466} = 0.504$$

$$B = 0.001665 \times \frac{6.466}{0.01745} = 0.615$$

DISCUSSION

Lloyd T. Hendrix[2]

The author is to be thanked for doing NPSH test work on fluids other than water. The California Natural Gasoline Association had a subcommittee which did experimental tests on hydrocarbons. There were about 240 tests covering two pumps and a range of materials from kerosene to a butane-propane mixture. I had the good fortune to be associated with this work.

In my opinion, for all of the work done on NPSH, the greatest problem is in selecting the vapor pressure to be used. For example, water used for the normal approval tests for pumps can range from being saturated with air to being completely deaerated. If it is saturated entering the pump suction line, by the time it gets to the pump the pressure is low enough to release two to three actual cubic feet of vapor per one hundred cubic feet of water. Even if the water NPSH were always run with deaerated water, there would still be the problem of selecting the vapor pressure for the hydrocarbon mixture. An article I wrote for the June, 1958, *Petroleum Refiner* discusses this in more detail, but the point I want to make is that we are asking for trouble by applying correction factors to the water NPSH for design work involving hydrocarbons. Our best system would be to use water NPSH determined on deaerated water as the minimum feet of liquid above pump suction, and assume the vapor pressure of the liquid to be the pressure above the liquid in the surge vessel if the system is above atmospheric pressure. Otherwise, for atmospheric systems use something similar to the method shown in the *Refiner* article. This allows for dissolved air or gas coming out of solution and takes advantage of the fact that the pump will handle some vapor.

Finally, I would like to compliment the author on a fine piece of work. He might be interested in work being done by Mr. George Bosco of Aerojet General on dynamic bubble point vapor pressures for various liquids. Results of this work should be completed in six to eight months.

Robert B. Jacobs[3]

I wish to commend the author for undertaking an investigation which was long overdue, for the manner in which he has carried out his experimental work, and for his insight into the more subtle aspects of this problem. I hope that he has the opportunity to carry on this work, and to resolve some of the many questions which he has raised.

It is rather heartening to note that a correlation based upon the naive assumptions made in references [1 and 2] can be valid for even a few cases; in addition to the author's results, I would like to point out that the relative NPSH requirements for hydrogen and nitrogen in a pump with a specific speed of 1350 were accurately predicted by the analysis in reference [2]. However, I should hasten to add that accurate prediction of the relative NPSH requirements between cold water and the liquefied gases was not obtained. I therefore agree with the author that different modes of cavitation must be postulated, and that quite different phenomena may be dominant for one mode than for another.

Several questions came to mind regarding the test apparatus and procedure. In Fig. 2(*a*), was the "heating or cooling" coil installed as shown, or was it submerged in the liquid; if it was as shown, was it an effective temperature and/or pressure control? It seems that once all the liquid in the standpipe was saturated, only pressure control of the vapor space in the standpipe would be necessary.

A question regarding the accuracy of the temperature measure-

[2] Chief Process Engineer, Natural Gas Division, Richfield Oil Corporation, Bakersfield, Calif.
[3] Natural Bureau of Standards, Boulder, Colo.

ments comes to mind when I note that an NPSH accuracy of ±0.5 ft with butane at 90 F requires a temperature accurate to about ±0.17 deg F. The question again arises in connection with the procedure used for determining that the temperature did not change in the suction line for the high temperature water test; to detect a 0.5-ft change in NPSH with water at 400 F requires a temperature measurement that will detect a change of 0.06 deg F. Was it ascertained that the liquid leaving the standpipe actually had the same vapor pressure as that at the liquid vapor interface (in the high-temperature water experiments)? The vapor pressure of the fluid leaving the tank in Fig. 7(*b*) can be appreciably greater than that at the liquid surface because of local boiling along the steam coil.

I hope that the author will not forsake the use of the vapor bulb method for measuring NPSH, for those cases where it is desirable, because of the difficulties which he encountered. He has probably thought of the two most likely causes for the difficulties which he experienced. The heat conduction through the pressure lines could be effectively eliminated by tempering these lines, either by running them along the pipe before bringing them out through the insulation or by having a longer tubing length inside of the pipe. The effect of the bulb on the flow can, of course, be reduced by decreasing the size of the bulb; the bulb which the author used seems rather large, but perhaps the displacement in his manometer system required this size. As the bulb must only be large enough to assure that the liquid-vapor interface remains in the bulb, the bulb size can be minimized by using a differential pressure indicator that requires a minimum volume displacement. Another alternative, which involves other problems when the bulb is above atmospheric temperature, is to measure the vapor pressure through a tap which communicates with the vapor space.

The author's discussion is most provocative and interesting. In his discussion of the assumptions employed in the calculation of the amount of vapor formed, he does not comment on the assumption of stable equilibrium, although he mentions it in a later section. This assumption may be one of the least tenable in view of the short times that it may take for fluid particles to traverse low-pressure regions, and of the many factors which can effect the nucleation and growth of vapor regions.

Perhaps, when the author speaks of a fluid at high temperature and pressure tending to cavitate more uniformly, he has water in mind and therefore may be justified in using these properties. When discussing fluids in general, however, it may be more meaningful to refer to those combinations of properties which influence the volume of vapor that will be formed. For example, hydrogen at 1 atmosphere and −424 F is not at high pressure and temperature, but apparently cavitates like hot water. This same limitation applies when the author mentions surface-tension effects.

There is a question in my mind concerning what is meant by suppressing cavitation entirely, and therefore concerning the statement that the same NPSH is required for all fluids to suppress cavitation entirely. I visualize that the time for nucleation in one fluid may be so long that it will pass through a low-pressure region with no vapor formation, while for another fluid vapor may form. If cavitation is considered to be entirely suppressed in the first case, then the statement concerning the same NPSH requirements for all fluids may not be true. In this connection, I would like to know what influence the author thinks the presence of gas may have had on his cold water tests. I think that the author's suggestion of investigations into the existence of metastable states, factors effecting nucleation and bubble growth, and the influence of heat conduction will assist in resolving many of the fundamental problems in this area.

I realize that in many complex situations we try solutions which our intuitions suggest and then, if the results are satisfactory, we try to find a justification for our actions. Is this the case for the correlation attempted in Fig. 15, or does the author have reason to think that this correlation should be successful?

I would again like to commend the author for making a significant contribution in a very difficult area.

Igor J. Karassik[4]

The research studies carried out by the author and the report that he has presented fill an important blank space in our knowledge of centrifugal-pump operation under what might be termed marginal suction conditions. For this valuable contribution both designers and users of pumps should be truly grateful to him.

Because of my long term association with problems dealing with pumping water at high temperatures, I shall limit my remarks to that portion of the paper which deals with the effect of temperature on the NPSH requirements when handling water. In the past, there had been some scattered evidence indicating that the required NPSH of centrifugal pumps was appreciably reduced as water temperature increased. A few individual tests were reported here and there to illustrate this contention. At the same time, there persisted considerable scepticism directed at this claim. But I submit that the essential theory that NPSH is reduced with temperature—as it is so aptly proved in this report—can be readily supported by a strictly logical demonstration.

In this particular case, we need merely to consider the effect of temperature on the performance of centrifugal pumps, operating at a given speed and supplied with a fixed NPSH, when handling (*a*) cold water at 70 F and (*b*) hot water at 705.4 F (critical temperature for water).

It is obvious that in the case of cold water at 70 F, the break in the head-capacity curve will occur at some capacity determined by the geometry of the impeller and by the speed at which the pump is operating as indicated in Fig. 16.

When it comes to handling water at 705.4 F, that is the critical temperature at which no evaporation takes place (as long as the pressure is maintained at 3206.2 psia), the volume occupied by water is the same as that occupied by steam. Under these conditions, a slight reduction in the available NPSH can have no appreciable effect on the performance characteristics of the pump (when expressed as head in foot-pounds per pound, plotted against volume) since no true cavitation can take place. This statement is predicated on the fact that a change from water to steam occurs without a change in volume occupied by either fluid. In other words, the head-capacity curve of a pump handling 705.4 F water with less than the theoretically required NPSH will coincide with the head-capacity curve with cold water and ample NPSH, as shown in Fig. 16.

Having established the two limits of performance characteristics

[4] Consulting Engineer and Manager of Planning, Harrison Division, Worthington Corporation, Harrison, N. J. Mem. ASME.

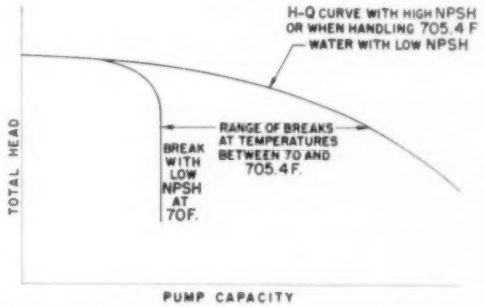

Fig. 16 Effect of temperature on maximum capacity at fixed pump speed and with fixed NPSH

at 70 F and at 705.4 F, I submit that the relationship between the location of the break and the pumping temperature is a continuous function. Therefore, all breaks at temperatures between these two extreme temperatures must take place between the two limits of capacity indicated.

This would indicate that the practice of establishing the required NPSH without regard to the operating temperature has been conservative and unrealistic. I am convinced that the thermodynamic analysis presented here can yield a workable mathematical method to predict the required NPSH with relation to temperature.

A word of caution is necessary at this point. It would be highly unwise to rush headlong to the conclusion that the values of recommended NPSH for boiler feed pumps should immediately be drastically reduced. We must remember that boiler feed pumps are frequently required to operate over wide ranges of temperature and that a given installation cannot very well take advantage of a permissible reduction in NPSH requirements at the top operating temperature if operation at lower temperatures will wipe out any assistance gained by the effect we have described. The effect is very useful in affording us some measure of additional protection during the transient conditions which prevail with regard to suction phenomena when severe load reduction occurs in a steam power plant. Let us preserve this protection and not give in to the temptation to cut corners.

On the other hand, the author's analysis should be of extreme interest to us with reference to the application of boiler circulating or of reactor cooling pumps. If we were to express the facts indicated in Fig. 16 in a different manner, we can say that until now a curve of permissible operating speeds plotted against available NPSH for a fixed capacity represented a single curve as shown in Fig. 17, labeled "A." In the light of the facts as we now understand them, this curve can be replaced by a family of curves arranged in such a way that an increase in operating temperature results in some increase in the permissible operating speed of the pump, until such time as at 705.4 F, the NPSH plays no further part in determining the maximum permissible operating speed. This is indicated in Fig. 17 by curves "B," "C," and "D."

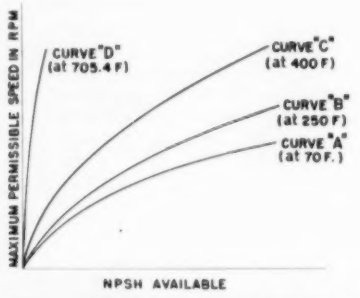

Fig. 17 Maximum permissible speed versus NPSH for a given pump and a given capacity at various water temperatures

It would therefore appear that some tendency may have existed in the past to be overly timid and conservative in selecting operating speeds for boiler circulating pumps. Because they and reactor circulating pumps normally operate at temperatures from 550 to 650 F, it should be obvious that higher operating speeds are permissible—or, in turn, lower NPSH values are required for a given speed.

It is true that provision must be made to meet conditions of operation when the temperature is lower than normal rated temperature. This will occur during start-up or during emergencies. But we can deal very effectively with this problem by virtue of the fact that this type of installation favors the use of two-speed motors for reasons other than NPSH considerations. When operating at lower speed and, of course, at reduced capacities, the required NPSH is also much reduced. Therefore, if an installation takes advantage of the beneficial effect of temperature on NPSH, it can be protected against the loss of this effect at lower temperatures merely by shifting operating speeds.

For instance, if an installation of nuclear reactor circulating pumps is designed to handle 600 F water, it can be provided with an automatic protective control in the form of a thermostatic switch. Assuming that the available NPSH would make the operation unsafe at temperatures under 450 F, this switch would automatically transfer operation to the lower of the two motor speeds whenever the temperature fell to 450 F. This lower speed operation would then continue until either manual resetting or restoration of temperature would permit a switch-over back to the higher speed.

Alfred H. Nissan[5]

This paper is a welcome addition to the literature on cavitation; it adds weight to the two probably most significant conclusions which are emerging from the considerable research on the subject. The first is that it is probably incorrect to speak of cavitation as a single phenomenon: There are at least two modes and there may be more. The second is that there is a great deal of work to be done both on the physics as well as on the engineering aspects of the phenomena which collectively contribute to and constitute the complex events of "cavitation."

Since Rayleigh first analyzed the behavior of liquids under cavitating conditions in 1917, he and all subsequent workers have repeatedly shown evidences that there were unknown though very significant factors coming into play. Thus 30 years later, Wislicenus[6] in his authoritative book on "Fluid Mechanics of Turbomachinery" had this to say: ". . . . Although it is usually possible to make some qualitative predictions regarding the influence of viscosity on other hydraulic characteristics, particularly the power and efficiency of the machine, *no general information is available to indicate even the direction in which an increase in viscosity . . . . . will influence the cavitation characteristics of the machine*" (my italics). This statement is, as far as I am aware, still true today. As late as 1957, Robertson, et al.,[7] showed that the scaling laws in cavitation for streamlined bodies were different from those for bluff objects and that even for the same objects there were different inception indexes. And now the author contributes further evidence that the same pump will behave differently with the same liquid at one temperature from its behavior at another. A clue to one of these missing factors, other than the unknown influence of viscosity, may be in Iyengar and Richardson's work[8] on the presence and size distribution of air nuclei in liquids. By means of absorption spectra of sound waves ranging in frequency from about 150 to 1000 kc/sec in liquids under different conditions, these authors conclude that air bubbles ranging in diameter from a few up to about 40 microns control the kind of cavitation which is most generally observed, i.e., in cold water under ordinary conditions. In hydrocarbons or in water under high pressures, these nuclei disappear and a different mode of cavitation arises—harder to the ear in its sound effects, and demanding a higher threshold before it manifests itself. I would ask the author whether he investigated the

[5] Research Professor, School of Engineering, Rensselaer Polytechnic Institute, Troy, N. Y.

[6] G. F. Wislicenus, "Fluid Mechanics of Turbomachinery," McGraw-Hill Book Company, New York, N. Y., 1947.

[7] J. M. Robertson, J. H. McGinley, and J. W. Holl, *La Houille Blanche*, No. 4, 1957, p. 550.

[8] K. S. Iyengar and E. O. Richardson, *British Journal of Applied Physics*, vol. 9, 1958, p. 154; *Nature*, vol. 181, 1958, p. 1328.

possibility that air nuclei contributed to the divergence in behavior of the pump which he observed when water under high temperatures—and pressures—and organic liquids were compared with cold water or, alternatively, whether the liquids were freed entirely from air. My second question is whether the author could see direct evidences in the pump—such as the condition of the impeller—to support the two modes of cavitation depicted in Fig. 13.

I think there can be no dissent from the author's conclusion that a great deal more fundamental work should be done on cavitation phenomena.

Frank C. Stanek[9]

The author deserves a vote of thanks for some interesting extensions to the prediction of cavitation performance when pumping unusual liquids.

For the most part, his data suggest NPSH values (for the N_s = 1200 impeller on hydrocarbons) which seem consistent with the experience of this discusser. Persons who intend to build on his test results should be cautioned to observe the condition of gas (air)-free liquid in the reservoir since it is easily possible to precipitate complete pumping failure with hydrocarbons at relatively high NPSH through unusual inlet line losses which can release significant volumes of dissolved or entrained air. Aircraft fuel pump designers are acutely aware of this peculiarity and have learned to avoid it or otherwise cope with it. The uninitiated should become familiar with SAE ARP-492 and its appropriate reference, the 1946 CRC Handbook, in order to appreciate the seriousness of this problem lest they be lulled into a false sense of security by seemingly adequate NPSH.

This discusser suggests that physical factors and thermodynamic properties other than those mentioned by Salemann, Stahl and Stepanoff may enter into the variations observed between the NPSH requirements for water, hydrocarbons, etc., at varying temperature:

(a) What about pressure ratio across a cavitating pump? Should not its magnitude affect cavitation performance? Isn't it logical that a given pump should perform less effectively for a given B value as pressure ratio increases? Evidence indicates that cavitation performance depreciates with decreasing inlet pressure.

(b) Certainly the shape of the saturated liquid and saturated vapor line on the Mollier diagram will determine the likelihood of recompressing vapors back into liquid phase. If the arrangement of these lines differs radically from one liquid to another, it is conceivable that the energy losses in a cavitating impeller may preclude the possibility of such recompression with a particular fluid. There is already some evidence of this with certain hydrocarbon fuels. If vapors can't be recompressed into liquid with restoration of local static pressure, the density effect of the mixture which is being handled by the impeller could account for some of the variations observed.

While points (a) and (b) do not constitute a constructive review of this paper, they may point the direction for additional research effort as well as to suggest why perfect correlations have yet to be obtained in cavitation tests.

A. M. Whistler[10]

The first point we should stress is that the NPSH figure we obtain from pump manufacturers is really no more than a number. This number is obtained by pumping water while throttling the suction. Pressure at the pump nozzle is noted. To this is added the kinetic energy of the water. A figure for vapor pressure is taken from the steam tables and subtracted from this sum.

The remainder is called NPSH. No one knows just what figure would be correct for vapor pressure. The water used in the customary test certainly contains air. Even if vacuum is applied the air is not entirely removed. It has to be boiled out. Even heating to boiling point doesn't remove all of it.

Hydrocarbons dissolve much more air than water does. Fig. 4 of the subject paper shows vapor pressure for kerosene. The bubble-point vapor pressure is some 8 times what it would be for pure kerosene. The routine test for vapor pressure of petroleum products is the REID method. Due to inherent characteristics of this method, it does not show the effect of air, and in most cases it will not detect other dissolved gases. The REID number is normally just slightly less than the true vapor pressure in an uncontaminated condition.

In the second paragraph of the paper, it is stated: "It has been known for some time that pumps operating on hydrocarbons can perform satisfactorily when supplied with less NPSH than the minimum required for cold water."

I believed this up to two years ago. Since that time I have inquired diligently as to the experiences of engineers in the oil industry. I have not found even one who has had any experience to back up this belief.

I know that several pump companies for a long time have shown NPSH curves for oil that are substantially lower than those for water. There is no differentiation as to pressure, etc. This method cannot be right.

On the other hand the Hydraulic Institute has a chart with a series of pressure lines. It looks much better. But did it come from one man?—or a group? And what was the background for the chart? No data points are shown. So far the answers of the foregoing questions are not available.

There have been several cases where oils have required much more "apparent" NPSH than water. The first record was on pumps unloading gasoline from tankers. It was found that the true vapor pressure was 14 psia ± as against some 7 or 8 obtained by the REID method. It is almost certain that dissolved air was the trouble.

The next case reported was pumping jet fuel. Tests on true vapor pressure were made by Aerojet on normal fuel and on a deaerated sample. The normal sample showed a bubble point of about 14 psia while the deaerated sample showed some 4 psia. The difference of 10 psia adds 28 feet to the apparent NPSH if air were not allowed for.

Another case was C.N.G.A. tests on absorption oil. The apparent NPSH was about three times that obtained on hot water at the factory. True vapor pressure was not obtained. But the oil was exposed to air.

The foregoing discussion was for purpose of showing that our base line NPSH curves are probably not absolute.

This observation, however, throws no light upon the subject of NPSH variation with liquids of different types. It might be helpful to work out a formula for the adiabatic vaporization of a liquid as its pressure energy is converted to kinetic. The formula is

$$\Delta h = \left(\frac{144}{\rho_1}\right)\left(\frac{P_1 - P_2}{T_1 - T_2}\right)\left(\frac{V\rho_v}{\rho_1}\right)\left(F + \frac{H}{100\,Cp}\right)$$

where Δh = suppression in pressure below initial bubble point in ft of liquid

F = slope of initial vaporization deg F/wt per cent vapor. For example, a mixture might start to vaporize at 100 F and be completely vaporized at 200 F. Then $F = (200 - 100/100) = 1.0$. For pure components $F = 0$.

H = latent heat Btu/lb

Cp = specific heat of liquid

[9] Thompson-Ramo-Wooldridge, Cleveland, Ohio.

[10] The Fluor Corporation, Ltd., Los Angeles, Calif. Mem. ASME.

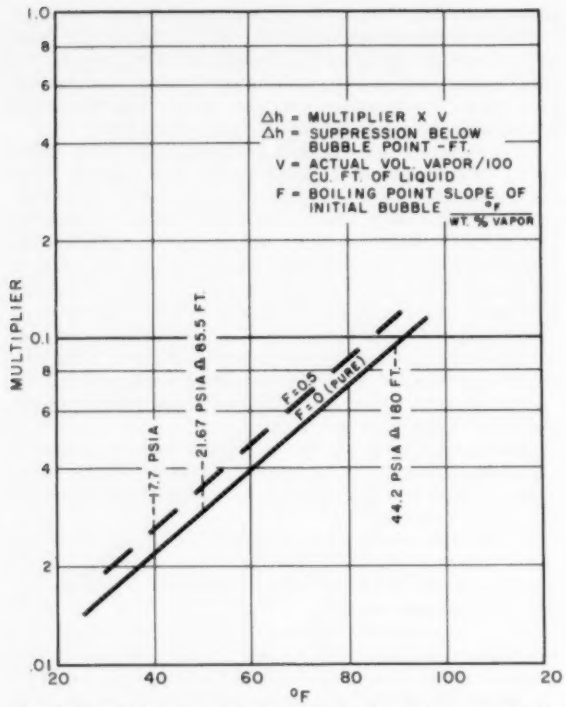
Δh = MULTIPLIER X V
Δh = SUPPRESSION BELOW BUBBLE POINT - FT.
V = ACTUAL VOL. VAPOR/100 CU. FT. OF LIQUID
F = BOILING POINT SLOPE OF INITIAL BUBBLE °F / WT. % VAPOR
MULTIPLIER
°F
17.7 PSIA
21.67 PSIA Δ 85.5 FT
44.2 PSIA Δ 180 FT
F=0.5
F=0 (PURE)

Chart I Normal butane; pressure suppression in adiabatic vaporization

V = actual cu ft of vapor formed per 100 cu ft of liquid

$\frac{P_1 - P_2}{T_1 - T_2}$ = slope of vapor pressure curve lb/sq in/deg F taken at point of operation

ρ_v = density of vapor lb/cu ft

ρ_l = density of liquid lb/cu ft

Space is not available to show the derivation. The assumptions made are (1) linear vapor pressure curve for the interval involved; (2) latent heat all comes from sensible heat of liquid; (3) constant densities, latent heats, and sensible heats, through the interval.

For any temperature point the formula boils down to:

$$\Delta h = \text{a multiplier} \times V$$

Chart I shows the multiplier for pure normal butane plotted against temperature. Chart II is the plot for water. To compare the two we might list computations assuming different amounts of vapor formed.

		Δh = ft suppression, Vapor, cu ft/100 cu ft liquid			
	Temp	3	60	90	Table 1
Normal butane	35°	0.57	1.14	1.71	2.5
	55°	1.02	2.04	3.06	3.5
	90°	2.82	5.65	8.45	8.80
Butane with 3% wt propane use butane with $F = 0.5$	35°	0.066	1.32	1.98	2.8
	55°	0.120	2.40	3.60	4.5
	90°	0.340	6.80	10.15	10.7
Water	70°	0.000016	0.00032	0.00048	0
	250°	0.4305	0.87	1.3	1.3
	300°	0.147	2.94	4.4	3.7

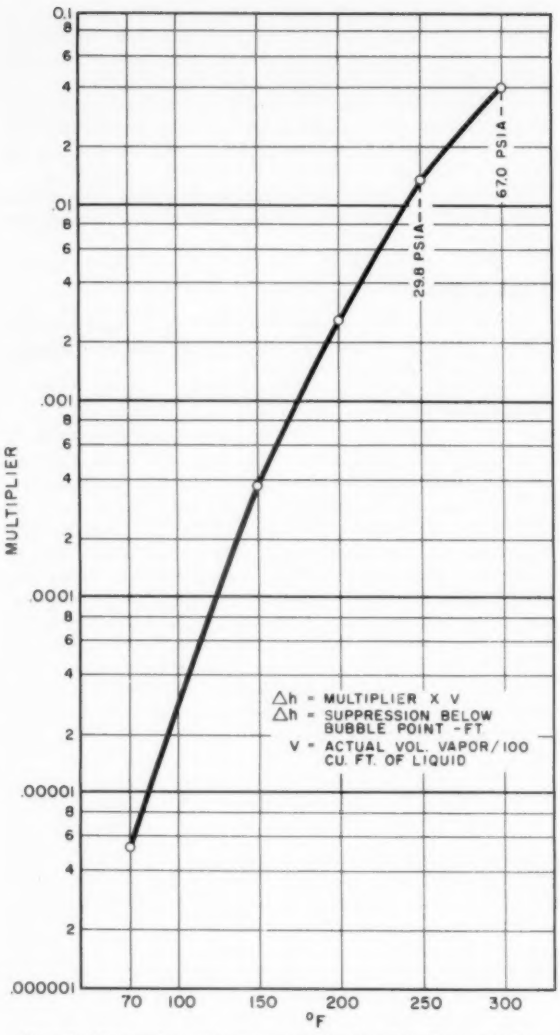
Δh = MULTIPLIER X V
Δh = SUPPRESSION BELOW BUBBLE POINT - FT.
V = ACTUAL VOL. VAPOR/100 CU. FT. OF LIQUID
MULTIPLIER
°F
67.0 PSIA
29.8 PSIA

Chart II Pure water; pressure suppression in adiabatic vaporization

In comparing this with Table 1, let us look at water first. To get suppressions like Table 1 we would need to vaporize 70 to 90 cu ft/100 cu ft of liquid. An answer like this is not acceptable without a lot more data.

Another point can be nailed to the wall. If we look at Fig. 8(*a*) for 72-F water we see that the head curve dropped regularly from 160 to 200 gpm before it became vertical. From our computations we can see that from a practical standpoint no suppression at all can be taken for water at 72 F. Therefore the only conclusion we can come to is that the 72-F water contained air.

From other similar tests we have seen the same can be said for kerosene, gasoline, and probably for benzene.

It is not quite clear just what the test procedure was. At the top of page 169 it says that the setup permitted testing by (1) suction line throttling, (2) varying pressure above the liquid, and (3) varying the level. But the next sentence states that, "The NPSH could therefore be computed from pressure and temperature measurements at the suction flange . . ."

It is also stated that for most liquids vapor pressure was maintained above the liquid level. But this could not be done for (1)

cold water, (2) gasoline at 70 F, (3) kerosene at 70 F unless a vacuum were maintained. And vacuum is not mentioned.

The results on butane check each other fairly well if we assume about 80 to 90 cu ft vaporized/100 cu ft of liquid. The F of 0.5 is assumed for the butane with propane. It might be a good guess.

When tests are made by throttled suction, the NPSH must be computed using a vapor-pressure figure obtained from reading the temperature in the suction line. This introduces three possible sources of error (1) the temperature, (2) the true vapor pressure, and (3) pressure. Temperature and pressure readings become more and more important as pressures go up. Compare the following:

Material	deg F	psia	$\frac{\text{psi}}{\text{deg F}}$	$\frac{\text{ft liq}}{\text{deg F}}$	$\frac{\text{ft}}{\text{psi}}$
n-Butane	35	16.0	0.32	1.23	3.86
	55	19.0	0.50	1.97	3.94
	90	43.5	0.65	2.66	4.07
Propane	35	72	1.2	5.25	4.35
	55	100	1.60	7.18	4.50
	90	168	2.30	10.95	4.76
H_2O	72	0.388	0.0129	0.03	2.31
	250	29.82	0.515	1.24	2.40
	300	67.01	0.99	2.5	2.53

One of the toughest problems is the true vapor pressure of a material. None of the commercial hydrocarbons are pure. Also the method of computing vapor pressure from analyses is not accurate enough for NPSH testing. And methods of analysis are not accurate enough either.

Summary

The following comments might be made:

1 This paper is an important step in progress toward better engineering.

2 It shows a definite indication that where NPSH tests are made on cold water

(*a*) Hydrocarbons exposed to air require as much or more than indicated by cold-water testing.

(*b*) For hydrocarbons under their own pressure the cold water NPSH contains a factor of safety.

3 It provides strong evidence NPSH requirements go down as pressure goes up.

4 It *may* predict that the allowable vaporization is not constant.

5 We should go slow on hard and fast generalization.

6 The actual suppression head below bubble point may not be nearly as great as indicated.

7 Future tests should be made by varying head with unthrottled suction.

Author's Closure

I believe that Mr. Hendrix overestimates the effect of dissolved gases on the performance of a pump. I agree that they definitely affect pump performance in the cavitating region, and if the amount released in the suction pipe is 2 or 3 per cent, it would, of course, cause a premature lowering of performance. But I do not believe that dissolved gas alone would cause an essentially vertical head breakdown line as on Fig. 8(*a*), where at 315 gpm a drop of NPSH from 14 ft to 13 ft causes the head to drop abruptly from 97 per cent of its noncavitating value and prevents any increase in flow.

From Fig. 1 of Mr. Hendrix's article in the *Petroleum Refiner*, we see that this change in NPSH would increase the "vapor" (actually air-vapor mixture) volume from 4 to 4.7 per cent.

I further propose that generally a far smaller percentage of dissolved gas comes out of solution than indicated by Fig. 1 in Mr. Hendrix's article or that water cannot as a rule be assumed to be saturated with air even when it is exposed to the atmosphere. I shall corroborate this with my experience with pumps handling entrained air. Generally, a 3 per cent mixture (by volume at suction pressure) is sufficient to cause a noticeable drop of head of about 3 per cent or more. If we take the NPSH requirement for a 3 per cent drop at 200 gpm from Fig. 8(*a*), a mixture of 6.5 per cent by volume is obtained from Mr. Hendrix's chart. That percentage of gas would, in the experience of the author, cause much more than a 3 per cent drop in head. Furthermore, at 160 gpm no change in head is measured with almost the same percentage of gas indicated.

The author is surprised to read Mr. Hendrix's proposal that one should assume "the vapor pressure of the liquid to be the pressure above the liquid in the surge vessel if the system is above atmospheric pressure." Since there is no problem about pure liquids, the sentence must apply to solutions and mixtures. Mr. Hendrix himself correctly states that the Reid equipment is not to be used. Now, if the surge vessel is $^1/_3$ full, its pressure would be the corrected Reid pressure.

First, I shall answer Mr. Jacobs' questions in order: Actually, there were heating and cooling coils at both ends of the standpipe, but none was used while data were taken. Rather, the temperature was allowed to rise or drop several degrees and was then restored while conditions were changed for the next point. A coil was placed into the vapor space with the discharge flow cascading over it to obtain better heat transfer, especially for the cooling phase.

Mr. Jacobs is correct in questioning the accuracy of the temperature measurements at 400 F. Precisely due to this difficulty the bulb method of NPSH measurements was attempted. The accuracy of ± 5 ft was not intended to include the 400 F tests and a special note should have been placed on Table 1.

With thermocouples wired with opposing emf, an accuracy of 0.25 deg F could be obtained. An estimate of the heat losses from the suction pipe resulted in a temperature drop of 0.20 deg F between tank and impeller. Therefore, the accuracy of the 410-deg point is in the order of 2 feet.

The author's method is not valid when the "threshold depression" required for the inception of cavitation is greater than the depression calculated for a small performance drop due to cavitation under equilibrium conditions. In this paper cavitation is considered to be entirely suppressed only when the static pressure of the liquid is above its vapor pressure.

The effect of the presence of air in cold water tests is discussed at length in the reply to Mr. Hendrix and Mr. Whistler.

Concerning the attempted correlation of $B(1)$ against V', the reasoning behind it was given, but perhaps not clear enough. The parameter $B(1)$, or $V'(1)$ for that matter, is a measure of the volume of vapor developed by a depression of 1 foot. Following Dr. Stepanoff, a very large B for a given depression would indicate that such a depression is not reasonably possible. The author's thinking is that, if such a depression does exist, the mode of cavitation must be such that only a small fraction of the fluid is affected. If a near homogeneous mixture of liquid and vapor results in the pump, the value of $B(1)$ should be small, since if it was large the performance drop would be large. Therefore, the author expected that V' calculated with an experimentally measured depression would correlate against $B(1)$, as it should correlate against a parameter which expresses the mode of cavitation.

Mr. Karassik does not pose any direct question pertaining to this paper. The author is in agreement with his theoretical proof that at the critical temperature no measurable performance change should result from a small pressure drop below 3206.2 psia.

On the subject of air again, in answer to Mr. Nissan, the author

must add that the cold water tests were run with an ejector creating a vacuum above the water level within 3 in. Hg of vapor pressure. In addition, tests were run at slightly above 212 deg F, with constant bleed of steam from the standpipe, and no significant difference was observed between results obtained at 72 and 212 deg F.

No evidence of erosion was found on the impeller. No support for the author's two modes of cavitation can be drawn from the condition of the impeller.

The author would like to add that noise generated by cavitation became "softer" at high temperatures on water, and was sometimes overshadowed by motor noise when pumping very hot water and hydrocarbons. Although a deficiency of air in cold water causes a "harder" crackling noise, probably due to the lack of cushioning air in the collapsing vapor bubbles, the higher density of water vapor at 400 deg is probably sufficient to cushion the collapse.

The author agrees with Mr. Stanek that pump geometry and operating conditions will influence cavitating performance, just as they influence cavitation inception.

Pressure ratio across a given pump should certainly affect cavitating performance. The direction, however, would depend on manner of changing the pressure ratio. Obviously, reducing the suction pressure will reduce the performance. Increasing the discharge pressure by decreasing flow did not seem to have much effect. Changing speed at constant specific speed should produce an improvement at higher speeds as the cavitating flow should become more and more localized, since all internal pressure differences rise with the square of speed, while B for a given pressure difference is constant.

Mr. Whistler's discussion is based on a number of general statements which may be true in the majority of cases, but are not always true. First is the statement that NPSH is obtained by the manufacturer running suction throttling tests on cold, air-saturated water. The author's employer, for example, tests many pumps on vacuum tanks and at 212 deg F and higher temperatures.

The author's statement pertaining to prior knowledge on operation of pumps on hydrocarbons is based on the text accompanying the NPSH correction chart for hydrocarbons published by the Hydraulic Institute. The chart, according to the Institute, is based on field data.

Mr. Whistler states several examples where hydrocarbons require more "apparent" NPSH than water. But he explains this himself as a matter of vapor pressure measurement, and not thermodynamic effects. Immediately following is the statement that "our base line NPSH curves are probably not absolute." There does not seem to be any but a trivial connection between the statements. Obviously, data that is known to be incorrect cannot be used for a "base line."

Mr. Whistler is the only one to take exception specifically to the author's contention that very high vapor to liquid ratios may exist in the pump. Perhaps he did not realize that the ratio of 70 to 90 ft^3 of vapor per 100 ft^3 of liquid does not necessarily exist uniformly throughout the cross section of the pump suction, but rather, only where cavitation exists, usually localized around the low pressure point of the impeller vanes, as shown in Fig. 13(a), in which the region was greatly enlarged for clarity. Even with such a large vapor percentage in a small region, the over-all percentage may stay reasonable.

The author doubts very much that a gradual breakoff of a cavitating performance curve permits the conclusion that either thermodynamic suppression or air is present. The gradual breakoff may also be the result of a gradual growth of the vapor region and subsequent deterioration of the flow conditions through the impeller. Only if under other conditions the curve becomes *more* abrupt, one should suspect that air or thermodynamics caused a more gradual breakdown in previous case.

It is evident from the numerous questions on test procedure that the author should have described it in detail. Tests on cold water were performed both by throttling and by applying vacuum to the suction tank, reducing the pressure to within 3.5 in. Hg abs. For hot water, vapor pressure was maintained above the liquid level by constant bleeding of vapor and by shutting off the heating or cooling while data were taken. Tests on kerosene were performed in the same manner. To avoid distillation and loss of material when testing other liquids the following procedure was used:

1 The system was completely filled from the storage tank and drained at high points to wash out most of the air.

2 With the main pump running, the system was brought above storage tank temperature. A small amount of liquid was then drained back to the storage tank and a vent opened at the top of the "standpipe" connected to the gas space of the storage tank. The pump was operated for an hour or more to drive off entrained and dissolved air.

3 All connections to the storage tank were closed and the system brought to the desired temperature. Barring air leakage into the system from the atmosphere, vapor pressure should exist in the vapor space even when the vapor pressure was below atmospheric pressure.

The author recognizes the difficulties in instrumentation and has avoided the throttling procedure and used special vapor-pressure instrumentation in attempts to overcome these difficulties. The work was concentrated about pure substances whose vapor pressures are known and easily measured. The butane used, for instance, was 99.5 per cent pure with the greatest part of the remaining 0.5 per cent made up of heavier hydrocarbons.

For field testing of mixtures whose composition and vapor pressure vary and are not known, the most promising method is the use of combination of bubble-point-pressure measuring apparatus and a vapor-pressure bulb as described here and by Mr. R. B. Jacobs.[11] It should be made visible from the outside to insure that there is no cavitation on the bulb, no gas already entrained passing the bulb, and to be able to observe the appearance of a vapor bubble in the bulb. Provision for evacuating the apparatus and filling with the fluid tested should be made.

In closing, the author would like to explain the meaning of the note "maximum capacity" on Figs. 8 and 9. The curves so designated indicate the NPSH at which the head breakdown curve approaches a vertical line. This question has arisen at the presentation and was not repeated in the submitted discussions.

[11] R. B. Jacobs, K. B. Martin, and R. J. Hardy, "Direct Measurement of Net Positive Suction Head," published in this issue, p. 147.

The Unsteady Wake Interaction in Turbomachinery and Its Effect on Cavitation[1]

HSUAN YEH[2]

Professor of Mechanical Engineering, University of Pennsylvania, Philadelphia, Pa. Mem. ASME.

J. J. EISENHUTH

Research Associate, Ordnance Research Laboratory, The Pennsylvania State University, University Park, Pa.

This paper attempts first to predict theoretically the influence on the nonsteady pressure perturbations on a blade row as a result of periodic wakes shed from an upstream blade row, and then to compare such theoretical predictions with a series of carefully conducted cavitation experiments at the Garfield Thomas Water Tunnel of the Ordnance Research Laboratory. The results indicate that the experimental values of pressure perturbations are somewhat lower than theoretically predicted values. The general trend, e.g., the influence of wake width and wake spacing, is in substantial agreement between theory and experiments.

In an axial-flow turbomachine, the relative motion between stationary and rotating blade rows presents a nonsteady flow problem. As a consequence, each blade experiences pressure and velocity perturbations which fluctuate with time. Kemp and Sears [1, 2][3] investigated the over-all effect of the fluctuating lift and induced drag of the blades, whereas Meyer [3] undertook a detailed study of the pressure and velocity perturbations themselves. Although such perturbations are undoubtedly significant in the (refined) flow analysis of all turbomachines, the pressure perturbation is especially important in liquid-handling turbomachines owing to the phenomenon of cavitation. Recent interest in turbopumps for liquid-fueled rockets strongly indicates a need for renewed research of this phenomenon. In addition to turbomachines, the application to propellers is obvious.

This paper attempts (*a*) to predict theoretically the influence on the nonsteady pressure perturbations on a blade row due to periodic wakes shed from an upstream blade row and (*b*) to compare such theoretical predictions with a series of carefully conducted cavitation experiments at the Garfield Thomas Water Tunnel of the Ordnance Research Laboratory. The results indicate that the experimental values of pressure perturbations are somewhat lower than theoretically predicted values. The general trend, e.g., the influence of wake width and wake spacing, is in substantial agreement between theory and experiments.

[1] This work was supported by the U. S. Navy Bureau of Ordnance under Contract No. NOrd 16597.

[2] Consultant to the Ordnance Research Laboratory, The Pennsylvania State University, University Park, Pa.

[3] Numbers in brackets designate References at end of paper.

Contributed by the Fluid Mechanics Subcommittee of the Hydraulics Division and presented at the Annual Meeting, November 30–December 5, 1958, New York, N. Y., of The American Society of Mechanical Engineers.

Note: Statements and opinions advanced in papers are to be understood as individual expressions of their authors and not those of the Society. Manuscript received at ASME Headquarters, July 31, 1958. Paper No. 58—A-114.

Nomenclature

a_n = Fourier components of velocity defect in wakes
c = chord of rotor-blade section
d = spacing distance between trailing edge of strut and leading edge of rotor at 0.9-radius section
D = diameter of rotor tip
$H_{0,1}^{(2)}$ = Henkel function of second kind, of order 0, 1, respectively
J = rotor advance ratio, $J = V_a/(nD)$
$J_{0,1}$ = Bessel function of first kind, of order 0, 1, respectively
n = revolutions per second of rotor
p = instantaneous pressure perturbation due to traveling wake
P_∞ = free-stream static pressure for incipient cavitation
P_v = vapor pressure of water at free-stream temperature
r = radius of rotor-blade section
r' = nondimensional radius, $r' = r/(D/2)$
s' = $x' - t'$
t = time, $t = 0$ when middle of a wake is a mid-chord
t' = nondimensional time, $t' = Vt/(c/2)$
u = velocity perturbation along chord
v = velocity defect in wake, in direction perpendicular to V
v_a = velocity defect in wake in axial direction
v_m = maximum velocity defect in wake, in direction perpendicular to V
v_{am} = maximum velocity defect in wake in axial direction
V = free-stream relative velocity approaching rotor-blade section
V_a = axial free-stream velocity (i.e., forward velocity of rotor)
x = distance along chord of rotor-blade section, measured from mid-chord
x' = nondimensional distance, $x' = x/(c/2)$
$Y_{0,1}$ = Bessel function of second kind, of order 0, 1, respectively
α = angle of attack
θ = $\cos^{-1} x'$
κ = (defined for periodic wakes only) $\kappa = \dfrac{\tau}{\lambda} = \dfrac{\nu}{\omega_0}$
λ = width of wake, defined by Fig. 3
λ' = nondimensional wake width, $\lambda' = \lambda/(c/2)$
ν = $2\pi/\lambda'$
σ_i = incipient cavitation index = $(P_0 - P_v)/{}^1/_2\rho V_a^2$
τ = distance between wakes (for periodic wakes)
τ' = $\tau/(C/2)$
ω = nondimensional wave number
ω_0 = (for periodic wakes only) = $2\pi/\tau'$ nondimensional primary-wave number

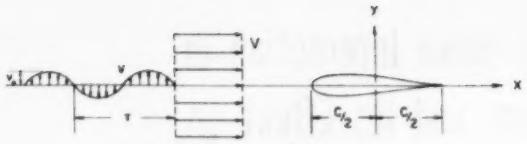

Fig. 1 Airfoil in sinusoidal gust

Analysis

Thin Airfoil Under Sinusoidal Gust. Consider a thin, rigid airfoil traveling with a horizontal velocity V relative to the surrounding air which carries a sinusoidal vertical gust v, Fig. 1. It is assumed that $v \ll V$. With the co-ordinate system x-y fixed on the airfoil (origin at mid-chord), the gust velocity v hitting the airfoil can be expressed by:

$$v = v_0 e^{i\omega(t'-x')} = v_0 e^{-i\omega s'} \tag{1}$$

where

v_0 = amplitude of gust velocity
ω = dimensionless frequency or wave number = (frequency)/$(2V/c) = \pi c/\tau$
t' = dimensionless time = $(2V/c)t$
x' = dimensionless distance in chordwise direction = $x/(c/2)$
s' = $x' - t'$

It can be noted that all distances have been nondimensionalized by $c/2$, i.e., half chord, and the time nondimensionalized by $(c/2)/V$. The space and time origins are chosen such that $x' = 0$ at mid-chord and $t' = 0$ when the maximum value of v is at mid-chord.

Under such a sinusoidal traveling gust, the unsteady pressure perturbation on the surface of the airfoil was obtained in 1940 by Küssner [4] as follows:[4]

$$p(\theta, t') = {}^1/_2\,\rho V v_0 e^{i\omega t'}\,[\{J_0(\omega) + iJ_1(\omega)\} + T(\omega)\{J_0(\omega) - J_1(\omega)\}]\tan\frac{\theta}{2} \tag{2}$$

where
$$T(\omega) = \frac{H_0^{(2)}(\omega) + iH_1^{(2)}(\omega)}{-H_0^{(2)}(\omega) + iH_1^{(2)}(\omega)}$$

and
$$\cos\theta = x'$$

It should be mentioned that the foregoing solution is based on a linearized theory which is possible if $v_m \ll V$. Physically the linearized theory amounts to assuming that the vorticity is carried by the main flow and not by the induced flow. As a consequence, the induced flow is a potential, although nonsteady, flow.

It is easy to show that Küssner's $T(\omega)$ is related to Theodorsen's $C(\omega)$ of reference [5] by the simple relation

$$T(\omega) = 2C(\omega) - 1$$

Furthermore, the entire square bracket of Equation (2) can be reduced to $2S(\omega)$ if we let

$$S(\omega) = (2/\pi\omega)/[\{J_0(\omega) - Y_1(\omega)\} - 2\{J_1(\omega) + Y_0(\omega)\}] \tag{3}$$

The function $S(\omega)$, expressed in a different form, was first used by Sears in [9]. The identification of $S(\omega)$ with the expression in Equation (3) was made in reference [10]. The value of $S(\omega)$ for ω between 0 and 50 was tabulated in [10, 11], the latter reference giving its asymptotic expression for large ω:

$$S(\omega) \to \left[\frac{1-i}{2(\pi\omega)^{1/2}}\right] e^{i\omega} \qquad \omega > 50 \tag{4}$$

[4] For the more general case $v = \bar{v}(x)e^{i\omega t'}$ where $\bar{v}(x)$ is an arbitrary function of x, expressions for p were obtained by Küssner and Schwarz in references [6, 7] and by Neumark in reference [8].

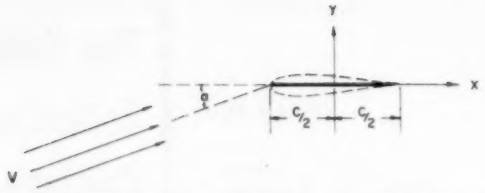

Fig. 2 Flat-plate airfoil at angle of attack with uniform stream

Thus Equation (2) becomes

$$p(\theta, t') = \rho V v_0 e^{i\omega t'} S(\omega)\tan\frac{\theta}{2} \tag{5}$$

Since the foregoing solutions are based on a linearized theory, the perturbations caused by gusts of different wave numbers can be superimposed. Now a periodic gust of arbitrary shape can be represented by a Fourier series

$$v(s') = \sum_{n=0}^{\infty} a_n e^{-in\omega_0 s'} \tag{6}$$

where a_n are the amplitudes of the Fourier components and ω_0 is the primary wave number. The total pressure perturbation is therefore

$$p(\theta, t') = \rho V \tan\frac{\theta}{2}\sum_{n=0}^{\infty} a_n e^{in\omega_0 t'} S(n\omega_0) \tag{7}$$

Concept of "Equivalent Angle of Attack." Consider a thin airfoil (idealized to a flat plate) making an angle of attack α with a uniform, parallel, steady flow of velocity V, Fig. 2. The velocity perturbation u on the surface of the airfoil is well known:[5]

$$u = V\sin\alpha\tan\frac{\theta}{2}$$

where $\cos\theta = x'$.

If the angle of attack is small, $\sin\alpha \approx \alpha$ and $u \ll V$. The Bernoulli equation for steady flows then shows that the pressure perturbation on the surface of the airfoil is

$$p = \rho V u = \rho V^2\alpha\tan\frac{\theta}{2} \tag{8}$$

Comparing Equations (7) and (8), it can be seen that the influence on the pressure perturbation on an airfoil due to a periodic traveling gust of arbitrary shape is equivalent to an angle of attack α such that

$$\alpha = \frac{1}{V}\sum_{n=0}^{\infty} a_n e^{in\omega_0 t'} S(n\omega_0) \tag{9}$$

α can be called the "equivalent angle of attack."

It should be pointed out that the concept of an equivalent angle of attack is useful and possible only because the chordwise distribution of pressure perturbation has the same functional form, i.e., $\tan\theta/2$, for gusts of all wave numbers and hence also for gusts of all shapes. It is, in fact, the same pressure distribution that the airfoil experiences in steady flows at a constant angle of attack. On the other hand, the absolute level of the pressure perturbation on the airfoil as a whole under a nonsteady gust is dependent both on time t' and on frequency ω. Thus the equivalent angle of attack also varies with time t', the primary wave number ω_0 and the wave form which determines the coefficients a_n.

Fourier Analysis of Wakes. In a turbomachine, the wakes shed

[5] See for example p. 38 of reference [12].

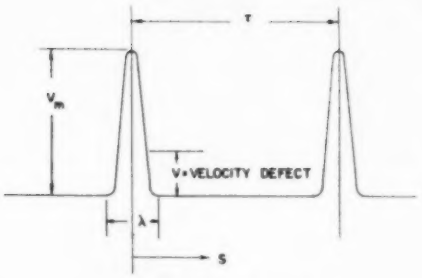

Fig. 3 Periodic wake profile

from one stator (or rotor) blade row constitute a periodic gust passing through its neighboring, downstream rotor (or stator) blade row.[6] A Fourier analysis of these periodic wakes can be performed easily by assuming the wake velocity profile to be a cosine curve. (For experimental evidence of this assumption see for example [13] for a single airfoil and [14] for an axial-flow compressor stage.)

In Fig. 3 which represents a periodic wake (velocity-defect) profile the following symbols are used:

v_m = maximum velocity defect
τ = distance between wakes, hence primary wave length
$\tau' = \tau/(c/2)$ = dimensionless primary wave length
$\omega_0 = 2\pi/\tau'$ = dimensionless primary wave number
λ = wake width, defined by Equation (10)
$\lambda' = \lambda/(c/2)$ = dimensionless wake width
$\kappa = \tau/\lambda = \tau'/\lambda'$ = wave length to wake-width ratio

The wake (velocity defect) profile is described by the following functions of abscissa s':

$$v = \frac{v_m}{2}(1 + \cos \kappa\omega_0 s') \qquad -\frac{\lambda'}{2} \leqslant s' \leqslant \frac{\lambda'}{2}$$

$$v = 0 \qquad -\frac{\tau'}{2} \leqslant s' \leqslant -\frac{\lambda'}{2} \quad \text{and} \quad \frac{\lambda'}{2} \leqslant s' \leqslant \frac{\tau'}{2} \tag{10}$$

This pattern repeats itself when s' increases or decreases by an amount τ'. Expressing $v(s')$ by a Fourier series

$$v = \sum_{n=0}^{\infty} a_n \cos n\omega_0 s' \tag{11}$$

Then, by standard Fourier analysis, one obtains

$$\begin{aligned} a_0 &= v_m/2\kappa \\ a_n &= v_m/2\kappa \qquad\qquad n = \kappa \\ &= \frac{v_m}{\pi n}\left[\frac{\kappa^2}{(\kappa+n)(\kappa-n)}\right]\sin\frac{n\pi}{\kappa} \qquad n \neq \kappa \end{aligned} \tag{12}$$

Next consider the limiting case as $\tau' \to \infty$, corresponding to a *single* wake of width λ'. Such a wake is described by

$$v = \frac{v_m}{2}\left(1 + \cos\frac{2\pi}{\lambda'}s'\right) \quad -\frac{\lambda}{2} \leqslant s' \leqslant \frac{\lambda'}{2} \tag{13}$$

$$v = 0 \qquad \text{all other values of } s'.$$

[6] Strictly speaking, such wakes produce not only a periodic vertical gust but also a horizontal one, since the wake velocity in general has components both parallel and normal to the direction of undisturbed relative flow of the downstream blade row. However, within the framework of linearized theory the upstream velocity disturbance parallel to the main relative flow causes no pressure perturbation on the blades and hence can be ignored.

The Fourier transform of v can be defined as

$$a(\omega) = \frac{1}{\pi}\int_0^\infty v(s')\cos\omega s' ds' = \frac{1}{2\pi}\int_{-\infty}^{\infty} v(s')e^{i\omega s'}ds' \tag{14}$$

such that

$$v(s)' = \int_0^\infty a(\omega)\cos\omega s' d\omega = \int_{-\infty}^{\infty} a(\omega)e^{-i\omega s'}d\omega \tag{15}$$

Note that ω here is a continuously varying dimensionless wave number defined by Equation (14) and is not related in any way to ω_0 defined for periodic wakes. Substituting Equation (13) into Equation (14) yields

$$a(\omega) = \left(\frac{v_m}{\pi}\right)\frac{\nu^2}{\omega(\nu^2-\omega^2)}\sin\frac{\pi}{\nu}\omega \tag{16}$$

where $\nu = 2\pi/\lambda'$ is a dimensionless wave number based on the wake width. At $\omega = \nu$, Equation (16) becomes

$$a_{(\omega=\nu)} = \frac{v_m}{2\nu} \tag{17}$$

Maximum Values of p or α. The expressions for p and α, Equations (7) and (9), contain the variable t' and hence are functions of time. In cavitation research, we are interested only in the maximum values of p (or α) since these values are responsible for setting off cavitation. For a single sinusoidal gust of wave length ω, the value of p (or α) is proportional to the real part of $e^{i\omega t'}S(\omega)$; its maximum value would therefore be reached when t' is such that $e^{i\omega t'}S(\omega)$ is purely real. This value of t' will therefore depend on ω. When the gust consists of a number of waves whose wave numbers are multiples of a primary wave number ω_0, it is not obvious at what t' the real parts of p and α would reach a maximum. The answer presumably would be different for different ω_0 and different wave forms. In general, for an arbitrary wake pattern, one would have to try successive values of t' and evaluate Equation (7) or (9). However, if the wake is narrow and spaced far apart, an approximate answer can be obtained by the following considerations:

Consider a narrow *single* wake represented by Equations (13) through (17). The equivalent angle of attack is then analogous to Equation (9)

$$\alpha(t') = \frac{1}{V}\int_{-\infty}^{\infty} a(\omega)e^{i\omega t'}S(\omega)d\omega \tag{18}$$

where $a(\omega)$ is given by Equations (16) and (17). Since the integral in Equation (18) cannot be integrated in closed form, we consider an approximate expression for the limiting case of a narrow wake $\lambda' \to 0$ and hence $\nu \to \infty$. Then $a(\omega) \approx v_m/\nu$ and is a constant. The integral in Equation (18) is then proportional to

$$T(t') \equiv \frac{1}{\pi}\int_{-\infty}^{\infty} S(\omega)e^{i\omega t'}\,d\omega \tag{19}$$

The integral $T(t')$ was evaluated by Meyer [3]. $T(t')$ has a discontinuity at $t' = -1$; it is 0 for $t' < -1$ and ∞ for $t' = -1$. For $-1 < t' < \infty$, $T(t')$ is a monotonically decreasing function of t'. Physically this means that before the wake hits the airfoil the influence of the wake is nil. As the center of the wake hits the leading edge of the airfoil, its influence is maximum. As the wake passes the leading edge, its influence decreases monotonically but never quite disappears even when the wake is far downstream and no longer on the airfoil.

Based on the foregoing consideration, one may conclude that, for a narrow wake, the maximum influence of the wake is felt when $t' = -1$, corresponding to the instant when the center of the wake hits the leading edge. The following calculations on the

maximum value of the equivalent angle of attack is therefore based on $t' = -1$. Although the fact that $T(t')$ becomes ∞ at $t = -1$ seems to cast some doubt as to the convergence of the calculation, this difficulty occurs only for the limiting case $\lambda' = 0$ but does not exist in actual cases where λ' may be small but still nonvanishing.[7]

Calculations. A series of calculations were made for periodic wakes represented by Fig. 3 and Equation (10). Three wake widths were chosen: $\lambda = 0.05\pi$, 0.10π, and 0.20π. In each case the maximum equivalent angle of attack, α_{max}, was calculated from Equations (9) and (12) using $t' = -1$ and a number of values of τ'. The results are plotted in Fig. 4.

It can be seen from Fig. 4 that:

1 The pressure perturbation resulting from periodic wakes decreases monotonically with increasing wake spacing, at first rapidly and then gradually. For the cases calculated, α_{max} appears to have reached an asymptotic value for $\tau' = 2\pi$. Thus for wake spacing τ larger than πc, τ has no influence on the pressure perturbation. (For ordinary turbomachines, however, τ is not quite that large.)

2 The pressure perturbation increases as the wake width λ' increases. In particular, the asymptotic values of α_{max} for large τ' can be plotted against λ'; such a plot is presented as the solid curve in Fig. 16. Consider the following asymptotic values of α_{max} at large τ':

$$\frac{\alpha_{max}}{v_m/V} = 0.1872 \text{ for } \lambda' = 0.10\pi$$

$$\frac{\alpha_{max}}{v_m/V} = 0.1300 \text{ for } \lambda' = 0.05\pi$$

Thus for the same maximum velocity defect, increasing the wake width by a factor 2 in this case increases the pressure disturbance by 43.7 per cent.

These theoretical calculations will now be checked by experiments.

Experiments

Experimental Facilities and Test Setup. The experimental phase of this study was conducted at the Garfield Thomas Water Tunnel of the Ordnance Research Laboratory. The large 48-in-diam tunnel in which the experiments were conducted is a variable-speed, variable-pressure water tunnel intended primarily for propulsion studies of body-propeller systems. It is a closed-circuit, closed-jet water tunnel, in which powered models can be used to drive single or counter-rotating propellers. The tunnel is 100 ft long and 32 ft high. The cylindrical test section is 48 in. diam and 14 ft long. The speed in the test section is continuously variable up to 48 knots. The pressure can be reduced to approximately 3 psia or raised to several atmospheres, giving a wide range of operating cavitation indexes.

The apparatus used in this experiment is shown in Figs. 5 and 6. The important components of the apparatus include a rotor whose blades pass through the wake of a strut which spans the tunnel test section. The diagram in Fig. 7 illustrates more clearly the details of the setup for typical cross sections of the strut and rotor blade. Spacing distances d, measured from the trailing edge of the strut to the leading edge of a rotor blade at the 0.9 radius station of the rotor blade, were varied from 1.25 to 19.25 in. This variation was achieved by moving the strut axially by means of hub spacers. The strut itself has a biconvex, circular arc cross section with a constant maximum thickness of 1.22 in. and a constant chord length of 10.3 in. Two series of tests were made;

[7] It can be shown that the integral of (18), after substituting the expression (16) for $a(\omega)$ and making use of the asymptotic form of $S(\omega)$ given by (4), is convergent for all t' including $t' = -1$ if λ' does not vanish.

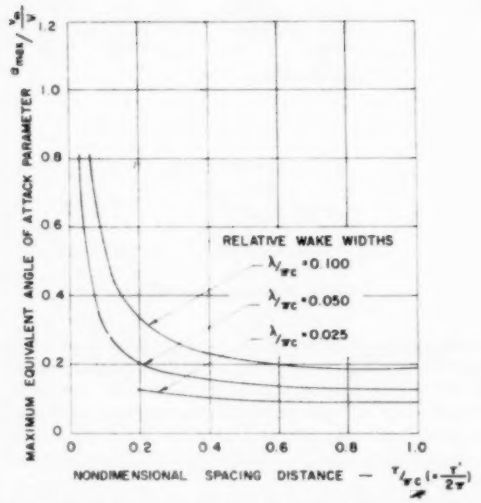

Fig. 4 Maximum equivalent angle of attack as influenced by distance between wakes

namely, one with a smooth strut and the other with a roughened strut. For the roughened strut, two rows of pins were installed near the leading edge in order to increase the size of the wake.

The rotor, two-bladed and 24 in. diam, was designed for an advance ratio [$J = V_a/(nD)$] of 1.3. The hub diameter is 8 in. The blade-section shapes are NACA 16-series symmetrical airfoils with a constant chord length of 4 in. and with thickness ratios varying from 0.12 at the hub to 0.06 at the tip. Each section was set at the angle which would align it with the relative flow at the design advance ratio. The 0.9 radius section has a thickness ratio of 0.087 and was designed to be the critical[8] section in cavitation at the design advance ratio. Experiments indeed showed that cavitation occurred first at this radius.

The cavitation tests were run by first setting a particular test section velocity V_a and rotor rpm and then varying the test-section pressure to determine the point of incipient cavitation. The procedure followed in determining the pressure of incipient cavitation was first to lower the pressure until cavitation was present and then to increase the pressure to the point where the cavitation disappeared. The pressure at which cavitation disappeared was used to calculate the incipient cavitation number. The cavitation observations were made visually by means of a stroboscopic light.

Attention was paid particularly to the cavitation characteristics of the 0.9-radius section of the rotor blades and the data presented in this paper are for this section. The incipient cavitation conditions were recorded first with the rotor in the free-stream condition (strut removed). The strut was then installed and the same type of measurement was made as the blades passed through the wake of the strut.

Wake Survey. Figs. 8 and 9 show typical wake data for the smooth and roughened struts, respectively. Compared with these data are wake curves calculated according to Equation (10) using the depths and widths of wakes that would make the measured data best fit the assumed curves. The data for the smooth strut fit the assumed curves quite well. The data for the roughened strut, on the other hand, do not fit the curves very well for closer spacing distances. At the closer distances the measured wakes are generally narrower toward the wake centers and wider toward the wake edges than the calculated wakes, Fig. 9. Beyond a spacing of $d/c = 1.0025$ the measured and

[8] It had the highest cavitation number.

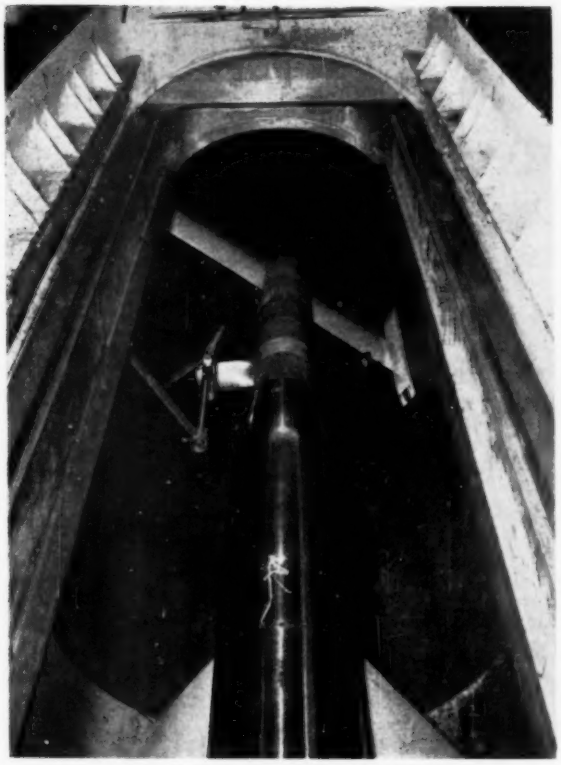

Fig. 5 Top view of experimental apparatus

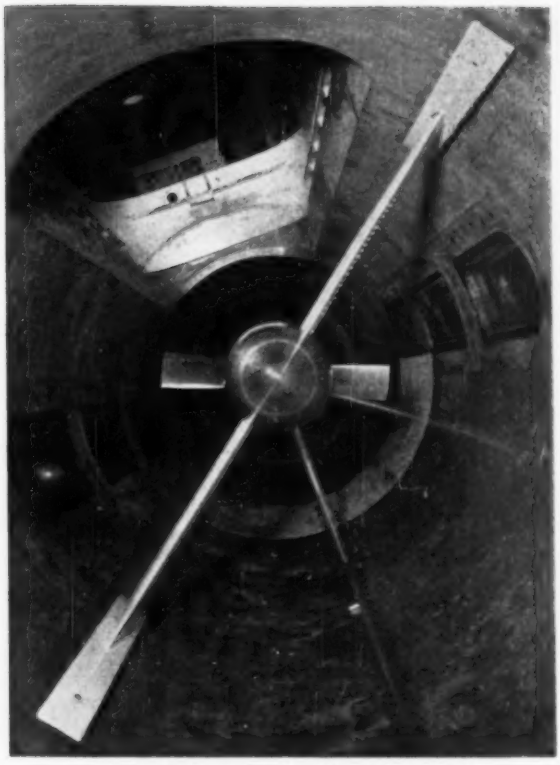

Fig. 6 Head-on view of experimental apparatus

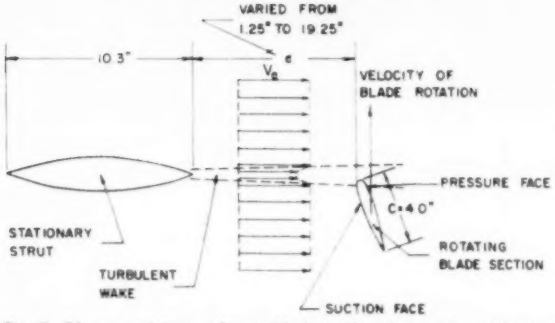

Fig. 7 Diagram of strut and rotor-blade sections in experimental setup

calculated wakes compare very well as seen by $d/c = 4.8125$ in the same figure.

Fig. 10 shows the variation of wake width and depth with spacing. The depths and widths that were used in the plot were those that permitted the best matching of measured and assumed wakes.

Results of Cavitation Measurements. By choosing various combinations of tunnel velocity and rotor rpm it was possible to cover a range of J-values. After determining the pressure of incipient cavitation for the 0.9-radius section at each J condition, the incipient cavitation numbers defined by

$$\sigma_i = \frac{P_0 - P_v}{\frac{1}{2}V_a^2} \tag{20}$$

could be determined. By convention the forward velocity V_a was chosen in calculating σ_i.

A plot of incipient cavitation number versus advance ratio for the 0.9-radius section in the *undisturbed* stream is shown in Fig. 11. A scale of angle of attack α is also given on the plot. These data are composed with a predicted curve obtained from the theoretically determined minimum pressure coefficients [15, 16] for the airfoil and by application of available theories for propellers [17].[9] Although the levels of σ_i are different, the shapes of the predicted and experimentally determined curves are very similar.

Figs. 12, 13, 14, and 15 show typical incipient cavitation-number values for the 0.9-radius section passing through the wake of the strut. The data are presented in a form similar to that of Fig. 11. For comparison purposes, the experimentally determined curve of the blade section in the undisturbed stream is also plotted in each figure. It can be seen immediately that except at the lower advance ratios (higher angles of attack) there is no effect of the smooth strut wake on the cavitation performance of the section, Figs. 12 and 13. With the roughened strut the effect is very noticeable at all operating conditions, Figs. 14 and 15. A characteristic of all the curves for the roughened-strut case is the leveling of the curve with increasing section angles of attack over a certain range of J.

[9] Consistent with propeller theory, the tangential component of induced velocity is assumed to increase discontinuously from zero to its full value as the flow passes through the infinitely thin propeller disk. At the point on the cavitation curve where the slope changes abruptly, and for points on the upper leg of the curve the minimum pressure coefficient occurs almost at the leading edge of the airfoil. It was assumed then that the pertinent velocity picture which would apply would be that occurring just in front of the propeller. The only induced velocity occurring in this picture would be the axial component. Once this "critical" corner of the curve and the point at the design advance ratio where no induced velocities occurred were located, a linear variation of σ_i with J was assumed between the points.

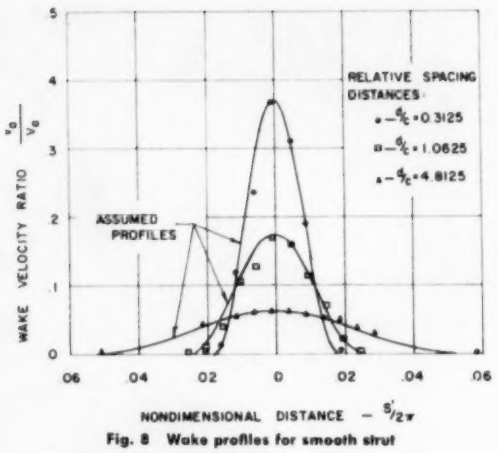
RELATIVE SPACING DISTANCES:
• – s/c = 0.3125
□ – s/c = 1.0625
△ – s/c = 4.8125
ASSUMED PROFILES
WAKE VELOCITY RATIO – v_a/V_0
NONDIMENSIONAL DISTANCE – s'/2r

Fig. 8 Wake profiles for smooth strut

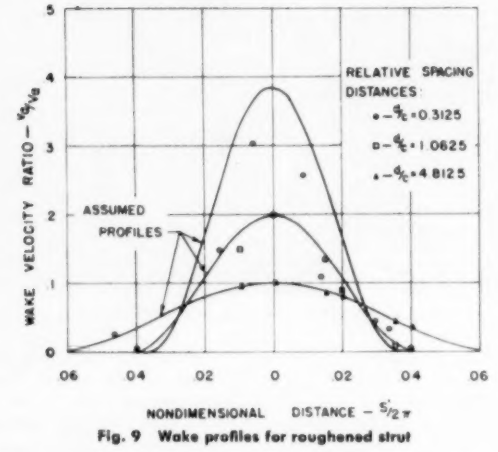
RELATIVE SPACING DISTANCES:
• – s/c = 0.3125
□ – s/c = 1.0625
△ – s/c = 4.8125
ASSUMED PROFILES
WAKE VELOCITY RATIO – v_a/V_0
NONDIMENSIONAL DISTANCE – s'/2r

Fig. 9 Wake profiles for roughened strut

It should be mentioned that the visual observations of cavitation are inherently difficult particularly in this case because of the necessity of using a stroboscopic light. Cavitation observations generally are characterized by scatter of the data, so even with the use of great care in the observations, the scatter that is present in the data is to be expected. Among the safeguards used in the tests were the reduction of air content below the saturation level and the elimination of entrained air bubbles in the stream.

The cavitation observed for the rotor in the undisturbed stream was generally what would be expected. At and near the design advance ratio, visible cavitation occurred aft of the mid-chord near the region of minimum pressure. As the angle of attack was increased, the region of minimum pressure moved forward and the cavitation bubbles were indeed observed farther and farther toward the leading edge until in the range of the "critical corner" of the cavitation curve the cavitation started at the leading edge of the blade. The cavitation bubbles present were discrete bubbles occurring randomly on the blade surface. Near the pressure for incipient cavitation the frequency of the bubbles decreased markedly until there was none present. In determining the pressure for incipient cavitation, then it was necessary to take considerable care in determining that all signs of cavitation had disappeared.

With the data behind the smooth strut it was already mentioned that in the higher J-region no effect from the strut was observed. There was no marked change in the character of the cavitation in the lower J-region from that which occurred for the

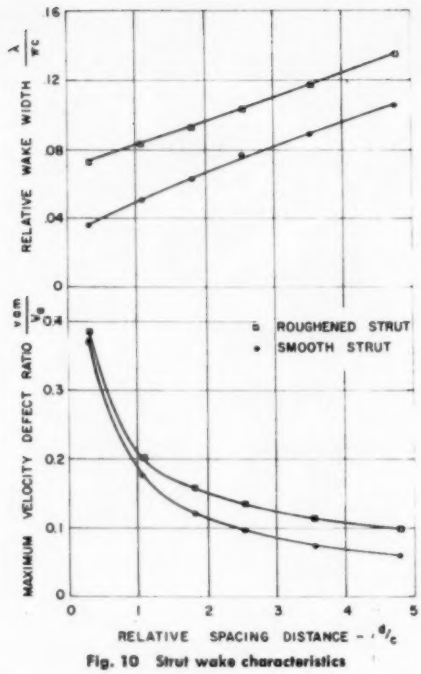
RELATIVE WAKE WIDTH – λ/r_c
MAXIMUM VELOCITY DEFECT RATIO – v_am/V_0
• SMOOTH STRUT
□ ROUGHENED STRUT
RELATIVE SPACING DISTANCE – s/c

Fig. 10 Strut wake characteristics

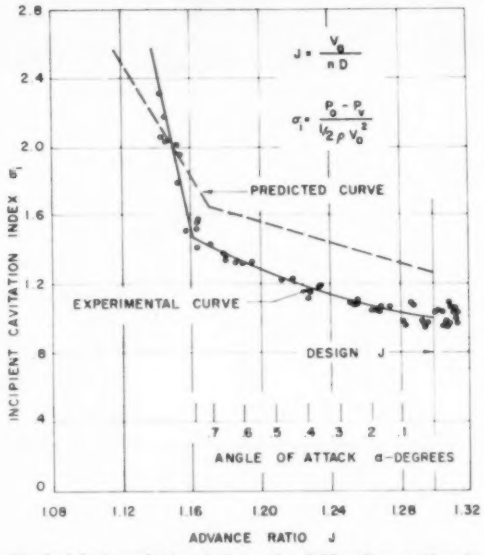

Fig. 11 Incipient cavitation indexes for 0.90-radius section in free stream

case of no wakes, except that the pressure for incipient cavitation increased.

In the observations with the roughened strut, however, the character of the cavitation changed. In this case a radial band of bubbly cavitation occurred on the blade surface; this band moving chordwise on the blade from the leading edge to the trailing edge as the blade passed through the wake. The band decreased progressively in radial extent when the wake passed from about mid-chord to the blade trailing edge. The radial extent of the band in this trailing region of the blade was roughly centered at the 0.9-radius station. For $d = 0.3125$ the band was visible at

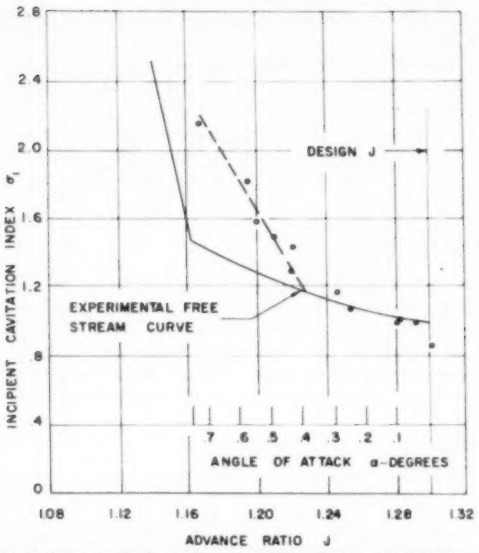
INCIPIENT CAVITATION INDEX σ_i
DESIGN J
EXPERIMENTAL FREE STREAM CURVE
7 6 5 4 3 2 1
ANGLE OF ATTACK α-DEGREES
ADVANCE RATIO J

Fig. 12 Incipient cavitation indexes for 0.90-radius section behind smooth strut, $d/c = 0.3125$

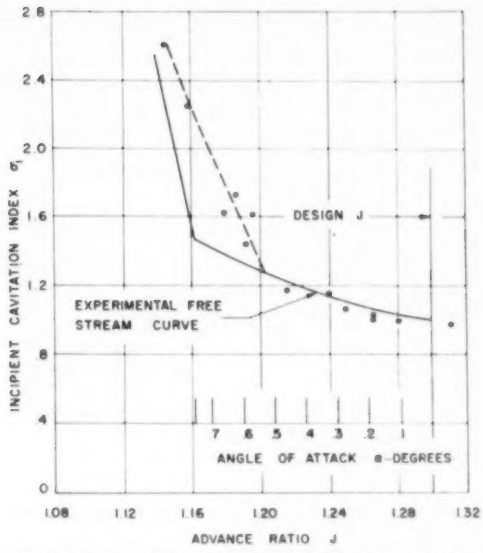
INCIPIENT CAVITATION INDEX σ_i
DESIGN J
EXPERIMENTAL FREE STREAM CURVE
7 6 5 4 3 2 1
ANGLE OF ATTACK α-DEGREES
ADVANCE RATIO J

Fig. 13 Incipient cavitation indexes for 0.90-radius section behind smooth strut, $d/c = 1.0625$

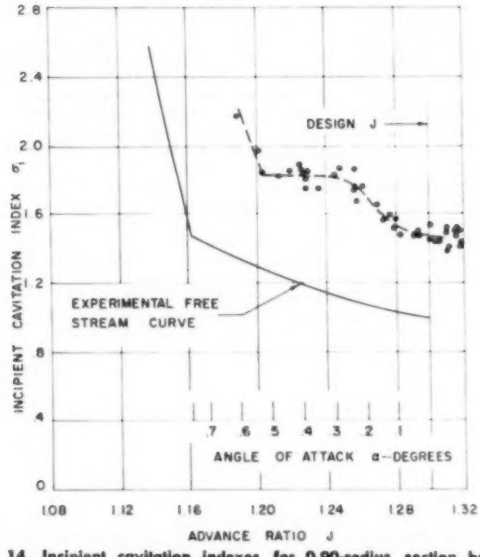
INCIPIENT CAVITATION INDEX σ_i
DESIGN J
EXPERIMENTAL FREE STREAM CURVE
7 6 5 4 3 2 1
ANGLE OF ATTACK α-DEGREES
ADVANCE RATIO J

Fig. 14 Incipient cavitation indexes for 0.90-radius section behind roughened strut, $d/c = 0.3125$

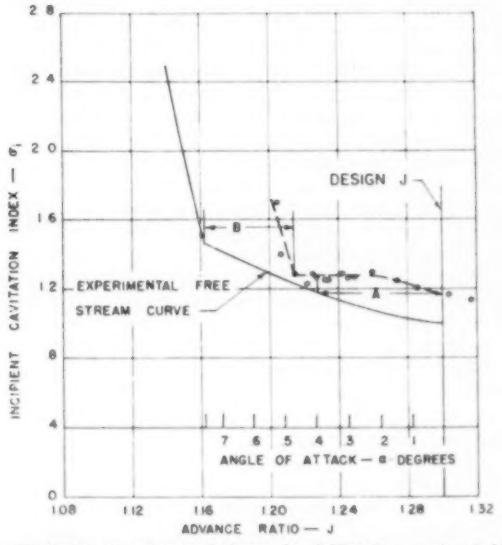

Fig. 15 Incipient cavitation indexes for 0.90-radius section behind roughened strut, $d/c = 4.8125$

all advance ratios for every chordwise position of the wake. For larger d's and at pressures near incipient cavitation the band was visible at every chordwise position of the wake only at J's below about 1.28. For J's larger than 1.28 cavitation occurred only at positions aft of mid-chord. For all d's and in the J-range where the leveling of the curve occurred, the band would disappear abruptly as the increasing pressure reached a certain value. This pressure value for a given tunnel velocity and a particular d was the same for all J's. The differences in σ_i were then dependent upon when the last discrete bubbles would disappear. It should also be mentioned that the band of cavitation was present, at least for some conditions on both sides of the blade; i.e., the suction and pressure faces of the blade. Because of the physical setup it was difficult to observe the pressure-face cavitation, so attention was focused only on the suction-face cavitation.

Discussion of Cavitation Test Results. The prediction of the interference effect due to viscous wakes between stationary and rotating vanes is given in terms of a maximum equivalent angle of attack. In comparing the experimental data typified by Figs. 12, 13, 14, and 15, it is necessary to arrive at some system of measuring the maximum equivalent angle of attack. With the smooth strut, as indicated previously, there was no effect in the higher advance ratio range. There was an effect, however, in the lower J-range close to the "critical" corner of the undisturbed stream data curve. This effect could be measured as the difference in angle of attack between the points at which the slopes abruptly changed for the undisturbed and wake-affected data.

On the other hand, by virtue of the shapes of the curves, the maximum equivalent angle of attack varied with advance ratio

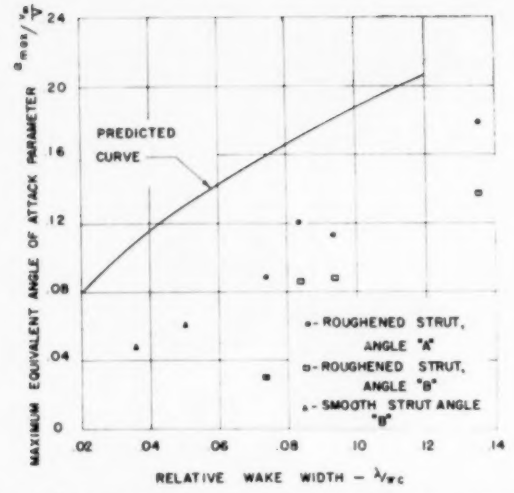
MAXIMUM EQUIVALENT ANGLE OF ATTACK PARAMETER
PREDICTED CURVE
o - ROUGHENED STRUT, ANGLE "A"
□ - ROUGHENED STRUT, ANGLE "B"
Δ - SMOOTH STRUT ANGLE "B"
RELATIVE WAKE WIDTH

Fig. 16 Maximum equivalent angle of attack data for various wake sizes

for the roughened-strut case. One may consider either the difference between angles of attack at the "critical" corners of the undisturbed and wake-affected curves or the equivalent angle of attack for a σ_i occurring at $J = 1.3$ on the wake-affected curve. For this reason two equivalent angles were measured for each set of roughened-strut data. The measurement of these angles is more clearly shown in Fig. 15 as the horizontal distances A and B. Only the angles designated by B, of course, are measured for the smooth-strut data.

The results of the equivalent angle-of-attack measurements are finally presented in Fig. 16. This figure offers a comparison of a predicted and measured maximum equivalent angle-of-attack parameter versus a nondimensional-wake width, for sufficiently high values of distance between wakes. (Since the value of $\tau/\pi c$ in these experiments is 2.7 at the 0.9-radius section, the asymptotic values of predicted α_{max} at large $\tau/\pi c$ apply. If $\tau/\pi c$ were not sufficiently large, the comparison would have to be made on the theoretical curves of Fig. 4.) The figure shows that the experimental results are generally lower than the predicted curve. The trends of the results are, however, comparable.

Conclusions

The influence of a nonsteady pressure perturbation on a blade due to periodic, traveling wakes is shown to be equivalent to a quasi-steady angle of attack of the main flow without wakes. For narrow wakes the equivalent angle of attack reaches a maximum when the middle of the wake hits the leading edge of the blade. Theoretical calculations predict this maximum equivalent angle of attack for various wake widths and wake spacings.

Experiments on cavitation appear to verify qualitatively the theoretical predictions, although the pressure perturbation appears to be less in experiments than in theory. The trend of the influence of wake width and wake spacing seems in substantial agreement between the theory presented here and experiments. In attempting to analyze the apparent difference in quality between the smooth and roughened-strut data, the varying equivalent angle of attack with varying operating conditions for the roughened strut, and the final difference in levels of predicted and measured data, it is difficult to arrive at any quantitatively exact conclusions. Such factors as the deviation of the roughened-strut wake data with the theoretical definition of the wakes, unknown characteristics of the cavitation phenomenon itself, the influence of finite airfoil thickness, and so on, may all be contributing reasons.

The theoretical considerations also do not take into account nonlinear effects associated with the local realignment of vorticity as the wake passes the leading edge and over the surface of the blade section.[10] Although such nonlinear influences are small for small velocity defects in the wake, the application of the theory to future cases should be considered in the light of its limitations.

Acknowledgments

This investigation was supported by the U. S. Navy Bureau of Ordnance under Contract No. NOrd 16597. The authors wish to express their appreciation to Dr. George F. Wislicenus under whose guidance and direction the investigation was conducted and to members of the Garfield Thomas Water Tunnel staff for their assistance in the performance of the experimental work.

References

1 N. H. Kemp and W. R. Sears, "Aerodynamic Interference Between Moving Blade Rows," *Journal of the Aeronautical Sciences*, vol. 20, 1953, pp. 585–598.

2 N. H. Kemp and W. R. Sears, "The Unsteady Forces Due to Viscous Wakes in Turbomachines," *Journal of the Aeronautical Sciences*, vol. 22, 1855, pp. 478–483.

3 R. X. Meyer, "The Effect of Wakes on the Transient Pressure and Velocity Distributions in Turbomachines," TRANS. ASME, vol. 80, 1958, p. 1544.

4 H. G. Küssner, "Das zweidimensionale Problem der beliebig bewegten Tragfläche unter Berücksichtigung von Partialbewegungen der Flüssigkeit," *Luftfahrt-Forschung*, band 17, 11/12, 1940, 355–361.

5 T. Theodorsen, "General Theory of Aerodynamic Instability and the Mechanism of Flutter," NACA Report No. 496, 1934.

6 H. G. Küssner and L. Schwarz, "Der schwingende Flügel mit aerodynamisch ausgeglichenem Ruder," *Luftfahrt-Forschung*, band 17, 11/12, 1940, pp. 337–354.

7 L. Schwarz, "Berechnung der Druckverteilung einer harmonisch sich verformenden Trägflache in ebener Strömung," *Luftfahrt-Forschung*, band 17, 11/12, 1940, pp. 379–386.

8 S. Neumark, "Pressure Distribution on an Airfoil in Nonuniform Motion," Reader's Forum, *Journal of the Aeronautical Sciences*, vol. 19, 1952, pp. 214–215.

9 W. R. Sears, "Some Aspects of Non-Stationary Airfoil Theory and Its Practical Applications," *Journal of the Aeronautical Sciences*, vol. 8, 1941, pp. 104–108.

10 N. H. Kemp, "On the Lift and Circulation of Airfoils in Some Unsteady Flow Problems," Reader's Forum, *Journal of the Aeronautical Sciences*, vol. 19, 1952, pp. 713–714.

11 H. Yeh, "Sears Function in Unsteady Flows," Reader's Forum, *Journal of the Aeronautical Sciences*, vol. 24, 1957, pp. 546–547.

12 W. F. Durand, "Aerodynamic Theory," vol. 2, Durand Reprinting Committee, California Institute of Technology, Pasadena, Calif., January, 1943.

13 A. Silverstein, S. Katzoff, and W. K. Bullivant, "Downwash and Wake Behind Plain and Flapped Airfoils," NACA Report 651.

14 H. Yeh, H. M. Croner, and D. E. Andrews, "Preliminary Measurements of Nonsteady Velocities in a Single Stage Axial Flow Compressor," WADC Technical Report 55-249, June, 1956.

15 I. H. Abbott, A. E. von Doenhoff, and L. S. Stivers, Jr., "Summary of Airfoil Data," NACA Report No. 824, 1945.

16 W. F. Lindsey, D. B. Stevenson, and B. N. Daley, "Aerodynamic Characteristics of 24 NACA 16-Series Airfoils at Mach Numbers Between 0.3 and 0.8," NACA TN 1546, September, 1948.

17 B. W. McCormick, J. J. Eisenhuth, and J. E. Lynn, "A Study of Torpedo Propellers—Part I," Ordnance Research Laboratory, The Pennsylvania State University, March 30, 1956.

[10] Meyer [3] calculated the localized pressure perturbation at the blade close to the wake due to these nonlinear effects. His results showed that the additional, localized pressure gradient is positive at first, followed by a negative value of lesser magnitude. This seems to indicate that the nonlinear effects tend to suppress cavitation instead of promoting it. However, there is the additional possibility of a realignment of vorticity even before the wake completely passes the leading edge of the airfoil. The possibility of a nonlinear effect that promotes cavitation, therefore, cannot be ruled out, especially if the wake is not very narrow.

DISCUSSION

R. X. Meyer[11]

The authors are to be congratulated on a highly interesting and novel contribution. The concept of the "equivalent angle of attack" introduced for the first time by the authors, should prove to be particularly fruitful. It permits bridging the gap between the simpler theories concerned with thin airfoils—in which the leading edge appears as a singularity—and applications to actual profiles, where no such singularity arises.

In their conclusions, the authors also discuss the type of nonlinear effect considered in reference [3] as cited by the authors. This effect is due to the gradual transport of the vorticity by the perturbation velocity, and is of importance only in the neighborhood of the wake, and increases as the wake is swept downstream. Near the leading edge, the effect should be small, because the time available for the vorticity transport is short. Since the analysis presented by the authors is only concerned with the vicinity of the leading edge, the omission of this nonlinear effect is doubtlessly justified.

[11] Member Senior Staff, Space Technology Laboratories, Inc., Los Angeles, Calif.

Authors' Closure

The authors wish to thank Dr. Meyer for his comments. We agree with the thoughts expressed in his second paragraph.

Thermal-Stress Ratchet Mechanism in Pressure Vessels[1]

D. R. MILLER

Consulting Engineer,
Knolls Atomic Power Laboratory,
General Electric Company,
Schenectady, N. Y. Mem. ASME

The combination of cyclic thermal stresses and sustained internal pressure in a vessel is shown to be a source of progressive expansion of the vessel if the stresses are sufficiently high. Criteria presented allow determination of limits to be imposed on stresses in order to prevent progressive expansion or to allow estimation of the expansion per cycle where stresses are sufficient to produce growth. The effect of strain-hardening of the metal on progressive reduction of the growth rate is discussed.

THE PROGRESSIVE thinning of a sheet subjected to a sustained tensile load and a superimposed cyclic bending load has been discussed by Hill [1].[2] Parkes [2] has discussed the problem of incremental collapse of an aircraft wing as a result of fluctuating thermal stresses superimposed on the normal wing loading. Observations of progressive distortion of pressure vessels subjected to repeated thermal stresses have been reported by Weil and Rapasky [3]. Coffin [4] also has observed growth due to combined steady and cyclic loads.

This paper deals with the problem of cyclic heat flux through the walls of a vessel subjected to a sustained internal pressure. It is shown that if the thermal strains and the membrane stress resulting from pressure are sufficiently high, an increment of growth will be produced by each cycle of heat flux.

Analysis

The characteristics of the ratchet-growth mechanism will be developed first for an elementary model for simplicity and clarity. Then the analysis will be extended to thin-walled pressure vessels with heat flow from one surface to the other or with heat flow through their walls due to heat generation within the walls, as occurs in the case of nuclear radiations. All of the derivations are based on maintaining the instantaneous average tensile stresses at the level compatible with the external load and making stress distributions compatible with the instantaneous differential thermal strains and with the prior stress-strain history.

Three-Bar Assembly. Consider the three-bar assembly shown in Fig. 1. The bars are assumed to be made of an elastic-plastic material nominally without strain-hardening and are assumed to be attached to a rigid support and to a rigid block to which the tensile load P is applied. Each of the outer bars has half of the cross-sectional area of the middle bar.

Let us assume that the load P is maintained at the value necessary to cause yielding of the assembly. Now assume that the outer bars are heated an amount T above the temperature of the middle bar. During heating the outer bars tend to reduce their load because of their thermal elongation. However, the middle bar cannot increase its load, and the thermal elongation of the outer bars is unrestrained. This produces an equal plastic elongation of the middle bar. Now, if the outer bars are cooled to their original temperature, they tend to shrink and to take more than their share of the external load. Since they are unable to accept additional load, the outer bars elongate plastically by the same amount that the middle bar elongated during heating of the outer bars. Each subsequent cycle of heating and cooling of the outer bars produces a plastic elongation of the three-bar assembly equal to the unrestrained thermal elongation of the heated outer bars.

In a practical assembly there would be some strain-hardening. In the following analysis it will be assumed initially that the strain-hardening is exactly sufficient to offset the increase in true stress resulting from reduction of cross section during growth.

Now consider the case where the external load causes the tensile stress $n\sigma_y$. Let the outer bars be cyclicly heated an amount T_1

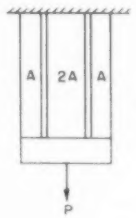

Fig. 1 Three-bar assembly

[1] The paper is based on work sponsored by the United States Atomic Energy Commission under contract No. W-31-109 Eng 52 with the General Electric Company.

[2] Numbers in brackets designate References at end of paper.

Contributed by the Metals Engineering Division and presented at a joint session with the Joint ASTM-ASME Committee on Effect of Temperature on the Properties of Metals at the Annual Meeting, New York, N. Y., November 30–December 5, 1958, of THE AMERICAN SOCIETY OF MECHANICAL ENGINEERS.

NOTE: Statements and opinions advanced in papers are to be understood as individual expressions of their authors and not those of the Society. Manuscript received at ASME Headquarters, August 4, 1958. Paper No. 58—A-129.

Nomenclature

α = coefficient of linear thermal expansion
β = growth-rate attenuation constant
σ_y = tensile yield stress
σ_t = maximum tensile thermal stress calculated on an elastic basis
σ_m = tensile membrane or average stress due to internal pressure or applied load
$\epsilon_y = E/\sigma_y$
ϵ_N = total tensile strain after N cycles
ϵ_∞ = total tensile strain after an infinite number of cycles
ν = Poisson's ratio in the elastic range
$m = \sigma_t/\sigma_y$
$n = \sigma_m/\sigma_y$
y = growth strain due to one cycle of temperature variation
E = Young's modulus of elasticity
E_p = ratio of incremental stress to incremental strain in plastic region
N = number of temperature cycles
T = temperature excursion

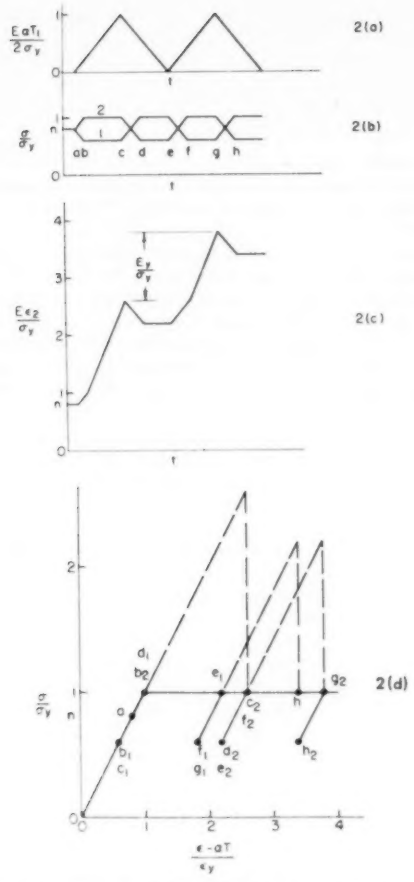

Fig. 2 Stresses and deformation of three-bar assembly

above initial temperature and then returned to their initial temperature. The temperature, stress, and elongation variations with time during cycling of temperature are shown in Fig. 2 for a particular set of conditions. The numeral 1 denotes the outer bars which are cyclically heated and cooled and the numeral 2 denotes the constant-temperature inner bar in Fig. 2(*b*) and in the subscripts. Note that these plots are established by alternately applying and removing the differential strain αT_1 and maintaining the total force developed in the three-bar assembly equal to the external force.

Based on construction of Fig. 2, the following relation was derived for the growth per cycle after a steady-state cycle is established:

$$\frac{y}{\epsilon_y} = 2m - 4(1 - n), \quad \text{for} \quad 1 \geq n > 0 \tag{1}$$

For this expression to be valid for $n = 0$, the compressive yield stress would have to be greater than the tensile yield stress. A negative value indicated by use of equation (1) indicates that no growth occurs.

Now consider the system of Fig. 1 with a nominal stress-strain characteristic composed of an elastic portion and a plastic portion of constant slope, E_p. It will be assumed initially that conditions are such that no compressive plastic flow occurs during the temperature cycle. The graphical construction for this case is shown in Fig. 3. The inner bar is assumed to remain at constant

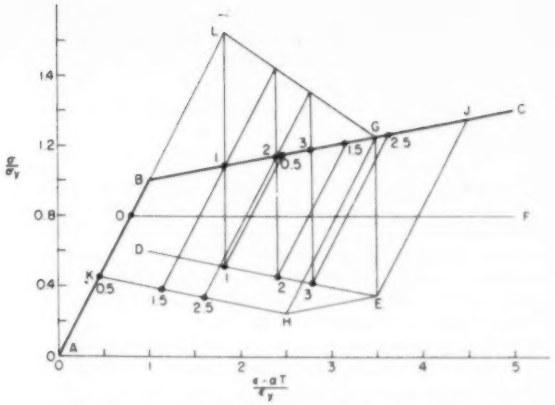

Fig. 3 Effect of strain-hardening in three-bar assembly

temperature, and the outer bars are assumed to be heated and then returned to the temperature of the inner bar. The initial conditions are represented by point *O*. As the outer bars are heated their load falls off, and the central bar picks up load and extends beyond the elastic limit. This condition is represented by points 0.5. When the outer bars are cooled, they pick up load and strain beyond the elastic limit while the inner bar drops load and shortens elastically. The end of the first cycle is represented by points 1. A similar process is repeated thereafter with decreasing increments of plastic strain in succeeding cycles. The total strain beyond the elastic limit approaches exponentially that corresponding to the condition where no further growth occurs. This is evident from the construction shown in Fig. 3. If N is an integral number of cycles of temperature variation, the total strain can be computed from

$$\frac{\epsilon_N}{\epsilon_y} - 1 = \left(\frac{\epsilon_\infty}{\epsilon_y} - 1\right)(1 - e^{-\beta N}) \tag{2}$$

The dimensionless total strain at the end of the first cycle is

$$\frac{\epsilon_1}{\epsilon_y} = 1 + \frac{E}{E_p}\left\{2n - 1 - \frac{2\left(2m + \frac{E}{E_p} + 2n - 1\right)}{\left(1 + \frac{E}{E_p}\right)^2} - \frac{(2n-1)\left(\frac{E}{E_p} - 1\right) - 2m}{1 + \frac{E}{E_p}}\right\} \tag{3}$$

When the asymptotic strain is obtained, the cyclic stresses are entirely elastic, and the dimensionless total strain at an instant when the system is isothermal is

$$\frac{\epsilon_\infty}{\epsilon_y} = 1 + \frac{E}{E_p}\left[n - 1 + \frac{m}{2}\left(1 - \frac{E}{E_p}\right)\right] \tag{4}$$

The parameter β can be computed using the relation

$$\beta = \log_e\left(\frac{\frac{\epsilon_\infty}{\epsilon_y} - 1}{\frac{\epsilon_\infty}{\epsilon_y} - \frac{\epsilon_1}{\epsilon_y}}\right) \tag{5}$$

The construction of Fig. 3 can be made as follows:

1 Plot the stress-strain curve *A-B-C*, the load line *O-F*, the line *D-E* as a mirror image of *B-C* with respect to *O-F*.

2 Locate line 1-1 at an abscissa computed from equation (3), and locate line *G-E* at the abscissa computed from equation (4).

3 Draw the parallelogram *G-J-E-H*.

4 Draw *K-H* parallel to *D-E*.

5 Extend line 1-1 to intersect the extension of line *A-B* and draw *L-G*.

6 Complete the construction as indicated.

The points 0.5, 1.5, and 2.5 represent conditions when the outer bars are at maximum temperature, and points 1, 2, and 3 represent conditions when the system is isothermal. When the system is strain-hardened enough to prevent further growth, the conditions with the outer bars at maximum temperature are represented by points *J* and *H*, and the isothermal condition is represented by points *G* and *E*.

The foregoing evaluation of the three-bar assembly also would be applicable to slow isothermal temperature cycling of a thin-walled pressure vessel fabricated from plate of which the two half thicknesses are materials differing in thermal-expansion coefficient but having the same stress-strain characteristics. Strict applicability requires that the maximum-shear-stress criterion for the incidence of plastic flow be valid. This criterion is approximately valid and is used here for simplicity. In the case of the bimetallic vessel the quantity ϵ_y for the three-bar assembly would be replaced by $\epsilon_y(1 - \nu)$ for the pressure vessel in equations (1) to (5), inclusive.

Pressure Vessel With Uniform Heat Flux. A thin-walled pressure vessel with a cyclic uniform heat flux through its walls and with a sustained internal pressure will be subject to progressive growth if the loadings are sufficiently high. For simplicity of analysis it will be assumed that the maximum-shear-stress criterion for initiation of plastic flow is valid.

The analysis of this case is more complicated than that of the three-bar assembly, because the stress distribution is more complex and because of the possibility of compressive yielding in the regions of the highest thermal stresses. Two conditions of combined circumferential thermal and pressure stress which are on the verge of producing progressive growth are shown in Figs. 4(*a* and *b*). The former represents a case where no compressive plastic strain occurs, and the second represents a case where it does occur. The thermal strain is assumed to vary linearly in the radial direction, and the hoop stress caused by pressure is assumed constant, as is approximately true for a vessel whose wall thickness is small in comparison with its radius. The material is assumed to be elastic-plastic without strain-hardening in the nominal membrane stress-strain characteristic, and the tensile and compressive yield stresses are assumed to be equal.

The following is the identification of various lines in Fig. 4(*a*):

1 *A-B-G-H* represents the pressure load at 70 per cent of yield.

2 *A-D-K-H* represents the thermal stress and pressure stress combined as they would be if the system were elastic. The upper boundary *L-D* corresponds to the outside surface, if the heat flux is outward.

3 *A-C-E-J-H* corresponds to the actual combined thermal and pressure-stress distribution while the heat flux is applied.

4 *A-L-E-F-H* corresponds to the stress distribution existing after removal of the heat flux.

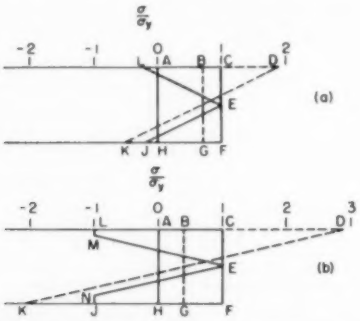

Fig. 4 Stress distributions with linear temperature variation

It should be noted that the vessel has received a permanent increase in diameter equal to that which would have resulted in an increase in membrane stress from 70 to 100 per cent of the yield point.

Fig. 4(*b*) is similar to Fig. 4(*a*) except that lines *L-M* and *N-J* denote the depth to which yielding occurs in compression and in tension once during each cycle of temperature variation.

Fig. 5, curve A, shows how the maximum thermal stress σ_t, computed with elastic behavior assumed, must be limited if cyclic growth is to be avoided. For values of $(\sigma_t/\sigma_y) < 2$, curve A is a straight line, representing conditions of Fig. 4(*a*) where plastic flow occurs only during the first cycle of application of heat flux. The remainder of curve A is an hyperbola, representing the conditions of Fig. 4(*b*) where cyclic plastic flow occurs during each cycle of temperature variation. It is to be expected that this cyclic plastic flow might contribute substantially to the risk of fatigue failure.

If the thermal stresses are larger than those indicated by Fig. 5, an increment of growth occurs with each cycle of temperature variation. The dimensionless growth per cycle for the present case is

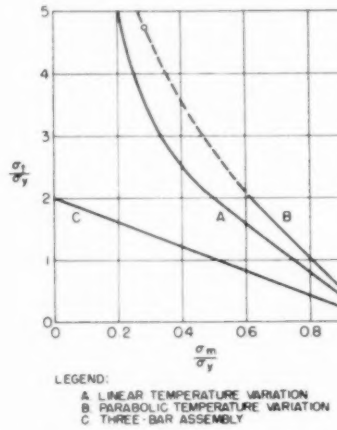

Fig. 5 Thermal stress beyond which cyclic growth occurs

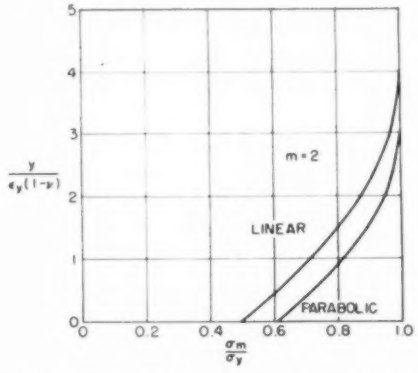

Fig. 6 Growth per cycle in shells with linear and parabolic temperature distribution

$$\frac{y}{\epsilon_y} = 2\{m - 2[m(1-n)]^{1/n}\}(1-\nu) \qquad (6)$$

for conditions where no compressive plastic flow occurs during the cycle. The characteristics of equation (6) are shown for a particular value of m by the upper curve of Fig. 6.

Pressure Vessel With Heat Generated Within Its Wall. A thin-walled pressure vessel with uniform heat generation within its walls will have an approximately parabolic variation of temperature in the radial direction through its wall. The case considered here is one where heat is removed only from one surface or equally from both surfaces. If heat is removed equally from both surfaces, the stress distribution of the outer half is the same in form as that of a shell with heat removed entirely from the outer surfaces. Hence only the case of heat removal from one surface need be considered. The assumptions made with respect to material characteristics for the pressure vessel with linear temperature variation are used here as well.

Fig. 7 represents the stress distributions for two cases with a parabolic temperature distribution. Fig. 7(*a*) represents the case where any increase in thermal stress or membrane stress would cause plastic flow to occur during each cycle. This case determines the point of transition from the linear to the nonlinear portion of curve B of Fig. 5. This point is at an ordinate of 2 and an abscissa of 0.615. *A-D-K-H* represents the combined thermal and pressure-stress distribution which would exist if the system were elastic. *A-C-E-H* shows the actual combined stress distribution while the heat flow is a maximum, and *A-L-E-F-H* shows the stress distribution when the heat flow is zero.

Fig. 7(*b*) represents a case where plastic flow occurs once during each cycle in the region of maximum stress. This case is for $\sigma_t/\sigma_y = 4.74$ and $\sigma_m/\sigma_y = 0.288$. With a higher thermal stress and with the membrane stress reduced enough to prevent growth, cyclic plastic flow would occur at and near the zero heat-flux surface as well as in the region of maximum heat flux.

The case of Fig. 7(*b*) is plotted on curve B of Fig. 5. Above this point, curve B approaches curve A asymptotically. The dashed portion of curve B of Fig. 5 was drawn on the basis of judgment to fit the linear portion and the plotted point.

If the thermal stresses are sufficient to cause growth but insufficient to cause compressive plastic flow, the dimensionless growth per cycle is

$$\frac{y}{\epsilon_y} = \frac{3m(1-\nu)}{2}\left\{\left[\frac{1}{2} + \cos\left(\frac{\theta + 4\pi}{3}\right)\right]^2 - \left(\frac{1-n}{m}\right)^{2/n}\right\} \qquad (7)$$

where

$$\theta = \cos^{-1}\left[\frac{4}{m}(1-n) - 1\right] \qquad (8)$$

The characteristics of equation (7) are shown in the lower curve of Fig. 6 for a particular value of m.

Correlation Between Three-Bar Assembly and Pressure Vessels. In the linear range of the curves of Fig. 5, the limits on the maximum thermal stresses beyond which cyclic growth occurs at a particular membrane-stress-to-yield-stress ratio for the three cases which have been considered are in the proportions 1:2:2.6 for the three-bar assembly, the linear, and the parabolic stress distributions. It is of interest to note that the three limiting cases correspond to equal values of average tensile thermal stress in the zone where tensile thermal stresses would be present if the material were elastic.

It is also of interest to note that the slopes of the lowermost portions of the curves in Fig. 6 coincide with the slopes of the

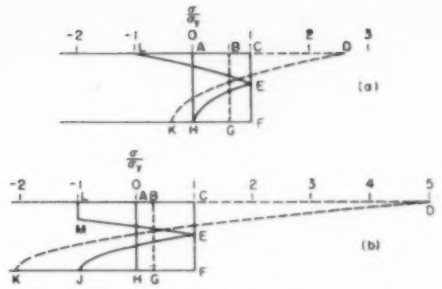

Fig. 7 Stress distributions with parabolic temperature variation

(y/ϵ_y)-functions for the three-bar assembly which have the same horizontal-axis intercepts. In the limiting case of $n = 1$, the growth per cycle corresponds to the full maximum thermal differential expansion.

The determination of total growth as a function of the number of temperature cycles is more complex for the pressure vessels than for the three-bar assembly because of the nonlinear character of equations (6) and (7). With a particular strain-hardening characteristic and initial growth rate, the pressure-vessel growth rate falls with increasing strain more than does the growth rate of the three-bar assembly. If it is desired to plot the growth as a function of the number of cycles for a particular pressure vessel, the growth-rate and total-growth curves can be plotted on the basis of numerical computations, and successive adjustments of m and n as strain-hardening proceeds.

Discussion

The formulas and curves presented in the foregoing provide criteria suitable for design for avoidance of growth of pressure vessels due to cycling of heat flux through the walls while pressure loading is maintained. The formulas for growth rates also will be useful in estimating the growth rates which will occur with combinations of high thermal strains and pressure loadings. Some other criterion than the maximum-shear-stress criterion for the initiation of plastic flow might have provided more valid derivations, but it is doubtful that the increased accuracy would be of enough value in practical cases to justify use of a more complex flow criterion.

Curve B in Fig. 5 was used in modification of the design of a pressurized tube to be installed in the Engineering Test Reactor as part of a test loop. The modification was made after prediction, on the basis of the analysis just presented, that the growth which would occur in the original design was prohibitive. The tube is to be in a high neutron and gamma-ray flux which will produce high differential thermal strains in the wall of the tube. A scale model of the modified design was tested with internal pressure and with electric-current heating to simulate design loadings, and the test confirmed the absence of growth. Consideration is being given to performing tests on the model under more severe loadings to enable a comparison of the actual growth characteristics with those which would be predicted by the formulas presented in the paper.

Some cases where growth might be predicted in the basis of the present analysis or by similar analyses are:

1 Pressure vessels subjected to temperature transients in the contained fluid, heated from their exteriors or heated within their walls by nuclear radiations.

2 Temperature cycling of pressure vessels clad with material differing from the base metal in coefficient of thermal expansion.

3 Bimetallic joints in pressure piping subjected to slow cycling

of temperature. (Metals differing in thermal-expansion coefficients.)

4 Temperature cycling of pressure vessels made of a metal consisting of crystal phases differing in thermal-expansion coefficients.

5 Turbine blades and disks subjected to severe temperature transients and centrifugal loading.

6 Pressurized piping subjected to high bending or torsional loadings.

7 High-speed aircraft wings subjected to combined thermal and mechanical loads.

8 Electrical conductors in motors subjected to mechanical and thermal-expansion loads.

The growth problem in vessels heated with electrical heaters attached to the walls can be alleviated by avoiding hot spots caused by heaters being locally in direct contact with the walls.

At temperatures where creep is significant it is to be expected that, with combined sustained external loads and cyclic differential thermal strains, the creep deformations will be increased by the thermal-strain cycling.

It should be recognized that the growth ratchet as analyzed here is characteristic of cases where pressure or other external loading continuously maintains membrane or average stresses across a member at a constant value. In some cases local membrane or bending stresses will be reduced by application of a single cycle of sufficiently high differential thermal strain. This phenomenon has been discussed by Langer [5].

There are several potential sources of progressive deformation as a result of temperature cycling not considered in the foregoing which deserve mention, since in some cases they also may interact with external loads so as to increase the growth rate. Burke and Turkalo [6] have demonstrated and explained the occurrence of progressive distortion of zinc bicrystals due to cycling of temperature in the absence of external loads. The progressive distortion is attributed to the difference between the mode of plastic flow at high temperature (grain-boundary flow) and that at low temperature (transcrystalline slip). The source of internal stresses tending to cause plastic flow is the anisotropy of thermal expansion during cycling. Another anisotropic material in which progressive distortion can be produced by temperature cycling alone is uranium [7].

Progressive deformation has been postulated by the author in a bimetallic three-bar assembly subjected to a sufficiently high range of isothermal temperature cycling. In this system progressive growth can occur if the two metals both have tensile yield stresses lower than their compressive yield stresses. This system behaves somewhat like the three-bar assembly discussed in the text of the paper, in which the external load replaces the difference between tensile and compressive yield stresses.

An isotropic material also may experience a progressive distortion owing to temperature cycling as has been shown by the progressive approach to a spherical shape of a steel cube subjected to repeated heating and cooling [8]. This distortion may be due to the high cyclic thermal stresses produced by rapid heating and cooling and/or to density changes caused by phase transformations combined with the cyclic variations in yield strength which accompany the local temperature changes. A case where a similar, and probably analogous, phenomenon can be visualized is that of a rod thermally insulated from, and at its end attached to, a concentric tube of the same material and of the same cross-sectional area. If the tensile and compressive yield strengths of the material are equal, and if both yield strengths fall as temperature increases, the assembly becomes progressively shorter and larger in diameter when a suitable temperature cycle is imposed. Thus, if first the tube is heated sufficiently, it will yield in compression because its yield strength is lower than that of the rod. If now the rod is heated to the temperature of the tube, the tube will be in tension and the rod will be in compression. When the temperature of the rod reaches that of the tube, there may have been some tensile plastic flow in the tube, but it will have been smaller than the original compressive plastic flow in the tube. If now the tube is cooled to the initial temperature of the rod, the rod will yield in compression. If the rod is now cooled to the initial temperature, the entire assembly will have experienced plastic shortening of its longitudinal axis. From the similarity of the assumed temperature cycle to that for a solid cylinder subjected to rapid heating and cooling of its exterior, it appears that a solid cylinder will become progressively shorter in length and larger in diameter if exposed to sufficiently severe alternating changes of surface temperature. Similarly, a cube would progress toward a spherical shape.

Progressive distortion has been observed to occur when the thermal expansion of a container exceeds that of its solid particulate contents. Thus a very long, vertical, thin-walled, austenitic-stainless-steel tube filled with fine ferritic-steel shot would be expected to become progressively larger in diameter with repetitive slow cycling of temperature. This is true because the shot would slump down when the assembly was hot, but could not be forced upward again by shrinkage of the tube diameter while the assembly was cooled.

Acknowledgment

The author was aided in formulation of the concepts and analyses presented here by discussions with several colleagues, in particular Messrs. T. H. Glasser and J. C. Westmoreland, whose query prompted this investigation, and Dr. W. E. Cooper who aided in evaluation of the effects of strain-hardening.

References

1 R. Hill, "The Mathematical Theory of Plasticity," Oxford University Press, London, England, 1950, pp. 287–294.

2 E. W. Parkes, "Wings Under Repeated Thermal Stress," *Aircraft Engineering*, vol. 26, 1954, pp. 402–406.

3 N. A. Weil and F. S. Rapasky, "Experience With Vessels of Delayed-Coking Units," preprint of paper submitted to a session on pressure vessels, American Petroleum Institute, Division of Refining, Los Angeles, Calif., May 13, 1958.

4 L. F. Coffin, "The Resistance of Materials to Cyclic Thermal Strains," Paper No. 57—A-286.

5 B. F. Langer, "Design Values for Thermal Stress in Ductile Materials," presented at ASME-AWS Joint Metals Engineering Conference, April, 1958, Paper No. 58—Met-1.

6 J. E. Burke and A. M. Turkalo, "Deformation of Zinc Bicrystals by Thermal Ratcheting," *Journal of Metals*, vol. 4, 1952, pp. 651–656, *Trans. AIME*, vol. 194, pp. 651–656.

7 H. H. Chiswick, "The Plastic Deformation of Uranium on Thermal Cycling," *Trans. ASM*, vol. 49, 1957, pp. 622–654.

8 L. C. Bibber, "Dimensional Changes in Steel," *The Welding Journal*, vol. 27, 1948, pp. 1009–1024.

DISCUSSION

L. F. Coffin, Jr.[3]

The author has presented a very interesting analysis of certain systems subjected simultaneously to mean stresses and cyclic thermal stresses and has determined criteria for cyclic growth in such cases. In these analyses he has focused his attention principally on those cases where the mean stresses are comparatively high and the thermal stresses relatively low such that the plastic deformation which occurs at any point in the structure is monotonic in nature. In such cases it is appropriate to use idealized representations for real material behavior, as given in Figs. 2 and 3. There is, in addition, much engineering interest in this particular range of steady and thermal stresses.

When the cyclic thermal stresses become severe so as to pro-

[3] General Electric Research Laboratory, General Electric Company, Schenectady, N. Y. Mem. ASME.

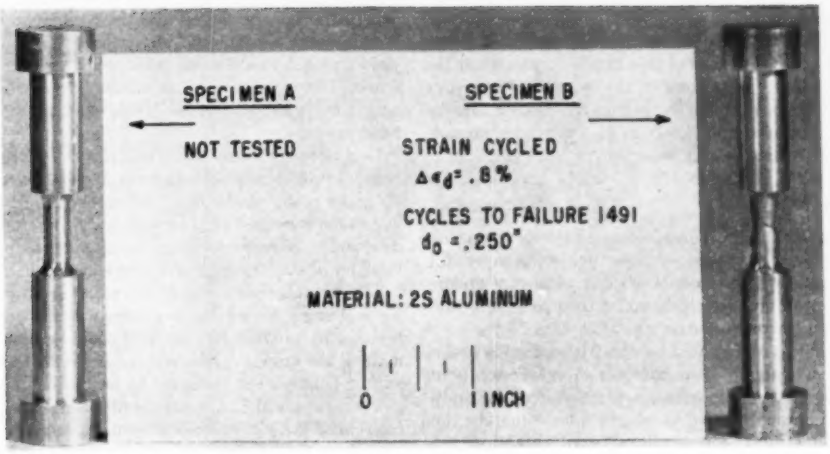

Fig. 8 Cylindrical test specimens of 2S aluminum

duce, upon unloading, a reversed plastic strain, the deformation path of certain portions of the structure, under growth conditions subjected to monotonic plastic deformation, are coupled with cyclic plastic deformations. Such may be the case, when, for example, thermal-stress fatigue is the limiting design condition in the structure. It begins to be important when the stress at any point is carried sufficiently far in the reverse direction to be influenced by the Bauschinger effect. Upon such situations uncertainties regarding material behavior occur and assumptions must then be made.

The writer for some time has been investigating the room-temperature behavior of ductile metals subjected to large cyclic plastic strains (0.5 to 30 per cent) with superimposed mean stresses or strains.[4] Under these conditions numerous observations of monotonic deformations as a consequence of small mean stresses and cyclic plastic strains have been observed, including, for example, the twisting of an aluminum bar by shearing stresses of the order of 63 psi under the simultaneous action of a longitudinal fully reversed cyclic plastic-strain range of magnitude 0.0086 in. per in.

Another interesting example of the case by which metals can be deformed when subjected to cyclic plastic strain is shown in Fig. 8. Here an initially uniform cylindrical test specimen of 2S aluminum is subjected to 1500 cycles of a push-pull axial loading with a diametral strain range of 0.8 per cent. The resulting specimen shape is shown in the right-hand figure. It is of particular interest to note that the central section of the specimen has necked down while the ends of the specimen have increased in thickness, although there has been no net change in length of the specimen since the strain was produced by a cyclic displacement of the ends of the specimen. Less soft materials do not show this effect to the same degree as aluminum. The effect can be explained in terms of a slight tensile mean stress at the center and a compressive mean stress near the ends arising from second-order effects concerning the instantaneous stresses during cycling.

The combined action of cyclic and monotonic plastic strain can have a significant influence on the stress-strain behavior in ductile metals. The author has calculated that, when strain-hardening is taken into account, the increment of plastic deformation in systems undergoing racheting decreases in a negative exponential fashion with the number of cycles, whereas, in the absence of strain-hardening, the deformation increment remains

[4] L. F. Coffin, Jr., "The Stability of Metals Under Plastic Strain," General Electric Research Laboratory Report RL-2137, to be published.

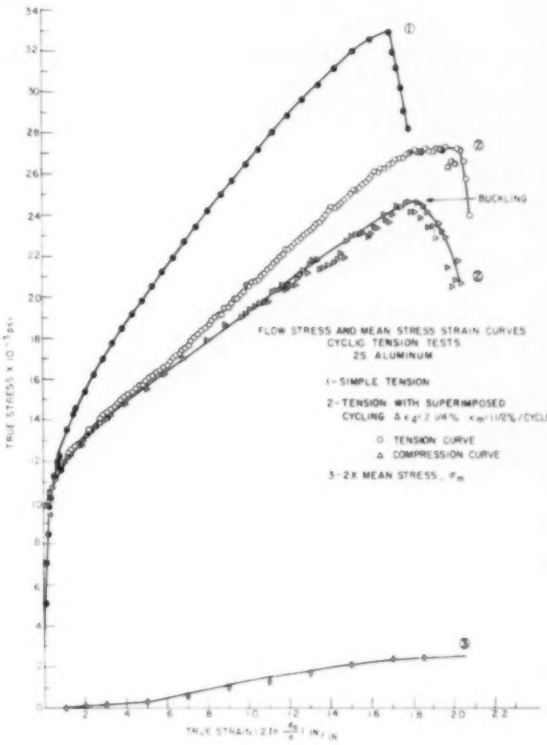

Fig. 9

constant. Thus any tendency to change the strain-hardening characteristics of the material will have a pronounced influence on the magnitude and extent of the plastic deformation achieved by this type of loading.

In Fig. 9 is shown the influence of the superposition of a cyclic plastic strain upon the monotonic stress-strain curve. These data are achieved by what is called a cyclic tension test,[4] in which the combined cyclic and monotonic strain is achieved in a push-pull type of machine. Note in particular the significant decrease in strain-hardening produced by the superposition of a cyclic

strain of a $2^1/_4$ per cent range for each $1^1/_2$ per cent monotonic deformation (curve 2) when compared to the simple monotonic test (curve 1). Differences such as this can have a marked influence on the magnitude and extent of the monotonic deformation produced by "racheting." These effects must be clearly recognized when attempting an analysis in which the plastic-strain path involves reversals in direction.

Author's Closure

Dr. Coffin's discussion is an interesting supplement to the paper. It lends support to the theory presented in the paper and also points out a case where the author's formulas may underestimate the amount of growth which would be produced by the ratchet phenomenon treated in the paper.

The cyclic tension test represented by Fig. 9 is analogous to the author's three-bar assembly. If we consider cases where n is so small that it can be neglected in equation (1), and if we multiply Coffin's transverse strains by two to obtain approximately the corresponding axial strains, the predicted axial extension per cycle is

$$y = 2\Delta\epsilon_a - \frac{4\sigma_y}{E} \qquad (9)$$

At a flow stress of 37,500 psi (assuming $E = 10^7$ psi) equation (9) gives the actual growth per cycle. At a flow stress of 20,000 psi equation (9) gives an extension of 0.037 in./in. instead of the actual value of 0.03 in./in. The discrepancy between theory and experiment may be caused by a small difference between the compressive and tensile yield strengths. A small excess of tensile yield strength would offset the effect of a small tensile mean stress. Small differences in yield strengths would be of little significance with the membrane-stress levels commonly used in pressure vessels.

In a pressure vessel in which growth is accompanied by local plastic cyclic strains such as occur in the case represented by Fig. 4(*b*), the cyclic plastic flow may either retard continued growth due to the increased yield strength resulting from work hardening, or it may produce cyclic-strain softening to partially offset the work hardening resulting from the elongation.

The formulas presented in the paper are probably most useful for enabling a designer to determine whether growth is a potential problem in a particular case, and enabling him to obtain an estimate of the growth which will occur if growth is expected. The author believes the formulas to be reasonably accurate for engineering applications where membrane stresses are a substantial fraction of the yield or creep strength, and where the material is initially in the annealed condition. If the material were initially in a work-hardened condition, it might be possible for a stable system to begin to grow after softening occurs due to exposure to elevated temperature or due to plastic-strain cycling.

At the present state of knowledge of the ratchet problem it would be prudent to make a simulated-service test or in-service checks for comparison with theoretical predictions of growth in any case where substantial growth is expected, unless the hazards associated with expansion of the pressure vessel are small.

AARON COHEN

Convair Astronautics,
San Diego, Calif.

EDWARD HOMER

Electron Tube Division,
Radio Corporation of America,
Harrison, N. J.

Refractory Metal Facings for Protection of Metal Surfaces Subjected to Repeated High-Temperature Pulses

Because the operating frequency of a magnetron has a direct relationship to the size of the resonant structure, the power at a given frequency that can be obtained from a magnetron may be limited by the temperature which the resonating structure can withstand. A rise in the temperature of the resonant structure is caused by the impact of high-energy electrons emitted from the cathode at high peak-power levels for short durations. This paper deals with the analytical determination of the temperature of the resonant structure, a solution to the heat problem in which a thin coating of refractory metal is used to prevent the vulnerable components from melting, and some experimental results to verify the analysis.

THE GEOMETRY of a typical magnetron is shown in Fig. 1. Early investigation of the anode vane temperature and stresses revealed that the vane surface melted after operation for approximately 6 hr with 1-microsec pulses of 1.94 to 2.25 megawatts per sq in. The required conditions were an output power of 3.1 megawatts per sq in. with a 2.5-microsec pulse width and 250 hr of operation.

In analyzing this problem the following assumptions were made:

1 An area of A sq in. of the vane surface is uniformly bombarded by electrons during n pulses having a duration of t_0 microsec each.

2 All the energy of the bombarding electrons is converted to heat at the surface of the vane.

3 The dissipation produced in N vanes by n pulses is Q/A watts per sq in. Each vane, therefore, dissipates Q/AN watts per sq in.

4 The back of the vane is maintained at a temperature of L deg C by liquid cooling of the anode block.

5 Radiation is negligible compared to conduction and therefore may be disregarded.

6 Because the temperature over the face of the vane is uniform, it is permissible to use the equation for one-dimensional heat flow [1][1]

$$U_t(x, t) = kU_{xx}(x, t), \qquad t > 0 \tag{1}$$

7 Since the temperature at the back of the vane remains constant, the vane can be considered a semi-infinite strip. Therefore,

$$U(x, 0) = 0 \tag{2a}$$

$$\lim_{x \to \infty} U(x, t) = L, \qquad t > 0 \tag{2b}$$

$$-KU_x(0, t) = \phi(t), \qquad t > 0 \tag{2c}$$

$$V_t(x, t) = kV_{xx}(x, t), \qquad t > 0 \tag{3a}$$

$$V(x, 0) = 0 \tag{3b}$$

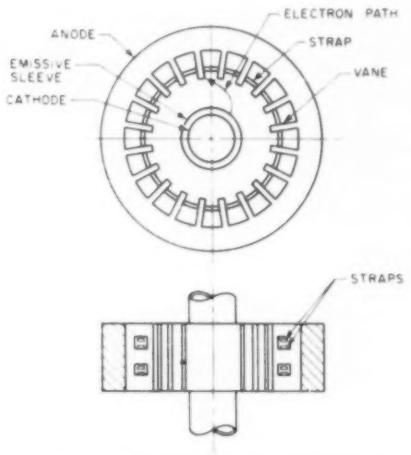

Fig. 1 Geometry of a typical magnetron

$$-KV_x(0, t) = \phi(t) \tag{3c}$$

$$V(x, t) = U(x, t) - L \tag{3d}$$

$$\lim_{x \to \infty} V(x, t) = \lim_{x \to \infty} U(x, t) - L \tag{3e}$$

$$\lim_{x \to \infty} V(x, t) = 0 \tag{3f}$$

$$U(x, t) = L + \frac{1}{K}\sqrt{\frac{k}{\pi}} \sum_{n=1}^{\infty} \int_0^t \frac{\phi(t - n\tau)}{\sqrt{\tau}}\, e^{-\frac{x^2}{4k\tau}}\, d\tau \tag{4}$$

$$U(0, t) = L + \frac{1}{K}\left(\frac{k}{\pi}\right)^{1/2} \sum_{n=1}^{\infty} \int_0^t \frac{\phi(\tau)}{(t - n\tau)^{1/2}}\, d\tau \tag{5}$$

If Equation (10) in the Appendix is evaluated for $n = 1$, or the first pulse, the solution has the familiar form

$$U(x, t) = L + \frac{\phi_0}{K}\left\{2\left(\frac{kt}{\pi}\right)^{1/2} e^{-\frac{nx^2}{4kt}} - x \operatorname{erfc}\left[\frac{nx}{2\,(kt)^{1/2}}\right]\right\}_0^t \tag{6}$$

For repeated pulses Equation (10) becomes

[1] Numbers in brackets designate References at end of paper.

Contributed by the Metals Engineering Division and presented at a joint session with the Joint ASTM-ASME Committee on Effect of Temperature on the Properties of Metals at the Annual Meeting, New York, N. Y., November 30–December 5, 1958, of THE AMERICAN SOCIETY OF MECHANICAL ENGINEERS.

NOTE: Statements and opinions advanced in papers are to be understood as individual expressions of their authors and not those of the Society. Manuscript received at ASME Headquarters, September 2, 1958. Paper No. 58—A-188.

$$U(x, t) = L + \frac{\phi_0}{K} \sum_{n=1}^{\infty} \left\{ \frac{2}{n} \left(\frac{kt}{\pi} \right)^{1/2} e^{-\frac{nx^2}{4kt}} - x \operatorname{erfc} \left[\frac{nx}{2(kt)^{1/2}} \right] \right\} \quad (7)$$

In Equations (1) through (7), $U(x, t)$ is the temperature at any point x for any pulse duration t,

ϕ_0 = watts per sq in.
K = thermal conductivity, watt-in./sq in. deg C
k = thermal diffusivity = $\frac{K}{\rho c}$, in²/in-sec
ρ = density
c = specific heat
t = pulse duration, sec

As an example, the temperature of a vane after the first pulse can be calculated from Equation (6) as follows:

$$\phi_0 = \frac{9.38 \times 10^6 \text{ watts}}{\text{sq in.}}$$

$$K = \frac{8.8 \text{ watt-in}}{\text{sq in. deg C}} \qquad \text{(reference [4])}$$

$$\frac{\phi_0}{K} = \frac{1.07 \times 10^6 \text{ deg C}}{\text{in.}}$$

$$k = \frac{0.1575 \text{ in}^2}{\text{in-sec}} \qquad \text{(reference [4])}$$

t = 2.5 microsec

L = 150 deg C

Therefore,

$$U(1 \times 10^{-3}, 2.5 \times 10^{-6}) = 150 + 1.07 \times 10^6 \times \left\{ 2 \left[\frac{(0.1575)(2.5 \times 10^{-6})}{\pi} \right]^{1/2} e^{-\frac{(10^{-3})^2}{4(0.1575)(2.5 \times 10^{-6})}} - 10^{-3} \left(1 - \operatorname{erf} \frac{10^{-3}}{2[(0.1575)(2.5 \times 10^{-6})]^{1/2}} \right) \right\}$$

$$U(10^{-3}, 2.5 \ \mu\text{sec}) = 273 \text{ C} \quad (8)$$

Curves showing the results of such calculations for various vane materials are plotted in Fig. 2. These curves show the depth of penetration of the temperature produced by the first pulse. Equation (7), on the other hand, yields the temperature in the vane at any point $x > 0$ after any number of pulses. Equation (7), however, is difficult to handle and does not provide much more information than does Equation (8).

Equation (5) gives the temperature at the face of the vane after n pulses. A typical calculation using Equation (5) is shown in the following. The calculation is for a copper vane, and the conditions are the same as those used in the preceding example.

$$U(0, 2.5 \ \mu\text{sec}) = 150° + (755° + 19.1° + 15.9° + 11.9° + 9.5° + 7.9° + \ldots\ldots\ldots\ldots\ldots) \quad (9)$$

It is evident that this series converges after a finite number of pulses. It is also evident that the high-temperature conditions are produced by the first pulse.

Experimentation

Immediate Steps to Reduce Erosion. To check the results of the foregoing analytical investigation, a series of experiments was conducted to determine the effects of high-temperature operation on copper-vane magnetrons of various designs. The existing design employed three-section OFHC[2] copper vanes, brazed together and to the copper straps with silver-copper eutectic brazing alloy, Fig. 3. Erosion of the vane face began at the brazed joints and was heaviest at the strap-clearance "windows." It was evident that the tendency to erosion in these areas resulting from the "thermal block" of the "windows" was increased by the presence of the low-melting-point (779 C) brazing material. During assembly, the brazing metal often flowed over the entire vane face. When the completed tube was operated, additional silver-copper brazing metal from the joints flowed over the eroding face, alloying with the copper and creating still more low-melting-point material. This progressive decomposition can be seen in Fig. 4, a photomicrograph of a small area of an eroded three-section vane. Although as much as 0.012 in. of the copper-vane face has eroded, a thin layer of silver-copper alloy still extends from the brazed joint and along the face.

The first step taken to reduce such erosion was the substitution

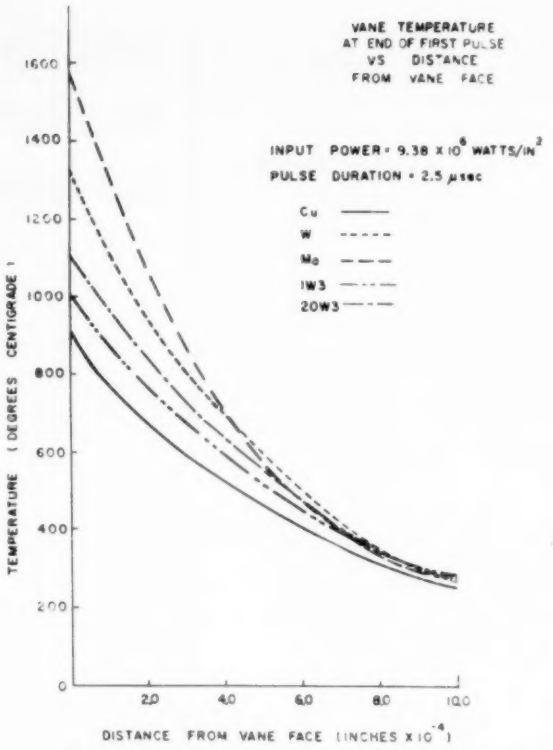

Fig. 2 Curve of vane temperature at end of first pulse

[2] Made by American Metal Company, Ltd.

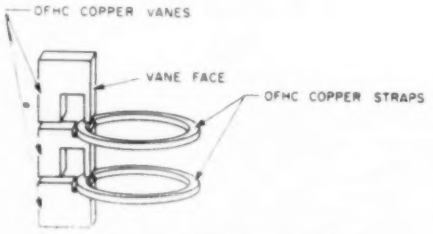

Fig. 3 Three-piece vane assembly

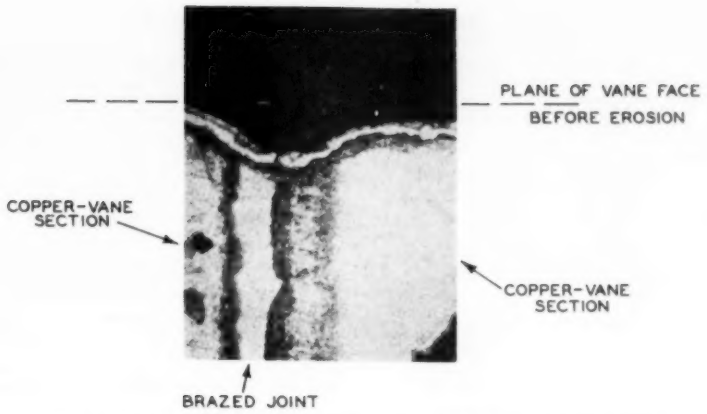

Fig. 4 Photomicrograph of section through an eroded three-piece copper vane

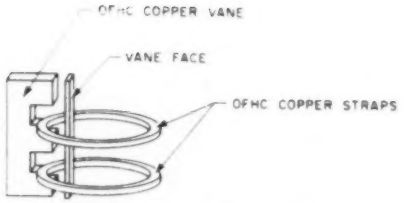

Fig. 5 Two-piece vane assembly

for the silver-copper eutectic alloy of Nicoro[5] (35 per cent Au, 48 per cent Cu, 17 per cent Ni, flow point 1025 C), a brazing metal having higher melting point and surface tension. Vane-strap assemblies were brazed with Nicoro at 1040 C, forming joints having nearly the melting point of the base metal. Because of its high surface tension and high liquidous viscosity, the Nicoro was confined to the joints and did not flow over the vane face.

Depite this improvement, the vanes continued to erode even during operation at one-half power. The next step taken was substitution for the three-piece vane assembly of the two-piece design shown in Fig. 4 so as to remove all brazing material from the vane face. The braze shown in Fig. 5 was made approximately 0.014 in. deep.

It was mandatory to determine if the temperature during operation was sufficient to melt the brazed joint. By insertion of the proper values in Equation (7) it was determined that the build-up of temperature at a depth $x > 0$ from the face is small compared with that at the surface. For example, for any number of pulses

$$U(10^{-3}, 2.5\ \mu\text{sec}) = (123^\circ + 77^\circ + 32^\circ + 16.5^\circ + \ldots\ldots) + 150^\circ$$

It was concluded, therefore, that the brazed joint was not in danger of melting. Although a tube using two-piece copper vanes of the type shown in Fig. 5 was not tested, subsequent tests using a dummy-anode tube (to be described) confirmed the analytical findings, and erosion would be substantially reduced.

Equations (5) and (7) can be used to calculate the temperature at any depth in the vane after any number of pulses of any pulse duration, and for any material. On the basis of such calculations the most critical region was found to be within a few thousandths of an inch of the vane face.

Another subject investigated was the effect of windows in the vanes. Because the "window" shown in Fig. 5 is only 0.14 in. behind the surface of the vane the resulting concentration of heat-flow lines can cause hot spots. However, an analog field plot of this configuration, assuming steady-state conditions, showed that the temperature at the face of the vane in front of the window was only about 25 deg C higher than that without the window [3]. It was concluded, therefore, that the windows have little effect on the melting of the vanes.

It was difficult to obtain a precise stress analysis because of the rapid repetition rate of the temperature cycle. The following expression, derived by Timoshenko [3, 5], indicates that the stress is much higher than the yield point of any material that can be used for a vane:

$$\delta = -\frac{\alpha T E}{1 - \tau}$$

where

δ = stress
α = coefficient of thermal expansion
T = amplitude of temperature variation on surface
E = Young's modulus
τ = Poisson's ratio

Timoshenko's expression, however, was developed for a much slower periodic temperature cycle, and, therefore, may not be applicable to the present case. The only conclusion that can be drawn is that the yield point of the copper vanes may have been exceeded in the magnetrons tested.

Final Solutions Considered. Both the initial analysis and the evidence obtained from experimental tubes indicated that magnetrons using pure copper vanes could not be operated at full power. Effort was directed, therefore, to the development of a protective vane facing which would have the highest possible electrical and thermal conductivity. Three general fabrication techniques were investigated:

1 Brazing of a refractory conductor to the vane face.

2 Application of a conductive refractory facing by other means.

3 The use of vanes constructed entirely of a refractory conductive material.

The two-piece, copper-vane assembly shown in Fig. 5 was suitable for use with a brazed refractory face. Analysis showed that the significant parameters of a usable refractory are its density, thermal conductivity, specific heat, and melting point.

High electrical conductivity, low vapor pressure, and a low coefficient of thermal expansion are also desirable. The materials finally selected for evaluation, and their characteristics, are listed in Table 1.

[5] Trade name of Western Gold & Platinum Company.

Table 1 Characteristics of various vane-face materials

	Tungsten	Molybdenum	1W3 Elkonite	20W3 Elkonite	Hevimet	OFHC Copper (for comparison)
Composition, per cent	100% W	100% Mo	65% Cu 35% W	45% Cu 55% W	90% W 6% Ni 4% Cu	100% Cu
Spectrographic analysis, tracer quantities	Not analyzed	Not analyzed	Fe, Si, Ag, Ni, Mg, Mn, Pt	Fe, Si, Ag, Ni, Mn, Pt	Mg, Mn, Si, Fe, Ag, Pt	Not analyzed
Electrical resistivity, microhm-cm	5.48	5.17	4.60	6.00	6.8	1.67
Coeff. of expansion, $\frac{\text{in.} \times 10^{-6}}{\text{in.} \times °C}$	4.6	5.5	12.6	9.8	5.6	16.6
Density, gm/cc	19.0	9.9	12.6	14.7	Not available	8.9
Thermal conductivity, $\frac{\text{cal cm}}{\text{cm}^2 °C}$	0.476	0.346	0.773	0.652	Not available	9.00
Specific heat, $\frac{\text{cal } °C}{\text{gm}}$	0.034	0.062	0.059	0.048	Not available	0.093

The vane-face temperatures predicted analytically for these materials are shown in Fig. 2.

The Elkonites 1W3 and 20W3 are not alloys in the strict sense, since there is no copper-tungsten binary system. It was thought that with these metals, the copper might be vaporized from the vane face, leaving a tungsten lattice to absorb the heat, and retaining the electrical properties of the copper in the region behind the face.

All the materials listed in Table 1 could be brazed easily with Nicoro in a hydrogen atmosphere. In each case the vane straps were first brazed to the copper-vane backs either with Nicoro powder or by plating the straps with nickel and gold in a 1 to 4 proportion by weight and firing in hydrogen at 1040 C.

The most serious problem encountered in these assemblies was the difference in the thermal-expansion rates of the copper and the refractory facings. The thermal-expansion coefficients shown in Table 1 may be used to predict the mismatch along the length of the vane over the temperature range 25 to 1040 C. The distortion experienced in making the assemblies agreed well with the predictions.

The greatest mismatch—that for the copper-tungsten combination—was about 1 per cent of the vane length. Since this difference did not affect tube operation adversely, no effort was made to circumvent it. It was extremely important, however, that the resulting distortion be directed along the vane length, and that there be no other bowing or bending of the vane parts. This restriction was achieved in jigging technique, by constraining the vane on all surfaces except one end during and after the braze, and in particular by moving the vane face into juxtaposition with the copper vane as the Nicoro shim between the parts melted. The jigging arrangement is shown in Fig. 6.

Although the resulting assembly includes locked-in stresses up to the yield point of the copper, these stresses are partially offset during tube operation by the elevated temperature of the vane tip. None of the vane tips constructed by this method cracked in normal handling and operation, even though one tube was held at −55 C for several hours.

The bimetal thermal distortion of the brazed assembly made it desirable to find a means for fabricating a copper-refractory metal laminate from which complete vanes could be machined to final dimensions. The following techniques were tested:

1 "Flame spraying" tungsten and molybdenum on Monel and copper using Metco[4] flame-spraying equipment. In this process the base metal is preheated with an oxyacetylene flame, and a tungsten or molybdenum wire is then fed at a predetermined rate into the flame, where it is vaporized and blown against the base metal by compressed air.

[4] Trade name of Metallizing Engineering Company.

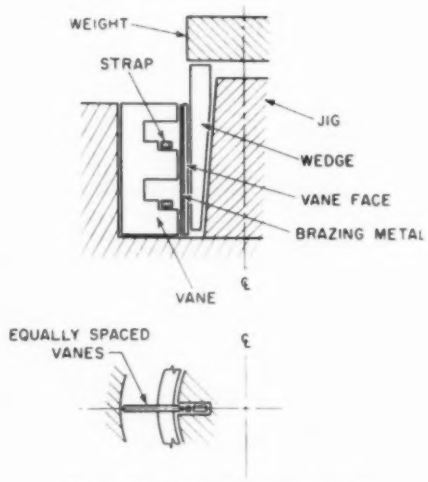

Fig. 6 Jig for two-piece vane assembly

(a) *Tungsten on Copper.* It was not possible to spray pure tungsten metal on copper and form a substantial bond. When thoriated tungsten was sprayed on a 0.450 × 7-in. copper face, it was possible to obtain about 0.005 in. of "packed" tungsten particles ranging in size from 100 to 500 microns. The coating was porous, compared with pure tungsten metal, and could be scraped into powder with a metal tool. This sample did not withstand machining into test vanes.

(b) *Molybdenum on Copper.* About 0.010 in. of porous molybdenum was sprayed on a copper strip 0.017 in. thick. The copper oxidized heavily, and there was very little bond at the interface. Better results probably could have been obtained by spraying in an inert atmosphere.

(c) *Molybdenum on 403 Monel.* This sample had the least bimetal distortion, and a good bond between the metals, with some diffusion at the interface. Porosity was similar to that of the molybdenum on copper [2]. The sample was clamped and brazed to a copper backing, then sectioned into testable vanes. Some molybdenum flaked off during machining.

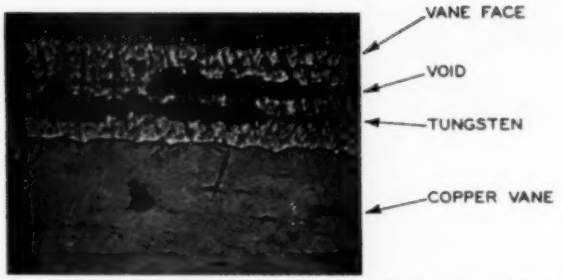

Fig. 7 Photomicrograph of section through Linde "flame-plated" tungsten-on-copper vane

Porosity and poor bonding of the metals were the limiting factors in the flame-spraying method.

2 A more elaborate "flame-plating" setup using higher temperatures and supersonic particle velocities (developed by Linde Air Reduction Company) was used to spray 0.005 in. of pure tungsten metal on a 0.450 × 7-in. copper face. The tungsten was dense and machined as well as ordinary tungsten metal. The bond to the base metal was excellent, considering that no actual alloying took place. Fig. 7 is a photomicrograph of the sample which shows the penetration of the tungsten into the copper. Also visible is a stratum of voids in the tungsten, which the vendor claims was caused by the use of two separate spraying runs to deposit the tungsten. Test vanes made from this bar have not yet been evaluated.

The Linde sample was the most promising of the sprayed-metal techniques.

3 Three other techniques studied but not tested, were as follows:

(*a*) Vacuum casting of OFHC[2] copper on tungsten to form a machinable laminate.

(*b*) An electroplating method under development by the Balic Company for depositing tungsten oxide on copper and subsequently reducing the deposit to pure tungsten metal.

(*c*) Machining of vanes entirely from a refractory metal. As shown in the following table, the maximum temperatures for the faces of such vanes would be higher than those for the laminated vanes described in the foregoing.

Refractory material	Solid, deg C	Laminated on copper, deg C
Tungsten	1595	1465
Molybdenum	1906	1690

In such designs copper straps would be distorted by the expansion mismatch between the low-expansion refractory vanes and the enclosing copper anode. Any tube design based upon the use of solid refractory-metal vanes would have to take into consideration the poor electrical characteristics of this material. Solid molybdenum vanes were used in the test anode to be described.

Evaluation

The next step in the solution of this problem was to evaluate experimentally the various materials which had been investigated analytically and assembled into test vanes. For this purpose a test anode was designed which would allow vanes of the various materials to be tested.

This anode was a split type having 18 permanent molybdenum dummy vanes and provision for two demountable test vanes, Fig. 8.

A cooling jacket was placed around the anode, and thermocouples were installed on the body of the anode. The assembly was placed in a vacuum bell-jar setup, and operated as a diode

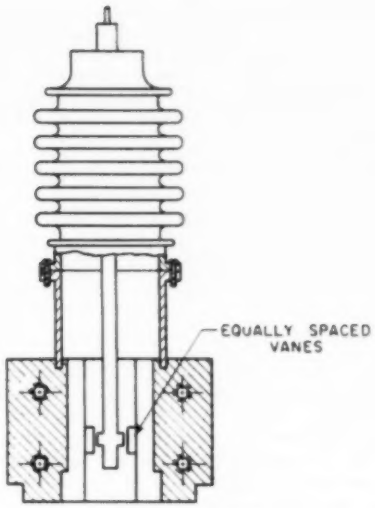

Fig. 8 Test anode

with its cathode pulsed at the repetition rate required to meet the analytical conditions. Peak powers of the order of 7.04 megawatts per sq in. were obtained for very short durations. Although these tests were conducted for comparative purposes rather than for absolute results, it was difficult to maintain conditions sufficiently stable to permit precise evaluation of the results. However, enough conditions were held approximately constant so that the following comparison between the various materials can be made. The peak power inputs for the various tests, varied from 5.61–7.04 megawatts per sq in. This power was held from 2 to 120 sec.

The relative durability of the test vanes was evaluated by numerical integration of the erosion of each vane and correlation with the power-time exposure in the test anode. The depth of erosion at the side of the vane was measured at 0.01-in. intervals along the vane length, and the total erosion area in this plane was then approximated by Simpson's rule. Because in many instances the erosion varied across the vane thickness the integration was repeated for the opposite vane face and the areas summed.

The total erosion thus measured was an index of the *relative* durability of the vanes tested and not an absolute indication of the volume of metal eroded. Because of the varying eccentricity of the test cathode during each test, one vane of each pair being tested was usually more heavily eroded than its diametrical opposite in the anode. The relative durability was then determined from the average erosion of the two vanes.

Relative durability of the vanes is defined empirically as

$$\mu = \frac{\phi_{PK} t}{\sigma}$$

where

ϕ_{PK} = peak pulse power, megawatts per sq in.
t = time, sec
σ = relative erosion
μ = relative durability index

Since each set of vanes was pulsed at varying power levels for different lengths of time, the $\phi_{PK} t$ product for each test was obtained by summing the individual products for each power level during the test. The results are shown in Table 2. The test vanes of sprayed tungsten and Hevimet were not evaluated.

Table 2 Relative durability of vane-face materials

Vane-face material	Units of erosion, Vane No. 1	Vane No. 2	Power-time product, $\phi_{PK}t$ mw-sec/sq in.	Relative durability, μ
Tungsten	16	368	5000	4.180
Molybdenum	Nil	517	2829	1.740
Elkonite 20W3	257	632	1490	0.537
Elkonite 1W3	24	2875	350	0.094
Copper[a] (no windows)	330	337	727	0.350
Copper	230	2650	691	0.077

[a] Results for this solid-copper vane are included as a matter of interest. The durability factor, however, cannot be compared directly with those of the other vanes tested.

Conclusion

The experimental values of μ compare well with the analytical results. The tungsten-faced vanes are roughly two orders of magnitude better than copper. Although this improvement could have been anticipated from the calculations and from the high melting point of tungsten, it was felt that because the thermal conductivity of tungsten is so much lower than that of copper, the temperature rise might outweigh the high melting point. The experimental data, however, verified the analytical work. On the basis of these results the thickness of the tungsten face was reduced from 0.014 to 0.009 in. Subsequent tests of the new design showed no erosion at full power.

The results for the Elkonite disproved the original assumption of a sustaining tungsten lattice, and indicated instead that the copper content of these materials is the bond for random tungsten particles. Therefore it might be possible to produce a more durable tungsten-copper combination by use of a technique employed in machining certain types of impregnated cathodes; that is, by first pressing and sintering pure tungsten to the desired density, then impregnating with copper.

Contrary to the plotting-paper analog result, most of the erosion occurred over the window areas. This intense localized erosion is attributed to the peculiarities of the test diode rather than the thermal block formed by the windows, because solid vanes without windows were most heavily eroded in the same area.

Acknowledgment

The authors are particularly indebted to Donald E. Nelson, Carl L. Sonnenschein, and Victor J. Stein of the RCA Electron Tube Division for their guidance and encouragement in this study.

APPENDIX

Making the substitution $\lambda = \dfrac{x}{2(k\tau)^{1/2}}$

$$U(x, t) = Lt + \frac{x}{K}(k/\pi)^{1/2} \sum_{\eta=1}^{\infty} \int_{\frac{x}{2(kt)^{1/2}}}^{\infty} \frac{\phi(t - \eta x^2/4K\lambda^2)}{\lambda^2} e^{-\lambda^2} d\lambda, \qquad x > 0 \quad (10)$$

The most important case is for $x = 0$, that is, the face of the vane.

$$U(0, t) = L + \frac{1}{K}(k/\pi)^{1/2} \sum_{n=1}^{\infty} \int_0^t \frac{\phi(\tau)}{(t - n\tau)^{1/2}} d\tau \quad (11)$$

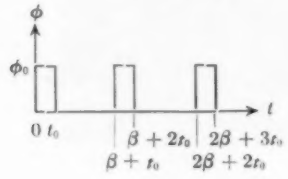

$$\begin{aligned}
&\phi(\tau) = \phi_0 && 0 < t < t_0 \\
&\phi(\tau) = 0 && t_0 < t < \beta + t_0 \\
&\phi(\tau) = \phi_0 && \beta + t_0 < t < \beta + 2t_0 \\
&\phi(\tau) = 0 && \beta + 2t_0 < t < 2\beta + 2t_0 \\
&\phi(\tau) = \phi_0 && 2\beta + 2t_0 < t < 2\beta + 3t_0
\end{aligned}$$

$$U(0, t) = L + \frac{\phi_0}{K}(k/\pi)^{1/2} \sum_{n=1}^{\infty} \left[-\frac{2}{n}(t - n\tau)^{1/2} \right]_0^{t_0}, \quad x = 0 \quad (12)$$

$$U(0, t) = L - \frac{2\phi_0}{K}(k/\pi)^{1/2} \sum_{n=1}^{\infty} \left[\frac{1}{n}(t - nt_0)^{1/2} - \sqrt{t} \right]$$

$$U(0, t) = L - \frac{2\phi_0}{K}(k/\pi)^{1/2} \left\{ \left[(t_0 - t_0)^{1/2} - \sqrt{t_0} \right] + \frac{1}{2}\left[(\beta + 2t_0 - 2t_0)^{1/2} - \sqrt{(\beta + 2t_0)^{1/2}} \right] + \frac{1}{3}\left[(2\beta + 3t_0 - 3t_0)^{1/2} - (2\beta + 3t_0)^{1/2} \right] + \cdots \right\}$$

$$U(0, t) = L + \frac{2\phi_0}{K}(k/\pi)^{1/2} \left[(t_0)^{1/2} + \frac{1}{2}\left[(\beta + 2t_0)^{1/2} - \sqrt{\beta} \right] + \frac{1}{3}\left[(2\beta + 3t_0)^{1/2} - (2\beta)^{1/2} \right] + \cdots \frac{1}{n}\left\{ \left[(n - 1)\beta + nt_0 \right]^{1/2} - \left[(n - 1)\beta \right]^{1/2} \right\} \right]$$

References

1 Churchill, "Modern Operational Mathematics in Engineering," McGraw-Hill Book Company, Inc., New York, N. Y., 1944, pp. 107–109.

2 Peirce, "A Short Table of Integrals," Ginn and Company, Boston, Mass., third edition, 1929, pp. 116–119.

3 Ingersoll and Zobell, "Heat Conduction," McGraw-Hill Book Company, Inc., New York, N. Y., 1948, pp. 45–50, pp. 200–205.

4 Moore, "Heat Transfer Notes for Electrical Engineering," Ann Arbor, Mich., 1951, pp. 3–5, pp. 9–10.

5 S. Timoshenko, "Theory of Elasticity," McGraw-Hill Book Company, Inc., New York, N. Y., 1934, pp. 210–212.

The Failure of Structural Metals Subjected to Strain-Cycling Conditions

R. W. SWINDEMAN

D. A. DOUGLAS

Metallurgy Division, Oak Ridge National Laboratory, Oak Ridge, Tenn.[1]

Data showing the isothermal strain-cycling capacity of three metals, Inconel, Hastelloy B, and beryllium are presented. It is noted that at frequencies of 0.5 cycle per min the data satisfied an equation of the form $N^{\alpha}\epsilon_p = K$, where N is the number of cycles to failure, ϵ_p is the plastic strain per cycle, and α and K are constants whose values depend on the material and test conditions. Data on Inconel are given to establish the effect of grain size, specimen geometry, temperature, and frequency. It is found that, at temperatures above 1300 F, grain size and frequency exert a pronounced effect on the rupture life. Fine-grained metal survives more cycles before failure than coarse-grained material. Long time cycles shorten the number of cycles to failure when the strain per cycle is low. Thermal-strain-cycling data for Inconel are compared to strain-cycling data at the same mean temperature. Good correlation is found to exist between the two types of tests.

Introduction

MANY OF THE failures encountered in engineering devices result from dynamic loads which are imposed on the structure either mechanically or thermally. Most often, fatigue failures are considered to be the result of rapidly fluctuating stresses which introduce damage in the material on a very microscopic scale. Thus in low-temperature fatigue, no bulk plastic straining of the metal can be discerned. However, at elevated temperatures, where relaxation of stress can occur, measurable amounts of plastic strain may be induced during each stress reversal. This is particularly true in the case of restrained structures when they are subjected to large thermal fluctuations. Quite often, under such conditions, the thermally induced stresses occur over relatively long time cycles and are large enough to exceed the elastic limit of the metal. Thus in studying the behavior of materials loaded in this manner it is more meaningful to think of the metal as experiencing a number of strain reversals which ultimately lead to failure, rather than to attempt to base such failures on an indeterminate stress state. It is this problem of thermal strain fatigue which will be discussed in this paper.

Recent studies have revealed that the plastic-strain history of a metal under dynamic load conditions provides extremely useful data for calculating the metal life consumed and the service life remaining under expected operating conditions. This idea was conceived by Manson [1][2] and then demonstrated experimentally by Coffin [2] by thermally cycling stainless steel under conditions of restraint until failure occurred. The relationship between plastic strain and cycles to failure was found to be of the form $N^{\alpha}\epsilon_p = K$ where N is the cycles to failure, ϵ_p is the strain per cycle, and α and K are constants which depend on the material and test conditions.

Most of the subsequent work has been within the temperature range where the rate of work-hardening was appreciably greater than the recovery rate. The work to be discussed in this presentation concerns metals at temperatures where creep and relaxation are the dominant factors.

Equipment

The fact that creep and relaxation are dominant in the temperature range of interest made it both feasible and attractive to substitute mechanical loads for thermal fluctuations as a means of producing strain cycles. The apparatus used at the Oak Ridge National Laboratory has been previously described in detail [3, 4] and is represented by the schematic drawing in Fig. 1. By use of pneumatic pressure on the piston, strain in tension and compression can be imposed on both rod and tubular specimens. The strain amplitude is controlled either by a rigid reference member or by a motion-transmitter device which actuates solenoid valves, when the strain reaches a preset value. The plastic strain can be measured in any desired cycle by bleeding off all pressure in the piston chamber and directly reading the displacement from the zero position of the dial gage. As part of this investigation, additional testing of specimens is being carried out at the University of Alabama under the direction of Dr. W. D. Jordan of the Mechanical Engineering Department. In this program, which is sponsored by the ORNL, tubular specimens are thermally cycled in test devices which are modifications of the one described by Coffin [5] in his original work. Thus by utilizing each of these types of test apparatus, it is possible to explore separately the effects of material variables, thermally and mechanically produced strains, geometry of specimen, temperature, and frequency.

Results and Discussion

Most of this investigation has been conducted with Inconel as the test material; however, a few tests were made using Hastelloy B and beryllium. Thus representative data can be compared between metals of quite widely different degrees of strength, ductility, and fabrication history. In Fig. 2 are conventional plots of the plastic strain per cycle ϵ_p versus N, the number of cycles to failure. The co-ordinates are plotted on logarithmic scales so that if Manson's relationship $N^{\alpha}\epsilon_p = K$ is satisfied, the data points should define a straight line. It is apparent that this con-

[1] Operated by Union Carbide Corporation for the Atomic Energy Commission.

[2] Numbers in brackets designate References at end of paper.

Contributed by the Metals Engineering Division and presented at a joint session with the Joint ASTM-ASME Committee on Effect of Temperature on the Properties of Metals at the Annual Meeting, New York, N. Y., November 30–December 5, 1958, of THE AMERICAN SOCIETY OF MECHANICAL ENGINEERS.

NOTE: Statements and opinions advanced in papers are to be understood as individual expressions of their authors and not those of the Society. Manuscript received at ASME Headquarters, September 2, 1958. Paper No. 58—A-198.

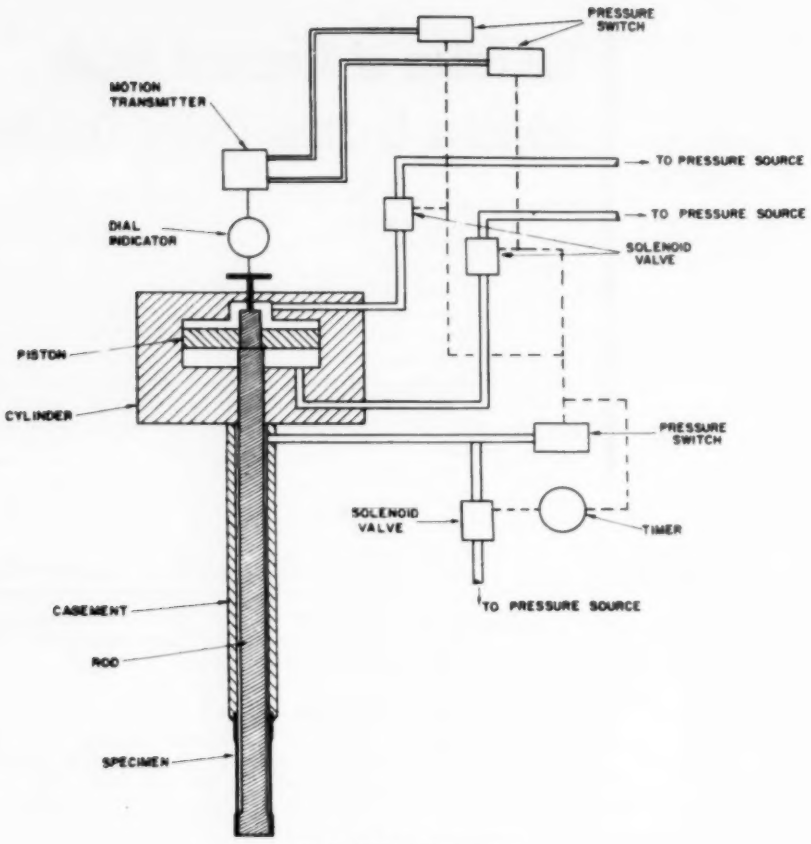

Fig. 1 Strain cycle apparatus

dition is satisfied for each material, but it is also evident that there is a variation in the slope of the line from one metal to another. These slopes are approximately +0.58 for Hastelloy B, +0.76 for Inconel, and +0.81 for beryllium. Such values are in contrast to the findings of Coffin [6] who shows α to be very nearly +0.5 for several different metals, all tested at temperatures below 1200 F.

It also has been noted that, for any given material, K can be varied by changes in the metallurgical structure. Fig. 3 is a plot of the strain-cycling properties of Inconel rod specimens machined from the same heat but differing in the annealing treatment before test. The specimens given an anneal of 1650 F had a finer grain size and were much more resistant to fracture than the specimens given a 2050-F anneal prior to test. Comparative data for rod material at 1300, 1500, and 1600 F, which has been reported previously in the literature [4], indicate that grain-size effects are most pronounced at 1500 and 1600 F. At 1300 F, however, coarse and fine-grained materials have nearly identical strain-cycling properties. Inconel is a solid-solution-type alloy which is not subject to phase changes or aging reactions so that this difference in behavior seems clearly dependent on the relative grain size. It is also noteworthy that the slopes of the two lines are parallel and thus the α-value is consistent for both types of specimens.

The question of whether specimen geometry seriously affects the strain-cycling properties also merits consideration. In Fig. 4, the strain-cycling properties at 1500 F of rod and tube specimens are compared. Tube data fall slightly short of the rod curve but this may be attributed to two factors: (*a*) There is a difference in the method of sensing failure inasmuch as the tubes are considered to fail when the first crack propagates through the wall whereas rods are tested to complete failure; (*b*) the rod specimens possess a slightly finer grain size than the tube specimens. The tube data shown include test results from two different heats of metal and the agreement indicates that the cycling properties are not particularly sensitive to small variations in alloy composition.

Naturally one of the most important considerations in regard to test variables is the influence of temperature on the number of cycles to failure. This is particularly important where it is desired to apply isothermal mechanical strain-cycling data to design problems where thermal cycling is involved. In Fig. 5 are plotted the results for tests at 1300, 1500, and 1600 F. The band represents the scatter of points obtained on an extensive test program of tubes and rods at 1500 F. Nearly all of the data for rods at 1300 F and tubes at 1600 F fall inside this band. The 1600-F rod data fall consistently above the band, but this is due to the grain-size effect previously mentioned. It appears, therefore, that within this particular range there is no major change in fracture behavior as a function of temperature. The fact that Inconel is metallurgically stable, that no grain growth occurs, and that the deformation mechanism is uniform throughout this span are important points to bear in mind when considering these results.

Since temperature appears to have no major influence on the number of cycles to fracture from 1300 to 1600 F, it would appear reasonable to expect mechanical strain-cycle results under isothermal conditions to correlate with those obtained by thermally

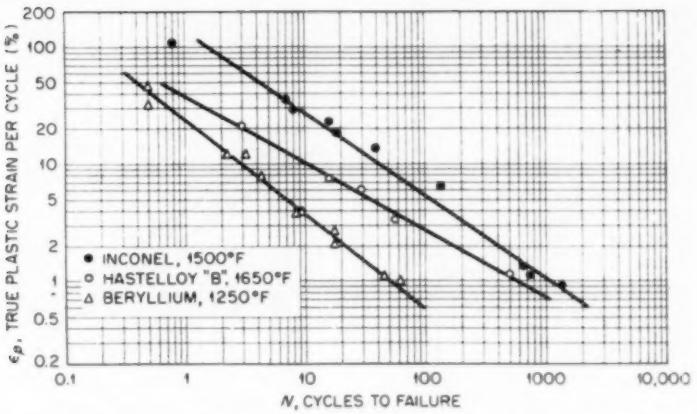

Fig. 2 Comparison of strain-cycling properties of Inconel, Hastelloy B, and beryllium

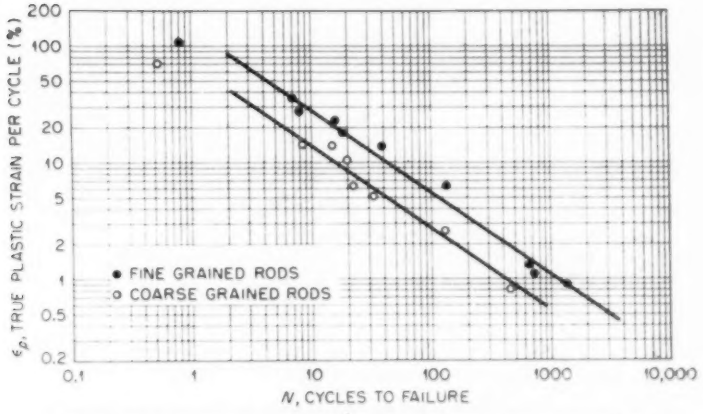

Fig. 3 Effect of grain size on strain-cycling properties of Inconel at 1500 F

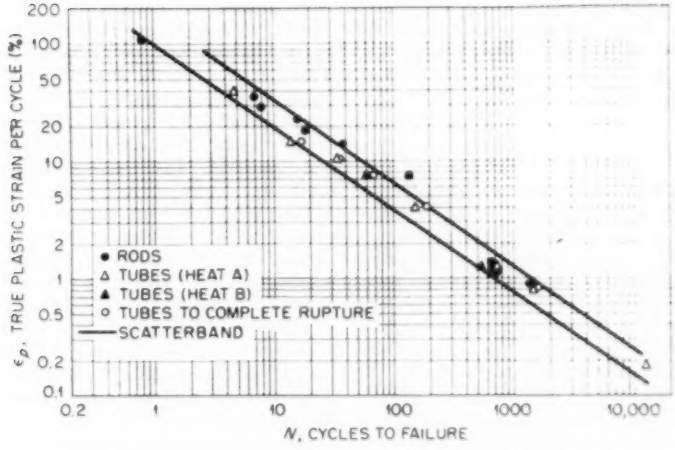

Fig. 4 Strain-cycling properties of Inconel tubes and rods at 1500 F

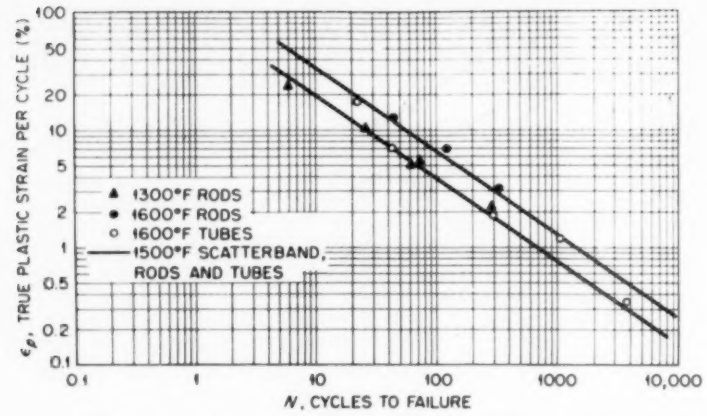

Fig. 5 Effect of temperature on strain-cycling properties of Inconel

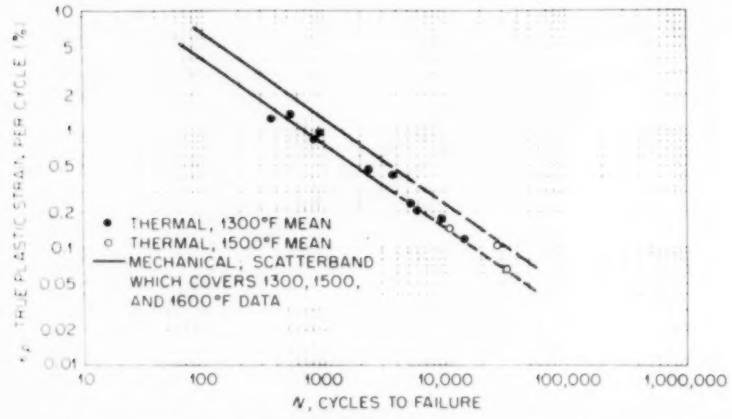

Fig. 6 Comparison of thermal and mechanical strain-cycling properties of Inconel

cycling about a corresponding mean temperature. In Fig. 6 are data illustrating the validity of this assumption. The thermal excursions about the 1300 F mean covered the range from 1000 to 1600 F. At the 1500 F mean the temperature extremes were 1400 and 1600 F. It is evident that in the absence of metallurgical instabilities a metal responds to the mechanically produced strain in the same manner as to one thermally induced.

Frequency

One very important variable to be considered in studying the effect of dynamic loads on the behavior of metals at elevated temperatures is that of frequency. It is well known that the test frequency can be changed over a wide range without producing a marked effect on the *S-N* curve in low-temperature fatigue tests. On the other hand, several investigators have found that frequency does exert an influence on the cycles to rupture at high temperatures. This is especially true at lower frequencies where creep or relaxation may become active. Moore and Alleman [7] have conducted fatigue studies for 0.17 per cent carbon steel at 1200 F employing two frequencies; namely, 200 and 2500 stress cycles per min (cpm). Specimens cycled at the high frequency of 2500 cpm, outlasted the low-frequency test by a factor of 10.

Hyler [8] has conducted fatigue studies on Inconel at 1200 and 1600 F, using frequencies of 60 and 600 cpm. He observed essentially no difference in the *S-N* diagram at 1200 F but an appreciable frequency effect was seen at 1600 F. Specimens cycled at 600 cpm endured 10 times more cycles than those at the lower frequency. Fatigue studies on lead have yielded similar results. Dolan [9] reports data for reversed-flexure fatigue tests on lead at room temperature for frequencies of 1, 6, 44, and 248 cpm. Curves relating the strain per cycle and the number of cycles to rupture were determined for each frequency. A comparison of the curves revealed that the cycles to rupture increase with increasing frequency. Unfortunately the strain values range only from 0.1 to 1 per cent and the reported strains include both elastic and plastic components.

Since the plastic strain per cycle was not determined in any of these studies, the direct use of these data for studying the frequency effect on the strain-cycling behavior is not possible. The results, however, raise the question of whether or not the difference in the plastic strain absorbed could explain the variation in properties with frequency. Since plastic strain is generally considered a reliable measure of damage to a structure it would appear that specimens strained within the same limits of plastic deformation should survive an equivalent number of cycles before fracture, regardless of the rate at which the strain is introduced. However, since design problems involving temperature fluctuations are often concerned with slow thermal cycles, a series of tests to investigate frequency effects was initiated.

The majority of the data discussed previously was obtained using a constant load, thus the specimen creeps until the limiting

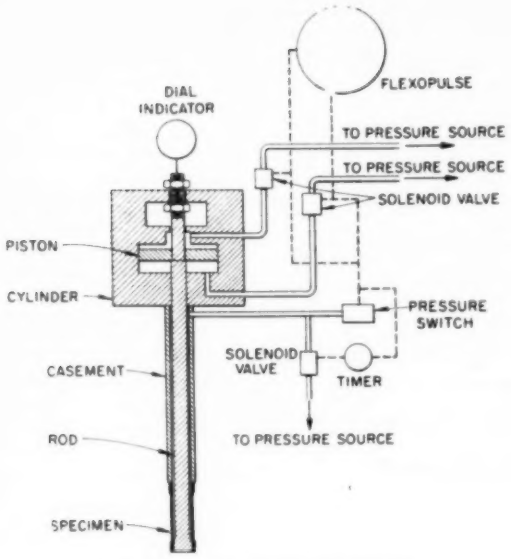

Fig. 7 Strain-cycle apparatus (modified)

strain condition is reached in the desired time interval. This type of test is quite easy to regulate for short time cycles, but the prescribed load required to produce specific strains in 10 or 30 min is difficult to obtain. Thus a slight modification of the equipment was made to provide adjustable but rigid reference limits as shown in Fig. 7. In this test the specimen is strained to the selected limit very rapidly and held at this strain for the selected time interval. During this period the elastic strain is gradually converted into plastic strain by the relaxation process. It is therefore quite simple to control frequency and vary it from times as short as $^1/_2$ min per cycle up to whatever time cycle seems practical. The plastic strain in any given cycle can be measured as before by releasing the load so that specific values are obtained. In Fig. 8 is a comparison of results obtained by the creep method and the relaxation method. Since creep and relaxation are manifestations of the same deformation phenomena the excellent correlation shown between the two types of tests was expected.

Fig. 9 presents the data from a series of tests at 1500 F using the standard 2-min-per-cycle period in comparison with results when a 30-min-time cycle was used. At the high percentages of plastic strain per cycle, good correlation exists, but a significant deviation is clearly shown for the low strain values. The data for 1650 F at 30 mpc follow a trend similar to that at 1500 F, but at 1300 F, as shown in Fig. 10, the only test point which falls outside of the 2-min-per-cycle data occurs below 1 per cent strain and even here the deviation is not appreciable.

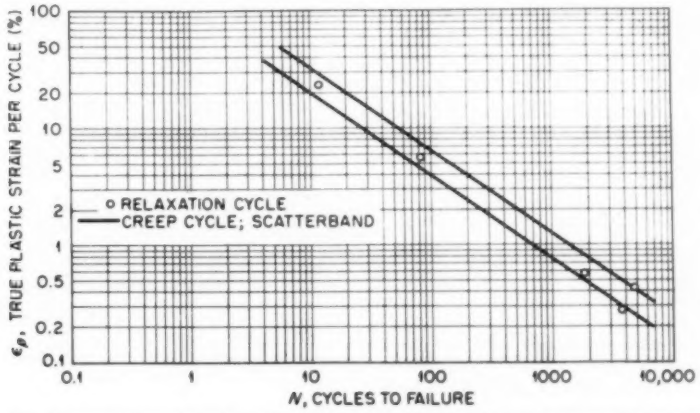

Fig. 8 Comparison of strain-cycling properties of Inconel subjected to creep and relaxation cycles at 1500 F

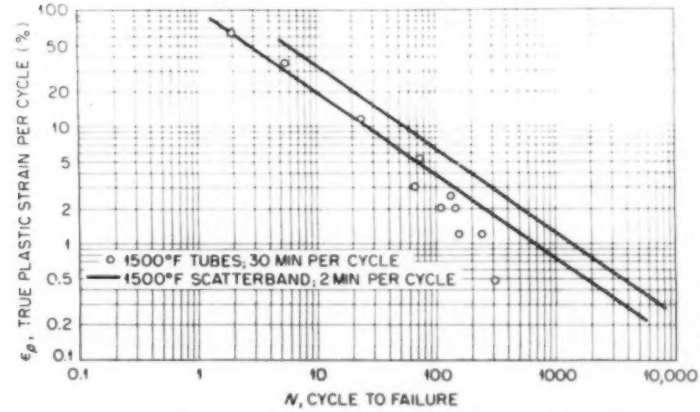

Fig. 9 Effect of frequency on strain-cycling properties of Inconel at 1500 F

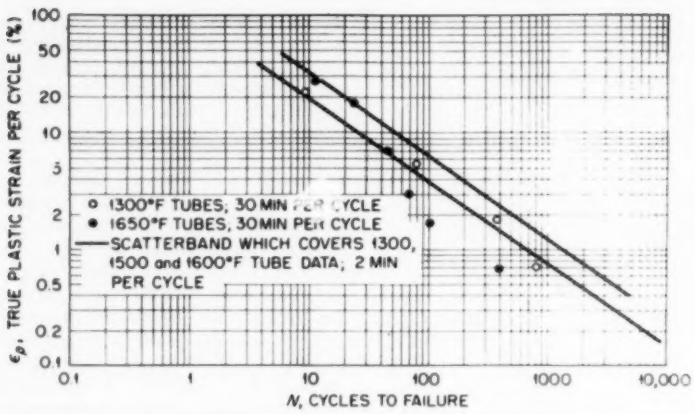

Fig. 10 Effect of temperature on strain-cycling properties of Inconel tested at 30 min per cycle

There is, of course, considerable engineering interest in the fact that, for the same amount of repeated plastic deformation, a metal subjected to slowly fluctuating loads will survive for only a fraction of the cycles of a specimen cycled more rapidly. This is especially important since the frequency appears to exert the greatest influence for values of strain below 2 per cent which are also equivalent to the thermal strains most often encountered during service. There is no evidence to indicate that the longer thermal exposure encountered in the low-frequency tests is detrimental so it must be concluded that the mechanisms controlling fracture at high temperatures are strongly influenced by time as well as plastic flow.

Conclusions

This investigation into the high-temperature behavior of metals under dynamic loads reveals the following significant points:

1 The relationship $N^{\alpha}\epsilon_p = K$ is verified for several metals at elevated temperatures providing that the cycle time is relatively short. The exponent α is found to be dependent on the material and varied from +0.58 to +0.81. Since many metals have exhibited a slope of +0.5 in low-temperature tests the greater slopes seen at the high temperatures indicate a dependence on temperature or deformation mechanism rather than directly on material composition. In this study Inconel is shown to have no significant variation in α over a 300-F range, which suggests that the deformation mechanism is the major factor affecting the slope. Thus there may be a break in the strain-cycling curve similar to the one observed for the equicohesive temperature in creep. The K-factor is found to be changed significantly by changes in grain size; thus it is believed that the displacement of the rupture curve can be attributed to metallurgical changes.

2 Metals respond in the same manner to plastic strain whether it is introduced by thermal changes or mechanically imposed loads. This statement must be qualified to the extent that the deformation mechanism and metallurgical structure must not be altered by the temperature fluctuations.

3 There is a marked change in the number of equivalent strain cycles a metal can survive as a function of the rate at which the strains are reversed. This phenomenon is apparently confined to the high-temperature region and establishes the fact that plastic deformation is not the sole mechanism controlling the fracture life of a metal.

Acknowledgments

The authors would like to acknowledge the contributions of K. W. Boling, E. Bolling, and E. B. Patton of the Mechanical Properties Group in performing the tests.

References

1 S. S. Manson, "Behavior of Materials Under Conditions of Thermal Stress," NACA TN 2933, 1953.

2 L. F. Coffin, "A Study of the Effects of Cyclic Thermal Stresses on a Ductile Metal," TRANS. ASME, vol. 76, 1954, p. 931.

3 J. R. Weir, R. V. Meghreblian, and D. A. Douglas, "High Temperature Properties in Relation to Design," Proceedings of the Third Sagamore Conference, 1956, p. 441.

4 C. R. Kennedy, "Plastic Strain Absorption as a Criterion for High Temperature Design," Proceedings of the Fourth Sagamore Conference, 1957, p. 193.

5 L. F. Coffin and R. P. Wesley, "Apparatus for Study of Effects of Cyclic Thermal Stresses on Ductile Metals," TRANS. ASME, vol. 76, 1954, p. 923.

6 L. F. Coffin, "Strain Cycling and Thermal Stress Fatigue," Proceedings of the Fourth Sagamore Conference, 1957, p. 219.

7 H. F. Moore and N. J. Alleman, "Progress Report on Fatigue Tests of Low-Carbon Steel at Elevated Temperatures," *Proc. ASTM*, vol. 31–1, 1931, p. 114.

8 W. S. Hyler, Battelle Memorial Institute, unpublished work.

9 T. J. Dolan, "How Can We Appraise for High-Temperature Service?", *Metals Progress*, vol. 61–3, 1952, p. 55.

DISCUSSION

L. F. Coffin, Jr.[3]

The authors have presented a most interesting and timely paper on the resistance of certain metals to cyclic strain at very high temperatures. There are two points of particular interest to the writer contained in this paper, one the comparison of thermal and mechanical strain cycling data and the other, the effect of speed of cycling on the low cycle fatigue resistance of metals.

With respect to the comparison of thermal and mechanical strain cycling, it is reassuring to note that the authors find the differences encountered to be small, Fig. 6. The writer has compared the mechanical and thermal strain fatigue resistance of AISI Type 347 stainless steel [6] on the basis of the plastic

[3] Metallurgy and Ceramics Research Department, General Electric Company, Schenectady, N. Y. Mem. ASME.

strain range and found a noticeable difference in behavior between the two types of cycling, such that for a given plastic strain range, the constant temperature tests at 350, 500, and 600 C withstood a greater number of cycles to failure than test specimens subjected to constrained cyclic temperature, the mean value of which was 350 C. It is of interest to note further that the curves of plastic strain range versus cycles to failure were in all cases straight lines having the slope of $-1/2$. This is equivalent to $\alpha = 1/2$ using the authors' notation. The causes of possible differences between the two types of tests were discussed in detail [6] to justify the belief that the two types of tests should be equivalent in terms of the plastic strain range. Included were such factors as difference in specimen material and geometry such as size and surface area, and temperature distribution. It appears to the writer that the same sources of difficulty exist in the present tests. In particular longitudinal temperature variations in the thermal stress tests lead to unmeasured strain concentrations. Thus the conclusion that response of the material to these two types of strain is not felt to be fully justified. Before complete confidence can be placed in the assumption of the equivalence in mechanical and thermal cycling tests, still greater care will be required than heretofore in performing the comparative tests.

With respect to the effect of frequency of cycling, or more accurately the hold time, on the low cycle fatigue resistance of metals, the presentation of information in this area is most welcome. That the hold time could be important in thermal cycling was noted by the writer (Reference [2], Fig. 26) for AISI type 347 stainless steel. Recently we have been giving more attention to this problem, particularly since it is of such importance to systems subjected to infrequent reversals in loading which operate at temperatures where time-dependent processes are important. This may be of interest here, particularly since it might help to clarify differences in the exponent α from 0.5.

It has been observed [6, 10][4] that, for a large number of metals, cyclic-strain fatigue data can best be represented by the relationship $N^{1/2}\Delta\epsilon_p = C$ regardless of the metal, the temperature of test (provided time-dependent processes are not operative), and the manner of testing. Further, the constant C could be determined by substituting, at $N = 1/4$, the fracture ductility defined as the true strain at fracture for the plastic strain range. Thus the low cycle fatigue curve could be reliably predicted from a knowledge only of the fracture ductility and the slope of $-1/2$. Although it is not now known why such a relationship between cyclic and monotonic loading exists, nevertheless considerable use can be made of the fact.

In the case of materials subjected to cyclic strain at temperatures where creep and other diffusional processes can occur, it is of interest to speculate as to the reliability of the above relationship. It is well known that the ductility of metals obtained from a stress rupture test is generally reduced as the time of test is increased, although eventually the ductility may again rise. It would be expected then that the ductility changes should be of influence in low cycle fatigue tests when the time for failure in low cycle fatigue is comparable to those producing ductility decreases in stress rupture. This is particularly so, since, during the hold time, the deformation process is predominantly relaxation and hence time dependent. Thus a knowledge of the ductility-time for rupture behavior at any temperature would be of value in predicting the fatigue resistance of metals where failure times become long. In Fig. 11 is shown a construction which may be of benefit in explaining how the ductility decrease would affect the cyclic plastic strain-cycles to failure curve. To the left at $N = 1/4$, the open circles represent the ductility at various rupture times τ_1, τ_2, τ_3, and τ_4. The dashed lines represent the expected fatigue curves for the particular ductilities at these times. For a particular series of low cycle fatigue tests where each test lasts a different time, the actual result would be given by the solid line. This is obtained by finding, for a particular plastic strain range, that dashed line curve whose ductility is equal to the rupture ductility of the metal obtained for the same time as the cyclic test, and determining from this curve the cycles to failure. The triangles in Fig. 11 represent such points, through which the solid line is drawn.

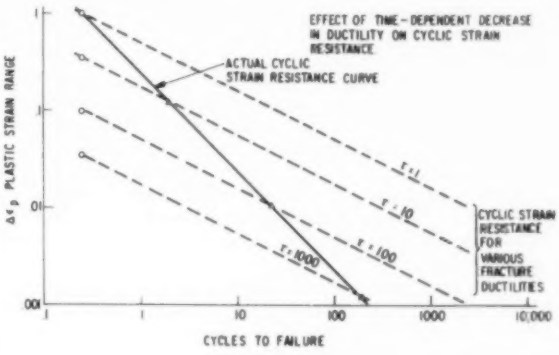

Fig. 11

Thus for high temperatures where, as the authors clearly point out, time-dependent mechanisms occur, it would be expected that the value of α would increase from 1/2 to some higher value, depending on the hold time. The fact that all of the values of α for Inconel are above 0.5 supports this point of view, and further, that, as the hold times are further increased from a period of 2 minutes per cycle to 30 minutes per cycle, the value of α increases further. It would be of interest to see if $\alpha = 0.5$ for low temperatures where time dependent processes are less important. Further the writer wonders how the fracture ductility values defined here appear when plotted on the various curves in the paper for $N = 1/4$ cycles.

With respect to the origin of the relationship $N^{\alpha}\epsilon_p = K$ for predicting failure from low cycle fatigue, like many observations, predictions, and theories it is believed that the form of this relationship was independently developed by Mr. Manson and the writer. The writer arrived at such a relationship while attempting to show that the total plastic strain to failure was constant, which, as it turned out, was not the case. The authors are referred to technical reports from the Knolls Atomic Power Laboratory [11, 12] and prior classified progress reports for earlier references of this work by the writer.

References

10 J. F. Tavernelli and L. F. Coffin, Jr., "A Compilation and Interpretation of Cyclic Strain-Fatigue Tests," ASM 1958 Preprint No. 112.

11 L. F. Coffin, Jr., and R. P. Wesley, "An Apparatus for the Study of Cyclic Thermal Stresses on Ductile Metals," KAPL 820, Knolls Atomic Power Laboratory, Oct. 27, 1952 (unclassified).

12 L. F. Coffin, Jr., "A Study of the Effects of Cyclic Thermal Stresses on a Ductile Metal," KAPL 853, Knolls Atomic Power Laboratory, June 3, 1953 (unclassified).

Ian O. MacConochie[5]

The authors have proved rather conclusively the validity of the equation $N^{\alpha}\epsilon_p = K$ as describing the failure line for some situations. However, the writer would like to suggest a mathe-

[4] Numbers from 10 to 12 in brackets designate additional References at end of this discussion. Other numbers in brackets designate References at end of the paper.

[5] Assistant Professor, School of Engineering, University of South Carolina, Columbia, S. C. Assoc. Mem. ASME.

matical approach to the problem of fatigue while at the same time reminding the reader that the theory has been developed for the idealized case of fatigue of a single crystal. In its present form when not considering the stress gradients within the entire specimen it is suggestive of a very high endurance strength at low number of cycles for a single crystal. It is hoped that in the near future it will be possible to modify the theory to apply it to aggregates of crystals.

The present theory is based upon the knowledge that on each cycle of stress (safe or unsafe) slip occurs between atomic lattices along planes of maximum atomic density. The number of such slippages taking place and the extent thereof depending upon the stress present and the number of stress reversals preceding the given event [13, 14].

On every stress reversal some atomic aggregates interlock on screw and edge defects precluding further slip along those planes. For each atomic lattice which interlocks more strain must be absorbed by the remaining lattices. Stated more precisely:

The number of atomic lattices moving on any stress cycle n is inversely proportional to the number of lattices X which have not moved. That is, as the number of lattices remaining unmoved diminish, the number of lattices moving on each subsequent cycle increases.

For a given crystal made up of a large number of such lattices failure occurs when all the atomic lattices have moved and interlocked on screw or edge dislocations and no other slip is possible.

In stating this mathematically:

Let: B equal total slip (i.e., fully work-hardened)
A equal amount of slip (strain) taking place on the first cycle being a function of temperature, stress applied, and rate of application of stress
X equal amount of slip after n cycles
n equal the number of cycles

Thus:

$A \cdot \dfrac{B}{X}$ is the number of crystals changing on any cycle

or

$$\frac{dX}{dn} = \frac{-AB}{X}$$

dX being the amount of slip taking place in the given cycle and dn being one cycle in this case.

Then:

$$X\,dX = -AB\,dn \tag{1}$$

Integrating:

$$X^2 = -2ABn + C_1 \tag{2}$$

Evaluating constant C_1

when $X = B$, $n = 0$, therefore $C_1 = B^2/2$

Hence: Substituting constant in equation (2) becomes:

$$X^2 = -2ABn + B^2 \tag{3}$$

At failure all the lattices have undergone slip (i.e., $X = 0$)
Equation (3) becomes:

$$n = \frac{B}{2A} \tag{4}$$

For n equal 1, i.e., the first cycle

$$B = 2A$$

Stated in another way, if $A \geqq \dfrac{B}{2}$ the part fails on the first cycle.

Now let S = the stress applied.

As stated A, the amount of slip on the first cycle, is proportional to the stress applied.[6]

Therefore let $A = K$ (constant)$\cdot S$

For failure criteria: (S-n curve)

$$n = \frac{B}{2A} = \frac{B}{2(KS)} \tag{5}$$

Since B, the total number of atomic lattices present, is not known, let K equal $\dfrac{B}{\text{some number}}$; since B is constant, K is still constant.

Equation (5) becomes:

$$n = \frac{B}{2 \cdot \dfrac{B}{\text{number}} \cdot S} = \frac{\text{number}}{2S} \tag{6}$$

To further amplify this theory it will be assumed that the crystals of some metals (such as steel) have an endurance limit. That is, if the stress applied to a crystal is sufficiently low no slip will occur (internally) along the edges of atomic aggregates.

Thus let S_0 equal endurance strength of a crystal, and n becomes $= \dfrac{\text{some number}}{2(S - S_0)}$.

The discusser wishes to acknowledge the assistance of Professor Bickley of the Mathematics Department of Imperial College, London.

References

13 H. C. Gough and H. L. Cox, "Mode of Deformation of a Single Crystal of Silver," *Journal of the Institute of Metals*, vol. 45, no. 1, 1931.

14 M. S. Hunter and W. G. Fricke, Jr., "Metallographic Aspects of Fatigue Behavior of Aluminum," *ASTM Proceedings*, vol. 54, 1954.

Walter Sawert[7]

The authors are to be congratulated for their fine contribution on the subject of low cycle fatigue strength. The results of their work indicates that many variables have to be considered to answer intelligently the question, "How many reversed plastic strain cycles can be tolerated for a component under expected operating conditions?"

The authors do not elaborate on some items which could be important to many readers. (This may be due to the necessity for condensing their work for publication.) For example, in their graphs the authors plot ϵ_{pl}, true plastic strain per cycle, versus N_f cycles to failure. How is true plastic strain per cycle defined?

Also, one gets the impression that the measured plastic displacement Δl has been divided by a given gage length. This procedure, to compute true plastic strain, would be valid only under two assumptions:

(1) The axial temperature distribution over the gage length is uniform.

(2) The plastic straining is uniformly applied over the gage length.

The second assumption might be correct for small plastic strains up to about 10 per cent, but probably not at 100 per cent for a $^1/_2$ or $^3/_4$ of a cycle.

Since grain size effects are pronounced, what are the actual grain sizes of "coarse and fine grain" specimens?

[6] Gough and Cox found that the spacing of slip bands is approximately inversely proportional to the intensity of the shear stress.

[7] Mechanical Metallurgist, EOS-JED-AGT, General Electric Company, Evendale, Ohio. Mem. ASME.

Authors' Closure

The authors appreciate Dr. Coffin's comments, which amplify several points discussed in the paper.

One aspect with which Dr. Coffin appears to take issue is the behavior of metals under conditions where strains are induced thermally as opposed to mechanically induced strains. As pointed out in our paper, under conditions where metallurgical stability exists over the temperature range of the test, the metal behaves the same, regardless of how the strain is introduced. The mechanical strain-fatigue data generated at our laboratory are compared with data obtained by Dr. W. D. Jordan at the University of Alabama, using thermally induced strains. We agree with Dr. Coffin that a system using resistance heating to produce thermal fluctuations will always tend to produce strain concentrations. However, Dr. Jordan has established the distribution of these strains by optical measurements between markers along the gage of the specimens. Also, extensive studies were conducted to determine the temperature profile during cycling, and hysteresis loops were obtained by autographically recording each cycle during the test life. It is a very carefully conceived and executed test program, and it is hoped that these data will be published in the near future. Thus, the authors feel that the excellent correlation between thermal and mechanical strain fatigue tests reported in this paper should not be discounted on the basis of the experimental techniques employed by Dr. Jordan. If Dr. Coffin is serious in his belief that the true strain at fracture in a tensile test and a curve with a slope of $-1/2$ will describe the strain fatigue characteristics of metals, it is difficult to see why it should matter whether the additional strains are induced mechanically or thermally.

This brings up a second point in the discussion, which is the deviation of the data reported in this paper from a slope of $-1/2$. Coffin inquires if α would equal 1/2 at low temperatures for this metal. We believe that this is true, although the upper temperature limit for such a case is not known. The basis for our belief is the data reported by co-workers of Coffin, at General Electric, in which Inconel is shown to exhibit a slope of $-1/2$ in the temperature range from ambient to 800 F. Thus, the construction suggested by Dr. Coffin to explain the high slopes at elevated temperature in terms of the creep ductilities is of interest. It is important in this analysis, however, that the strain-cycling ductility approach the creep ductility for the same strain rate as N approaches 1/4. Second, if the equation $N^{\alpha}\epsilon_p = K$ is to hold, the creep ductility must exhibit a very particular decrease with increasing time.

We have included Table 1 to show the variation in the creep ductility obtained in our laboratory from short-time constant-load tests on Inconel rods at 1500 F. Natural strains calculated from gage length and diametric measurements both indicated that the ductility does not significantly change in the time interval from about 0.1 to 10 hr.

If these data were employed for the construction proposed by Coffin, then the isochronous strain-cycling curve for $\tau = 0.1$ hr would fall very near $\tau = 1$, and $\tau = 10$, while $\tau = 100$ would be significantly below these curves. The constant frequency curve would therefore exhibit a slope of $-1/2$ for times ranging from 0.1 to 10 hr and thereafter show a gradual increase in the range where the isochronous curves are not coincident.

In addition, one must be cautious in attempting to employ tensile or constant-load creep data in such an analysis. The fracture ductility obtained from either measurement, gage length or diametric, does not truly reflect the ductility which should be associated with the strain-cycle life. When the creep ductility is high, the stress increases with the creep strain, thereby shortening the life. Moreover, if necking occurs, it will produce strain concentrations in the gage length as well as increase the strain rate and the ductility in the neck.

Table 1 Creep ductilities for fine-grained Inconel rods tested at 1500 F

Time to rupture, hr	Ductility, ϵ_f: Diametric measurement,[a] %	Ductility, ϵ_f: Gage length measurement,[b] %	Environment
0.083	175	49	Air
0.096	181	54	Air
0.175	183	74	Argon
0.594	210	72	Air
0.71	167	68	Argon
1.0	207	70	Air
1.3	221	78	Air
1.6	207	60	Air
5.5	169	67	Argon
34	122	68	Argon
175	39	35	Argon
Tensile test (0.05 in/in/min)	225	75	Air

[a] $\epsilon_f = 2 \ln \left(\frac{D_0}{D} \right)$

[b] $\epsilon_f = \ln \left(\frac{l}{l_0} \right)$

In strain fatigue, necking does not normally occur and, for ϵ_p less than 20 per cent, the stress is effectively constant throughout the test. Thus, we feel that the ordinary tensile and creep ductilities are not adequate criteria for predicting strain-fatigue results.

Finally, in regard to the matter of references, the authors wish to emphasize that they certainly had no intention of depreciating the originality or the significance of the many contributions which Dr. Coffin has made in the field of thermal-strain fatigue. The references are listed in the order that they came to the authors' attention and, as always, this runs the risk of unintentionally slighting some deserving person. Actually, the personnel at the Oak Ridge National Laboratory have borrowed heavily from the ideas and information reported in the literature by both Mr. Manson and Dr. Coffin. It is our hope that they both are as original and as productive in the future so that we may continue to remain in their debt.

The authors appreciate Professor MacConochie's suggestions on a mathematical approach to the problem of fatigue. However, we would like to suggest a number of difficulties which we are sure Dr. MacConochie is aware of but may not be readily apparent to every reader.

1 It is assumed that work hardening takes place and that fracture occurs when each crystal has slipped ($X = B$).[8]

2 Likewise it is assumed that there is a finite endurance limit for the metal under study. Once again one must remember that at high temperatures where time-dependent deformations can occur, such an assumption is not valid.

Thus the authors wish to caution the reader that one must always differentiate between theories which are applicable where low-temperature behavior exists in contrast to conditions where high temperature or time-dependent flow can occur.

Mr. Sawert's inquiry regarding the definition of the true plastic strain per cycle ϵ_p is appreciated. This quantity is considered to be the sum of the tensile and compressive strains without regard to sign. For greater than one cycle

$$\epsilon_p = 2 \ln \left(\frac{l_{\max}}{l_{\min}} \right) \times 100$$

[8] While it is true that in high-frequency fatigue tests the hysteresis loop may show some narrowing, in low-cycle fatigue, especially at high temperatures, work hardening is not always observed. Moreover, even at low temperatures there is increasing evidence that the number of slip planes does not significantly increase after the first few cycles.

where l_{max} and l_{min} are the maximum and minimum lengths, respectively. For tests lasting less than one cycle, however, where the first $^1/_4$ cycle is in compression, the tensile and compressive strains must be summed and "normalized" to obtain the equivalent strain in a full cycle. Thus

$$\epsilon_p = \left[\ln\left(\frac{l}{l_{mn}}\right) + \ln\left(\frac{l_f}{l_{mn}}\right)\right]\frac{100}{N}$$

where l is the initial length, l_f is the length at fracture, and N is the cycle fraction. This assumes that the maximum tensile and compressive strains will be the same and that no necking or buckling occurs. One way to obtain a strain of 100 per cent per cycle in a specimen with a $^1/_2$-in. gage length would be to introduce 22 per cent compression and 28 per cent extension. This is without regard to whether the specimen ever reaches 28 per cent extension from the mean length. Studies have been made of the axial strain distribution along the length of creep and strain-cycling rod specimens. Diametric measurements indicate that no significant strain concentration occurs up to 25 per cent extension.

The ASTM grain size numbers of the fine and coarse-grained tubes were 5 and 1, respectively, and for rods, 7 and 1.

R. B. JERMAN[1]
R. C. WILLIAMS[2]
D. O. LEESER[3]

Evaluation of Material Wear and Self-Welding in Sodium-Cooled Reactor Systems

Laboratory and prototype component tests were made to determine the degree of adhesion and self-welding of various bearing-couple materials in liquid sodium. A few tests were run in nitrogen and in argon. Temperatures were from 500 F to 1000 F and the static loads on the bearing surfaces were up to 10,000 psi. The harder materials showed better wear resistance generally than did the softer materials. However, each material has a service life depending upon the temperature, unit loads, nature of service, and environment.

Introduction

THE SELECTION OF MATERIALS for reactor vessels, piping, and other stationary structural components for a liquid-sodium-cooled reactor is based on strength requirements and compatibility with the sodium coolant. Since the compatibility requirement has been quite adequately satisfied by standard stainless steels, the design of such permanent structural elements is relatively conventional. On the other hand, conventional design usually assumes maintenance and replacement of bearings, whereas in a reactor, replacement of bearings may be prohibitive because of induced radioactivity. Furthermore, bearings operating in a sodium-cooled reactor are subjected to the additional hazard of galling or self-welding. The liquid sodium will remove all traces of film, grease, and oxide from metal surfaces and leave the surface in a very active or nascent condition which will promote the adhesion of two mating material surfaces by providing optimum conditions for interdiffusion or self-welding and galling.

The critical nature of the bearing problem along with the lack of basic test data has prompted designers of both water-cooled and liquid-metal-cooled reactors to essentially bypass the bearing problem. This has been accomplished by an often awkward placement of bearings in low-temperature regions of the reactor, which are usually well above the liquid media. Low loads and low speeds have also been dictated to insure an adequate trouble-free life.

Because of the extreme necessity for positive operation of internal moving parts, the Atomic Power Development Associates, Inc., (APDA) initiated a series of tests to investigate the galling and self-welding of bearing surfaces. The program consisted of a group of laboratory tests conducted by the Allis-Chalmers Manufacturing Company and a group of component and prototype tests performed in the laboratories of The Detroit Edison Company, Allis-Chalmers Manufacturing Company, and Argonne National Laboratories.

Laboratory Tests

1 Experimental Procedure and Test Equipment

The principal objective of the laboratory tests was to determine the adhesion characteristics of various bearing-couple materials, when subjected to slow speeds and moderate bearing loads in liquid sodium. Some additional tests were run in argon and in nitrogen gas. Two types of tests were used; one was a static load test, under liquid sodium at an elevated temperature, to investigate the tendency for direct adhesion. The other type of test was essentially identical, but an intermittent small-angle twist was applied while the bearing couple was under static load.

The external appearance of the apparatus which was used for both the static and the torque tests is shown in Fig. 1. A sectional view of the apparatus which identifies the various parts and shows how the lever arm system was used to apply pressure to the bearing-couple sample is given in Fig. 2. The desired pressure was maintained on the bearing couple by the tension of the spring scale. The two halves of the bearing couple are identified, in Fig. 2, as "specimen cap" and "specimen table"; the cap is 1 inch and the table $2^1/_2$ in. in diameter.

After thoroughly degreasing and cleaning the specimens and test apparatus, the unit was assembled, purged with nitrogen, and

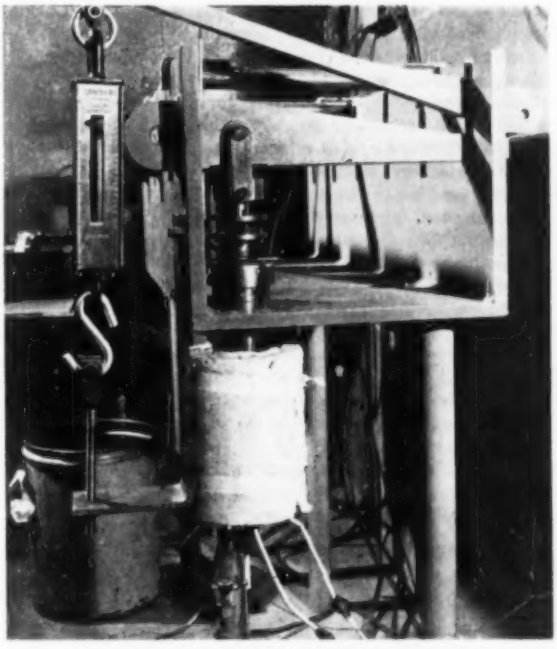

Fig. 1 Sodium-weld test apparatus

[1] Allis-Chalmers Manufacturing Company, Milwaukee, Wis.
[2] Atomic Power Development Associates, Inc., Detroit, Mich.
[3] Atomic Power Development Associates, Inc., Detroit, Mich. Mem. ASME.

Contributed by the Metals Engineering Division and presented at the Annual Meeting, New York, N. Y., November 30–December 5, 1958, of THE AMERICAN SOCIETY OF MECHANICAL ENGINEERS.

NOTE: Statements and opinions advanced in papers are to be understood as individual expressions of their authors and not those of the Society. Manuscript received at ASME Headquarters, November 6, 1958. This paper was not preprinted.

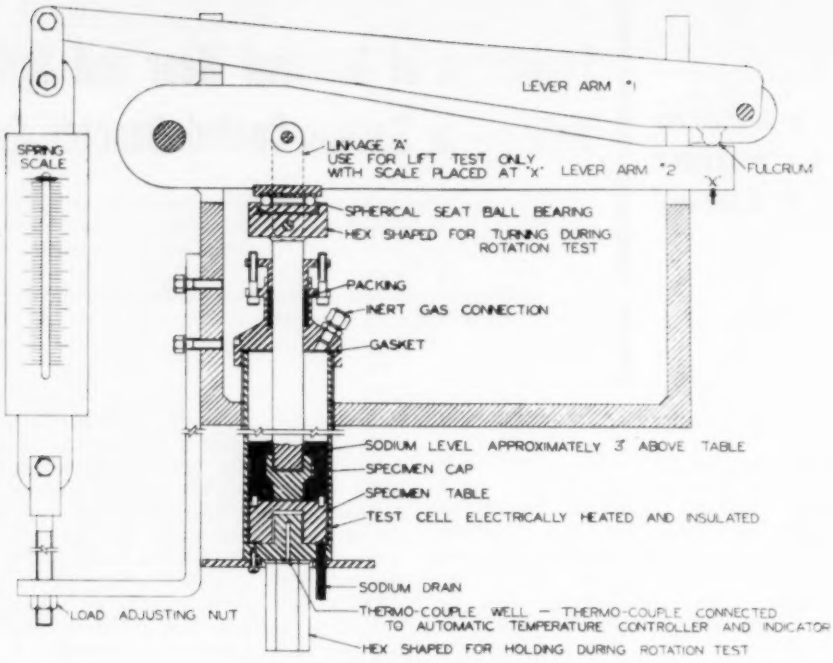
LEVER ARM #1
SPRING SCALE
LINKAGE 'A' USE FOR LIFT TEST ONLY WITH SCALE PLACED AT 'X'
LEVER ARM #2
FULCRUM
'X'
SPHERICAL SEAT BALL BEARING
HEX SHAPED FOR TURNING DURING ROTATION TEST
PACKING
INERT GAS CONNECTION
GASKET
SODIUM LEVEL APPROXIMATELY 3" ABOVE TABLE
SPECIMEN CAP
SPECIMEN TABLE
TEST CELL ELECTRICALLY HEATED AND INSULATED
SODIUM DRAIN
THERMO-COUPLE WELL — THERMO-COUPLE CONNECTED TO AUTOMATIC TEMPERATURE CONTROLLER AND INDICATOR
LOAD ADJUSTING NUT
HEX SHAPED FOR HOLDING DURING ROTATION TEST

Fig. 2 Section view of weld test apparatus

filled with liquid sodium through a tube at the bottom of the unit to a level of $3^1/_2$ in. above the bearing-couple interface.

(*a*) *Static Adhesion Test.* An initial load of 1000 psi was applied to the bearing couple and the temperature of the sodium was raised to 500 F and held for 50 minutes. The load was then removed and the force necessary to lift the cap from the table was measured. This procedure was repeated at 100 F increments, holding the load each time for 50 minutes at temperature prior to determining the adhesion of the cap; 10 additional minutes were allowed for raising the temperature. After the 1000-psi load series was completed, the 500 to 1000 F temperature cycle was run at 2500, 5000, and 10,000-psi loads. The test was discontinued when the 10,000-psi load at 1000 F was reached or when welding occurred, whichever was sooner.

(*b*) *Torque Tests.* The same equipment and temperature-load cycles were used for a series of torque tests. The load and temperature settings were obtained in the same manner as for the static-adhesion tests. When the ambient conditions were reached, the cap part of the bearing-couple was rotated 90 degrees with respect to the table by turning the cap through two 45-deg increments with a 30-sec interval. The cap was turned by means of a hand torque wrench applied to an external hexagonal nut which was attached to the specimen cap through an extension rod, see Fig. 2. The torque loads were read from the 24-in. torque wrench. After 50 minutes at temperature, the cap was once again rotated 90 deg, with respect to the table, in 45-deg increments at 30-sec intervals. This procedure was repeated at the succeeding temperature levels up to 1000 F and at the pressure levels up to 10,000 psi, or until seizure occurred.

II Test Specimens and Materials

The general design of the bearing-couple is shown in Figs. 3 and 4 and consists of the flat surface of the cap pressing against the flat top of the table. Each specimen contact surface was given a 63-rms finish prior to testing; the hard materials tested were ground while the softer materials were machined to this finish. The hardness of all materials was taken on the as-received condition, unless otherwise specified.

The materials chosen for testing, listed in Table 1, were all known to have satisfactory corrosion resistance to high-temperature liquid sodium. The test specimens were fabricated entirely of the base material, and in the cases of surface treatment the test surfaces were either nitrided, hard-faced, or chromium-plated, as indicated in Table 1. The coating of boron nitride in a nickel matrix was tested for the dry lubricant properties of boron nitride. While this coating was wear tested in an argon atmosphere only, several static corrosion tests have indicated acceptable compatibility with liquid sodium at 950 F. The special preparation of this coating is given in a footnote to Table 1.

III Experimental Results and Discussion

Tables 2, 3, 4, and 5 are test data from four of the laboratory bearing-couple tests. These four tests are presented in detail as typical examples of the results obtained. While these data indicate trends of material behavior as a function of load and temperature, the actual test values are not considered to be as significant as the general physical appearance of the surfaces of the specimens after testing, see Figs. 3, 4, 5, and 6. The post-test surface conditions of all of the samples tested are given in Table 1, along with pretest hardness and the maximum temperature, torque, and load levels attained during the individual tests.

While the significance of the actual numbers obtained from the tests, as exemplified in Tables 2 through 5, is not definite because of the difficulty in interpreting the data in terms of test variables, certain features of the data do deserve consideration as indicative of the physical processes occurring during the tests.

(*a*) None of the bearing couples showed any appreciable tendency for direct adhesion during the static load tests. Tables 2 and 3 show a "force-to-lift, 4–6 advantage" column; the numerical value of 20 in this column represents an instrumental constant, and the deviations from 20 are not considered significant. Presumably, the temperature, times, and bearing pressures inves-

tigated were insufficient to precipitate self-welding, however, the time variable alone could completely alter the results.

(*b*) The torque test was a more severe test than the static adhesion test. The results show the influence of at least two variables. The data in Table 1 show the generally improved resistance to galling of the harder materials, although specimen No. 5, as compared to either No. 6 or No. 14, does not follow this generalization. Sample No. 14, however, is complicated by two other factors; first, the superficial Rockwell 15N hardness number may not accurately reflect the true surface hardness of the nitrided surfaces, and secondly, the nitrided surface may in itself be more resistant to wetting by the sodium or may be less subject to galling than a metallic surface. Thus the hardness and the detailed nature of the surface are found to be important variables.

(*c*) The nature of the surface can affect the basic nature of the test in another way. If the surface is sufficiently rough for even minute particles of metal to become detached, the effect may be accumulative and thus lead to widespread galling by an avalanche process. Under these conditions, a material susceptible to galling might be given a sufficiently smooth surface and be operated in a totally grit-free environment, and thus show a normal life, all the while existing in a metastable galling-susceptible condition. On the other hand, a material not susceptible to galling could be put into service with a rough surface and might subsequently polish smooth, or if accidentally subjected to grit would clear itself. Certain of the samples appear to fall into these two distinct categories.

Table 4 shows a very pronounced decrease in coefficient of friction, for sample 14A, from about 1.4 to 0.04 during testing, and it is suggested that this resulted from the polishing down of the original 63-rms surface to a smoother surface. Table 5, shows some reduction in coefficient of friction for sample 14B, but it is not as marked as for sample 14A. Likewise, the physical appearance of 14B is rougher than that of 14A, as shown in Figs. 4 and 5. On the other hand, Table 2 shows about a constant coefficient of friction for a moderately successful test, sample No. 6, and Table 3 shows a rapidly rising coefficient of friction for a very poor bearing-couple, sample 8.

(*d*) It would be desirable to know something further concerning the direct effect of sodium on the characteristics of the bearing-couples. Although the data are entirely insufficient to substantiate a firm statement, the results of tests 15A and 15B show a distinct advantage of running this particular couple in sodium rather than in nitrogen. Tests 1 and 2 might have provided further information, however, since they had differing initial hardnesses and both galled quite badly, a further comparison cannot be made.

Prototype Tests

I Pressure Actuated Valve (Johnson Valve)

This test, performed at Allis-Chalmers, consisted of repetitive cycles of a free piston (diaphragm) pressure actuated valve, shown in Figs. 7, 8, and 9 operating in liquid sodium at temperatures from 500 to 1000 F. The actual test surface was the $4^3/_{16}$ in. long, $^1/_{16}$ in. thick Stellite No. 6 hard-faced cylindrical portion of a piston sliding in the bore of a Type 347 stainless steel valve body. The $^3/_8$ in. long, $5^3/_8$ in. OD cylindrical portion of the flange located on one end of the piston was also faced with $^1/_{16}$-in. thick layer of Stellite No. 6.[4]

A total of 800 operating cycles of the valve were performed at 50 F increments from 500 to 1000 F. Of the total 697 hours immersion in molten sodium, 219 were used for valve operation. The valve was actuated by a system of electrically operated pressure valves so arranged that the sodium was pressurized continuously by nitrogen to the closing and opening chambers. Approximately 2 minutes' time was required to complete a full cycle. The only difficulty encountered was that of gas lines plugging with condensed sodium. It was only the combination of gas line plugging and loss of sodium through the solenoid vent valves that caused the test to be terminated after 219 hours and 7263 operating cycles. The sliding surfaces of the valve operated without sticking or seizure between 500 and 100 F. Other than discoloration from exposure to heat and to impure sodium, the interior surfaces of the valve showed no sign of wear other than light rub marks around the bore. Light rubbing was expected, even though there was a 6-mil clearance between the valve bore and the piston, particularly, when the piston seated at the end of the "closing" cycle.

II Quick-Release Pin

In the early design stages of suitable delatching mechanism for the APDA reactor control rods, the ball-type release mechanism was considered to be of some merit. To prove out the principle of operation a standard quick-release pin capable of carrying a 10,000-lb tensile load was given two series of tests. The first series consisted of 500 load-release cycles in air with a 1000-lb applied load. The second series consisted of 1000 load-release cycles in 570 F sodium with a 200-pound applied load.

The quick-release pin, shown in Fig. 10, was fabricated of AISI 4130 steel (35 R_c hardness) for the pin body, AISI 4130 steel (59 R_c) for the plunger, Type 440 C stainless steel (59 R_c) for the load-carrying balls, and for the pin guide AISI 4140 (40 R_c) steel for the air test and chromium carbide (70 R_c) for the sodium test. The pin body is the tensile member and contains four openings for the load-carrying $^1/_4$-in. diameter balls. These balls are locked into position by the plunger, which is recessed about $^1/_4$ in. from its lower edge to form a pocket into which the balls retract upon releasing. To delatch, the plunger is depressed until the balls retract into the plunger recess.

For the load-release tests performed in air at room temperature, the quick-release pin was suitably restrained and loaded by means of hydraulic jack. A tensile load of 1000 lb was applied to the pin and the plunger depressed until the load was released. The force required to release the 1000-lb load gradually increased from 60 lb at the start to about 100 lb at the end of 500 cycles. Except for slight deformation of the pin guide, the pin released satisfactorily for the total of 500 cycles. The load-carrying balls, plunger, and pin body did not undergo any significant wear.

For the load-release tests performed in sodium at 570 F, the quick release pin was tested in the apparatus shown in Figs. 11 and 12. The equipment is shown with the sodium pot attached to the bottom in Fig. 11; Fig. 12 shows the ball release mechanism at the left. The release mechanism is loaded by the coil springs. The load was applied to the pin by four compression springs calibrated to load the pin to 230 pounds. The springs were cocked by hand through a lever system. A second level located directly beneath the cocking lever was used to trip or depress the pin plunger and release the load. A total of 1000 cycles were performed quickly and efficiently by this method. The force required to release the pin from its latched position varied from a minimum of 20 lb to a maximum of 28 lb. The pin guide used in the sodium test was made from chromium carbide and did not deform as did the AISI 4140 guide used in the air test. The load-carrying balls were slightly scored by the sharp edges of the chrome carbide pin guide. There was no significant wear marks on the other parts of the pin as a result of load-release tests in sodium.

III Reciprocating Shaft Seal and Bellows Seal

A test unit designed to verify the operating characteristics of 2 basic seal types; a ring-type pressure breakdown bushing and an expansion bellows, was operated for 10,000 cycles in 500-F

[4] A product of the Haynes Stellite Division of the Union Carbide & Carbon Corp.

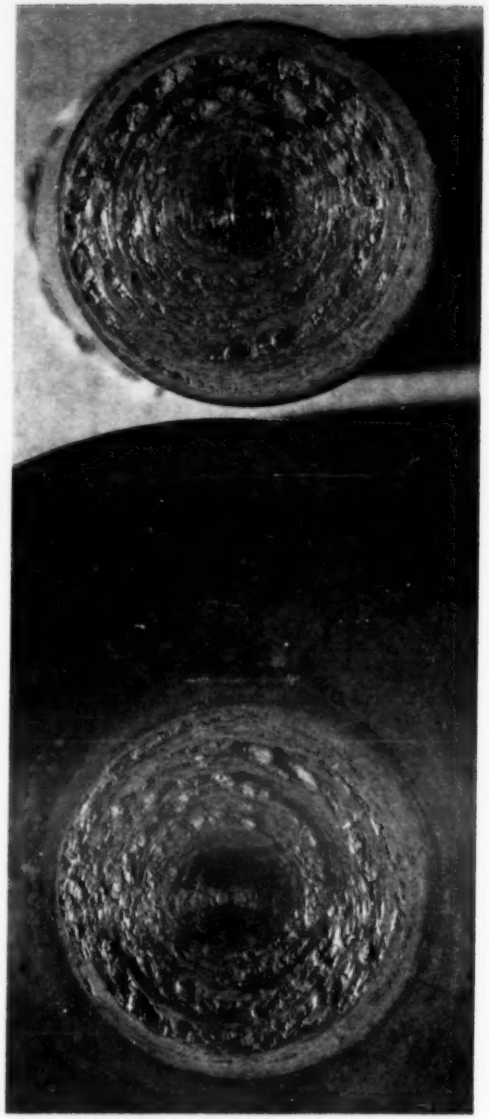

Fig. 3 Photograph of completed test couple no. 1 (X 2½)

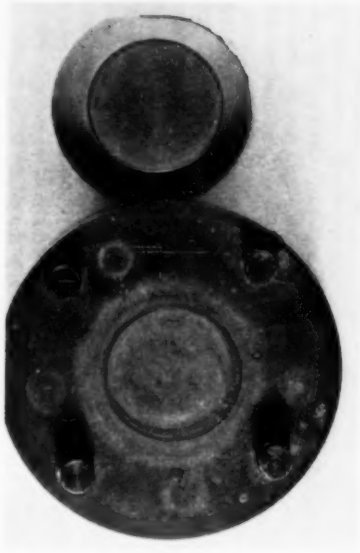

(X 1)

Fig. 4 Photograph of completed test couple no. 14A

(X 2½)

Fig. 6 Photograph of completed test couple no. 19 (X 2½)

(X1)

Fig. 5 Photograph of completed test couple no. 14B

(X 2½)

Table 1 Material combinations

Test combination no.	Material	Acceptability	Pretest hardness	Max torque: Max temp (1)	Max torque: Max load (2)	Post-test surface condition
1	347 Stn. Stl. Cap	C	85–86 Rb	Welded		
	347 Stn. Stl. Table		85–86 Rb	700°	10,000 psi	Galled and welded
2	347 Stn. Stl. Cap	C	24 Rc	Welded		
In nitrogen atmosphere	347 Stn. Stl. Table		22 Rc	700°	10,000 psi	Galled and welded
3	Armco	C	45–50 Rb	Welded		
	Stellite No. 6 (3)		55–65 R 30N	500°	10,000 psi	Galled and welded
4	Inconel "X" Cap	A	36 Rc	340		High spots polished
	Inconel "X" (Annealed) Table		27–28 Rc	1000°	10,000 psi	High spots polished
5	Ampco No. 18 Cap	C	97–97.5Rb	160		Welded plastic deformation 1/4 in. deep
	Stellite No. 1 Table (3)		48–52 Rc	1000°	2,500 psi	High spots polished
6	347 Stn. Stl. Cap	B	85–86 Rb	260		Scored lightly and worn
	Inconel "X" (Hardened) Table		36–38 Rc	900°	10,000 psi	Scored lightly
7	347 Stn. Stl. (Chrome Plated)	C	48 Rc	300		Galled and worn slightly
	347 Stn. Stl. (Chrome Plated)		48 Rc	1000°	10,000 psi	Galled, plastic deformation, metal pick-up
8	420 Stn. Stl. (Hardened) Cap	C	56.2–71.5 R30N	Erroneous[a]		Worn and flaked
	Sae 52100 Table		6.5–10 Rc	600°	2,500 psi	Scored, plastic deformation, metal pick-up
9	Stellite No. 6 Cap (3)	A	55.5–65 R30N	200		Polished
	Colmonoy No. 6 Table (3)		49–54 Rc	1000°	10,000 psi	Pitted, smooth
10	304 Stn. Stl. (Chrome Plated)	C	22.5–24 R30N	Erroneous[a]		Galled
	304 Stn. Stl.		34.5–36 R30N	1000°	10,000 psi	Galled
11	410 Stn. Stl. (Hardened)	C	40.5–42.5 R30N	250		Heavy gall
	304 Stn. Stl.		34.5–36 R30N	900°	10,000 psi	Heavy gall, metal pick-up
12	431 Stn. Stl. (Hardened)	C	51–63 R30N	180		Galled
	304 Stn. Stl.		33.2–34 R30N	800°	10,000 psi	Galled, metal pick-up
13	446 Stn. Stl. Cap	C	24.2–28 R30N	160		Spalled and torn
	304 Stn. Stl. Table		34.5–35 R30N	700°	10,000 psi	Scored, metal pick-up
14-A	Malcomized 347 Stn. Stl. Cap (4)	A	82–88 R15N	50		Smooth
	304 Stn. Stl. Table		53.5–56 Ra	1000°	10,000 psi	Smooth
14-B	Malcomized 347 Stn. Stl. Cap (4)	A	77–73 R15N	120		Fairly smooth
2 Mils ground from cap and table faces of combination No. 14-A	304 Stn. Stl. Table		51.5–53 Ra	1000°	10,000 psi	Smooth
15-A	Stellite No. 6 Cap (3)	C	60.5–69 Ra	240		Galled with some exchange of metal at and near the circumference
In nitrogen atmosphere	304 Stn. Stl. Table		52–53 Ra	1000°	2,500 psi	Slightly galled at and near the circumference
15-B	Stellite No. 6 Cap (3)	B	60.5–70.5 Ra	300		Smooth in center slightly worn near circumference
	304 Stn. Stl. Table		52–53 Ra	1000°	10,000 psi	Fairly smooth
16	Stellite No. 6 Cap (3)	A	64.5–70 Ra	170		Smooth, slightly polished around circumference and center smooth
	Stellite No. 6 Table (3)		77 Ra	1000°	10,000 psi	
17	Stellite No. 6 Cap (3)	B	67–72 Ra	190		Slightly worn at circumference
	347 Stn. Stl. (Chrome Plated)		62–66 Ra	1000°	10,000 psi	Slightly worn near circumference
18	"S" Inconel Cap	B	62.5–66 Ra	130		Smooth to pitted in several spots
	"S" Inconel Table		64–65.5 Ra	1000°	10,000 psi	Smooth to pitted in several spots
19	Nitrided 304 Stn. Stl. Cap (5)	B	94 R15N	160		Fairly smooth
	304 Stn. Stl. Table		50 Ra	1000°	10,000 psi	Fairly smooth
20	BN in Nickel Matrix on 304 (6)	C	2–2.5 MoH	440		Slightly galled, exchange of metal

Table 1 (Cont.)

Test combination no.	Material	Acceptability	Pretest hardness		Max torque: Max temp (1)	Max torque:	Max torque: Max load (2)	Post-test surface condition
In argon atmosphere	304 Stn. Stl. Table		50	Ra	900°		1000 psi	Worn and slightly galled, exchange of metal
21-A	BN in Nickel Matrix on 304 (7)	A−	3.5	Rb		105		Fairly smooth
In argon atmosphere	304 Stn. Stl. Table		60	Ra	1000°		1000 psi	Fairly smooth
21-B	BN in Nickel Matrix on 304 (7)	C	3.5	Rb		120		Slightly galled, exchange of metal
In argon atmosphere	304 Stn. Stl. Table		60	Ra	1000°		2500 psi	Worn and galled, exchange of metal
22-A	SAE B 1112 Cap	B	83–86	Ra		50		Slightly galled
	347 Stn. Stl. Table		77–78	Ra	1000°		1000 psi	Build-up from B 112 steel
22-B	SAE B 1112 Cap	A				70		
	347 Stn. Stl. Table				1000°		2500 psi	Polished, no additional galling Polished, fairly smooth
22-C	SAE B 1112 Cap	A				90		Polished, no additional galling
	347 Stn. Stl. Table				1000°		5000 psi	Polished, fairly smooth
22-D	SAE B 1112 Cap	A				130		Polished, slight spherical deformation
	347 Stn. Stl. Table				1000°		10,000 psi	Polished, slight convex deformation
23	BN in Nickel Matrix on 304 (8)	C				400		Galled
In argon atmosphere	BN in Nickel Matrix on 304 (9)				800°		1000 psi	Galled
24	347 Stn. Stl. Cap	A−	51	Ra		130		Smooth, superficial grooving
	Post Heat-Treated Nitrided 347 Stn. Stl. Table (10)		46	Ra	1000°		10,000 psi	Unchanged
25	Post Heat-Treated Nitrided 347 Stn. Stl. Cap. (10)	A	65	Ra		120		Unchanged
	Post Heat-Treated Nitrided 347 Stn. Stl. Table (10)		46	Ra	1000°		10,000 psi	Unchanged
26	347 Stn. Stl. Cap Post Heat-Treated Nitrided	B+	51	Ra		240		Smooth, 1 groove approx. 1 mil deep
	347 Stn. Stl. Table (Lapped to 32 rms Finish) (10)		50	Ra	1000°		10,000 psi	Smooth
27	Post Heat-Treated Nitrided 347 Stn. Stl. Cap (lapped to 32 rms finish)	B+	63	Ra		90		Smooth, center slightly grooved
	Post Heat-Treated Nitrided 347 Stn. Stl. Table (lapped to 32 rms finish) (10)		49	Ra	1000°		10,000 psi	Smooth, center slightly grooved

A Acceptable under conditions similar to test.
B Limited acceptability under similar conditions (some surface damage).
C Unacceptable.
(1) Test temperatures were 500, 600, 700, 800, 900, and 1000 F.
(2) Test pressure loadings were 1000, 2500, 5000, and 10,000 psi.
(3) Stellite No. 1, Stellite No. 6, and Colmonoy No. 6 were welded onto Type 304 stainless steel specimens.
(4) Malcomizing is a furnace nitriding process patented by V. T. Malcolm of the Chapman Valve Mfg. Co. Nitride case depths were approximately (6) mils.
(5) Nitrided by the A. F. Holden Co. (salt bath process). Six mil case depth.
(6) Coating applied to specimen from a dispersion of NiO and BN in isopropyl alcohol and nitromethane prepared to yield a 20–80 volume ratio of boron nitride to nickel matrix. The "as-deposited" coating was dried under infrared lamps and then subjected to a reduction step in hydrogen at 500 C. The reduced coating was isostatically pressed at 25 tons/in^2. The coating was then sintered in purified hydrogen at 950 C for $^1/_2$ hour and allowed to cool slowly for 2 hours. Final coating thickness was approximately 2 mils. (Vitro Laboratories, West Orange, N. J.).
(7) 50–50 volume ratio of boron nitride to nickel matrix. Coating thickness approximately 3–4 mils.
(8) 10–90 volume ratio of boron nitride to nickel matrix. Coating thickness approximately 6 mils.
(9) 20–80 volume ratio of boron nitride to nickel matrix. Coating thickness approximately 2 mils.
(10) Specimens were malcomized at 1050 F for 48 hours and post heat-treated at 1200 F for (4) hours.
[e] Erroneous due to apparatus seizure.

Table 2 Material weld test no. 6 in sodium at elevated temperatures

Inconel "X" (hardened) cap vs. stainless steel 347 table
Cap hardness, 36–38.0 Rockwell "C"
Table hardness, 85–86 Rockwell "B"

Time in hot Na	Load, psi	Temp, deg F	First test sequence, force to lift 4-6 advantage	Second test sequence — Torque to turn in ft lb start of test	Second test sequence — Torque to turn in ft lb end of test	Coefficient of friction Start of test	Coefficient of friction End of test
50	1000	500	20	20	20	0.72	0.72
50	1000	600	20	20	20	0.72	0.72
50	1000	700	20	20	20	0.72	0.72
50	1000	800	20	20	20	0.72	0.72
50	1000	900	20	30	20	1.08	1.08
50	1000	1000	20	30	30	0.11	0.11
50	2500	500	20	30	30	0.432	0.432
50	2500	600	20	50	50	0.720	0.72
50	2500	700	20	60	40	0.86	0.58
50	2500	800	20	50	60	0.72	0.86
50	2500	900	20	50	60	0.72	0.86
50	2500	1000	20	70	60	1.01	0.86
50	5000	500	20	50	40	0.36	0.29
50	5000	600	20	70	80	0.50	0.58
50	5000	700	20	90	80	0.65	0.58
50	5000	800	15	110	90	0.79	0.65
50	5000	900	15	130	80	0.94	0.58
50	5000	1000	20	140	100	1.00	0.72
50	10,000	500	20	100	100	0.36	0.36
50	10,000	600	20	140	150	0.50	0.54
50	10,000	700	20	200	180	0.72	0.65
50	10,000	800	20	220	160	0.79	0.58
50	10,000	900	20	230	260	0.83	0.43
50	10,000	1000	20	200	140	0.72	0.50

Table 3 Material weld test no. 8 in sodium at elevated temperatures

SAE 52100 cap 004 vs. hardened 420 stainless steel 516
Cap hardness, 6.5–10 Rockwell "C"
Table hardness, 56.4–71.5 Rockwell "C"

Time in hot Na	Load, psi	Temp, deg F	First test sequence, force to lift 4-6 advantage	Second test sequence — Torque to turn in ft lb start of test	Second test sequence — Torque to turn in ft lb end of test	Coefficient of friction Start of test	Coefficient of friction End of test
50	1000	500	20	80	100	2.9	3.6
50	1000	600	20	90	80	3.2	2.9
50	1000	700	20	100	100	3.6	3.6
50	1000	800	20	40	40	1.4	1.4
50	1000	900	20	100	110	3.6	3.96
50	1000	1000	35	120	120	4.3	4.3
50	2500	500	20	180	220	2.6	3.2
50	2500	600	20	360	400	5.2	5.8
50	2500	700	20	450	360	6.5	5.2
50	2500	800	20	320	350	4.6	5.0
50	2500	900	20	350	350	5.0	5.0
50	2500	1000	20	340	330	4.9	4.7
50	5000	500	20	620	570		
50	5000	600	20				
50	5000	700	20	Collar seized to shaft			
50	5000	800	20				
50	5000	900	25				
50	5000	1000	30				
50	10,000	500	25				
50	10,000	600	20				
50	10,000	700	20				
50	10,000	800	25				
50	10,000	900	25				
50	10,000	1000	65				

Table 4 Material weld test no. 14A in sodium at elevated temperatures

Malcomized 347 stainless cap vs. 304 stainless table
Cap hardness, 82–88 R-A
Table hardness, 52–53 R-A

Time in hot Na, min	Load, psi	Temp, deg F	Torque to turn —in ft lb— Start of test	Torque to turn —in ft lb— End of test	Coefficient —of friction— Start of test	Coefficient —of friction— End of test
50	1000	500	30	20	1.1	0.72
50	1000	600	30	30	1.1	1.1
50	1000	700	30	40	1.1	1.4
50	1000	800	40	30	1.4	1.1
50	1000	900	30	30	1.1	1.1
50	1000	1000	30	30	1.1	1.1
50	2500	500	50	40	0.72	0.58
50	2500	600	30	20	0.43	0.29
50	2500	700	20	20	0.29	0.29
50	2500	800	20	20	0.29	0.29
50	2500	900	32	30	0.46	0.43
50	2500	1000	20	30	0.29	0.43
50	5000	500	20	10	0.14	0.07
50	5000	600	10	10	0.07	0.07
50	5000	700	10	0	0.07	0
50	5000	800	10	0	0.07	0
50	5000	900	10	0	0.07	0
50	5000	1000	5	0	0.04	0
50	10000	500	10	20	0.04	0.07
50	10000	600	20	10	0.07	0.04
50	10000	700	10	0	0.04	0
50	10000	800	20	10	0.07	0.04
50	10000	900	10	10	0.04	0.04
50	10000	10000	20	30	0.07	0.11

Table 5 Materials weld test no. 14B in sodium at elevated temperatures

Malcomized 347 stainless cap vs. 304 stainless table
Cap hardness, 71–73 R-A
Table hardness, 52–53 R-A

Time in hot Na, min	Load, psi	Temp, deg F	Torque to turn —in ft lb— Start of test	Torque to turn —in ft lb— End of test	Coefficient —of friction— Start of test	Coefficient —of friction— End of test
50	1000	500	30	20	1.1	0.72
50	1000	600	20	20	0.72	0.72
50	1000	700	30	20	1.1	0.72
50	1000	800	30	40	1.1	1.4
50	1000	900	40	40	1.4	1.4
50	1000	1000	40	40	1.4	1.4
50	2500	500	50	60	0.72	0.86
50	2500	600	50	50	0.72	0.72
50	2500	700	50	60	0.72	0.86
50	2500	800	60	60	0.86	0.86
50	2500	900	50	60	0.72	0.86
50	2500	1000	70	50	1.00	0.72
50	5000	500	40	70	0.29	0.50
50	5000	600	80	90	0.58	0.65
50	5000	700	80	100	0.58	0.72
50	5000	800	90	70	0.65	0.50
50	5000	900	100	100	0.72	0.72
50	5000	1000	80	90	0.58	0.65
50	10000	500	40	70	0.14	0.25
50	10000	600	40	80	0.14	0.29
50	10000	700	60	60	0.25	0.22
50	10000	800	80	80	0.29	0.29
50	10000	900	100	80	0.36	0.29
50	10000	1000	120	100	0.43	0.36

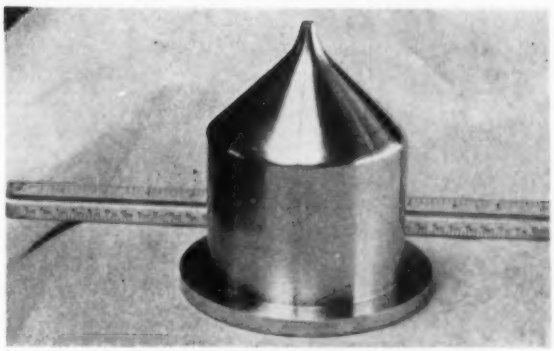

Fig. 7 Pressure actuated valve, sliding seal plug

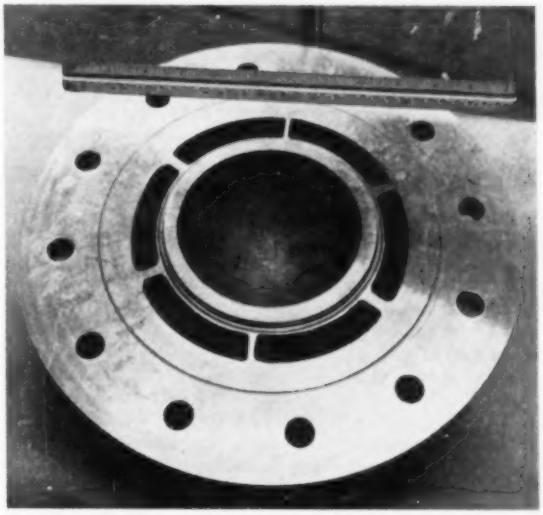

Fig. 8 Pressure actuated valve, inner flange view of cast entrance section

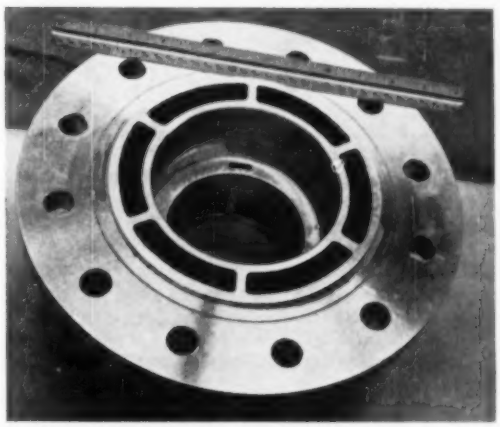

Fig. 9 Pressure actuated valve, inner flange view of cast exit section showing the sliding surfaces and seat

Fig. 10 Quick-release pin (after 1000 load cycles in 570 F sodium)

NaK. The test determined the applicability of these seals for reactor accessory drives involving reciprocating motion. The test cell, shown in Fig. 13, was designed and fabricated by American Machine and Foundry Company.

The breakdown bushing was designed for operation with a reciprocating shaft which might be as much as $^3/_{16}$ in. radially displaced from the center line of the seal housing. The seal contained a total of 8 sliding rings with a diametral clearance of 0.0008 in. at room temperature between the shaft and 4 main seal rings. The four primary shaft seal rings were made of Stellite No. 3 and four floating rings were made from K-Monel. The stationary diaphragm rings were made of K-Monel also, with the exception of the clamping diaphragm which was made from Type 440 C stainless steel. The entire outer seal housing was Type 440 C stainless steel. The shaft was made from Type 440 C stainless steel that was hardened, chrome plated, and carefully polished. All floating components and stationary contact surfaces were lapped for good fits. The expansion bellows, Fig. 14, was made from 12-mil-thick Type 347 stainless steel. All joints were fused by inert gas shielded arc welding. The completed bellows consisted of 45 convolutions and was flanged at both ends so that one end could be sealed to the reciprocating shaft and the other end sealed to the stationary test cell housing.

In operation, NaK was supplied to the test unit beneath the floating-ring bushing by a reverse flow Einstein-Szilard pump. A 70-psi differential was provided across the floating ring seal, and leakage flow was measured by a Fischer-Porter armored flowrator and checked against an electromagnetic flowmeter. The expansion bellows was positioned above the floating-ring bushing and above the NaK level. The reciprocating shaft was operated by an air cylinder located at the top of the test unit. The shaft stroke was 6 in. and a full cycle consisted of the shaft moving from the full up to the full down position and the return stroke.

The tests performed by the Allis-Chalmers Co. consisted of 772 cycles run at a rate of 1 full cycle in 2 minutes, 1609 cycles run at the rate of 2 full cycles in 1 minute, and 7619 cycles run at the rate of 1 full cycle in 1 minute. The measured leakage rate across the seal with a 70-psi differential was 0.3 gpm. Calculated leakage was 0.204 gpm, which corresponds to a calculated diametral clearance between shaft and seal (at 500 F) of 0.0019 in.

The seal operated very well throughout the test without any evidence of wear, galling, or grabbing. The condition of the reciprocating shaft was excellent with only polish marks visible to the eye. The rubbing surfaces of all the seal rings were checked on a Brush Surface Analyzer. The regions which appeared to be the roughest on measurement, were found to have a surface finish of 3 to 4 microinches.

The sealing bellows failed after 9990 cycles. The failure was a complete separation of the upper-most convolution from the heavier end core which was welded in turn to the seal flange.

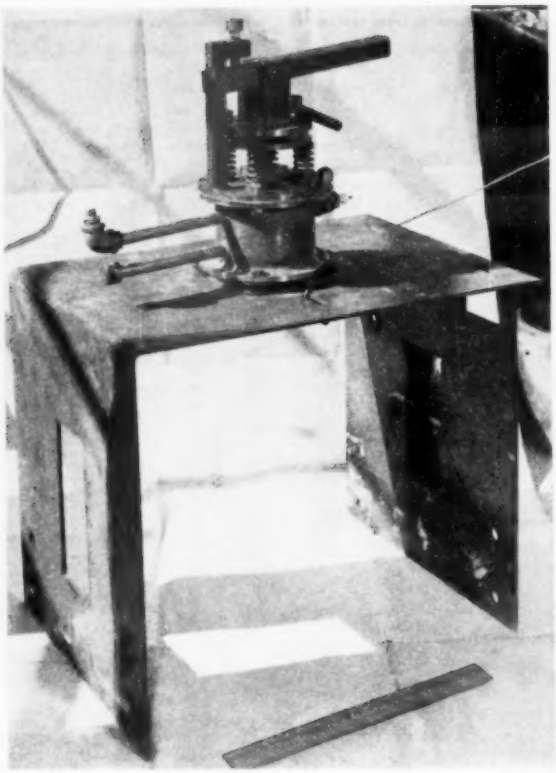

Fig. 11 Quick-release pin test set-up

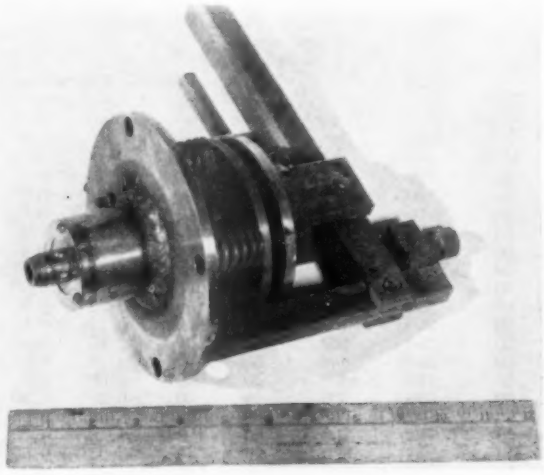

Fig. 12 Quick-release pin test set-up

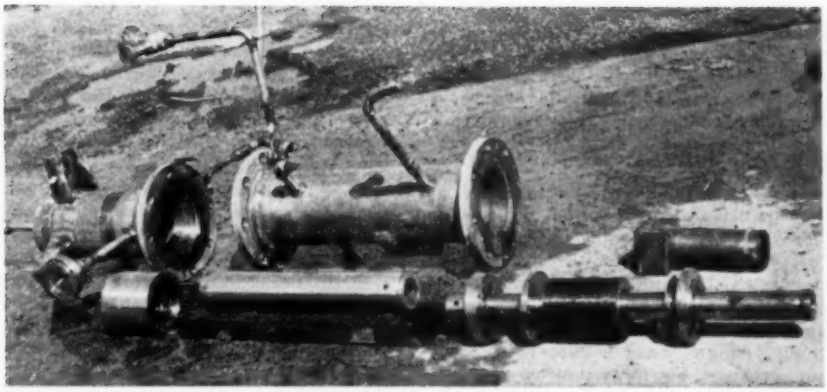

Fig. 13 Bellows and seal tester, exploded view of components after 10,000 cycles in 500-F NaK

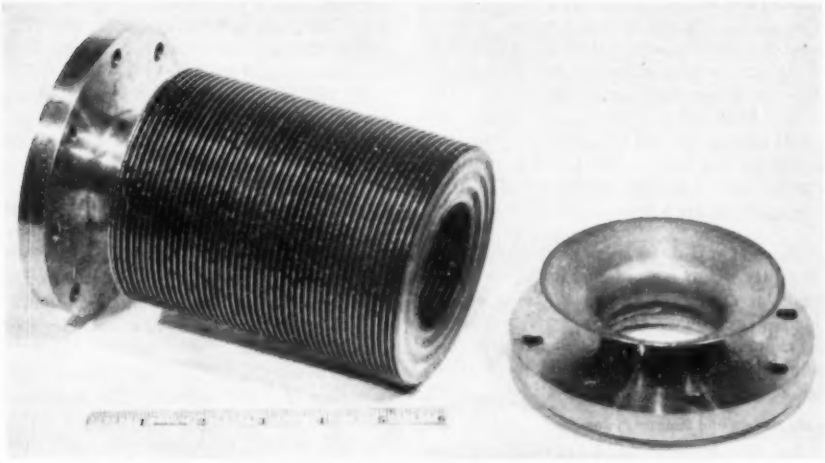

Fig. 14 Bellows and seal tester (after 10,000 cycles in NaK), bellows failure

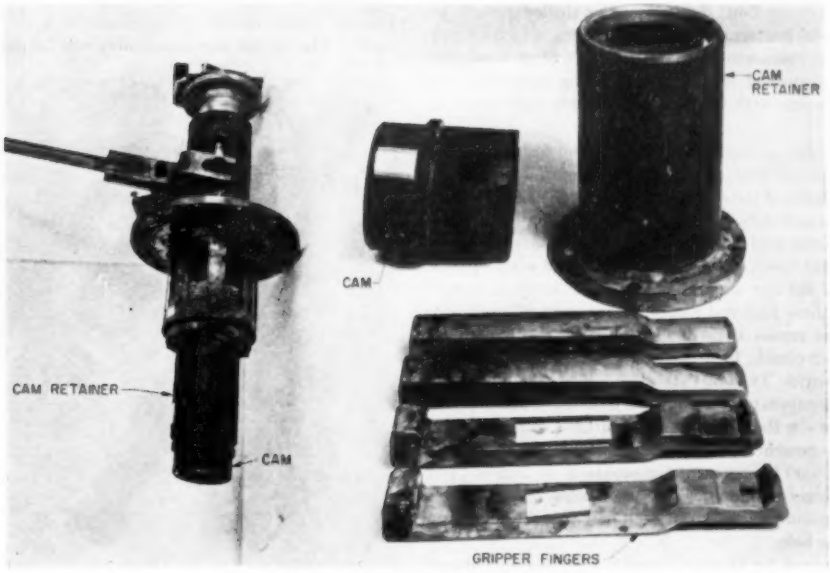

Fig. 15 Gripper mechanism test unit

There was no evidence that this was a gradual failure, since the system was reasonably gas tight up to this time and any leaks would have been indicated by an additional inert gas consumption. The bellows failure was attributed to tiny burnups of weld metal at the diaphragm joint which acted as stress raisers.

IV Fuel Subassembly Gripper Mechanism

The gripper mechanism is the working end of the offset handling mechanism which will be used for the loading and unloading of fuel and radial blanket subassemblies within the reactor vessel. Even though the gripper will be operated only when the reactor is shut down, it is located at all times within the reactor vessel, exposed fully to the rigors of reactor sodium and all its transients. In operation, gripper fingers are cammed into the pickup and release positions by reciprocating motion of the gripper body.

A full size gripper mechanism, Fig. 15, fabricated by AMF was tested. Except for the cast Stellite No. 6 fingers, the gripper was fabricated from Type 304 stainless steel. The cam surfaces were hard chrome plated and the internal wear ring was welded-on Stellite No. 6. The test, conducted at the Argonne National Laboratory, consisted of repetitive hand actuated pickup and release operations of the gripper with a dummy fuel subassembly handling lug. These operations were performed entirely under sodium at temperatures from 550 to 1100 F. The sodium was kept at temperature 24 hours a day and the gripper was operated during the normal day working hours. Except for a shutdown and an inspection period after 2 months operation and 1610 cycles, the gripper was operated for a total of 319 days and 3160 gripping cycles.

Wear was insignificant on any of the bearing surfaces. A fine crack, attributed to faulty welding, was found in the wear ring. The fingers exhibited some burnishing at the points of contact with the handling lug. The chrome-plated cam surfaces appeared intact except at the camming edges where the fingers were actuated. Other than the plating being rubbed off at these points, the wear was negligible.

V Core Subassembly Nozzle and Support Plates

A Tests in Nitrogen. The Fermi plant core and radial blanket subassemblies are supported by two 2-in. thick Type 347 stainless steel plates. The 2 plates are spaced 18 in. apart and have top-chamfered $1^3/_4$-in. and 2-in. diameter holes drilled completely through on 2.693-in. centers. The plate sections, which support the individual core subassemblies vertically, are considered critical wear areas because of the frequent loading operations and close vertical tolerance with the core subassembly hold-down device.

Based on the results of the laboratory self-weld tests described, a nitride wear-resistant surface was suggested as the best means of protecting the holes of the support plates as well as the lower or nozzle ends of the core subassemblies. The use of a nitride case offers some economic and fabrication advantages over properly fitted wear-resistant inserts in each of the 182 holes within the reactor core area of the two support plates. For the confirmatory prototype tests, three material combinations were selected: (1) Type 304 stainless versus Type 304 stainless; (2) nitride Type 304 stainless versus nitride Type 304 stainless; and (3) Type 304 stainless versus nitride Type 304 stainless. The 3 combinations were tested at a temperature of 750 F in a nitrogen atmosphere. The materials were in the form of a block drilled with a 2-in. diameter hole to represent the upper support plate and a 2-in. diameter tube (collar) to represent the subassembly nozzle. The hole was 5 mils larger in diameter than the nozzle. In the three combinations mentioned, the first of each pair was the collar and the second was the hole.

The test, conducted by Detroit Edison's Engineering Laboratory and Research Department, consisted of side loading the collar against the hole and measuring the force required to move the collar down and up through the hole. Before the side load was applied, the collar was inserted into the hole to a depth of $^1/_8$ in. to limit the sharp edge effect of the chamfered hole. Side loads of 100, 200, 400, and 800 lb were to be applied to each material combination.

As expected, the bare stainless versus bare stainless combination was unsatisfactory; with only a 50-lb side load on the collar, seizure occurred and further testing was discontinued. The bare stainless collar and nitrided stainless hole combination exhibited erratic vertical loading and testing was discontinued after seizure at the 400-lb side load. The collar was significantly galled after the 200-lb side load test and, with the 400-lb side load, the metal build-up from the collar was sufficient to cause seizure. At this point the vertical force rose to 1100 lb. The nitrided hole itself was not damaged.

The nitrided stainless versus nitrided stainless combination behaved satisfactorily at all side loadings. The average vertical force required to move the collar against the hole at side loadings of 100, 200, 400, and 800 lb was 53, 233, 375, and 625 lb, respectively. The mating surfaces were little more than slightly polished as a result of the test.

B Tests in Sodium. The bottom or nozzle end of the fuel subassembly, Fig. 16, consists of an inner cylinder, a spring, and an outer cylinder. The reactor hold-down device exerts a downward force on the fuel subassemblies, and this force is transmitted to the nozzle springs allowing the subassemblies to be properly positioned and restrained against the lifting force of the upward-flowing sodium coolant. Galling and/or seizure of the nozzle would lead to serious mechanical difficulties. The points of rubbing contact of primary importance are those of the inner cylinder against the nozzle nose at the bottom. The outer surface of the nose piece and the outer cylinder have rubbing contact with the support plate.

Tests were made by the Allis-Chalmers Company on two nozzle assemblies in 750-F sodium. The nozzles were repeatedly inserted and withdrawn from the holes of simulated support plates (top and bottom) by a shaft connected to an air motor which provided the proper nozzle speed, length of travel, and cycling control. All parts of the first nozzle assembly were fabricated from Type 304 stainless steel except the spring and the simulated support plates, which were fabricated from Type 343 stainless steel. The second nozzle assembly was fabricated from the same

Fig. 16 Fuel element nozzle assembly

materials as the first and, in addition, the surfaces of the simulated support plate and nozzle which contacted each other were surface hardened by nitriding and lapped to a 32-rms finish.

Test No. 1, conducted under sodium at 750 F, had the nozzle end cycling in and out of the support plate hole with a $2^1/_2$-in. stroke, including a $^1/_2$-in. overstroke, at the rate of 24 cycles a minute with room temperature clearances between the support plate hole and the nozzle of approximately 6 mils. In spite of the fact that the inner and outer cylinders of the nozzles were in metal-to-metal contact with each other, the unit operated quietly and without mishap up to the 30th cycle when a slight chattering became more evident until the unit stopped at the 48th cycle. By manually adjusting the air motor the unit was made to operate to the 62nd cycle. However, this was accomplished with much chattering so the test was terminated.

Upon dismantling the unit, it was found that severe uniform galling had occurred around the entire circumference between the inner and outer cylinder at the top and between the outer cylinder and the upper support plate. Some galling had also occurred, in one section only, between the outer surface of the nose piece and the lower support plate and the inner-cylinder retaining ring and pin were "ripped" from the inner cylinder.

Test No. 2 was conducted with sodium temperature maintained at 750 F and cycling with a $2^1/_2$-in. stroke, including a $^1/_2$-in. overstroke, at 3 different rates: (*a*) 150 cycles at 3 cycles a minute, (*b*) 100 cycles at 6 cycles a minute, and (*c*) 750 cycles at 12 cycles a minute. During the test a slight scraping sound was audible, but otherwise the movements were quiet and steady. On inspection after 1000 cycles, slight rubbing was indicated between the outer cylinder and the upper support plate and slight rubbing on the inner surface of the outer cylinder from the spring. Other than the areas of slight rubbing there was no evidence of wear.

The unit was cleaned, reassembled with a new Type 347 stainless steel spring and tested for an additional 5000 cycles at the rate of 12 cycles a minute. The strokes were smooth and quiet; no evidence whatsoever of any galling or seizure. Upon reinspection, the rub marks between the upper outer cylinder and the upper support plate were more pronounced than they were after the 1000-cycle run, and there were rub marks between inner and outer cylinder at the top. Evidence of galling was notably lacking. This test seems to bear out the fact that the materials used for this type of operation are more critical than the running clearances. With essentially the same clearances, only 62 cycles were completed for the first test, whereas 6000 cycles were completed for second test.

Summary and Conclusions

In laboratory tests, the harder material combinations showed generally better wear and self-welding resistance than did the softer materials. Results of hard material and soft material combinations, such as Ampco No. 18 versus Stellite No. 1 and Armco iron versus Stellite No. 6, indicate that temperature effects on material strength and hardness will dictate the type of material failure. Ampco No. 18 underwent severe plastic deformation and the Stellite No. 1 was polished but neither exhibited any galling. Armco iron was severely galled and the Stellite No. 6 had considerable metal pick-up but neither was plastically deformed.

The results of the prototype tests indicate that sodium has little, if any, effect upon the bearing or wearing characteristics of the materials tested. The resistance to galling and self-welding is dependent on the design and the load application. Sodium cannot be relied upon to act as a lubricant for reactor components subject to wear. Mating surfaces must be protected by a hard material and/or hardening treatment that is known to possess or impart adequate wear resistance even when operating dry.

Under simulated, nonradioactive, reactor-operating conditions, the Stellite No. 6 performed exceptionally well as did the nitrided stainless steels. However, each has limitations even though exhibiting comparable wear resistance. Stellite No. 6, since it can be applied in a relatively thick layer or even cast to shape, appears best suited for repetitive wear applications such as a rotating or reciprocating shaft rubbing against a stationary sleeve or the grippers of a latch mechanism. A nitride case, since it is relatively thin, appears best suited for stainless steel applications requiring resistance to self-welding and wear resulting from nonrepetitive or infrequent cyclic operation.

Acknowledgments

The authors wish to thank the staffs of the Allis-Chalmers Manufacturing Company, the Engineering Laboratory and Research Department of The Detroit Edison Company, and the Argonne National Laboratory, who performed the several laboratory and prototype tests.

Irradiation of Haynes-25 and Inconel-X Compression Springs in High-Temperature High-Pressure Water

R. L. MEHAN

Knolls Atomic Power Laboratory,
General Electric Company,
Schenectady, N. Y.

Irradiation tests were performed on Haynes Stellite Alloy 25 and Inconel-X springs irradiated in the compressed condition in an in-pile high-temperature water loop. The loop was operated at 560 to 600 F and the springs of both materials received integrated fluxes of 5.9×10^{19} and 4.2×10^{19} nvt fast, respectively. Postirradiation testing and examination revealed no serious deleterious effects resulting from these exposures. It was found the spring constant increased 5 to 8 per cent after exposure and the free length decreased 2 to 3 per cent. The effect of irradiation on the plastic-flow curve was slight as revealed by three-point loaded bend tests on 0.160-in-diam rods irradiated with the springs.

IT IS KNOWN from past experimental work that metals subjected to neutron bombardment undergo changes in mechanical properties. In general, strength properties increase and ductility decreases. These effects tend to increase with increasing neutron exposure. Because of this radiation-damage effect, materials chosen for use in nuclear reactor cores where neutron exposures are appreciable must be scrutinized carefully for possible harmful changes in properties resulting from this exposure. When the exposure takes place in a corrosive environment such as high-temperature high-pressure water, corrosion effects must also be considered.

Ideally a test to investigate material behavior under a combined radiation-damage-corrosion environment should take place in an environment similar to that anticipated in service. However, the practical difficulties and cost in conducting such an in-pile test are so great that most investigators generally perform preirradiation and postirradiation tests, that is, the comparison of some selected property before and after radiation. Such a test is somewhat objectionable because the material behavior could well be different while actually being tested under anticipated service conditions rather than after this exposure. However, it is a first approximation of the material response to combined radiation-damage-corrosion effects.

The investigation described in this paper is a result of such pre and postirradiation tests. It was desired to know if Haynes-25 and Inconel-X springs undergo any harmful changes when exposed to relatively low neutron fluxes while in high-temperature high-pressure water at 580 F. The primary questions the tests were designed to answer were:

1 Are there any deleterious effects of irradiation *per se* on plastic properties when these materials are exposed to total integrated fast fluxes in the order of 10^{19} neutrons per cm^2 (*nvt*) at temperatures of about 580 F?[1]

2 Are there any combined effects of corrosion and irradiation detectable by a preirradiation and postirradiation comparison test that have a harmful effect on spring properties?

To answer these questions, two separate irradiations were performed in an in-pile, high-pressure water loop, both irradiations being nearly identical except for exposure time. Because of the considerably higher flux present in the experimental facility compared to the anticipated service conditions, one irradiation was performed for a short time—less than 500 hr—to determine the effect of integrated flux alone. The information obtained from this test was deemed insufficient to assess the significance of corrosion because of the short time the springs had been in contact with water under irradiation. Consequently, a second irradiation lasting for more than 2000 hr was performed to assess the effect of long-term exposure more adequately. The integrated flux received by the springs in this second irradiation was far higher than anticipated in service; however, it was thought that if the springs and spring materials performed satisfactorily under these relatively severe conditions no serious difficulties would be encountered under the actual service conditions.

Materials

The two materials investigated were Haynes Stellite Alloy 25 and Inconel X. The material was received as 0.162-in-diam wire in the as-drawn condition. The percentage of cold work received by the wire after the last annealing treatment for the Inconel X was 15 per cent, and 35 to 40 per cent for the Haynes 25. Chemical analyses for these materials are shown in Table 1.

[1] Fast neutrons in this report are defined as neutrons with energies greater than 1.0 Mev.

Contributed by the Metals Engineering Division and presented at the Annual Meeting, New York, N. Y., November 30–December 5, 1958, of THE AMERICAN SOCIETY OF MECHANICAL ENGINEERS.

NOTE: Statements and opinions advanced in papers are to be understood as individual expressions of their authors and not those of the Society. Manuscript received at ASME Headquarters, August 4, 1958. Paper No. 58—A-94.

Nomenclature

τ_{max} = maximum shear stress, psi
δ = deflection, in.
P = load, lb
r = spring mean radius, in.
d = wire diameter, in.
c = spring index ($2r/d$)
n = active coils
G = modulus of rigidity (11.5×10^6 psi for Inconel X and 13×10^6 psi for Haynes 25)
K = spring constant, lb/in.
α = pitch angle, deg

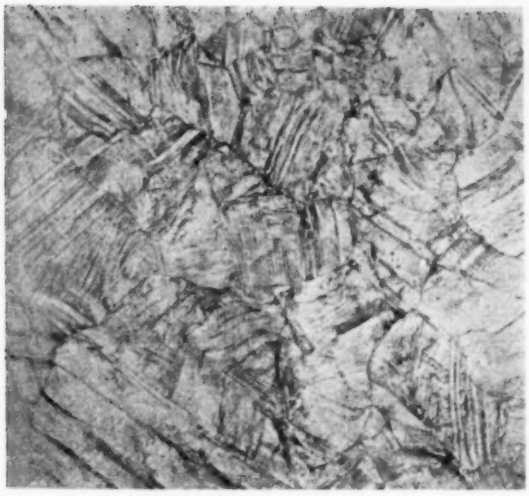

Fig. 1 Photomicrograph of Haynes-25 wire in fully heat-treated and preirradiated condition used for manufacture of irradiation springs. Etch: aqua regia; 100 X.

Table 1 Chemical analysis for Haynes 25 and Inconel X used in spring irradiation

Element	Weight per cent — Inconel X	Haynes 25
C	0.04	0.03
Mn	0.75	1.51
S	0.004	
Si	0.30	0.70
Cr	15.5	19.8
Ni	72.6	10.0
Fe	7.05	1.79
W		14.8
Cb + Ta	0.71	
Ti	2.27	
Al	0.88	
Cu	0.04	
Co		51.4

This wire was tested in the heat-treated condition before it was coiled into springs to determine the optimum heat treatment. The optimum heat treatment was established by experiment, and the results of an average of three of these tests were:

	Inconel X	Haynes 25
Heat-treatment, deg F—hr	1350 F—16 hr	1100 F—2 hr
Tensile strength, psi	192,000	214,000
0.2 per cent yield strength, psi	156,000	194,000
Elongation in 1 in., per cent	15.1	5.7
Reduction of area, per cent	35.3	14.8

Typical photomicrographs of this material are shown in Figs. 1 and 2.

From this starting stock, ten springs of each material in the cold-drawn condition were manufactured to the following specifications:

Wire diameter, in.	0.162
Spring diameter, in.	1.75
Active turns	4
Deflection per lb	16.1×10^{-3}
Solid height, in.	0.970
Free length, in.	2.38

The springs were wound in the cold-drawn condition, heat-treated at the optimum temperatures and times shown, and pickled.

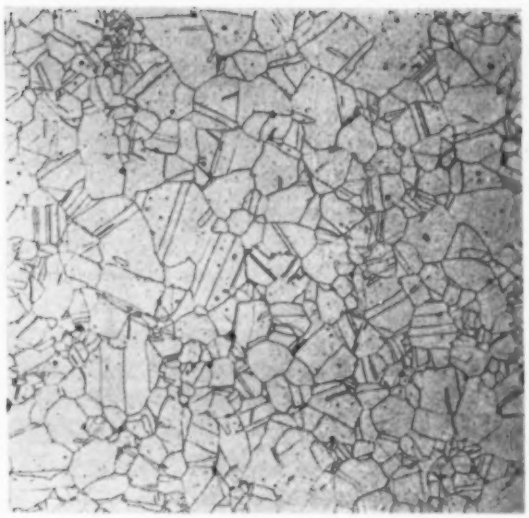

Fig. 2 Photomicrograph of Inconel-X wire in fully heat-treated and preirradiated condition used for manufacture of irradiation springs. Etch: aqua regia; cupric chloride; 100 X.

In addition to the springs, about 12 3-in. sections of each wire composition were cold-straightened, heat-treated, and pickled. These rods were subsequently irradiated with the springs.

Test Procedure and Irradiation Conditions

To investigate the combined effect of irradiation and exposure to high-temperature water on spring properties and plastic behavior of the spring materials, five types of tests or measurements were employed before and after exposure:

1 Change in free length of springs
2 Load-deflection tests in elastic range on springs
3 Tests to solid height on springs
4 Bend tests to failure on 3-in. sections of straightened wire
5 Metallographic examination of straightened wire

Both irradiation assemblies contained three springs each of Haynes 25 and Inconel X compressed to a calculated stress of 80,000 psi. The method of calculating the stress appears in the Appendix. In addition, each assembly contained five straightened wires of each material. Fig. 3 shows an irradiation assembly in schematic form and Fig. 4 a photograph of an assembly before in-pile insertion. Fig. 3 shows that the irradiation assembly was so designed that water was in contact with the rods and springs during exposure.

Before insertion into an assembly, each spring was load-deflection tested on a 300-lb-capacity Dillon Testing Machine. The slope of the load-deflection line, obtained by averaging three separate tests, was taken as the spring constant K. The spring constant K was measured in an identical manner after irradiation. All postirradiation tests were performed remotely in shielded cells in the KAPL Radioactive Materials Laboratory.

Each spring was photographed with a calibrated scale for determination of free length before insertion into an irradiation slug. A similar photograph was obtained after irradiation. Every effort was taken to insure that the orientation of the spring in the pre and postirradiation photographs was the same. A typical photograph of a spring is shown in Fig. 5. The difference between the two heights was taken as the change in free length of the spring caused by the exposure conditions.

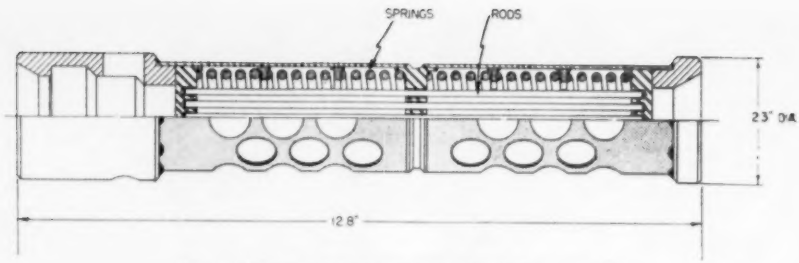

Fig. 3 Schematic drawing of spring irradiation assembly

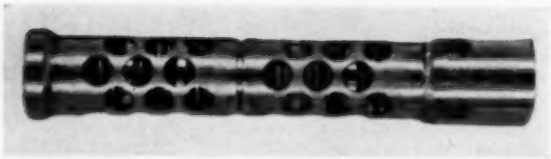

Fig. 4 Photograph of spring test assembly before insertion in-pile; approximately $^1/_4$ X

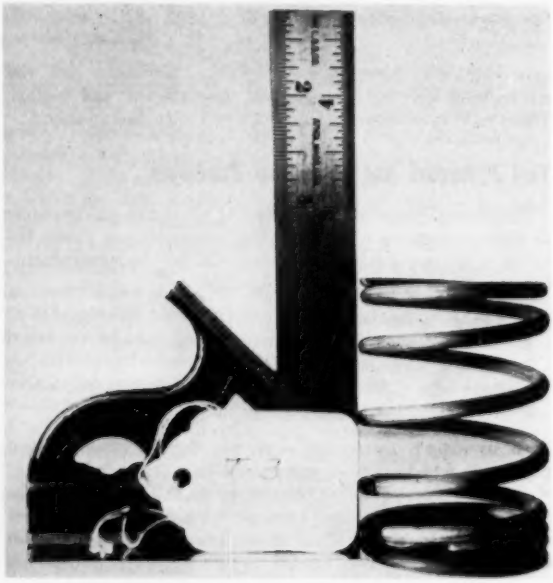

Fig. 5 Preirradiation photograph of Inconel-X spring illustrating method of obtaining free-length changes

Preirradiation compression tests to solid height were not performed on springs to be inserted in the reactor, but rather on duplicate springs of identical condition. The purpose of these tests was to determine if any incipient cracks would open up when the coils were taken well into the plastic range. All tests were repeated three times to give any incipient crack a chance to open up. Both pre and postirradiation springs were carefully examined under 10 to 15 × magnification for any evidence crack formation. For both load-deflection tests and solid-height tests on unirradiated and irradiated springs, the same 300 lb-capacity Dillon Testing Machine was used, but on different load ranges.

Bend tests of the 0.160-in-diam rods obtained from the straightened spring wire were performed at room temperature. The rods were tested as a three-point-loaded beam and were deflected to failure. Postirradiation tests were performed on a specially designed apparatus previously described [1].[3] Although preirradiation tests were performed on a different piece of apparatus, the support and plunger geometries were identical and it is felt the pre and postirradiation tests were similar.

Hardness tests were performed on the rods after bend testing and well away from any area of plastic deformation. Both pre and postirradiation tests were performed on standard Rockwell hardness apparatus; the latter was modified for remote testing. Postirradiation metallographic examinations were only made on the rods exposed to 4.2×10^{19} *nvt*.

The irradiation assemblies shown in Figs. 3 and 4 were irradiated in a low-flux portion of a high-temperature high-pressure in-pile loop. The nominal water conditions, temperature of exposure, and neutron flux are shown in Table 2.

Table 2 Exposure conditions for the scram-spring irradiation

Condition	Short-time irradiation	Long-time irradiation
Irradiation temperature, deg F	560–600	560–600
Integrated fast flux, *nvt*	5.9×10^{18}	4.2×10^{19}
Operating pressure, psi	2250	2250
Water conditions		
Oxygen, ppm	<0.1	<0.1
pH	5.8 to 6.4	5.8 to 6.4
Ion-exchange purification	None	None
Specific resistance, ohm-cm	300,000	300,000

Test Results

The results of load-deflection tests on Haynes-25 and Inconel-X springs, both preirradiation and postirradiation, are shown in Table 3. These data indicate that the primary effect of the exposure conditions is to increase the slope of the curve (or to increase the spring constant K). The effect seems to increase with increasing exposure for the Haynes 25 but not for the Inconel X. To check the significance of these results, the data for two springs (B-1 and T-4 in Table 3) were analyzed statistically. The results of these tests indicated that spring B-1 showed a highly significant increase in slope but the increase in slope of spring T-4 was not significant on the 5 per cent level. It was further established that approximately a 2.3 per cent increase in slope was needed for a statistically significant increase. As shown in Table 3, all the Haynes-25 springs showed a significant increase in K while only a fraction of the Inconel-X springs increased significantly.

The effects of the exposure conditions on the free length of the springs subjected to the short-time exposure are shown in Table 4. The long-time-irradiated springs were not examined for free-length changes. As can be seen from Table 4, the result of the exposure decreased the free lengths of the springs in the order of 2 per cent.

[3] Numbers in brackets designate References at end of paper.

The crush tests to solid height on each spring from both irradiations were repeated three times for each spring, and the subsequent examination under 10 to 15 × magnification of the inside and outside of all the active spring coils failed to reveal any incipient cracks. Each spring was examined by two observers before the foregoing conclusions were reached. Examination was made difficult by the presence of longitudinal drawing marks on some of the spring wires, but by suitable manipulation of lighting it was possible to conclude that no cracks were associated with these drawing marks.

These four tests, free-length change, load-deflection curves, crush tests, and visual examination comprised the examination of the springs. No effects were found as a result of irradiation in high-temperature water that could be considered harmful from an engineering aspect.

The results at room temperature of the three-point loaded bend tests on Inconel-X and Haynes-25 rods are given in Figs. 6 and 7. Three figures show that the effect of the irradiation-imposed conditions on the plastic behavior in bending for these materials is slight. The apparatus used was not sensitive enough to detect any differences in the elastic modulus.

Hardness results were statistically analyzed and are shown in Table 5. For the short-term irradiation, a statistically significant decrease in hardness was noted for the Inconel X while the Haynes 25 remained unchanged. For the long-term irradiations, both hardnesses decreased by a small but statistically significant amount. The Inconel X did not decrease in hardness to as large an extent as in the short-term irradiation. For practical engineering purposes, it should be noted that these hardness changes, although statistically significant, are quite small and are probably unimportant.

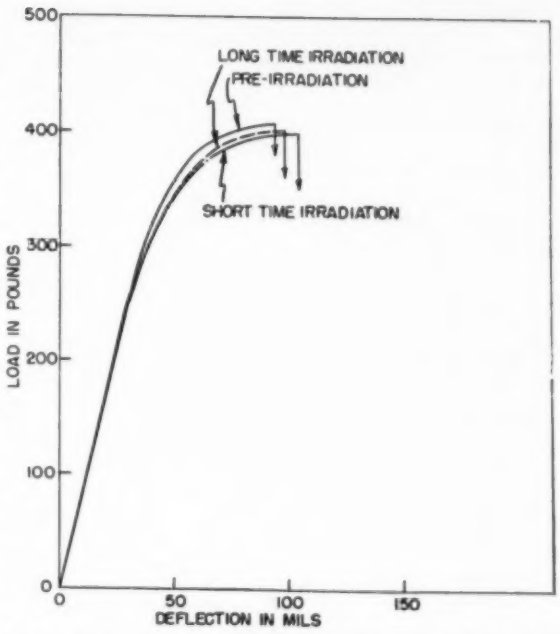

Fig. 6 Free-beam bead tests of 0.160-in-diam Haynes-25 rods before and after irradiation. Rods were loaded as a simple three-point beam over a $1^1/_2$-in. span.

Table 3 Results of load-deflection tests for irradiated Haynes-25 and Inconel-X springs

Irradiation test	Material	Number	Preirradiation K^a	Preirradiation N^b	Postirradiation K^a	Postirradiation N^b	Increase, per cent
Short-time test	Haynes 25	B-1	0.0710	16	0.0758	21	6.4[c]
(5.9×10^{18} *nvt* fast)	Haynes 25	B-4	0.0708	15	0.0757	16	5.3
	Haynes 25	B-7	0.0716	15	0.0739	20	3.2
	Average		0.0711	46	0.0748	57	5.0
	Inconel X	T-3	0.0592	16	0.0617	14	4.1
	Inconel X	T-4	0.0581	16	0.0591	15	1.8[d]
	Inconel X	T-6	0.0574	16	0.0586	15	2.1
	Average		0.0582	48	0.0598	44	2.7
Long-time test	Haynes 25	B-2	0.0703	16	0.0765	18	8.1
(4.2×10^{19} *nvt* fast)	Haynes 25	B-8	0.0697	16	0.0761	18	8.4
	Haynes 25	B-9	0.0693	16	0.0757	18	8.4
	Average		0.0698	48	0.0761	54	8.3
	Inconel X	T-1	0.0566	16	0.0572	18	1.1
	Inconel X	T-2	0.0576	15	0.0697	18	5.1
	Inconel X	T-8	0.0576	16	0.0593	18	2.9
	Average		0.0573	47	0.0591	54	3.0

[a] Slope of load-deflection curve in lb per in., each entry represents three separate tests.
[b] Total number of observations to obtain a particular slope.
[c] Difference statistically significant, 5 per cent level, by covariance analysis.
[d] Difference not statistically significant, 5 per cent level, by covariance analysis.

Table 4 Free-length change of irradiated Haynes-25 and Inconel-X springs (short-time irradiation)

Material	Spring no.	Preirradiation free length, in.	Postirradiation free length, in.	Change, per cent
Haynes 25	B-1	2.234	2.172	−2.78
	B-4	2.219	2.172	−2.12
	B-7	2.234	2.172	−2.78
Inconel X	T-3	2.359	2.297	−2.63
	T-4	2.406	2.359	−1.95
	T-6	2.344	2.297	−2.01

Postirradiation photographs of transverse sections of Haynes-25 and Inconel-X rods from the long-term irradiation are shown in Figs. 8 and 9. As expected, no discernible difference was found between preirradiation and postirradiation metallographic structures.

Discussion

The most interesting phenomenon observed in this investigation was the increase noted in the load-deflection slopes after

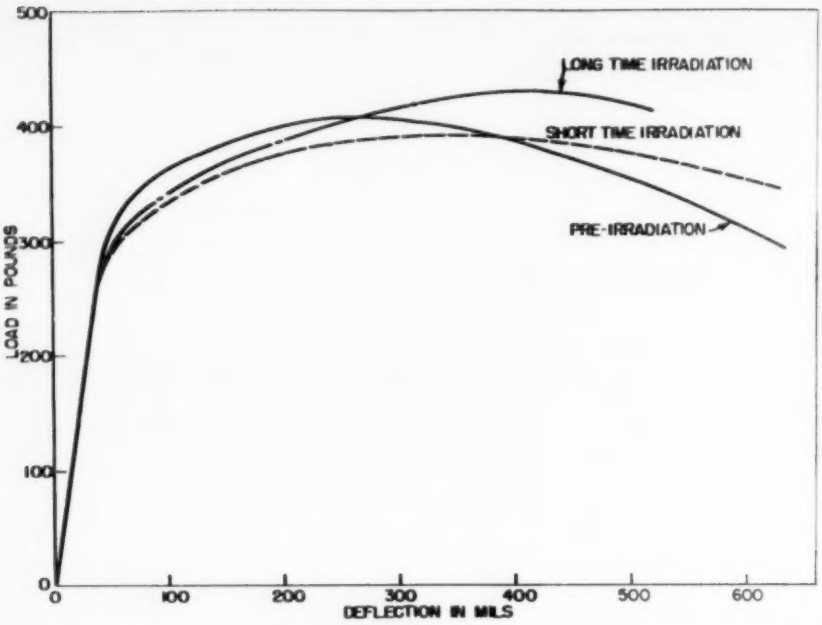

Fig. 7 Free-beam bend tests of 0.160-in-diam Inconel-X rods before and after irradiation. Rods were loaded as a simple three-point beam over a $1^1/_2$-in. span.

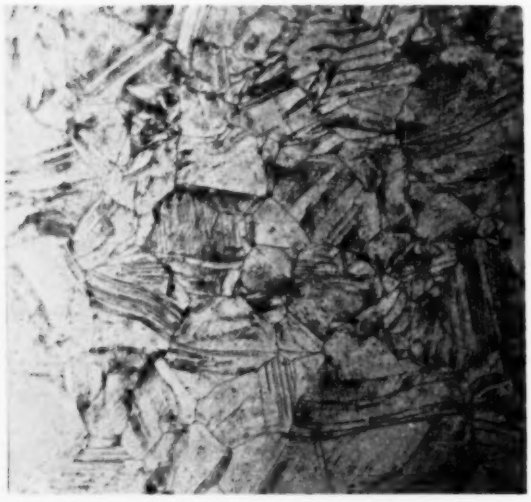

Fig. 8 Photomicrograph of Haynes-25 wire after long-time exposure in the high-pressure water loop. Etch: aqua regia; 100 X.

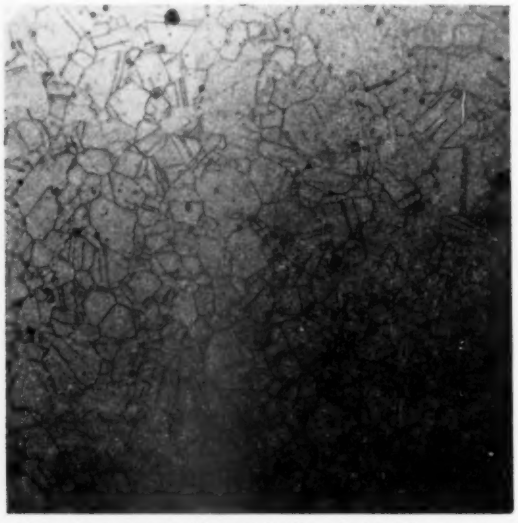

Fig. 9 Photomicrograph of Inconel-X wire after long-time exposure in the high-pressure water loop. Etch: aqua regia; cupric chloride; 100 X.

Table 5 Hardness values of irradiated Haynes 25 and Inconel X

Material	Irradiation	Rockwell-A hardness — Preirradiation			Rockwell-A hardness — Postirradiation			Significant difference (5 per cent level of significance)
		X[a]	N[b]	S[c]	X[a]	S[b]	S[c]	
Haynes 25	Short-time	71.1	14	1.44	70.3	12	0.771	No
Inconel X	Short-time	68.1	7	0.476	64.8	12	2.63	Yes
Haynes 25	Long-time	71.1	14	1.44	69.5	8	0.669	Yes
Inconel X	Long-time	68.1	7	0.476	66.1	7	0.996	Yes

[a] Arithmetic average of observations.
[b] Number of observations.
[c] Standard deviation.

irradiation. This result was unexpected and in direct contradiction to the results reported [2] by Zeno on Inconel, Inconel X, and type 302 stainless-steel compression springs irradiated at 572 F. Zeno showed a 9.3 per cent decrease in slope for Inconel X and a decrease in free length of approximately 6.0 per cent in.

In the results of this investigation, the observed increase in slope might have been caused by either geometrical or material changes. A brief consideration of these various factors will now be presented.

In the simple theory (pitch angles neglected) the expression for the spring constant is

$$K = \frac{d^4 G}{64 n r^3} \tag{1}$$

To account for the observed increase of K either the numerator of equation (1) must increase, the denominator decrease, or a combination of the two must occur. It is difficult to visualize either d or r changing because of any exposure-induced phenomena, especially in the direction necessary.

The number of active turns, n, was for a time suspected as the culprit in increasing the spring constant. To check this supposition, a Haynes-25 spring was loaded under identical conditions to the irradiation springs and exposed in helium at 600 F for 1164 hr. No change was noted in the number of active turns. The other results of this test were:

Increase in spring constant, per cent	0.94
Decrease in free length, per cent	0.64
Loss in load (at 23 lb), per cent	3.45

As can be seen, this check experiment showed results similar to those noted on the irradiation springs, only to a slighter extent. The effect did not seem to be caused by a change in the number of active coils, that is, there was no rotation of the ends of the springs with respect to each other about the longitudinal axis. It appears that the number of active turns does not change appreciably under these conditions.

Unfortunately, it was not possible to directly measure the active turns of the irradiated springs. The results of the preceding experiment indicate that a change in n does not occur. It is possible, however, that the different exposure conditions of the irradiated springs accelerated creep-relaxation effects at the spring ends and thus decreased the number of active turns.

To complete the survey of possible geometrical changes, the more exact theory for open-coiled helical springs with ends fixed against rotation (the probable condition in this experiment because of the friction between the ends and supporting plates) was considered. The equation for the deflection can be shown to be

$$\delta = \psi_1' \frac{64 P r_0^3 n}{G d^4} \tag{2}$$

where

$$\psi_1' = \frac{\sin \alpha - \sin \alpha_0}{\cos^2 \alpha_0 \sin \alpha - \sin \alpha_0 + \dfrac{EI}{GI_p} \tan \alpha \, (\cos \alpha_0 - \cos \alpha)} \tag{3}$$

The values of ψ_1' are shown graphically by Wahl [3] for various pitch angles. From this plot or from equation (3) it can be seen that ψ_1' will decrease with decreasing pitch angle for springs in compression.

For the springs under consideration the pitch angle was approximately 11 deg. From the observed decrease in free length (for the 324-hr irradiation) it can be estimated that the pitch angle may decrease about 1 deg to an approximate final value of 10 deg. From these values it can be estimated that the spring constant K will increase about 0.5 per cent because of the change in ψ_1'. This is a factor of 10 less than that observed in the irradiation springs.

From the preceding discussion it can be seen that geometrical changes do not seem sufficient to account for the increase in the spring constant. There is, however, a possibility of changes occurring in the shear modulus G. It is possible for the shear modulus to be reduced approximately 5 per cent because of overstraining [3]. This loss can be recovered by low-temperature heat treatments. Timoshenko [4], quoting work performed by I. Muir in 1899, also notes the decrease in elastic properties after cold work and the subsequent recovery with low-temperature annealing.

Unfortunately, it is not possible to assign this cause definitely as the reason for the observed increase in spring constant. This is because it cannot be definitely stated whether or not the springs were heat set in the manufacturing procedure. If they were heat set it seems probable that any increase in shear modulus would take place in the heat-setting operation and not subsequently because of in-pile temperature effects. Conversely, if they were not heat set, the possible increase in shear modulus caused by in-pile temperature effects provides an attractive explanation for the experimental results.

There is a slight possibility that the neutron bombardment in some obscure way may change the elastic constants. This explanation is not considered very probable in view of information [5] showing that elastic properties are substantially unaffected by pile irradiations at ambient temperatures. However, the possibility exists that material and exposure conditions interact in some complex fashion to produce the observed increase in spring constant.

This discussion shows that the observed increase in spring constant is difficult to rationalize. It is felt, however, that this effect is not serious from the engineering standpoint. Both spring materials displayed negative changes in free length that may perhaps have been accelerated by the exposure conditions as shown by the one Haynes-25 comparison spring exposed to temperature alone. Zeno [2] felt such an effect was operative; however, these changes in free length do not seem excessive.

The effect of radiation on the plastic-flow curve is shown quite well in the three-point loaded bend tests in Figs. 6 and 7. The effect on the plastic-flow curve is quite small and it can be inferred that radiation damage at 560 to 600 F under the experimental conditions of this investigation has little effect on mechanical properties. This statement is also borne out by the hardness results which did not display the usual increase after irradiation but rather decreased, probably because surface effects on the metal outweighed any tendency for radiation hardening.

Conclusions

Haynes-Stellite-Alloy-25 and Inconel-X springs irradiated in the compressed condition between 560 and 600 F in water showed no serious harmful effects caused by the exposure conditions as revealed by postirradiation testing. The spring constant increased for both materials as a result of the exposure conditions, the maximum change being about 8 per cent for Haynes 25 and 5 per cent for Inconel X. The reason for this increase is not clear but may be attributed to changes in the elastic constants.

No cracks or defects were found on the surfaces, either inside or outside, as a result of the exposure conditions. Testing to solid height did not result in any failure detectable by visual examination.

The effect of radiation damage was slight as revealed by three-point loaded bend tests on 0.160-in-diam rods of Haynes 25 and Inconel X. This conclusion is verified by observed decreases in Rockwell hardness instead of the increases usually noted in radiation-damage experiments.

Acknowledgment

An investigation involving pile irradiations is necessarily dependent on the efforts of many people. Without the help of various personnel in the KAPL Radioactive Materials Laboratory this experiment could not have been conducted.

The assistance of F. W. Wiesinger in conducting the many load-deflection tests for the preirradiation-property determinations and his assistance in postirradiation testing and data reduction is appreciated.

References

1 W. D. Valovage and G. L. Cutler, "Remotely Operable Bend Test Apparatus," Fifth Hot Laboratory and Equipment Conference, Philadelphia, Pa., March, 1957.

2 R. S. Zeno, unpublished data, January, 1951.

3 A. M. Wahl, "Mechanical Springs," Penton Publishing Company, Cleveland, Ohio, 1944, p. 64.

4 S. Timoshenko, "Strength of Materials, Part 2," D. Van Nostrand Company, Inc., Princeton, N. J., 1956, p. 423.

5 J. W. Glen, "A Survey of Irradiation Effects in Metals," *Advances in Physics*, vol. 4, October, 1955, p. 424.

6 These formulas may be found in Wahl, reference [3], equation (16), and p. 47, equation (48).

APPENDIX

From the theory of elasticity, the following formulas may be derived [6]:

$$\tau_{max} = \frac{16Pr}{\pi d^3}\left[\frac{4c-1}{4c-4} + \frac{0.615}{c}\right] \tag{4}$$

and

$$\delta = \frac{64nPr^3}{d^4G}\left[\frac{1}{1+\frac{3}{16}\frac{1}{c^3-1}}\right] \tag{5}$$

The term in brackets in equation (5) is essentially equal to one for the present spring geometry and may be neglected.

For each spring an experimental load-deflection curve was determined. The slope of this curve is equal to the spring constant and, from equation (5), we obtain

$$\frac{P}{\delta} = K = \frac{d^4G}{64\,nr^3} \tag{6}$$

From equation (4) the load necessary to produce any desired shear stress (80,000 psi in this case) may be found.

$$P = \tau_{max}\frac{\pi d^3}{16r}\frac{1}{\frac{4c-1}{4c-4}+\frac{0.615}{c}} \tag{7}$$

By knowing experimentally the K value, equation (6), and substituting in equation (6) the calculated load P from equation (7), the deflection necessary to obtain a stress of 80,000 psi is found. The springs were compressed to this value in the irradiation assembly.

R. C. DRUTOWSKI

Research Laboratories,
General Motors Corporation,
Detroit, Mich.

Energy Losses of Balls Rolling on Plates

The apparatus for measuring the rolling force of a ball supported between two plates is described. The rolling force is an extremely small quantity compared to the normal force. Instantaneous values of the rolling force vary greatly from point to point on the sample surface and this variation is explained in terms of surface roughness and material homogeneity. The energy losses of balls rolling on plates are shown as functions of load, material, and surface roughness. The rolling of a ball on a plate is examined as a cyclic process in which elastic hysteresis losses appear to be the primary source of energy dissipation. An analysis involving the Hertzian contact stress field is used to derive an equation relating the rolling force and the material damping capacity.

THE PROBLEM of the rolling ball at first examination appears to be no problem at all. After all, "nothing rolls like a ball" and ball bearings are accepted without question as very low friction devices. Because of this low friction, a great deal of ball-bearing development has been mainly concerned with the life of the bearing. For most ball bearings, if the life is long under a given speed and load, the bearing is considered satisfactory.

However, for the class of ball bearings known as instrument ball bearings, friction torque is of importance. For many applications, both a low starting torque and a low running torque are desirable. The work on the energy losses during rolling was started with the purpose of generating information which might lead to the minimizing of the friction torque of these instrument ball bearings.

The variables affecting the friction torque of a ball bearing may be divided into two groups. In the first group are those variables affecting the rolling itself, such as ball and race materials, surface finish, and contact stress. The second group includes additional variables inherent in the assembled ball bearing such as those resulting from ball-separator design and the degree of fit of the parts. Our work is concerned with the first group of variables and for simplicity we have adopted the experimental arrangement of a ball rolling between flat plates.

In addition to its practical aspects, the problem of the rolling ball is an interesting one to pursue in the light of the information it may give on the way energy is lost during rolling. The rolling of a ball is a cyclic process since the stress field resulting from the ball contact moves with the ball. Relating the energy losses to this cyclic stressing may eventually increase our understanding of the inelastic behavior of materials.

Historically, the problem of the freely rolling ball, that is, one under almost no tangential traction, was not understood until a few years ago when Tabor published his work [1][1] on rolling friction. Prior to that time investigators tried to account for rolling friction in terms of surface interaction. Osborne Reynolds [2], in 1876, explained rolling friction in terms of microslip caused by differential elastic displacement in the contact area. Heathcote [3], in 1921, attributed the rolling friction of a ball in a groove to interfacial slip, the slip being caused by different parts of the contact area being different distances from the axis of rotation. Tomlinson [4], in 1929, proposed an explanation based on molecular adhesion. Tabor's experiments prove that none of these mechanisms is important except for Heathcote's and then only for balls in deep grooves. Tabor reached the conclusion that the energy required in rolling a ball on a plate is dissipated in hysteresis losses of the elastically strained metals. This conclusion is confirmed by the work done in this laboratory.

[1] Numbers in brackets designate References at end of paper.

Contributed by the Lubrication Division and presented at the Annual Meeting, New York, N. Y., November 30–December 5, 1958, of THE AMERICAN SOCIETY OF MECHANICAL ENGINEERS.

NOTE: Statements and opinions advanced in papers are to be understood as individual expressions of their authors and not those of the Society. Manuscript received at ASME Headquarters, September 10, 1958. Paper No. 58—A-190.

Test Apparatus and Procedure

As shown in Fig. 1, a ball of radius R is located between two flat parallel plates under a load N. To overcome the resistance to rolling at the contact areas of the ball and the plates, a torque must act on the ball. Assuming deformation of ball and plates is negligible, this torque is the force F times the diameter $2R$ of the ball. The frictional work for an advance s of the ball on the plates is then $2FR$ times the angular displacement of the ball s/R in radians. With identical plates this frictional work $2Fs$ is evenly divided between the two contact areas.

The rolling-friction force is an extremely small quantity compared to the normal force and the rolling test apparatus had to be designed so that the normal force acting vertically did not interfere with the measurement of the small friction force acting horizontally. To accomplish this the bottom plate is supported on a high-pressure film of oil. This oil film supports the load while offering practically no resistance (at the low shear rates encountered) to the lateral movement of the plate in response to the rolling-friction force.

The rolling-friction test apparatus is shown in Fig. 2. The lower sample plate is located in a holder which is bolted to a support plate. The support plate rests on four $^3/_8$-in. $\times$ $1^1/_8$-in. oil pads, one at each corner. The cutaway portion of the figure shows the interface at which the high-pressure oil film is maintained. To measure the rolling force, an elastic restraint in the form of two parallel beams is placed on the lower plate holder. The figure shows one of the rolling-force beams. The second beam is located at the other end of the plate holder. One end of each beam is fastened to the holder while the other end is fixed to the oil-pad housing. A parallel beam arrangement was chosen to restrict rotation of the plate when displacement occurs. Deflection of the sample, which is proportional to the acting friction force, is measured by means of strain gages mounted on the beams.

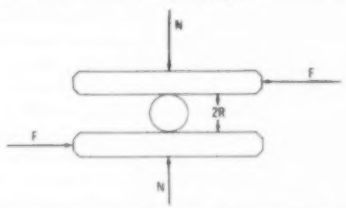

Fig. 1 Experimental arrangement of rolling-friction samples

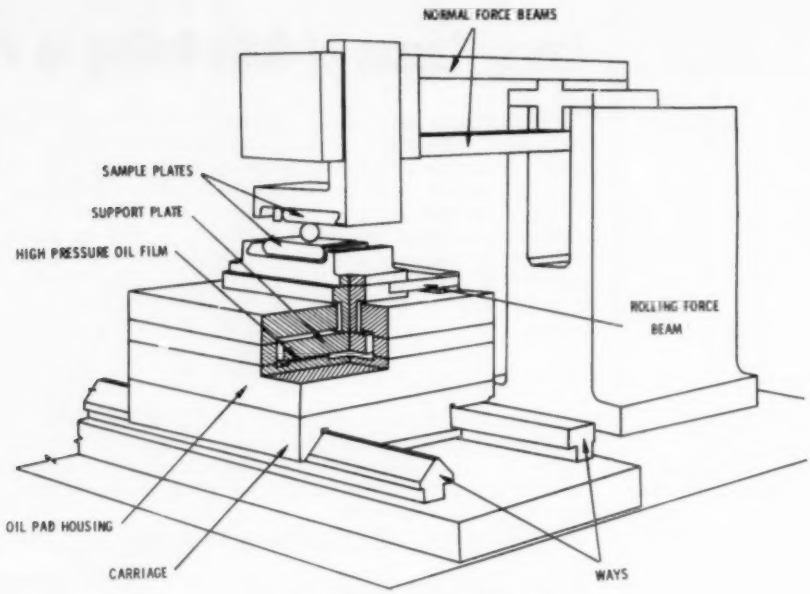

Fig. 2 Rolling-friction test apparatus

The signal from the strain gages is amplified and fed into an oscillograph.

The upper plate is attached securely to the free end of a much stiffer pair of parallel beams. The vertical deflection of this upper plate when contact is established between the ball and the plates determines the normal loading. Strain gages mounted on these beams feed another channel of the oscillograph and give a continuous indication of the normal load during the course of a run.

Rolling of the ball between the plates is maintained by attaching the oil-pad housing to a carriage which is moved along straight ways by a hydraulic ram (not shown). The upper plate is stationary. The velocity of the carriage can be varied from 0.0001 to 1 ips. and is controlled in either direction. The ball center moves at an average speed of half the speed of the carriage. While the carriage and oil-pad housing are moved uniformly the motion of the lower sample plate, which is elastically connected to the oil-pad housing, is continuously modified by the action of the friction force. The difference in the displacement of the oil-pad housing and the plate sample is proportional to the acting friction force and is measured.

A rolling-friction run consists of rolling the ball back and forth over the same track many times. Because of the sensitivity of the friction-force measurement and the large normal loads employed, small geometrical deviations of the ball from a perfect sphere or the plates from perfect parallel planes cause a horizontal component of the normal force to be added to the actual rolling force. To eliminate these geometrical force components, the determination of the average rolling resistance is based on two passes, one in each direction. Reversing the direction of rolling reverses the direction of the true rolling force, but does not affect the direction of the geometrical force components. Thus the difference between the average recorded friction force for forward and reverse rolling is equal to twice the true rolling force. Instantaneous values of the measured force during the run, however, still will include these geometrical misalignment components.

The reproduction of an actual friction trace in Fig. 3 shows the great variation in the friction force. This trace was obtained for the rolling of a smooth $^1/_2$-in-diam hardened-steel ball on a

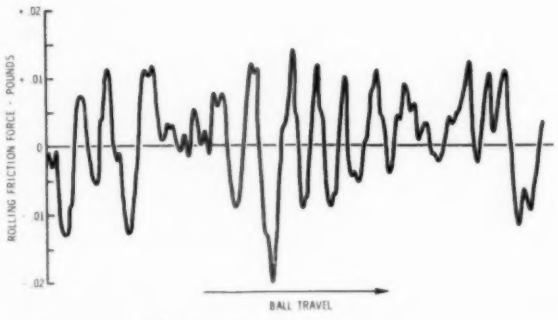

Fig. 3 Rolling-friction force trace

hardened-steel surface of 15-microin. roughness over a distance of approximately 2 in. Rolling was perpendicular to the lay, i.e., perpendicular to the direction of the surface scratches, at a load of 36 lb. The reproduced trace is a portion of the run for which an average rolling-friction force of 0.0021 lb was calculated. The great variation in the friction trace is due primarily to the roughness of the plates and the peaks are many times greater than the average value of the friction force. The number and size of these peaks define the force necessary to start rolling at any point on the sample surface and thus they are analogous to starting-torque values for ball bearings.

For the first pass of a ball on new plates the friction force is greater than for succeeding passes over the same track. Fig. 4 contains the reproductions of the friction traces for passes in the same direction over the same portion of the track. Most of the reduction in the rolling force occurs between the 1st and 3rd passes while any subsequent reduction is slight. The larger friction value for the beginning passes represents the work of plastic deformation in addition to the rolling work. After the surfaces become sufficiently deformed to carry the load, equilibrium conditions are reached and further deformations are all elastic. The results of this plastic work are plainly evident under large loads because a groove is actually formed in the plates. However, even

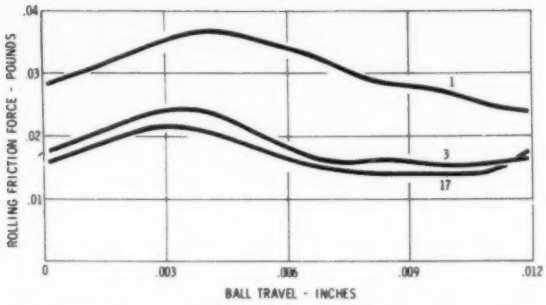

Fig. 4 Rolling-friction force as a function of number of passes

for light loads where no apparent plastic deformation occurs this larger force for the beginning passes is observed. For hardened steel, equilibrium values of the rolling force are usually reached after just a few passes. Unless otherwise noted the equilibrium value is used in this paper.

Variation of Sample Material

Friction versus load curves for monel, cemented carbide, stainless steel, and chrome-alloy-steel balls rolling on hardened 52100 steel plates are shown in Fig. 5. The average rolling-friction forces plotted in this figure are the equilibrium values obtained after plastic deformation has ceased. All plates were hardened to a value of Rc 50 and were unidirectionally abraded on emery paper to a roughness of 15 microin. The balls were all $^1/_2$-in-diam and had a surface roughness of less than 1 microin. The balls were rolled perpendicular to the surface lay of the plates at an angular velocity of 0.12 radians per sec. The curves reflect material properties such as modulus of elasticity, hardness, and elastic hysteresis of the samples. The modulii of elasticity of the ball and plate affect the magnitude of the contact stress for a given load. The hardness determines the amount of plastic deformation at a given load before equilibrium rolling is established. For the Monel ball, plastic deformation starts at the lowest load employed so that the whole curve represents rolling at contact stresses which cause plastic deformation. For the cemented-carbide ball, plastic deformation starts at a load of approximately 30 lb so that the lower half of the curve represents elastic rolling while the upper half represents plastic deformation. For the stainless-steel ball and the chrome-steel ball, plastic deformation starts at approximately 60 lb so that almost the entire curve is for elastic rolling. The curve for the stainless-steel ball is higher than that for the chrome-steel ball because of the higher elastic hysteresis of the stainless steel. From these curves it is apparent that the equilibrium rolling force increases rapidly once the contact stress becomes large enough to cause plastic deformation on initial rolling.

In each of the curves of Fig. 5 the rolling force is a monotonically increasing function of load. To check possible relationships between these two variables, the data for a $^1/_2$-in-diam cemented-carbide ball rolling on a polished 52100 steel plate (Rc 60) are plotted on logarithmic graph paper in Fig. 6. The data can be fitted by two straight lines indicating that for low loads the equilibrium rolling force increases as the 1.2 power of the load while for the higher loads the equilibrium rolling force increases as the 2.4 power of the load. For these particular samples, plastic deformation of the plate was observed at a load of approximately 30 lb. Thus the increase of the equilibrium rolling force with an increase in load is greater in the plastic region than in the elastic region. It is felt that the difference between these two regions is primarily a function of the increase in stress amplitude, and thus

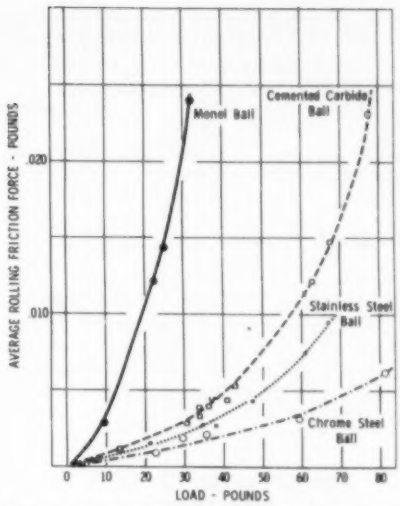

Fig. 5 Rolling force versus load curves for four 1/2-in-diam balls rolling on 52100 steel plates

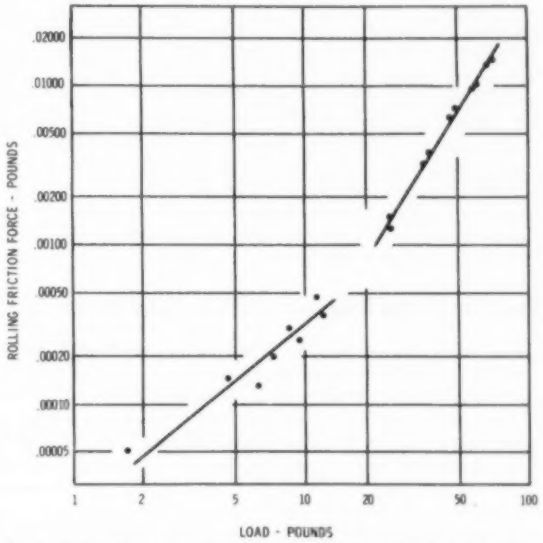

Fig. 6 Rolling force versus load for a cemented-carbide ball rolling on a hardened steel surface

of hysteresis, with load. The amount of plastic deformation even for the highest loads is very small and the groove thus formed is not sufficiently deep to bring into play slip of the Heathcote type.

For survey purposes, rough determinations of the equilibrium rolling force were made for a large number of plate materials. A $^1/_2$-in-diam ball of chrome-alloy steel (700 diamond pyramid hardness) at a load of 22 lb was used for all these tests. The plot of the equilibrium rolling force versus hardness of the plate material is given in Fig. 7. The following is a list of the plate materials used with the diamond-pyramid hardness values given in parentheses: Silver (40); copper (44); various bronzes (78, 87, 102, 111, 129, 143, 154, 258); 1045 steel (183, 267, 560, 616); 1095 steel (203, 310, 400, 530, 766); 52100 steel (190, 270, 630, 735, 790); titanium (235); s Monel (247, 312, 380); various tool steels (402, 760, 785, 804); tungsten (464); stainless steel (230, 760); and cemented carbide (900). While the scatter in the data is ap-

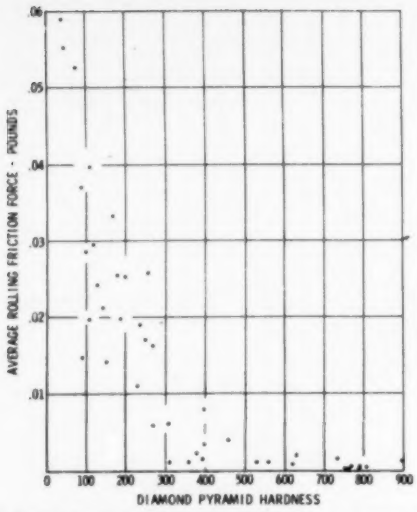

Fig. 7 Rolling friction versus plate hardness for a chrome-alloy-steel ball rolling at constant load on various plate materials

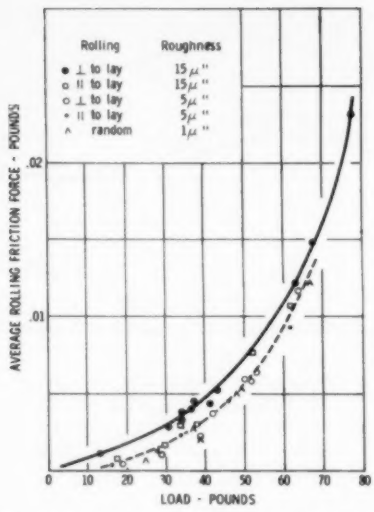

Fig. 8 Rolling friction versus load curves for varying plate roughness and orientation of lay

preciable two definite regions in Fig. 7 are discernible: For plate-hardness values of less than 300 DPH, the rolling friction is high and increases rapidly with decrease of hardness; and for plate-hardness values greater than 400 DPH, the rolling friction is low and is not affected greatly by changes in hardness. For plate hardness less than 300 DPH, the plates are plastically deformed on initial rolling which means high equilibrium rolling forces. The amount of plastic deformation increases as plate hardness decreases. For plate hardness greater than 400 DPH the rolling is elastic thus giving a low friction force dependent primarily on elastic hysteresis of the samples.

Variation of Plate Roughness and Orientation of Lay

Fig. 8 shows the equilibrium rolling force versus load curves for $^1/_2$-in-diam cemented-carbide balls rolling on hardened (50 Rc) plates of 52100 steel of varying roughness and orientation of lay. The plates were polished unidirectionally on varying grades of emery paper with the exception of the 1-microin. plate which was polished randomly on an abrasive-charged-cloth wheel. The ball roughness was less than 1 microin. Data for five combinations were obtained: Rolling perpendicular and parallel to the lay of the 15-microin. surface; rolling perpendicular and parallel to the lay of the 5-microin. surface; and, rolling on the 1-microin. surface which had a random orientation of the roughness. For loads less than about 60 lb, the data divide themselves between two curves, one for perpendicular rolling on the 15-microin. surface, and the other for rolling on the 5-microin. and 1-microin. surfaces; the values for rolling parallel to the lay on the 15-microin. surface fall between these two curves. For higher values of the load the indication is that the two curves become one.

While roughness and orientation of lay have only a small effect on the average rolling friction they have a greater effect on the size and number of rolling-friction peaks during a run. The rolling-friction peak histograms in Fig. 9 are for runs all made at about the same load (35 lb) on surfaces of varying roughness and orientation of lay. The histograms are graphical representations of the frequency distributions of the friction peaks measured with respect to the average of the trace. The histogram for rolling perpendicular to the lay of the 15-microin. surface covers the most area and is the broadest indicating the largest number of friction peaks per inch of rolling and the largest maximum peak (0.045 lb,

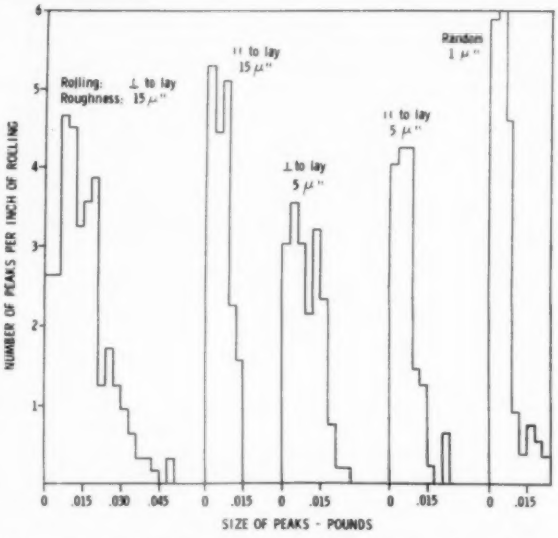

Fig. 9 Histograms of rolling-friction peaks of a cemented-carbide ball rolling at constant load on steel surfaces of varying roughness and orientation of lay

ten times the average friction force for this run). The average peak size is 0.015 lb. Next in order of decreasing average peak size is rolling perpendicular to the lay on the 5-microin. surface with a value of 0.009 lb. Parallel rolling on the 15-microin. surface and on the 5-microin. surface and rolling on the random polished 1-microin. surface all have an average peak value of about 0.006 lb. When rolling parallel to the lay of a rough surface, the ball effectively sees a much smoother surface than when rolling perpendicular to the lay.

Effect of Material Homogeneity

The appreciable number of friction peaks measured for even the smoothest steel surfaces may indicate that the friction peaks are not only due to geometrical irregularities but may be due

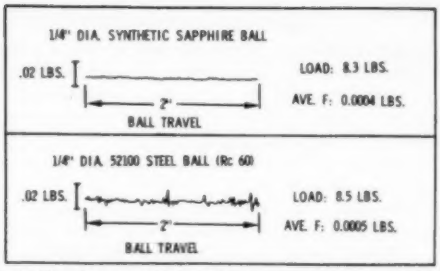

Fig. 10 Rolling-force recordings illustrating effect of material homogeneity

partly to the inhomogeneity of the samples themselves. To test this hypothesis, homogeneous samples of fused quartz and of synthetic sapphire were subjected to rolling tests. Fig. 10 shows the results. The top trace is for $^1/_4$-in-diam synthetic sapphire ball rolling between quartz plates while the bottom trace represents a $^1/_4$-in-diam hardened 52100 steel ball rolling between the same plates. The load and the average rolling force were approximately the same for both combinations. All the surfaces were equally highly polished so that if surface irregularities caused the variation in the rolling force for the steel ball they also should have caused the same variation for the synthetic sapphire. The fact that they did not is held as evidence that the inhomogeneous structure of the steel is the cause for the friction variations.

Relationship Between Rolling Force and Material Damping

The rolling of a sphere on a plate is a cyclic process. The stresses resulting from the contact of ball and plate are carried along with the moving contact. Elements of volume in the samples are cyclically stressed as the stress field passes through them. This cyclic stressing is accompanied by a hysteresis loss which appears to be the primary source of energy dissipation during rolling.

Fig. 11 shows the ball and plate in the vicinity of the contact area subdivided into blocks of thickness Δx, each bounded by the sample surfaces and by planes perpendicular to the direction of rolling. The strain energy stored in each of these blocks is a function of the contact pressure and the elastic constants of the material. The stored strain energy in the blocks in the ball V_1 and in the blocks in the plate V_2 is plotted as a function of the distance of each block from the center of the contact area. The exact shape of these curves is not known but the essential fact is that the strain energy is a maximum for the block at the center of the contact area. As the ball rolls a distance Δx the energy dissipated is Δx times the friction force F and the strain energy in the blocks is changed according to these curves. Effectively this energy change between blocks is equivalent to one block in the ball and one block in the plane being subjected to the cycle of zero strain energy to maximum strain energy to zero strain energy. By definition, the specific damping capacity is the ratio of the energy dissipated during a cycle to the maximum strain energy stored during the cycle. Thus the specific damping capacity for the rolling ball is

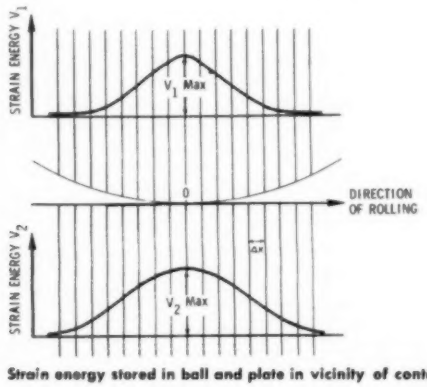

Fig. 11 Strain energy stored in ball and plate in vicinity of contact area

$$\mathrm{SDC} = \frac{F\Delta x}{V_{1\max} + V_{2\max}} \tag{1}$$

Since F is determined experimentally, all that is needed for calculation of the specific damping capacity is the value of $V_{\max}$ for ball and plate. Choosing a co-ordinate system with the origin at the center of the contact area, the x-axis extending in the direction of rolling, and the z-axis extending into the sample, the complete stress distribution in the y-z-plane for a sphere contacting a plane is given by Huber [5]:

$$\left.\begin{aligned}
\sigma_x &= q_0\left\{\frac{1-2\nu}{3}\frac{a^2}{y^2}\left[1-\left(\frac{z}{\sqrt{u}}\right)^3\right]\right. \\
&\quad \left.+\frac{z}{\sqrt{u}}\left[2\nu+\frac{(1-\nu)u}{a^2+u}-(1+\nu)\frac{\sqrt{u}}{a}\tan^{-1}\frac{a}{\sqrt{u}}\right]\right\} \\
\sigma_y &= -q_0\left\{\frac{1-2\nu}{3}\frac{a^2}{y^2}\left[1-\left(\frac{z}{\sqrt{u}}\right)^3\right]\right. \\
&\quad +\left(\frac{z}{\sqrt{u}}\right)^3\frac{a^2u}{u^2+a^2Z^2}+\frac{z}{\sqrt{u}}\left[\frac{(1-\nu)u}{a^2+u}\right. \\
&\quad \left.\left.+(1+\nu)\frac{\sqrt{u}}{a}\tan^{-1}\frac{a}{\sqrt{u}}-2\right]\right\} \\
\sigma_z &= q_0\left(\frac{z}{\sqrt{u}}\right)^3\frac{a^2u}{u^2+a^2z^2} \\
\tau_{yz} &= q_0\frac{yz^2}{u^2+a^2z^2}\frac{a^2\sqrt{u}}{a^2+u}
\end{aligned}\right\} \tag{2}$$

where u is defined by the equation

$$\frac{y^2}{a^2+u}+\frac{z^2}{u}=1 \tag{3}$$

and

$$q_0 = \frac{3}{2}\frac{P}{\pi a^2} \tag{4}$$

P is the force pressing the sphere against the plane, a is the radius of the circular contact area, ν is Poisson's ratio, and E is Young's modulus. The strain energy in the element of volume,

$$\Delta x\left(\int_0^\infty\int_{-\infty}^{\infty} dydz\right)_{x=0}$$

is $V_{\max}$ and is given by

$$V_{\max} = \frac{\Delta x}{E}\int_0^\infty\int_{-\infty}^{\infty}\left[\frac{1}{2}(\sigma_x^2+\sigma_y^2+\sigma_z^2)\right. \\ \left.-\nu(\sigma_x\sigma_y+\sigma_y\sigma_z+\sigma_z\sigma_x)+(1+\nu)\tau_{yz}^2\right]dydz \tag{5}$$

Assuming $\nu = 0.3$ and substituting equations (2) and (4) in equation (5) the resulting double integral was evaluated by numerical integration on an IBM 701 electronic computer giving the following answer:[2]

[2] This differs from the value used by Tabor (*British Journal of Applied Physics*, vol. 6, 1955, p. 79) for the elastic work involved in rolling. For a Poisson's ratio of 0.3 Tabor's value for the constant is 0.256.

Table 1 Specific damping capacities calculated from rolling-friction data

Material	SDC per cent
52100 steel (Rc 60)	0.7
1020 steel (Rb 80)	2.8
MnCu Alloy (Rb 70)	14.9

$$V_{max} = 0.1315 \frac{P^2}{a^2 E} \Delta x \tag{6}$$

Equation (1) for the specific damping capacity thus becomes

$$\text{SDC} = \frac{F}{0.1315 \frac{P^2}{a^2} \left(\frac{1}{E_1} + \frac{1}{E_2} \right)} \tag{7}$$

where E_1 and E_2 are, respectively, the Young's moduli for ball and plate. Equation (7) is only applicable for values of the load which do not cause any plastic deformation. When plastic deformation does occur the geometry is no longer a sphere contacting a flat plate and equations (2) are no longer valid. Table 1 shows the specific damping capacities for three different materials, determined from rolling tests made at a mean compressive contact stress of 55,000 psi. The values calculated for 52100 steel and 1020 steel agree roughly with accepted specific damping capacities for alloy and mild steels determined from other tests. The agreement is not exact because the stress distribution for the rolling ball is different from that employed in the usual tests, and the SDC is known to depend on actual test configuration [6]. The high rolling force measured for the MnCu alloy with the consequent high SDC of 14.9 per cent is also to be expected. The MnCu is a special alloy developed at the U. S. Bureau of Mines [7] with an unusually high damping capacity.

Conclusions

1 The hypothesis that the energy lost in rolling a ball on a plate is dissipated in hysteresis losses of the elastic strained metals is confirmed by our experimental results. Rolling-energy measurements can be translated into material hysteresis losses giving reasonable specific damping capacities.

2 The average rolling force is not very dependent on surface roughness and orientation of lay.

3 The frequency distribution of rolling-force peaks is a function of surface roughness, orientation of lay, and material homogeneity. These peaks are many times larger than the average rolling force.

4 The equilibrium rolling force increases more rapidly with load in the range where plastic deformation occurs than it does in the load range where only elastic rolling occurs.

References

1 D. Tabor, "The Mechanism of Rolling Friction—II The Elastic Range," *Proceedings of the Royal Society*, series A, vol. 229, 1955, pp. 198–220.

2 O. Reynolds, "On Rolling Friction," *Transactions of the Royal Society*, vol. 166, 1876, pp. 155–174.

3 H. L. Heathcote, "The Ball Bearing: In the Making, Under Test and on Service," *Proc. Institution of Automotive Engineers*, vol. 15, 1921, pp. 569–662.

4 G. A. Tomlinson, "A Molecular Theory of Friction," *Philosophical Magazine*, vol. 7, 1929, pp. 905–939.

5 M. T. Huber, "Zur Theorie der Berükrung Fester Elastischer Körper," *Annalen der Physik*, vol. 14, 1904, pp. 153–163.

6 A. M. Freudenthal, "The Inelastic Behavior of Engineering Materials and Structures," John Wiley & Sons, Inc., New York, N. Y., 1950, p. 326.

7 J. W. Jensen and J. A. Rowland, Jr., "Manganese-Copper High-Damping Alloys," *Product Engineering*, vol. 27, May, 1956, pp. 135–137.

On the Effect of Lubricant Inertia in the Theory of Hydrodynamic Lubrication

A. A. MILNE

Department of Scientific and Industrial Research, Mechanical Engineering Research Laboratory, Thorntonhall, Glasgow, Scotland

A theoretical study is made of the corrections required to the basic lubrication equations to allow for small effects of lubricant inertia in the laminar regime. The problem is approached by first determining the stream function for a wedge-shaped oil film with purely viscous flow and then obtaining the first-order correction for inertia. For the particular case when the convergence of the film is small, the resulting expressions for pressure gradient and tangential drag are compared with those obtained by other methods. Close agreement is found with Kahlert's equations, but the present expressions are more general in form. It would appear that, in general, the effect of lubricant inertia is to cause a slight increase in the load capacity of a bearing.

In the classical theory of hydrodynamic lubrication it is assumed that the effect of lubricant inertia is small compared with that of lubricant viscosity. The relative magnitude of the various terms in the equations of motion has been examined by Kahlert [1],[1] among others, and it may be shown that the ratio of the inertia to the viscous terms is of the order of magnitude of $(\rho U h^2/\eta L)$, where U is the bearing surface velocity, h is the representative film thickness, and L is the representative bearing length. Insertion of typical values shows that in most applications of hydrodynamic lubrication theory the inertia effect is indeed negligible, but with current trends toward higher operating speeds and the use of lower-viscosity fluids the effect is likely to become of increasing importance; in recent work there are even suggestions that turbulent conditions have been encountered [2, 3]. This paper is concerned with some theoretical considerations of the probable influence of inertia upon bearing performance under conditions in which the lubricant inertia has a significant effect but the flow is still laminar.

In previous treatments it has been assumed *ab initio* that the lubricant film is very thin. Under such conditions Slezkin and Targ [4] suggested that the inertia effect might be averaged across the film; a modified form of Reynolds equation is then readily obtained for steady conditions and this has been partially integrated by Osterle, Chou, and Saibel [5]. It is interesting to note that a similar expression may be obtained by a slight modification of boundary-layer theory [6]. These methods, while of interest, involve the rather dubious assumption of a parabolic velocity profile in the lubricant film and lead to appreciably different estimates of the inertia correction from that obtained by Kahlert [1] in a more satisfactory treatment. Kahlert used an iteration procedure for examining the influence of inertia upon the velocity distribution and studied the effect upon performance of both the slider and the journal bearing in some detail. Ladanyi [7] studied the influence of bearing-surface acceleration but ignored effects caused by variations in particle velocity within the film.

The present paper approaches the problem from a different starting point. It has been shown previously [8] that certain aspects of the theory of hydrodynamic lubrication can be discussed in terms of a two-dimensional stream function; this approach does not depend upon the classical initial assumption of a thin film. When purely viscous effects are under consideration the stream function must satisfy the biharmonic equation and the given boundary conditions; the particular case of a wedge-shaped oil film has been treated in some detail [8] while the film between eccentric cylinders has been discussed by Wannier [9]. An exact solution for the stream function when the inertia terms are retained appears unlikely to be obtained for the geometrical configurations of practical interest. The method to be adopted, therefore, follows that described by Anzelius [10] in which a series form of the stream function is assumed, the sequence of terms in descending powers of the kinematic viscosity representing successive approximations for the inertia correction. In the problems investigated by Anzelius the convergence appeared to be acceptable. On the assumption that the inertia effect is relatively small the first two terms of the stream function for a wedge-shaped oil film will be derived. For the particular case when the convergence is small the resulting expressions for pressure gradient and frictional drag will be compared with those obtained by other methods.

Theory

It will be assumed that the fluid is incompressible, that the viscosity is constant, that there are no extraneous forces, and that the motion is steady. Under these conditions the differential equations of motion of a fluid in two dimensions are [11]

$$\left.\begin{aligned} \rho\left(\frac{u\partial u}{\partial r}+\frac{v\partial u}{r\partial\theta}-\frac{v^2}{r}\right) &= -\frac{\partial p}{\partial r}-\frac{\eta\partial}{r\partial\theta}\left(\frac{\partial v}{\partial r}+\frac{v}{r}-\frac{\partial u}{r\partial\theta}\right) \\ \rho\left(\frac{u\partial v}{\partial r}+\frac{v\partial v}{r\partial\theta}+\frac{uv}{r}\right) &= -\frac{\partial p}{r\partial\theta}+\frac{\eta\partial}{\partial r}\left(\frac{\partial v}{\partial r}+\frac{v}{r}-\frac{\partial u}{r\partial\theta}\right) \end{aligned}\right\} \quad (1)$$

where ρ is the density of the fluid and η is the viscosity. Introducing a stream function ψ such that

$$u=-\frac{1}{r}\frac{\partial\psi}{\partial\theta},\quad v=\frac{\partial\psi}{\partial r} \quad (2)$$

[1] Numbers in brackets designate References at end of paper.

Contributed by the Lubrication Division and presented at the Annual Meeting, New York, N. Y., November 30–December 5, 1958, of The American Society of Mechanical Engineers.

Note: Statements and opinions advanced in papers are to be understood as individual expressions of their authors and not those of the Society. Manuscript received at ASME Headquarters, September 3, 1958. Paper No. 58—A-195.

and eliminating the pressure gives the following equation for ψ:

$$\eta\nabla^4\psi = \frac{\rho}{r}\left(\frac{\partial\psi}{\partial r}\frac{\partial\nabla^2\psi}{\partial\theta} - \frac{\partial\psi}{\partial\theta}\frac{\partial\nabla^2\psi}{\partial r}\right) \tag{3}$$

Following Anzelius [10] the stream function may be considered as a series in the form

$$\psi = \psi_0 + \left(\frac{\rho}{\eta}\right)\psi_1 + \left(\frac{\rho}{\eta}\right)^2\psi_2 \ldots\ldots \left(\frac{\rho}{\eta}\right)^k\psi_k \tag{4}$$

where

$$\left.\begin{aligned} &\nabla^4\psi_0 = 0 \\ \text{and}\quad &\nabla^4\psi_{k+1} = \left(\frac{1}{r}\right)\sum_{m+n=k}\left(\frac{\partial\psi_m}{\partial r}\frac{\partial\nabla^2\psi_n}{\partial\theta} - \frac{\partial\psi_m}{\partial\theta}\frac{\partial\nabla^2\psi_m}{\partial r}\right)\end{aligned}\right\} \tag{5}$$

This stream function may be determined by first obtaining a solution for the biharmonic equation $\nabla^4\psi_0 = 0$ and subsequently evaluating the successive terms in the series. The first term ψ_0 is the solution for purely viscous flow and for laminar motion solutions are already available for the particular cases of a slider bearing [8] and for a journal bearing [9]. The successive terms, $\psi_1, \psi_1 \ldots$ represent the corrections that require to be introduced to account for inertia effects. The calculation of the first correction term for the case of a slider bearing will now be discussed.

Consider two planes in relative motion inclined at an angle to each other and held apart by the hydrodynamic pressure in the fluid between them. Under steady conditions let it be assumed that the planes move with velocities U_1 and U_2 toward the origin. The boundary conditions to be satisfied are therefore

$$\left.\begin{aligned} &(1,2)\quad \theta = 0;\ \psi = Q,\ \frac{1}{r}\frac{\partial\psi}{\partial\theta} = U_1 \\ &(2,3)\quad \theta = \beta;\ \psi = 0,\ \frac{1}{r}\frac{\partial\psi}{\partial\theta} = U_2\end{aligned}\right\} \tag{6}$$

where Q is the flow per unit length delivered by a line source at the origin.

The stream function for purely viscous, steady flow has been given previously [8] and is

$$\psi_0 = r(A\sin\theta + B\theta\cos\theta + C\theta\sin\theta) + (E + F\theta + G\cos 2\theta + H\sin 2\theta) \tag{7}$$

where

$$\left.\begin{aligned} A &= (U_1\beta^2 + U_2\beta\sin\beta)/(\beta^2 - \sin^2\beta) \\ B &= (-U_1\sin^2\beta - U_2\beta\sin\beta)/(\beta^2 - \sin^2\beta) \\ C &= [U_1(\sin\beta\cos\beta - \beta) + U_2(\beta\cos\beta - \sin\beta)]/(\beta^2 - \sin^2\beta) \\ E &= Q(\sin\beta - 2\beta\cos\beta)/2(\sin\beta - \beta\cos\beta) \\ F &= 2Q\cos\beta/2(\sin\beta - \beta\cos\beta) \\ G &= Q\sin\beta/2(\sin\beta - \beta\cos\beta) \\ H &= -Q\cos\beta/2(\sin\beta - \beta\cos\beta)\end{aligned}\right\} \tag{8}$$

Inserting this value for ψ_0 in equation (5) we obtain an expression for the second term in the stream function in the form

$$\nabla^4\psi_1 = \frac{1}{r^2}[A_1\sin 2\theta + B_1\cos 2\theta + C_1\theta\sin 2\theta + D_1\theta\cos 2\theta] + \frac{1}{r^3}[E_1\sin\theta + F_1\cos\theta + J_1\sin 3\theta + K_1\cos 3\theta + L_1\theta\sin 3\theta + M_1\theta\cos 3\theta] + \frac{1}{r^4}[N_1\sin 2\theta + O_1\cos 2\theta + P_1\sin 4\theta + Q_1\cos 4\theta] \tag{9}$$

where

$$\left.\begin{aligned} A_1 &= -2AB - B^2 + C^2 \\ B_1 &= 2AC + 2BC \\ C_1 &= -4BC \\ D_1 &= -2B^2 + 2C^2 \\ E_1 &= -2BH + 2GC - 2BF \\ F_1 &= -2BG - 2CH + 2CF \\ J_1 &= -8AH - 6BH - 6CG \\ K_1 &= -8AG - 6BG + 6CH \\ L_1 &= 8BG - 8CH \\ M_1 &= -8BG + 8CH \\ N_1 &= -8FH \\ O_1 &= -8FG \\ P_1 &= -8H^2 + 8G^2 \\ Q_1 &= -16GH\end{aligned}\right\} \tag{10}$$

The particular integral of equation (9) may be written in the form

$$\psi_1 = r^2[A_2\theta\sin 2\theta + B_2\theta\cos 2\theta + C_2\theta^2\sin 2\theta + D_2\theta^2\cos 2\theta] + r[F_2\theta^2\sin\theta + H_2\theta^2\cos\theta + J_2\sin 3\theta + K_2\cos 3\theta + L_2\theta\sin 3\theta + M_2\theta\cos 3\theta] + [N_2\theta\cos 2\theta + O_2\theta\sin 2\theta + P_2\sin 4\theta + Q_2\cos 4\theta] \tag{11}$$

where

$$\left.\begin{aligned} A_2 &= -\frac{1}{16}B_1 - \frac{5}{64}C_1 \\ B_2 &= \frac{1}{16}A_1 - \frac{5}{64}D_1 \\ C_2 &= -\frac{1}{32}D_1 \\ D_2 &= \frac{1}{32}C_1 \\ F_2 &= -\frac{1}{8}E_1 \\ H_2 &= -\frac{1}{8}F_1 \\ J_2 &= \frac{1}{64}J_1 - \frac{3}{128}M_1 \\ K_2 &= \frac{1}{64}K_1 + \frac{3}{128}L_1 \\ L_2 &= \frac{1}{64}L_1 \\ M_2 &= \frac{1}{64}M_1 \\ N_2 &= \frac{1}{16}N_1\end{aligned}\right\} \tag{12}$$

$$O_2 = -\frac{1}{16} O_1$$

$$P_2 = \frac{1}{192} P_1 \qquad (12) \text{ cont'd}$$

$$Q_2 = \frac{1}{192} Q_1$$

To satisfy the boundary conditions we introduce a complementary function

$$\psi_1' = r^2[A_2 \sin 2\theta + B_2 \cos 2\theta + C_2\theta + D_2] + r[E_2 \sin \theta + F_2 \cos \theta + G_2\theta \sin \theta + H_2\theta \cos \theta] + [N_2 + O_2\theta + P_2 \sin 2\theta + Q_2 \cos 2\theta] \quad (13)$$

such that

$$\left.\begin{aligned} &(1, 2) \quad \theta = 0: \ \psi_1 + \psi_1' = 0, \ \frac{\partial}{\partial\theta}(\psi_1 + \psi_1') = 0 \\ &(3, 4) \quad \theta = \beta: \ \psi_1 + \psi_1' = 0, \ \frac{\partial}{\partial\theta}(\psi_1 + \psi_1') = 0 \end{aligned}\right\} \quad (14)$$

hence determining the arbitrary constants $A_2 - Q_2$.

The complete solution, therefore, is

$$\psi = \psi_0 + \left(\frac{\rho}{\eta}\right)(\psi_1 + \psi_1') + K \quad (15)$$

where K consists of terms of higher order in (ρ/η) that may be neglected in the first approximation.

Pressure Gradient

The pressure gradient along the planes is given [11] by

$$\frac{\partial p}{\partial r} = -\frac{\eta}{r}\frac{\partial}{\partial\theta}\left[\frac{\partial v}{\partial r} + \frac{v}{r} - \frac{1}{r}\frac{\partial u}{\partial\theta}\right] \quad (16)$$

and for the stream function given by (15) this becomes

$$\frac{\partial p}{\partial r} = \eta\left[\frac{2}{r^2}(B\cos\theta + C\sin\theta) + \frac{8}{r^3}(H\cos 2\theta - G\sin 2\theta)\right] + \rho\left[\frac{4}{r}\{2A_2\sin 2\theta + 2B_2\cos 2\theta - C_2(3\cos 2\theta - 4\theta\sin 2\theta) + D_2(3\sin 2\theta + 4\theta\cos 2\theta) - C_2\} + \frac{2}{r^2}\left\{\begin{aligned} &-F_2(3\cos\theta - 2\theta\sin\theta) \\ &- 3G_2(\sin\theta + 3\theta\cos\theta - \theta^2\sin\theta) \\ &+ H_2(3\sin\theta + 2\theta\cos\theta) \\ &+ 12J_2\cos 3\theta - 12K_2\sin 3\theta \\ &+ L_2(13\sin 3\theta + 12\theta\cos 3\theta) \\ &+ M_2(13\cos 3\theta - 12\theta\sin 3\theta) \\ &+ G_2\sin\theta + H_2\cos\theta \end{aligned}\right\} + \frac{4}{r^3}\left\{\begin{aligned} &N_2(3\cos 2\theta - 2\theta\sin 2\theta) \\ &+ O_2(3\sin 2\theta + 2\theta\cos 2\theta) \\ &+ 16P_2\cos 4\theta - 16Q_2\sin 4\theta \\ &+ 2P_2\cos 2\theta - 2Q_2\sin 2\theta \end{aligned}\right\}\right] \quad (17)$$

which, along $\theta = 0$, is

$$\frac{\partial p}{\partial r} = \eta\left[\frac{2B}{r^2} + \frac{8H}{r^3}\right] + \rho\left[\frac{4}{r}\{2B_2 - 3C_2 - C_2\} + \frac{2}{r^2}\{-3F_2 + 8J_2 + 13M_2 + H_2\} + \frac{4}{r^3}\{3N_2 + 16P_2 + 2P_2\}\right] \quad (18)$$

where

$$C_2 = \frac{1}{2(1 - \cos 2\beta - \beta\sin 2\beta)} \times \left[\begin{aligned} &A_2\{(1 - \cos 2\beta)(2\beta - \sin 2\beta)\} \\ &+ B_2\{(1 - \cos 2\beta)^2 - 2(1 - \cos 2\beta) + 2\beta\sin 2\beta\} \\ &+ C_2\{2\beta(1 - \cos 2\beta)(\beta - \sin 2\beta)\} \\ &+ D_2\{2\beta(\beta\sin 2\beta + \cos^2 2\beta - \cos 2\beta)\} \end{aligned}\right]$$

$$H_2 = \frac{1}{(\beta^2 - \sin^2\beta)} \times \left[\begin{aligned} &F_2\{(\beta\cos\beta + \sin\beta)(-\beta^2\sin\beta) \\ &- (\beta\sin\beta)(-\beta^2\cos\beta - 2\beta\sin\beta)\} \\ &+ H_2\{(\beta\cos\beta + \sin\beta)(-\beta^2\cos\beta) \\ &- (\beta\sin\beta)(\beta^2\sin\beta - 2\beta\cos\beta)\} \\ &+ J_2\{(\beta\cos\beta + \sin\beta)(3\sin\beta - \sin 3\beta) \\ &- (\beta\sin\beta)(3\cos\beta - 3\cos 3\beta)\} \\ &+ K_2\{(\beta\cos\beta + \sin\beta)(\cos\beta - \cos 3\beta) \\ &- (\beta\sin\beta)(3\sin 3\beta - \sin\beta)\} \\ &+ L_2\{(\beta\cos\beta + \sin\beta)(-\beta\sin 3\beta) \\ &- (\beta\sin\beta)(-\sin 3\beta - 3\beta\cos 3\beta)\} \\ &+ M_2\{(\beta\cos\beta + \sin\beta)(\sin\beta - \beta\cos 3\beta) \\ &- (\beta\sin\beta)(\cos\beta - \cos 3\beta + 3\beta\sin 3\beta)\} \end{aligned}\right]$$

$$P_2 = \frac{1}{4(1 - \cos 2\beta - \beta\sin\beta)} \times \left[\begin{aligned} &N_2\{-(1 - \cos 2\beta)^2\} \\ &+ O_2\{(1 - \cos 2\beta)(\sin 2\beta - 2\beta)\} \\ &+ P_2\{4\sin 2\beta(2\beta + \sin 2\beta\cos 2\beta - 2\sin 2\beta)\} \\ &+ Q_2\{4\sin 2\beta(1 - \cos 2\beta)^2\} \end{aligned}\right] \quad (19)$$

and $A_2 - Q_2$ are given by the relationships (12), (10), and (8).

Consider now the case when β is so small that $\beta^2 \ll 1$. The foregoing expressions reduce to

$$\frac{\partial p}{\partial r} = \eta\left[-\frac{6(U_1 + U_2)}{r^2\beta^2} - \frac{12Q}{r^3\beta^2}\right] + \frac{\rho}{r}\left[\left(-\frac{U_1^2}{7} + \frac{4U_1U_2}{35} - \frac{U_2^2}{7}\right)\left(\frac{Q}{r\beta}\right)\left(\frac{3(U_1 + U_2)}{35}\right) + \frac{Q^2}{r^2\beta^2}\left(\frac{54}{35}\right)\right] \quad (20)$$

This expression may now be applied to a section of film in a hydrodynamic slider bearing. The first group of terms represents the ordinary pressure gradient term while the second represents the first approximate correction for inertia effects. The expression enables a quantitative estimate to be made of the relative importance of the various factors.

Frictional Drag

The shearing stress in the fluid is given by:

$$p_{r\theta} = \eta\left[\frac{\partial v}{\partial r} - \frac{v}{r} + \frac{1}{r}\frac{\partial u}{\partial \theta}\right] \tag{21}$$

and for the stream function given by (15) this becomes

$$P_{r\theta} = \eta\left[\frac{2}{r}(B\sin\theta - C\cos\theta) + \frac{4}{r^2}(G\cos 2\theta + H\sin 2\theta)\right]$$

$$+ \rho\left[2\left\{\begin{array}{l} A_2(-2\cos 2\theta + 2\theta\sin 2\theta) \\ \quad + B_2(2\sin 2\theta + 2\theta\cos 2\theta) \\ \quad - C_2(\sin 2\theta + 4\theta\cos 2\theta - 2\theta^2\sin 2\theta) \\ \quad + D_2(-\cos 2\theta + 4\theta\sin 2\theta + 2\theta^2\cos 2\theta) \\ \quad + 4A_1\sin 2\theta + 4B_1\cos 2\theta \end{array}\right\}\right.$$

$$+ \frac{2}{r}\left\{\begin{array}{l} F_2(-\sin\theta - 2\theta\cos\theta) \\ \quad + H_2(-\cos\theta + 2\theta\sin\theta) \\ \quad + 4J_2\sin 3\theta + 4K_2\cos 3\theta \\ \quad + L_2(-3\cos 3\theta + 4\theta\sin 3\theta) \\ \quad + M_2(3\sin 3\theta + 4\theta\cos 3\theta) \\ \quad - G_2\cos\theta + H_2\sin\theta \end{array}\right\}$$

$$\left.+ \frac{4}{r^2}\left\{\begin{array}{l} N_2(\sin 2\theta + \theta\cos 2\theta) \\ \quad + O_2(-\cos 2\theta + \theta\sin 2\theta) \\ \quad + 4P_2\sin 4\theta + 4Q_2\cos 4\theta \\ \quad + P_2\sin 2\theta + Q_2\cos 2\theta \end{array}\right\}\right] \tag{22}$$

while along $\theta = 0$,

$$p_{r\theta} = \eta\left[-\frac{2C}{r} + \frac{4G}{r^2}\right]$$

$$+ \rho\left[\begin{array}{l} 2\{-2A_2 - D_2 + 2B_2\} \\ + \frac{2}{r}\{-H_2 + 4K_2 - 3L_2 - G_2\} \\ + \frac{4}{r^2}\{-O_2 + 4Q_2 + Q_2\} \end{array}\right] \tag{23}$$

where

$$B_2 = \frac{1}{4(1 - \cos 2\beta - \beta\sin 2\beta)} \times$$

$$\left[\begin{array}{l} A_2(\sin^2 2\beta - 4\beta^2\cos 2\beta) \\ + B_2(-2\beta + 2\beta\cos 2\beta - \sin 2\beta \\ \quad + \sin 2\beta\cos 2\beta + 4\beta^2\sin 2\beta) \\ + C_2(-4\beta^2\cos 2\beta - 2\beta^2\sin 2\beta \\ \quad + 2\beta\sin^2 2\beta) \\ + D_2(-2\beta^2 + 2\beta\sin 2\beta\cos 2\beta \\ \quad + 4\beta^2\sin 2\beta - 2\beta^2\cos 2\beta) \end{array}\right]$$

$$G_2 = \frac{1}{(\beta^2 - \sin^2\beta)} \times$$

$$\left[\begin{array}{l} F_2\{-\beta^2\sin^2\beta - (\beta\cos\beta - \sin\beta) \\ \quad (\beta^2\cos\beta + 2\beta\sin\beta)\} \\ + H_2\{-\beta^2\sin\beta\cos\beta + (\beta\cos\beta - \sin\beta) \\ \quad (\beta^2\sin\beta - 2\beta\cos\beta)\} \\ + J_2\{\beta\sin\beta(3\sin\beta - \sin 3\beta) \\ + (\beta\cos\beta - \sin\beta)(3\cos\beta - 3\cos 3\beta)\} \\ + K_2\{\beta\sin\beta(\cos\beta - \cos 3\beta) \\ + (\beta\cos\beta - \sin\beta)(3\sin 3\beta - \sin\beta)\} \\ + L_2\{-\beta^2\sin\beta\sin 3\beta - (\beta\cos\beta - \sin\beta) \\ \quad (\sin 3\beta + 3\beta\cos 3\beta)\} \\ + M_2\{\beta\sin\beta(\sin\beta - \beta\cos 3\beta) \\ + (\beta\cos\beta - \sin\beta)(\cos\beta - \cos 3\beta + 3\beta\sin 3\beta)\} \end{array}\right]$$

$$Q_2 = \frac{1}{4(1 - \cos 2\beta - \beta\sin 2\beta)} \times$$

$$\left[\begin{array}{l} N_2\{4\beta^2\sin 2\beta - (1 - \cos 2\beta) \\ \quad (2\beta + \sin 2\beta)\} \\ + O_2\{\sin^2 2\beta - 4\beta^2\cos 2\beta\} \\ + P_2\{4(\cos 2\beta - 1)(2\beta - \sin 2\beta\cos 2\beta) \\ \quad - 8\sin^2 2\beta(\sin 2\beta - 2\beta)\} \\ + Q_2\{4\sin^2 2\beta(\cos 2\beta - 1) \\ \quad - 8\sin 2\beta\cos 2\beta(\sin 2\beta - 2\beta)\} \end{array}\right] \tag{24}$$

and A_2 to Q_2 are given by the relationships (12), (10), and (8).

Again, if β is so small that $\beta^2 \ll 1$ then along $\theta = 0$

$$p_{r\theta} = 2\eta\left[\frac{(2U_1 + U_2)}{r\beta} + \frac{3Q}{r^2\beta^2}\right]$$

$$+ \rho\beta\left[\begin{array}{l} \left\{-\frac{U_1^2}{35} - \frac{U_1U_2}{42} + \frac{4U_2^2}{105}\right\} \\ + \frac{Q}{r\beta}\left\{-\frac{U_1}{7} + \frac{2U_2}{35}\right\} + \frac{Q^2}{r^2\beta^2}\left(-\frac{6}{35}\right) \end{array}\right] \tag{25}$$

and this expression also may be applied to a hydrodynamic slider bearing to obtain a first approximate correction for inertia effects.

Comparison With Kahlert's Analysis

It is interesting to compare the expressions in the previous section for the particular case when β is small with those derived by Kahlert [1]. Kahlert started with the usual approximations of hydrodynamic lubrication theory, retaining in addition the inertia terms, and showed that for a thin lubricant film the two-dimensional equations of flow reduced to

$$\rho\left(\frac{u\partial u}{\partial x} + \frac{v\partial u}{\partial y}\right) = -\frac{dp}{dx} + \frac{\eta\partial^2 u}{\partial y^2} \tag{26}$$

together with the continuity equation. He assumed a velocity and pressure distribution in the form

$$\left.\begin{aligned} u_2 &= u_1 + u_k \\ p_2 &= p_1 + p_k \end{aligned}\right\} \tag{27}$$

where terms with the subscript 1 represented conditions when the inertia terms are negligible, and those with the subscript k represented the small corrections required to account for inertia. He inserted values for u_1 and p_1 known from classical theory into (26) and derived values for the correction terms in the form

$$u_k = -\frac{1}{2\eta}\frac{dp_k}{dx}\, yh\left(\frac{y}{h} - 1\right) + \frac{U^2}{\nu}\frac{dh}{dx}\,\frac{y}{h}\left[\frac{K_1}{6}\left(\frac{y^2}{h^2} - 1\right) + \frac{K_2}{12}\left(\frac{y^3}{h^3} - 1\right) + \frac{K_3}{20}\left(\frac{y^4}{h^4} - 1\right) + \frac{K_4}{30}\left(\frac{y^5}{h^5} - 1\right)\right] \tag{28}$$

and

$$\frac{dp_k}{dx} = -\frac{12\eta}{h^3}\,Q_k - \frac{3\eta U^2}{\nu h}\left[\frac{K_1}{6} + \frac{K_2}{10} + \frac{K_3}{15} + \frac{K_4}{21}\right]\frac{dh}{dx} \tag{29}$$

where

$$\left.\begin{aligned} K_1 &= -6\left(\frac{h_0}{h}\right) + 4 \\ K_2 &= -9\left(\frac{h_0}{h}\right)^2 + 27\left(\frac{h_0}{h}\right) - 14 \\ K_3 &= 18\left(\frac{h_0}{h}\right)^2 - 36\left(\frac{h_0}{h}\right) + 16 \\ K_4 &= -9\left(\frac{h_0}{h}\right)^2 + 15\left(\frac{h_0}{h}\right) - 6 \end{aligned}\right\} \tag{30}$$

and h_0 is the value of the film thickness where $dp_1/dx = 0$.

Substituting the given values for (30) in equations (28) and (29) and determining the correction terms we get

$$\frac{dp_k}{dx} = -\frac{12\eta}{h^3}\,Q_k + \frac{\rho U^2}{h}\,\frac{1}{70}\left[27\left(\frac{h_0}{h}\right)^2 - 3\left(\frac{h_0}{h}\right) - 10\right]\frac{dh}{dx} \tag{31}$$

and

$$\tau_{0k} = \eta\left[\frac{\partial u_k}{\partial y}\right]_{y=0} = \frac{6\eta Q_k}{h^2} + \rho U^2\,\frac{1}{70}\left[-3\left(\frac{h_0}{h}\right)^2 + 5\left(\frac{h_0}{h}\right) - 2\right]\frac{dh}{dx} \tag{32}$$

If we let

$$r\beta = h$$
$$Q = -(U_1 + U_2)h_c/2$$
$$\beta = dh/dx$$

then inspection of equations (20) and (25) shows that for terms in U_1^2 the expressions are identical with those in equations (31) and (32).

Kahlert considered only the case where the plane $y = 0$ was moving. If his method is extended to include the case when the plane $y = h$ is also moving, with a velocity U_2, then additional terms in equations (28) and (29) are required. It may be shown that these terms are similar in form to those given, the only difference being in the values of K_1, K_2, K_3, and K_4. Evaluation of these gives for the terms in U_1U_2 the values

$$\left.\begin{aligned} K_1 &= -6\left(\frac{h_0}{h}\right) + 2 \\ K_2 &= -18\left(\frac{h_0}{h}\right)^2 + 36\left(\frac{h_0}{h}\right) - 14 \\ K_3 &= 36\left(\frac{h_0}{h}\right)^2 - 60\left(\frac{h_0}{h}\right) + 24 \\ K_4 &= -18\left(\frac{h_0}{h}\right)^2 + 30\left(\frac{h_0}{h}\right) - 12 \end{aligned}\right\} \tag{33}$$

and for those in U_2^2

$$\left.\begin{aligned} K_1 &= 0 \\ K_2 &= -9\left(\frac{h_0}{h}\right)^2 + 9\left(\frac{h_0}{h}\right) - 2 \\ K_3 &= 18\left(\frac{h_0}{h}\right)^2 - 24\left(\frac{h_0}{h}\right) + 8 \\ K_4 &= -9\left(\frac{h_0}{h}\right)^2 + 15\left(\frac{h_0}{h}\right) - 6 \end{aligned}\right\} \tag{34}$$

and inserting these values in the appropriate expression yields equations for the pressure gradient and frictional drag identical with those in equations (20) and (25).

Discussion

The foregoing analysis presents a method of estimating a first approximation for the correction due to inertia effects in laminar flow between inclined planes; the final expressions are more general in form than those previously obtained. In principle, it should be possible to extend the analysis to higher degrees of approximation but it would appear that further terms in the series for the stream function are liable to become excessively complicated.

For the particular case when the angle between the planes is small the analysis may be applied to consideration of the effects of inertia in a lubricating film and the reduced expressions may be compared with those obtained by Kahlert. The two methods are essentially similar in principle but, in view of the considerable differences in detail, the final agreement is highly satisfactory. As Kahlert has already integrated equations equivalent to (31) and (32), and analyzed the performance of both journal and thrust bearings in some detail, it has not been thought necessary to repeat the analysis here. It would appear that, in general, the effect of lubricant inertia is to cause a slight increase in the load capacity of a bearing.

Acknowledgment

The work described was carried out as part of the research program of the Mechanical Engineering Research Board of the De-

partment of Scientific and Industrial Research, and this paper is published by permission of the Director of Mechanical Engineering Research; the author acknowledges the interest and encouragement of Dr. F. T. Barwell, Head of the Lubrication Division.

References

1 W. Kahlert, *Ingenieur-Archiv*, vol. 16, 1948, p. 321.

2 D. F. Wilcock, "Turbulence in High-Speed Journal Bearings," TRANS. ASME, vol. 72, 1950, pp. 825–834.

3 J. A. Cole, "Experiments on the Flow in Rotating Annular Clearances," Paper No. 15, International Mechanical Engineering Conference on Lubrication and Wear, 1957.

4 N. A. Slezkin and S. M. Targ, "The Generalized Equations of Reynolds," Comptes Rendus (Doklady) de l'Académie des Science de l'URSS, vol. 54, 1946, pp. 205–208 (in English).

5 J. F. Osterle, Y. T. Chou, and E. A. Saibel, "Effect of Lubricant Inertia in Journal-Bearing Lubrication," *Journal of Applied Mechanics*, vol. 24, TRANS. ASME, vol. 79, 1957, pp. 494–496.

6 A. A. Milne, *Wear*, vol. 1, no. 4, February, 1958, p. 349.

7 D. J. Ladanyi, "Effects of Temporal Tangential Bearing Acceleration on Performance Characteristics of Slider and Journal Bearings," U. S. NACA TN 1730, October, 1948.

8 A. A. Milne, "A Contribution to the Theory of Hydrodynamic Lubrication—A Solution in Terms of the Stream Function for a Wedge-Shaped Oil Film," *Wear*, vol. 1, August, 1957, pp. 32–39.

9 G. H. Wannier, "A Contribution to the Hydrodynamics of Lubrication," *Quarterly of Applied Mathematics*, vol. 8, 1950, pp. 1–32.

10 A. Anzelius, "Two Flow Problems in a Viscous Fluid" (in English), *Arkiv für Fysik*, vol. 9, 1955, pp. 391–398.

11 H. Lamb, "Hydrodynamics," Cambridge University Press, Cambridge, England, Sixth edition, 1932, p. 579.

F. W. OCVIRK

Associate Professor of Mechanical Engineering, Sibley School of Mechanical Engineering, Cornell University, Ithaca, N. Y. Mem. ASME

G. B. DuBOIS

Professor of Machine Design, Sibley School of Mechanical Engineering, Cornell University, Ithaca, N. Y.

Surface Finish and Clearance Effects on Journal-Bearing Load Capacity and Friction

A method of relating surface finish to minimum oil-film thickness and the corresponding load capacity of plain journal bearings is presented with supporting experimental data. The effect of clearance on load capacity and friction are shown on graphs indicating an optimum bearing clearance.

THE initial indication of the limiting failure load of a plain journal bearing is a sharp rise in friction coefficient, which is thought to be due to surface asperities protruding through the thickness of the hydrodynamic oil film. The increase in friction marks the threshold of bearing failure by overheating, although at moderate speeds some further increase in load may be achieved by "running-in" or wearing away the initial points of metallic contact.

Prediction of allowable safe bearing loads usually has been based on experience, using some parameter such as the Sommerfeld number, the load number, eccentricity ratio, or the minimum oil-film thickness. In general, these give allowable loads including a factor of safety, rather than the failure load. The ratio of the failure load to the allowable load is the factor of safety, a term which has been difficult to determine in bearing design. Better understanding of the factors related to the failure load capacity is needed.

Hydrodynamic lubrication theory predicts that an infinite load may be supported by a rotating journal bearing. The theory assumes an idealized bearing and journal with perfect geometrical shapes and surfaces, and does not incorporate the practical variables of roughened surfaces and load distortion. It is these practical variables which limit the loading to less than an infinite value. Hydrodynamic theory predicts load capacity for relatively thick films realistically, and also may predict values of loading for marginal films, if some criterion is established for determining the magnitude of the marginal film thickness.

This paper proposes a criterion for determining the limit of hydrodynamic lubrication based on the magnitude of the roughness of the surface finish of journal and bearing. Perfect alignment of the journal and bearing is assumed and only surface roughness is considered. Analytically determined design curves are presented giving the load capacity of a bearing corresponding with a minimum film thickness limited by the irregularities of a given surface finish. Experimental load-capacity data are compared with analytically determined data.

In the analytical curves presented, the form of plotting has been chosen to show directly the influence of clearance ratio and minimum film thickness on load capacity. The method of plotting also makes it possible to show the influence of clearance and film thickness on journal and bearing friction, showing the conditions for minimum friction. Although eccentricity ratio is the fundamental variable in the hydrodynamic equations, the equations are rearranged to give a form of plotting which emphasizes clearance and minimum film thickness rather than eccentricity ratio. In heavily loaded bearings, the changes in eccentricity ratio are relatively small for large changes in load whereas the changes in minimum film thickness are relatively greater.

The curves and data presented in this paper were determined in a bearing research investigation under the sponsorship and financial assistance of the National Advisory Committee for Aeronautics. The details of the research are presented in reference [1].[1]

Film Profile With Surface Roughness

Normally, the lubricating film is viewed as flowing circumferentially in an ideal wedge as shown in Fig. 1. The film at the point of closest approach is regarded as having a thin transverse profile between ideally smooth surfaces. The true film profile, however, is bounded by irregular surfaces in which the magnitude and distribution of irregularities depend upon the method of manufacturing the surfaces. The irregularities of the surface are usually determined with a surface-measuring instrument which gives an indication related to a mean height of the irregularities.

Tarasov [2] has examined the nature of the irregularities pro-

Contributed by the Lubrication Division and presented at the Annual Meeting, New York, N. Y., November 30–December 5, 1958, of THE AMERICAN SOCIETY OF MECHANICAL ENGINEERS.

NOTE: Statements and opinions advanced in papers are to be understood as individual expressions of their authors and not those of the Society. Manuscript received at ASME Headquarters, August 4, 1958. Paper No. 58—A-134.

[1] Numbers in brackets designate References at end of paper.

Nomenclature

C_d = diametral clearance, in.
D = bearing diameter, in.
e = eccentricity of journal and bearing axes, in.
e_l = lateral component of eccentricity, $e \sin \phi$, in.
F = friction force, lb
h_m = minimum film thickness at point of closest approach, in.
L = bearing length, in.
N = journal speed, rps
P = applied central load in bearing, lb
p = unit load on projected area, P/LD, psi
ϕ = attitude angle, angle between load line and line of centers of journal and bearing, deg
μ = viscosity of fluid, reyn

Dimensionless Numbers

C_d/D = clearance ratio
f = coefficient of friction, F/P
h_m/D = minimum-film-thickness ratio
L/D = length-diameter ratio
n = eccentricity ratio, $2e/C_d$
S = Sommerfeld number, $(\mu N/p)(D/C_d)^2$

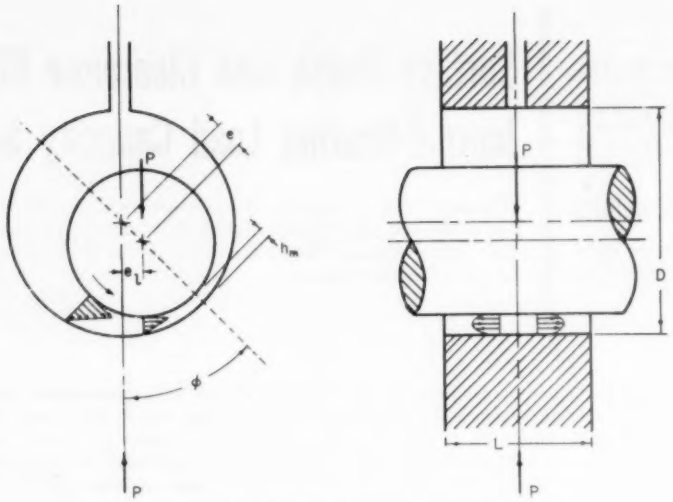

Fig. 1 Journal bearing with steady central load

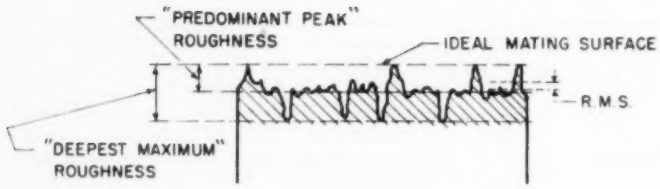

Fig. 2 Typical profile of commonly manufactured surfaces with roughnesses defined by Tarasov. Relation of actual roughness to profilometer values (rms) are given for common surfaces.

$$\text{TARASOV'S FACTOR} = \frac{\text{PREDOMINANT PEAK ROUGHNESS}}{\text{PROFILOMETER ROUGHNESS (RMS)}}$$

GROUND SURFACES	4 1/2
HYPROLAPPED	6 1/2
SANDPAPERED	7
SUPERFINISHED	7
LOOSE ABRASIVE LAP	10

duced by common machining processes. From 2500× magnification of surface profiles, he shows that in any given surface there are two orders of irregularities. For most of the surface extent there is a predominant roughness consisting of relatively small irregularities at small intervals. In addition, at relatively large intervals, there are high peaks and deep valleys. These are shown diagrammatically in Fig. 2. Tarasov shows three lines drawn on the profile, one tangent to the high peaks, one tangent to the deep valleys, and one through the relatively small but predominant irregularities. He defines roughness by the magnitudes of the irregularities measured from the top line, or ideal mating surface, as shown in Fig. 2. "Deepest maximum roughness" is the height from the ideal mating surface to the bottom of the deep valleys, and "predominant peak roughness" is the height of the irregularities from the ideal mating surface to the line through the predominant surface. For most surfaces, the greater roughness is approximately twice the smaller.

Tarasov compares the magnitudes of these roughnesses with those determined by profilometers and presents factors by which the profilometer readings in microinches rms should be multiplied to determine the foregoing values of roughness. In ground surfaces, for example, the predominant peak roughness is 4.5 times the profilometer value. It is to be noted that this is a ratio applying to any fineness of grinding. Factors for other types of finish are given in Fig. 2.

Applying Tarasov's idealizations of surface profiles to journal bearings, the minimum film profile may be visualized as in Fig. 3. The peaks of the journal and bearing surfaces are shown in initial contact. The condition shown may be regarded as the limit of hydrodynamic lubrication in the sense that a steep friction and temperature rise, and possible failure, may be expected because of metallic contact at the peaks. However, hydrodynamic support continues to exist because of the oil film between the predominant surfaces. It may be hypothesized that at initial contact of the surfaces the minimum film thickness is the sum of the predominant peak roughnesses of the two surfaces. For example, consider a smoothly ground finish of 10 microin. rms. If both parts have this finish, the corresponding minimum film thickness at first contact of the peaks is (2)(10)(4.5) = 90 microin. The calculated minimum film thickness at impending failure is therefore relatively much larger than the usual surface-finish reading.

Load Capacity Versus Minimum Film Thickness

Hypothesizing that the distance between the predominant surfaces at initial contact of the peaks as shown in Fig. 3 is the effec-

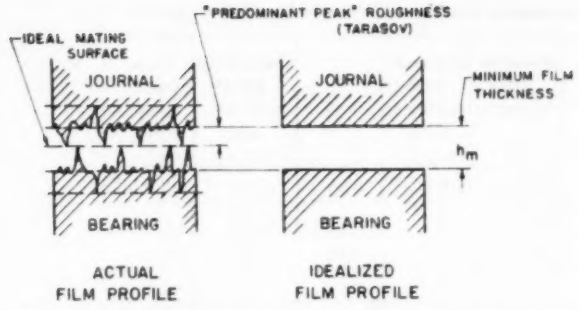

Fig. 3 Idealized profile of minimum film in a journal bearing at condition of minimum coefficient of friction when peaks of surfaces are at initial contact

tive film thickness, the corresponding load capacity can be determined by hydrodynamic theory. Although load capacity is conventionally determined as a function of eccentricity ratio, it is possible to relate load capacity to minimum film thickness as shown in the following steps:

According to the short-bearing approximation [3], the bearing variables are related to eccentricity ratio in the following equation:

$$\frac{p}{\mu N}\left(\frac{C_d}{D}\right)^2\left(\frac{D}{L}\right)^2 = \frac{\pi n}{(1-n^2)^2}\left[\pi^2(1-n^2)+16n^2\right]^{1/2} \quad (1)$$

In Equation (1), the term $(1 - n^2)^2$ may be factored to yield $(1 - n)^2(1 + n)^2$ in which $(1 - n)$ is related to the minimum film thickness h_m and diametral clearance C_d as follows:

$$h_m = \frac{C_d}{2}(1-n); \quad (1-n) = 2\frac{h_m}{C_d} \quad (2)$$

Substitution of Equation (2) in Equation (1) yields the following relationship in which minimum film thickness replaces the diametral clearance:

$$\frac{p}{\mu N}\left(\frac{h_m}{D}\right)^2\left(\frac{D}{L}\right)^2 = \frac{\pi n}{4(1+n)^2}\left[\pi^2(1-n^2)+16n^2\right]^{1/2} = f(n) \quad (3)$$

$$\frac{p}{\mu N}\left(\frac{D}{L}\right)^2 = \frac{f(n)}{\left(\frac{h_m}{D}\right)^2} \quad (4)$$

The left-hand term of Equation (4) is the film-capacity number in dimensionless form and is an indicator of film-load capacity. Numerical inspection shows that $f(n)$ in Equations (3) and (4) changes slowly for high values of eccentricity ratio corresponding to heavy loadings in bearings. For example, for values of n = 1.0, 0.7, and 0.5, the values of $f(n)$ are 0.785, 0.683, and 0.590, respectively. In Fig. 4, where Equation (4) is plotted on logarithmic scales, the solid lines for n = 0.7 and 1.0 are close together, showing relatively small dependence on eccentricity ratio for a given film thickness. In Fig. 4, the short bearing approximation gives the same line for any L/D less than 1.0, and for $L/D > 1.0$ a value of 1.0 should be used for L/D in the film-capacity number.

The Cameron and Wood analytical solution [4] is represented in Fig. 4 by dashed lines for n = 0.58 and 0.95, both for L/D = 1/2. The lines for n = 0.58 represents the maximum values obtainable from this solution for a given film thickness. This indicates that for a given film thickness the maximum load capacity as given by Cameron and Wood is reached at a bearing clearance which gives n = 0.58 at this film thickness. At n = 1.0 the film-capacity number approaches zero so that the line for n = 0.95 is shown.

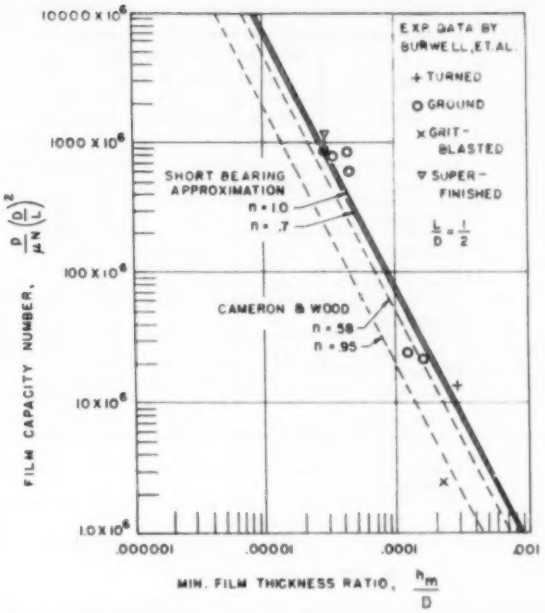

Fig. 4 Curves of film-load capacity against minimum film thickness compared with experimental data by Burwell, et al., for bearings of L/D of 1/2

Experimental Data

The experimental data points shown in Fig. 4 are from an experimental investigation of the effect of journal surface finish on bearing performance by Burwell, Kaye, van Nymegen, and Morgan [5] who present test data which have been reduced and plotted for comparison with the analytically determined curves. These data were obtained from friction runs of a pair of partial bearings against a common journal in a nutcracker-type machine as shown in Fig. 5, which also shows a table of the original data.

The primary objective of the tests was the determination of the Sommerfeld number at the point of minimum coefficient of friction and its relation to surface finish. As shown in the table of Fig. 5, the smoother the finish in microinches rms, the lower the value of Sommerfeld number at minimum friction. The hook point or point of minimum coefficient of friction presumably is the point where metallic contact of the surfaces begins. The table gives values of surface finish of the journals. For all of the bearings the surface finish was between 6 and 10 microin. rms. It is important to point out that all journal and bearing pairs were tested without previous running-in, and that because of the method of loading in a nutcracker type machine, journal bending did not become a variable in the tests. All bearings were of L/D approximately equal to 1/2.

The reduction of the Burwell, et al., data for plotting in Fig. 4 is shown in Table 1. The film-capacity number is determined from the Sommerfeld number, the clearance ratio, and L/D ratio given for the tests in Fig. 5 as follows:

$$\frac{p}{\mu N}\left(\frac{D}{L}\right)^2 = \left[\frac{p}{\mu N}\left(\frac{C_d}{D}\right)^2\right]\left(\frac{D}{C_d}\right)^2\left(\frac{D}{L}\right)^2 = \frac{1}{S}\left(\frac{D}{C_d}\right)^2\left(\frac{D}{L}\right)^2 \quad (5)$$

Table 1 Reduction of Burwell, et al., data to values of film-capacity number and minimum film-thickness number

TYPE OF FINISH	SURFACE ROUGHNESS MICROINCH R.M.S.			FACTOR GIVEN BY TARASOV	MINIMUM FILM THICKNESS h_m	MINIMUM FILM THICKNESS RATIO h_m/D	$\frac{D}{C_d}$	SOMMERFELD NO. AT POINT OF MIN. FRICTION	FILM CAPACITY NUMBER $\frac{P}{\mu N}\left(\frac{D}{L}\right)^2$ (4)
	JOURNAL (MAX.)	BEARING	SUM						
TURNED	130	8	138	$4\frac{1}{2}$ (1)	620×10^{-6}	291×10^{-6}	1150	0.38	13.5×10^6
GROUND	70	8	78	$4\frac{1}{2}$	351	165	1200	0.25	22.4
GROUND	50	8	58	$4\frac{1}{2}$	261	123	630	0.06	25.7
GRITBLASTED	40	8	48	10 (2)	480	226	280	0.12	2.54
GROUND	14	8	22	$4\frac{1}{2}$	99	46.5	520	0.0017	616
GROUND	13	8	21	$4\frac{1}{2}$	94.5	44.5	540	0.0013	870
CHEMICALLY ETCHED	11	8	19	— (3)	—	—	280	0.024	12.7
GROUND	8	8	16	$4\frac{1}{2}$	72	33.8	500	0.0012	808
GROUND	6	8	14	$4\frac{1}{2}$	63	29.6	480	0.001	894
SUPERFINISHED	1	8	9	7	63	29.6	500	0.0008-0.001	1212-881

(1) FOR GROUND SURFACES

(2) FOR LOOSE-ABRASIVE LAPPED SURFACES

(3) NOT GIVEN

(4) $\frac{P}{\mu N}\left(\frac{D}{L}\right)^2 = \frac{1}{S}\left(\frac{D}{C_d}\right)^2\left(\frac{D}{L}\right)^2$

The film-capacity number thus determined is for the condition where the friction coefficient is a minimum, and the surfaces are presumably about to make initial contact. The corresponding minimum film thickness is determined using the hypothesis that the film thickness is equal to the sum of the predominant peak roughnesses of the journal and bearing surfaces. As shown in Table 1, for each specimen the maximum journal roughness in microinches rms is multiplied by the proper Tarasov factor to determine the predominant peak roughness. For the grit-blasted surface, the correct Tarasov factor is not known and the value of 10 for loose-abrasive lapped surfaces was used giving a "wild point." For the bearing surfaces, an average value of 8 microin. rms is multiplied by the same Tarasov factor used for the journal, since the type of bearing finish is not given. In Table 1 are shown the values of h_m and h_m/D determined on the basis of the hypothesis.

As shown in Fig. 4 the experimental data thus obtained compare well with the analytically determined curves. The experimental data show the value of improved surface finish on bearing-load capacity. Considering the extremes of the data, the load capacity is increased almost one hundred fold in going from the turned surface to the superfinished surface. The analytical curves show that for high load capacity a very thin oil film between very smooth surfaces free of asperities is required. For design purposes a line can be drawn below the one shown to provide some factor of safety, since these lines represent incipient failure at the point of increasing friction.

Fig. 6 shows experimental data by three other experimenters for comparison with the analytical curves given by Equation (4). The data shown are not for the condition of minimum friction coefficient but are the results of experiments in which film thicknesses were measured. Each of the experimenters used a different technique in measuring journal position. In the Cornell experiments [3], eccentricity measurements were made with dial gages through a mechanical linkage leading to a rubbing contact with

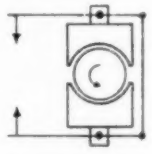

NUTCRACKER TYPE BEARING TEST MACHINE

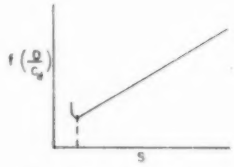

BURWELL DATA LOCATES THE HOOK-POINT OF FRICTION CURVES

L = 1.08 in D = $2\frac{1}{8}$ in

TYPE OF FINISH	SURFACE ROUGHNESS MICROINCH R.M.S.		$r/c = D/C_d$	SOMMERFELD NO. AT POINT OF MIN. FRICT.
	TRANSVERSE	PARALLEL		
TURNED	130	50	1150	0.30
GROUND	70	70	1200	0.25
GROUND	50	50	630	0.06
GRITBLASTED	30-50	–	280	0.12
GROUND	14	–	520	0.0017
GROUND	13	–	540	0.0013
CHEMICALLY ETCHED	11	–	280	0.024
GROUND	7	8	500	0.0012
GROUND	4	6	480	0.001
SUPERFINISHED	1	–	500	.0008-.0011

(1) FOR JOURNAL. (BABBITT BEARING SURFACE ROUGHNESS 6 TO 10 MICROINCH R.M.S.)

Fig. 5 Typical curve of coefficient of friction against Sommerfeld number obtained with a nutcracker machine by Burwell, et al. The table gives Sommerfeld numbers at minimum friction as a function of journal finish.

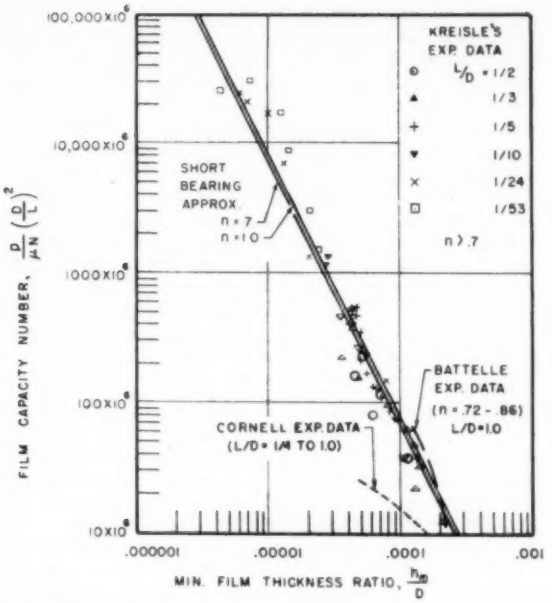

Fig. 6 Curves of film-load capacity against minimum film thickness compared with experimental data by Kreisle, by Battelle Memorial Institute, and by the authors

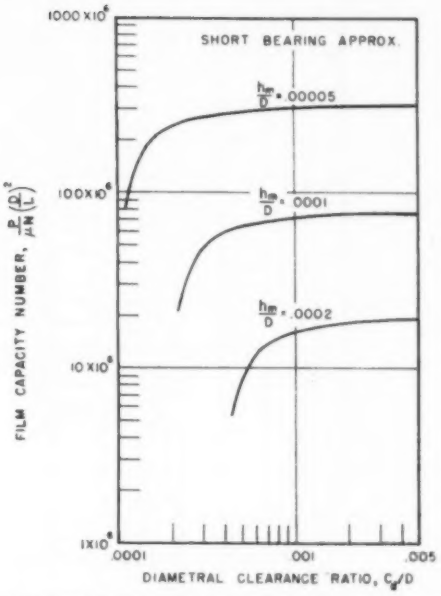

Fig. 7 Curves of film-load capacity against clearance ratio for a number of minimum film thicknesses as determined from the short-bearing approximation

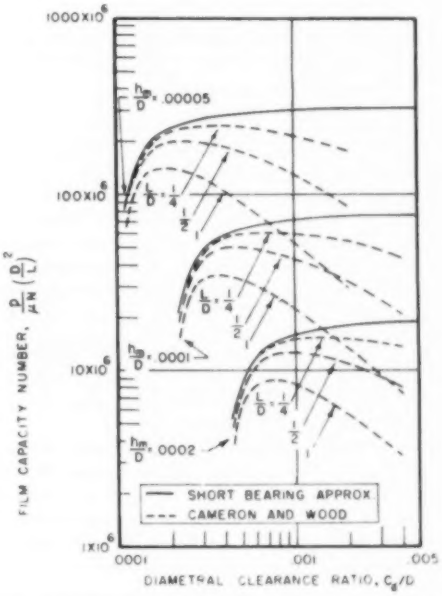

Fig. 8 Comparison of film-load capacities according to solution of Cameron and Wood with those of short-bearing approximation

the rotating journal. In Kreisle's experiments [6] eccentricity measurements were made but with an amplified inductance instrumentation which sensed the displacement of a nonrotating bearing under load. Kreisle's data are interesting in that he used bearings with L/D ratios as low as 1/53 which accounts for the high film-capacity numbers attained in Fig. 6. Both of these experimenters measured eccentricity so that minimum film thickness must be calculated using the measured clearance without regard to the influence of surface roughness on clearance.

Dayton, Allen, Fawcett, Miller, and Grimble [7] of Battelle Memorial Institute appear to be the first experimenters to have measured minimum film thickness directly. In the words of the experimenters, "In these tests, a high-audio frequency voltage is applied across the oil film from a small electrode on the journal surface to the bearing. A cathode-ray oscillograph connected in parallel permits observation of the dielectric breakdown through the thin region of the oil film. The breakdown voltages are used to compute the thickness of the minimum oil film."

Measurement of journal position or film thickness in a bearing with sufficient accuracy is difficult, as most experimenters will agree. Therefore, in comparing the analytical curves in Fig. 6 with the experimental data it is important to consider the methods used in obtaining the experimental data. In this respect, the experimental data by Burwell, et al., in Fig. 4 may be considered unique. Although these experimenters had not set out to measure minimum film thickness, their data may be interpreted as having done so. Their technique may be considered an accurate method of measuring minimum film thickness because of the direct relationship of the oil-film thickness to the surface roughness. In effect the surfaces contain a mechanical yardstick in their roughnesses.

Clearance and Load Capacity

The influence of clearance ratio on film-capacity number is shown in Fig. 7 as determined analytically from the short-bearing approximation. Each curve is for a given minimum film thickness and shows the load capacity of the film for a range of normally used clearance ratios. The curves in Fig. 7 are a cross plot of the analytical curves in Fig. 4. Referring to Fig. 4, for a fixed minimum film thickness, values of film-capacity number may be determined for each eccentricity ratio n from the sloping lines. With n and h_m known, the corresponding clearances may be determined from Equation (2) thus making possible the plotting of film-capacity number against clearance ratio as in Fig. 7. For

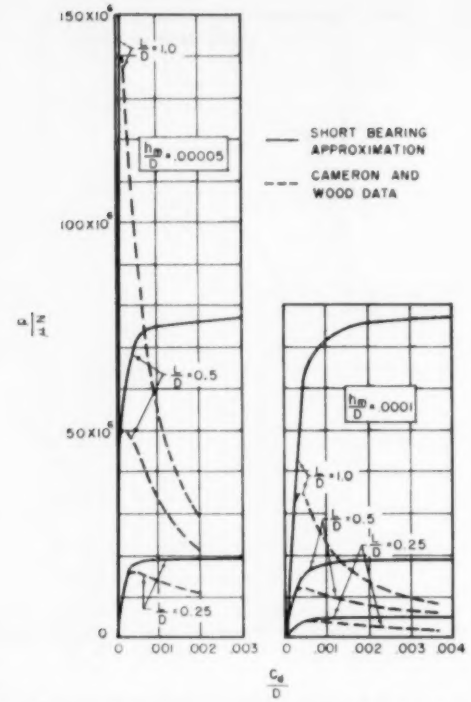

Fig. 9 Alternate plotting of some of the curves of Fig. 8 to show more clearly the effect of L/D ratio on film-load capacity for two minimum film thicknesses

a given minimum film thickness, the clearance required becomes greater as the eccentricity ratio increases, becoming infinite for an eccentricity ratio $n = 1.0$.

For those designers whose experience indicates that increasing the clearance of a bearing does not seriously affect the load capacity, the analytical curves of Fig. 7 are a mathematical confirmation. However, many designers feel that there is a best clearance for maximum load capacity [8]. This is confirmed by the mathematical solution of Cameron and Wood which is shown in Fig. 8, the curves in Fig. 7 being repeated for comparison. The Cameron and Wood curves show that, for heavily loaded bearings with very thin films, the maximum load capacity is obtained at small clearance ratios and that the load capacity falls off relatively rapidly as the clearance ratio is increased.

The effect of L/D ratio on bearing-load capacity is somewhat difficult to interpret in Fig. 8 since it is contained in the film-capacity number on the vertical scale. The effect of L/D is more clearly shown in Fig. 9 where load capacity is given in terms of $p/\mu N$ without the L/D term. In Fig. 9 both solutions show a decrease in load capacity with decreasing L/D as would be expected.

The differences between the two mathematical solutions on the effect of bearing clearance on load capacity are shown in Figs. 8 and 9, appearing greater in Fig. 9 which has linear scales. The differences of the two mathematical solutions are due to the different assumptions employed. Both account for end leakage. In the short-bearing approximation the velocity profile in the circumferential film flow is assumed linear as shown in Fig. 1, which leads to simplifications in the mathematical solution. The Cameron and Wood solution includes the effect of pressure gradient on these profiles which makes them curvilinear. Moreover, the Cameron and Wood solution is mathematically exact in satisfying Reynolds differential equation. However, neither solution takes into account the effect of pressure on viscosity, which may have an increasing effect on the load capacity at very high film pressures. Also neither solution takes into account the effect of the variations in oil-film temperature around the bearing on viscosity. This might alter the shape of the curves somewhat, reducing load capacity and friction at small clearances due to higher local film temperatures.

The limited experimental data in Fig. 4 appear to support the analytical curves of the short-bearing approximation. Unfortunately, the same data do not include a sufficient range of clearances at some constant minimum film thickness to be effectively compared with the analytical curve in Figs. 7 and 8. What is needed is a set of data from tests using the Burwell, et al., technique in which the series of specimens has the same finish but widely different clearances.

Friction Against Clearance

Figs. 10(a and b) show curves of friction in dimensionless numbers against clearance ratio for two L/D ratios. Several lines are shown on each curve for different minimum film thicknesses, the friction number increasing as the film thickness decreases.

The friction on the rotating journal and the stationary bearing are shown by different lines since the journal friction is greater than the bearing friction owing to the couple which is formed by the load vectors and the lateral displacement of the journal in the bearing as shown in Fig. 1. The difference of the two frictions increases with clearance because as the clearance increases the lateral displacement also increases. This method of plotting is valuable to show the effect of increasing clearance but the dimensionless variable lacks a diameter term to show the effect of diameter changes on torque. The dimensionless variable is related to force. However, it portrays clearly the effect of clearance changes on torque and power loss for a given bearing diameter. It is always the larger torque on the rotating element, labeled "journal" on these curves which is related to power loss and heat generation. The dashed lines labeled "bearing" are included for clarity and possible use by experimenters who measure friction on the stationary element.

The journal lines show that the power loss and heat generated pass through a minimum at some clearance ratio depending on both L/D and minimum film thickness. The clearance for minimum power loss decreases as the L/D ratio increases. It is interesting to note that for the shorter bearings in Fig. 10(a) the minimum friction is at reasonable clearance ratios greater than 0.001. However, since the curves for journal friction are relatively flat in the region of minimum friction the choice of clearance is wide and a large clearance may be specified. A large clearance has the advantage that larger oil flows and greater cooling of the oil is indicated.

The curves of Figs. 10(a and b) were determined from the short-bearing approximation which gives friction as an eccentricity-ratio function in which the term $(1 - n)$ appears. By substituting Equation (2) for $(1 - n)$ and manipulating algebraically, the following expression results giving friction as a function of minimum film thickness:

$$\frac{F/LD}{\mu N} = \frac{\psi(n)}{\dfrac{h_m}{D}} \tag{6}$$

in which

$$\psi(n) = \frac{\pi^2(1 - n^2)^{1/2}}{(1 + n)} + \frac{n(1 - n)\sin\phi(L/D)^2}{2C_n} \tag{7}$$

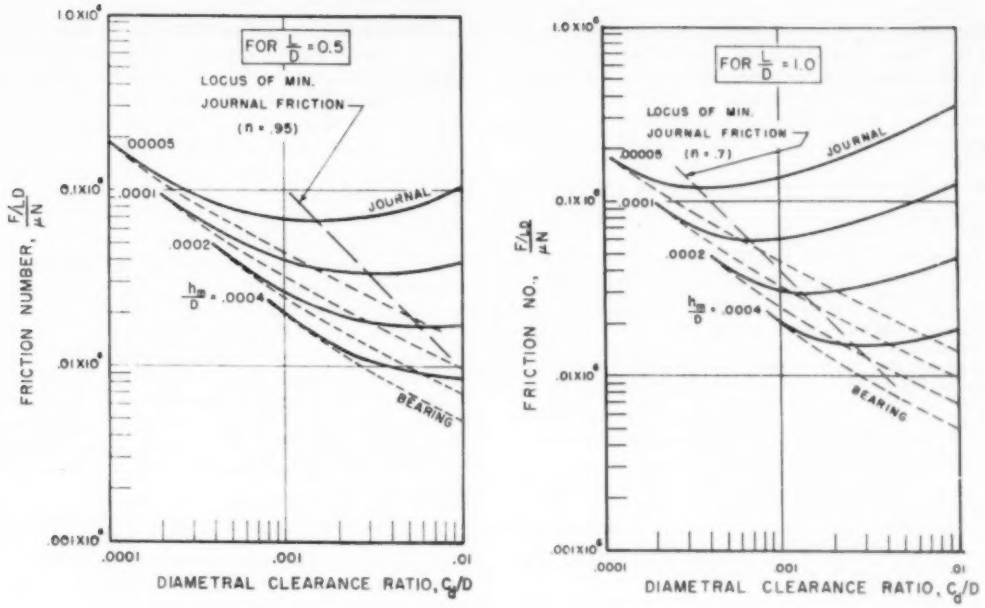

Fig. 10 Curves of journal and bearing friction against clearance ratio for a number of minimum film thicknesses as determined from the short-bearing approximation for bearings (a) of $L/D = 1/2$ and (b) of $L/D = 1.0$

where

$$C_n = \frac{(1 - n^2)^2}{\pi n}\left[\frac{1}{\pi^2(1 - n^2) + 16n^2}\right]^{1/2} \qquad (8)$$

In Equation (6) the friction number has a form similar to unit loading since F/LD is unit friction force based on projected area of the bearing. In this equation friction varies inversely as the first power of the minimum film thickness whereas load capacity varies as the second power. The curves of Figs. 10(a and b) have been plotted from Equation (6) in which Equation (2) is used to determine clearance ratio for a fixed value of h_m and various values of n. $\psi(n)$ is determined from Equations (7) and (8). The first term in Equation (7) gives values which result in friction number for the bearing, and the second term represents the added friction due to the load couple which must be added to determine the friction number for the journal. The second term is not only a function of eccentricity ratio but of L/D and the attitude angle ϕ as well.

Use of the Curves

In the design of heavily loaded bearings, many variables other than surface finish and clearance are of importance. Among these are elastic deflection and curvature of shaft and journal under load, out-of-roundness, out-of-straightness, waviness of the surfaces, and any other factors which influence the profile of the minimum film and the load capacity of the film. However, if short bearings are chosen, many of these variables have a lessened influence, and the importance of surface finish may be increased.

The curves of this paper are useful chiefly in specifying surface finish and clearance. The curves of Fig. 4 may be used to determine an allowable minimum film thickness for a design situation in which the load, speed, and viscosity are known and the dimensions D and L are assumed. Using Tarasov's factors the surface finishes may be specified to give a film profile free of touching asperities. The factor of safety may be incorporated by specifying surface finishes somewhat finer than indicated. In cases where exceptionally smooth but costly finishes are indicated, a rougher finish could be made smoother by various methods of polishing or burnishing the surface, or by a careful run-in of the bearing.

According to the short-bearing approximation in Fig. 7 the choice of clearance is not critical so long as the clearance ratio is greater than 0.001. While this is a simplification, the independence of load capacity from clearance has not been verified experimentally for large clearance ratios. The Cameron and Wood curves in Figs. 8 and 9, on the other hand, show that for maximum load capacity clearance ratios smaller than commercially used are required. These differences in theory are interesting. However, because of the differences, it is difficult to make a definite recommendation on clearance choice until experimental data are available. If actual behavior shows that clearance ratio does not have a great effect on load capacity, then the choice of clearance ratio may be made using Figs. 10(a and b) to give minimum power loss.

Conclusions

The chief contribution of this paper is the presentation of curves of load capacity and friction in a manner which aids in clarifying the effect of film thickness and clearance ratio on the performance of plain journal bearings. The criterion for determining the load capacity of a bearing in terms of surface roughness and Tarasov's factors appears to be well supported by the Burwell, et al., experimental data for $L/D = 1/2$.

Concerning the effect of clearance on load capacity, the short-

bearing approximation shows a relatively minor effect and the Cameron and Wood curve a relatively great effect, so that conclusions in this regard should be held in check until experimental data are made available for comparison.

References

1 F. W. Ocvirk and G. B. DuBois, "Relation of Journal Bearing Performance to Minimum Oil-Film Thickness," Technical Note 4223, National Advisory Committee for Aeronautics, Washington, D. C., April, 1958.

2 L. P. Tarasov, "Relation of Surface-Roughness Readings to Actual Surface Profile," TRANS. ASME, vol. 67, 1945, pp. 189–196.

3 G. B. DuBois and F. W. Ocvirk, "Analytical Derivation and Experimental Evaluation of Short-Bearing Approximation for Full Journal Bearings," Report 1157, National Advisory Committee for Aeronautics, 1953.

4 A. Cameron and W. L. Wood, "The Full Journal Bearing," *Proceedings of The Institution of Mechanical Engineers*, vol. 161, WEP nos. 47–54, 1949, pp. 59–72.

5 J. T. Burwell, J. Kaye, D. W. van Nymegen, and D. A. Morgan, "Effects of Surface Finish," *Journal of Applied Mechanics*, vol. 8, TRANS. ASME, vol. 63, 1941, pp. A-49–58.

6 L. F. Kreisle, "Very Short Journal-Bearing Hydrodynamic Performance Under Conditions Approaching Marginal Lubrication," TRANS. ASME, vol. 78, 1956, pp. 955–963.

7 R. W. Dayton, C. M. Allen, S. L. Fawcett, N. E. Miller, and R. E. Grimble, "A Fundamental Study of Bearing Behavior," Contract N5 ori-111, Office of Naval Research and Battelle Memorial Institute, May 16, 1952.

8 A. Kingsbury, "Optimum Conditions in Journal Bearings," TRANS. ASME, vol. 54, 1932, RP—54-7, pp. 123–148.

DISCUSSION

C. M. Allen[2]

The authors have once again demonstrated their very apt capabilities in the performance of a precise and definitive research program on sleeve bearings. The discusser would like to raise but two points concerning their paper.

The first is concerned with the effects of surface roughness of a bearing-shaft combination on load-carrying ability. Unfortunately, surface-roughness indications tell only a portion of the story. True, Tarasov's[3] factors for identifying "deepest and predominant peak maximum roughness" are helpful in considering the possible effects surface roughness may have on load-carrying ability of journal bearings. However, even these factors do not provide any insight concerning the nature of the surfaces themselves in that they describe only topography. A smooth, freshly ground hardened-steel surface has clumps of smeared metal (at least the ones produced at Battelle do) on the surface which, when studied with the electron-microscope, reveal loosely adherent fins of grinding fuzz. When such a surface is run in a bearing under very moderate loads, the clumps of smeared metal are subjected to the hydrodynamic forces of the lubricant film. There are several instances of intimate contact between the bearing and shaft even under rather lightly loaded conditions. When the ground surface of the shaft is examined after a short running period, and one must be fortunate enough to find the same area previously examined with the electron-microscope, it can be shown that some of the smeared fins of metal have been removed. It is well known that worn-in bearings have greater load-carrying ability than a freshly assembled bearing-shaft set. With ground surfaces, it would appear that a reasonably long period of operation is necessary to wear in a bearing assembly.

Lapped shaft surfaces appear to be freer of smeared fins of metal, and by observing the dielectric breakdown of the oil film[4] it can be seen that lapped surfaces wear in more rapidly than smoothly ground surfaces even though the profilometer surface roughness is of the same order. The evidence for this is that the incidence of asperity contact is observed to be much greater for ground surfaces than for lapped surfaces. Lapped and electropolished shaft surfaces have the least incidence of asperity contact between bearing and shaft, other conditions being equal, than do either ground or lapped shaft surfaces. Consequently, there is a relatively short period of wearing in and less difference between initial and final bearing load capacity.

Perhaps it will have been noticed that no comments have been made concerning the surface of the bearing. Since bearings are generally machined by cutting tools, and sometimes even burnished, it is suspected that a similar type of wearing in behavior prevails, but it is considered to be less important because of the lower modulus and strength of conventional bearing-material surface relative to the shaft. Therefore it does not appear that the surface roughness of the bearing should be weighted as heavily as the surface roughness of the relatively hard-steel shaft surface when considering the resulting nature of the lubricant film on load-carrying capacity.

The authors comment that we at Battelle were the "first experimenters to . . . measure . . . minimum film thickness directly."[5] I would like to say that I doubt we were first and that the method referred to is not in the strictest sense direct, but rather the oil-film thickness is obtained by indirect means by inference of electrical oil-film conductance data. The actual procedure used to obtain quantitative data on the minimum oil-film thickness is too involved to discuss here. The system used was to impress a high audiofrequency voltage across the oil film between an electrode embedded in the shaft and the bearing surface. Data on the breakdown potential were obtained and reduced to minimum lubricant film thickness by a series of computations. It is believed that the method could be made to provide quite accurate data for thin hydrodynamic films if a suitable electrode could be made. The inherent problem is one of having an electrode stable with respect to the shaft surface when exposed to the pressures of the oil film. Further, it is believed that once the electrode system was accurately calibrated, the entire shaft surface could be used as an electrode thus obviating the mechanical nuisance associated with the electrode. Of course, the conditions of the calibration and subsequent experiments must be comparable.

B. Sternlicht[6]

The authors should be complimented for trying to establish better understanding of surface finish on journal-bearing performance. This problem is very complex and deserves considerable attention. Because of its complexity, there are a number of questions which must be considered and which I would like to pose to the authors. Among these are:

1 Can Reynolds equation be used in analysis of bearings where film thickness is of the same order of magnitude as surface finish?

2 As the asperities of the journal move relative to the asperities of the bearing at any point within the fluid film, dh/dx varies. Therefore "squeeze-film" effects are present; these may be quite important in raising load-carrying capacity. Have the authors considered the importance of this effect?

3 Local temperatures and pressures are very important in analysis of thin fluid film for not only will they change the fluid

[2] Division Consultant, Battelle Memorial Institute, Columbus, Ohio.

[3] Reference [2] of authors' paper.

[4] C. M. Allen, "The Dielectric Strength of Oil Films in Plain Bearings," *Mechanical Wear*, American Society for Metals, 1950, pp. 181–191.

[5] R. W. Dayton, C. M. Allen, et al., "A Fundamental Study of Sleeve Bearing Behavior," Office of Naval Research, Contract N5 ori-111, Battelle Memorial Institute Report, May 16, 1952.

[6] Consulting Engineer—Hydrodynamics, General Electric Laboratory, Schenectady, N. Y. Assoc. Mem. ASME.

viscosity but will also deform the surface. What consideration have the authors given to this point?

4 What order of misalignment will cause a tenfold variation in film-capacity number for minimum film-thickness ratio equal to 1×10^{-4} and 1×10^{-5}?

A few additional comments may be in order. The authors show that clearance ratio does not have great effect on load-carrying capacity. Yet, we know that clearance ratio has a large effect on horsepower loss which in turn markedly affects the viscosity of the fluid in the bearing clearance. We also know that load-carrying capacity of a bearing is dependent on viscosity of the fluid at every point within the convergent film. Thus practice and theory, as presented by the authors, does not agree. The disagreement stems from the fact that the analysis presented by the authors considers isothermal conditions while in practice close to adiabatic conditions prevail. High-speed bearings, therefore, have to use high clearance ratio while low-speed bearings use low clearance ratio for the same imposed load and eccentricity ratio.

Several years back the discusser conducted some experiments on minimum friction as a function of Sommerfeld number. The following observation was made: By running-in the bearing, the Sommerfeld number could be decreased by 70 per cent before the "hook-point" of friction curve would change. This observation was also made by other investigators and therefore is not new. However, the importance of this observation was that the surface finish of the journal and bearing as measured before and after the run-in period did not change. Apparently better conformity rather than surface finish resulted after the run-in period. This observation points out that load or film-capacity number can be tripled without any change in minimum film-thickness ratio. From this standpoint, Figs. 4 and 6 are very misleading for everything is plotted on a log-log scale, but there are 4:1 variations in load-carrying capacity between theory and experiment for the same minimum film-thickness ratio.

Another interesting observation may be cited. Large numbers of babbitted bearings operated continuously for years without distress. Once the units were stopped and restarted under much lighter load, each of the units failed. Observation of the unfailed bearings showed that the babbitt crept in spots conforming to the specific load. However, this conformed film shape was not capable of supporting other loads. This point is brought out to show the complexity in modes of failure and design criteria. The designer should be cautioned in setting minimum film thickness as the only criteria in design. Most bearing failures occur due to misalignment, deformation, excessive temperature, dirty oil, fatigue due to dynamic loads, and so on. Thus there remain a lot of questions about analysis where film thickness is of the same order of magnitude as the surface finish. These remarks are not made in order to detract from the valuable contribution made by the authors, but merely to caution the designer when he sets minimum film thickness as criteria in design.

Authors' Closure

The authors wish to thank Mr. Allen and Mr. Sternlicht for their kind interest and for pointing out that there are many surface characteristics which influence the load capacity of journal bearings. While it is indeed true that the relationship of surface condition to load capacity is complex, it is desirable to sort out the many factors in their order of importance. The topography of the surface may be of the first order influence on load capacity in many cases where short bearings and perfect alignment are concerned.

However, there are other first order factors as the discussers point out. Mr. Allen's comment of the time required to loosen and remove the particles smeared on a ground surface is interesting and may seriously decrease load capacity in the running-in period. Mr. Sternlicht refers to surface conformability and misalignment as important variables. The authors agree that these are also first order variables and would wish to refer to an NASA paper by F. H. Raven and R. L. Wehe soon to be published, who show the effect of shaft bending (and the corresponding misalignment in support bearings) on load capacity.

Both Mr. Allen and Mr. Sternlicht discuss the advantages of running-in a bearing to increase load capacity. Mr. Allen's observation that lapped surfaces may be run-in more rapidly than ground surfaces when both have the same profilometer roughness is interesting. Tarasov shows that the high peaks of the surface are infrequent compared to the relatively small irregularities of the predominant surface. Therefore, it may be expected that the profilometer, which is an averaging device, reports the height of the small irregularities rather than the high peaks, which have a low statistical influence because of their infrequency. For the same profilometer reading both the ground and lapped surfaces may have the same small irregularities, but according to Tarasov's factors, the high peaks of the lapped surface may be twice as high as the ground surface. This may in part explain that a lapped surface may be run-in more rapidly because the higher peaks are more quickly worn off.

Mr. Sternlicht cites a case in which the load capacity of a bearing was greatly increased by running-in but that the profilometer measurement showed no change before and after running. Again, this may be explained in part by the fact that running-in deforms the occasional high peaks and has little influence on the predominant irregularities reported by the profilometer.

Mr. Sternlicht asks whether Reynolds equation applies when the irregularities are of the same order of height as the film thickness. This is a difficult question considering the complexity of incorporating the condition of an irregular boundary. In their paper, the authors have assumed that Reynolds equation applies in the conventional sense at the condition where the high peaks are at initial contact. This seems reasonable considering that the peaks are infrequent and from $4^1/_2$ to 10 times higher than the predominant irregularities thus making the minimum film thickness relatively greater than the predominant irregularities. This also applies to squeeze film effect in Mr. Sternlicht's second question. Considering the infrequent occurrence of the high peaks, the squeeze film effect may apply to such a small area as to be negligible. However, the squeeze film effect would increase as the peaks are worn off and boundary conditions are approached.

Many of Mr. Allen's and Mr. Sternlicht's comments probably apply to the thinner films attainable after the high peaks have been worn off whereas the Burwell, et al., data presented are based on new surfaces at initial friction hook point conditions.

It is certainly true as Mr. Sternlicht points out that a film viscosity variable with temperature will be nearer the actual operating condition (including heat transfer) than assuming constant film viscosity (isothermal condition). It would be interesting to compare the results of a solution based on an adiabatic film with those presented in the paper.

The authors feel that the comments of the discussers are particularly valuable in furthering the insight into the effects of bearing surface on bearing performance.

Statistical Optimization of Regulators Employing a Binary Error Criterion

J. H. MILSUM

Associate Research Officer, Simulation Group, National Research Council of Canada, Ottawa, Ontario, Canada

The problem is considered of minimizing total costs of a regulator subject to both a steady reference input and a statistical load disturbance. A binary error criterion is used which directly relates the error magnitude to the economic penalty entailed by the error. In contrast it is not easy to relate the mean-square error to economic penalty. Experimental work shows that the amplitude probability density distributions in saturating loops are altered sufficiently from the Gaussian that the statistical linearization technique does not predict results with satisfactory accuracy in many cases of interest. The use of modified distributions alleviates this problem, but analog computer experiments provide the most satisfactory attack for complicated situations and are easily instrumented.

Introduction

REGULATORS must maintain acceptable output quality with respect to some predetermined constant reference, usually in the presence of random disturbances. Any departure of product quality from ideal is called the error and generally incurs some economic penalty. Almost all process controllers, discrete manufacturing processes, and regulators of speed, voltage, temperature, and so forth, fall into this category. Economic optimization requires minimization of all costs or maximization of profit and is generally too complex for complete solution (Fig. 1). It is useful therefore to make a partial optimization by minimizing the sum of error penalty and of power costs, with the overhead charges assumed predetermined. This is an essential stage in the complete optimization including overhead costs.

Historically, attention has concentrated on minimizing the mean-square value of the error (MSE), and techniques have been developed for linear servomechanisms subject to noisy input signals [1].[1] Recent work by Kazakov [2] and Booton [3] extended the technique to systems with static nonlinearities (SNL). An SNL is defined as an element in which output and input are not proportional over the whole range, and their relationship is independent of frequency. The particular class of SNL considered in this paper is the saturation of controller output.

The MSE is difficult to relate to the cost penalty of imperfect quality, and instead a binary error criterion is considered. This

Contributed by the Instruments and Regulators Division and presented at the Annual Meeting, November 30–December 5, 1958, New York, N. Y., of THE AMERICAN SOCIETY OF MECHANICAL ENGINEERS.

NOTE: Statements and opinions advanced in papers are to be understood as individual expressions of their authors and not those of the Society. Manuscript received at ASME Headquarters, July 15, 1958. Paper No. 58—A-71.

[1] Numbers in brackets designate References at end of paper.

Nomenclature

Abbreviations

APD = amplitude probability density distribution
BEC = binary error criterion
CHU = Centigrade heat unit
MAD = mean absolute deviation
MSE = mean-square error
MV = manipulated variable
PDS = power density spectrum
RMS, rms = root mean square
SNL = static nonlinearity

Symbols

c = controlled variable
c_p = specific heat CHU/lb-deg C
C = capacity CHU/deg C
d = disturbance input variable
e = error variable
g = controller transfer function
h = plant or process transfer function
I = integral involved in Parseval's formula
k = gain constant
k_μ = equivalent mean gain
k_σ = equivalent rms gain
l = limited output
L = dimensionless inverse limited output, $L = \frac{\sigma_n}{l}$
m = manipulated variable, degrees-of-freedom of χ^2-distribution
M = ratio of mean and rms values, $M = \mu/\sigma$
n = noise variable or input
N_m = dimensionless MAD manipulated variable, $N_m = \frac{\nu_m}{\sigma_n}$
P_R = probable reject rate, or penalty
q = function of —
Q = heat flow, CHU/sec (Q_{max}, maximum value)
r = reference input variable
R = dimensionless reference input, $R = \frac{r_0}{\sigma_n}$
S = complex variable
t = time; normalized Gaussian variable, $t = \frac{X - \mu}{\sigma}$
T = time constant of system
W = fluid flow rate, lb/sec; $\overline{W}$, average value
γ = relative cost of rejection and power
δ = tolerance of "error channel" in BEC
Δ = dimensionless error tolerance, $\Delta = \frac{\delta}{\sigma_n}$
$\Delta\theta$ = average temperature change
θ = temperature
μ = mean value of stochastic variable
ν = MAD of stochastic variable
π = dimensionless variable, $\pi_1 = \Sigma_e L = \frac{\sigma_e}{l}\pi_2 = M_e \Sigma_e L = \frac{\mu_{ee}}{l}$
σ = RMS value of stochastic variable
Σ = dimensionless RMS value, $\Sigma_e = \frac{\sigma_e}{\sigma_n}$
τ = dimensionless time constant
Φ = power density spectrum of stochastic variable; error function, $\Phi\left(\frac{x}{\sqrt{2}}\right) = \frac{2}{\sqrt{\pi}}\int_0^{x/2} e^{-x^2} dx$
ω = frequency, radians/sec

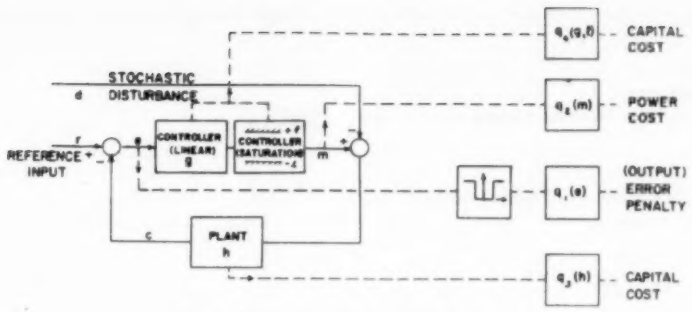

Fig. 1 Cost components in controlled system

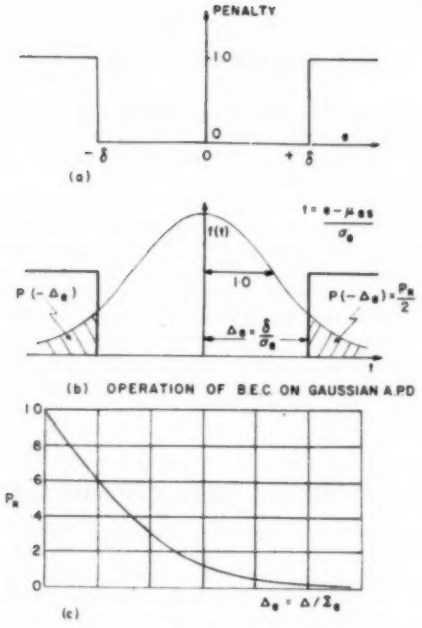

Fig. 2 The binary error criterion

binary error criterion (BEC) either accepts the product with zero penalty if the error lies within a predetermined tolerance, or rejects the product with constant penalty if the tolerance is exceeded [Fig. 2(*a*)]. The "no go" gage of quality control is an important example.

The probable reject rate P_R is defined as the proportion of time during which the error exceeds the permitted tolerance, or alternatively the proportion of discrete products which is rejected. If the amplitude probability density distribution (APD) of the error signal is Gaussian, as usually assumed in linear systems subject to random inputs, then the probable reject rate corresponds to the two-tail cumulative distribution [Fig. 2(*b* and *c*)]. Regulator saturation modifies the APD of the signal in the loop, but the method of statistical linearization enables the MSE to be predicted with sufficient accuracy. This method assumes that linear filtering within the loop reshapes the non-Gaussian distribution, produced by the nonlinearity, to Gaussian form at the error point. The Gaussian APD is described uniquely by its first and second moments [mean (μ) and mean-square (σ^2) values, respectively], and the change of these moments across a nonlinearity may be calculated easily. The reject rate given by the BEC is determined by the area under the tails of the APD and is consequently sensitive to higher moments. Hence the assumption of a Gaussian APD may not be acceptable for calculations in nonlinear loops, and unfortunately no analytical method exists for calculating the higher moments.

The power input to a system, in many cases, is a controller output, called here the manipulated variable, MV. The RMS value (σ) and mean absolute deviation (MAD, ν, the mean value of the rectified signal) are two suitable measures of the power. They are stably related for a wide range of APD's, and for the Gaussian case,

$$\frac{\nu}{\sigma} = \sqrt{\frac{2}{\pi}} \approx 0.8 \qquad (1)$$

Both may be computed by the method of statistical linearization, but with unknown accuracy.

This paper investigates the interrelation of the error and MV for varying system parameters in randomly disturbed, saturating loops, in order that the partial optimization just discussed may be performed. The results of analog computer investigations show that non-Gaussian models of the error APD must be used in many cases if statistical linearization is to predict the BEC and MV with acceptable accuracy.

Linear Analysis

A simple regulatory system consisting of single-lag plant and proportional controller with saturation limits is analyzed, and comparison is made with experimental results. The experiments cover much more general situations, however.

A simple but general model of random disturbances is obtained if both the APD and power-density spectrum (PDS) are Gaussian. The Gaussian model is characterized by two parameters, the mean μ and dispersion (σ, standard deviation) but for the PDS, $\mu = 0$, and the dispersion time (T_s) [4, 5] is the only parameter. In contrast, the conventional quadratic spectrum has two parameters (ω_n and ζ).

In the experimental work [5] the Gaussian PDS was closely approximated by a four-equal-lag filter operating on "white" noise, and the lag time-constant T_n is therefore employed, instead of T_s, for the appropriate closed-loop mean-square calculations. Note, however, that $T_s = 2T_n$ in this case [5].

In the simplest application where the mean value of the reference and disturbance signals is zero and the system is linear, the MSE and mean-square MV can be obtained by use of Parseval's theorem,

$$\sigma_e^2 = \frac{1}{2\pi}\int_{-\infty}^{+\infty} \Phi_e(j\omega)\cdot d\omega$$

$$= \frac{1}{2\pi}\int_{-\infty}^{+\infty} \Phi_n(j\omega)\cdot|H_e(j\omega)|^2\cdot d\omega \qquad (2)$$

where

σ_e^2 = MSE
$\Phi_e(j\omega)$ = PDS of error
$\Phi_n(j\omega)$ = PDS of disturbance
$H_e(j\omega)$ = closed-loop transfer function relating error to disturbance

and similarly for σ_n^2 and σ_m^2.

The computation is simplified by use of special tables of integrals [6] and in this case is obtained

$$\sigma_n^2 = I_1 = \frac{\Phi_0}{2\pi}\int_{-\infty}^{+\infty}\left|\frac{1}{(1+j\omega T_n)^4}\right|^2 d\omega$$

$$= \frac{5\Phi_0}{32T_n} \tag{3}$$

$$\sigma_e^2 = I_3 = \frac{\Phi_0}{2\pi}\int_{-\infty}^{+\infty}\left|\frac{1}{(1+j\omega T_n)^4(1+j\omega T_n\cdot\tau_i)}\right|^2 d\omega$$

$$= \frac{5\Phi_0\cdot q(\tau_i)}{32T_n\cdot k_i^2} \tag{4}$$

$$\sigma_m^2 = (k_c\sigma_e)^2$$

$$= \frac{5\Phi_0}{32T_n}\left(\frac{k_c}{k_i}\right)^2\cdot q(\tau_i) \tag{5}$$

where

$q(\tau_i)$ is a rational function of τ_i
Φ_0 = magnitude of white PDS
k_c = controller gain (therefore also loop gain)
$k_i = 1 + k_c$

$$\tau_p = \frac{T_p}{T_n}$$

$$\tau_i = \frac{\tau_p}{k_i}$$

The more convenient nondimensional representation becomes

$$\Sigma_e \equiv \frac{\sigma_e}{\sigma_n} = \frac{\sqrt{q(\tau_i)}}{k_i} \tag{6}$$

$$\Sigma_m \equiv \frac{\sigma_m}{\sigma_n} = \frac{k_c}{k_i}\cdot\sqrt{q(\tau_i)} \tag{7}$$

and the familiar results are plotted in Fig. 3, for varying controller gain k_c and plant "speed" τ_p showing the inevitable compromise requirement between error and power.

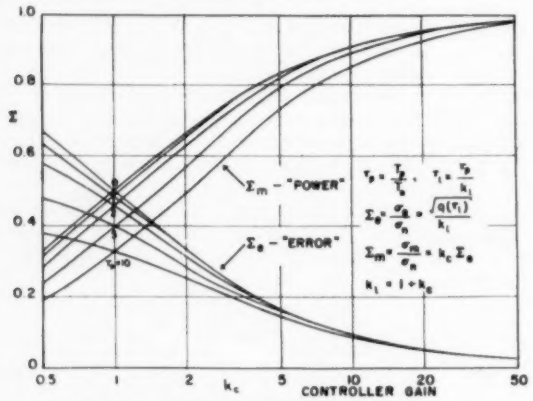

Fig. 3 RMS error and MV—single-lag plant

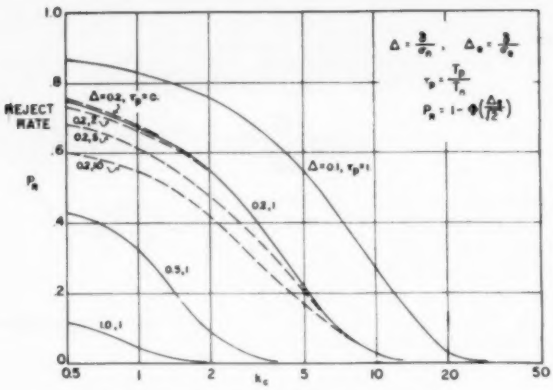

Fig. 4 Binary error criterion—single-lag plant

The corresponding BEC curves are shown in Fig. 4, with the dimensionless tolerance $\Delta = \delta/\sigma_e$, and τ_p as parameters. The curves for the reject rate proportion P_R are similar in shape but not identical with the Σ_e curves.

The error curves are quite different for the more usual regulator case of nonzero reference input (and perhaps also nonzero-mean disturbance). However, the system can be compensated for such steady errors by "oversetting" of the input or by including integral action in the controller so that the curves reproduced above are in fact applicable. On the other hand, the mean value of the MV contributes directly to the power requirements, and the appropriate total RMS (Σ_{m_t}) and MAD (N_m) values of the MV may be calculated [5], as a function of a new dimensionless reference-input parameter, $R = \frac{|r|}{\sigma_n}$.

Analysis With Saturating Regulator-Statistical Linearization

Practical regulators may saturate in the manipulated variable or any of its derivatives, and often the remaining loop components may be considered linear. Even this simplified situation is not amenable to closed-loop computation unless only the MV itself saturates rather than its derivatives. Sharp saturation is therefor added to the simple gain controller of the section Linear Analysis [Fig. 5(*a*)]; however, for convenience in later calculations the limiter is considered comprised of a linear gain, k_c, and a limiter with unit gain in the linear region [Fig. 5(*b*)].

Statistical linearization [2, 3, 5] is an approximation which conceptually replaces a static nonlinearity by a linear component. This linear component is defined by an equivalent mean gain, k_μ, and equivalent rms gain, k_σ; which gains are computed as the ratios of the first and second moments (mean and mean-square values) of the output APD in relation to the first and second moments of the input APD, respectively, [Fig. 5(*c*)]. Booton [3] defines k_σ differently by using that equivalent rms gain which results in least mean-square error of approximation, and the significance of the difference is examined in references [2 and 5]. In all these computations the error signal is assumed to have a Gaussian APD.

The mutual interdependence, via the closed loop, of the input and output of the nonlinearity precludes direct closed-loop computations in many cases of interest; instead trial-and-error or indirect calculations must be made. However, the simple relay [Fig. 5(*d*)] does permit direct computation in some simple closed-loop configurations, having one less parameter than the limiter. This is a special case of great interest since relays are widely used in practice, and since limiters approximate increasingly to the

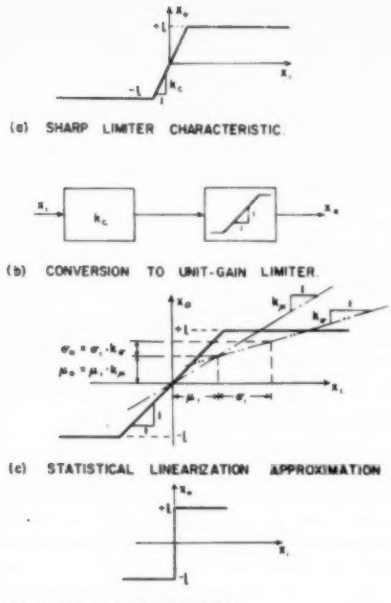
(a) SHARP LIMITER CHARACTERISTIC.
(b) CONVERSION TO UNIT-GAIN LIMITER.
(c) STATISTICAL LINEARIZATION APPROXIMATION
(d) RELAY CHARACTERISTIC.

Fig. 5 Statistical linearization of limiter

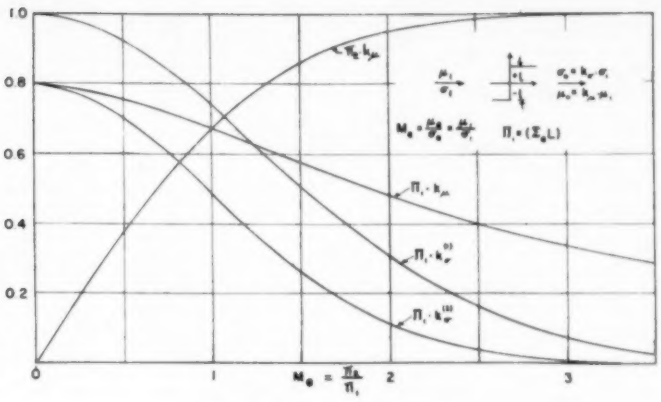

Fig. 6 Equivalent gains for relay

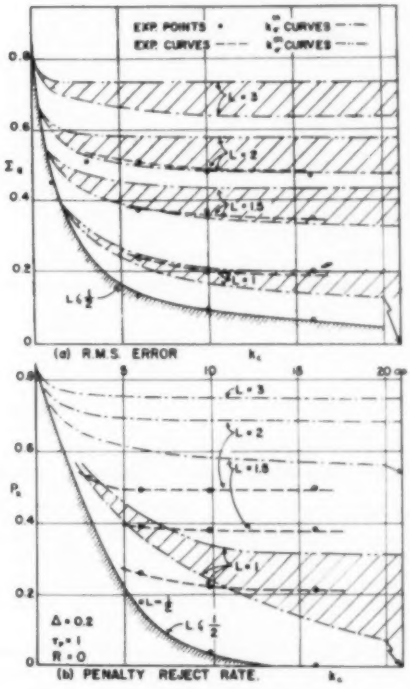

Fig. 7 BEC and MSE for limiter in loop

relay with increasing linear gain. As an example, Fig. 6 shows the various equivalent gains for the relay against appropriate dimensionless parameters. The equivalent gains all decrease to zero as the mean:dispersion ratio (M_e) of the input increases. Note that the predicted rms output approaches only $\sigma_0/l = 0.8$ for the Booton prediction $k_\sigma^{(2)}$ whereas the physically required value of unity is produced by the second moment approximation $k_\sigma^{(1)}$.

As already noted, the input to the nonlinearity has been assumed to have a Gaussian APD in previous work and also in Fig. 6. Filtering within the linear remainder of the loop has been assumed to produce this result, and experimental work has shown that the mean and rms error signals may be predicted with satisfactory accuracy by this assumption. However, no measurements of the APD at the input and output of the nonlinearity have been reported, since they were not necessary for these predictions of mean-square error. There is no difficulty in extending the statistical linearization concept to non-Gaussian distributions should this be found necessary (provided only that the new distributions be known).

The predicted curves of dimensionless rms error $\Sigma_e = \dfrac{\sigma_e}{\sigma_n}$, and BEC error, probable reject rate P_R against linear gain of the controller k_c are compared in Fig. 7 with the results of an analog computer investigation, both for the first-order system with sharp saturation in the controller. Similarly the results for the dimensionless rms and MAD manipulated variables are shown in Fig. 8. The presentation is limited here to the simplest case (i.e., zero-mean) in order that the principles may be illustrated within present space limitations. The extension to nonzero means is of course necessary for realistic appraisal of the regulator problem and is reported in reference [5].

Fig. 7(a) confirms that the two prediction methods bracket the test results, with better prediction by use of $k_\sigma^{(1)}$ in the heavily saturated region ($L \equiv l/\sigma_n > 1$). For $L < 1/2$, saturation effects are negligible, and linear prediction is possible as considered in reference [6]. Examination of Fig. 7(b) for the BEC, however, reveals that no satisfactory agreement exists between the experimental values and those predicted by statistical linearization. Note that the natural dimensionless parameter for the BEC is $\Delta = \dfrac{\delta}{\sigma_n}$ and an arbitrary, but realistic value of 0.2 has been chosen. It is interesting that the reject rates depend less on loop gain than predicted by linearization, and that, in fact, the dependency is very similar to that of the rms error.

Fig. 8 shows the similar plots for the manipulated variable (both rms and MAD) and again there is consistent disagreement. For significant values of L and k_c the predicted values are high, but prediction improves as k_c is decreased.

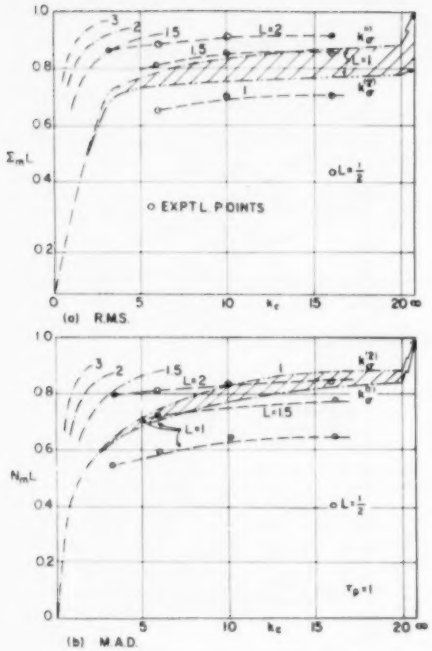

Fig. 8 RMS and MAD manipulated variable for limiter in loop

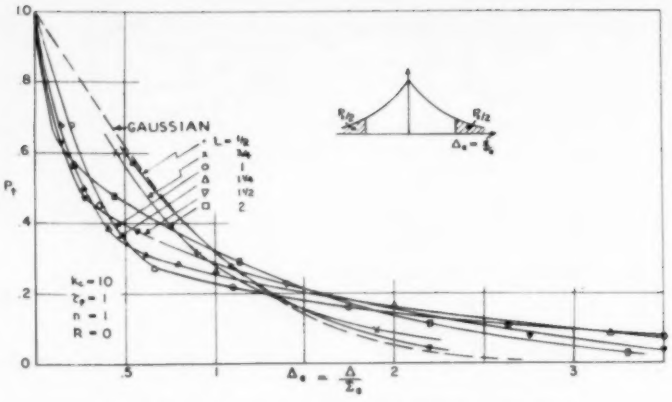

Fig. 9 Two-tail cumulative distribution of error, for varying L

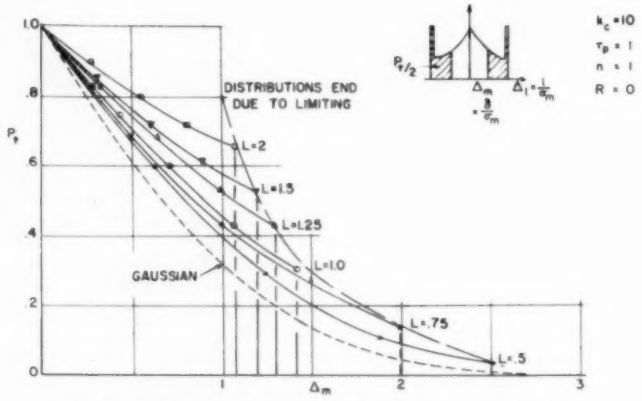

Fig. 10 Two-tail cumulative distribution of MV, for varying L

Experimental Study Modification of Statistical Linearization

The results discussed indicate that the relevant probability distributions in the saturating loop should be investigated, since the assumption of Gaussian APD in the error yields unsatisfactory predictions. Such investigations were made on a high-speed analog computer using simply constructed, special, equipment, and are reported in detail in reference [5]. In particular the two-tail cumulative probability distributions for the case mentioned for varying L are reproduced in Figs. 9 and 10 for the error and manipulated variable, respectively. The Gaussian curves are superimposed as a datum and show that the error and MV distributions are affected by saturation in significant degree and in mutually inverse manner. The error distribution undergoes two basic effects,

(i) the "two-tail" slope becomes larger than Gaussian (and hence also the APD) in the region of small amplitude with increasing L.

(ii) the probability of exceeding a given amplitude, P_p, becomes larger than Gaussian in the large amplitude region.

In particular for $L \geqslant 1$ there is about 0.1 probability of exceeding a dimensionless amplitude of $\Delta_s = \dfrac{\delta}{\sigma_e} = 3$ whereas the equivalent Gaussian probability is almost zero. Between these extreme amplitudes the curves of varying L intermingle in complicated fashion.

The mutually inverse effects on the MV distribution involve,

(i) the slopes of the two-tail distribution always being less than Gaussian.

(ii) large pulses on the APD corresponding to frequent occurrence of the saturated value.

The error distribution curves generally resemble the chi-square (χ^2) distributions for small degrees of freedom, when modified to a back-to-back form. Unfortunately the complex configuration changes with varying L preclude any direct, inclusive analytic treatment. However, since the substantially saturating distributions differ from the Gaussian in a generally similar manner, an averaged, empirical distribution (and corresponding to the χ^2-curve for 1 degree of freedom ($m = 1$) with a modified rms value) was used in the hope of improving accuracy of prediction. This distribution, and the relevant scatter plot, is shown in Fig. 11(a) and the improved predictions in Fig. 11(b). Since the empirical model of error APD was obtained for a single-lag plant having little filtering action, one cannot immediately assume universal applicability of the result. The greater filtering of more complex plants does indeed tend to bring the error distributions back toward the Gaussian, but the characteristic long "tails" are retained. Thus prediction of reject rate can always be improved by judicious combination of the results for the Gaussian and empirical models.

In order to predict the manipulated variable, the statistical linearization method was modified by computing power transfer

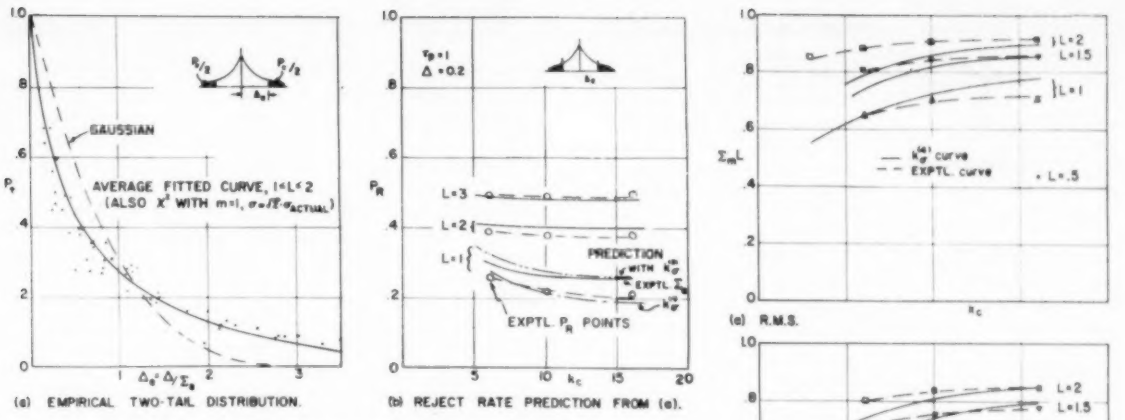

Fig. 11 Prediction of reject rate, using empirical error distribution

Fig. 12 Prediction of manipulated variable, using χ^2-distribution of error

across the nonlinearity with the new error APD; actually the exact χ^2-distribution for $m = 1$ was used for ease of calculation. In this manner new equivalent gains were computed [5]. The improved predictive accuracy is illustrated in Fig. 12 for both rms and MAD values. Prediction is acceptable for large k_c, but the values become increasingly low with respect to the experimental values as gain is decreased (and therefore as filtering is increased) since the error APD increasingly approaches Gaussian. Again the results from Gaussian and χ^2-analyses bracket the actual results.

Experiments were made on the more usual regulator configuration with constant reference level. Since less manipulated variable is thereby available in one direction to nullify the random disturbance effects, asymmetric signal distributions may be expected within the loop. However, knowledge of the two-tail distribution sufficed for the present study. Since the usual regulator tolerates little error, and probably operates with a large $R:L$ ratio, tests were confined to $L = 1/2$ and 1 over a wider R range. The general results are similar to those for symmetric saturation, which is understandable since the principal effects of increasing L and R are the same, namely, more saturation. For moderately low reject rates ($P_R < 0.4$) an effective saturation L' may be defined for combined L and R effects as

$$L' = L(1 + kR) \tag{8}$$

where $k \approx 1$.

For large $R:L$ ratios the two-tail distributions eventually change to forms quite unlike the averaged model, and further investigations would be needed. In particular, the unrectified distributions would need to be measured

Thermal Example

The process considered is essentially a water-heater which supplies hot water to many different chemical processes at a randomly varying rate which may be assumed Gaussian-distributed. Outlet water temperature characterizes the product quality, which is subject to a BEC, since both boiling water (100 C) and water below 70 C fail to perform the required duty and entail product rejection. The heating rate is error actuated by a proportional-and-saturating controller, and input water temperature is 10 C. A fast level control is assumed to maintain constant volume in the heater.

Assuming ideal mixing, good insulation, and a negligible work term, conservation of energy yields

$$Q_m = C \cdot \left(\frac{d\theta_e}{dt}\right) + W(t) \cdot c_p \cdot (\theta_e - \theta_i) \tag{9}$$

and the controller equation is

$$\left.\begin{aligned} Q_m &= k(\theta_r - \theta_e) \text{ in linear range} \\ &= Q_{\max} \text{ at upper bound} \\ &= 0 \text{ at lower bound} \end{aligned}\right\} \tag{10}$$

where the nomenclature and assumed values are

Q_m = MV heat flow, CHU/sec
$Q_{\max}$ = 15000 CHU/sec
θ_e = water temperature in heater, deg C
θ_i = inlet water temperature = 10 C
θ_r = reference temperature = 85 C
C = thermal capacity of tank = 1000 CHU/ deg C
c_p = specific heat = 1 CHU/lb − deg C
k = controller gain, CHU/sec − deg C
$W(t)$ = variable flow rate, lb/sec

The primitive block diagram of Fig. 13(*a*) illustrates this closed loop. The time varying nature of $W(t)$ initially renders the analysis of this paper inapplicable, but matters may be simplified by assuming, with little inaccuracy,

$$W(t) \cdot c_p \cdot (\theta_e - \theta_i) = \bar{W} \cdot c_p \cdot (\theta_e - \theta_i) + W_1 \cdot c_p \cdot \Delta\theta \tag{11}$$

where $\bar{W}$ = mean value of $W(t)$ = 100 lb/sec
$W_1 = W - \bar{W}$
= Gaussian-APD variable with rms value σ_{W1} = 100 lb/sec and PDS time constant (as per text) T_s = 10 sec
$\Delta\theta$ = mean value of $(\theta_e - \theta_i)$ = 75 C

Thus the modified block diagram of Fig. 13(*b*) is obtained; for direct application of the present analysis, however, it is convenient to work with signals of the same dimension, as in Fig. 13(*c*). Except for controller asymmetry, the layout is identical with that assumed in the main discussion. In fact, small error is involved in considering the controller symmetrical since the tests

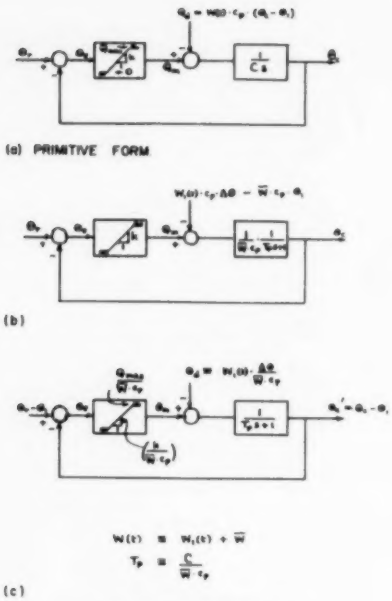

Fig. 13 Thermal example

described heretofore showed that negative outputs are seldom called for in the regulator situation.

The following equivalences with earlier nomenclature now apply:

$$
\begin{aligned}
r_0 &\equiv (\theta_r - \theta_1) = 75\ \text{C} \\
d &\equiv \theta_d = \frac{\Delta\theta}{\bar{W}\cdot c_p}\cdot W_1 = 0.75 W_1\ ^\circ\text{C} \\
m &\equiv \theta_m = \frac{Q_m}{\bar{W}\cdot c_p} = 0.01\, Q_m\ ^\circ\text{C} \\
T_p &\equiv \frac{C}{\bar{W}\cdot c_p} = 10\ \text{secs} \\
\tau_p &\equiv \frac{T_p}{T_n} = 1 \\
k_s &\equiv \frac{k}{\bar{W}\cdot c_p} = 0.01\, k \\
l &\equiv \frac{Q_{\max}}{\bar{W}\cdot c_p} = 150\ \text{C} \\
\delta &\equiv 100 - 85\ \text{C} = 15\ \text{C} \\
\sigma_n &= \sigma_{W1}\cdot\frac{\Delta\theta}{\bar{W}\cdot c_p} = 75\ \text{C} \\
\therefore L &= \frac{\sigma_n}{l} = {}^1/_2 \\
R &= \frac{r_0}{\sigma_n} = 1 \\
\Delta &= \frac{\delta}{\sigma_n} = 0.2
\end{aligned}
\qquad (12)
$$

Assuming that the heating cost is 0.2 dollar per 10^4 CHU then the power cost (Fig. 1) is [5];

$$q_3(m) = 0.3\,\frac{\nu_m}{l} = 0.3\, N_m L\ \$/\text{sec} \qquad (13)$$

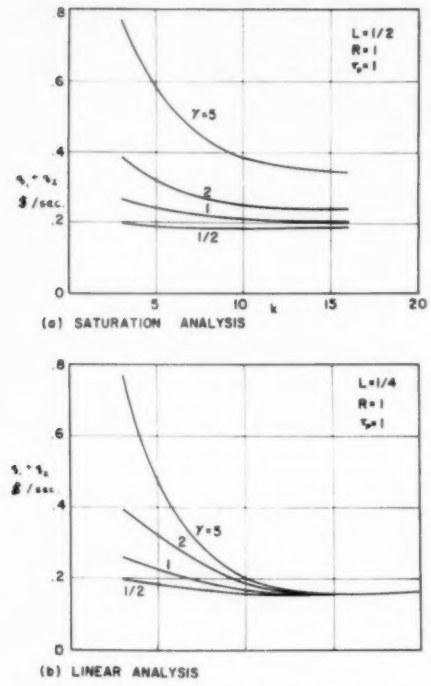

Fig. 14 Operating costs for thermal example

For generality of analysis it is desirable to study the combined error and power costs for different ratios of rejection penalty and power cost.

Therefore we define:

$$\gamma \equiv \frac{\text{cost of rejection/sec}}{\text{cost of } Q_{\max} \text{ power/sec}} = \frac{\text{cost of rejection/sec}}{0.3}, \qquad (14)$$

then

$$q_1(e) = q_1(P_R) = 0.3\cdot\gamma\cdot P_R. \qquad (15)$$

The combined cost of Equations (13) and (15) is plotted in Fig. 14(a) for several values of γ, using the experimental results reported earlier. Note that by Equation (8) the equivalent $L' = (1 + R)L = 1$. A minimum cost for small finite k occurs only when the penalty for rejected product is small ($\gamma < {}^1/_2$). For larger, and more realistic γ-values the combined costs decrease slowly with increasing gain, so that a relay control would be cheapest in all respects.

It is desirable to consider changes in heater size ($Q_{\max}$) also. Here only the effect of doubling $Q_{\max}$ (to 30,000 CHU/sec) will be examined.

This change alters the saturation level so that $L = {}^1/_4$, and as shown in the section Experimental Study Modification of Statistical Linearization a linear analysis is now a valid approximation since $L' = {}^1/_2$. The results are shown in Fig. 14(b), and are generally similar to the first case except that all γ-curves approach a unique curve above $k = 10$, because $P_R \to 0$. Thereafter the slowly increasing combined costs have a limiting value 0.17. Thus for large γ a larger heater should be considered, and the next stage of cost analysis performed, i.e., including controller cost $q_2(g, l)$, (see Fig. 1). In this example the boiler cost $q_3(h)$ has been considered fixed, but the analysis can be extended, of course, to optimize with this additional variable.

Conclusions

A wide range of test results confirms that statistical linearization predicts the system rms error with acceptable accuracy. As suggested by Kazakov the average of the two available methods provides best prediction. On the other hand, the BEC reject rate is not accurately predictable from these rms error calculations with the assumption of a Gaussian error-APD. The two-tail rectified error distributions, measured over wide ranges of saturation level, reference and disturbance levels, and plant complexity, differ from the Gaussian, particularly in having greater probability in the tails, thus directly affecting the prediction of the BEC. An empirical, averaged error distribution corresponding to a quasi-χ^2 distribution predicts the reject rate with reasonable accuracy, unless there is very considerable filtering in the loop, in which case the empirical and Gaussian models provide upper and lower bounds for prediction. Similarly the MV is not predicted satisfactorily with the Gaussian error model if substantial saturation exists. A modified power transfer calculation (statistical linearization) across the nonlinearity, with a χ^2-error model, improves the predictive accuracy, but any one model is limited as to range of improvement. Unfortunately, no obvious way exists of relating analytically the changes in the distribution to the causal parameter changes.

For regulators operating with reference inputs of ordinary value these conclusions are also valid.

These empirical distribution models do improve prediction, but for any specific problem in which an accurate economic minimum is desired between error penalties and power costs, an analog computer study should be performed. It is one purpose of this paper to show that such studies are relatively easy and cheap to instrument and carry out.

Acknowledgments

Acknowledgment is made of the assistance of many people at M.I.T. and in particular of H. M. Paynter. The National Research Council of Canada supplied continuing support of these studies. Philbrick Researches Inc. generously helped with advice and equipment in the instrumentation stage.

References

1 J. G. Truxal, "Automatic Feedback Control System Synthesis," McGraw-Hill Book Company, Inc., New York, N. Y., 1955.

2 I. E. Kazakov, "Approximate Probability Analysis of the Operational Precision of Essentially Nonlinear Feedback Control Systems," Automatyki i Telemekaniki, Moscow, USSR, 1955.

3 (i) R. C. Booton, "Nonlinear Control Systems With Random Inputs," *Trans. IRE*, Professional Group on Circuit Theory, no. 1, 1954.
or Report No. 61, DACL, M.I.T., March, 1952.
(ii) R. C. Booton, "The Measurement and Representation of Nonlinear Systems," *Trans. IRE*, Professional Group on Circuit Theory, No. 4, 1954.

4 H. M. Paynter, "On an Analogy Between Stochastic Processes and Monotone Dynamic Systems," Proceedings of Conference on Control Technology, Heidelberg, Germany, September, 1956.

5 J. H. Milsum, "Problems in Optimizing of Stochastically Disturbed, Saturating Regulators, Employing a Binary Error Criterion," ScD thesis, M.I.T., August, 1957.

6 Newton, Gould, and Kaiser, "Analytical Design of Linear Feedback Controls," John Wiley & Sons, New York, N. Y., 1957.

DISCUSSION

T. P. Goodman[2]

One interesting feature of the author's work is his use of an electronic random-noise generator in combination with an analog computer to perform statistical experiments. The use of electronically-generated random voltages for purposes of illustrative display on an oscilloscope has been well known for some years; a decade ago, J. C. R. Licklider and E. Dzendolet pointed out the potentialities of such a display:[3]

"A thousand cases—or a million—parade themselves before one's eyes in a single second. In 10 seconds one is almost willing to say that he has seen an infinite population. Moreover, the population is normal. Its standard deviation can be varied by turning a knob. Random samples can be drawn at will: 2 cases, or 20, or 200."

From the use of random-voltage signals merely to illustrate results which have been obtained analytically the author has taken a major step forward to the use of random-voltage signals to obtain experimentally statistical results which cannot readily be obtained analytically.

In the writer's view, this procedure represents an important computational method which is comparable to the "Monte Carlo" method[4] in which statistical calculations are performed on a digital computer by using sequences of random numbers as input data.

It would be of interest to have the author's comments on how his analog-computer method compares with the digital Monte Carlo method for the types of problems which he has considered.

H. M. Paynter[5]

The author has in this notable paper, and in his associated exhaustive research work, manifested an interesting and fruitful point of view with respect to the role of analog models in theoretical investigations; namely, that they serve as worthy experimental media, since any useful or practical theory dealing with the real world must, "in passing," so to speak, also adequately describe the observed behavior of computing systems.

The author also has put in proper context the function of any given optimalizing criterion in system design and operation. The "accept-reject" alternative frequently has more practical significance than "minimum squared error" or other more conventional measures. Perhaps it is also worth while to point out that in any given analog study of a proposed configuration, the complete economic balances displayed in Fig. 1 of the paper can all actually be *directly computed continuously* and optimized *ad hoc*. Such studies are breathtakingly "short and sweet" on presently available commercial machines.

Author's Closure

In the Monte Carlo method the sequence of random numbers fed into a digital computer is indeed the sampled-data equivalent of the random continuous voltage used in the analog computer simulation. Each simulation has advantages for different physical situations.

In most engineering systems the signals are continuous (although in the microscopic limit they may be considered comprised of discrete steps). Hence it is natural to use continuous signals in their simulation, especially since the time scale may be speeded up dramatically, as mentioned by both discussers. This is particularly true of control systems, even including those of the sampled-data type.[6] A technically trivial, but commercially

[2] Mechanical Systems Department, General Engineering Laboratory, General Electric Co., Schenectady, N. Y. Assoc. Mem. ASME.

[3] J. C. R. Licklider and E. Dzendolet, "Oscillographic Scatterplots Illustrating Various Degrees of Correlation," *Science*, vol. 107, 1948, pp. 121–124.

[4] E. Bowman and R. B. Fetter, "Analysis for Production Management," R. D. Irwin, Inc., Homewood, Ill., 1957.

[5] Massachusetts Institute of Technology, Cambridge, Mass.; also, American Center for Analog Computing, Boston, Mass. Mem. ASME.

[6] H. Chestnut, A. Dabul, D. Leiby, "Analog Computer Study of Sampled-Data Systems," AIEE 58-1324.

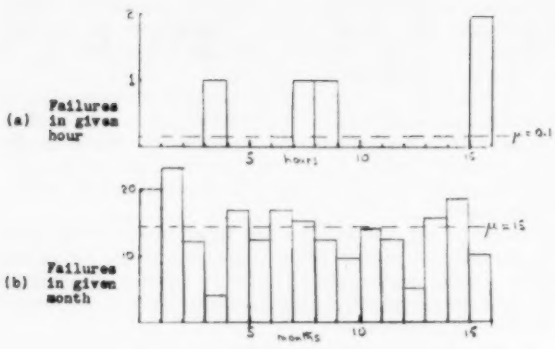

Fig. 15 Machine tool failure rates

important corollary is that large systems subject to random climatic variables with huge destructive potential, such as flooding, freezing, and earthquaking, may quickly be studied over long periods of real time to obtain extreme value probabilities. Parenthetically, this latter task is often hampered, however, by an inadequate knowledge of the environment's statistics.

Discrete steps characterize other physical systems, such as batch production, machine tool failure, random walks, and inventory control. The latter typifies the high accuracy requirement of some of such systems, which make the discrete counting action of digital computers more suitable. Machine tool failure illustrates another situation in which mean failure rate (for example, 1 failure per 10 hours, from among 100 machines) is very low compared with the discrete step represented by one failure, Fig. 15(*a*). In such cases a continuous waveform would be a very unsatisfactory simulation. This remains true as long as the hour-by-hour performance is of interest, which is the case in determining allotment of maintenance staff, for example.[4] If, however, the failure rate per week, month, or year (time scale compression of order 10^2 or 10^3) contained sufficient information, then the revised failure rate curve, Fig. 15(*b*), could perhaps be simulated satisfactorily by a continuous waveform. The relevant parameter, ratio of standard deviation and mean, has been reduced by this time scale compression and consequent loss of information. Again the challenging possibilities of sample-and-hold techniques on the analog computer[5] should be mentioned as an alternative method.

In answer to Dr. Goodman's last question, the author considers that the digital Monte Carlo method would be very wasteful for the reported experiments. The noise used in the experimental work was roughly flat out to 100 cps, and since there was still significant energy content beyond 100 cps, the minimum sampling rate for real time operation would be 1000 samples per second. Assuming 100 computing steps per sample, then a digital computer with operating time of 10 μ sec per step would be needed. With currently available computers, this implies an IBM 704 or UNIVAC class machine at a cost above one million dollars to operate in the same time scale as that of the approximately $1000 worth of analog equipment used.

The author concurs with Professor Paynter's concluding remarks about continuously optimizing control and is in fact intending to publish further work on this subject in the near future.

Both discussers are thanked for their interest and kind remarks.

An Introduction to the Time-Modulated Acceleration Switching Electrohydraulic Servomechanism

STEPHEN A. MURTAUGH, JR.

Research Mechanical Engineer, Systems Synthesis Department, Cornell Aeronautical Laboratory, Buffalo, N. Y.; formerly, Systems Engineer, Moog Servocontrols, Inc., East Aurora, N. Y.

A discussion of a new concept in electrohydraulic control is presented in this paper. The usual hydraulic servomechanism design uses a d-c amplifier and a flow-control servo valve to obtain hydraulic flow proportional to the position or velocity error of the load. In the acceleration switching servo these components are replaced by an electronic multivibrator and an especially designed electrohydraulic-servo valve called an acceleration switching valve. System control is obtained through modulation of the multivibrator square-wave dwell time by which the driven-load acceleration is regulated. The servo valve behaves as a pure integrator throughout most of its operating frequency range. Use of this technique has resulted in increased reliability, excellent servo valve resolution, negligible center-shift due to temperature extremes, and near infinite pressure-gain characteristics.

A NEW concept in the field of electrohydraulic servomechanisms, the acceleration switching technique represents a different approach to the design of electrohydraulic closed-loop control systems. The benefits a system designer may expect from using an acceleration switching servo are such as to improve materially both system performance and reliability, especially when the control is required to respond to small input signals and/or to operate in an environment of temperature extremes or contaminated fluids.

Electrohydraulic servos are commonly used to position the control surfaces of modern military aircraft and missiles where the requirement exists for exacting performance at high power levels. The degree of success with which electrohydraulic servomechanisms have been utilized in these and in other applications is often limited by several factors with which the servo valve is directly concerned. Servo-valve resolution or threshold can limit the ability of the system to respond to minute signal inputs. Extreme precautions must be taken to insure that the system hydraulic fluid is free of contamination, otherwise servo-valve reliability would be jeopardized. In order to obtain zero steady-state error under load it is necessary to add integral control which complicates the loop dynamics. Finally, operation at elevated temperatures is aggravated by the drift tendency, or center shift, of the servo valve. The acceleration switching servo has proved to reduce the foregoing effects materially, resulting in dependable, trouble-free, electrohydraulic control systems capable of providing system response and stability previously unobtainable.

It is the purpose of this paper to develop and explain some of the important characteristics of the acceleration switching servo, reviewing some of the previously published reports on the subject to provide an understanding of the fundamental factors governing the use and operation of the acceleration switching technique.

Contributed by the Instruments and Regulators Division and presented at the Annual Meeting, New York, N. Y., November 30–December 5, 1958, of THE AMERICAN SOCIETY OF MECHANICAL ENGINEERS.

NOTE: Statements and opinions advanced in papers are to be understood as individual expressions of their authors and not those of the Society. Manuscript received at ASME Headquarters, August 28, 1958. Paper No. 58—A-159.

Acceleration Switching Servo

The idea of acceleration switching (also known as pulse length modulation) originated several years ago at the Applied Physics Laboratory of Johns Hopkins University [1].[1] The acceleration switching concept essentially is a method of controlling the time-rate-of-change of flow to an output member in a manner such that a desired position or velocity of the driven load is obtained. This control is a result of the valve-spool velocity rather than spool position being made the control parameter. Load control is achieved by using an especially designed two-stage, four-way, servo valve, called an acceleration switching (AS) valve, to drive a

[1] Numbers in brackets designate References at end of paper.

Nomenclature

A = output member (actuator) piston area, sq in.
A_s = spool end area, sq in.
C = static gain of valve-actuator combination, in/sec^2—unbalance
f = switching frequency, cycles per second (cps)
K = acceleration switching valve static gain, in^3/sec^2—unbalance
K_d = valve driver gain, unbalance/volt
K_p = sensitivity of output member transducer, volts/in.
ΔP = total pressure drop across spool orifice, psi
P_s = pressure drop across spool, psi
Q = valve useful oil flow, in^3/sec.
Q/x = spool-orifice flow gain, in^2/sec-in.
s = Laplace operator
Δt = time unbalance
T_1 = dwell time of positive polarity square wave, sec
T_2 = dwell time of negative polarity square wave, sec
W = bushing slot width, in.
x = valve-spool displacement, in.
x_{p-p} = peak-to-peak valve-spool displacement, in.
$\dot{x}$ = valve-spool velocity, ips
$\dot{x}_{max}$ = maximum valve-spool velocity, ips
ϵ = transformed error signal, volts
θ_0 = output member displacement, volts
θ_0/ϵ = open-loop gain from valve input signal to actuator-displacement voltage
θ_i = reference input signal, volts
θ_f = modified feedback signal, volts
τ = time constant, sec

conventional design hydraulic actuator in a closed-loop system, Fig. 1. The AS valve transfer function is essentially that of an integration or, in operational notation, K/s. Dynamic performance of the AS valve-actuator combination thus becomes equivalent to a double integration, or C/s^2. This means that the output member (actuator) accelerates the load to the position called for by the system input. Performance benefits realized from this technique include essentially zero center shift while operating through temperature extremes, steady-state error due to load forces is virtually eliminated, resolution is enhanced, and reliability (especially in the presence of contaminated fluid) is considerably improved. The AS servo valve is driven by a constant-amplitude, fixed-frequency square wave which is generated in the valve-driver amplifier, Fig. 2. Usually this amplifier consists of two stages; namely, a summing stage to compare the input and feedback signals and to amplify the difference (or error), plus a free-running multivibrator which provides a specific switching frequency and drives the valve coils. When an input signal is applied to the system, an unbalanced voltage is produced on the multivibrator-tube grids. This unbalance causes the dwell time of the square wave of one polarity to increase and the dwell time of the other polarity to decrease, while the switching frequency remains essentially constant, Fig. 3. As a result of this differential modulation of the square-wave dwell time the multivibrator output has an average or d-c value which is proportional to the error voltage. Variation of the error results in a corresponding change in the multivibrator output average value. The valve driver gain is expressed as time-unbalance per volt input. The valve signal is thus a time-unbalance proportional to error voltage, rather than a current magnitude which varies with error voltage.

The time-unbalance input to the AS valve produces a time rate of change of flow to the load actuator, causing a load acceleration proportional to the time unbalance. By controlling the output acceleration, the effects of steady-state loading errors are reduced substantially. It is this acceleration control by a switching input from which the name "acceleration switching servo" is derived.

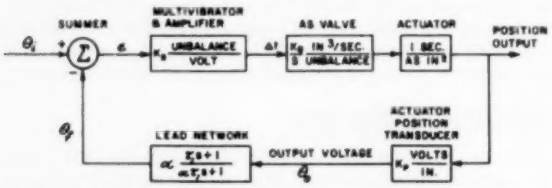

Fig. 1 Block diagram for typical acceleration-switching position servo

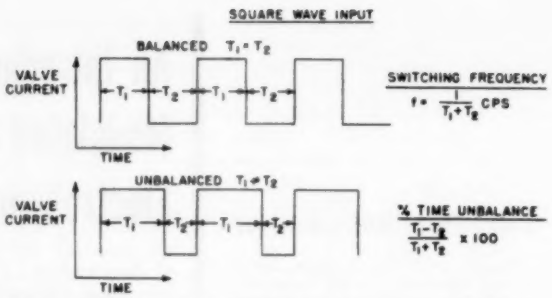

Fig. 3 Modulation of switching-frequency, square-wave dwell time

AS Valve Operation

The acceleration switching servo valve, Fig. 4, is controlled by a time-modulated square-wave signal generated in the valve driver. In turn, the valve meters the flow of high-pressure hydraulic fluid to the actuating cylinder which drives the load. The square-wave valve input drives the torque-motor flapper hard over against the nozzles, alternately sealing each nozzle at the switching frequency. The spool is free to move in the bushing, as there are no restraining springs at the ends of the spool. During the time the flapper is sealing one nozzle, the constant flow through the opposite inlet orifice is directed to the corresponding end of the valve spool, causing the spool to move at essentially constant velocity. When the polarity of the square wave reverses, the flapper moves rapidly across the nozzle gap to seal the opposite nozzle, causing the spool to reverse quickly its direction of motion. By using identical inlet orifices, the spool velocity is maintained equal in both directions. The matching of inlet orifices is considerably more critical in the AS valve than in a proportional flow-control servo valve. Inlet orifices are matched within ±0.1 per cent, to obtain equal spool velocity in both directions,

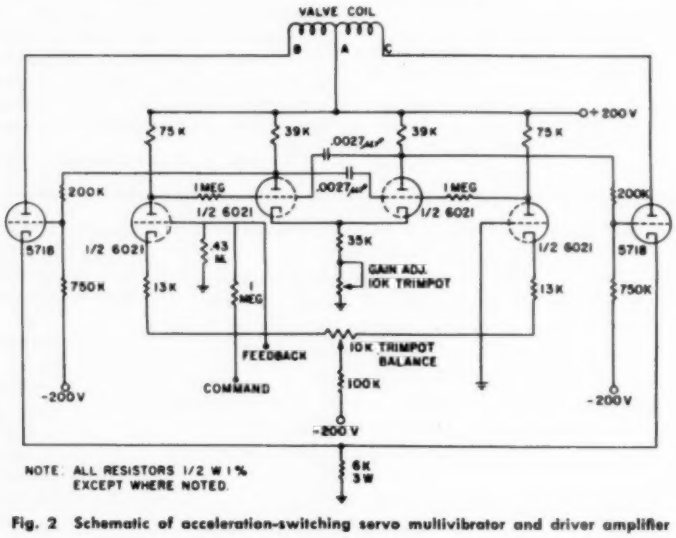

Fig. 2 Schematic of acceleration-switching servo multivibrator and driver amplifier

while flow control-valve inlet orifices are not matched closer than ±2 per cent.

The spool activity occurs at the repetition rate of the square wave and results in a small-amplitude shuttling motion of the spool about a nominal zero position. With a balanced or zero input, therefore, the average spool velocity is zero. The amplitude of the peak-to-peak spool displacement at the switching frequency is but a fraction of the total allowable spool travel and is dependent on the spool diameter, inlet-orifice pressure drop, and the switching frequency.

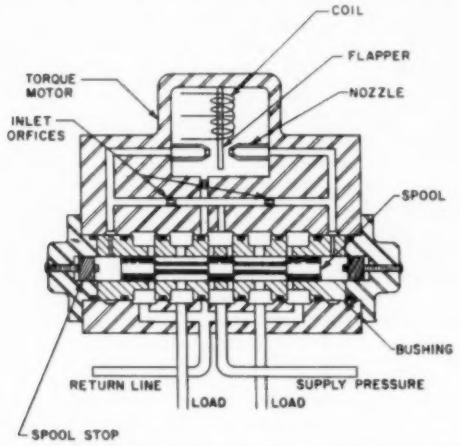

Fig. 4 Schematic diagram of an acceleration-switching servo valve

With an unbalanced input signal, the flapper dwells at one nozzle for a longer interval than at the other nozzle during each switching cycle. This directs more flow through one inlet orifice than through the other so that a spool average velocity results. A 100 per cent unbalance, or saturation signal, causes the flapper to continually seal one nozzle only, inducing the spool to move at maximum velocity in one direction. An integration is achieved in this operation for the spool displacement is a function of the time integral of the error signal. Considering that the spool moves at constant velocity when one nozzle is sealed, and assuming a rectangular spool port opening, a constant rate of change of useful flow is produced by the valve. This flow rate working into a constant area actuator produces a constant acceleration of the actuator piston. The spool position at any time determines the flow to the actuator which gives the actuator an instantaneous velocity which, when integrated, gives piston or load displacement. The idealized transfer function of an AS valve is defined as being that of a pure integrator K/s where $1/s$ indicates in operational notation the integration in the valve and K is the valve static gain. Valve gain is defined as the rate of change of valve useful flow (acceleration of the load actuator) per unit time unbalance of the valve square-wave switching signal, (in³/sec³)/(time unbalance). The amplitude of this transfer function attenuates at 20 db per decade and the phase angle remains at 90-deg lag for input frequencies above a minimum value. Fig. 5 shows

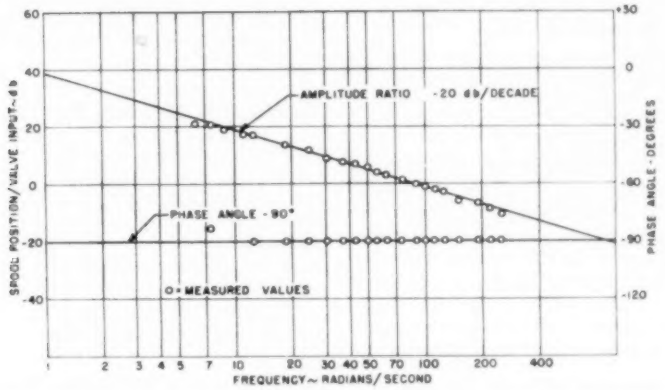

Fig. 5 Frequency response for an acceleration-switching servo valve compared with an ideal integrator K/s

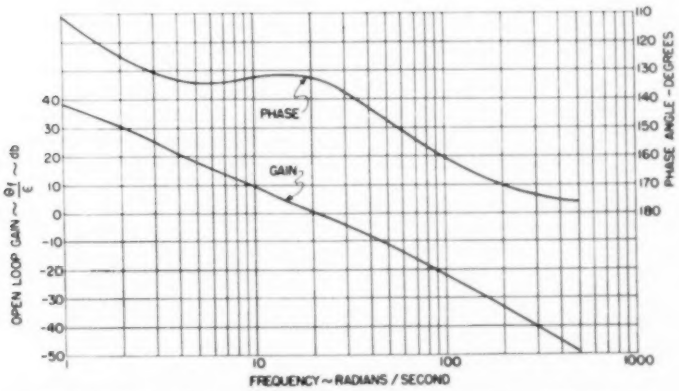

Fig. 6 Open-loop frequency response for a typical acceleration-switching servo

the valve frequency response as determined by measuring spool position and valve-input signal for a range of input frequencies. The actual transfer function departs from this ideal form as will be discussed later. Fig. 6 shows the open-loop frequency response of a typical AS servo.

AS Valve Performance

The performance characteristics obtained from a properly designed and assembled AS valve include the following:

1 AS valve gain is essentially constant for valve inputs varying from 0 to ±100 per cent time unbalance. A spool bushing null cut to the axis (having zero overlap and underlap) is required in order to obtain a constant valve gain for all input-signal amplitudes.

2 The amplitude ratio and phase lag of the AS valve are very nearly those of a pure integrator; i.e., 20 db-per-decade attenuation, and constant 90-deg phase lag.

3 The AS valve exhibits negligible center shift when operated at elevated temperatures. This means the valve maintains its balance and the actuator does not shift its zero operating point as temperature is cycled (providing the valve driver remains balanced). Center-shift measurements made on production valves show less than 1 per cent time unbalance (center shift) as temperature is cycled from 80 to 400 F, while the valves operate in a position servo with 3000-psi system pressure. The effect of temperature on AS valve gain appears to be rather small, typical valves having had less than ±4 per cent gain change over a fluid temperature range of 100 to 500 F. Conventional servo valves exhibit center shift and gain variation on the order of 15 per cent or more over this same temperature range.

4 System pressure variations do not cause center shift of the AS valve, thus insuring that the load will not move due to system or back-pressure variations. Typical center shifts measured amount to less than 0.5 per cent for a 3000-psi valve when valve pressure drop is changed from 2000 to 3500 psi.

5 Infinite pressure-gain characteristics (load pressure versus time unbalance) reflect the ability of the AS valve virtually to eliminate steady-state errors due to varying actuator loading. Tests made on systems using production valves indicate the servo will withstand load pressures up to the equivalent of more than 90 per cent of system pressure without causing a measurable steady-state position error. This of course is dependent on the resolution of the entire servo system. AS valve pressure gain is at least an order of magnitude greater than that achieved by conventional servo valves.

6 Excellent resolution is obtained due to the continuous spool motion, which practically eliminates spool stiction. The spool is not required to assume a given position to obtain a desired load position or velocity. System resolution is dependent primarily on the feedback element. Measurements taken on systems using production valves show the AS servo will faithfully reproduce system sinusoidal inputs corresponding to less than 0.01 per cent time unbalance. Hysteresis and dead-zone effects are practically nonexistent. The spool-switching activity eliminates any dead zone of operation due to either spool null overlap or hydraulic-amplifier hysteresis.

7 Increased reliability is realized because driving forces considerably greater than those used in conventional servo valves are used to drive the flapper and are available to drive the spool. The torque-motor design is simplified since linear displacement of the flapper versus input current is not required. Thus a smaller torque motor with a larger force output can be used. This increased force output of the torque motor reduces the possibility of foreign materials accumulating and/or obstructing the motion of the moving parts, thereby minimizing the effect of contaminated fluids on valve operation and hence increasing system reliability. Several models of the AS valve have been in use for more than a year. During this time no silting or sludge problems have been experienced. No valve deterioration or increase in leakage has been measured, despite continuous testing of the valves. In addition, the large forces available to drive the spool and flapper cause them to be relatively insensitive to maneuvering accelerations.

8 AS valve gain is theoretically 1.4 times as sensitive to input and drain-pressure variations as is flow-control valve gain. This is because the AS valve gain varies directly with valve pressure drop whereas flow-control valve gain changes directly with the square root of valve pressure drop. The AS valve gain is the product of spool maximum velocity and spool orifice flow gain. Both of these quantities vary in direct proportion to the square root of the valve pressure drop. Therefore the AS valve gain is more sensitive to both system and return pressure variations than is a conventional servo valve gain. Actual measurements made show that the valve gain does not actually decrease in direct proportion to the change in valve pressure drop. Valve gain was measured on a 2.0 cu in. per sec rated flow AS valve at 3000 psi and then at 1500-psi valve pressure drop. The gain actually decreased 44 per cent instead of 50 per cent. This gain-change discrepancy is attributed to flow force effects on the spool.

AS servo-valve performance cannot be specified by the same characteristics as those used to specify proportional-flow control valves. Since both the flapper and the spool are in continuous motion at the switching frequency (even with a zero input signal to the system) and because the valve-input signal is a time-modulated square wave, the majority of the performance criteria must be based on dynamic considerations. In addition, these dynamic tests are most conveniently made with the valve operating in a closed-loop servo.

AS Valve Characteristics

Switching Frequency. The switching frequency chosen for the system is important for several reasons. The higher the repetition rate used, the lower will be the valve leakage, for the spool is switching even when zero input is applied to the valve. The higher the repetition rate chosen, the less will be the effect on the output member, for as the spool moves in response to the torque-motor switching, it in turn causes the output member to have a small-amplitude switching motion. This noise content will vary directly with the spool switching displacement and inversely with the actuator area and the switching frequency. The actuator noise content can be eliminated effectively by proper selection of these variables. Switching frequencies of 165 to 250 cps have been used successfully with double-ended actuators of less than 1 sq in. area. As switching frequency is increased, the flapper transit time becomes a larger per cent of the time for each half cycle. In addition, the delay from the time the square-wave signal is impressed on the torque-motor coil to the time the flapper moves becomes a larger per cent of the half-cycle time. These effects will limit the upper switching frequency value, because of their effects on valve performance.

Gain. The valve useful flow Q is defined by the expression

$$Q = \frac{K}{s}\,\Delta t \text{ cu in. per sec}$$

where Δt = time unbalance

$$= \frac{T_1 - T_2}{T_1 + T_2} \text{ (nondimensional)}$$

This expression may be rearranged to give an expression for valve gain

$$K = \frac{Qs}{\Delta t} = \left(\frac{Q}{x}\right)\left(\frac{xs}{\Delta t}\right) = \left(\frac{Q}{x}\right)\left(\frac{\dot{x}}{\Delta t}\right) \frac{\text{in}^3/\text{sec}^2}{\text{time unbalance}}$$

Assuming that the spool moves at a constant velocity which is equal in both directions, a plot of spool displacement versus time reveals the spool activity to be triangular at the switching frequency. If a rectangular bushing slot is used, the valve gain is seen to be as in the foregoing; the spool-orifice flow gain times the spool velocity. The valve gain may be determined dynamically by instrumenting the valve spool properly such as to obtain measurements of the spool-orifice flow gain and the spool velocity while switching. Since both the maximum spool velocity and the spool-orifice flow gain vary with supply pressure, valve gain will be dependent on the hydraulic pressure at which the system operates.

In an actual valve the maximum spool velocity is equal to the spool velocity while switching (normally measured with zero valve-input signal) providing the time required for the spool to reverse direction after each switch is negligible. The spool velocity is computed from:

$$\dot{x}_{\max} = 2fx_{p-p}$$

Usually, x_{p-p} is 0.003 to 0.005 in. The time required for the spool to reverse its direction of motion when switching back and forth at the switching frequency is referred to as truncation time. A limit is held on the truncation time to assure that the spool is moving freely in the bushing and not excessively rounding off the triangular spool position wave form. If the truncation is excessive, the assumption of maximum spool velocity being equal to spool velocity while switching with zero input would be erroneous. Normally, the truncation is less than 5 per cent of the time for each switching cycle.

The dynamic valve gain also may be measured by operating the valve in a closed-loop servo, driving the valve with various amplitudes of a sinusoidal signal, and measuring the load-actuator peak-to-peak acceleration. This is accomplished by supplying a sinusoidal input of a given frequency to the system and varying the input amplitude to produce from 0 to 100 per cent time unbalance. By measuring both the actuator displacement and the valve-input signal and then dividing the displacement by the input voltage the open loop gain is obtained. This gain is equivalent to the product of the valve driver gain, valve dynamic gain, actuator dynamic gain, and the actuator-potentiometer sensitivity. This may be expressed as

$$\frac{\theta_0}{\epsilon} = K_d \frac{K}{s} \frac{1}{A_s} K_p$$

When all quantities in the equation except valve gain K are known, valve gain can be determined for any input amplitude. By varying the input amplitude, the independence of valve gain on input-signal amplitude is demonstrated. Typical values of valve gain realized in production valves vary from 70 to 1800 in^3/sec^2/time unbalance.

Valve Unbalance. The unbalance refers to the symmetry or null of the valve about its zero input operating point. It is specified in per cent of time unbalance. When the valve-driver gain is known, the valve unbalance may be measured as a d-c voltage at the input to the multivibrator when there is zero input to the test servo. An unbalance of less than ±3 per cent is readily achieved on production valves.

Leakage. AS valve leakage is measured while the valve is switching at the nominal repetition rate with zero servo input. The higher the system switching frequency, the lower will be the leakage for a given spool velocity, for the spool will expose less area of the bushing ports during each cycle of operation as the frequency is increased. Therefore higher switching frequencies can be used to reduce the valve leakage and, at the same time, eliminate any possibility of the actuator responding to the switching frequency. The total leakage of the valve consists of (a) the hydraulic amplifier flow, and (b) the flow to the load as a result of spool switching activity at zero input. The total leakage at zero input as measured on a 4.6 cu in. per sec rated flow AS valve with 1850-psi valve drop is 0.63 cu in. per sec when switching at 125 cps. Leakage of 1.14 cu in. per sec while switching at 140 cps was measured on a 10.9 cu in. per sec rated flow AS valve at 3000-psi drop. The leakage flow to the load is dependent on the spool-bushing null cut as discussed in the following.

Spool-Bushing Null. The null cut of the spool-bushing combination is important in an AS valve for two reasons:

1 The linearity of the dynamic spool-orifice-flow gain curve (Q versus x) will depend on the null cut. A null cut to the axis will give a constant slope to the curve of valve useful flow versus spool displacement (Q/x const); underlap or overlap will cause the valve gain to vary with the input-signal amplitude.

2 Leakage while switching is affected by the null cut, an underlap causing greater leakage and an overlap causing less leakage than a null cut to the axis (zero over and underlap).

Transfer Function. The dynamic valve gain has been defined to be that of a pure integrator. This is an approximation which was sufficient for use in designing systems using low flow valves in high-response servos. However, in measuring the AS valve-frequency response, it is seen that the valve actually has a transfer function of

$$\frac{K\tau}{\tau s + 1}$$

where τ is the hydraulic-amplifier time constant. The change of the valve-transfer function from an integration to a first-order lag occurs because of the flow-reaction forces acting on the valve spool. The hydraulic-amplifier time constant τ is a function of the valve rated flow and can be predicted for any given valve. The larger the flow, the smaller τ, is. It has been shown [2, 4] that the hydraulic-amplifier time constant may be expressed as

$$\tau = \frac{S^2}{K_1 K_2 W \Delta P}$$

where

$$K_1 = \text{flow reaction-force coefficient} = \left.\frac{\partial Q}{\partial \Delta t}\right|_{P_s = \text{const}}$$

$$K_2 = \text{hydraulic-amplifier-orifice coefficient} = \left.\frac{\partial Q}{\partial P_s}\right|_{\Delta t = \text{const}}$$

Therefore the time constant can be controlled by the spool diameter and the bushing slot width used. Since it is desired to have the AS valve transfer function approximate that of an integrator over as much as possible of its operating-frequency range, the hydraulic-amplifier time constant should be as large as is convenient. This is accomplished by increasing the spool diameter and decreasing the bushing slot width (which increases the spool travel necessary to produce a desired flow). Flow-force compensation, such as using a spool with shaped lands, will tend to nullify the flow forces, and should result in increased values of τ. Another effect on the time constant has been noted during assembly and test of groups of identical valves. Depending on the care taken in the assembly of the torque motor and balancing of the hydraulic amplifier, considerable variation in the predicted value of τ could be obtained. If the valve time constant is of importance in a given system, the valve specification should require that the predicted and actual time constant be in agreement within certain limitations.

Typical values of τ obtained are between 0.05 and 0.50 sec, the larger values of τ occurring in low-flow valves. A time constant of 0.14 sec is obtained for a valve with 1.8 gpm rated flow at 933-psi pressure drop across the valve [6]. The valve has a total bushing slot width of 0.114 in. and a $^1/_4$-in-diam spool. A valve with a rated flow of 0.33 gpm at 933-psi drop has a time constant of 0.38 sec, bushing-slot width of 0.080 in., and a $^1/_4$-in-diam spool.

So far, no comprehensive describing-function theory has been developed for the AS valve. However, the representation of the transfer function as a first-order lag is useful because it does allow prediction of closed-loop servo response with reasonable accuracy.

Miscellaneous. A correctly adjusted AS valve is relatively immune gainwise to switching-frequency changes. Valves have been tested at repetition frequencies from 150 to 250 cps. The valve-gain variation was less than ±1 db over this frequency range.

Elimination of the spool-centering springs obviates any changes in valve performance due to variations in spring forces or rates, or frictional side loads.

The open-loop frequency response of a typical AS servo is shown in Fig. 6. The valve static gain was 85.4 cu in. per sec^2, valve time constant 0.50 sec, valve-driver gain 0.03 time unbalance per volt, actuator area 0.18 sq in., and feedback-transducer sensitivity 63 volts per in. The lead network used in the feedback path had $\alpha = 0.2$ and $\tau_1 = 0.12$ sec.

Disadvantages. The increase in complexity of the servo electronics due to the addition of the multivibrator to the amplifier and the increase in null leakage over linear flow-control-valve systems are the major disadvantages of an AS servo. However, it is felt that in many systems the increase in reliability, improved resolution, and the excellent elevated-temperature operation will more than offset the disadvantages.

If load-position control is desired, it is necessary to insert a phase-correction circuit to compensate for the additional integration of the valve within the servo loop. This compensation network may be placed in either the forward or the feedback path. If placed in the feedback path, the network also may serve to shape system-response characteristics. In a velocity-control servo, the AS valve provides the necessary integration to provide essentially zero steady-state velocity errors.

Conclusion

Nearly one hundred acceleration switching valves have been built. These have been used by several customers in various position and velocity-control systems. Considerable development testing has been conducted on these valves in an effort to understand the mechanism of the acceleration switching concept. The advantages and disadvantages have been observed and additional areas to be studied have been discovered. The analysis of the valve-transfer characteristics can be studied further, particularly with respect to using flow-force-compensated spools to provide larger values of the hydraulic-amplifier time constant. Possibly a describing-function theory such as has been developed for linear valves can be derived for AS valves. The effects of structural and fluid compliance on the AS servo performance and band width should be studied in detail.

It is felt that the characteristics of the AS valve and the time-modulation concept present potential advantages to the electrohydraulic-system designer. It is with the intention of setting forth the collected results of some of the lessons learned that this paper is presented. It is hoped that the device may prove to be beneficial in surmounting the linearity and reliability problems often encountered in the use of linear servo valves.

Acknowledgment

The author wishes to express his appreciation to Mr. Woodrow Seamone of the Applied Physics Laboratory, Johns Hopkins University, Silver Spring, Md., for the many helpful discussions relating to the acceleration switching concept.

References

1 J. G. Chubbuck, "Are High Performance and Low Cost Compatible in Hydraulic Servos?" *Control Engineering*, vol. 4, March, 1957, pp. 98–103.

2 W. Seamone, "Design and Performance Criteria of the Acceleration Switching Hydraulic Servo," Johns Hopkins University, Applied Physics Laboratory, APL/JHU CF-2652, June 19, 1957.

3 S. A. Murtaugh, "An Introduction to the Acceleration Switching Technique," Moog Valve Company, Inc., East Aurora, N. Y., MR-237, August, 1957.

4 W. Seamone, "Transfer Characteristics of the Acceleration Switching Transfer Valve," John Hopkins University, Applied Physics Laboratory, BBC-5 Memo no. 580, October 3, 1957.

5 J. E. Gibson, F. B. Tuteur, and T. J. Mapes, "A New Hydraulic Servo Valve for Pulse-Length-Modulation Operation," ASME Annual Meeting, December 1957, Paper No. 57—A-128.

6 W. S. Harris, "Using the Acceleration Switching Valve," *Control Engineering*, vol. 5, April, 1958, pp. 123–125.

7 W. S. Harris, S. A. Murtaugh, "Problem Forum" Letters, *Control Engineering*, vol. 5, July, 1958, pp. 10–12.

DISCUSSION

J. E. Gibson[2] and F. B. Tuteur[3]

The author is to be complimented on this presentation of the pulse-length-modulated (PLM) or acceleration-switching (AS) mode of valve operation. It is gratifying that someone has finally produced solid experimental evidence to back up the claims of increased reliability, and so on, that previously had been made for this type of valve operation on a more or less theoretical basis. The method was apparently developed independently about ten years ago by Jackson[4] and five years ago by Chubbuck,[5] and is presently utilized in valves produced commercially by at least two firms. The principle is also outlined in a recent text co-authored by the writers.[6]

The reasons for suggesting the name "pulse-length-modulation" in this text and in the author's reference [5], perhaps deserve some explanation. Both the mathematics and the physics of the PLM principle carry over into the operation of hydraulic valves and cross fertilization of techniques from other areas is always fruitful. More important, however, is the lack of generality of the term "acceleration switching." The principle of operation is not dependent on acceleration switching. The author, quite correctly, has shown that the "per cent time unbalance" controls the acceleration of an ideal, unloaded piston, in the absence of flow-reaction forces. But in the practical valve the integration becomes a time constant. Moreover, as was shown in the author's reference [5], PLM operation is entirely practical in valves with spring-restrained pistons. Here, even in the ideal, the first stage or driver does not produce piston acceleration. Thus PLM is a more general and, we hope, more descriptive term.

The author apparently concurs with proposed advantages of the method listed by the writers (reference [5] of the author), ex-

[2] Associate Professor of Electrical Engineering, Purdue University, Lafayette, Ind.

[3] Associate Professor of Electrical Engineering, Yale University, New Haven, Conn.

[4] K. R. Jackson, U. S. Patent No. 2,655,940, 1950.

[5] J. G. Chubbuck, "Acceleration Switching Hydraulic Servo," The Johns Hopkins University, Applied Physics Laboratory Report, May, 1955.

[6] J. E. Gibson and F. B Tuteur, "Control Systems Components," McGraw-Hill Book Company, Inc., New York, N. Y., 1958.

cept perhaps with number 6, tolerances. It would be most enlightening to hear the author's comments on manufacturing tolerances and cost. It was our thought that a simple, single-stage valve driven by a simple rugged mag amp to operate in the PLM mode would result in economical manufacture. The author states that in his valve, inlet orifices must be selected more carefully and spool bushings must be cut for zero lap. These facts along with the rather elaborate electronic driver required would seem to place the valve in the luxury category.

It seems to us, however, that while it is undoubtedly true that a linear flow-gain curve can be obtained only with a zero-lapped spool, this is no less true in a valve operated in a continuous mode. Also, if a valve has overlap, it will show an actual dead band when operated in a continuous mode, while for operation in the PLM mode there would be only a reduction in flow gain, at least as long as the amplitude of spool oscillation exceeds the overlap length. The increase of leakage obtained with an underlapped spool is also at least qualitatively the same for both modes. Thus we feel that the requirement for careful lap adjustment should not be charged against the PLM mode of operation since the PLM mode is no worse than the continuous mode for underlap, while for overlap it is actually better.

The same argument applies to the exactness with which inlet orifices have to be matched. It seems to us that for both operating modes a mismatch in orifice holes will result in some valve unbalance, which must be compensated for by a small offset signal. We would be very much interested in a further statement by the author as to why this problem should be worse in the PLM mode than in the continuous mode of operation. In connection with this, is it not true that the superior performance of the PLM mode in regard to center shift as a function of temperature and pressure is primarily due to the accurate match between inlet orifices?

A disadvantage not mentioned by the author is that the square-wave switching signal applied to the valve torque motor results in very high voltage pulses because of the inductance of the torque-motor winding. This was found to be particularly serious when the switching method was applied to single-stage solenoid valves. Voltage spikes of such magnitude were produced that the coil insulation broke down. Also, the voltage pulses were picked up by sensitive preamplifier stages in the servo loop and caused all sorts of malfunctioning. It was found, however, that by connecting a suitable value of capacitance and resistance across the coil, the voltage pulse could be reduced considerably without affecting the current wave shape within the coil too much. This problem is not so serious with torque motors used to operate a first-stage flapper valve since the inductance is much smaller than that of a solenoid.

G. A. Levine[7]

The paper very nicely describes the concept and characteristics of the acceleration switching servomechanism. The item not brought out, though, is that the ASV system is not just a laboratory curiosity but an item currently employed in some of the Navy BuOrd guided-missile programs. Rather than delve into "Why acceleration switching?" the following discussion will highlight several current applications with the special qualities brought out by the ASV system.

(*a*) In a homing antenna problem, the original system required dither as well as spinning of the valve spool in order to obtain the necessary resolution. Owing to the very small force requirements, and the inability to manufacture sufficiently small metering slots, a total spool stroke of 0.005 in. produced the maximum flow. The valve was thus required to operate with minimum spool stroke measured in ten thousandths of an inch. The switching servo was introduced in this application and demonstrated hysteresis-free operation with the required resolution. Subsequent tests in the laboratory, with a pickup mounted on the spool, showed capability of following a sinusoidal command with a spool motion of 40/1,000,000 of an inch.

(*b*) The success of the antenna application led to the consideration of the ASV for a flight-control servo system. The special problems here were: (1) Desirability for positional dynamic resolution of 500:1; (2) handle a severe mechanical, structural resonance; (3) overcome a large and random load; and (4) operate in an extreme high-temperature oil and ambient environment.

The resolution was demonstrated in the first application. As pointed out by the author, the system has theoretically[8] infinite steady-state load stiffness due to the spool integration. By proper servo design, the band pass can be made equal to or greater than the load resonant[9] frequency. The last item of concern was high-temperature qualities. Since the valve has been converted into a high force level mechanism with no basic intelligence function, it should be ideal in high-temperature systems. There are no springs which can relax, and change valve gain, plenty of force to scrape varnished oil off the spool and sleeve, constant spool motion to prevent build-up of sludges, wet torque-motor design providing cooling to the coils, insensitivity to charging permeance of the magnets (as long as the electromagnetic force produces flapper motion), and insensitivity to relative motion between flapper and nozzles. High-temperature tests[10] with 400 to 500 F oil temperatures and ambient temperatures reaching 700 F have demonstrated the excellent characteristics of this valve. Bias shifts appear to be around 5 per cent and gain changes are equally small.

(*c*) Carrying out various research and development projects often requires use of high-force level or high-speed servos. Two such applications in which ASV servos are being used are in conjunction with thrust-vector control of the exhaust jet of a rocket nozzle. In one of these applications, the engine fuel is 90 per cent hydrogen peroxide, which is extremely dangerous when in proximity with oils. The servo was thus required to operate with distilled water as the fluid. This servo, using a stock wet-coil valve, has been used during the past 6 months with no apparent degradation of performance. Another servo has been used mounted on the exhaust cone of a rocket engine, which has a rather severe vibration and temperature environment. While this is not exceptional for hydraulic servos, it has demonstrated that the ASV system can "take it" in true environments as well as in the test laboratory.

What then are the drawbacks? The author lists higher leakage, more complicated electronics, lead network, lack of perfect spool integration due to the Bernoulli spring force, and to this is added the possibility of switching activity exciting line resonance as problems. Focusing attention on the electronics, a lead-lag network is required to stabilize a system whose open-loop transfer function approximates a (K/s^3). This network is composed of two resistors and one capacitor, which can hardly be considered complex. The valve driver differs from conventional valve drivers in that it produces a series of current square waves which are time unbalanced as a function of signal input, instead of a dif-

[7] Mechanical and Hydraulics Project (Bumblebee Controls Group), Applied Physics Laboratory, The Johns Hopkins University, Silver Spring, Md.

[8] W. Seamone and L. A. Wenrich, "An Experimental Study of Hydraulic Servo Torque Characteristics as a Function of Frequency," The Johns Hopkins University. Applied Physics Laboratory Report CF-2753, September, 1958.

[9] W. Seamone, discussion of this paper, p. 270.

[10] W. Seamone and K. E. W. Duning, "Hydraulic (Acceleration Switching) Servo Dynamic Performance Under Extreme High Temperature Environment," The Johns Hopkins University, Applied Physics Laboratory Report CF-2737, June, 1958.

ferential current output proportional to voltage input. The vacuum-tube version requires four subminiature tube bottles instead of three, the extra element being the multivibrator. This electronic disadvantage is equalized if the linear valve system requires dither. Development work is progressing at *APL/JHU* to make a transistorized driver which may simplify the electronics further.

The effect of Bernoulli force in canceling out the spool integration becomes significant in higher flow servos (3–5 hp and up). This is especially true if the servo band pass is less than about 8–10 cps, since the time constant cannot be ignored in calculation of the closed-loop frequency response. An experimental spool, contoured[11] for reduction of these forces, has been procured and as soon as manpower becomes available will undergo a series of experiments to determine if this effect can be minimized for high flow valves.

In conclusion, for a hydraulic servo less than 3–5 hp, the ASV has demonstrated:

1 Superior resolution.
2 Less sensitivity to external loads.
3 Less sensitivity to environmental extremes, these being (*a*) acceleration, (*b*) vibration, (*c*) temperature.
4 Stable operation with the servo band pass equal to or exceeding the load resonant frequency without any major modifications.
5 Good reliability due to high force levels involved.

W. Seamone[12]

The author is to be congratulated on his excellent discussion of the techniques involved in the acceleration-switching servomechanism. This type of servomechanism has undergone extensive theoretical and experimental studies at the Applied Physics Laboratory in order to define more precisely its dynamic characteristics under various operating conditions. The results of recent studies will be outlined briefly and may help clarify some of the points discussed by the author.

Servo torque stiffness has been examined for both linear flow control and acceleration-switching servos over the frequency spectrum from zero to 50 cps. These servos were of comparable band width and were compared on the basis of unit positional error per externally applied dynamic load. The results of these tests indicated the static torque stiffness of the acceleration switching servo was approximately an order of magnitude greater than for the conventional linear system. However, since there is an integration involved in achieving this high torque gain for the switching case, the torque stiffness drops off with frequency and is approximately the same as for the linear servo over most of the frequency spectrum above 2 to 5 cps.[8]

The author has raised the question on the effect of fluid compliance on valve performance. A theoretical study has been made of the effects of hydraulic dynamic pressure fluctuations in the supply line to the transfer valve. The pressure fluctuations are generated by the sudden changes in flow across the spool edge at the spool switching frequency. The results of this study have indicated a small-amplitude, limit-cycle oscillation can exist in the valve if the acoustic frequency of the line coincides with the multivibrator switching frequency. The presence of a hydraulic-line resonance condition has been shown to affect the valve time constant and may account for some of the variations in valve time constant noted by the author. The problem of hydraulic resonance is avoided by designing the hydraulic connecting circuitry such as to separate the acoustic line frequency and multivibrator switching frequency. A complete report on this subject is currently in preparation.

One of the serious problem areas confronting many servo designers is the limitation of servo band width imposed by a resonant load. Application of some new techniques recently developed at the Applied Physics Laboratory has shown considerable promise in extending allowable servo band width. These techniques have been applied to the acceleration switching servo driving a highly resonant load and have resulted in the attainment of servo band width in excess of the load resonant frequency. Stable control is achieved by the judicious selection of system parameters and does not require any additional components or circuitry to the system. This technique is currently being given extensive theoretical and experimental treatment and will be the subject of a technical paper in the near future.

Several questions have been raised concerning potential problem areas in the use of an acceleration-switching-type system. The results of many hundreds of hours of testing during development and usage of this system at the Applied Physics Laboratory will be reviewed to show to what extent problems actually have materialized.

Effect of Valve Switching Activity. Owing to the double integration in the forward loop of the servo, the actual switching activity on the actuator is generally negligible. There is no apparent increase in wear on the actuator seals and no noticeable hydraulic line vibration in current applications. Systems have been in operation for many hundreds of hours and have indicated no appreciable increase in leakage or change in performance during this period, thus making this system ideal for systems requiring long life.

A machine-tool acceleration switching servo (milling machine) has been used for intermittent operation at APL for over a year with excellent performance and reliability.

Flapper Bias. The question has been raised concerning effects of flapper mechanical bias on valve bias. Again, experience has shown the valve to be very insensitive to any flapper changes as evidenced by achieving less than 3 to 5 per cent valve-bias change on production valves under all types of operating conditions of temperature, vibration, acceleration, and so on.

Reliability. The over-all reliability of the servo has been demonstrated in many ways:

(*a*) Servos have been operated for many hours without the benefit of filters between the pump and the servo valve (the upstream orifices are protected internally in the valve). No degradation or unreliable operation has been observed under these conditions.

(*b*) The addition of a 2-lb friction block to the spool has shown negligible effect on valve operation. The only effect is the slight truncation of the triangular wave form of the spool. This added friction does not add hysteresis or dead space to the valve.

Actual Problem Areas. During the course of development of the acceleration-switching system, three serious problem areas have required solutions:

(*a*) Early models of switching valves exhibited a bouncing of the flapper upon contacting each nozzle. The net effect was to make the valve gain sensitive to repetition rate. This problem has been eliminated by a redesign of the torque motor by the valve manufacturer.

(*b*) The feedback linkage must be free of dead space to avoid low-amplitude, limit-cycle oscillation as a result of the double integration in the loop.

(*c*) The hydraulic connecting circuitry to the valve must not have the oil acoustic frequency coincide with the multivibrator switching frequency, otherwise this coupled resonance condition will cause a limit-cycle oscillation. This condition must be

[11] Shih-Ying Lee and J. F. Blackburn, "Steady-State Axial Forces on Control-Valve Pistons," TRANS. ASME, vol. 74, 1952, pp. 1005–1011.

[12] Project Supervisor, Mechanical and Hydraulics Project (Bumblebee Controls Group), Applied Physics Laboratory, The Johns Hopkins University, Silver Spring, Md.

avoided by proper design of the connecting circuitry to separate the two frequencies.

In summary, the advantages of the acceleration-switching servo have outweighed the problem areas in specific applications at the Applied Physics Laboratory. The servo designer is encouraged to include this type of servo along with the conventional linear systems to broaden the techniques from which he may choose in his design of future systems.

J. L. Shearer[13]

This well-written paper gives a good picture of the state of the art in this field. It is interesting to note the extreme care required in selection of fixed upstream orifices in order to avoid null shift caused by dissymmetry of flapper-valve, bridge-flow characteristics. It would appear that unequal leakage effects at the ends of the spool valve also might cause comparable difficulties.

In connection with the double integration claimed for AS valves, it would appear that the second integration due to the action of the spool valve would be subject to the same imperfections as in a conventional valve; i.e., droop in flow due to increase in load pressure.

It would appear that the effects of flow forces in the spool valve on the operation of the first stage have not been evaluated fully.

All-in-all, it is difficult to visualize how an AS valve is appreciably better or easier and cheaper to make than a conventional high-performance electrohydraulic servo valve. The acceleration-switching technique does, of course, provide a means of obtaining high-level dither to minimize the effects of static friction throughout the system. It might be worth while investigating what happens to the effects of magnetic hysteresis in the torque motor in an AS valve as a result of this dither.

Author's Closure

The discussers have been very generous with the additional information which they have contributed The relating of their experiences in AS valve and systems design has greatly added to the value of this paper. I am grateful to them for their comments.

First, a few remarks in regard to AS valve manufacturing tolerances and costs are in order. The author's opinions are based on his experience with AS valve design to meet customer specifications. It is not denied that a simple valve design could be realized which would result in reduced cost, particularly if a design which is not limited to flow control valve design concepts is developed. It is agreed that a satisfactory PLM valve can be made using relaxed tolerances. It is the customer specifications which the valve performance must meet that dictates the tolerances, test operations, and total cost. Until such time as system designers contemplating the use of PLM have become sufficiently familiar with the characteristics of such systems so as to avoid over-specification of the valve performance, and until such time as a new simple valve design is evolved no major manufacturing costs reductions can occur.

The AS valves built by the author were modifications of existing servo valve designs. Because of the newness of this unconventional approach, the parameters of the systems for which these valves were to be used, such as switching frequency and driver current amplitude, could not be firmly established. Therefore, a generalized type of AS valve had to be produced which would provide both constant acceleration gain and minimum valve unbalance for switching frequencies from 140 to 190 cps and driver currents from 12 to 19 ma. To meet such requirements much valve adjustment and testing was necessary. In addition, it was desirable that the acceleration gain remain constant for all valve inputs from 0 to 100 per cent time unbalance. This necessitated close tolerances on the spool-bushing null, the slot width, and the inlet orifices. Spool bushing fits were also controlled to achieve low friction and small truncation times. When faced with this type of specification for an undefined system, the valve manufacturing and testing costs cannot be minimum. However, if a system is designed to use a specific switching frequency and driver current, if the linearity of gain with time unbalance requirement is reasonable, and if the leakage is not of primary concern, then certainly some cost reduction should result.

An AS valve with overlap will show more than a reduction in flow gain as mentioned by Professors Gibson and Tuteur. With the spool oscillation amplitude greater than the overlap length, a nonlinear rate of change of flow with input amplitude is obtained, the flow gain increasing with input amplitude. Thus a smaller gain is obtained for small inputs than for large inputs. Concerning the exactness in matching inlet orifices, a mismatch which is tolerable in a flow control valve gives an exaggerated time unbalance in the AS valve. In a standard servo valve, the first stage is rate canceled so that an inlet orifice mismatch will result in the flapper seeking an off-center null position. With an AS valve, the inlet orifices control the spool velocity; a mismatch results in unequal spool velocities as the spool oscillates, causing a valve unbalance. The effects are not equivalent in the two modes; however, the PLM valve with spool springs may behave differently than the AS valve. It is true that inlet orifice matching is important to center shift as a function of pressure and temperature. However, the independence of AS valve center shift from the flapper position between the nozzles, as temperature varies because of the nonlinear nature of the first stage operation, is also a primary factor in the superior performance of the PLM mode. Recent AS valve development has shown that the matching of inlet orifices is not so critical as was thought at the time this paper was written. Present production has relaxed the accuracy of mismatch by an order of magnitude which is a step toward reduction of manufacturing costs.

Break-down of coil insulation due to the switching voltage spikes may be a disadvantage of the single-stage solenoid PLM valve, but it has never occurred in the two-stage valve torque motor. The coil insulation used was the same as in the standard servo valve. No trouble with voltage pulse pick-up occurred either, probably because of the attention given to the multivibrator and amplifier design by the group at the Applied Physics Laboratory of Johns Hopkins University.

Leakage effects at the ends of the spool are probably nonexistent because of the very low differential pressure between the spool ends and the return lines. In answer to Professor Shearer's comments regarding the dearth of advantages which accrue from the ASV system, I believe the abundance of systems test results presented by Messrs. Levine and Seamone have adequately proven the claims made for the method. Actual experience in the development of an acceleration switching system would provide verification of the predicated performance for anyone interested.

[13] Associate Professor of Mechanical Engineering, Massachusetts Institute of Technology, Cambridge, Mass. Mem. ASME.

Theoretical and Experimental Analysis of Hydrodynamic Gas-Lubricated Journal Bearings[1]

J. A. COLE AND J. KERR.[2] Additional references might usefully be included in the authors' introduction surveying earlier work on gas lubrication. The pioneer work of O. C. Brewster (1, 2)[3] deserves a mention, and also the comprehensive investigation by G. W. K. Ford, D. M. Harris, and D. Pantall (3), which includes experimental results with several gases. Y. Katto and D. Soda (4) have given a theoretical solution for the infinitely wide isothermal bearing, and V. Constantinescu (5, 6) has worked on the theory for infinite and finite bearings, considering both isothermal and polytropic flow regimes.

Several points arise regarding the authors' computational procedure. The boundary conditions are not stated explicitly, but are obviously that the film pressure equals the ambient pressure at the bearing sides: Was the computing procedure also arranged to exclude film pressures below the absolute zero of pressure? The iteration procedure for α seems unnecessary: Could not this have been avoided by taking the origin $\theta = 0$ at the point of maximum film thickness, then resolving the film pressure forces in directions parallel and perpendicular to the line of centers, and finally calculating load capacity and attitude angle from these components? In this connection, it appears from a comparison of Figs. 4 and 6 that film pressure generation commences in the diverging film, some 18 deg before the maximum film thickness position: Is this correct?

The expression of the results in terms of the conventional Sommerfeld number (Fig. 5) is very helpful to those accustomed to incompressible fluid lubrication. The ambient pressure is not stated, but is presumably atmospheric. However, the analysis of the infinitely wide bearing by Ausman, authors' reference (8), leads to the result:

$$S\epsilon = \frac{1}{12\pi^2} + 12\left(\frac{\bar{S}}{k}\right)^2$$

for moderate eccentricity ratios, S being the conventional Sommerfeld number based on load pressure, and $\bar{S}$ the modified Sommerfeld number based on ambient pressure. From this, it appears that eccentricity ratio and Sommerfeld number are not directly related even at a fixed value of the ambient pressure, since viscosity and speed occur separately (in $\bar{S}$). The authors' comments on this situation would be appreciated.

Since a compressible viscous fluid sheared in a converging film would be expected to generate lower pressures than an incompressible fluid, the result in Fig. 5 that for $L/D = 1.5$ the compressible case gives a higher load capacity than the incompressible case is very surprising. Is this due to the modified attitude-eccentricity locus?

The reference to turbulence is rather mystifying and calls for elaboration: How is turbulence taken into account when solving the simplified Navier-Stokes equations, and what are the results?

The question of the index n used in the pressure-density relation $p \propto \rho^n$ is of fundamental importance to the subject, and the value of the paper would be enhanced if the authors would give their results for the case $n = 1$, and, if available, for values of n between 1 and 1.4. It seems very unlikely that the value $n = \gamma$ would apply to a flow regime involving viscous friction.

The experimental results are of particular interest to the writers, as they have recently published (7) results obtained with 1-in-diam bearings at speeds up to 60,000 rev/min. The two investigations agree, on different grounds, that bearings of conventional clearance ratio (0.001) operating in atmospheric air should carry approximately 1 lb/sq in. load per 1000 rev/min.

[1] By B. Sternlicht and R. C. Elwell, published in the May, 1958, issue of TRANS. ASME, vol. 80, pp. 865-878.

[2] Department of Scientific and Industrial Research, Mechanical Engineering Research Laboratory, Glasgow, Scotland.

[3] Numbers in parentheses designate References at the end of this discussion.

References

1 O. C. Brewster, "High Speed Rotor," 1952 U. S. Patent No. 2603539.

2 O. C. Brewster, discussion on "A Simple High-Speed Air Spinner for Centrifugal Testing of Small Mechanical Devices," by C. F. Bild and P. F. Vial, TRANS. ASME, vol. 75, 1953, p. 515.

3 G. W. K. Ford, D. M. Harris, and D. Pantall, "Principles and Applications of Hydrodynamic-Type Gas Bearings," *Proceedings, The Institution of Mechanical Engineers*, vol. 171, 1957, pp. 93–128.

4 Y. Katto and D. Soda, "Theory of Lubrication by Compressible Fluids With Special Reference to Air Bearings," Proceedings, Second Japanese National Congress on Applied Mechanics, 1952, pp. 267-270.

5 V. Constantinescu, "Sur la Théorie des Paliers à Gaz," *Revue de Mécanique Appliquée*, vol. 1, no. 1, 1956, pp. 141-155.

6 V. Constantinescu, "Sur le Problème Tridimensionnel de la Lubrification aux Gaz," *Revue de Mécanique Appliquée*, vol. 1, no. 2, 1956, pp. 123-138.

7 J. A. Cole and J. Kerr, "Observations on the Performance of Air Lubricated Bearings," Conference on Lubrication and Wear, 1957, The Institution of Mechanical Engineers, Paper No. 95.

Authors' Closure

The authors wish to thank Messrs. Cole and Kerr for the added discussion which they have submitted on our paper published in the ASME TRANS., May, 1958. The added references they presented are most valuable and serve as an additional bibliography on hydrodynamic gas bearings.

With reference to the boundary conditions, our paper presents results for atmospheric pressures at the ends of the bearings. We do not understand the question raised about pressures below absolute zero; we assume that Messrs. Cole and Kerr mean pressures below 14.7 psia, and our results show pressures below atmospheric (e.g., Figs. 4, 11, 12, 13, and 14). These pressures below atmospheric in hydrodynamic gas bearings act to raise the load carrying capacity, for they create suction. This is one reason why compressible theory yields a higher load carrying capacity than incompressible theory. It is possible to eliminate the iterative procedure for α; in fact, many of the cases were solved in this manner. However, the computer program is set up for the solution of grooved and partial bearings and, in this case, the iteration of α is more convenient. The question of pressures above atmospheric in the diverging part of the bearing ahead of the maximum film thickness is being further investigated. The origin of these atmospheric pressures may not have been sketched too accurately in Fig. 4. These curves were sketched from 12 calculated points 30 deg apart, since the mesh size used in calculations was 12×12. Tests, however, show (Fig. 12) that ahead of maximum film thickness, pressures above atmospheric are indeed present. We are, therefore, in the process of calculating on IBM 704 some additional cases using a finer mesh ($m \times n = 72 \times 36$). This will be reported in a future paper.

Messrs. Cole and Kerr's reduction of Mr. Ausman's results

for infinitely wide bearing [reference (8)] appears to be in error. It should read

$$S = \frac{\frac{1}{6\pi^2}\sqrt{1+\left(\frac{S}{k}\right)^2}}{\epsilon}$$

We have shown in our paper that for ambient pressures at the bearing ends, a dimensionless parameter involving the Sommerfeld number can be used. This parameter allows calculation of the compressible Reynolds equation to the same form as that employed for incompressible fluids (Equation [4] and [6]). In this process, the h^3 term is being replaced by $p\,h^3$ and the existence of pressures below atmospheric is permissible. It is further shown that equation [6] can be written in another form (equation [17]) where the effect of ambient pressures is seen. We have, therefore, clearly shown that for atmospheric pressure at the ends of the bearing the eccentricity ratio is a function of the conventional Sommerfeld number.

It is well known that compressibility raises the load carrying capacity as shown in Fig. 5. One reason for this was pointed out earlier. It is quite surprising that Messrs. Cole and Kerr question this point. Calculation of some of their own experimental results [reference (7) of their discussion] will confirm this point.

When Fig. 6 of our paper is compared with the results for laminar and super laminar speeds [reported in reference (9)] it is seen that our eccentricity locus resembles that for the turbulent condition more closely than it does that for the laminar conditions. This observation, however, should not be taken to imply that our solution is valid for turbulent conditions. It is interesting to note also, from reference (9), that the load carrying capacity obtained there is higher under turbulence than it is under laminar conditions, for an isothermal path. The compressible hydrodynamic gas bearing has also higher load carrying capacity than does the incompressible laminar condition. Since many hydrodynamic gas bearings operate at high Reynolds numbers, it is recommended that inertia effects be included in the analysis when the Reynolds number is above transition.

We were pleased by the interest expressed by Messrs. Cole, Kerr, and others, in the variation of the index n of the pressure-density relationship. We are in fact presently preparing a paper in which n is varied between 1 to 1.4 and in which the energy and Reynolds equations are solved simultaneously using a 72 × 36 grid. We expect this paper to be published within the next few months.

It was also gratifying to see that Messrs. Cole and Kerr arrived at the same results we did, in establishing design criteria for load carrying capacity of hydrodynamic gas bearings operating in atmospheric air.

The comments which we received from the various discussions were most stimulating. The interest shown in our paper has encouraged us to write the afore-mentioned second paper on hydrodynamic gas bearings, in which we will cover several of the points raised in the discussions and present additional information on this subject.

Journal of BASIC ENGINEERING

Information for Authors

• Manuscripts should be submitted in final form to the Editor. Each manuscript must be accompanied by a statement that it has not been published elsewhere nor has it been submitted for publication elsewhere. A paper which would occupy more than 8 pages of the Journal may be returned to the author for abridgment.

• The author should state his business connection, the title of his position, and his mailing address. A short abstract (50 to 100 words) should be included on the first page immediately preceding the introductory paragraph of the paper.

Three copies of the manuscript are required. One of these must be a carefully prepared printer's copy, typed in double spacing, on one side of the page only, with wide margins, on $8^1/_2$ by 11-in. opaque white paper. Mimeographed manuscripts, if prepared with exceptional care, can be accepted provided they are completely edited.

• As far as possible, all mathematical expressions should be typewritten. Greek letters and other symbols not available on the typewriter should be carefully inserted in ink. Care should be taken to distinguish between capital and lowercase letter, between zero (0) and the letter (*O*), between the numeral (1) and the letter (*l*), etc. A letter representing a vector cannot be printed with an arrow above or below it. The letter should be underscored with a single wavy line, wherever it appears in the text, to designate boldface type.

• A list of symbols carefully marked for the use of the editor (thus: κ, Greek l.c. kappa), if it has not been included in the body of the paper, should accompany the manuscript on a separate page.

• Before preparing a manuscript the author should study printed articles in the Journal, with special attention to the form and style of mathematical expressions, tables, footnotes, references, and abstract. Numbers that identify mathematical expressions should be enclosed in parentheses. Numbers that identify references at the end of the paper should be enclosed in brackets. Care should be taken to arrange all tables and mathematical expressions in such a way that they will fit into a single column when set in type. Equations that might extend beyond the width of one column (fractions that should not be broken or long expressions enclosed in parentheses) should be rephrased to go on two or more lines within column width. Fractional powers are preferred to root signs and should always be used in more elaborate formulas. The solidus should be used instead of the horizontal line for fractions wherever possible.

• A normal paper should not exceed 8 pages in the Journal. It is about 8000 words or 20 double-spaced typewritten pages exclusive of drawings. A Technical Brief should not exceed 750 words or about one page in the Journal inclusive of drawings.

• Originals and two copies of figures must accompany the manuscript. Line drawings should not be larger than $8^1/_2 \times 11$ in. and should be planned for reduction to column width. Lettering should be large enough to be clearly legible when the illustration is reduced. The originals of line drawings must be in India ink on white or pale blue tracing paper or tracing cloth. Photographs of equipment or test specimens must be glossy prints and should be used sparingly. Captions for figures should be typed double-spaced and included as the last page of the manuscript. The figure number and author's name should be written in the margin or on the back of each illustration.

• Titles of papers should be brief.

• Authors can obtain copies of the ASME Manual MS-4, "An ASME Paper," from the Editor and are urged to do so before drafting their papers in final form.

• Papers published in Journals of the Transactions of the ASME must be presented at a Meeting, either in person or by title.

• An author is entitled to 25 preprints free of charge (in the case of two authors, 15 each; three or more authors, 10 each). Larger quantities of preprints or reprints can be ordered from Editorial Department, The American Society of Mechanical Engineers, 29 West 39th Street, New York 18, N. Y. Quotations will be sent on request.

Please address all communications to:

Editor, ASME,

29 West 39th Street,

New York 18, N. Y.

ASME Publications Committee

An Excellent On-the-Job Reference for Draftsmen and Designers.

AMERICAN DRAFTING STANDARDS MANUAL

This is the most complete Standard on the subject that has been produced to date. It has been written to acquaint draftsmen with the drafting methods and practices which have been approved by literally hundreds of industries and to show them how to apply these techniques to their own work.

The Manual is being published in seventeen sections, of which the following are now available. If you are not using them, it will pay you to do so for, with their aid, mistakes can be eliminated, efficiency increased, and the best type of workmanship produced.

SIZE AND FORMAT (Section 1), Y14.1 — 1957. **$1.00**

Deals with sheet sizes, the basic format, location of title and revision blocks, positioning of lists of material and drawing numbers, and print fold. Illustrated.

LINE CONVENTIONS, SECTIONING AND LETTERING (Section 2), Y14.2 — 1957. **$1.50**

Scope: Line symbols, visible and hidden lines, section, center and dimension lines; extension lines and leaders; cutting plane lines; break and phantom lines; section lining on detail and on assembly drawings; direction and spacing of general purpose section lines; the cutting plane, full and half sections; location of sectional views; lines behind the cutting plane; broken-out, revolved, removed, offset, auxiliary, and thin sections; sections through webs, shafts, bolts, pins, foreshortened projections and rotated features; intersections in section; sizes of lettering for different purposes. Twenty-seven diagrams supplement and illustrate the text.

PROJECTIONS (Section 3), Y14.3 — 1957. **$1.50**

Covering arrangement of views for multiple view orthographic projections, this Section describes and illustrates practices in the choice and arrangement of the views; use of partial, alternate, removed and revolved views; auxiliary views; conventional breaks; and rounded and filleted intersections; developed views; descriptive geometry applications.

PICTORIAL DRAWING (Section 4), Y14.4 — 1957. **$1.50**

Here the various kinds of pictorial drawings are defined and the correct method of using them described. Axonometric, oblique, and perspective drawings are fully considered, and a number of examples presented showing the variety of positions in which the axes may be placed. Suggestions are given on the proper pictorial arrangement of sectional views, thread representation, the use of break lines, indicating fillets and rounds, unidirectional and pictorial plane dimensioning, shading, and phantom drawing.

DIMENSIONING AND NOTES (Section 5), Y14.5 — 1957. **$2.00**

Defines terms used in dimensioning drawings; illustrates how dimensions and notes should be used to specify design requirements on mechanical drawings, and includes dimensioning practices for the control and form tolerancing of geometric surfaces.

SCREW THREADS (Section 6), Y14.6 — 1957. **$1.50**

Presents the approved methods of placing screw thread data on drawings and a considerable amount of information on thread tolerances useful to draftsmen. Typical drawing notes are shown along with specific practices for dimensioning.

GEARS, SPLINES, AND SERRATIONS (Section 7), Y14.7 — 1958. **$1.50**

Although this Section is not intended to be a textbook on gear design, it does give reasons for the methods shown and specified, so that the user will have some basic understanding of the need for more detailed gear-tooth dimensioning and specifications. Also included are the delineation and specification of Splines and Serrations.

METAL STAMPINGS (Section 10), Y14.10 — 1959. **$1.50**

Sets forth practices used by small parts manufacturers in the production of metal stampings as produced on standard types of punch presses. Here too, will be found help in laying out and delineating a product which will be subjected to metal stamping processes. References to methods of fabrication, die clearances, etc., are also included, although this type of information is not specified on the production drawing.

FORGINGS (Section 9), Y14.9 — 1958. **$1.50**

This document represents the best judgment produced by years of experience in forging and will supply the needs of the draftsman who must transform a design sketch to a production drawing.

PLASTICS (Section 11), Y14.11 — 1958. **$1.50**

With the increasing applications of Plastics in industry, this Section should prove extremely useful in the drafting room. It gives recommended practices in the representation and dimensional sizes of various features which must be incorporated in drawings.

FLUID POWER DIAGRAMS (Section 17), Y14.17 — 1959. **$1.50**

Contains the procedures to be followed in the delineation of drawings which depict fluid power systems using a fluid (liquid or gas) within enclosed circuits to transmit and control power. Types covered are: Pictorial diagram which may be used for quotation and piping the installation; Cutaway diagram which is most often used for instruction purposes; Graphical diagram which may be used for quotation, piping and installation, and for analyzing circuit operation; and a Combination diagram which is used to emphasize purpose and operation of a portion of a system.

20% discount to ASME members

THE AMERICAN SOCIETY OF MECHANICAL ENGINEERS
29 W. 39th Street **New York 18, N. Y.**